# STRUCTURAL COEFFICIENT FOR HIGH POLYMER MODIFIED ASPHALT MIXES
# BE321

## JUNE 2019

## FINAL REPORT


**Principal Investigator**

Pavement Engineering & Science Program
Western Regional Superpave Center
Department of Civil & Environmental Engineering
University of Nevada
Reno, NV 89557

**Project Manager**

Rhonda K. Taylor, P.E.
State Pavement Design Engineer
Pavement Management Section

Florida Department of Transportation
605 Suwannee St. MS 32
Tallahassee, Florida 32399-0450

**Disclaimer**

The opinions, findings, and conclusions expressed in this publication are those of the authors and not necessarily those of the State of Florida Department of Transportation

# SI* (MODERN METRIC) CONVERSION FACTORS

## APPROXIMATE CONVERSIONS TO SI UNITS

| Symbol | When You Know | Multiply By | To Find | Symbol |
|---|---|---|---|---|
| | | **LENGTH** | | |
| in | inches | 25.4 | millimeters | mm |
| ft | feet | 0.305 | meters | m |
| yd | yards | 0.914 | meters | m |
| mi | miles | 1.61 | kilometers | km |
| | | **AREA** | | |
| $in^2$ | square inches | 645.2 | square millimeters | $mm^2$ |
| $ft^2$ | square feet | 0.093 | square meters | $m^2$ |
| $yd^2$ | square yard | 0.836 | square meters | $m^2$ |
| ac | acres | 0.405 | hectares | ha |
| $mi^2$ | square miles | 2.59 | square kilometers | $km^2$ |
| | | **VOLUME** | | |
| fl oz | fluid ounces | 29.57 | milliliters | mL |
| gal | gallons | 3.785 | liters | L |
| $ft^3$ | cubic feet | 0.028 | cubic meters | $m^3$ |
| $yd^3$ | cubic yards | 0.765 | cubic meters | $m^3$ |
| | | NOTE: volumes greater than 1000 L shall be shown in $m^3$ | | |
| | | **MASS** | | |
| oz | ounces | 28.35 | grams | g |
| lb | pounds | 0.454 | kilograms | kg |
| T | short tons (2000 lb) | 0.907 | megagrams (or "metric ton") | Mg (or "t") |
| | | **TEMPERATURE (exact degrees)** | | |
| °F | Fahrenheit | 5 (F-32)/9<br>or (F-32)/1.8 | Celsius | °C |
| | | **ILLUMINATION** | | |
| fc | foot-candles | 10.76 | lux | lx |
| fl | foot-Lamberts | 3.426 | $candela/m^2$ | $cd/m^2$ |
| | | **FORCE and PRESSURE or STRESS** | | |
| lbf | poundforce | 4.45 | newtons | N |
| $lbf/in^2$ | poundforce per square inch | 6.89 | kilopascals | kPa |

## APPROXIMATE CONVERSIONS FROM SI UNITS

| Symbol | When You Know | Multiply By | To Find | Symbol |
|---|---|---|---|---|
| | | **LENGTH** | | |
| mm | millimeters | 0.039 | inches | in |
| m | meters | 3.28 | feet | ft |
| m | meters | 1.09 | yards | yd |
| km | kilometers | 0.621 | miles | mi |
| | | **AREA** | | |
| $mm^2$ | square millimeters | 0.0016 | square inches | $in^2$ |
| $m^2$ | square meters | 10.764 | square feet | $ft^2$ |
| $m^2$ | square meters | 1.195 | square yards | $yd^2$ |
| ha | hectares | 2.47 | acres | ac |
| $km^2$ | square kilometers | 0.386 | square miles | $mi^2$ |
| | | **VOLUME** | | |
| mL | milliliters | 0.034 | fluid ounces | fl oz |
| L | liters | 0.264 | gallons | gal |
| $m^3$ | cubic meters | 35.314 | cubic feet | $ft^3$ |
| $m^3$ | cubic meters | 1.307 | cubic yards | $yd^3$ |
| | | **MASS** | | |
| g | grams | 0.035 | ounces | oz |
| kg | kilograms | 2.202 | pounds | lb |
| Mg (or "t") | megagrams (or "metric ton") | 1.103 | short tons (2000 lb) | T |
| | | **TEMPERATURE (exact degrees)** | | |
| °C | Celsius | 1.8C+32 | Fahrenheit | °F |
| | | **ILLUMINATION** | | |
| lx | lux | 0.0929 | foot-candles | fc |
| $cd/m^2$ | $candela/m^2$ | 0.2919 | foot-Lamberts | fl |
| | | **FORCE and PRESSURE or STRESS** | | |
| N | newtons | 0.225 | poundforce | lbf |
| kPa | kilopascals | 0.145 | poundforce per square inch | $lbf/in^2$ |

*SI is the symbol for the International System of Units. Appropriate rounding should be made to comply with Section 4 of ASTM E380.
(Revised March 2003)

# TECHNICAL REPORT DOCUMENTATION PAGE

| 1. Report No. | 2. Government Accession No. | 3. Recipient's Catalog No. |
|---|---|---|
| 4. Title and Subtitle<br>Structural Coefficient for High Polymer Modified Asphalt Mixes | | 5. Report Date<br>June 2019 |
| | | 6. Performing Organization Code |
| 7. Author(s)<br>Jhony Habbouche (ORCID: 0000-0002-6216-3134), Elie Y. Hajj (ORCID: 0000-0001-8568-6360), and Peter E. Sebaaly (ORCID: 0000-0001-9660-8552) | | 8. Performing Organization Report No.<br>WRSC-UNR-FDOT-BE321-DEL6 |
| 9. Performing Organization Name and Address<br>Pavement Engineering & Science Program<br>Department of Civil and Environmental Engineering<br>University of Nevada<br>Reno, NV 89557 | | 10. Work Unit No. |
| | | 11. Contract or Grant No.<br>BE321 |
| 12. Sponsoring Agency Name and Address<br>Florida Department of Transportation<br>605 Suwannee Street, MS 30<br>Tallahassee, FL 32399 | | 13. Type of Report and Period Covered<br>Final Report, March 2017–June 2019 |
| | | 14. Sponsoring Agency Code |
| 15. Supplementary Notes | | |


16. Abstract

This report summarizes the information and findings from this study aiming to determine the structural coefficient for high polymer (HP) asphalt concrete (AC) mixes. In this research, HP AC mixes are defined as asphalt mixtures manufactured using asphalt binders modified with Styrene-Butadiene-Styrene (SBS) at the approximate rate of 7.5% by weight of binder. The following activities and analyses were completed to achieve the overall goal of this research study:

- Reviewed and summarized current and past literatures on the performance of HP asphalt binders and AC mixes. In summary, while several previous studies highlighted the positive impact of the HP modification of asphalt binders and mixes, there was a lack of understanding of the HP AC mix structural capacity as expressed through the structural coefficient for the AASHTO 1993 guide.
- A total of eight polymer modified (PMA) and eight HP AC mixes were designed and evaluated in the laboratory for their engineering properties and performance characteristics. The 16 mixes were used in a full mechanistic analysis using the 3D-Move model. Overall, HP AC mixes showed better performance characteristics when compared with their respective PMA AC mixes. The estimated initial fatigue-based structural coefficients ranged from 0.33 to 1.32. Using advanced statistical analyses an initial fatigue-based structural coefficient for HP AC mixes of 0.54 was determined and verified for other distress modes (e.g., rutting, reflective cracking).
- The determined structural coefficient was verified using full-scale testing. Two extensively instrumented experiments were conducted in the PaveBox facility at University of Nevada; experiment No. 1 evaluated a flexible pavement with PMA AC layer and experiment No. 2 evaluated a flexible pavement with a reduced thickness of HP AC layer. In general, the reduced thickness of the HP AC layer resulted in similar vertical surface deflections except under the center of the applied surface load (higher deflections), higher vertical stresses at the middle of the base layer, and similar vertical stresses at 6 inch and 24 inch below the subgrade surface. In addition, the mechanistic analysis showed that the HP pavement will result in better fatigue and rutting performance in the AC layer, slightly higher rut depths in the unbound layers but similar total rut depths.

In general, the overall results of the laboratory evaluation, pavement modeling, and full-scale testing support the use of a structural coefficient of 0.54 for HP AC mixes in Florida. A testing plan for the Florida Department of Transportation (FDOT) Accelerated Pavement Testing (APT) has been recommended to further validate the recommended structural coefficient. The main thrust of the APT plan is to identify unique cases where additional rutting may occur in the crushed aggregate base (CAB) layer under the reduced thickness of the HP AC layer.


| 17. Key Words | 18. Distribution Statement |
|---|---|
| modified binder, performance, mechanistic analysis, full-scale pavement, instrumentation | No restrictions. |

| 19. Security Classif. (of this report) | 20. Security Classif. (of this page) | 21. No. of Pages | 22. Price |
|---|---|---|---|
| Unclassified | Unclassified | 434 | |

**Form DOT F 1700.7 (8-72)** Reproduction of completed page authorized.

## ACKNOWLEDGMENTS

The research reported herein was performed under FDOT Project BE321 (FDOT BE321) by the Pavement Engineering & Science (PES) Program and Western Regional Superpave Center (WRSC) at the University of Nevada, Reno (UNR). Dr. Peter E. Sebaaly, P.E., professor of civil engineering at UNR, was the principal investigator (PI). Dr. Elie Y. Hajj, associate professor of civil engineering at UNR, was the Co-PI and UNR–Project Manager. Mr. Jhony Habbouche is also an author of this report. Thanks are also due to Dr. Adam J.T. Hand for his help during the identification and procurement process of materials from Florida, and for his assistance in acquiring a large scale asphalt mixer. Thanks are also due to Mr. Connor Overstreet, Mr. Nicholas Peery, Mr. Christian OQuinn Jr, Mr. Sailesh Bista, Mr. Ghadi Sebaaly, Mr. Habtamu Merga, Mr. Ahmad Warrag, Mr. Andrew Myers, Mr. Marc Lattin, and Mr. Murugaiyah Piratheepan at UNR for their work in the laboratory testing and full-scale experiments.

## EXECUTIVE SUMMARY

Asphalt concrete (AC) mixtures have been used as driving surfaces for flexibles pavements since the early 1900s. With the increase of highway traffic volume and axle loads, the introduction of modified asphalt binders provided transportation agencies an effective tool to design balanced asphalt mixtures that can resist conflicting distresses such as permanent deformation and fatigue cracking while maintaining good long-term durability (i.e., reduced moisture damage and aging). While polymer-modified asphalt (PMA) mixtures, with 2-3% polymer content, have shown improved long-term performance, it is also believed that asphalt mixtures with high polymer (HP) content (i.e., >6% polymer content) may offer additional advantages in flexible pavements subjected to heavy and slow-moving traffic loads. The main objective of this study is to determine the structural coefficient for AC mixes in the state of Florida manufactured with a high polymer (HP) modified asphalt binder that contains approximately 7.5% Styrene-Butadiene-Styrene (SBS) polymer.

The study combines the following five major aspects: (1) *Literature Review*: information and findings from the literature review on the performance of HP asphalt binders and mixtures in the laboratory and in the field were collected. In addition, attempts to determine a structural capacity for HP AC mixes using available data compiled as part of the literature review were executed. (2) *Extensive laboratory evaluation of HP asphalt binders and mixtures:* aggregates from Southeast Florida (FL) and Georgia Granite (GA), RAP material from Georgia Granite (GA), and highly and conventionally polymer modified asphalt binders, PG76-22 and HP binder, were identified for the development of 16 laboratory AC mixes (i.e., eight PMA and eight HP). The designed AC mixes were evaluated in terms of engineering properties (i.e., stiffness) and performance characteristics (i.e., resistance to rutting, fatigue cracking, top-down cracking, and reflective cracking). (3) *Advanced mechanistic analysis under heavy moving loads using 3D-MOVE:* the developed properties and characteristics of PMA and HP AC mixtures were implemented in the 3D-MOVE model to determine the responses and performance of PMA and HP pavement sections under various loading conditions. Using the pavement responses from 3D-MOVE along with the performance models for the PMA and HP AC mixtures for fatigue cracking, structural coefficients of the HP modified asphalt mixtures were determined using the fixed service life approach. The determined fatigue-based coefficients were verified against other distress modes (i.e., AC and total rutting, top-down cracking, and reflective cracking). (4) *Full-scale pavement testing using PaveBox:* the 11 feet width by 11 feet depth by 7 feet height PaveBox, available at UNR facilities, served as a full-scale laboratory tool to verify the structural coefficients developed and checked previously through laboratory testing and computer modeling.

The review of available literature led to the numerous findings and recommendations:

- The reviewed laboratory studies indicated: a) Increasing the SBS polymer content from 0, 3, 6, to 7.5% continues to improve the performance properties of the asphalt binder and mixture, b) HP modification tends to slow down the oxidative aging of the asphalt binder, and c) HP asphalt binder should not be used to overcome the negative impact of RAP on the resistance of the AC mixture to various types of cracking.
- The reviewed field projects indicated: a) HP AC mixes have been used over a wide range of applications from full depth AC layer to thin AC overlays under heavy traffic, b) HP

AC mixes did not show any construction related issues, and c) while early performance is encouraging, almost all HP field projects lack long-term performance information.

- While several previous studies highlighted the positive impacts of the HP modification of asphalt binders and mixtures, there is still a serious lack of understanding on the structural value of the HP AC mix as expressed through the structural coefficient for the AASHTO 1993 Guide. The attempt by the research team to determine an $a_{HP\text{-}AC}$ based on the available information led to the conclusion that empirically-based $a_{HP\text{-}AC}$ can underestimate the structural value of the HP AC mix while determining the $a_{HP\text{-}AC}$ based on the mechanistic analysis of a single failure mode (i.e., fatigue cracking) may overestimate the structural value of the HP AC mix.

The laboratory evaluation of PMA and HP AC mixes as well as the advanced mechanistic analyses of PMA and HP flexible pavement structures led to numerous findings and recommendations summarized as follows:

- Overall, HP AC mixes showed better engineering property and performance characteristics when compared with the corresponding PMA control AC mixes which can be credited to the high polymer modification of the asphalt binder (i.e., HP binder).
- The estimated initial fatigue-based structural coefficients ranged from 0.33 to 1.32. Using advanced statistical analyses and considering all factors and their interactions, an initial fatigue-based structural coefficient of 0.54 was determined for HP AC mixes.
- The initial fatigue-based structural coefficient for HP AC mixes of 0.54 was verified for the following distresses; rutting in AC layer, shoving in AC layer, total rutting, top-down cracking, and reflective cracking. The verification process concluded that the structural coefficient of 0.54 for HP AC mixes would lead to the design of HP pavements that offer equal or better resistance to the various distresses as the designed PMA pavements with the structural coefficient of 0.44. This conclusion held valid for the design of both new and rehabilitation projects.
- Based on the data generated in the execution of the experimental plan and the analyses presented, it was recommended that HP AC mixes be incorporated into the current FDOT Flexible Pavement Design Manual with a structural coefficient of 0.54.

The structural coefficient determined for HP AC mixes through laboratory testing and pavement modeling was verified using full-scale testing. Two full-scale experiments were conducted in the PaveBox facility at UNR; experiment No. 1 evaluated a flexible pavement with PMA AC layer and experiment No. 2 evaluated a flexible pavement with HP AC layer. The design thickness of the PMA AC layer was 4.25 inch (108 mm) based on a structural coefficient of 0.44 while the design thickness of the HP AC layer was reduced to 3.50 inch (89 mm) based on the recommended structural coefficient of 0.54. Both pavements had the same crushed aggregate base (CAB) and subgrade (SG) layers. The full-scale pavements were instrumented to measure the responses to load in terms of surface deflections, tensile strains at the bottom of the AC layer, and vertical stresses in the CAB and SG layers. In addition, AC mixtures were sampled during construction and evaluated for their dynamic modulus, fatigue, and rutting characteristics. The first analysis compared the measured pavement responses from the two pavements. In general, the reduced thickness of the HP AC layer resulted in higher vertical surface deflections, higher vertical stresses at the middle of the CAB layer, similar vertical stresses at 6 inch (152 mm) and 24 inch (610 mm) below the SG surface, and similar or lower tensile strains at the bottom of the

AC layer. The second analysis compared the responses of the two pavements calculated through mechanistic modeling. The mechanistic analysis showed the HP pavement generated; better fatigue and rutting performance in the AC layer, higher rutting in the unbound layers but similar total pavement rutting.

In general, the overall results of the laboratory testing, pavement modeling, and full-scale testing using the PaveBox supported the selection of 0.54 as structural coefficient for HP AC mixes in Florida. A testing plan for the FDOT Accelerated Pavement Testing (APT) has been recommended to further validate the recommended structural coefficient for HP AC mixes. The main thrust of the APT plan is to identify unique cases where additional rutting may occur in the CAB layer under the reduced thickness of the HP AC layer.

## TABLE OF CONTENTS

## LIST OF FIGURES

## LIST OF TABLES

# CHAPTER 1. INTRODUCTION

## 1.1. BACKGROUND

Asphalt concrete (AC) mixtures have been used as driving surfaces for flexible pavements since the early 1900s. As highway traffic increased in volumes, axle loads, and tire pressures, the demand for high quality and durable AC mixtures became more critical. The flexible pavement engineering community has kept up very well with these demands through the introduction of new technologies for the manufacturing of asphalt binders and mixtures, advanced pavement testing and evaluation techniques, and new construction equipment. Typically, the resistance of AC mixtures to permanent deformation (rutting and shoving) requires stiff asphalt binder and low asphalt binder content while its resistance to cracking (fatigue, top-down, block, and thermal) requires flexible asphalt binder and higher asphalt binder content. Specifically, the introduction of modified asphalt binders provided transportation agencies additional tools to effectively design balanced asphalt mixtures that can resist these conflicting distresses while maintaining a good long-term durability (i.e., reduced moisture damage and aging).

Figure 1-1 shows typical behavior of neat, modified, and ideal asphalt binders as a function of anticipated temperatures over the life of the asphalt binder in the asphalt mixture as part of the flexible pavement structure *(1)*. The typical behavior leads to the following observations:

- A neat asphalt binder will be easier to produce and construct, however, it may experience: a) rutting under high pavement temperatures due to its softer behavior, b) fatigue cracking (bottom-up and top-down) at intermediate pavement temperatures due to its non-flexible behavior, and c) thermal cracking at low pavement temperatures due to its brittle behavior.
- A modified asphalt binder will be generally more difficult to produce and construct requiring higher temperatures, however, it may experience: a) less rutting under high pavement temperatures due to its stronger behavior, b) less fatigue cracking (bottom-up and top-down) at intermediate pavement temperatures due to its flexible behavior, and c) less thermal cracking at low pavement temperatures due to its more ductile behavior.
- An ideal asphalt binder exhibits the most desirable behaviors and offers excellent resistance to all three modes of distresses. Unfortunately, the break in the behavior curve has proven to be impossible to achieve, and therefore, the ideal binder does not currently exist.

Modified asphalt binders have been produced using a wide range of technologies to modify the properties of the neat asphalt binder in order to accommodate the project-specific load and climatic conditions. Throughout the past 50 years, asphalt binders have been modified with polymers, ground tire rubber, chemicals (e.g., acid), recycled engine oils, etc., to achieve the desired properties.

Several state department of transportation (DOT), including Florida DOT (FDOT), have recognized the benefits of polymer modified asphalt (PMA) in AC mixes in resisting multiple modes of climate and load induced distresses in flexible pavements. For the past 20 years, the Nevada DOT (NDOT) has specified PMA binders (i.e., around 3% Styrene-Butadiene-Styrene (SBS)) for all asphalt mixtures to be used in the construction and rehabilitation of the state's road

network. The PMA AC mixes are mandated throughout the entire depth of the AC layers, not just in the top lift, due to its observed benefits in resisting rutting, fatigue cracking, and thermal cracking.

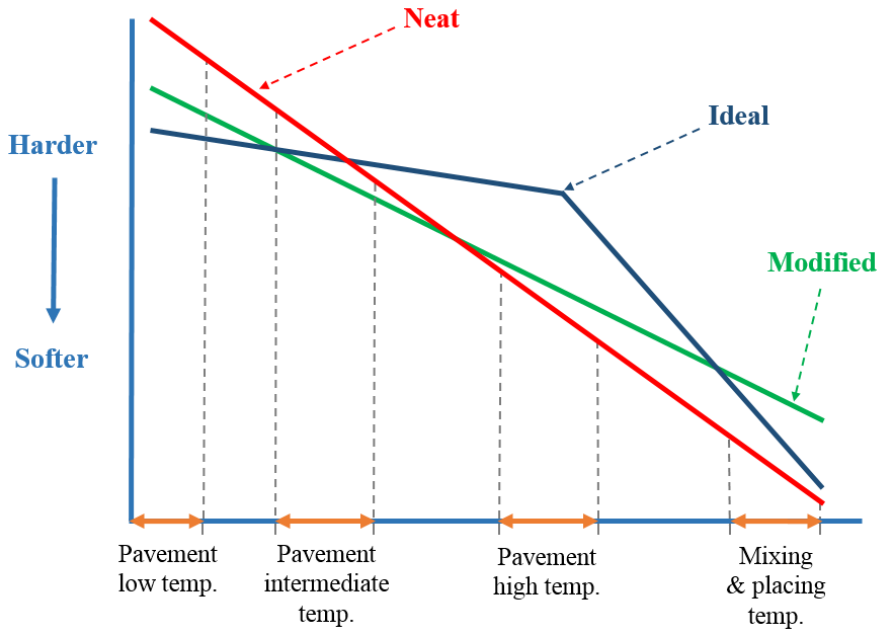


**Figure 1-1. Typical behavior of asphalt binders through pavement life.**

## 1.2. AASHTO FLEXIBLE PAVEMENT DESIGN METHODOLOGY

The American Association of State Highway and Transportation Officials (AASHTO) Guide for Design of Pavement Structures (AASHTO 1993 Guide) constitutes the primary method used by FDOT for designing new and rehabilitated highway pavements. The AASHTO 1993 Guide design method is based on information obtained at the American Association of State Highway Officials (AASHO) Road Test, which was performed from 1958 to 1960 near Ottawa, Illinois. The road test was composed of six two-lane test loops, four large loops and two small ones, subjected to truck traffic. The main objective of the road test was to determine the effect of different axle loadings (i.e., configuration and load) on the performance and behavior of pavements. The loaded trucks were mounted with bias-ply tires with inflation pressure of 70 psi (483 kPa). No super single tires, triple, or quad axles were utilized. The road test was only subjected to a maximum of 2 million equivalent single axle loads (ESALs) *(2)*.

The primary objective of the AASHO Road Test was to assess and evaluate the pavement deterioration induced by traffic loads. The first pavement design guide, known as AASHO Interim Guide for the Design of Rigid and Flexible Pavements was developed using the AASHO Road Test results. Many versions were subsequently released including the AASHTO 1993 Guide which is still used today by many transportation agencies including FDOT. The overall approach of the AASHTO 1993 Guide is to design, both flexible and rigid pavements, for a specified serviceability loss at the end of the design life of the pavement. In the AASHTO design methodology, Equation 1-1 or the monograph presented in Figure 1-2 are used to design flexible pavements *(2)(3)*.

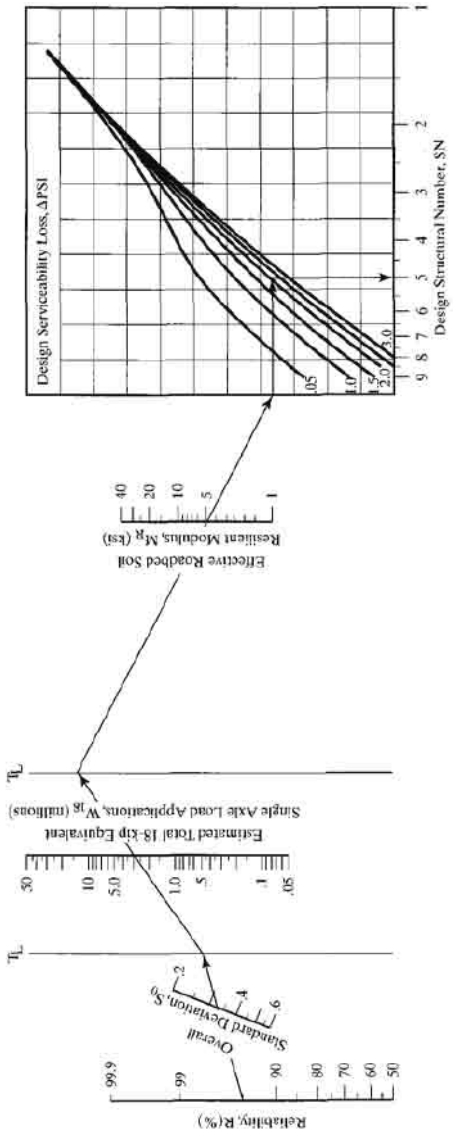


**Figure 1-2. AASHTO 1993 Nomograph for designing flexible pavements** *(2)***.**

$$logW_{18} = Z_R S_0 + 9.36 * \log(SN+1) - 0.20 + \frac{\log\left[\frac{\Delta PSI}{4.2-1.5}\right]}{0.4+\frac{1094}{(SN+1)^{5.19}}} + 2.32 * logM_R - 8.07 \quad \textbf{Equation 1-1}$$

Where;
$W_{18}$: applied traffic in terms of number of EASLs;
$M_R$: resilient modulus of the layer being protected, psi;
$Z_R$: normal deviations associated with the design reliability R and variability $S_0$;
$\Delta PSI$: loss in present serviceability index; and
$SN$: structural number required to protect a given layer with the $M_R$.

The desired level of design reliability increases with the increase in design traffic. According to AASHTO 1993 Guide, an 85% reliability may be selected for a low volume road (defined as less than 500 ESALs per day) while a 95% reliability or higher is suggested for a medium volume

road (subjected to a traffic between 500 and 1750 ESALs per day) or a high volume road (subjected to a traffic greater than 1750 ESALs per day). For flexible pavement, the standard deviation *($S_0$)* is typically assumed to be 0.49. The standard normal deviate *($Z_R$)* is calculated as the difference between the current traffic *($logW_{18}$)* and the traffic to reach the terminal present serviceability index (PSI) labeled as $p_t$ over the standard deviation *($S_0$)*. In addition, the subgrade effective resilient modulus *($M_R$)* is used to account for seasonal changes and effects *(2), (3)*.

The AASHTO 1993 Guide method uses the PSI to represent the performance of the pavement defined as a subjective measure of the ride quality by the road user. The PSI varies between an upper and lower limit of 5 and 0 representing the best and worst pavement conditions, respectively. The serviceability loss *($\Delta PSI$)* at the end of the design life is specified; representing the difference between the initial serviceability *($p_i$)* of the pavement when opened to traffic and the terminal serviceability *($p_t$)* that the pavement is expected to reach before rehabilitation, resurfacing, or reconstruction is required.

The empirical relationship among design traffic, pavement structure, and pavement performance for flexible pavements is solved to determine the required structural capacity of the pavement section, known as the structural number *(SN)*. The total pavement *SN* is defined as the summation of the layer thicknesses times the corresponding structural layers and drainage coefficients as expressed in Equation 1-2.

$$SN = \sum_{i=1} a_i D_i m_i \qquad \textbf{Equation 1-2}$$

Where;
*SN*: total structural number required for design traffic;
$a_i$: structural coefficient for the $i^{th}$ layer;
$D_i$: thickness of the $i^{th}$ layer, inch; and
$m_i$: drainage coefficient for the $i^{th}$ layer except the AC layer.

No direct method exists for establishing new structural coefficients as new AC mixtures are created. The current structural coefficients were estimated based on many factors including material stiffness, and compressive and/or tensile strength. Figure 1-3 shows a chart used to estimate the structural coefficient of dense-graded AC surface course based on its elastic (resilient) modulus *($E_{AC}$)* at a temperature of 68°F (20°C) in accordance with the AASHTO 1993 Guide. These coefficients were determined based on limited parameters used in the AASHO road test where a single type subgrade soil, gravel base, and AC mix were considered. Furthermore, no advanced paving materials including Superpave-designed AC mixes and polymer modified AC mixes were used.

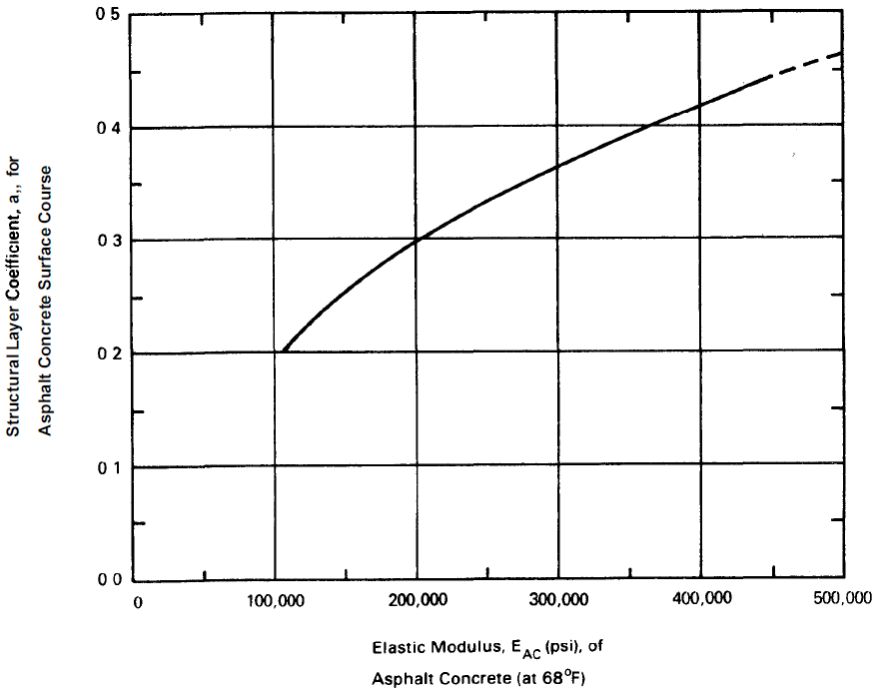


**Figure 1-3. Chart estimating structural coefficient of dense-graded asphalt concrete based on the elastic (resilient) modulus after AASTHO 1993** *(2)***.**

## 1.3. FDOT PAVEMENT DESIGN PRACTICE

FDOT recently updated and published a manual for designing flexible pavements in Florida (September 2016) *(4)*. This manual provides guidance for conducting new and rehabilitated flexible pavement designs according to the AASHTO 1993 Guide. Additional information regarding materials testing and obtaining traffic data are provided. It should be mentioned that FDOT has not yet adopted the 2008 AASHTO Mechanistic-Empirical (M-E) Pavement Design Guide (MEPDG) for flexible pavement design which was developed as part of the National Cooperative Highway Research Program (NCHRP Project 1-37A) *(5)*. The existence of several major revisions to the models used in the AASHTOWare® Pavement M-E software has been cited as the reason for non-adoption by Florida DOT *(3)*.

## 1.4. PROBLEM STATEMENT AND OBJECTIVES

Based on previous experience, a structural coefficient of 0.44 was found to be well representative of PMA AC mixes in Florida when designed in a pavement section following the AASHTO 1993 Guide. In some states, this coefficient was recalibrated to account for the conventional polymer modification of asphalt mixtures (2-3% polymer). For example, in Alabama, the resulting average AC structural coefficient was 0.54 with a standard deviation of 0.08 leading to approximate reduction in the thickness of the AC layer of 18% based on a study conducted by the National Center for Asphalt Technology (NCAT) in 2009 *(3)*. If the positive impact of the polymer on the layer is assumed to be maintained at higher contents, then the use of a high polymer (HP) modified asphalt binder may lead to a higher AC structural coefficient and a reduced AC layer thickness for the same design traffic and serviceability design loss *(3)*.

Consequently, the objective of this FDOT research study is to determine the structural coefficient for asphalt mixes that contain a HP modified binder. With this determination, the FDOT Flexible Pavement Design Manual may be modified to adopt the structural value for mixtures containing this binder type. For this purpose, the major tasks to be carried out in this research are:

- Conduct an extensive review of literature by compiling information about HP AC mixes, their evaluation in the laboratory, their implementation on actual existing demonstration field projects, and their performance all around the United States, Central America, and Europe.
- Establish mix designs for PMA and HP AC mixes following the FDOT Superpave mix design specifications using representative local materials from multiple sources in the state of Florida.
- Evaluate the engineering properties and performance characteristics of the designed PMA and HP AC mixes, and implement the developed properties and characteristics into an advanced flexible pavement modeling process to determine the responses and performance under various structural and loading conditions. This task will lead to preliminary structural coefficients for HP AC mixes.
- Verify the structural coefficients assigned to the HP modified asphalt mixtures, developed and checked in the previous tasks for various type of distresses using a full-scale laboratory testing of asphalt pavement structures (e.g., PaveBox).
- Develop a practical plan to validate the recommended structural coefficient for HP AC mixes under the FDOT Accelerated Pavement Testing (APT) facility.

## 1.5. ORGANIZATION OF REPORT

In this research, HP AC mixes are defined as asphalt mixtures manufactured using asphalt binders modified with SBS or Styrene-Butadiene (SB) at the approximate rate of 7.5% by weight of binder. PMA AC mixes are defined as asphalt mixtures manufactured using asphalt binders modified with SBS or SB at the approximate rate of 3% by weight of binder. Both asphalt binders (i.e., PMA and HP) must meet the corresponding FDOT Specifications 2018 mandated in Section 916. This document constitutes the final report and presents the outcome of the FDOT comprehensive research study (Grant BE321). This document is divided into multiple chapters that address various key aspect of this study:

- ***Review of Literature:*** Chapter 2 addresses the key aspects of HP modified asphalt mixes and their performance in the laboratory and on existing field projects. A general background on PMA asphalt binders and mixes evaluated in the laboratory is provided. Information on actual demonstration field projects with limited and extensive performance data accomplished using HP AC mixes are also presented. In addition, a preliminary analysis of structural coefficient for mixes manufactured using HP asphalt binders is provided.
- ***Experimental Design and Test Description:*** Chapter 3 presents the experimental design for the development of structural coefficient for HP AC mixes. In addition, this chapter provides detailed information related to the raw materials used in this study and a detailed description for each performance test conducted for the purpose of the project completion.

- ***Mix Designs and Test Results:*** Chapter 4 presents in detail the mix designs developed in the laboratory. In addition, it provides the analysis of all test results generated from the performance evaluation of the laboratory AC mixes.
- ***Flexible Pavement Modeling:*** Chapter 5 describes the overall approach implemented in the mechanistic analysis procedure for flexible pavement modeling. The objective of this part of the study is to incorporate the measured engineering property and performance characteristics of the evaluated PMA and HP AC mixes into the mechanistic modeling of flexible pavement responses to traffic loads.
- ***Determination of Structural Coefficient for HP AC Mixes:*** Chapter 6 presents the efforts to determine the critical responses of the designed pavement structures for the identified distresses of AC pavements including; fatigue cracking, AC rutting, total rutting, top-down cracking, and reflective cracking using the 3D-Move model, and to determine the structural coefficient for HP AC mixes. First, the determined critical responses are used to estimate the fatigue performance life of the designed pavement structures followed by the development of the initial structural coefficient for HP AC mixes based on the equal fatigue performance life approach. Finally, the fatigue-based initial structural coefficients are verified for the other modes of distress.
- ***Verification of Structural Coefficient for HP AC Mixes using Full-Scale Pavement Testing:*** Chapter 7 presents in detail the effort to verify the structural coefficient determined through laboratory testing and computer modeling in two instrumented full-scale asphalt pavements subjected to stationary dynamic loadings.
- ***Summary of Findings, Conclusions, and Development of Recommendations: APT Implementation Plan:*** Final conclusions and recommendations based on the literature review, laboratory testing and evaluation, advanced mechanistic modeling, and full-scale testing are provided in Chapter 8. In addition, an implementation plan of the final recommended structural coefficient for HP AC mixes using the APT setup at FDOT facilities is provided in this chapter.

# CHAPTER 2. REVIEW OF LITERATURE

Polymer modification of asphalt binders is not a new concept and has become progressively more common over the past several decades. While several agencies utilize unmodified asphalt binders, many have increasingly become reliant upon polymer modified asphalt binders with a fair portion of those located in climatic regions that experience significantly wider temperature range conditions and higher levels of oxidation. Therefore, it is becoming ever more important to characterize the benefits afforded with the polymer modification process. This chapter constitutes a critical state-of-the-art review of HP asphalt binders and mixtures evaluated in the laboratory and field. It summarizes the information and findings from the literature review on the performance of HP asphalt binders and mixtures. Two major objectives were targeted in this review: (a) identify all current and previous studies that have been conducted to evaluate the engineering properties and performance characteristics of HP asphalt binders and HP AC mixes and (b) determine a preliminary structural coefficient of HP AC mixes for use in the structural design of flexible pavements *(6)*.

The literature presented in this chapter focused on three major areas of interest: (a) laboratory evaluation of HP modified asphalt binders and mixtures, (b) performance of pavement sections constructed with HP AC mixes, and (c) techniques to determine the structural coefficient of HP AC mixes. In addition, it documents studies that evaluated asphalt binders and mixtures that were manufactured at multiple levels of modification but do not fit the HP category as defined in this research. These studies were incorporated in the review only in cases where they include the properties of the control materials since they offer insights on the impact of the incremental increase in the polymer content on the properties of asphalt binders and mixtures *(6)*.

## 2.1. LABORATORY EVALUATION OF HP MODIFIED ASPHALT BINDERS AND MIXES

The objectives of this section are: a) present an overall background on the history of asphalt binder modification using polymers and b) provide some detailed information about recent laboratory studies that evaluated the performance of HP asphalt binders and mixtures. More detailed information about the laboratory evaluation of HP modified asphalt binders and mixes are provided in Appendix A.

### 2.1.1. History of Polymer Modified Asphalt Binders

The increase in traffic volume and axle loads coupled with reduced budgets of public agencies required better performance from the designed pavement structure. The modification of asphalt binders was identified as a suitable solution to provide the improved performance *(7)*. The processes providing the modification of asphalt binders using natural and synthetic polymers were patented as early as 1843 in Europe *(8), (9)*. The significantly higher costs of the early polymer modified asphalt binders limited their use in the United States (US) till mid-1980s when newer and less expensive polymers were developed *(10)*. A survey conducted in 1997, indicated that 47 out of 50 states allowed the use of modified asphalt binders and some DOTs (35 out of 47) confirmed that their use is quickly increasing *(11)*. At that time, many research teams around

the world focused on evaluating the benefits to pavement performance attributed to the use of polymer modified asphalt binders. A study done for Ohio DOT (OHDOT) showed that AC mixtures manufactured using modified asphalt binders performed much better in terms of resistance to fatigue cracking and permanent deformation when compared with mixtures manufactured using neat asphalt binders *(12)*. A significantly higher viscosity was observed for modified asphalt binders at 140°F (60°C) in accordance with a study done in Nevada in 2003 *(13)*. In a 2003 study discussing the concept of hot mix asphalt (HMA) perpetual pavements, Newcomb claimed the benefit of using a modified asphalt mixture in the bottom lift of the AC layer in increasing the fatigue life of the pavement structure *(14)*. Consequently, agencies estimated an addition of four to six years of pavement service life when constructed using a modified asphalt binder.

A 2003 study by the US Army Corps of Engineers showed that the type of modifier may affect the performance of the asphalt binder in resisting multiple distresses such as rutting, fatigue, thermal cracking, and moisture damage *(15)*. In comparison to neat asphalt binders, modifiers typically invoke specific enhancements to the physical properties and rheological performance of asphalt binders, such as improving the ductility, expanding the relaxation spectra, and increasing its overall strength. For example, ductility and resistance to rutting can be improved by the use of natural rubber in asphalt binder despite its problems with compatibility and decomposition *(16)*. The use of tire rubber improved the resistance to rutting and reflective cracking but still required high mixing temperatures and long digestion times to prevent the separation of the modified asphalt binder *(16)*. Meanwhile, the addition of Styrene-Butadiene-Rubber (SBR) modifier to asphalt binders helped in improving the low-temperature ductility, elastic recovering as well as the cohesive and adhesive properties of the binder *(16)*. Within the past 20 years, the SBS modifier replaced the SBR because of its wider compatibility and greater tensile strength property *(17)*. In general, improvement in asphalt binder ductility in conjunction with the improved elastic behavior due to polymer modification can have a positive influence on the cracking resistance of asphalt mixtures. Previous studies have shown the capability of polymer modifiers to lessen the deteriorative oxidative age hardening effects *(18)*. Accordingly, more durable asphalt pavements can be expected from the use of polymer modified AC mixtures.

Currently, SBS is a well-recognized elastomer which is commonly used in asphalt mixtures due to its elasticity and ability to be recycled. Asphalt binders modified with SBS polymers have shown improved performance at low temperatures when compared to un-modified binders and binders modified with chemically reactive polymers (e.g., Polyphosphoric Acid…). In 2003, Mohammed et al. evaluated the possibility of recycling SBS modified asphalt mixtures as part of the pavement rehabilitation process *(19)*. Cores were sampled from US 61 in Louisiana and the eight-year-old SBS modified binder was extracted and recovered. The recovered polymer modified asphalt binder was blended with virgin binder and evaluated at different temperatures. The blend was found to be much stiffer than anticipated at both low and high temperatures with a higher rutting resistance and a lower fatigue resistance. A 2004 FDOT study showed the use of SBS polymer in asphalt binder was able to reduce the rate of micro-damage accumulation and therefore benefited cracking resistance *(18)*. However, it was found that there is no effect for using SBS on healing or aging characteristics of the asphalt mixture.

The most commonly used polymer modified asphalt binders limit the SBS content to around 3% due to cost and construction issues. Recent studies showed that these issues can be overcome by modifying the conventional structure of the SBS polymer to produce a modified asphalt binder with increased durability and reduced costs. In 2010, researchers at Delft University developed a new SBS polymer structure that allowed the use of SBS at levels of 7 – 8% by weight of asphalt binder *(20)*.

Figure 2-1 illustrates a typical polymer modified asphalt binder with 2.5% polymer where the polymer is not in continuous phase *(21)*. Increasing the polymer content up to 7.5% changes the structure from asphalt binder with a dispersed swollen polymer phase to a swollen polymer with a dispersed asphalt binder phase. At this stage, the HP asphalt binder is more like an asphalt-modified rubber rather than a rubber-modified asphalt where the rubber makes the continuous phase in the structure. The phase reversal achieved by the addition of high polymer content produces a more elastic asphalt binder with improved resistance to permanent deformations (i.e., rutting and shoving) and cracking (i.e., fatigue, thermal, and reflective).

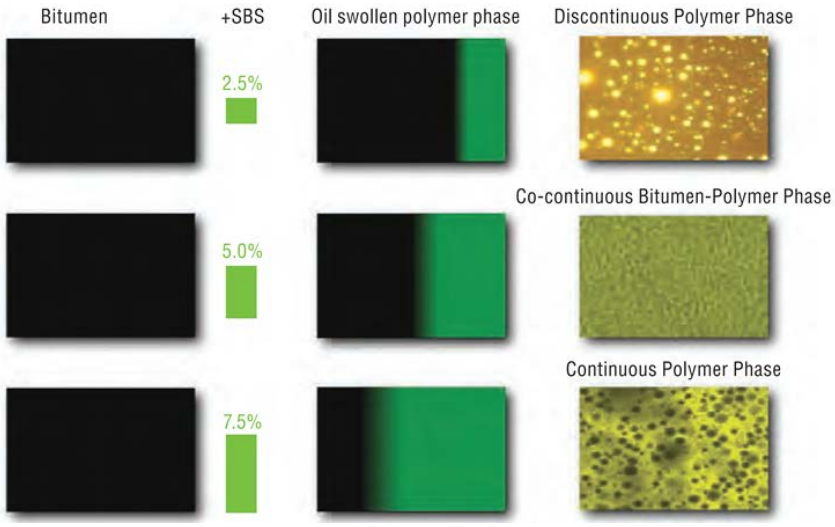


**Figure 2-1. Effect of increasing SBS polymer content on asphalt binder/polymer morphology *(21)*.**

### 2.1.2. Laboratory Evaluation of Polymer Modified Asphalt Binders and Mixtures in Florida

In 2001, FDOT conducted a study to evaluate the effect of increasing the polymer content of asphalt binders in terms of resistance to rutting distress *(22)*. Three asphalt binders meeting the current FDOT specifications (FDOT specifications, 2018) *(23)* were evaluated in this study: a PG67-22 neat binder, a PG76-22PMA binder at 3% SBS content, and a PG82-22PMA binder at 6% SBS content. All asphalt binders were collected at the plant and laboratory tests such as dynamic shear rheometer (DSR) *(24)*, multiple stress creep recovery (MSCR) *(25) (26)*, and binder fracture energy *(27)* were conducted for analysis and characterisation *(22)*. In addition, AC mixtures were designed with 0.5-inch (12.5 mm) nominal maximum aggregate size (NMAS) fine gradation using granite aggregate and the three asphalt binders previously defined. The

cracking resistance of the mixtures was evaluated using the Superpave indirect tension test (IDT) *(28)*. Finally, similar AC mixes were evaluated in terms of resistance to rutting and fatigue cracking via accelerated loading performed using the FDOT Heavy Vehicle Simulator (HVS) through measuring the actual rut depth developed in the wheel path and the actual tensile strains at the bottom of the AC layer, respectively.

On one hand, the DSR results showed that the PG82-22PMA binder exhibited the greatest stiffness, elasticity and rutting resistance, as shown by its high $G^*$, low $\delta$, and high $G^*/sin(\delta)$, respectively (Refer to Figure 2-2). On the other hand, the MSCR test results indicate that the two PMA binders exhibit greater viscoelastic behavior than the neat binder shown by the higher recovery and lower non-recoverable creep compliance values accompanied with a lower sensitivity to the stress level (Refer to Figure 2-3). Meanwhile, a greater fracture energy was observed for the PG82-22PMA when compared with the PG76-22PMA and PG67-22 binders indicating a better fracture resistance for AC mixes manufactured with the PG82-22PMA binder. The IDT test results showed minor difference between the measured fracture energy values between the PG82-22 PMA and PG76-22PMA AC mix; however, a 66% reduction in the creep rate was observed for the PG82-22PMA AC mix as compared to the PG76-22PMA AC mix (Refer to Figure 2-4).

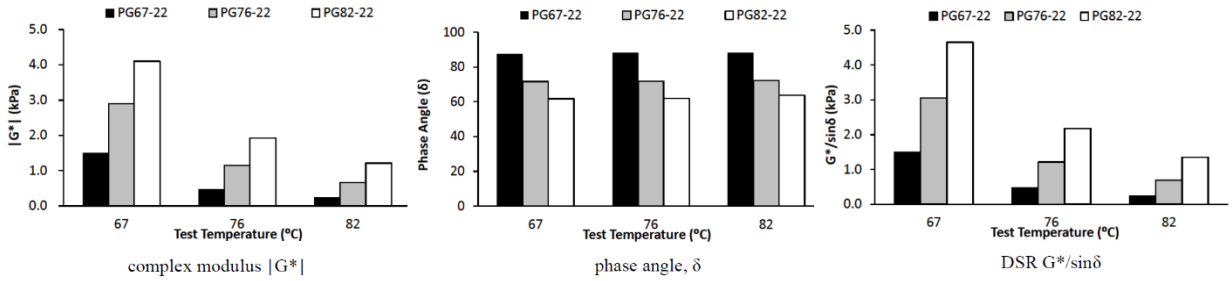


**Figure 2-2. DSR properties of PG67-22, PG76-22PMA, and PG82-22PMA binders *(22)*.**

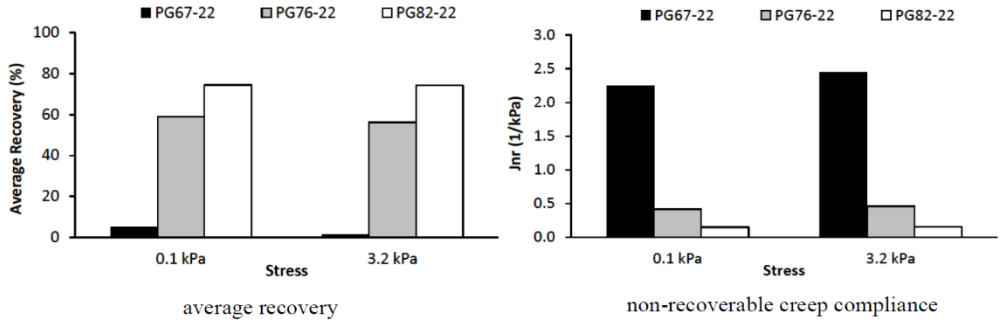


**Figure 2-3. MSCR test results at 64°C (147°F) for PG67-22, PG76-22PMA, and PG82-22PMA binders *(22)*.**

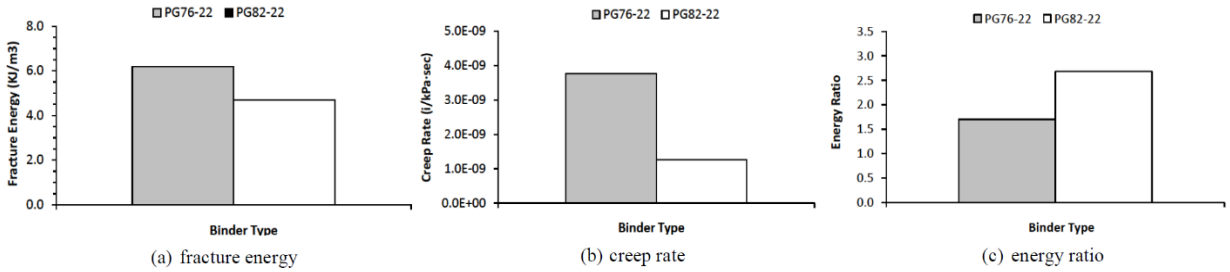


**Figure 2-4. IDT fracture properties for PG76-22PMA and PG82-22PMA asphalt mixtures *(22)*.**

The accelerated loading was performed using the FDOT HVS, electrically powered, mobile, and fully automated. The overall experiment evaluated the rutting and fatigue performance of the different mixtures. The APT pavement structures are illustrated in Figure 2-5. The HVS rutting performance showed that both polymer modified mixtures (i.e. PG76-22PMA and PG82-22PMA) significantly out-performed the neat mix (i.e. PG67-22) showing a rut depth reduction of 29% and 49% after 100,000 passes, respectively. Meanwhile, the PG82-22PMA AC mix performed significantly better than the PG76-22PMA in both measured rut depth (reduction of 28%) and shear area (reduction of 40%) (Refer to Figure 2-6). Additionally, the HVS fatigue performance showed significant reductions in measured tensile strains at the bottom of AC layer for the two PMA AC mixes with the percent reduction increasing with the higher polymer content (i.e. PG82-22PMA) *(22)* (Refer to Table 2-1).

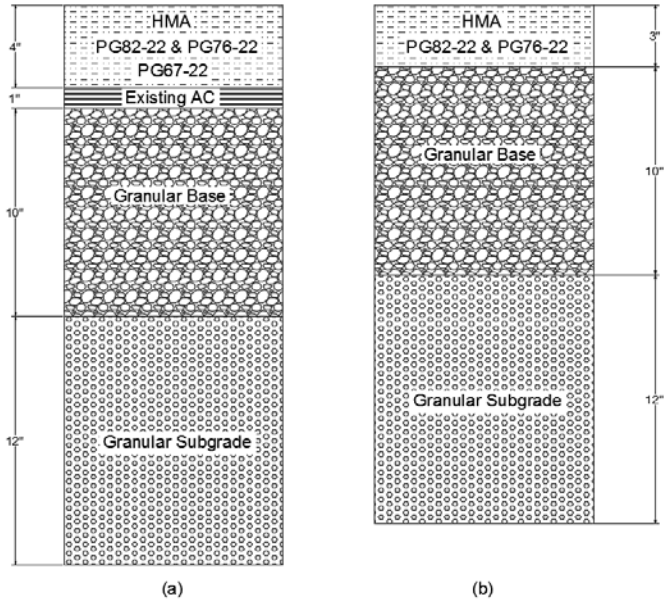


**Figure 2-5. APT pavement structures for evaluating: (a) rutting and (b) fatigue.**

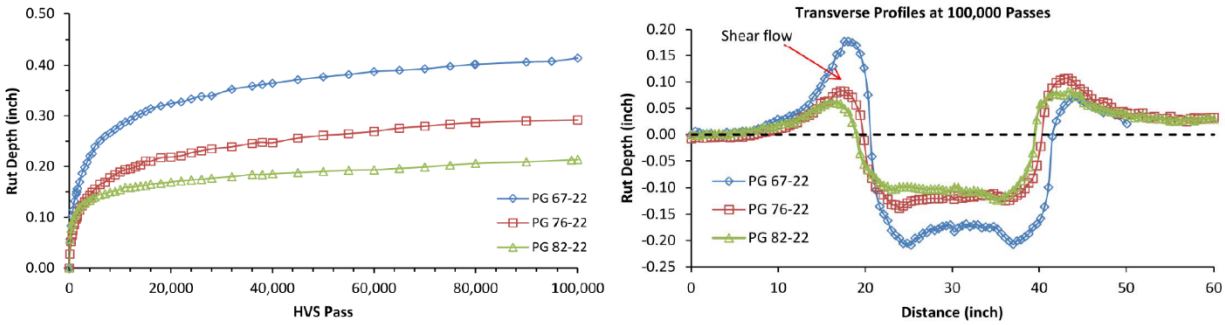


**Figure 2-6. APT rutting test results: (a) rut depth progression and (b) Transverse profiles after 100,000 passes *(22)*.**

**Table 2-1. Summary of the Rutting Performance of the APT Section *(22)*.**

| Pass Number | PG67-22 | | PG76-22PMA | | PG82-22PMA | |
|---|---|---|---|---|---|---|
| | Rut, inch (mm) | Shear Area/ WP Area | Rut, inch (mm) | Shear Area/ WP Area | Rut, inch (mm) | Shear Area/ WP Area |
| 100 | 0.06 (1.52) | 0.21 | 0.03 (0.76) | 0.44 | 0.06 (1.52) | 0.23 |
| 5,000 | 0.24 (6.10) | 0.60 | 0.16 (4.06) | 0.50 | 0.14 (3.56) | 0.28 |
| 10,000 | 0.28 (7.11) | 0.63 | 0.19 (4.83) | 0.52 | 0.15 (3.81) | 0.20 |
| 20,000 | 0.32 (8.13) | 0.61 | 0.22 (5.59) | 0.49 | 0.17 (4.32) | 0.30 |
| 100,000 | 0.41 (10.41) | 0.72 | 0.29 (7.37) | 0.45 | 0.21 (5.34) | 0.27 |

### 2.1.3. Effect of Long-Term Aging on HP Modified Asphalt Binders

In addition to improving the resistance of the AC mixtures to rutting and cracking, the high polymer content may improve the resistance of the asphalt binder to long-term aging. An asphalt binder with low susceptibility to long-term aging would significantly reduce the potential of the asphalt mixture to all types of cracking: bottom-up fatigue, top-down fatigue, thermal, reflective, and block. This phenomenon was evaluated in a recent research study by the Pavement Engineering and Science (PES) Program at University of Nevada, Reno (UNR) where the long-term aging susceptibility of three asphalt binders: neat, polymer modified with 3% SBS (PMA), and high polymer modified with 7.5% SBS (HP) were evaluated *(7)*. The main objective of the study was to observe and quantify the influence of binder modification on the oxidative aging characteristics of asphalt binders.

The evaluated asphalt binders were aged at different temperatures (i.e. 50°C, 60°C and 85°C) and for different durations (e.g. 0.5, 1, 15, 25, 60, 180 and 240 days) to measure the aging kinetics as a function of time and temperature. The aged binders were rheologically evaluated in

the DSR by determining the dynamic shear modulus ($G^*$) and phase angle ($\delta$) master curves. Figure **2-7** shows the measured properties of the aged asphalt binders using the Glover- Row parameter ($G$-$R$) at a temperature of 15°C and a frequency of 0.005 rad/s. Each data point plotted in this figure represents a specific asphalt binder condition in terms of temperature and time (i.e. combinations defined earlier). It is anticipated that lower $G^*$ and lower $\delta$ represent lower susceptibility to long-term aging. In addition, a steeper slope between $G^*$ and $\delta$ represents lower susceptibility to long-term aging. In other words, a steep curve located closer to the left side of the chart indicates lower susceptibility to long-term aging.

The data presented in Figure 2-7 *(7)* show that the HP asphalt binder is the least susceptible to long-term aging, followed by the PMA binder, while the neat asphalt binder is the most susceptible to long-term aging. Furthermore, the data show that the neat asphalt binder was the first binder to reach the $G$-$R$ cracking criterion of 87 psi (600 kPa) after about 170 days of oven aging while the PMA and HP asphalt binders lasted for about 190 and 230 days before reaching the same failure criterion.

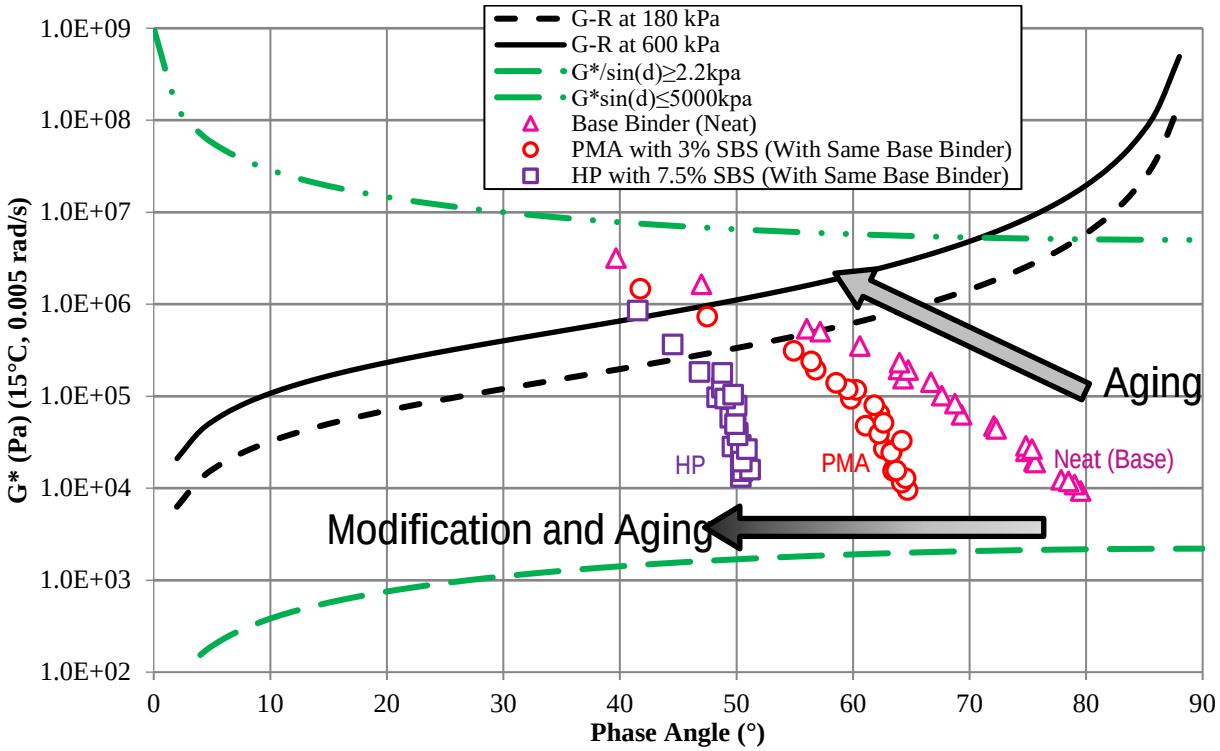


**Figure 2-7. Comparison of Glover-Rowe *(G-R)* parameters for neat, PMA, and HP asphalt binders in a black space diagram.**

### 2.1.4. Laboratory Evaluation of HP Binders in Poland: ORBITON HiMA

Researchers at ORLEN Asfalt in Poland hypothesized that a crack can pass through a conventionally modified asphalt binder by finding weak spots between the polymer network sections. Meanwhile, the crack passage through a highly modified asphalt binder is more difficult because of the barrier formed by the polymer network as depicted in Figure **2-8** *(29)*.

Limiting crack propagation in asphalt mixtures remains a clear example illustrating the benefits of a continuous polymer network acting in the asphalt binder and mixtures as an elastic reinforcement.

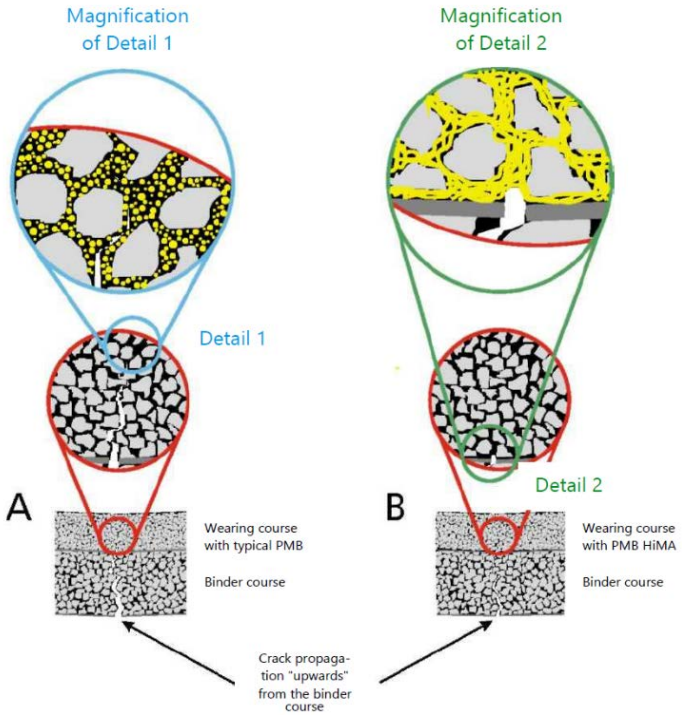


**Figure 2-8. Crack propagation illustration through: (a) conventional PMA mixes, and (b) HP mixes *(29)*.**

In 2011, three new HP asphalt binders were developed by these researchers: (a) ORBITON 25/55-80 HiMA designated to be used for typical asphalt base courses of long-life pavements (i.e. perpetual) with slow traffic, (b) ORBITON 45/80-80 HiMA designated to be used for wearing and binder courses of pavements subjected to very heavy loads and/or low temperatures and (c) ORBITON 65/105-80 HiMA designed to be used for special technologies such as stress absorbing membrane interlayers (SAMI), and emulsion applications in slurry seals *(29)*. All three binders were modified with 7.5% SBS by weight of the binder. The properties of the three HP binders and AC mixes were evaluated in the laboratory at the low temperature using the bending beam rheometer (BBR) test by measuring the stiffness and coefficient of relaxation after 60 seconds (i.e. $S(60)$, and $m$) static load simulating the slow rate of thermal stresses *(30)*, and thermal stress restrained specimen test (TSRST) by measuring the fracture strength and fracture temperature *(31)*, respectively. Additionally, the HP binders were evaluated at the intermediate temperature using the DSR test (i.e., $G^*\sin\delta$) *(24)*. For the high temperature, the HP binders and AC mixes were evaluated using the DSR *(24)* and MSCR *(25)* tests, and the wheel tracker rutting test, respectively.

For the low temperature evaluation, the measured $S(60)$ and $m$-value properties of the evaluated binders show that the BBR critical low temperature continues to decrease as the SBS content

increases from 0%, 3%, to 7.5% except for the third HP binder designed for use in SAMI and slurry seals. In addition, the TSRST fracture temperature of the evaluated AC mixes continues to decrease as the SBS content increases from 0%, 3%, to 7.5%. These results clearly show the benefits of using HP binders towards improving the resistance of AC mixes to thermal cracking. Meanwhile, for the intermediate temperature, the measured $G^*sin(\delta)$ properties of the evaluated asphalt binders show that the DSR critical intermediate temperature continues to decrease as the SBS content increases from 0%, 3%, to 7.5%. These results clearly show the increases resistance of the HP binders to fatigue cracking. At the end for the high temperature, the MSCR data showed increased rutting resistance of the evaluated binders as the SBS content increases from 0%, 3%, to 7.5% *(29)*.

### 2.1.5. Evaluation of Thin Overlay Mixes using HP Asphalt Binders

Over the last 35 years, the focus of state DOTs changed from the construction of new roads to maintenance and rehabilitation of existing infrastructure by using several pavement preservation techniques. These techniques are defined as a set of cost-effective practices designed to extend pavement life, improve safety, and save public funds. Thin asphalt concrete overlay (thickness ≤ 1.5 inch (38 mm)) is considered a preservation treatment for AC pavements. State DOTs in the Northeast Pavement Preservation Partnership (NEPPP), the Pennsylvania Asphalt Pavement Association (PAPA), academia, and industry, developed a pilot specification for high-performance thin overlay (HiPO) mixtures manufactured using HP asphalt binders and reclaimed asphalt pavement (RAP). HiPO was intended as a mean to extend the available funds for pavement preservation and for essentially delaying the future need for pavement rehabilitation. Several distresses and issues that shorten the service life of conventional overlays such as reflective cracking, thermal cracking, fatigue cracking and rutting were addressed while developing the HiPO mixtures specifications AASHTO Transportation System Preservation Technical Services Program (TSP2) *(32)*. Following the publication of the HiPO Specifications *(32)*, the New Hampshire (NH), Vermont (VT) and Minnesota (MN) DOTs showed interest in using this specification for demonstration field projects. The main interest in the HiPO specification is that it allows the use of RAP up to 25% by dry weight of aggregate and an HP asphalt binder with 7.5% of SBS polymer, graded as PG76-34 or PG82-28 *(33)*. The experimental plan included work to develop a Superpave mix design with an NMAS of 3/8-inch (9.5 mm) based on input from interested DOTs following the pilot specification. The evaluations included performance tests to evaluate the plant-produced mixtures collected from the field projects in terms of resistance to reflective *(34)*, thermal *(31)* and fatigue cracking *(35)* as well as rutting *(36)*. Additional tests, not mandated as part of the specifications, were conducted such as Hamburg wheel tracking device (HWTD) for further rutting evaluation as well as the semi-circular bending (SCB) test for further evaluation of resistance to cracking.

All evaluated mixtures exhibited an average overlay test (OT) cycles to failure greater than the minimum required 300 cycles. However, the Vermont with RAP mix did not exhibit cycles to failure within ± 10% of the number of cycles exhibited by the corresponding mix without RAP indicating the need of assessing the applicability of using 24% RAP without changing the grade of the binder. For the thermal cracking properties, the addition of RAP decreased the thermal cracking resistance of the VT mixture as presented by the warmer thermal fracture temperature. In parallel, the results for the fatigue cracking showed that the two mixtures with RAP (NH and

VT) showed a similar number of cycles to failure which is significantly lower of the number of cycles to failure for the VT mixture with no RAP. At the end, the APA rutting data showed that the NH with RAP mixture did not meet the APA rutting criterion in the pilot specification of minimum 0.16 inch (4.0 mm) after 8000 loading cycles. Both VT mixtures with and no RAP met the APA rutting criterion *(33)*.

### 2.1.6. New Hampshire DOT Highways: 2011 Auburn-Candia Resurfacing

In 2011, FHWA awarded the New Hampshire DOT (NHDOT) a $2 million grant for new technologies as part of resurfacing NH Route 101 from Auburn to Candia. The evaluation of HP and neat AC mixes were incorporated into this project. The experiment evaluated the following mixtures: mix A (0.5-inch NMAS (12.5-mm)) and 35% RAP using neat PG52-34 with Evotherm, mix B (0.75-inch NMAS (19.0-mm)) and 20% RAP using neat PG64-28, and mix C (0.375-inch NMAS (9.5-mm)) and no RAP using a PG70-34HP binder with 7.5% SBS *(38)*. This study was incorporated into the literature review to examine the ability of the HP binder to produce an AC mix with comparable properties to other AC mixes from the same aggregate source with higher NMAS and RAP contents. Figure 2-9 illustrates the aggregate gradation of the three evaluated mixtures. The three mixtures were designed using the Superpave mix design methodology with 75 design gyrations. The optimum asphalt binder content for mixes A, B, and C are 5.50%, 4.90%, and 6.50%, respectively.

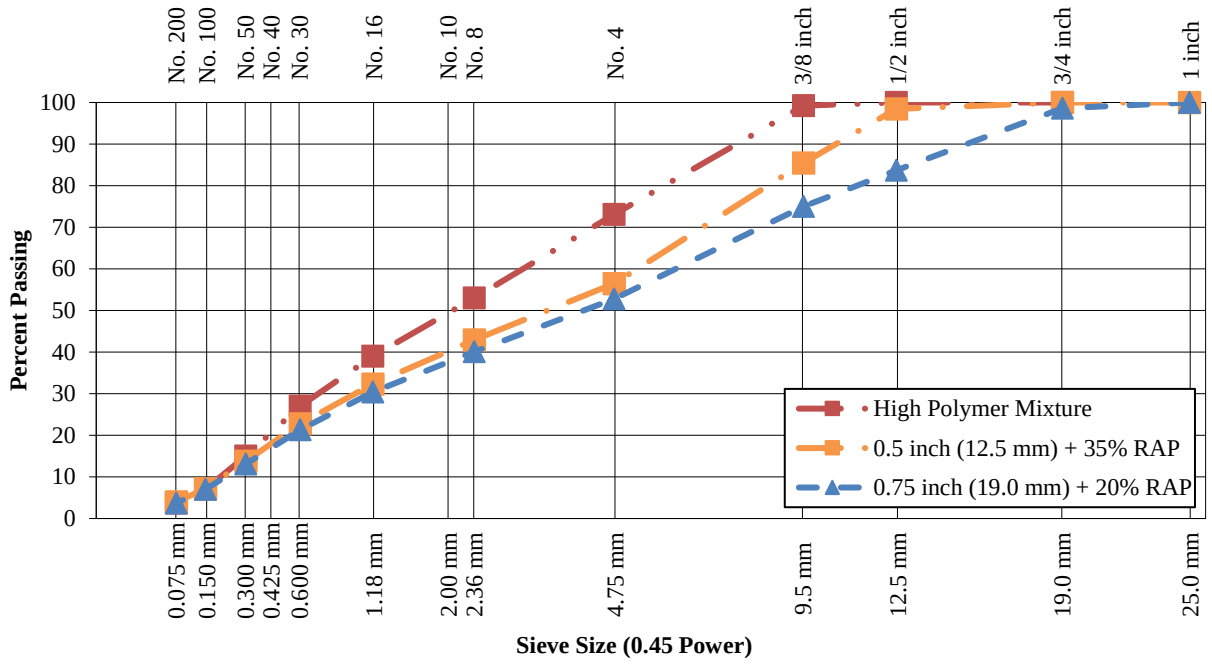


**Figure 2-9. Aggregate gradations of NHDOT mixes A, B, and C.**

The three AC mixes were evaluated in terms of their engineering property (|E*|) *(39) (40)*, resistance to rutting by determining the flow number (FN) *(39)*, resistance to fatigue cracking by conducting a flexural beam fatigue testing at multiple strain levels *(35)*, resistance to reflective cracking by conducting the Texas Overlay test (OT) *(34)*, and resistance to thermal cracking by

conducting the TSRST test *(31)*. The Dynamic modulus (E*) represents the engineering property of the AC mix and provides an indication on its overall quality. Mix B exhibited the highest E* property while mix C (HP) exhibited the lowest modulus. This indicates that the HP binder was unable to overcome the impact of RAP, higher NMAS with coarser gradation, and higher optimum binder content on the E* property of the AC mix.

The AMPT machine was used to determine the flow number (FN) of the three mixes (A, B, and C) *(39)*. The testing temperature was 122°F (50°C) selected as the design high temperature at 50% reliability as determined using the long-term pavement performance bind (LTPPBind) software version 3.1. This temperature was computed at a depth of 0.80 inch (20 mm) below the pavement surface. The Francken model was used to determine the tertiary flow. The highest FN was measured on the HP mix C at 346 followed by mix B at 237 and mix A at 128 cycles. This indicates that the HP binder was able to overcome the impact of RAP, higher NMAS with coarser gradation, and higher OBC on the FN property and produced an HP AC mix that is more resistant to rutting.

Flexural beam fatigue testing was performed to determine the fatigue characteristics of the three mixes *(35)*. Beams were trimmed from slabs compacted using the IPC Global Pressbox slab compactor. In order to account for the relative locations of the various mixtures within the pavement structure, mixes A and B were tested at strains of 250, 500, and 750 micro-strain while higher strains of 750, 1000, 1,250 micro-strain were applied to test mix C. All tests were conducted at a loading frequency of 10Hz and a temperature of 59°F (15°C). The 50% reduction in initial beam stiffness (determined at cycle 50) was adopted as a failing criterion. Figure 2-10 presents the beam fatigue results and fatigue relationship of the evaluated mixes *(38)*. A considerably better fatigue relationship was observed for the HP mix C when compared with mixes A and B.

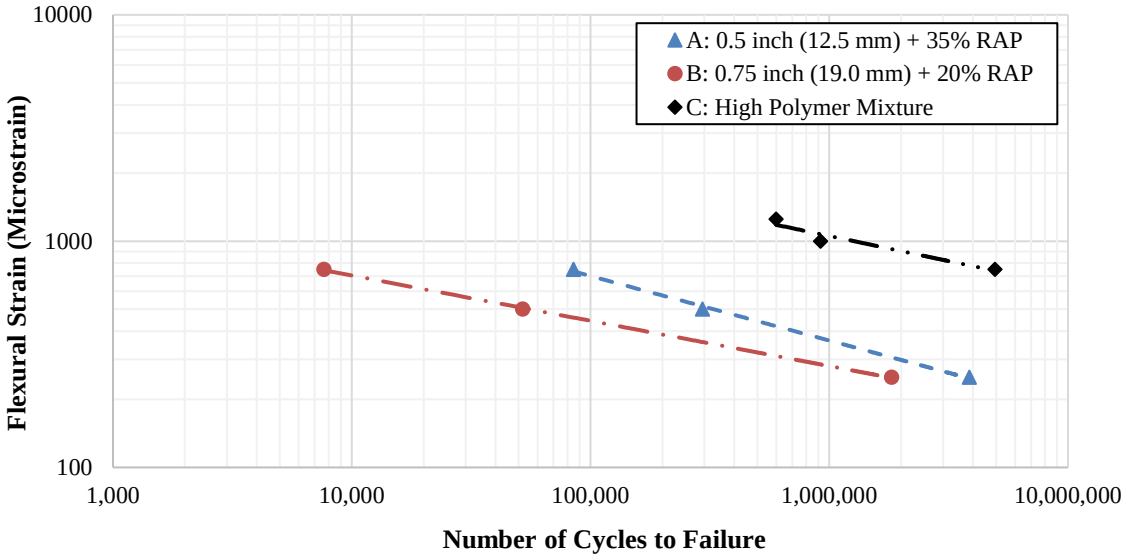


**Figure 2-10. Fatigue characteristics of mixes A, B, and C at 59°F (15°C).**

It should be noted that, a significant difference in the laboratory fatigue resistance will not necessarily translate to the same difference in fatigue performance in the field. Many factors may highly affect the fatigue life of an asphalt pavement such as stiffness, tensile strain under field loading, the fatigue characteristic of the asphalt mixture, pavement structure, and the interaction of all these factors. In a mechanistic pavement analysis, an AC layer with a higher stiffness will show a lower laboratory fatigue life in a strain-controlled mode of loading, on the other hand, it will produce a lower tensile strain under field loading which may result in a longer fatigue life in the field. Therefore, a full mechanistic analysis would be necessary to effectively evaluate the impact of HP mixes on the fatigue performance of AC pavements.

The Texas OT was used to evaluate the mixtures' resistance to reflective cracking at a testing temperature of 50°F (10°C) *(34)*. Failure was defined as the number of cycles to reach a 93% drop in initial load which is measured from the first opening cycle. The best performance was observed for the HP mix C with a number of cycles to failure of 968. Mixes A and B showed much lower resistance to reflective cracking with similar number of cycles to failures of 18 and 17, respectively *(38)*. The TSRST was used to evaluate the resistance of the mixes to thermal cracking *(31)*. The thermal fracture temperatures were observed to be -26, -22, and -37°C for mixes A, B, and C, respectively. The lowest fracture temperature was observed for the HP mix C followed by mix A while mix B showed the warmest fracture temperature. It should be noted that only the HP mix C exhibited a fracture temperature lower than the low temperature PG of the binder. Mixes A and B exhibited fracture temperatures that are significantly warmer than the low temperature PG of their respective binder.

In summary, it should be recognized that the presence of RAP in mixes A and B and the higher optimum binder content of mix C contributed to the increase in its relative resistance to all three modes of cracking: fatigue, reflective, and thermal. However, the fatigue life of the HP mix C at 750 micro-strain is over 600 times the fatigue life of mixes A and B, the reflective cracking life of the HP mix is 54 times the reflective cracking life of mixes A and B, and the thermal fracture temperature is 11 - 15°C lower than the thermal fracture temperature of mixes A and B. It is believed that a significant portion of this large increase in the resistance of the HP mix C to fatigue, reflective, and thermal cracking can be attributed to the properties of the HP binder. In addition to exhibiting a superior resistance to all modes of cracking, the HP mix C also exhibited higher resistance to rutting than mixes A and B with RAP.

## 2.2. EVALUATION OF FIELD HP AC MIXES PROJECTS WITH LIMITED PERFORMANCE DATA

### 2.2.1. Introduction

Several field demonstration projects were constructed in the US, Canada, Southern America, Europe, and Australia to evaluate the performance of HP AC mixes as summarized in Table 2-2. Figure 2-11 shows the locations of some of the projects on the U.S.A. map. This section presents the available information from some of the identified projects in terms design, testing, construction, and the up to date field performance of the HP AC mixes. The field projects presented in this section have very limited information concerning their long-term performance.

Test sections on the NCAT Test Track with extensive field performance data will be presented in the following section (Section 2.3).

**Table 2-2. Summary of Existing Field Projects Using HP AC Mixes.**

| Country/Agency | Project Description | Construction Year |
|---|---|---|
| Brazil/ Ministry of Roads | Mill and AC Overlay on Highway PR-092 | 2011 |
| USA/ Advanced Material Services LLC | Corvette Museum Race Track / Nashville / Bowling Green | 2013 |
| USA/ City of Bloomington, MN | Mill and AC Overlay on Normandale Road | 2012 |
| USA/Georgia DOT | Thin AC Overlay at junction of Routes 138 and 155 | 2012 |
| USA/HiPO Projects (New Hampshire and Vermont) | New Hampshire Route 202 | 2011 |
| | Vermont US-7 | 2011 |
| USA/ Oklahoma DOT | Mill and AC Overlay on Interstate I-40 | 2012 |
| USA/ Oregon DOT | Thin AC Overlay on Interstate I-5 | 2012 |
| USA/Virginia DOT | I-95 | --- |
| USA/ NCAT | Section N7 at the National Center for Asphalt Technology Test Track | 2009 |

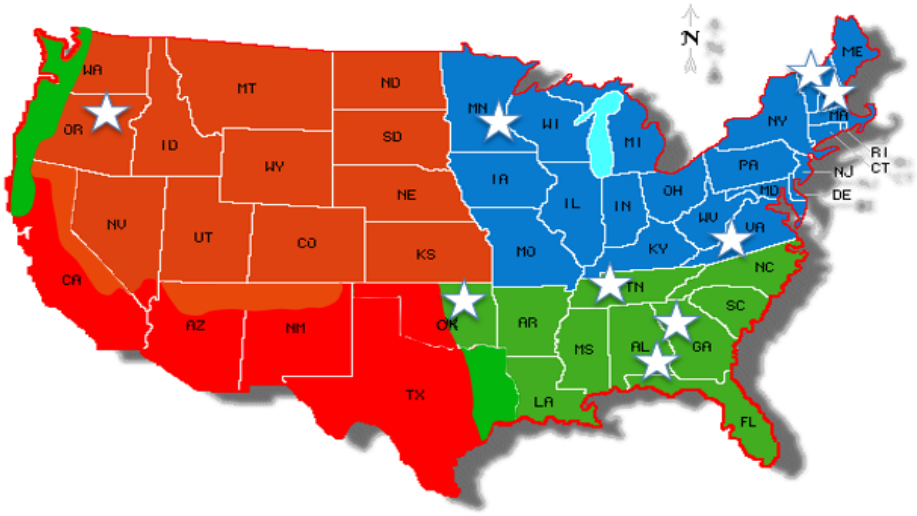


**Figure 2-11. Location of some HP field mixture projects in U.S.A.**

### 2.2.2. High Polymer Modified Asphalt Mixture Trial in Brazil

The first HP AC mix trial in Brazil was constructed in 2011 on a small test section located on Highway PR-092 in the state of Paraná *(41)*. PR-092 is known to be one of the most important and busiest roads in Parana State carrying approximately 1,800 vehicles and 4,200 heavy agricultural trucks per day. The HP binder was modified with 7.5% SBS by weight of binder. The standard pavement structure proposed by the Parana State DOT consisted of a 12 inch (305

mm) total thickness: 7.9 inch (200 mm) base course of cement-treated RAP, 1 inch (25 mm) Stress Absorbing Membrane Interlayer (SAMI), 1.6 inch (40 mm) binder course, and 1.6 inch (40 mm) PMA wearing course. The HP AC trial alternative consisted of 6.5 inch (165 mm) of dense-graded HMA reflecting a 46% reduction in the total structural section. Even-though this project does not include any performance properties on the HP binder, mixture, and field section, its value to the literature review remains through its hypothetical increase in the structural coefficient for the HP AC mix. Since the overall structural section was reduced by 46%, it can be concluded that the structural coefficient of the HP AC mix can be 46% higher than the structural coefficient of the combination of standard AC mix and cement-treated RAP base.

### 2.2.3. Winning the Race Track Challenge using HP Mixes

The National Corvette Museum Motorsports Park in Bowling Green, Kentucky has one of the high-performance tracks that attract professional and talented drivers to push their limits and fine-tune their machines. The facility has two circuits featuring technical turns with straightaways and elevation changes: a 2-mile (3.2-km) with 13-turn high-speed west course and a 1-mile (1.6-km) with 10-turn east course. Designing asphalt mixes for race tracks significantly differ from designing mixes for highway pavements. On a race track, raveling and bleeding remain the main concerns. The project required more than 58,000 tons of AC mix, including 20,000 tons of mix optimized for the track surface. The HP binder was modified with 7.5% SBS and graded as PG82-22. The HP AC mix was designed following the Marshall Mix design methodology (75-blow) *(42)*.

The Evotherm warm-mix asphalt additive was added to improve the HP AC mix workability which was expected to be stiff and difficult to compact. An important key point of the HP asphalt binder remains its softening point. It is defined as the temperature at which the asphalt binder changes phase from a semi-solid to a more viscous liquid leading to the migration of the fines to the surface due to the effect of extremely hot tires. For the race track, the minimum required softening point is 180°F (82°C) necessitating the use of polymers. The mixture was manufactured using an aggregate gradation that provides an optimum macro-texture accompanied with minimizing the damage induced from lateral shear forces of fast tires. Silica-rich limestone from the Fort Payne formation in Springfield, TN was selected as the best and most cost-effective material to enhance friction and skid-resistance on the race track. Pavement macro-texture remains a driving consideration for race tracks operating under wet or dry conditions, rain or shine, such as for National Corvette Museum Motorsports Park *(42)*.

The pavement structure consisted of an 8.5 inch (216 mm) dense-graded layer of aggregate base followed by a 5 inch (127 mm) PG64-22 asphalt base course and two 1.5 inch (38 mm) lifts of the HP AC mix serving as the wearing course layer. The value of this project to the literature is that it shows the various applications where HP binders have been successfully used in the US.

### 2.2.4. Mill and AC Overlay on Normandale Road, City of Bloomington

In 2012, the City of Bloomington, MN, constructed two projects with HP AC mixes to overcome the effects of weak water-saturated bases and subgrades as well as the heavy traffic that comes

with its prime location south of Minneapolis and St. Paul, adjacent to the international airport and the sprawling Mall of America within its limits *(43)*.

The first project was located on Normandale Service Road at 84th Street. It consisted of milling 6 inch (150 mm) of the existing AC layer and replacing it with three 2 inch (51 mm) HP mix lifts of 3/8-inch (9.5 mm) NMAS. The constructed section was 400 ft (122 m) long and 25 ft (7.6 m) wide, part of a larger reconstruction project in the area. Both the base and subgrade layers were characterized as soft and wet materials *(43)*.

The second project was located on West 98th Street from Logan Ave. South to Penn Ave. South involving the use of HP and conventional PMA mixes (i.e., PG58-28). The HP section was designed with a 25% thinner overlay layer compared to the conventional overlay. The reduction in overlay thickness was meant to overcome the increase in costs, while still reducing reflective and thermal cracking known as major issues in Minnesota, and achieving better durability *(43)*.

The HP binder for both projects included 7.5% SBS. The HP mixes were expected to help the city place more cost-effective and durable asphalt pavements resulting with reduced pavement thicknesses, and/or built pavement section on top of questionable existing base and subgrade layers. The HP mixes consisted of a 0.375-inch (9.5-mm) NMAS containing 6% of HP asphalt binder by total weight of mix. The mix was foamed at 300°F (149°C), placed at a temperature of 265°F (130°C), and compacted to a density of 92% verified by cores.

The value of this project to the literature review is two folds: a) it represents a situation where the HP AC mix is used to overcome the effect of weak base and subgrade which represents a scenario identified in the FDOT project statement, and b) a hypothetical structural coefficient can be estimated from the 25% reduction in the thickness of the HP AC layer.

### 2.2.5. HP Modified Asphalt Mixtures on Busy Intersection in Georgia

In 2010, Georgia DOT (GDOT) decided to evaluate a HP AC mix designed for better pavement durability and higher resistance to rutting and shoving at the junction of two busy state highways (Routes 138 and 155) in Stockbridge, Henry County. The main concern of the GDOT was rutting and shoving at the intersection especially with the huge increase of braking actions induced by heavy trucks *(20)*.

Due to the traffic level at the evaluated intersection, GDOT specified a Superpave mix design with a PG76-22 asphalt binder modified with a 7.5% SBS. The actual binder met the requirements of PG82-28. The granite aggregate gradation was characterized as dense with 0.5 inch (12.5 mm) NMAS. The work on site consisted of milling 1.5 inch (38 mm) of the existing AC layer and replacing it with the HP modified mix at 7% in-place air voids *(20)*.

Based on general observations reported from the job site, the HP modified mix had similar workability as the regular SBS modified mix *(20)*.

### 2.2.6. High-Performance HP Overlays in New Hampshire and Vermont

The NEPPP pilot performance-based HiPO overlay mixtures presented in section 2.1.5 were implemented on two demonstration projects located in New Hampshire and Vermont. The first project, located in New Hampshire, placed 1,500 tons of HP mixes with 25% RAP material on Route 202 in Rochester at a 1.0 inch (25 mm) thickness overlay for a 1.75-mile (2.7-km) length. The existing pavement was in bad conditions and no milling was done prior to the placement of the HiPO overlay. A conventional New Hampshire DOT mixture was placed on an adjacent section for comparison purposes *(33)*.

In summer 2011, the Vermont DOT placed a HiPO mixture on two 1-mile (1.6 km) sections on US-7 in Danby, VT. One of the mixes did not contain RAP, while the other mix had 24% RAP. The existing pavement was rated as fair to good after 14 years of service with some isolated areas of permanent deformation, some transverse cracking, and some shrinkage cracking. Surface preparation preceded the overlay placement included spot filling of permanent deformation areas, crack sealing along the length of the project, patching of cracks and potholes. Some milling was performed at transition areas and across bridges *(33)*.

In terms of field performance of the HiPO mixes placed on the two demonstration projects; minimal reflective cracking was observed on the New Hampshire section including RAP (25% of cracking that has returned) which can be due to the lack of surface preparation since the existing pavement was in poor conditions. No reflective cracking was observed on the Vermont section. Additionally, after 2 years of service, no signs of environmental related cracking nor rutting have been observed on all sections *(33)*.

### 2.2.7. HP Modified Overlay Mix on I-40 in Oklahoma

The project consisted of a 2-mile (3.2-km) mill-and-overlay on I-40 at the eastern end of Caddo County west of Oklahoma City. The objective of using a HP AC mix for the overlay was to increase durability, possibly reduce the thickness of the AC layer, and allow the DOT to complete a larger resurfacing program with the same amount of funds. Three different AC mixes were manufactured using a HP modified asphalt binder graded as PG76-28E. The “E” stands for “extremely high grade” based on the MSCR test with a minimum of 95% recovery at a stress level of 3.2 kPa. The HP modified asphalt binder contained 7.5% SBS. An improvement in overall performance, resistance to raveling, reduced fatigue cracking and rutting were expected by the Oklahoma DOT (ODOT) based on the findings from the National Center for Asphalt Technology’s (NCAT) Test Track study *(44)*.

The project consisted of milling 5 inch (127 mm) from the existing AC surface and placing the HP AC overlay at 8 inch (200 mm) thick which was expected to perform equivalent to a conventional 10.5 inch (267 mm) PMA overlay. The 8 inch (200 mm) HP AC overlay was constructed as follows: an intermediate 1.5 inch (38 mm) rich layer of 0.375-inch (9.5-mm) NMAS running at binder content of 5.6 to 5.8% followed by two lifts of 2.5 inch (64 mm) Oklahoma S3 base coarse with a 0.75 inch (19 mm) NMAS and capped with a 1.5 inch (38 mm) lift of Oklahoma S5 mixture with a 0.375-inch (9.5-mm) NMAS. A 0.75 inch (19 mm) open-graded friction course (OGFC) was placed on top to provide high friction and good drainability

to eliminate hydroplaning and truck tire spray. The purpose of having a HP modified rich mixture at the bottom is to increase resistance to reflective cracking from the existing AC layer. It was reported that the produced HP AC mix for this project was highly workable at a temperature of 325°F (163°C).

Even-though this project does not offer information on the properties of the HP binder and AC mix, its value to the literature review will be in two folds; a) a hypothetical structural coefficient can be determined based on the relative thicknesses of the HP and PMA layers, and b) the long-term performance of the section will be valuable if it can be obtained by the research team.

### 2.2.8. HP Modified Thin Overlay Mix on I-5 in Oregon

This demonstration project consisted of a 2 mile (3.2 km) segment on the northbound lanes of I-5 near Medford, OR. The project was part of a nationwide demonstration program involving thin pavement overlays incorporating HP asphalt binders. The mix design was produced based on the specifications developed by the NEPPP for the HiPO overlay mix presented in section 2.1.5. The objective of using the HiPO asphalt mix on this project was to evaluate the thin overlay pavement preservation option under heavy traffic *(45)*.

The PMA binders contained 3% SBS while the HP binder contained 7.5% SBS and both binders were graded as PG70-22ER. The "ER" extension stands for passing the Oregon DOT (ODOT) specification on the minimum Elastic Recovery *(ER)* of 50% per AASHTO T301 *(46)*. The major difference between the two binders is the *ER* value; the PMA binder had an *ER* of 64% while the HP binder had an *ER* of 89%. The PMA and HiPO mixes were produced with identical aggregate gradations and volumetric properties. The mixes were manufactured using 0.375-inch (9.5-mm) NMAS aggregate with 6.4% asphalt binder by total weight of mix and 20% RAP. It should be mentioned that no special plant adjustments were reported to accommodate the production of the HiPO mix.

The existing pavement on I-5 had a 0.75 inch (19 mm) open-graded friction course (OGFC) mostly deteriorated due to wear and raveling. Historically, 2 inch (51 mm) of the existing pavement would be milled and replaced with a new AC mix followed by an OGFC. In this project, ODOT decided to micro-mill 1 inch (25 mm) and replace with the new AC mix. Two 1-mile (1.6-km) travel-lanes were milled to 1 inch (25 mm) and replaced with the HiPO mix followed by a 1-mile section of the same two travel-lanes milled and replaced with ODOT's 0.375-inch (9.5-mm) NMAS dense-graded PMA mix at the same thickness. Prior to paving of the travel lanes, ODOT required the contractor to place the HiPO mix on the shoulder to check its workability and appearance. A latex-modified asphalt tack coat, CRS-2Ph, was used to ensure a strong bond between the existing pavement and the overlay. No problems were reported during the production, laydown, and compaction of the PMA and HiPO mixes, except the CRS-2Ph was switched to CSS-1h traditional tack coat on the second and final shift of paving to cut down on clumping *(45)*.

Even-though this project does not offer information on the properties of the HP binder and mixture, its value to the literature review will be in the long-term performance of the HiPO thin overlay under heavy traffic if it can be obtained by the research team.

## 2.3. EVALUATION OF FIELD HP AC MIXES PROJECTS WITH EXTENSIVE PERFORMANCE DATA

### 2.3.1. Introduction

As presented earlier, several studies have shown that HP AC mixes have the potential to improve the resistance to cracking and rutting with a potential reduction in the AC layer thickness when compared to PMA AC mixes. While the laboratory evaluations done on HP asphalt binders and AC mixes were promising, it remains necessary to fully understand and evaluate the performance and in-situ characteristics of the HP AC mixes on actual field projects. For this purpose, a full-scale experiment was conducted at the NCAT Test Track in 2009. This section documents some detailed information about the work done and presents the findings from the full-scale experiment.

### 2.3.2. NCAT Test Track Sections

The full-scale experiment at the NCAT Test Track was sponsored by Kraton Performance Polymers LLC to fully understand the in-situ characteristics of HP AC mixes when used on actual pavement sections. It consisted of two mains sections: (1) a control section, labeled as S9-PMA, designed and constructed using a PMA AC mix, and (2) a HP section, labeled as N7-HP, designed and constructed to be thinner than the control section using HP AC mix. The section labeling is a combination of a letter and a number: N and S denotes North and South, respectively, meanwhile the digit represents the section number (1 through 13 on each tangent). Figure 2-12 illustrates the as-designed structures, mix types, and layers thicknesses of both pavement sections (i.e., S9-PMA and N7-HP) *(21)*.

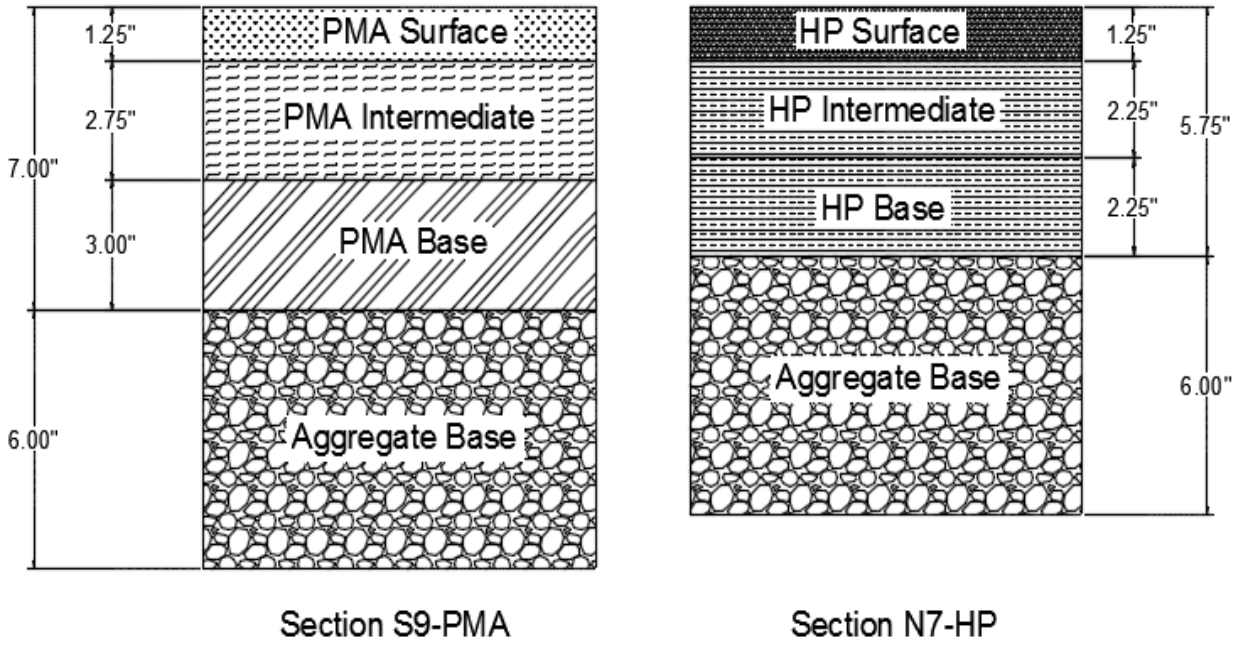


**Figure 2-12. NCAT Test Track S9-PMA and N7-HP cross-sections design: materials and layer thicknesses *(21)*.**

Random longitudinal (RL) stations were established at different locations within and between wheel paths throughout each section prior to construction. These locations played a major role during construction. They constituted the locations of nuclear density testing, and survey points for thickness. They also served as locations for falling weight deflectometer (FWD) testing and determination of transverse profile. For both sections, the subgrade was classified as an AASHTO A-4(0) metamorphic quartzite soil and compacted to target density and moisture content. The average dry unit weights of the subgrade material for section S9-PMA and N7-HP were 123.4 and 121.8 lb/ft$^3$ (1,977 and 1,951 kg/m$^3$) with a moisture content of 9.2% and 9.4%, respectively. The aggregate base was a crushed granite material placed at 6 inch (150 mm) thick. The average dry unit weights of the aggregate base material for section S9-PMA and N7-HP were 140.2 and 140.6 lb/ft$^3$ (2,246 and 2,252 kg/m$^3$) with a moisture content of 5.0 and 4.1%, respectively. Direct measurements for the pavement structure responses to traffic loads were made using strain gauges and pressure cells embedded at different locations and depths within the pavement structure layers. Table 2-3 summarizes the as-built AC layer properties for the two sections *(21)*.

**Table 2-3. As-Built AC Layers Properties.**

| **Lift** | **Surface** | | **Intermediate** | | **Base** | |
|---|---|---|---|---|---|---|
| **Section** | **S9-PMA** | **N7-HP** | **S9-PMA** | **N7-HP** | **S9-PMA** | **N7-HP** |
| **Thickness, inch (mm)** | 1.2 (30) | 1.0 (25) | 2.8 (71) | 2.1(53) | 3.0 (76) | 2.5 (64) |
| **NMAS, inch (mm)** | 0.375 (9.5) | 0.375 (9.5) | 0.75 (19.0) | 0.75 (19.0) | 0.75 (19.0) | 0.75 (19.0) |
| **% polymer - SBS** | 2.8 | 7.5 | 2.8 | 7.5 | 0.0 | 7.5 |
| **Performance Grade** | 76-22 | 88-22 | 76-22 | 88-22 | 67-22 | 88-22 |
| **Asphalt, %** | 6.1 | 6.3 | 4.4 | 4.6 | 4.7 | 4.6 |
| **Air voids, %** | 6.9 | 6.3 | 7.2 | 7.3 | 7.4 | 7.2 |
| **Plant Temperature, °F (°C)** | 335 (168) | 345 (174) | 335 (168) | 345 (174) | 325 (163) | 340 (171) |
| **Paver Temperature, °F (°C)** | 275 (135) | 307 (153) | 316 (158) | 286 (141) | 254 (123) | 255 (124) |
| **Compaction Temperature, °F (°C)** | 264 (129) | 297 (147) | 273 (134) | 247 (119) | 243 (117) | 240 (116) |

### 2.3.3. PMA and HP Mix Designs

All AC mixes were designed using the Superpave mix design methodology with 80 design gyrations. Table 2-4 and Figure 2-13 present the aggregate gradation of each lift of the AC layer for both sections. The optimum binder content was determined at 4% air voids and satisfying all volumetric properties criteria. Table 2-5 summarizes the mix design information for the different lifts (i.e., surface, intermediate, and base) for both PMA and HP AC mixes. Similar volumetric properties were observed for the PMA and HP AC mixes despite the large difference in the binder PG resulting from the additional polymer in the HP binder *(21)*.

**Table 2-4. Aggregate Gradations of PMA and HP Mixes – NCAT Test Track.**

| Sieve Size | Surface Layer Mixes | | Intermediate Layer Mixes | Base Layer Mixes | |
|---|---|---|---|---|---|
| | PMA | HP | PMA & HP | PMA | HP |
| 1 inch (25.0 mm) | 100 | 100 | 100 | 100 | 100 |
| 0.75 inch (19.0 mm) | 100 | 100 | 93 | 93 | 93 |
| 0.5 inch (12.5 mm) | 100 | 100 | 82 | 84 | 82 |
| 0.375 inch (9.5 mm) | 100 | 100 | 71 | 73 | 71 |
| No. 4 (4.75 mm) | 78 | 77 | 52 | 55 | 52 |
| No. 8 (2.36 mm) | 60 | 60 | 45 | 47 | 45 |
| No. 16 (1.18 mm) | 46 | 45 | 35 | 36 | 35 |
| No. 30 (0.6 mm) | 31 | 31 | 24 | 25 | 24 |
| No. 50 (0.3 mm) | 16 | 16 | 12 | 14 | 12 |
| No. 100 (0.15 mm) | 10 | 9 | 7 | 8 | 7 |
| No. 200 (0.075 mm) | 5.8 | 5.7 | 3.9 | 4.6 | 3.9 |

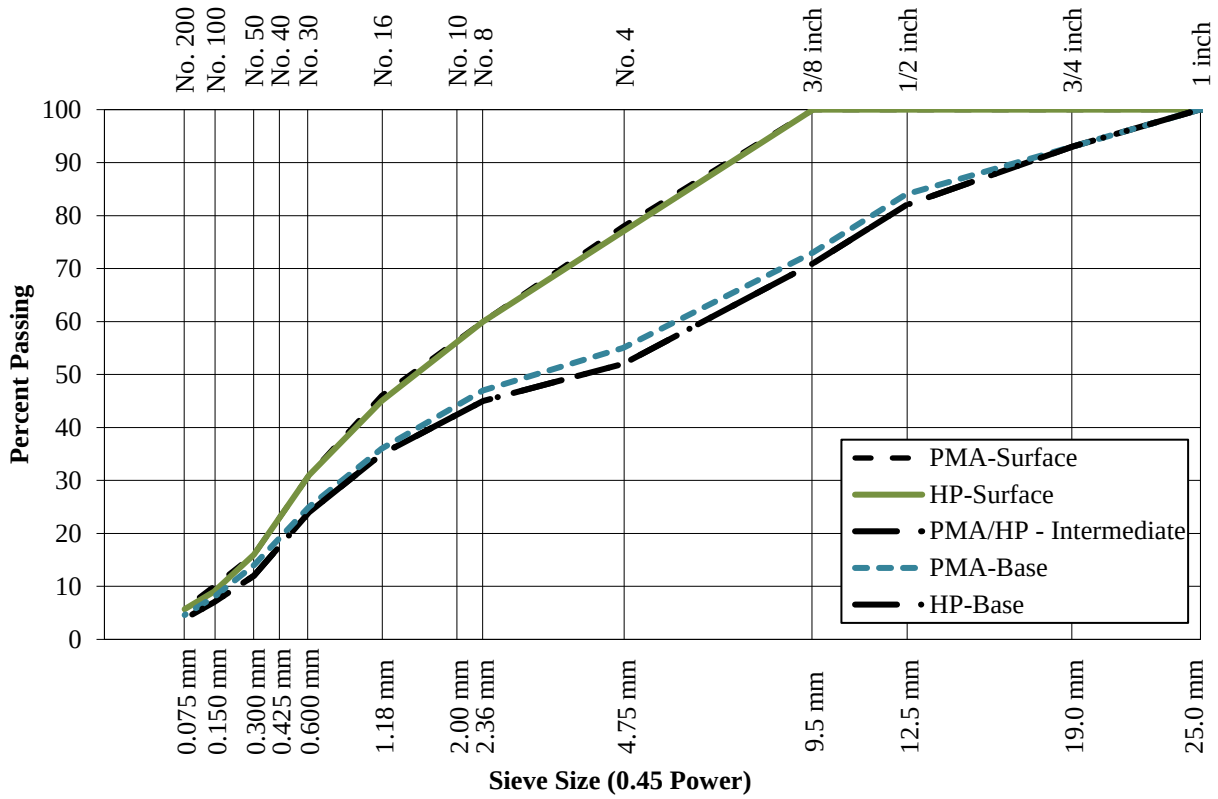


**Figure 2-13. Aggregate gradations of PMA and HP mixes – NCAT Test Track.**

**Table 2-5. Summary of NCAT PMA and HP Mixes (Surface, Intermediate, and Base Lifts) Mix Designs.**

| Mix Type | PMA | | | HP | |
|---|---|---|---|---|---|
| Lift ID | Surface | Intermediate | Base | Surface | Intermediate & Base |
| Asphalt PG Grade | 76-22 | 76-22 | 67-22 | 88-22 | 88-22 |
| % SBS Polymer | 2.8 | 2.8 | 0.0 | 7.5 | 7.5 |
| Design Air Voids, % | 4.0 | 4.0 | 4.0 | 4.0 | 4.0 |
| Optimum Binder Content (by total weight of mix), % | 5.8 | 4.7 | 4.6 | 5.9 | 4.6 |
| Effective Binder ($P_{be}$), % | 5.1 | 4.1 | 4.1 | 5.3 | 4.2 |
| Dust Proportion, DP | 1.1 | 0.9 | 1.1 | 1.1 | 0.9 |
| Maximum Specific Gravity, $G_{mm}$ | 2.483 | 2.575 | 2.574 | 2.474 | 2.570 |
| Voids in Mineral Aggregate (VMA), % | 15.8 | 13.9 | 13.9 | 16.2 | 14.0 |
| Voids Filled with Asphalt (VFA), % | 75.0 | 71.0 | 71.0 | 75.0 | 72.0 |

### 2.3.4. Laboratory Evaluation of Binders and Plant-Produced Mixtures

Loose mixtures were collected in five-gallon pails during production and were brought back to the NCAT laboratory for further evaluation. Corresponding asphalt binders used during production were all sampled at the plant and brought back to the laboratory.

#### *2.3.4.1 Properties of Asphalt Binders*

All asphalt binders were sampled at the plant except for the PG76-22 used in the surface mixture lift of section S9-PMA which was replaced by the extracted and recovered binder from the field mixture. AASHTO M320-10 *(47)* was followed to test and grade all binders. It should be mentioned that the HP binder used for the surface lift in section N7-HP had a similar workability and compactability as of the PG76-22 binder in the laboratory and on field. In addition, the MSCR test was used to determine the PG of all asphalt binders in accordance with AASHTO MP 19-10 *(48)*. Table 2-6 summarizes all the PG's and MSCR results.

**Table 2-6. Asphalt Binder Testing: PG and MSCR Test Results.**

| Mixture | Binder Grading | | MSCR | | | | |
|---|---|---|---|---|---|---|---|
| | True Grade | PG | Test Temp., °C | $J_{nr0.1}$, $kPa^{-1}$ | $J_{nr3.2}$, $kPa^{-1}$ | $J_{nrdiff}$, % | PG |
| Base Lift of S9-PMA | 69.5 – 26.0 | 64 – 22 | 64 | 1.68 | 1.95 | 16.1 | 64-22 H* |
| Interm. Lift of S9-PMA | 78.6 – 25.5 | 76 – 22 | 64 | 0.84 | 1.15 | 36.9 | 64-22 H |
| Surface Lift of S9-PMA | 81.7 – 24.7 | 76 - 22 | 64 | 0.98 | 1.37 | 39.8 | 64-22 H |
| All lifts of N7-HP | 93.5 – 26.4 | 88 – 22 | 64 | 0.004 | 0.013 | 200.7 | Not Graded |

*H denotes a heavy traffic level

*2.3.4.2 Properties of Plant-Produced Mixtures*

The experimental plan *(21)* included tests to evaluate loose mixtures collected from the plant in terms of moisture susceptibility using the tensile strength ratio test *(49*), stiffness using the unconfined and confined dynamic modulus tests *(39) (40)*, resistance to fatigue cracking using the flexural beam fatigue test *(35)*, resistance to rutting using the flow number test *(39*), and resistance to top-down cracking using the IDT creep compliance and strength test *(28)*.

*Moisture Susceptibility*

Four mixtures: Surface-S9-PMA, Base-S9-PMA, Surface-N7-HP, and Base-N7-HP, were evaluated for moisture susceptibility following AASHTO T283 *(49)*. Results are summarized in Table 2-7 show the HP AC mixes exhibited significantly higher unconditioned and conditioned tensile strength properties than the corresponding PMA AC mixes. However, all four mixtures met the requirement of a minimum tensile strength ratio of 80%.

**Table 2-7. Summary of Moisture Susceptibility Properties of the PMA and HP Mixtures.**

| Mixture | Treatment | Tensile Strength, psi (kPa) | Tensile Strength Ratio, TSR, % |
|---|---|---|---|
| Surface-S9-PMA | Conditioned | 137.2 (946) | 94 |
| | Unconditioned | 145.4 (1,003) | |
| Base-S9-PMA | Conditioned | 116.2 (801) | 86 |
| | Unconditioned | 134.6 (928) | |
| Surface-N7-HP | Conditioned | 197.1 (1,359) | 89 |
| | Unconditioned | 222.1 (1,531) | |
| Base-N7-HP | Conditioned | 208.4 (1,437) | 88 |
| | Unconditioned | 237.6 (1,638) | |

*Dynamic Modulus Property*

Dynamic modulus (E*) testing was performed on each of the plant-produced mix placed on the sections S9-PMA and N7-HP in accordance with AASHTO T378 *(39)* and AASHTO R84 *(40)*. The E* property provides an indication of the stiffness and the overall quality of the asphalt mixture. All measured data had a coefficient of variation (COV) lower than 13% indicating good repeatability of the results. The testing was done unconfined and with a 20 psi (138 kPa) confinement pressure on all evaluated mixtures. Figure 2-14 and Figure 2-15 illustrate the unconfined and confined E* master curves for all the evaluated mixtures, respectively. Examination of the E* master curves leads to the following observations:

- For both confined and unconfined testing conditions, the dynamic modulus values reported for the HP AC mixes are higher than for the PMA AC mixes indicating a stiffer mix.
- No impact was observed on the ranking of PMA and HP AC mixes in terms of dynamic modulus with the addition of confinement. However, higher values for both mixes were reported under the confinement condition which was conventionally expected.

- All AC mixes, PMA and HP, for each confinement condition (i.e., unconfined and confined) exhibit similar dynamic modulus at a low temperature and high frequency (i.e., upper right end of the master curve).

Overall, it can be noticed that the high polymer content of the HP AC mixes had a much greater impact on the measured E* values for the surface course when compared with the intermediate and base course layers. The confinement had significant effects on the E* values especially at the lowest reduced frequencies (i.e., below 1 Hz) *(21)*.

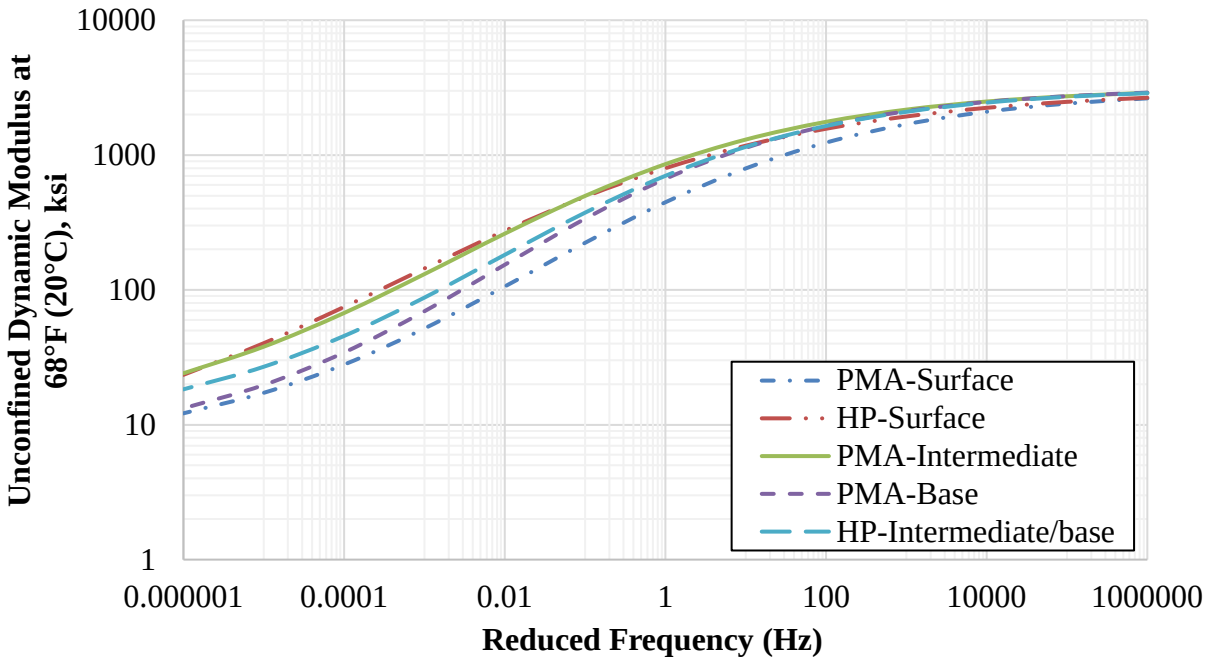


**Figure 2-14. Unconfined dynamic modulus master curves.**

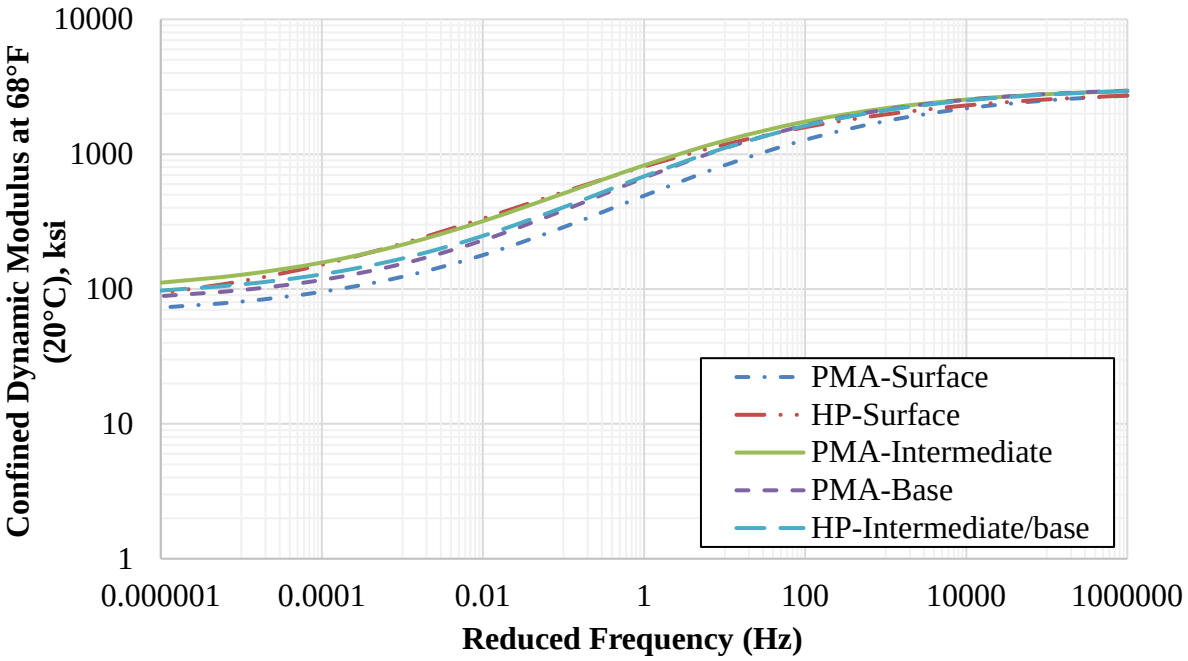


**Figure 2-15. Confined dynamic modulus master curves.**

*Fatigue Cracking Properties*

Flexural beam fatigue testing was performed in accordance with AASHTO T 321 *(35)* to determine the fatigue characteristics of the plant-produced mixtures placed on sections S9-PMA and N7-HP. Beams were tested at multiple strains at a temperature of 68°F (20°C). The 50% reduction in initial beam stiffness (determined at cycle 50) was adopted as a failure criterion. Figure 2-16 illustrates the fatigue characteristics of PMA-Base and HP-Base AC mixes. The following observations can be made:

- The HP AC mix showed significantly higher number of load cycles to failure when compared with the PMA AC mix.
- At a flexural strain level of 400 micro-strain (expected strain level at bottom of AC), the average fatigue life of the HP AC mix was observed to be approximately 33 times higher than the fatigue life of the PMA AC mix at a temperature of 68°F (20°C) *(21)*.

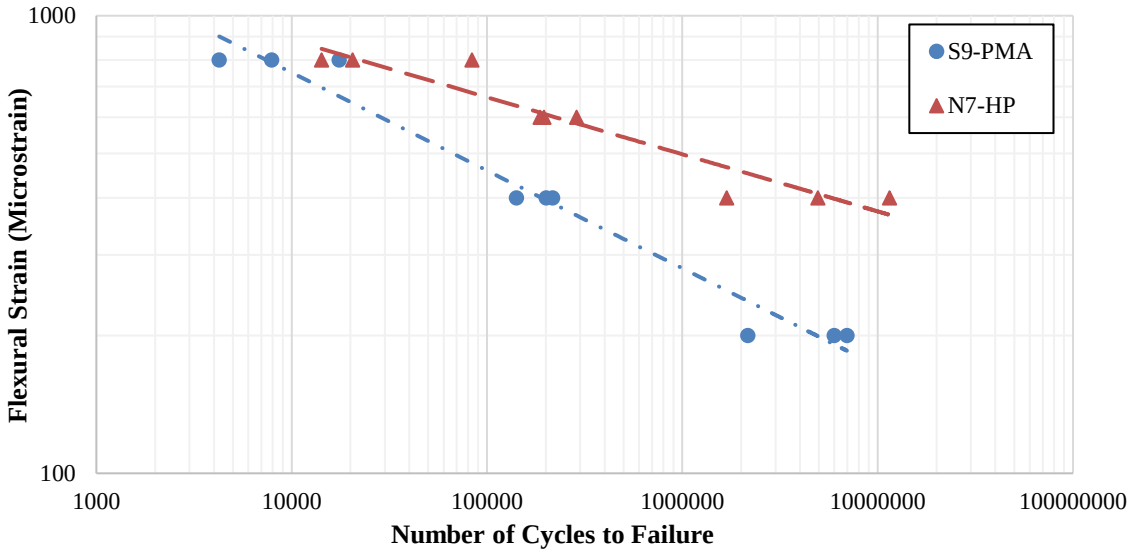


**Figure 2-16. Fatigue characteristics of PMA-Base and HP-Base mixes at 68°F (20°C).**

*Rutting Properties*

Asphalt Pavement Analyzer (APA) Results: The APA was used to evaluate the rutting susceptibility of the PMA and HP AC mixes. The testing was performed according to AASHTO T340 *(36)* at a temperature of 147.2°F (64°C). All tested samples were subjected to a pressure of 100 psi (690 kPa) for 8,000 cycles. Table 2-8 summarizes the measured APA test results. Based on previous experience from sections on the NCAT test track, a mix with an average APA rut depth less than 0.21 inch (5.5 mm) should be able to withstand at least 10 million EASLs. Therefore, the evaluated mixes are not expected to fail in terms of rutting. The APA data of rut depth versus load cycles were fitted with a power function to determine the secondary stage rutting rate. The HP-surface AC mix showed the lowest secondary stage rutting rate followed by the HP-base AC mix. Combining the fatigue cracking data with the APA data indicates the possibility of designing a highly flexible HP pavement structure with high rut resistance *(3)*.

**Table 2-8. APA Testing Results of PMA/HP Surface/base AC Mixes.**

| Mixture ID | Average Rut Depth, inch (mm) | Standard Deviation (SDV), inch (mm) | COV, % | Rate of Secondary Rutting, inch/cycle (mm/cycle) |
|---|---|---|---|---|
| **PMA-Surface** | 3.07 (78.0) | 0.58 (14.7) | 19 | 0.000140 (0.003556) |
| **PMA-Base** | 4.15 (105.4) | 1.33 (33.8) | 32 | 0.000116 (0.002946) |
| **HP-Surface** | 0.62 (15.7) | 0.32 (8.1) | 52 | 0.0000267 (0.000678) |
| **HP-Base** | 0.86 (21.8) | 0.20 (5.1) | 23 | 0.0000280 (0.000711) |

Flow Number Properties: The FN property of the PMA/HP Surface/Base AC mixes were measured according to AASHTO T378 *(39)*. The testing temperature was 139°F (59.5°C) selected as the design high pavement temperature at 50% reliability determined using the long-term pavement performance bind (LTPPBind) software version 3.1 at a depth of 0.80 inch (20 mm) below the pavement surface. The Francken model was used to determine the on-set of the tertiary flow, i.e. FN. A higher FN value indicates a high resistance to rutting. As shown in Figure 2-17, the best rutting resistance was observed for the HP AC mixes especially the surface mix. The HP AC mixes exhibited FN values that are approximately 6 times greater than the FN of the PMA AC mixes.

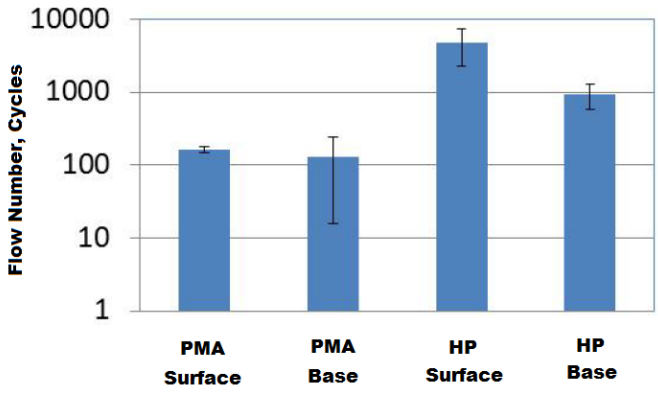


**Figure 2-17. Flow number test results for PMA/HP surface/base mixes *(21)*.**

*Thermal Cracking Properties*

The indirect tensile creep compliance and strength test was used to estimate the thermal stress and strain as well as the thermal cracking temperature of the mixtures in accordance with AASHTO T322 *(28)*. A cooling rate of 18°F (10°C) per hour starting at 68°F (20°C) was adopted to evaluate the change in terms of thermal stresses and failure timing. Table 2-9 summarizes the thermal properties of the evaluated mixtures. In the case of thermal cracking, the properties of the surface layer are more critical than the properties of the base layer. The measured thermal properties of the PMA and HP surface AC mixes are very close and appear to be within the repeatability of the test.

**Table 2-9. Indirect Tensile Strength, Failure Time, and Temperature for PMA/HP Surface/Base AC Mixes *(21)*.**

| Property | PMA-Surface | PMA-Base | HP-Surface | HP-Base |
|---|---|---|---|---|
| Indirect Tensile Strength at -10°C (50°F), ksi (MPa) | 0.68 (4.71) | 4.16 (28.68) | 4.55 (31.37) | 5.27 (36.34) |
| Failure Time, hour | 4.64 | 4.14 | 4.47 | 4.61 |
| Failure Temperature, °C | -26.4 | -21.4 | -24.7 | -26.1 |

### 2.3.5. Falling Weight Deflectometer Testing and Backcalculation

FWD testing of S9-PMA and N7-HP Sections started in August 2009. The testing was performed three times per month (on Mondays) for the S9-PMA section and on alternating Mondays for the N7-HP section. The testing was done at the same location of the random longitudinal stations already established prior to construction using a Dynatest Model 8000 FWD. A circular load plate of 11.8 inch (300 mm) diameter was used to conduct the FWD testing. Nine geophones were used to measure the deflections at the pavement surface. The geophones were spaced at; 0, 8, 12, 18, 24, 36, 48, 60, and 72 inch (0, 203, 305, 457, 610, 914, 1219, 1524, and 1829 mm) from the center of the load. Four different loads were applied three times at each testing location at: 6000, 9000, 12000, and 16000 lb (2727, 4090, 5455, and 7273 kg) *(21)*. In-situ pavement temperatures were recorded for each section during FWD testing.

NCAT researchers used the EVERCALC 5.0 software to backcalculate the layers moduli of the three-layer pavement section (AC over aggregate base and subgrade) from the measured FWD deflection data. The layer thicknesses were identified based on surveys at each offset and random location. Figure 2-18 to Figure 2-20 present the backcalculated moduli for the AC, granular base, and subgrade layers at the 9000 lb (4090 kg) load level, respectively.

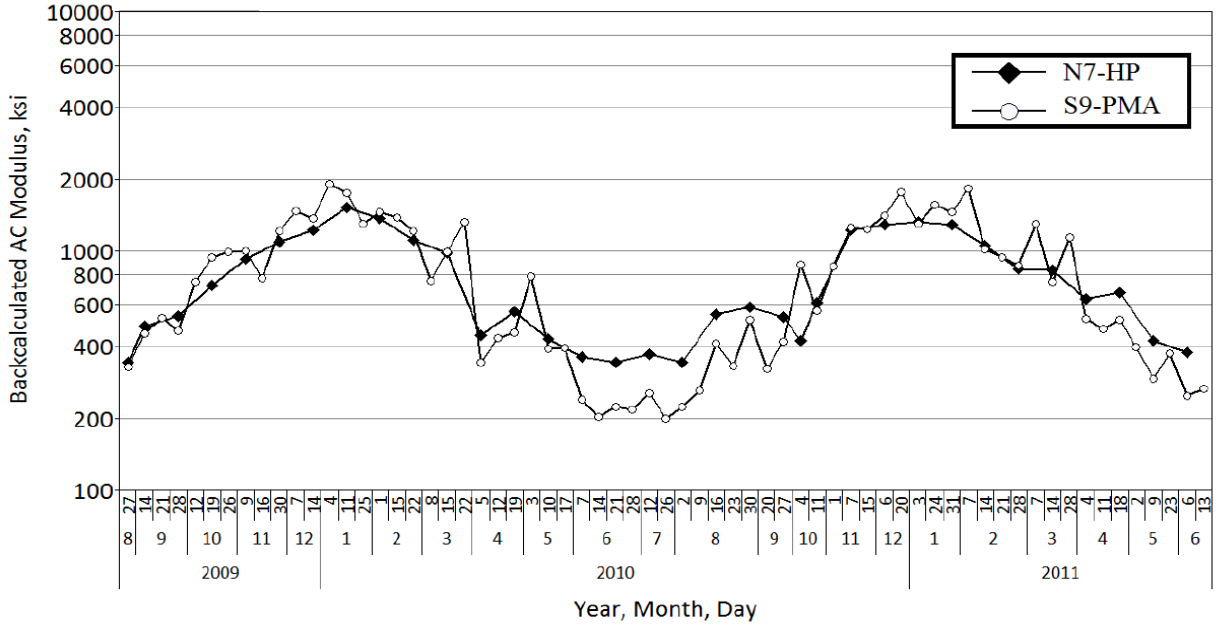


**Figure 2-18. Backcalculated AC modulus of sections N7-HP and S9-PMA *(21)*.**

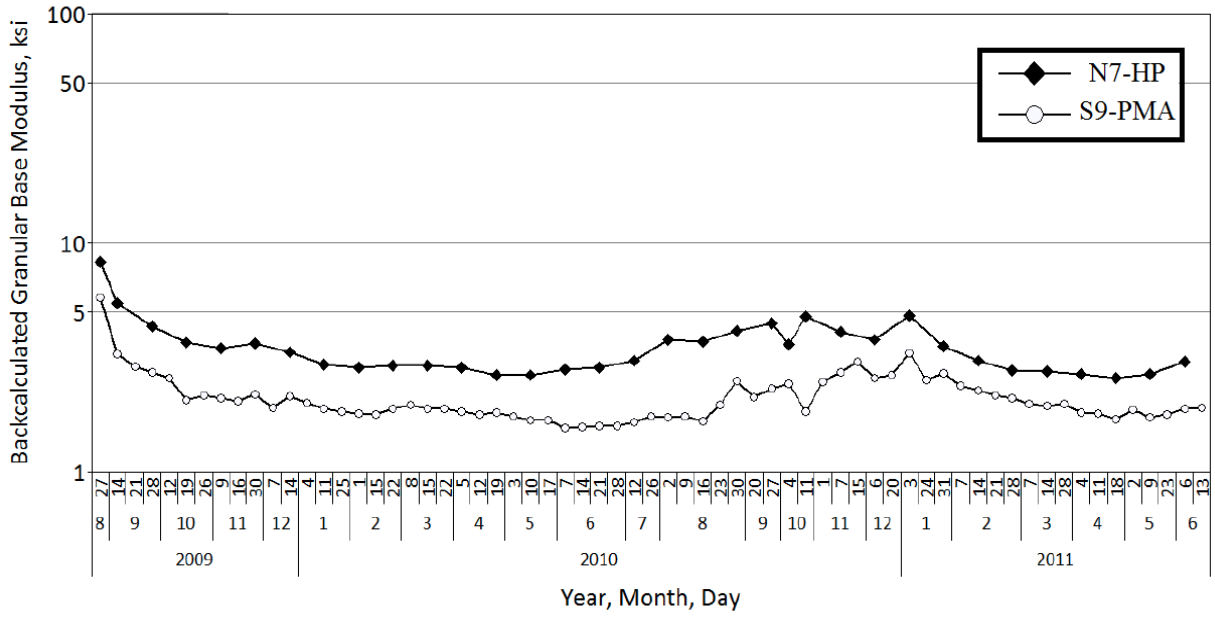


**Figure 2-19. Backcalculated granular base modulus of sections N7-HP and S9-PMA *(21)*.**

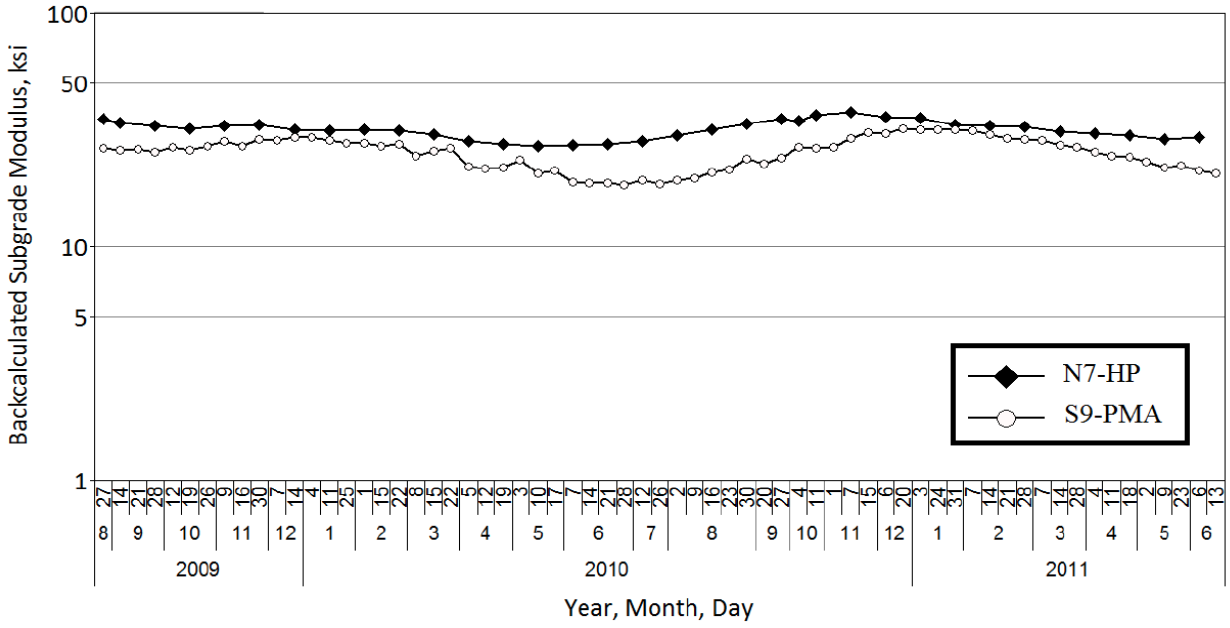


**Figure 2-20. Backcalculated subgrade modulus of sections N7-HP and S9-PMA *(21)*.**

A review of the backcalculated moduli data presented in Figure 2-18, Figure 2-19, and Figure 2-20 reveals the following observations:

- The variation in the backcalculated AC moduli clearly reveals the seasonal effects on the AC layer's stiffness.

- Relatively low backcalculated moduli values for the granular base layer were observed for both sections. The researchers indicated that these values were consistent with findings from previous laboratory triaxial resilient modulus testing conducted at NCAT.
- Relatively high backcalculated moduli values for the subgrade layer were observed for both sections when compared with the backcalculated moduli values for the granular base layer indicating the presence of strong subgrade material underneath both pavement sections (N7-HP and S9-PMA).

### 2.3.6. Pavement Responses to Traffic Load

As mentioned earlier, strain gauges and pressure cells were installed to measure strains and stresses at various locations and depths. Four primary measured pavement responses were collected: a) longitudinal strain at the bottom of the AC layer, b) transverse strain at the bottom of the AC layer, c) vertical stress in the aggregate base layer, and d) vertical stress in the subgrade layer. Weekly data were collected since traffic began on August 28, 2009. The following paragraphs summarize the response data collected during the period between August 28, 2009; and June 9, 2011 *(21)*.

*2.3.6.1 AC Layer Strain Responses*

*Longitudinal Strains*

Table 2-10 summarizes the measured longitudinal strains at the bottom of the AC layer under a single axle load at three temperatures of 50, 68, and 110°F (10, 20, and 44°C). Similar strains were observed on sections S9-PMA and N7-HP at the two lower temperatures. However, at the higher temperature, a lower longitudinal strain was measured on the N7-HP section when compared with strain on the S9-PMA section. The variability expressed by the standard deviation and COV was more than double for the N7-HP section when compared with S9-PMA. It should be mentioned that the AC layer in section S9-PMA is 1.25 inch (32 mm) thicker than the one in section N7-HP indicating that the increase in the HP mix modulus at the high temperature, caused by the higher polymer content, was enough to overcome the thickness advantage held by S9-PMA section.

**Table 2-10. Longitudinal Strain Measured at the Bottom of the AC Layer.**

| Section ID | Temperature, °F (°C) | Longitudinal Strain (micro-strain) | Standard Deviation (micro-strain) | COV (%) |
|---|---|---|---|---|
| S9-PMA | 50 (10) | 225 | 44 | 20 |
| | 68 (20) | 350 | 69 | |
| | 110 (44) | 979 | 192 | |
| N7-HP | 50 (10) | 225 | 101 | 45 |
| | 68 (20) | 337 | 152 | |
| | 110 (44) | 862 | 388 | |

Table 2-11 summarizes the measured transverse strains at the bottom of the AC layer under a single axle load at three temperatures of 50, 68, and 110°F (10, 20, and 44°C). The transverse

strains were observed to be lower than the measured longitudinal strains at the three corresponding temperatures. Less variability was observed with the measured transverse strains. At the two lower temperatures, higher strains were measured at N7-HP when compared with S9-PMA. At 110°F (44°C), the measured strains changed order where the S9-PMA showed higher values. This can be attributed to the interaction between layer thickness and modulus value.

**Table 2-11. Transverse Strain Measured at the Bottom of the AC Layer.**

| Section ID | Temperature, °F (°C) | Transverse Strain (micro-strain) | Standard Deviation (micro-strain) | COV (%) |
|---|---|---|---|---|
| S9-PMA | 50 (10) | 145 | 10 | 7 |
| | 68 (20) | 221 | 16 | |
| | 110 (44) | 590 | 42 | |
| N7-HP | 50 (10) | 184 | 48 | 26 |
| | 68 (20) | 256 | 67 | |
| | 110 (44) | 559 | 147 | |

Since fatigue cracking is controlled by the highest tensile strain at the bottom of the AC layer, the contribution of the HP mix towards the magnitude of the longitudinal strains is more critical. Using the measured longitudinal strains, the predicted fatigue life in terms of cycles to failure at 68°F (20°C) using the laboratory-determined transfer functions are 348,432 and 15,680,982 cycles for the S9-PMA and N7-HP section, respectively *(3).* It should be recognized that this analysis only compares the relative fatigue life of the two sections and there is no connection to the actual load repetitions to fatigue cracking of the two sections on the test track. Therefore, it can be concluded that the N7-HP section should have a relatively longer fatigue life than the S9-PMA section.

*2.3.6.2 Aggregate Base Vertical Pressure Responses*

Table 2-12 summarizes the measured vertical stresses in the base layer under a single axle load at three temperatures of 50, 68, and 110°F (10, 20, and 44°C). A lower vertical stress was observed in the base layer of the S9-PMA section when compared with the N7-HP section. This indicates that the geometry of the pavement structure plays a more significant role in the distribution of vertical stress than the properties of the AC mix.

**Table 2-12. Vertical Stresses Measured in the Base Layer.**

| Section ID | Temperature, °F (°C) | Average Pressure, psi (kPa) | Standard Deviation, psi (kPa) | COV (%) |
|---|---|---|---|---|
| S9-PMA | 50 (10) | 6 (41) | 0.6 (4.1) | 11 |
| | 68 (20) | 9 (62) | 0.9 (6.2) | |
| | 110 (44) | 25 (172) | 2.7 (18.6) | |
| N7-HP | 50 (10) | 9 (62) | 1.5 (10) | 16 |
| | 68 (20) | 13 (90) | 2.1 (14) | |
| | 110 (44) | 31 (214) | 4.9 (34) | |

*2.3.6.3 Subgrade Vertical Pressure Responses*

Table 2-13 summarizes the measured vertical stresses in the subgrade under a single axle load at three temperatures of 50, 68, and 110°F (10, 20, and 44°C). Slightly higher pressures were measured at the N7-HP section when compared with the S9-PMA section. This indicates that the geometry of the pavement structure plays a more significant role in the distribution of vertical stress than the properties of the AC mix but to a lesser extent at deeper locations.

**Table 2-13. Vertical Stresses Measured in the Subgrade Layer.**

| Section ID | Temperature, °F (°C) | Average Pressure , psi (kPa) | Standard Deviation, psi (kPa) | COV (%) |
|---|---|---|---|---|
| S9-PMA | 50 (10) | 5 (34) | 0.4 (2.8) | 9 |
| | 68 (20) | 7 (48) | 0.6 (4.1) | |
| | 110 (44) | 17 (117) | 1.4 (9.6) | |
| N7-HP | 50 (10) | 8 (55) | 0.8 (5.5) | 10 |
| | 68 (20) | 10 (69) | 1.0 (6.9) | |
| | 110 (44) | 17 (117) | 1.7 (11.7) | |

### 2.3.7. Pavement Performance

Approximately nine million ESALs were applied to the test sections (S9-PMA and N7-HP) as of June 27, 2011 while pavement performance was weekly monitored. Figure 2-21 illustrates the weekly measurements of rut depths for both sections. The rutting performance of the two sections remained close until approximately 3.5 million ESALs after which the observed rutting in the S9-PMA section started to significantly increase relative to rutting in the N7-HP section. Since the rut depths in both sections are relatively low (i.e., less than 0.25 inch (6.4 mm)), it can be assumed that the rutting is generated in the total AC layer (i.e., surface and base). Therefore, the rutting properties of the PMA and HP mixes presented in Table 2-8 and Figure 2-21 can be used to explain the relative rutting performance of the two sections as follows:

- The measured APA rut depths (Table 2-8) of the PMA AC mixes are significantly higher than the rut depths of the HP AC mixes. This indicates that the PMA section will experience overall higher rutting than the HP section under traffic loads as shown in Figure 2-21.
- The measured APA rates of secondary rutting (Table 2-8) of the PMA AC mixes are significantly higher than the APA rates of secondary rutting of the HP AC mixes. This indicates that after a certain level of traffic loading the PMA AC mixes will experience more progressive rutting than the HP AC mixes as shown in Figure 2-21.
- The flow numbers (Figure 2-17) of the PMA AC mixes are significantly lower than the flow numbers of the HP mixes indicating that the PMA AC mixes will experience tertiary flow much earlier than the HP mixes.
- The combination of the APA and FN data clearly shows that the PMA AC mixes will experience higher rutting than the HP AC mixes at a relatively lower number of load repetitions. In the absence of fully calibrated rutting models for the two mixes, it is believed that the combination of climatic conditions at the initial loading stage, pavement structure, and rutting characteristics of the two mixes has led to the clear separation in the

rutting performance of the two sections at approximately 3.5 million ESALs as shown in Figure 2-21.

Additionally, weekly roughness measurement (IRI) were collected on both sections as illustrated in Figure 2-22. The collected data revealed that section N7-HP was constructed at a much rougher level than section S9-PMA. However, the N7-HP section was able to maintain its construction level of roughness throughout the entire loading cycle. It should be noted that: a) surface roughness of short pavement sections, such as the NCAT Test Track sections, may not lead to performance issues because vehicle dynamics may not be fully activated over the short length of the section, and b) vehicle dynamics experienced over the length of such short section is more influenced by the roughness of the sections leading to it. The fact that section N7-HP performed well in rutting and did not experience a significant increase in roughness beyond its construction level indicates that the sections leading to it were not very rough.

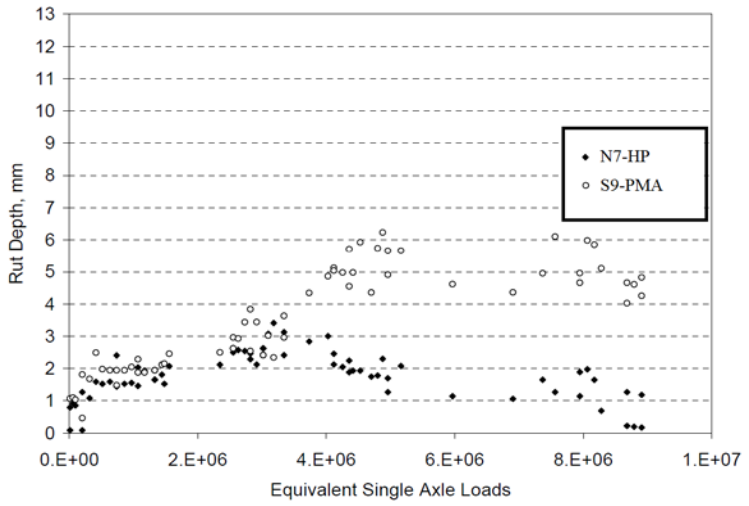


**Figure 2-21. Rut depths measured at various levels of applied ESALs *(21)*.**

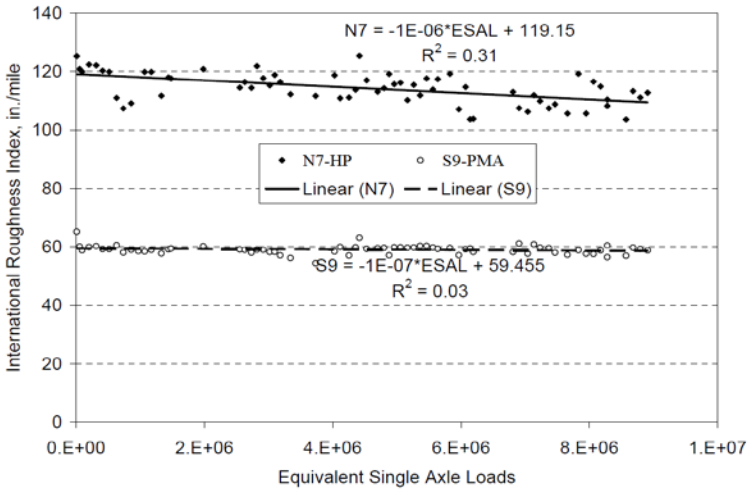


**Figure 2-22. Surface roughness measured at various levels of applied ESALs *(21)*.**

## 2.4. PRELIMINARY ANALYSIS OF STRUCTURAL COEFFICIENT FOR HP AC MIXES BASED ON NCAT STUDY

Based on previous experience, a structural coefficient of 0.44 was found to be representative of PMA AC mixes when designed in pavement sections for the state of Florida following the Flexible Pavement Design Manual *(4)*. In some other states, this structural coefficient was recalibrated to account for the conventional polymer modification of asphalt mixtures (2-3% polymer). If the positive impact of the polymer is assumed to be proportionally maintained at higher contents, then the use of a HP asphalt binder (7.5% polymer) can potentially lead to a higher AC structural coefficient *($a_{HP\text{-}AC}$)* and a reduced AC layer thickness for the same design traffic and serviceability loss *(3)*. The objective of this section is to illustrate several potential approaches to recalibrate the structural coefficient using the laboratory and field performance of HP AC mixes used in the experimental section N7-HP at the NCAT test track.

### 2.4.1. Background on Past Calibration Efforts

As mentioned previously, many factors may affect the determination of structural layer coefficients for new asphalt mixtures that were not used at the AASHO Road Test (e.g., recycled material, PMA and HP AC mixes). These factors include engineering properties, layer thickness, underlying support, position in the pavement structure, and stress state. Many studies have been conducted to determine these structural coefficients *(2), (3)*.

For AC mixes containing recycled materials, Van Wyk et al. (50) compared the deflection basins generated by non-destructive testing to theoretical deflection basins using BISTRO, a layered elastic software program. The pavement cross section was selected so the deflection basins matched adequately. Pavement responses such as tensile strains at the bottom of the AC layer, compressive strains at the top of subgrade, and surface deflections were computed on two similar pavement sections, one conventional and the other including RAP with similar design life. The structural number, the thickness and quality of base and subbase material, as well as the type of subgrade were maintained the same for both sections making the structural coefficient of the AC mix with RAP the only variable parameter. The structural number is a direct measure of the layer's thicknesses and their corresponding structural coefficients. It should be mentioned that this method accounts for the distress criteria (i.e., rutting and fatigue cracking) that constitutes the shortest pavement life.

Hossain et al. used FWD test data to determine the structural layer coefficient of crumb-rubber modified (CRM) mixes for Kansas DOT (KDOT) *(51)*. The layer conditions were then determined from the effective structural number calculated using backcalculated moduli, layer thicknesses and Equation 2-1 recommended by the AASHTO 1993 Guide. High variability in the structural layer coefficients was observed from this study.

$$SN_{eff} = 0.0045 * D * \sqrt[3]{E_p} \qquad \textbf{Equation 2-1}$$

Where;
*D*: total thickness of the corresponding pavement cross section above the subgrade, inch; and
$E_p$: effective modulus of the pavement cross section, psi.

In 2009, Timm et al. *(53)* used the performance of 11 test sections of neat and PMA AC mixes built on the NCAT Test Track between 2003 and 2006 as summarized in Figure 2-23 to establish the structural coefficient for PMA AC mixes for the Alabama DOT as described below:

- The performance of the test sections were converted into PSI using the relationship developed by Al-Omari and Darter *(53)* shown below:

$$PSI = 5 * e^{(-0.0038*IRI)} \qquad \textbf{Equation 2-2}$$

- Using the calculated PSI, the terminal serviceability *($p_t$)* and the change in PSI *($\Delta PSI$)* was determined for each section.
- Using the *$\Delta PSI$*, the resilient modulus property of the subgrade, and traffic in ESALs, the equivalent SN for each section was determined.
- Finally, the structural coefficient for each PMA section was determined using its equivalent SN and the thickness of the various layers including the PMA AC layer.
- The determined structural coefficients for the PMA AC mixes had an average value of 0.54 and a standard deviation of 0.08.

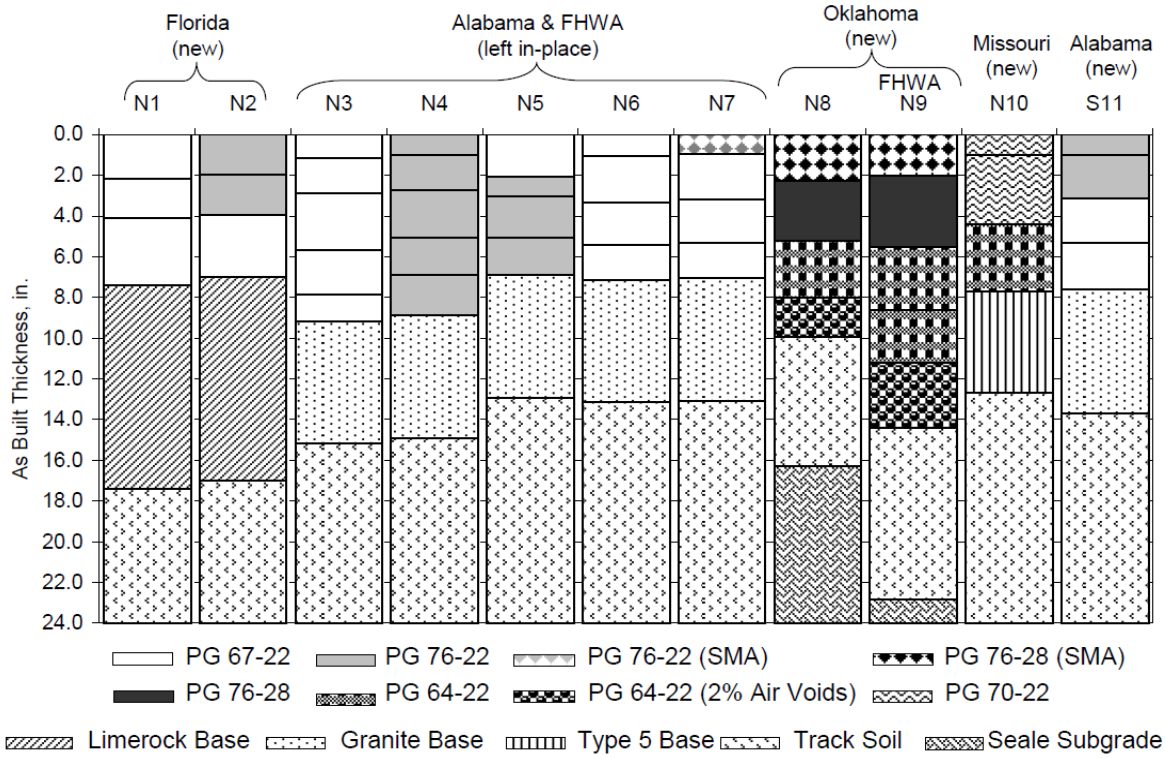


**Figure 2-23. NCAT Test Track structural sections *(3)*.**

### 2.4.2. Preliminary Analysis of NCAT Section N7-HP Structural Coefficient

The objective of this section is to illustrate different potential approaches for the recalibration of the structural layer coefficient of HP AC mixes using published data collected during the NCAT study; *Field and Laboratory Study of High-Polymer Mixtures at the NCAT Test Track (21)*. The

following four approaches were explored as part of this section and a preliminary structural coefficient for the HP AC mix was determined accordingly.

- Approach 1: consists of determining a structural coefficient for the HP AC mix using the fixed service life concept based on measured rutting performance.
- Approach 2: consists of determining a structural coefficient for the HP AC mix using collected FWD data, method of equivalent thickness (MET), and estimation of effective structural number *($SN_{eff}$)*.
- Approach 3: consists of determining a structural coefficient for the HP AC mix using the AASHTO 1993 Guide equation and associated loss in serviceability index.
- Approach 4: consists of determining a structural coefficient for the HP AC mix based on equivalent fatigue life using the 3D-Move Analysis model *(54)*.

Two pavement sections, a PMA and a HP, were considered as part of these analyses. The PMA section consisted of a 7 inch (178 mm) thick AC layer (Figure 2-12) while the AC layer thickness of the HP section was determined according to each of the examined approaches. Both sections had a 6 inch (150 mm) CAB layer placed on top of the same subgrade. A structural coefficient *($a_2$)* and a draining coefficient *($m_2$)* of 0.14 and 1.0 were assumed for the base layer, respectively.

In each approach, a percent difference between the estimated structural coefficients of the PMA AC and HP AC mixes used on the NCAT track will be calculated. This percent difference will be applied to the 0.44 structural coefficient for the PMA AC mix to estimate that of HP AC mix from Florida.

### *2.4.2.1 Approach 1: Determination of $a_{HP\text{-}AC}$ Based on Measured Rutting Performance*

As of June 27, 2011, approximately 8.9 million ESALs had been applied to test sections N7-HP and S9-PMA. At that time, there was no cracking evident on either of the sections. Weekly measurements of rut depths were collected and plotted (Refer to Figure 2-21). Both sections showed rut depth values lower than 0.25 inch (6.4 mm) after 8.9 million ESALs indicating a high resistance to rutting. Referring to Figure 2-21, similar rutting performance was observed on both sections up to an applied traffic of 3.5 million ESALs. Based on the observed rutting performance of the AC layers, the structural coefficient of the HP modified asphalt mix can be determined using the fixed service life approach. At the equivalent rutting performance of approximately 0.12 inch (3 mm) after 3.5 million ESALs, the 5.75 inch (146 mm) AC layer thickness for the HP pavement can be considered sufficient to achieve the same service life as the corresponding 7.00 inch (178 mm) AC layer thickness for the PMA pavement. The structural coefficient for the HP mix is then calculated as the ratio of the AC layer thickness of the PMA pavement to the AC layer thickness of the HP pavement times 0.44 which is the assumed structural layer coefficient of the PMA mix according to FDOT Equation 2-3. Accordingly, a structural coefficient of 0.54 is estimated for the HP mix based on the equivalent rutting performance after a traffic loading of 3.5 million ESALs.

$$a_{HP-AC-Rut} = \left(\frac{AC\ layer\ thickness\ of\ PMA\ pavement\ for\ rutting\ in\ AC}{AC\ layer\ thickness\ of\ HP\ pavement\ for\ same\ rutting\ in\ AC}\right) * 0.44 \qquad \textbf{Equation 2-3}$$

*2.4.2.2 Approach 2: Determination of $a_{HP\text{-}AC}$ Based on FWD Data*

As recommended by the AASHTO 1993 Guide, the effective structural number can be calculated from the total thickness of the pavement cross section above the subgrade and its effective modulus (refer to Equation 5.1). The analysis of the FWD data showed backcalculated moduli of 921,000 psi (6,350 MPa), 2,200 psi (15 MPa), and 27,800 psi (192 MPa) for the PMA AC, base, and subgrade layers, respectively *(21)*. The method of equivalent thickness (MET) is used to convert the top layers (i.e., AC and base layers) into a half space with a subgrade modulus of $M_r$ using Equation 2-4.

$$h_{e,n} = \{\sum_{i=1}^{n} h_i * \sqrt[3]{\frac{E_i}{M_R}}\} = \{D * \sqrt[3]{\frac{E_p}{M_R}}\} \qquad \textbf{Equation 2-4}$$

Where;
$h_{e,n}$: equivalent thickness of i[th] layer, inch;
$h_i$: thickness of i[th] layer, inch;
$E_i$: backcalculated modulus of i[th] layer, psi;
$M_R$: backcalculated modulus of the subgrade layer, psi;
$E_p$: effective modulus of the pavement cross section, psi; and
$D$: total thickness of the pavement cross section, inch.

Therefore, the equivalent layer thickness for the PMA section is calculated using Equation 2-5 as follows:

$$h_{e,n} = h_{PMA-AC} * \sqrt[3]{\frac{E_{AC}}{M_R}} + h_{base} * \sqrt[3]{\frac{E_{base}}{M_R}}$$
$$= 7 * \sqrt[3]{\frac{921{,}000}{27{,}800}} + 6 * \sqrt[3]{\frac{2{,}200}{27{,}800}} = 25.1\ inch\ (637\ \text{mm}) \qquad \textbf{Equation 2-5}$$

The effective modulus of the pavement cross section can be then calculated using Equation 2-6 where $D$ is equal to the summation of the thickness of both the PMA AC and base layers (i.e., 13 inch).

$$E_p = M_R * (\frac{h_{e,n}}{D})^3 = 27{,}800 * (\frac{25.1}{13})^3 = 199{,}140\ psi\ (1{,}373\ \text{MPa}) \qquad \textbf{Equation 2-6}$$

Accordingly, using Equation 2-1, the effective structural number of the PMA section is calculated as follows.

$$SN_{eff-PMA} = 0.0045 * D * \sqrt[3]{E_p} = 0.0045 * 13 * \sqrt[3]{199140} = 3.42 \qquad \textbf{Equation 2-7}$$

Therefore, using Equation 1-2, the structural coefficient of the PMA AC layer is calculated as follows and a value of 0.37 was determined (i.e., $a_{PMA\text{-}AC} = 0.37$).

$$SN_{eff-PMA} = a_{PMA-AC} * h_{PMA-AC} + a_{base} * h_{base} * m_{base}$$
$$3.42 = a_{PMA-AC} * 7 + 0.14 * 6 * 1 \qquad \textbf{Equation 2-8}$$

At 3.5 million EASLs, the PMA and HP sections were found to have an equivalent rutting performance. Therefore, the same effective structural number can be assigned for the HP pavement section. Thus assuming similar base layer properties, the structural layer coefficient for the HP AC mix can be calculated using Equation 1-2 and a value of 0.45 was determined (i.e., $a_{HP\text{-}AC} = 0.45$).

$$SN_{HP-AC} = a_{HP-AC} * h_{HP-AC} + a_{base} * h_{base} * m_{base}$$
$$3.42 = a_{HP-AC} * 5.75 + 0.14 * 6 * 1 \qquad \textbf{Equation 2-9}$$

This analysis showed an increase of 21.6% in the structural coefficient of the HP AC layer (i.e., $a_{AC\text{-}HP} = 0.45$) when compared with the structural coefficient of the PMA AC layer (i.e., $a_{PMA\text{-}AC} = 0.37$). Applying this percent difference on the recommended structural coefficient of PMA mixes in Florida, a value of 0.54 (i.e., denoting an increase of 21.6% from 0.44) is estimated for a FDOT HP AC mix.

*2.4.2.3 Approach 3: Determination of $a_{HP\text{-}AC}$ Based on Loss in Serviceability*

The PSI concept was developed during the AASHTO Road Test experiment to relate the ride conditions of the road with the opinion of the user. The original PSI equation has been modified throughout the years by State highway agencies to better describe local conditions. Equation 2-10 shows the PSI equation for flexible pavements *(55)*. As mentioned before, there was no cracking and patching reported on either of the sections after 8.9 million ESALs. Therefore, C and P values in Equation 2-10 were considered equal to zero.

$$PSI = 5 * e^{(-0.0041*IRI)} - 1.38 * RD^2 - 0.03 * (C + P)^{0.5} \qquad \textbf{Equation 2-10}$$

Where;
*PSI*: present serviceability index;
*IRI*: international roughness index, inch/mile;
*RD*: rut depth, inch;
*C*: cracking, $ft^2/1000ft^2$; and
*P*: patching, $ft^2/1000ft^2$.

After 8.9 million ESAL, average terminal serviceability values of 3.1 and 3.9 were calculated for the PMA and HP pavement sections, respectively ($p_{t\text{-}PMA}$=3.1, and $p_{t\text{-}HP}$=3.9). Considering an initial serviceability of 4.2 ($p_i$=4.2) for both sections, the change in PSI was found to be 1.1 and 0.3, respectively. A 50% reliability is considered for this analysis because high reliabilities are used to artificially increase the predicted traffic to account for uncertainty in the design process. Therefore, a normal deviate of zero value is then selected. Solving for all input parameters in Equation 1-1, the structural number of the PMA and HP pavement sections ($SN_{PMA\text{-}AC}$ and $SN_{HP\text{-}AC}$) was found to be 4.1 and 4.3, respectively. It should be mentioned that one-third of the backcalculated moduli value of the subgrade layer was considered following the recommendations from the AASHTO 1993 Guide procedure. Therefore, the corresponding structural coefficients of PMA and HP AC mixes were calculated using Equation 2-11 and Equation 2-12 and resulted in values of $a_{PMA\text{-}AC} = 0.46$ and $a_{HP\text{-}AC} = 0.60$. This analysis showed an increase of 29.2% in the structural layer coefficient for the HP AC layer when compared with

the structural coefficient of the PMA AC layer. Applying this percent difference on the recommended structural coefficient of PMA mixes in Florida, a value of 0.57 can then be assumed for FDOT HP AC mixes (i.e. $a_{HP\text{-}AC} = 0.57$).

$$SN_{PMA-AC} = a_{PMA-AC} * h_{PMA-AC} + a_{base} * h_{base} * m_{base}$$
$$4.1 = a_{PMA-AC} * 7 + 0.14 * 6 * 1 \rightarrow a_{PMA-AC} = 0.46 \quad \textbf{Equation 2-11}$$

$$SN_{HP-AC} = a_{HP-AC} * h_{HP-AC} + a_{base} * h_{base} * m_{base}$$
$$4.3 = a_{HP-AC} * 5.75 + 0.14 * 6 * 1 \rightarrow a_{HP-AC} = 0.60 \quad \textbf{Equation 2-12}$$

*2.4.2.4 Approach 4: Determination of $a_{HP\text{-}AC}$ Based on Equivalent Fatigue Life using 3D-Move Analysis*

As noted in previous sections (Section 2.3), field mixed laboratory compacted specimens of PMA and HP mixes were prepared and evaluated in terms of their resistance to fatigue cracking at a temperature of 68°F (20°C) using the flexural beam fatigue test. Equation 2-13 and Equation 2-14 show the fatigue relationship for PMA and HP mixes using the power model, respectively.

$$\varepsilon_{t-PMA} = 5374.2 * N^{-0.214} \quad \textbf{Equation 2-13}$$

$$\varepsilon_{t-HP} = 2791.8 * N^{-0.125} \quad \textbf{Equation 2-14}$$

Where;
$\varepsilon_t$: tensile strain at the bottom of the AC layer, micro-strain; and
*N:* Number of cycles to failure.

As shown previously, the predicted fatigue life in terms of cycles to failure at 68°F (20°C) using the laboratory-determined transfer function is expected to be 348,432 and 15,680,982 cycles for the S9-PMA and N7-HP sections, respectively *(3)*. Following the fixed service life approach for fatigue cracking, the required AC layer thickness for the HP pavement will be determined to achieve the same service life in terms of number of fatigue cycles to failure of the PMA pavement section. For that, the 3D-Move software was used and two analyses were conducted: static (i.e., stationary load), and dynamic (i.e., moving load).

The 3D-Move analytical model adopted here to undertake the pavement response computations uses a continuum-based finite-layer approach. The 3D-Move analysis model can account for important pavement response factors such as complex 3D contact stress distributions (normal and shear) of any shape, vehicle speed, and viscoelastic material characterization for the AC layers. This approach treats each pavement layer as a continuum and uses the Fourier transform technique. Since rate-dependent material properties (viscoelastic) can be accommodated by the approach, it is an ideal tool to model the behavior of AC layer and also to study pavement responses as a function of vehicle speed. Frequency-domain solutions are adopted in 3D-Move Analysis, which enables the direct use of the frequency sweep test data of AC mixture in the analysis. More information can be found in literature *(54)*.

*Input Parameters and Definition of Critical Points*

A single axle dual tires was applied as traffic loading on both sections for both static and dynamic analyses. For the dynamic analysis, a speed of 45 mph (72 km/h) was considered to simulate the speed of the loading trucks at the NCAT track. Table 2-14 summarizes the input values for the applied traffic. Table 2-15 and Table 2-16 summarize all the properties for the AC, base and subgrade layers from the PMA and HP sections, respectively. Table 2-17 and Table 2-18 summarize the dynamic modulus of the PMA and HP AC mixes, respectively. The RTFO properties for the PMA and HP asphalt binders are summarized in Table 2-19 and Table 2-20, respectively. Figure 2-24 illustrates the PMA pavement section and the points of interest at the bottom of the PMA AC layer (i.e., P1, P2, P3, P4, P5, and P6).

**Table 2-14. Characteristics of Applied Traffic Load.**

| **Single Axle Dual Tires** | |
|---|---|
| Axle Load, lb (kN) | 18,000 (80) |
| Tire Pressure, psi (kPa) | 120 (827) |
| Dual Tires Spacing, inch (mm) | 14 (356 mm) |
| Tire Load, lb (kN) | 4,500 (20) |

**Table 2-15. Summary of Input Properties for S9-PMA Test Section.**

| **Pavement Layer** | **Backcalculated Modulus** | **Thickness, inch (mm)** | **Characterization** |
|---|---|---|---|
| PMA Asphalt Concrete | Static: 921,000 psi (6,350 MPa)<br>Dynamic: Dynamic Modulus of PMA mix (Refer to Table 17) | 7 (178) | Viscoelastic |
| Aggregate Base | E = 2,200 psi (15 MPa) | 6 (150) | Linear Elastic |
| Subgrade | E = 27,800 psi (192 MPa) | Infinite | Linear Elastic |

**Table 2-16. Summary of Input Properties for N7-HP Test Section.**

| **Pavement Layer** | **Backcalculated Modulus** | **Thickness, inch** | **Characterization** |
|---|---|---|---|
| HP Asphalt Concrete | Static: 882,000 psi (6,081 MPa)<br>Dynamic: Dynamic Modulus of HP mix (Refer to Table 18) | To be determined | Viscoelastic |
| Aggregate Base | E = 3,600 psi (25 MPa) | 6 (150) | Linear Elastic |
| Subgrade | E = 33,000 psi (220 MPa) | Infinite | Linear Elastic |

**Table 2-17. Dynamic Modulus Input Values for S9-PMA AC Mix.**

| E*, psi (MPa) | Frequency (Hz) | | | | | |
|---|---|---|---|---|---|---|
| Temperature, °F (°C) | 0.1 | 0.5 | 1 | 5 | 10 | 25 |
| 14 (-10) | 2,186,700 (15,077) | 2,419,500 (16,682) | 2,506,000 (17,278) | 2,676,400 (18,453) | 2,737,700 (18,876) | 2,808,700 (19,365) |
| 40 (4) | 1,295,700 (8,934) | 1,621,400 (11,179) | 1,757,500 (12,118) | 2,052,200 (14,149) | 2,167,400 (14,944) | 2,307,300 (15,908) |
| 70 (21) | 458,600 (3,162) | 686,200 (4,731) | 802,000 (5,530) | 1,102,400 (7,601) | 1,240,800 (8,555) | 1,426,800 (9,837) |
| 100 (38) | 128,600 (887) | 208,700 (1,439) | 256,700 (1,770) | 406,900 (2,805) | 490,100 (3,379) | 617,700 (4,259) |
| 130 (54) | 43,900 (303) | 66,300 (457) | 80,300 (554) | 128,600 (887) | 158,400 (1,092) | 208,800 (1,440) |

**Table 2-18. Dynamic Modulus Input Values for N7-HP AC Mix.**

| E*, psi (MPa) | Frequency (Hz) | | | | | |
|---|---|---|---|---|---|---|
| Temperature, °F (°C) | 0.1 | 0.5 | 1 | 5 | 10 | 25 |
| 14 (-10) | 2,116,700 (14,594) | 2,372,600 (16,358) | 2,467,300 (17,011) | 2,652,300 (18,287) | 2,718,100 (18,741) | 2,793,700 (19,262) |
| 40 (4) | 1,147,700 (7,913) | 1,493,300 (10,296) | 1,640,800 (11,313) | 1,964,000 (13,541) | 2,091,000 (14,417) | 2,245,500 (15,482) |
| 70 (21) | 340,600 (2,348) | 541,500 (3,734) | 649,500 (4,478) | 944,000 (6,509) | 1,085,300 (7,483) | 1,279,900 (8,825) |
| 100 (38) | 85,500 (590) | 141,800 (978) | 177,200 (1,222) | 295,400 (2,037) | 364,900 (2,516) | 476,300 (3,284) |
| 130 (54) | 30,400 (210) | 44,400 (306) | 53,300 (367) | 85,000 (586) | 105,300 (726) | 140,900 (971) |

**Table 2-19. PMA Asphalt Binder Rheological Properties.**

| Asphalt Binder Properties – PMA Binder – NCAT Section S9 | | |
|---|---|---|
| Temperature, °F (°C) | G*, psi (Pa) | δ, ° |
| 168.8 (76) | 0.41045 (2,830) | 67.9 |
| 179.6 (82) | 0.24076 (1,660) | 70.0 |

**Table 2-20. HP Asphalt Binder Rheological Properties.**

| Asphalt Binder Properties – HP Binder – NCAT Section N7 | | |
|---|---|---|
| Temperature, °F (°C) | G*, psi (Pa) | δ, ° |
| 190.4 (88) | 0.34809 (2,400) | 50.4 |
| 201.2 (94) | 0.24149 (1,665) | 51.3 |

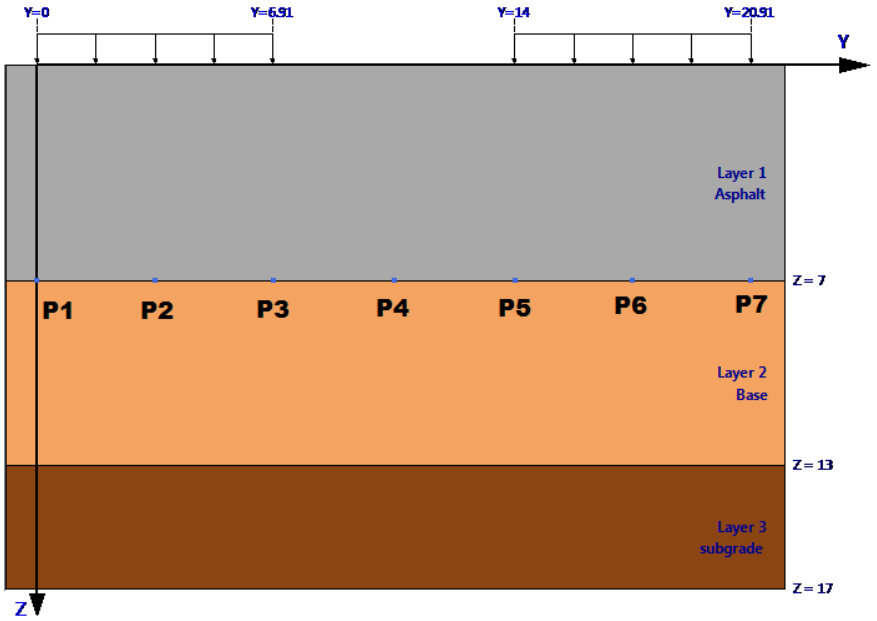


**Figure 2-24. Sketch of PMA-pavement section.**

*Static Analysis*

Table 2-21 summarizes the longitudinal and transverse strains at the bottom of the PMA AC layer. A critical tensile strain of 127.51 micro-strain was determined under the edge of the outer tire (point P5). Using Equation 2-13, this critical tensile strain resulted in 39,118,412 cycles to failure. Since both sections should be designed to show similar performance in terms of fatigue cracking, Equation 2-14 was used to determine an equivalent tensile strain of 313 micro-strain at the bottom of the HP AC layer. This led to a 3.75 inch thickness (46% reduction) for AC layer in the HP pavement section. The structural coefficient for the HP AC mix is then calculated as the ratio of the AC layer thickness of the PMA pavement to the AC layer thickness of the HP pavement times 0.44 (Equation 2-15). Accordingly, a structural coefficient of 0.82 is estimated for the HP mix based on the equivalent fatigue performance under an ESAL in a static analysis (i.e. $a_{HP\text{-}AC\text{-}Static} = 0.82$).

**Table 2-21. Longitudinal and Transverse Strains at the Bottom of PMA and HP AC Layers.**

| | PMA Section | | HP Section | |
|---|---|---|---|---|
| Point ID | $\varepsilon_{xx}$ (micro-strain) | $\varepsilon_{yy}$ (micro-strain) | $\varepsilon_{xx}$ (micro-strain) | $\varepsilon_{yy}$ (micro-strain) |
| P1 | -108.63 | -57.70 | -242.25 | -91.02 |
| P2 | -126.10 | -89.75 | -301.55 | -205.91 |
| P3 | -127.29 | -71.97 | -291.97 | -107.86 |
| P4 | -124.03 | -52.75 | -268.30 | -272.98 |
| P5 | -127.51 | -73.59 | -293.76 | -116.06 |
| P6 | -125.60 | -89.32 | -300.20 | -205.21 |
| P7 | -107.38 | -55.23 | -237.62 | -81.78 |

$$a_{HP-AC\ fat-Static} = \left(\frac{AC\ layer\ thickness\ of\ PMA\ pavement\ for\ fatigue\ in\ AC}{AC\ layer\ thickness\ of\ HP\ pavement\ for\ same\ fatigue\ in\ AC}\right) * 0.44 \qquad \textbf{Equation 2-15}$$

$$a_{HP-AC\ fat-Static} = \left(\frac{7.00}{3.75}\right) * 0.44 = 0.82$$

*Dynamic Analysis*

A critical tensile strain of 95.18 microns was determined under the inner edge of both inner and outer tires (points P3 and P5, respectively). Using Equation 2-13, this critical tensile strain resulted in 153,402,471 cycles to failure. Since both sections should be designed to show a similar performance in terms of fatigue cracking, Equation 2-14 was used to determine an equivalent tensile strain of 313 microns at the bottom of the HP AC layer (Refer to Figure 2-25). This led to a 3.50 inch thickness (50% reduction) for AC layer in the HP pavement section. The structural coefficient for the HP AC mix is then calculated as the ratio of the AC layer thickness of the PMA pavement to the AC layer thickness of the HP pavement times 0.44 (Equation 2-16). Accordingly, a structural layer coefficient of 0.88 is estimated for the HP mix based on the equivalent fatigue performance under a single ESAL in a dynamic analysis (i.e. $a_{HP\text{-}AC\text{-}dynamic}$ = 0.88).

$$a_{HP-AC-Fat-Dynamic} = \left(\frac{AC\ layer\ thickness\ of\ PMA\ pavement\ for\ fat.\ in\ AC}{AC\ layer\ thickness\ of\ HP\ pavement\ for\ same\ fat.\ in\ AC}\right) * 0.44 \qquad \textbf{Equation 2-16}$$

$$a_{HP-AC-Fat-Dynamic} = \left(\frac{7.00}{3.50}\right) * 0.44 = 0.88$$

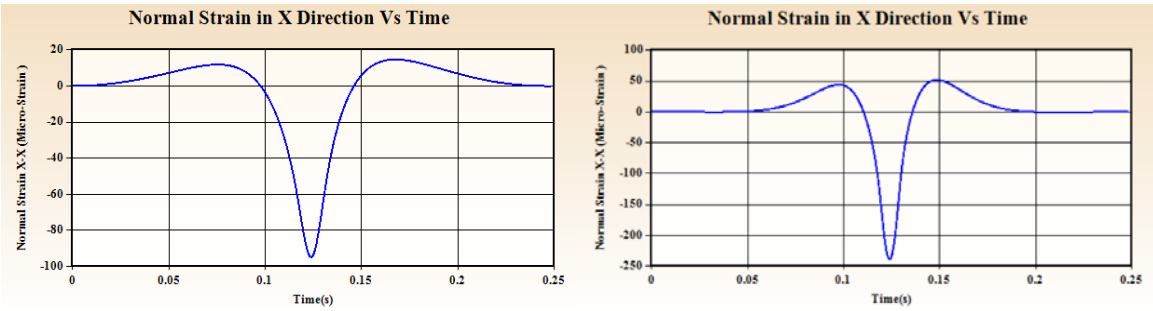


(a) (b)

**Figure 2-25. Longitudinal normal strain at P5 under dynamic loading at 45 mph: (a) PMA S9, and (b) HP N7 section.**

### 2.4.3. Summary

Four recalibration procedures and preliminary approaches were proposed to determine a new structural coefficient value for flexible pavement design of HP AC mixes ($a_{HP\text{-}AC}$) using the AASHTO 1993 Design methodology and based on the NCAT test track performance data. The first approach consisted of determining $a_{HP\text{-}AC}$ based on the rutting performance; a value of 0.54 was determined for the $a_{HP\text{-}AC}$. The second approach consisted of using the FWD backcalculation results, effective structural number, and method of equivalent thickness; a value of 0.54 was determined for the $a_{HP\text{-}AC}$. The third approach consisted of determining $a_{HP\text{-}AC}$ based on the road roughness and traffic loading; a slightly higher value of 0.57 was determined. The fourth and last

approach consisted of determining the $a_{HP\text{-}AC}$ based on fatigue data using the 3D-Move Analysis model; higher $a_{HP\text{-}AC}$ of 0.82 and 0.88 were determined for HP AC mixes under static and dynamic loading, respectively.

### 2.4.4. Findings

The first three approaches for the determination of the structural coefficient of the HP AC mix are all based on the AASHTO 1993 Guide concept with some slight variations in the analysis. Therefore, it is reasonable to expect that similar coefficients will be determined for the three approaches.

The fourth approach is based on the mechanistic analysis of the PMA and HP structures and their anticipated fatigue life. The research team wanted to present this approach to show that mechanistic-based layer coefficients maybe significantly different than the empirically determined coefficients. However, the use of the available data from the NCAT sections for the mechanistic-based approach suffered from the following serious limitations:

- Fatigue models for PMA and HP AC mixes were developed at a single temperature which does not allow the incorporation of the modulus effect. A true mechanistic analysis must incorporate the impact of AC mix modulus on the calculation of tensile strains and the determination of the fatigue life.
- No rutting models were developed for the PMA and HP AC mixes. The rutting properties from the APA and FN represent the empirical behavior of the mixtures at a single temperature and do not incorporate the modulus effect. A true mechanistic analysis must incorporate the impact of AC mix modulus on the calculation of vertical strains and the determination of the rutting life.

The large difference between the coefficients determined by the empirical approaches (1-3) and the mechanistic approach (4) should not jeopardize the applicability of the 3D-Move model for the following reasons:

- The fact that neither sections at the NCAT Test Track showed any fatigue cracking after 8.9 million ESALs indicates that the fatigue-based structural coefficients would be high which is consistent with approach 4.
- The current research will conduct fatigue and rutting testing at multiple temperatures which will allow the development of fatigue and rutting models that incorporate the impact of the modulus on the performance of the mixtures which is critical for a full mechanistic analysis.
- The current research will determine the structural coefficients based on multiple distress modes of: fatigue, rutting in AC, and total rutting and check their validity with other distresses of: top-down cracking, reflective cracking, and shoving.

The 3D-Move model has been validated through several studies to provide the same pavement analysis as the linear elastic model used in the AASHTO M-E Design when applied at static conditions (i.e. zero speed). The additional benefit of the 3D-Move model is that it incorporates vehicle speed and braking stresses.

# CHAPTER 3. EXPERIMENTAL DESIGN AND TESTS DESCRIPTION

This chapter presents the experimental design for the development of structural coefficient for HP AC mixes. It should be noted that HP AC mixes are defined as asphalt mixtures manufactured using asphalt binders modified with SBS or SB at the approximate rate of 7.5% by weight of binder. PMA AC mixes are defined as asphalt mixtures manufactured using asphalt binders modified with SBS or SB at the approximate rate of 3% by weight of binder. In addition, this chapter provides detailed information about the materials used in this study and detailed descriptions of performance tests conducted in this project.

## 3.1. EXPERIMENTAL DESIGN

The overall objectives of the experimental design are: a) define the steps necessary to carry-out a laboratory evaluation to determine the engineering properties and performance characteristics of PMA and HP AC mixes, b) define the process of incorporating the measured properties and performance characteristics into the mechanistic approach to determine the structural coefficient for HP AC mixes in Florida, and c) define the process to validate and verify the determined structural coefficient through large-scale testing (i.e., UNR PaveBox). Figure 3-1 presents a flow chart of the recommended experimental design showing the interactions among its major parts and their various components. The experimental design consists of five major parts: I) Laboratory evaluation of HP binders and AC mixes, II) Flexible pavement modeling, III) Determination of Structural Coefficients, IV) Verification: large-scale pavement testing using PaveBox, and V) development of an APT implantation plan.

The objective of the laboratory evaluation (Part I) is to determine the necessary engineering properties and performance characteristics of common PMA and HP AC mixes used in Florida. These mixes are established following the FDOT Superpave mix design specifications *(23)* using two representative sources for aggregates and asphalt binders.

The objective of the flexible pavement modeling (Part II) is to implement the developed properties and characteristics into an advanced flexible pavement modeling process to determine the responses and performance under various structural and loading conditions. In addition, initial structural coefficients will be determined for the evaluated HP AC mixes in Florida using the service life approach based on the performance life of the PMA and HP AC pavement sections (Part III).

The objective of the full-scale pavement testing using PaveBox (Part IV) is to verify the structural coefficient developed and checked in Part III using a 11x11 feet (335.3x335.3 cm) square by 7 feet (213.4 cm) height full-scale structure called “PaveBox”. The findings from Part IV will be used to make any necessary modifications to the structural coefficient for HP AC mixes determined under Part III. Finally, an implantation plan of the final recommended structural coefficient for HP AC mixes using the APT setup at FDOT facilities is provided (Part V).

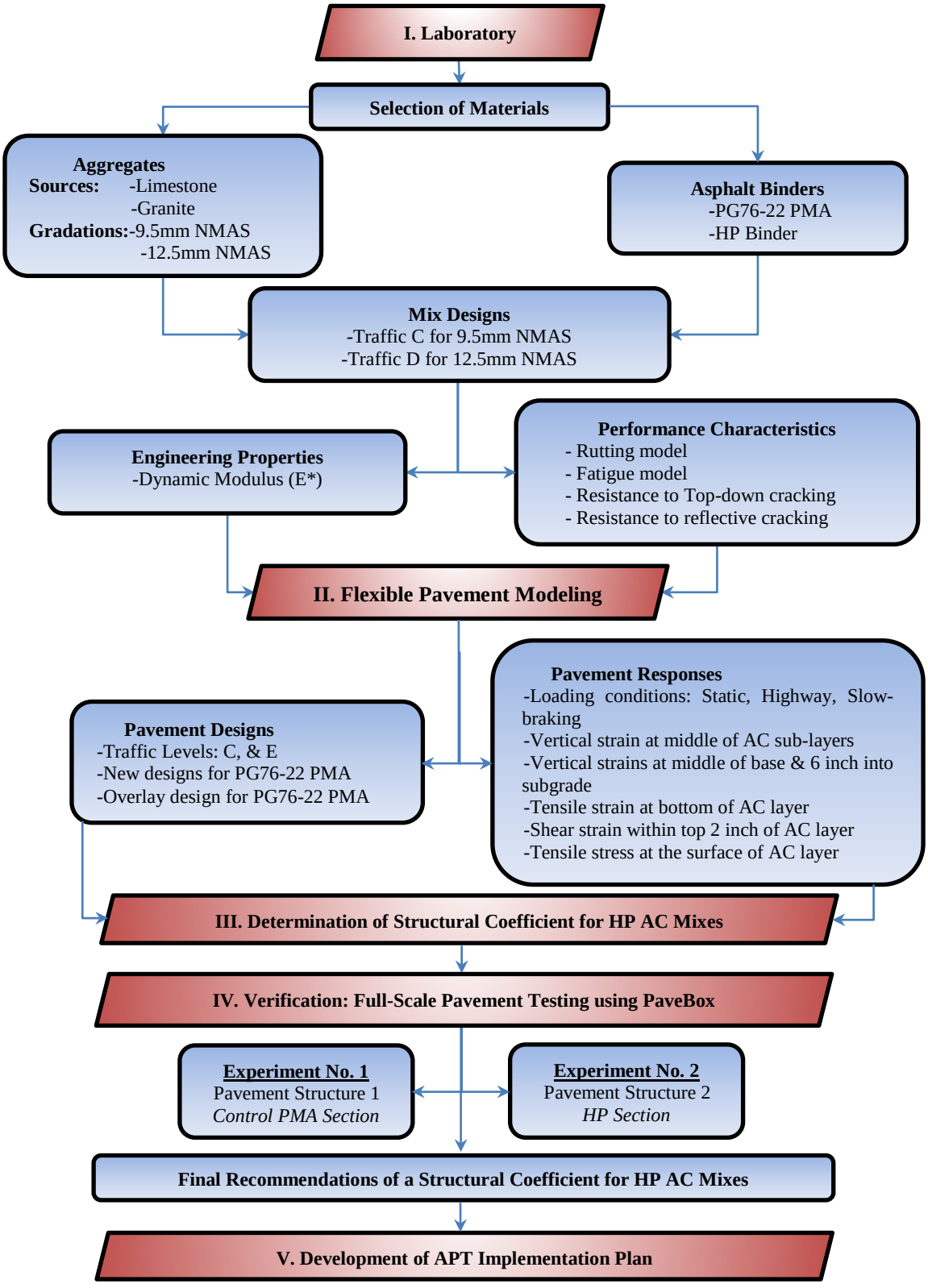


**Figure 3-1. Flowchart of the experimental plan.**

## 3.2. MATERIALS

This section involves the selection of the materials to be used in the fabrication of PMA and HP AC mixes to be evaluated in the laboratory. Two sources of asphalt binders and two sources of aggregates were recommended by the project panel as listed below:

- Asphalt binders: Ergon Asphalt and Emulsion of Jackson, MS, and Vecenergy of Rivera Beach, FL.
- Aggregates: White Rock Quarries and Junction City Mining.

### 3.2.1. Asphalt Binders

Two asphalt binder Performance Grades (PG) were targeted from each source: PG76-22PMA and HP Binder. The Ergon source was labeled as "A" and the Vecenergy source was labeled as "B". A total of ten 5-gallon buckets were obtained for each grade from each source along with the corresponding anti-strip liquid agent. All four binders are modified with SBS polymer which meets the polymer criterion of this research. The SBS contents of the PMA binders are 3.2 and 3.0% by weight of binder for Ergon and Vecenergy, respectively. The SBS contents of the HP binders are 7.6 and 8.0% by weight of binder for Ergon and Vecenergy, respectively. The grade and source of the base binder and the SBS content for each binder were provided by the suppliers (i.e., Ergon, and Vecenergy). The SBS contents of all binders meet the criteria set forth in this research; i.e., PMA binder approximately 3% and HP binder approximately 7.5% by weight of binder.

The liquid anti-strip was added in the laboratory to all sampled asphalt binders with a dosage rate of 0.5% by weight of the binder. This process was accomplished gradually throughout laboratory evaluation to ensure good effectiveness of the liquid anti-strip when mixed and stored with the asphalt binder. Figure 3-2 summarizes the steps followed to mix and incorporate the liquid anti-strip with the asphalt binder as follows:

- Heat the asphalt binder sampled in 5-gallon buckets to the mixing temperature and split it into one-gallon cans.
- Add the antistrip to the hot asphalt binder (dosage rate of 0.5% by weight of the asphalt binder).
- Mix the anti-strip thoroughly using a mechanical stirrer so there is a moderate visible recirculation for a minimum duration of 30 minutes. A heating membrane was used to control the temperature and keep it as close as possible to the mixing temperature throughout the mixing process.
- If desired, subdivide the asphalt binder into suitable portions for later use.

**Figure 3-2. Steps followed to mix the liquid anti-strip with asphalt binder.**

Table 3-1 to Table 3-4 summarize the properties of the four evaluated asphalt binders with and without anti-strip agent. The Superpave PG system *(47)* was used to determine the continuous grades of the four binders to confirm their PGs. All four binders met the corresponding FDOT Specifications 2018 *(23)* with the exception of the Ergon HP Binder without anti-strip agent with a percent recovery $R_{3.2}$ of 89.5%, which is slightly lower than the minimum required $R_{3.2}$ of 90%. However, the same Ergon HP Binder with the anti-strip agent met the specification with a $R_{3.2}$ of 92.5%. Since all binders will be used with anti-strip agents, this issue should not be of any concern to the research. The measured binders' data show a wide range in the measured properties of the binders obtained from Ergon and Vecenergy at all levels of temperature and aging stages. This will ensure wide applicability of the research findings.

### 3.2.2. Aggregates

Two aggregates' mineralogy were targeted in this study: Southeast Florida limestone and Georgia Granite. The Southeast Florida limestone was obtained from White Rock Quarries and labeled as "FL." The Georgia Granite was obtained from Junction City Mining and labeled as "GA." Approximately six tons of aggregates were obtained from each source along with the corresponding reclaimed asphalt pavement (RAP) materials.

Two aggregate gradations were evaluated from each aggregate source with Nominal Maximum Aggregate Size (NMAS) of 9.5 mm and 12.5 mm. Gradation analyses were conducted for all aggregate stockpiles and RAP materials *(61)(62)*. The stockpile labeled "Generated Dust" (i.e., FL P200 or GA P200) was produced in the laboratory to generate passing No.200 (75-μm) materials. This stockpile was added to the Job Mix Formula (JMF) gradation to account for the dust generated during the production of the AC mixes.

Table 3-5 presents the gradations of all the individual stockpiles sampled from the FL source. Table 3-6 and Table 3-7 present the gradations of the stockpiles sampled from the GA source and used for gradations with NMAS of 9.5 mm and 12.5 mm, respectively.

Table 3-8 to Table 3-13 coupled with Figure 3-3 to Figure 3-8 present the stockpiles percent and JMF gradation for the various mixtures from the FL and GA aggregate sources. RAP materials (i.e., milled materials stockpile) were only used with AC mixtures manufactured using GA aggregates and PMA asphalt binders. It should be mentioned that the percent of generated dust added to each mixture was established based on the analysis of typical FDOT mix designs. In

addition, it should be noted that the recommended JMF gradations shown below were solely based on the blending of the stockpiles from each aggregate source.

**Table 3-1. Properties of the PMA Binder from Ergon Asphalt and Emulsion.**

| **SUPERPAVE PG ASPHALT BINDER: *ERGON PG76-22PMA*** | | | | |
|---|---|---|---|---|
| **Test and Method** | **Conditions** | **Measurements** | | **FDOT Specification 2018 Minimum/Maximum Value** |
| | | **Without Anti-Strip Agent** | **With Anti-Strip Agent** | |
| Source of base binder | | PG64-22 Exxon | PG64-22 Exxon | -- |
| Modifier | Polymer | SBS, 3.2% by weight of binder | SBS, 3.2% by weight of binder | -- |
| Additive | Anti-Strip Agent | -- | AD-here LOF 65-00 EU, 0.5% by weight of binder | -- |
| Original Binder | | | | |
| Flash Point, AASHTO T 48-06 *(56)* | Cleveland Open Cup | 581°F | 565°F | Minimum 450°F |
| Rotational Viscosity, AASHTO T 316-13 *(57)* | 275°F | 1.553 Pa.s | 1.504 Pa.s | Maximum 3.000 Pa.s |
| Dynamic Shear Rheometer, AASHTO T 315-12 *(24)* | G*/sin $\delta$ @ 76°C | 1.38 kPa | 1.35 kPa | Minimum 1.00 kPa |
| | Phase Angle, $\delta$ @ 76°C | 65 degrees | 66 degrees | Maximum 75 degrees |
| Rolling Thin Film Oven Test Residues (AASHTO T240-13) *(58)* | | | | |
| Rolling Thin Film Oven, AASHTO T 240-13 *(58)* | Mass Change | 0.17% | 0.85% | Maximum 1.00% |
| Multiple Stress Creep Recovery AASHTO M 332-14 *(59)* | $J_{nr,\ 3.2}$ @ 67°C | 0.19 $kPa^{-1}$ | 0.24 $kPa^{-1}$ | Maximum 1.00 $kPa^{-1}$ |
| | $J_{nr,diff}$ @ 67°C | 1.6% | 2.9% | -- |
| | $\%R_{3.2}$ @ 67°C | 84.1% | 81.4% | $\%R_{3.2} \geq 29.37(J_{nr,\ 3.2})^{-0.2633}$ $\geq 45.2\%$ |
| Pressure Aging Vessel Residue @ 100°C (AASHTO R 28-12) *(60)* | | | | |
| Dynamic Shear Rheometer, AASHTO T 315-12 *(24)* | G*sin $\delta$ @ 26.5°C, 10 rad/sec | 1,747 kPa | 2,282 kPa | Maximum 5000 kPa |
| Creep Stiffness, AASHTO T 313-12 *(30)* | S (Stiffness) @ -12°C, 60 sec.[(a)] | 155.0 MPa | 155.5 MPa | Maximum 300.0 MPa |
| | m-value @ -12°C, 60 sec.[(a)] | 0.336 | 0.355 | Minimum 0.300 |
| Continuous Grade[(b)] | -- | PG76.4-24.7 | PG75.7-26.5 | -- |

(a) Testing temperature is 10°C warmer than the actual low PG.

(b) Continuous grade based on AASHTO M320 *(47)*.

## Table 3-2. Properties of the HP Binder from Ergon Asphalt and Emulsion.

| SUPERPAVE PG ASPHALT BINDER: *ERGON HP Binder* | | | | |
|---|---|---|---|---|
| **Test and Method** | **Conditions** | **Measurements** | | **FDOT Specification 2018 Minimum/Maximum Value** |
| | | **Without Anti-Strip Agent** | **With Anti-Strip Agent** | |
| Source of base binder | -- | PG52-28 Exxon/Imperial | PG52-28 Exxon/Imperial | -- |
| Modifier | Polymer | SBS, 7.6% by weight of binder | SBS, 7.6% by weight of binder | -- |
| Additive | Anti-Strip Agent | -- | AD-here LOF 65-00 EU, 0.5% by weight of binder | -- |
| Original Binder | | | | |
| Flash Point, AASHTO T 48-06 (2015) *(56)* | Cleveland Open Cup | 536°F | 549°F | Minimum 450°F |
| Rotational Viscosity, AASHTO T 316-13 *(57)* | 275°F | 3.395 Pa.s | 3.450 Pa.s | Maximum 3.000 Pa.s[(a)] |
| Dynamic Shear Rheometer, AASHTO T 315-12 *(24)* | G*/sin $\delta$ @ 76°C | 4.62 kPa | 4.53 kPa | Minimum 1.00 kPa |
| | Phase Angle, $\delta$ @ 76°C | 47 degrees | 49 degrees | Maximum 65 degrees |
| Rolling Thin Film Oven Test Residues (AASHTO T240-13) *(58)* | | | | |
| Rolling Thin Film Oven, AASHTO T 240-13 *(58)* | Mass Change | 0.28% | 0.34% | Maximum 1.00 % |
| Multiple Stress Creep Recovery AASHTO M 332-14 *(59)* | $J_{nr,\ 3.2}$ @ 76°C | 0.08 $kPa^{-1}$ | 0.06 $kPa^{-1}$ | Maximum 0.10 $kPa^{-1}$ |
| | $J_{nr,diff}$ @ 76°C | 37.3 % | 19.9 % | -- |
| | $\%R_{3.2}$ @ 76°C | 89.5 % | 92.5 % | $\%R_{3.2} \geq 90.0$ % |
| Pressure Aging Vessel Residue @ 100°C (AASHTO R 28-12) *(60)* | | | | |
| Dynamic Shear Rheometer, AASHTO T 315-12 *(24)* | G*sin $\delta$ @ 26.5°C, 10 rad/sec | 636 kPa | 791 kPa | Maximum 5000 kPa |
| Creep Stiffness, AASHTO T 313-12 *(30)* | S (Stiffness) @ -12°C, 60 sec.[(b)] | 52.0 MPa | 49.0 MPa | Maximum 300 MPa |
| | m-value @ -12°C, 60 sec.[(b)] | 0.413 | 0.418 | Minimum 0.300 |
| Continuous Grade[(c)] | -- | PG93.5-33.5 | PG93.5-34.6 | -- |

(a) Binders with values higher than 3 Pa.s should be used with caution and only after consulting with the supplier as to any special handling procedures, including pumping capabilities *(23)*.

(b) Testing temperature is 10°C warmer than the actual low PG.

(c) Continuous grade based on AASHTO M320 *(47)*.

## Table 3-3. Properties of the PMA Binder from Vecenergy.

| SUPERPAVE PG ASPHALT BINDER: *VCENERGY PG76-22PMA* | | | | |
|---|---|---|---|---|
| **Test and Method** | **Conditions** | **Measurements** | | **FDOT Specification 2018 Minimum/Maximum Value** |
| | | **Without Anti-Strip Agent** | **With Anti-Strip Agent** | |
| Source of base binder | -- | PG67-22 Marathon | PG67-22 Marathon | -- |
| Modifier | Polymer | SBS, 3.0% by weight of binder | SBS, 3.0% by weight of binder | -- |
| Additive | Anti-Strip Agent | -- | AD-here LOF 65-00 EU, 0.5% by weight of binder | -- |
| Original Binder | | | | |
| Flash Point, AASHTO T 48-06 (2015) *(56)* | Cleveland Open Cup | 601°F | 604°F | Minimum 450°F |
| Rotational Viscosity, AASHTO T 316-13 *(57)* | 275°F | 1.207 Pa.s | 1.173 Pa.s | Maximum 3.000 Pa.s |
| Dynamic Shear Rheometer, AASHTO T 315-12 *(24)* | G*/sin $\delta$ @ 76°C | 1.34 kPa | 1.30 kPa | Minimum 1.00 kPa |
| | Phase Angle, $\delta$ @ 76°C | 71 degrees | 71 degrees | Maximum 75 degrees |
| Rolling Thin Film Oven Test Residues (AASHTO T240-13) *(58)* | | | | |
| Rolling Thin Film Oven, AASHTO T 240-13 *(58)* | Mass Change | 0.15 % | 0.25 % | Maximum 1.00 % |
| Multiple Stress Creep Recovery AASHTO M 332-14 *(59)* | $J_{nr,\ 3.2}$ @ 67°C | 0.54 $kPa^{-1}$ | 0.72 $kPa^{-1}$ | Maximum 1.00 $kPa^{-1}$ |
| | $J_{nr,diff}$ @ 67°C | 14.5 % | 22.3 % | Maximum $J_{nr,\ diff}$ = 75.0% |
| | $\%R_{3.2}$ @ 67°C | 46.0 % | 48.5 % | $\%R_{3.2} \geq 29.37(J_{nr,\ 3.2})^{-0.2633}$ $\geq$ 34.6 % |
| Pressure Aging Vessel Residue @ 100°C (AASHTO R 28-12) *(60)* | | | | |
| Dynamic Shear Rheometer, AASHTO T 315-12 *(24)* | G*sin $\delta$ @ 26.5°C, 10 rad/sec | 3,072 kPa | 2,548 kPa | Maximum 5000 kPa |
| Creep Stiffness, AASHTO T 313-12 *(30)* | S (Stiffness) @ -12°C, 60 sec.[a] | 146.5 MPa | 155.0 MPa | Maximum 300 MPa |
| | m-value @ -12°C, 60 sec.[a] | 0.339 | 0.341 | Minimum 0.300 |
| Continuous Grade[b] | -- | PG76.1-24.3 | PG75.8-24.6 | -- |

(a) Testing temperature is 10°C warmer than the actual low PG.
(b) Continuous grade based on AASHTO M320 *(47)*.

## Table 3-4. Properties of the HP Binder from Vecenergy.

| SUPERPAVE PG ASPHALT BINDER: *VCENERGY HP Binder* | | | | |
|---|---|---|---|---|
| **Test and Method** | **Conditions** | **Measurements** | | **FDOT Specification 2018 Minimum/Maximum Value** |
| | | **Without Anti-Strip Agent** | **With Anti-Strip Agent** | |
| Source of base binder | -- | PG52-28 Marathon | PG52-28 Marathon | -- |
| Modifier | Polymer | SBS, 8.0% by weight of binder | SBS, 8.0% by weight of binder | -- |
| Additive | Anti-Strip Agent | -- | AD-here LOF 65-00 EU, 0.5% by weight of binder | -- |
| Original Binder | | | | |
| Flash Point, AASHTO T 48-06 (2015) *(56)* | Cleveland Open Cup | 606°F | 597°F | Minimum 450°F |
| Rotational Viscosity, AASHTO T 316-13 *(57)* | 275°F | 3.439 Pa.s | 3.444 Pa.s | Maximum 3.000 Pa.s[(a)] |
| Dynamic Shear Rheometer, AASHTO T 315-12 *(24)* | G*/sin $\delta$ @ 76°C | 4.83 kPa | 4.72 kPa | Minimum 1.00 kPa |
| | Phase Angle, $\delta$ @ 76°C | 38 degrees | 36 degrees | Maximum 75 degrees |
| Rolling Thin Film Oven Test Residues (AASHTO T240-13) *(58)* | | | | |
| Rolling Thin Film Oven, AASHTO T 240-13 *(58)* | Mass Change | 0.12 % | 0.18 % | Maximum 1.00 % |
| Multiple Stress Creep Recovery AASHTO M 332-14 *(59)* | $J_{nr,\ 3.2}$ @ 76°C | 0.02 $kPa^{-1}$ | 0.02 $kPa^{-1}$ | Maximum 0.10 $kPa^{-1}$ |
| | $J_{nr,diff}$ @ 76°C | 9.0 % | 9.6 % | -- |
| | $\%R_{3.2}$ @ 76°C | 97.65 % | 97.73 % | $\%R_{3.2} \geq 90.0$ % |
| Pressure Aging Vessel Residue @ 100°C (AASHTO R 28-12) *(60)* | | | | |
| Dynamic Shear Rheometer, AASHTO T 315-12 *(24)* | G*sin $\delta$ @ 26.5°C, 10 rad/sec | 784 kPa | 774 kPa | Maximum 5000 kPa |
| Creep Stiffness, AASHTO T 313-12 *(30)* | S (Stiffness) @ -12°C, 60 sec.[(b)] | 46.2 MPa | 52.6 MPa | Maximum 300 MPa |
| | m-value @ -12°C, 60 sec.[(b)] | 0.433 | 0.443 | Minimum 0.300 |
| Continuous Grade[(c)] | -- | PG99.7-30.0 | PG98.5-30.1 | -- |

(a) Binders with values higher than 3 Pa.s should be used with caution and only after consulting with the supplier as to any special handling procedures, including pumping capabilities *(23)*.

(b) Testing temperature is 10°C warmer than the actual low PG.

(c) Continuous grade based on AASHTO M320 *(47)*.

**Table 3-5. Stockpiles Gradations for the FL Aggregate: NMAS 9.5 and 12.5 mm.**

| SIEVE SIZE | Stockpile ID | | | |
|---|---|---|---|---|
| | S1A Stone C41 | S1B Stone C51 | Screenings F22 | FL P200 |
| 1” (25.0 mm) | 100.0 | 100.0 | 100.0 | 100.0 |
| 3/4” (19.00 mm) | 99.6 | 100.0 | 100.0 | 100.0 |
| 1/2” (12.50 mm) | 60.8 | 99.7 | 99.9 | 100.0 |
| 3/8” (9.50 mm) | 12.1 | 91.4 | 99.8 | 100.0 |
| No.4 (4.75 mm) | 2.1 | 17.9 | 99.5 | 100.0 |
| No.8 (2.36 mm) | 2.0 | 6.3 | 90.5 | 100.0 |
| No.16 (1.18 mm) | 2.0 | 5.0 | 75.0 | 100.0 |
| No.30 (0.600 mm) | 1.9 | 4.4 | 60.7 | 100.0 |
| No.50 (0.300 mm) | 1.7 | 3.8 | 39.2 | 100.0 |
| No.100 (0.150 mm) | 1.4 | 2.8 | 9.1 | 100.0 |
| No.200 (0.075 mm) | 1.0 | 2.0 | 2.7 | 100.0 |

**Table 3-6. Stockpiles Gradations for the GA Aggregate: NMAS 9.5 mm.**

| SIEVE SIZE | Stockpile ID | | | | | | |
|---|---|---|---|---|---|---|---|
| | SR-8_334 | S1B Stone C53 | Screenings F22 | Screenings F23 | Sand 334-MS | Sand 334-LS | GA P200 |
| 3/4” (19.00 mm) | 100.0 | 100.0 | 100.0 | 100.0 | 100.0 | 100.0 | 100.0 |
| 1/2” (12.50 mm) | 97.8 | 100.0 | 100.0 | 100.0 | 100.0 | 100.0 | 100.0 |
| 3/8” (9.50 mm) | 89.6 | 98.0 | 100.0 | 100.0 | 100.0 | 100.0 | 100.0 |
| No.4 (4.75 mm) | 55.7 | 35.0 | 98.0 | 98.0 | 100.0 | 100.0 | 100.0 |
| No.8 (2.36 mm) | 34.1 | 4.0 | 73.0 | 77.0 | 97.0 | 100.0 | 100.0 |
| No.16 (1.18 mm) | 25.3 | 3.0 | 47.0 | 53.0 | 78.0 | 100.0 | 100.0 |
| No.30 (0.600 mm) | 20.1 | 2.0 | 32.0 | 38.0 | 40.0 | 88.0 | 100.0 |
| No.50 (0.300 mm) | 13.9 | 1.0 | 21.0 | 29.0 | 13.0 | 43.0 | 100.0 |
| No.100 (0.150 mm) | 8.5 | 1.0 | 13.0 | 20.0 | 1.0 | 9.0 | 100.0 |
| No.200 (0.075 mm) | 4.8 | 1.0 | 5.5 | 15.0 | 1.0 | 4.0 | 100.0 |

**Table 3-7. Stockpiles Gradations for the GA Aggregate: NMAS 12.5 mm.**

| SIEVE SIZE | Stockpile ID | | | | | | | |
|---|---|---|---|---|---|---|---|---|
| | Crushed RAP | S1A Stone C47 | S1B Stone C53 | Screenings F22 | Screenings F23 | Sand 334-LS | Sand F01 | GA P200 |
| 3/4” (19.00 mm) | 100.0 | 100.0 | 100.0 | 100.0 | 100.0 | 100.0 | 100.0 | 100.0 |
| 1/2” (12.50 mm) | 91.8 | 97.0 | 100.0 | 100.0 | 100.0 | 100.0 | 100.0 | 100.0 |
| 3/8” (9.50 mm) | 85.5 | 60.0 | 98.0 | 100.0 | 100.0 | 100.0 | 100.0 | 100.0 |
| No.4 (4.75 mm) | 61.2 | 15.0 | 35.0 | 98.0 | 98.0 | 100.0 | 100.0 | 100.0 |
| No.8 (2.36 mm) | 44.7 | 4.0 | 4.0 | 73.0 | 77.0 | 100.0 | 100.0 | 100.0 |
| No.16 (1.18 mm) | 36.6 | 2.0 | 3.0 | 47.0 | 53.0 | 100.0 | 99.0 | 100.0 |
| No.30 (0.600 mm) | 29.1 | 1.0 | 2.0 | 32.0 | 38.0 | 88.0 | 87.0 | 100.0 |
| No.50 (0.300 mm) | 18.3 | 1.0 | 1.0 | 21.0 | 29.0 | 43.0 | 53.0 | 100.0 |
| No.100 (0.150 mm) | 8.1 | 1.0 | 1.0 | 13.0 | 20.0 | 9.0 | 17.0 | 100.0 |
| No.200 (0.075 mm) | 4.1 | 1.0 | 1.0 | 5.5 | 15.0 | 4.0 | 0.3 | 100.0 |

**Table 3-8. Stockpiles Percent for the FL Aggregate: 9.5 mm NMAS Mixes with PMA and HP Asphalt Binders.**

| Product Description | Product Code | Producer Name | Product Name | Plant/Pit Number | Bin Percentage |
|---|---|---|---|---|---|
| S1B Stone | C51 | White Rock Quarries | S1B Stone | 87339 | 44.25 |
| Screenings | F22 | White Rock Quarries | Screenings | 87339 | 54.25 |
| Generated Dust | -- | -- | FL P200 | -- | 1.50 |

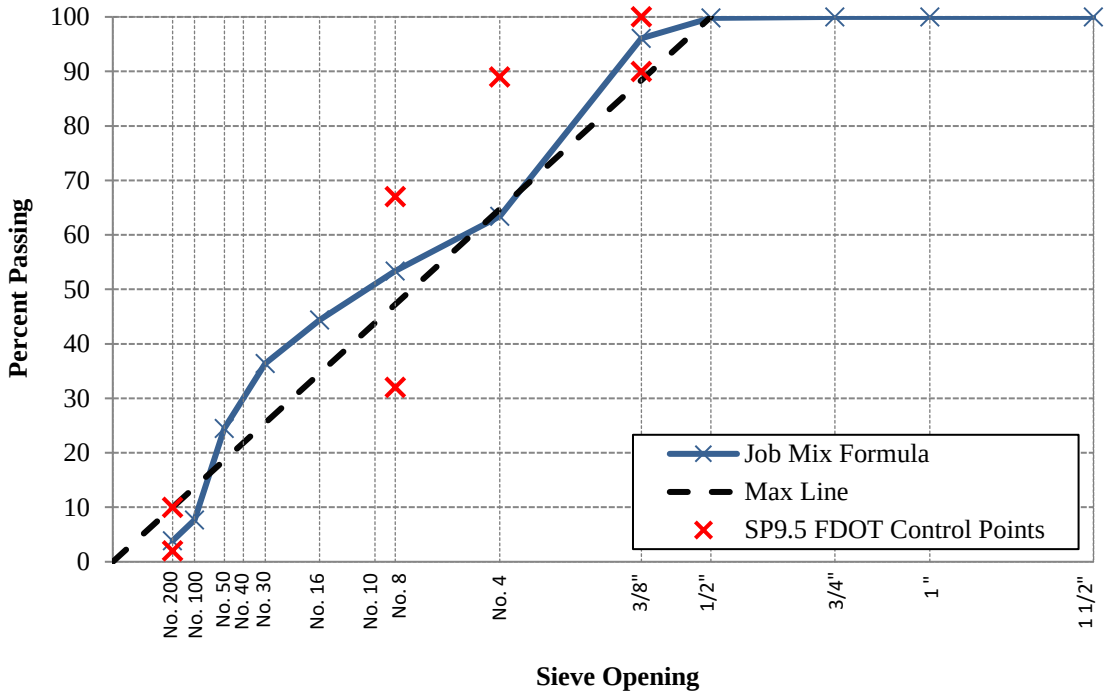


**Figure 3-3. JMF gradation for the FL aggregate: 9.5 mm NMAS mixes with PMA and HP asphalt binders.**

**Table 3-9. Stockpiles Percent for the FL Aggregate: 12.5 mm NMAS Mixes with PMA and HP Asphalt Binders.**

| Product Description | Product Code | Producer Name | Product Name | Plant/Pit Number | Bin Percentage |
|---|---|---|---|---|---|
| S1A Stone | C41 | White Rock Quarries | S1A Stone | 87339 | 13.50 |
| S1B Stone | C51 | White Rock Quarries | S1B Stone | 87339 | 31.50 |
| Screenings | F22 | White Rock Quarries | Screenings | 87339 | 53.50 |
| Generated Dust | -- | -- | FL P200 | -- | 1.50 |

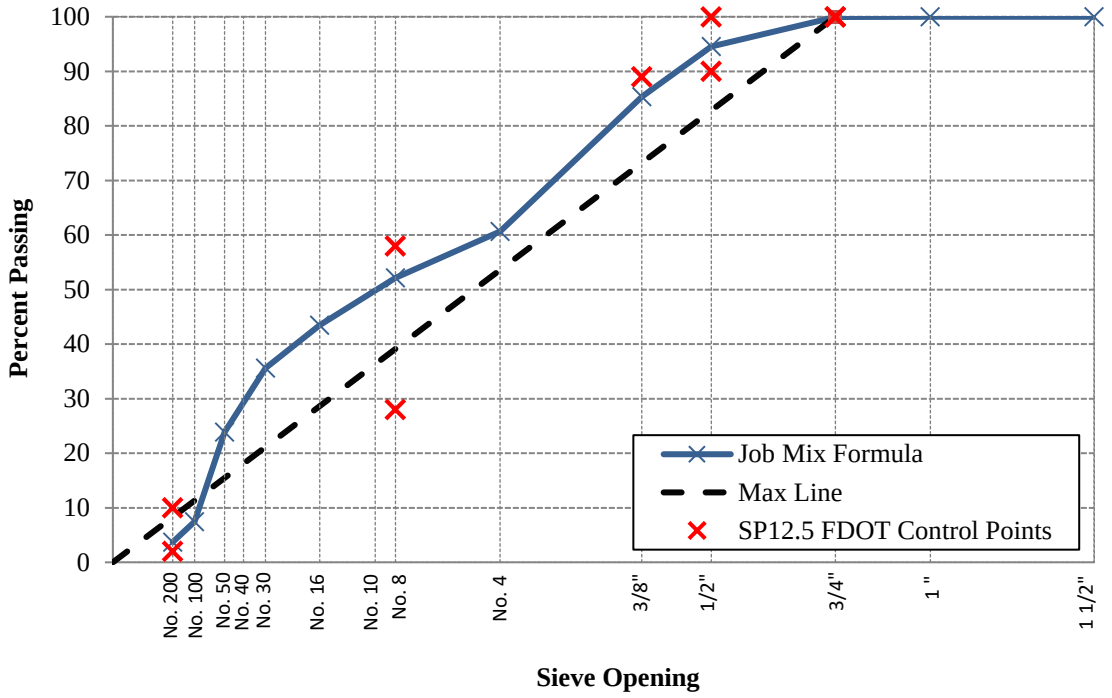


**Figure 3-4. JMF gradation for the FL aggregate: 12.5 mm NMAS mixes with PMA and HP asphalt binders.**

**Table 3-10. Stockpiles Percent for the GA Aggregate: 9.5 mm NMAS Mixes with PMA Asphalt Binders.**

| Product Description | Product Code | Producer Name | Product Name | Plant/Pit Number | Bin Percentage |
|---|---|---|---|---|---|
| Milled Material | 334-MM | Anderson Columbia Company. Inc. | 432737-1-52-01 (SR-8) | A0716 | 20.00 |
| S1B Stone | C53 | Junction City Mining | #89 Stone | GA553 | 31.95 |
| Screenings | F22 | Junction City Mining | W-10 Screenings | GA553 | 11.95 |
| Screenings | F23 | Junction City Mining | M-10 Screenings | GA553 | 21.95 |
| Sand | 334-MS | Mossy Head Sand Mine | Mossy Head | -- | 13.95 |
| Generated Dust | -- | -- | GA P200 | -- | 0.20 |

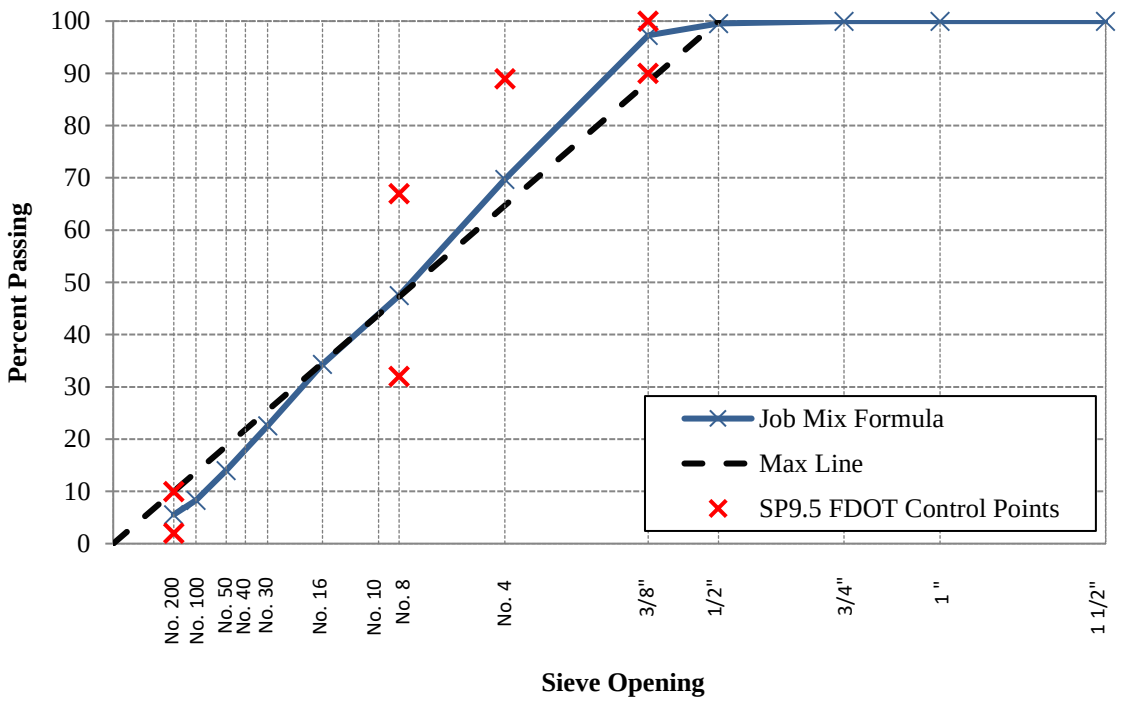


**Figure 3-5. JMF gradation for the GA aggregate: 9.5 mm NMAS mixes with PMA asphalt binders.**

**Table 3-11. Stockpiles Percent for the GA Aggregate: 12.5 mm NMAS Mixes with PMA Asphalt Binders.**

| Product Description | Product Code | Producer Name | Product Name | Plant/Pit Number | Bin Percentage |
|---|---|---|---|---|---|
| Crushed RAP | 334-CR | Anderson Columbia Company | 1-15 | A0716 | 20.00 |
| S1A Stone | C47 | Junction City Mining | #78 Stone | GA553 | 22.95 |
| S1B Stone | C53 | Junction City Mining | #89 Stone | GA553 | 14.95 |
| Screenings | F22 | Junction City Mining | W-10 Screenings | GA553 | 29.95 |
| Sand | F01 | Vulcan Materials Company | Silica Sand | 11057 | 11.95 |
| Generated Dust | -- | -- | GA P200 | -- | 0.20 |

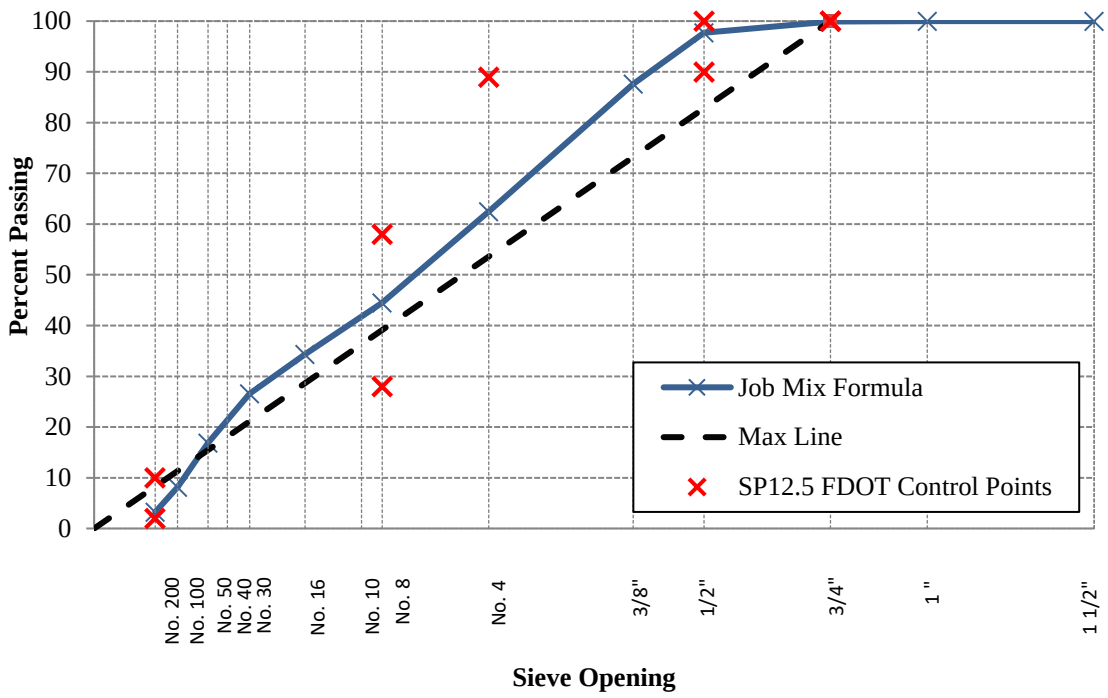


**Figure 3-6. JMF gradation for the GA aggregate: 12.5 mm NMAS mixes with PMA asphalt binders.**

**Table 3-12. Stockpiles Percent for the GA Aggregate: 9.5 mm NMAS Mixes with HP Asphalt Binders.**

| Product Description | Product Code | Producer Name | Product Name | Plant/Pit Number | Bin Percentage |
|---|---|---|---|---|---|
| S1B Stone | C53 | Junction City Mining | #89 Stone | GA553 | 33.95 |
| Screenings | F22 | Junction City Mining | W-10 Screenings | GA553 | 33.95 |
| Screenings | F23 | Junction City Mining | M-10 Screenings | GA553 | 15.95 |
| Sand | 334-LS | Anderson Columbia Company, Inc. | Blossom Loop | -- | 15.95 |
| Generated Dust | -- | -- | GA P200 | -- | 0.20 |

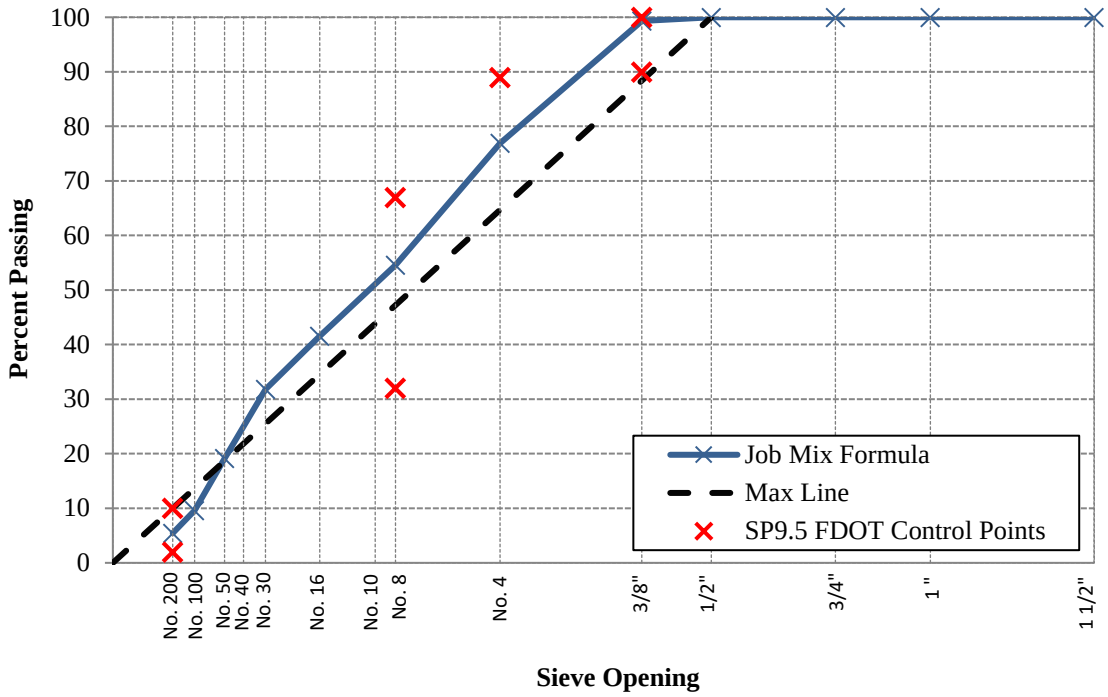


**Figure 3-7. JMF gradation for the GA aggregate: 9.5 mm NMAS mixes with HP asphalt binders.**

**Table 3-13. Stockpiles Percent for the GA Aggregate: 12.5 mm NMAS Mixes with HP Asphalt Binders.**

| Product Description | Product Code | Producer Name | Product Name | Plant/Pit Number | Bin Percentage |
|---|---|---|---|---|---|
| S1A Stone | C47 | Junction City Mining | #78 Stone | GA553 | 27.96 |
| S1B Stone | C53 | Junction City Mining | #89 Stone | GA553 | 12.96 |
| Screenings | F22 | Junction City Mining | W-10 Screenings | GA553 | 35.96 |
| Screenings | F23 | Junction City Mining | M-10 Screenings | GA553 | 11.96 |
| Sand | 334-LS | Anderson Columbia Company, Inc. | Blossom Loop | -- | 10.96 |
| Generated Dust | -- | -- | GA P200 | -- | 0.20 |

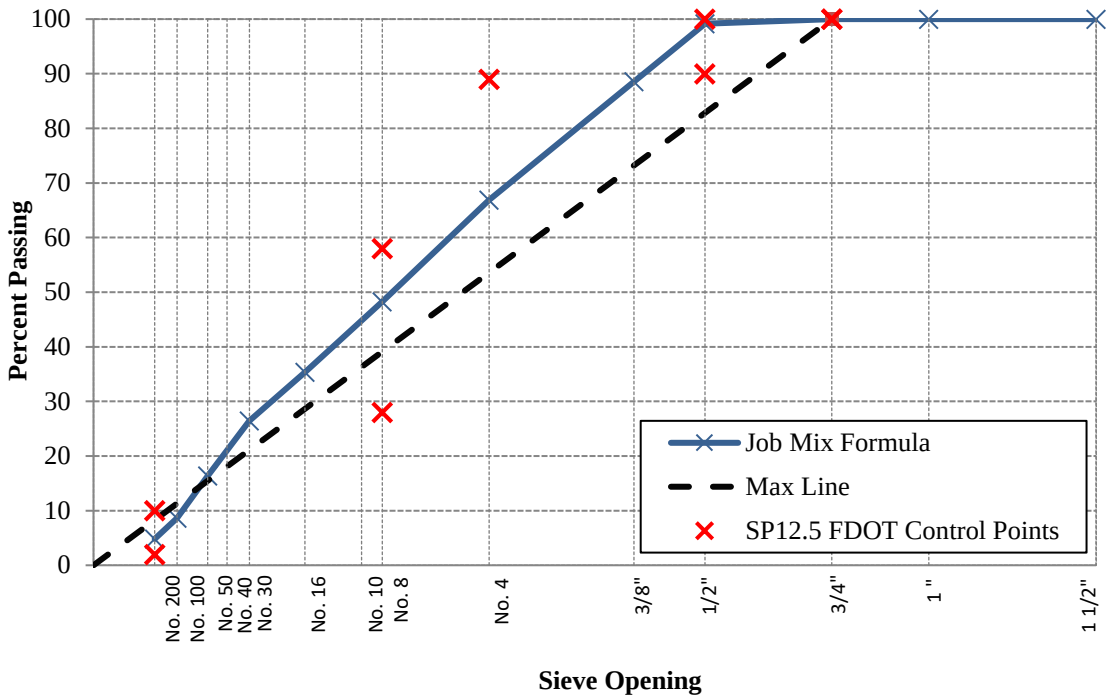


**Figure 3-8. JMF gradation for the GA aggregate: 12.5 mm NMAS mixes with HP asphalt binders.**

The following aggregate properties were measured on the recommended JMF gradations and checked against the FDOT Specifications 2018 *(23)*:

- Coarse Aggregate Angularity (ASTM D5821) *(63)*.
- Fine Aggregate Angularity (AASHTO T304) *(64)*.

- Flat and Elongated Particles (ASTM D4791) *(65)*.
- Sand Equivalent (AASHTO T176) *(66)*.

Table 3-14 summarizes the properties of the aggregates sampled from the two sources and measured on the recommended JMF gradations along with the corresponding FDOT Specifications 2018 *(23)*. The "95" and "125" in the gradation ID stands for NMAS of 9.5 mm and 12.5 mm, respectively. As shown in Table 3-14, all aggregate blends meet the respective FDOT specifications 2018 *(23)* with the exception of the coarse aggregate angularity for the Traffic Level E with a percent of two or more fractured faces of approximately 98% that is slightly lower than the required value of 100%.

**Table 3-14. Summary of Aggregate Properties for the Laboratory Aggregate Blends.**

| Traffic Level | Gradation ID | Coarse Aggregate Angularity[1] (%) | | Fine Aggregate Angularity (%) | | Flat and Elongated Particles (%) | | Sand Equivalent (%) | |
|---|---|---|---|---|---|---|---|---|---|
| | | Value | Criteria | Value | Criteria | Value | Criteria | Value | Criteria |
| C | FL95_PMA/HP | 100/92 | 85/80 | 48 | 45 Min. | 2 | 10% Max. | 84 | 45 Min. |
| | GA95_PMA | 100/97 | | 51 | | 8 | | 75 | |
| | GA95_HP | 100/93 | | 48 | | 7 | | 75 | |
| D & E | FL125_PMA/HP | 100/97 | 95/90 & 100/100 | 49 | 45 Min. | 4 | 10% Max. | 86 | 45 Min. & 50 Min. |
| | GA125_PMA | 100/98 | | 49 | | 5 | | 86 | |
| | GA125_HP | 100/98 | | 47 | | 6 | | 80 | |

[1]First value for one fractured face and second value for two fractured faces.

### 3.2.3. RAP Material

As mentioned previously, RAP materials (i.e., milled materials stockpile) were only used with AC mixtures manufactured using GA aggregates and PMA asphalt binders at a content of 20% by dry weight of aggregate (dwa). The characterization of the two RAP stockpiles (i.e., SR-8_334, and Crushed RAP) involved determination of asphalt binder content, and characterization of the recovered asphalt binder and extracted RAP aggregates. The asphalt binder content of the RAP stockpiles is required to establish the respective mix designs. On the other hand, the properties of the RAP asphalt binder are needed to determine the properties of blended asphalt binder (i.e., combination of virgin and RAP asphalt binders) using the blending chart approach.

The RAP materials were sampled, uniformly mixed, and reduced to get representative samples *(67)*. The Centrifuge method with solvent of trichloroethylene (TCE) was used for the extraction of the RAP asphalt binders. The asphalt binder content of each RAP stockpile was determined in accordance with AASHTO T164 *(68)*. The recovered aggregates were dried and evaluated in terms of size distribution to be used in establishing the aggregate gradation of the resultant mix design (i.e., virgin aggregates + RAP material) *(61) (62)*. However, the extracted asphalt binder could not be further evaluated in terms of PG grading (i.e., continuous grade) due to the potential high effect of TCE on the chemical and rheological properties of the extracted asphalt binder. Therefore, the findings in terms of asphalt binder contents of RAP stockpiles were only used for the establishment of corresponding mix designs of AC mixes containing RAP material.

Additional RAP asphalt binders were extracted using a solvent of Toluene-Ethanol at 85/15 proportion. The Toluene-Ethanol combination is anticipated to have lower impact on the chemical properties of the extracted asphalt binder. FM 3-D5404 *(69)* standard method was followed to recover the asphalt binder from the solvent solution using the rotavapor apparatus. Finally, the Superpave PG system (i.e., AASHTO M320 *(47)*) was used to determine the continuous grades of the two recovered RAP asphalt binders.

The RAP stockpile used with the GA PMA 9.5 mm mixes (i.e., SR8_334) had a binder content of 5.63% by total weight of mix (twm). The RAP stockpile used with the GA PMA 12.5 mm mixes (i.e., Crushed RAP) had a binder content of 6.68% by twm. The asphalt binders recovered from the SR-8_334 and Crushed RAP materials had a continuous grade of PG96.3-12.4 and PG103.9-11.0, respectively. These observations reveal that the Crushed RAP stockpile is stiffer and oxidized when compared with the SR-8_334 stockpile.

It has always been challenging to determine the properties of the blended asphalt binder in AC mixtures containing RAP materiel. The properties of the blended asphalt binder are required not only for establishing the resultant mix design but also to qualify the overall performance of AC pavements containing RAP material. One of the available approaches to estimate the properties of a blended asphalt binder is by developing blending charts. It should be mentioned that the blending chart approach is based on the assumption that full blending of virgin and RAP asphalt binders occurs, and a linear relationship between the critical PG temperatures (high, intermediate, and low) of the virgin and RAP asphalt binders exists. The developed blending chart can be analyzed as follows:

- For 0% RAP content, the critical temperature of the blend will be the grade of the virgin asphalt binder itself.
- For 100% RAP content, the critical temperature of the blend will be the grade of the RAP asphalt binder itself.
- The critical temperature of a blend with any RAP content can be estimated by a simple linear interpolation.

In this study, four combinations of virgin and RAP asphalt binders exist. The blending charts and the resulting PGs of the blended asphalt binders are summarized in Table 3-15 and illustrated in Figure 3-9 and Figure 3-10.

**Table 3-15. Summary of Continuous Performance Grades for Virgin, RAP, and Blended Asphalt Binders.**

| Virgin PMA Binder | RAP Content (%) | RAP Stockpile Continuous Grade | |
|---|---|---|---|
| | | SR-8_334 | Crushed RAP |
| Ergon (A) | 0[1] | 75.7-26.5 | 75.7-26.5 |
| | 20 | 79.8-23.7 | 81.3-23.4 |
| | 100[2] | 96.3-12.4 | 103.9-11.0 |
| Vecenergy (B) | 0[1] | 75.8-24.6 | 75.8-24.6 |
| | 20 | 79.9-22.2 | 81.4-21.9 |
| | 100[2] | 96.3-12.4 | 103.9-11.0 |

[1]Virign asphalt binder; [2]RAP asphalt binder.

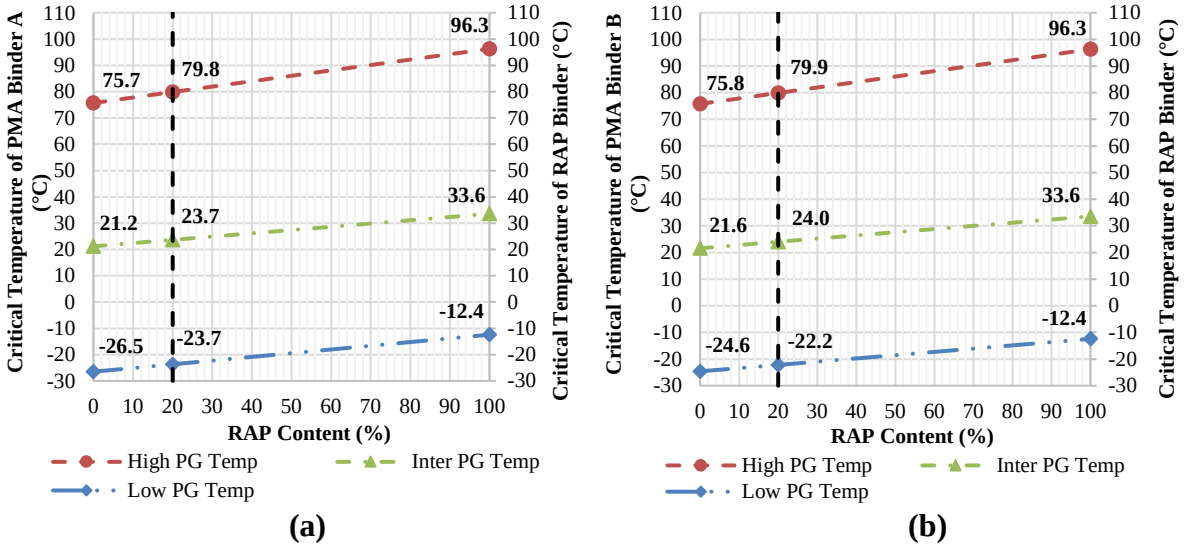


**Figure 3-9. Blending Chart for SR-8_334 RAP stockpile with: (a) virgin binder A; and (b) virgin binder B.**

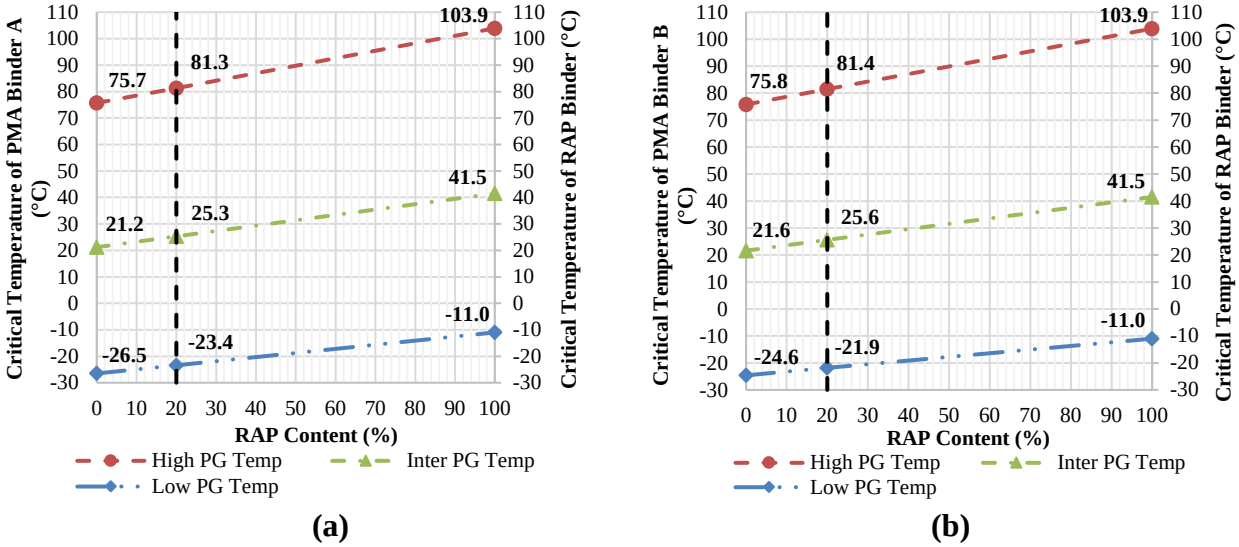


**Figure 3-10. Blending Chart for Crushed RAP stockpile with: (a) virgin binder A; and (b) virgin binder B.**

## 3.3. DESCRIPTION OF TEST METHODS

### 3.3.1. Engineering Properties: Dynamic Modulus Test

The 3D-MOVE and AASHTOWare® Pavement Mechanistic-Empirical (ME) software uses the dynamic modulus, E*, master curve of the AC layer to evaluate the structural response of the asphalt pavement under various combinations of traffic loads, speeds, and environmental conditions. The E* property of the AC mix is evaluated under various combinations of loading

and frequencies in accordance with AASHTO T378 *(39)*. The test was conducted using the Asphalt Mixture Performance Tester (AMPT) at frequencies of 10, 1, and 0.1 Hz (the 0.01 Hz was added only for the highest temperature) and at temperatures of 39, 68, and 122°F (4, 20, and 50°C) as summarized in Table 3-16.

**Table 3-16. Testing Conditions for the Dynamic Modulus.**

| Temperature | Frequencies |
|---|---|
| 39°F (4°C) | 10, 1, and 0.1 Hz |
| 68°F (20°C) | 10, 1, and 0.1 Hz |
| 122°F (50°C) | 10, 1, 0.1, and 0.01 Hz |

All mixtures were evaluated at the short-term aging conditions in accordance with AASHTO R30 *(70)*. The E* test specimen consisted of a 4.0 inch (100 mm) diameter by 6.0 inch (150 mm) height cored from the center of a SGC sample of 6.0 inch (150 mm) diameter by 7.0 inch (175 mm) height in accordance with AASHTO R83 *(71)*. All test specimens were compacted to 7.0±1.0% air voids. Using the viscoelastic behavior of asphalt mixtures (i.e., interchangeability of the effect of loading rate and temperatures) and the time-temperature superposition, the master curve was constructed for each mix in accordance with AASHTO R84 *(40)*. The data at various temperatures were shifted with respect to time until the curves merge into a smooth sigmoidal function at a single temperature knows as "*reference temperature*." The time-temperature superposition concept is only applicable within the linear viscoelastic region on thermo-rheologically simple materials such as AC mixtures. The measured master curves (one per AC mix) will be used to identify the appropriate E* for any combination of pavement temperature and traffic speed. Figure 3-11 shows the E* master curve for one of the AC mixes evaluated in this study (FL95_PMA(A) is an 9.5 mm NMAS AC mix manufactured using aggregate from FL source and PMA asphalt binder sampled from source A (refer to Section 4.1).

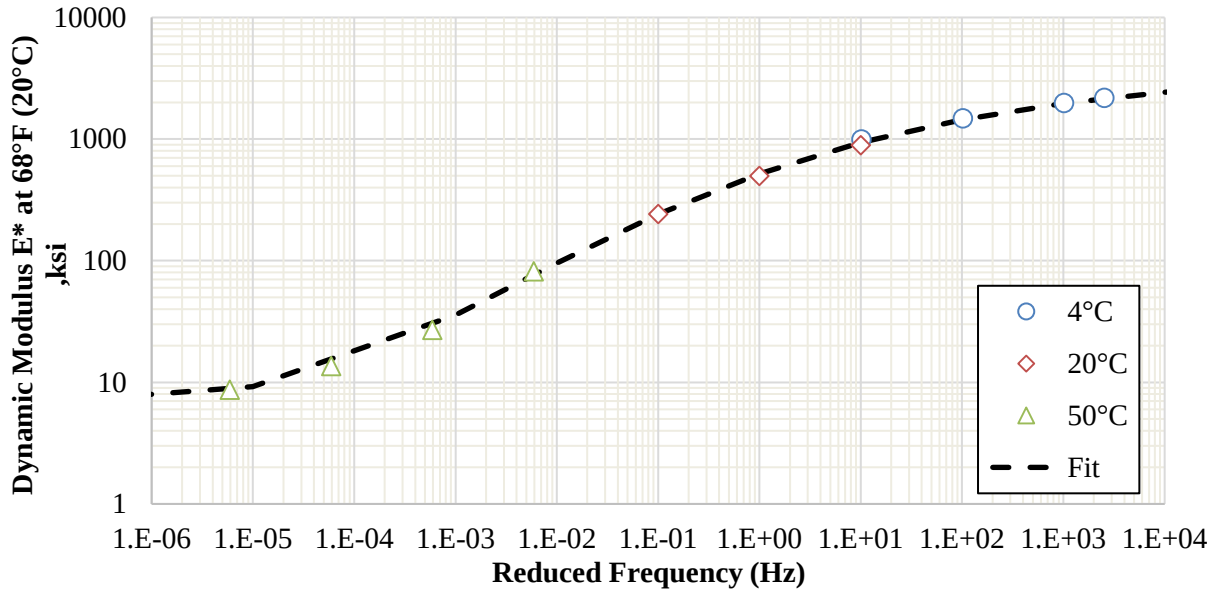


**Figure 3-11. Dynamic modulus master curve for FL95_PMA(A) AC mix.**

The general form of the dynamic modulus master curve equation is shown in a non-symmetrical sigmoidal model in Equation 3-1:

$$logE^* = \delta + \frac{E_{max} - \delta}{[1+\lambda e^{(\beta+\gamma \log(f_r))}]^{1/\lambda}} \qquad \textbf{Equation 3-1}$$

Where;
*E*:* dynamic modulus, ksi (or kPa);
*δ, β, γ, and λ*: fitting parameters;
$f_r$: reduced frequency, Hz; and
$E_{max}$: maximum value of the dynamic modulus, ksi (or kPa).

The shift factors at each temperature were calculated using the Arrhenius model (Equation 3-2 and Equation 3-3).

$$logf_r = logf + \log[a(T)] \qquad \textbf{Equation 3-2}$$

Where;
$f_r$*:* reduced frequency, Hz;
*f*: actual testing frequency, Hz; and
*a(T)*: shifting factor at temperature T.

$$\log[a(T)] = \frac{\Delta E_a}{R*ln10}\left(\frac{1}{T} - \frac{1}{T_r}\right) \qquad \textbf{Equation 3-3}$$

Where;
*a(T)*: shifting factor at temperature T;
$\Delta E_a$: activation energy;
*T*: testing temperature, °K; and
$T_r$: Reference temperature, °K.

The master curve constitutes an effective method to predict the asphalt mixture E* property beyond the testing conditions. In addition, the mechanical behavior of the asphalt mixtures is highly influenced by the phase angle. This parameter affects the distribution of the storage and loss moduli values known as elastic and viscous components of E*, respectively. An approximate relation between the dynamic modulus and phase angle is expressed in Equation 3-4.

$$\delta(w) \approx \frac{\pi}{2}\frac{d\log(|E^*|)}{d\log(w)} \qquad \textbf{Equation 3-4}$$

Where;
*δ(w)*: phase angle, degrees;
*E*:* dynamic modulus, ksi (or kPa); and
*w*: angular frequency, rad/s.

By using $T_r = 1/f_r$ and $w = 2\pi f_r$ and by calculating the first derivative of E* with respect to the angular frequency expressed in Equation 3.1, the modified phase angle model in terms of

reduced frequency at the reference temperature is expressed in Equation 3-5. Figure 3-12 shows the phase angle, *δ(w)*, master curve for one of the AC mixes evaluated in this study.

$$\delta(w) = -c * \frac{\pi}{2} * (E_{max} - \delta) * \gamma * \frac{e^{(\beta+\gamma \log(f_r))}}{[1+\lambda e^{(\beta+\gamma \log(f_r))}]^{[\frac{1+\lambda}{\lambda}]}} \qquad \textbf{Equation 3-5}$$

Where;
*δ(w)*: phase angle at reference temperature ($T_r$), degrees;
$E_{max}$: maximum value of the dynamic modulus, ksi (or kPa);
$f_r$: reduced frequency, Hz; and
*δ, β, γ, λ and c*: fitting parameters.

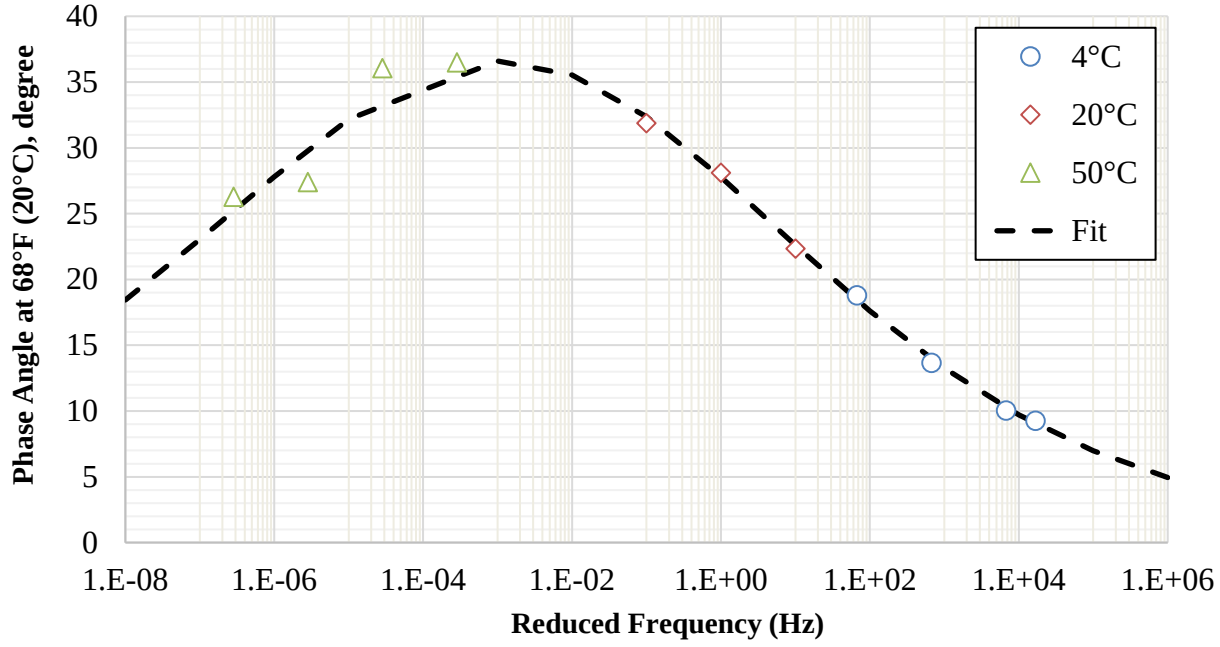


**Figure 3-12. Phase angle master curve for FL95_PMA(A) AC mix.**

### 3.3.2. Rutting Performance Characteristic

Permanent deformation can either be in the form of rutting or shoving. Rutting is caused by progressive movement of materials under repeated load. The rutting characteristics of the 16 mixtures were evaluated using the repeated load triaxial test (RLT) in accordance with the National Cooperative Highway Research Program (NCHRP) project 719 *"Calibration of Rutting Models for Structural and Mix Designs" (72).* All mixtures were evaluated at the short-term aging conditions in accordance with AASHTO R30 *(70)* since rutting is an early pavement life failure. The RLT test specimen consisted of a 4.0 inch (100 mm) diameter by 6.0 inch (150 mm) height cored from the center of a SGC sample of 6.0 inch (150 mm) diameter by 7.0 inch (175 mm) height in accordance with AASHTO R83 *(71).* All test specimens were compacted to 7.0±1.0% air voids.

The RLT test was conducted by applying a repeated deviator stress of 70 psi (482 kPa), a static confining pressure of 10 psi (69 kPa), and a contact stress of 3.5 psi (24 kPa). The deviator stress is applied through a pulse load with a repeated loading and unloading periods. Each loading cycle consists of 0.1 second loading followed by a rest period of 0.9 second. The axial deformation after each pulse is measured and the axial resilient strain ($\varepsilon_r$) is calculated. In addition, the cumulative permanent strain ($\varepsilon_p$) is calculated and plotted with respect to the number of loading cycles as shown in Figure 3-13 (FL95_PMA(B) is an 9.5 mm NMAS AC mix manufactured using aggregate from FL source and PMA asphalt binder sampled from source B (refer to Section 4.1). This relationship depicts three stages: primary, secondary, and tertiary. The primary stage exhibits a rapid increase in permanent strain with a decrease rate of plastic deformation. This is mainly due to a rearrangement of the mixture structure with an eventual concentration of stresses in the contact surface between the loading plate and the sample due to small irregularities, predominately associated with volumetric change *(73)*. Previous research has shown that densification is unlikely with pavements well compacted during construction and its contribution is only at first working stage of asphalt pavement. The secondary stage exhibits a constant rate of change of the permanent strain. Lower rate of deformation during the secondary stage suggests a more stable mixture after initial densification has been achieved, and the structure of the mix has finished its relocation due to initial traffic compaction. The tertiary stage exhibits high rates of permanent strain associated with plastic or shear deformation under no volume change *(72) (74)*. This change is reached when the specimen begins to deform significantly and individual aggregates composing the shape of the mixture are moving past each other.

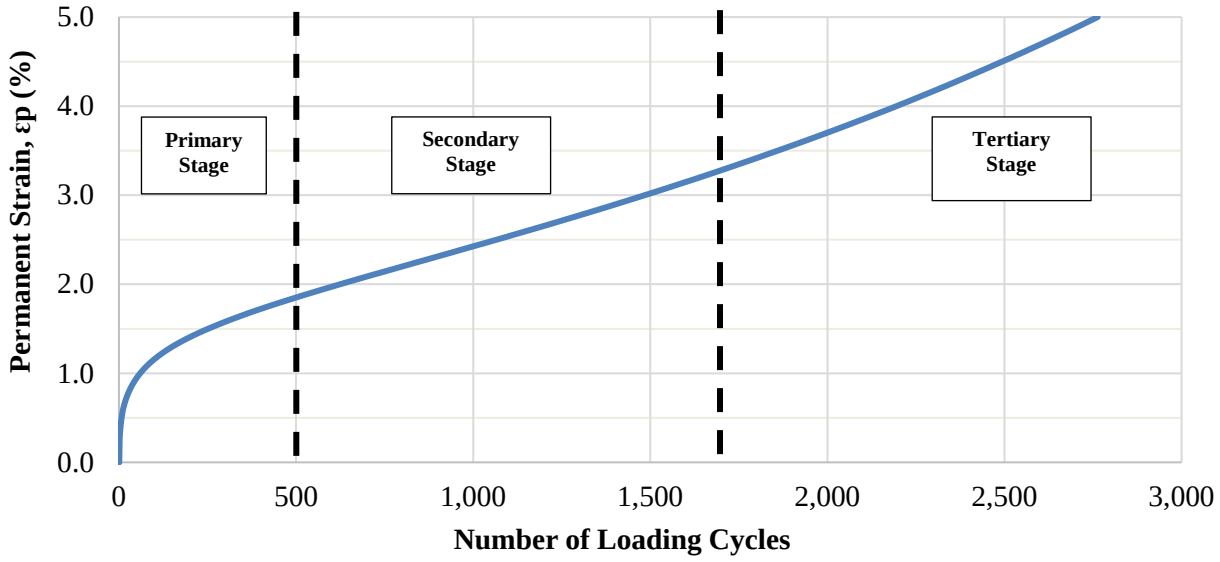


**Figure 3-13. RLT permanent deformation curve for FL95_PMA(B) AC mix at 122°F (50°C).**

The Francken model, expressed in Equation 3-6, is used to numerically model the permanent strain-loading cycle relationship. This well suited mathematical model combines both a power

model which characterizes the primary and secondary stages, and an exponential model which fits the tertiary stage.

$$\varepsilon_p(N) = A * N^B + C * (e^{D*N} - 1) \qquad \textbf{Equation 3-6}$$

Where;
$\varepsilon_p(N)$: permanent axial strain, inch/inch (or mm/mm);
*N*: number of loading cycles; and
*A, B, C, and D*: regression constants.

The RLT test was conducted at three different temperatures: 86, 104, and 122°F (30, 40, and 50°C) for some AC mixes and 104, 122, and 140°F (40, 50, and 60°C) for others. A rutting model for each mix was developed following Equation 3-7. Figure 3-14 shows the rutting curves for an AC mix evaluated in this study at the three testing temperatures.

$$\frac{\varepsilon_p}{\varepsilon_r} = K_z * \beta_{r1} * 10^{k_{r1}} * (T)^{\beta_{r2}*k_{r2}} * (N)^{\beta_{r3}*k_{r3}} \qquad \textbf{Equation 3-7}$$

Where;
$\varepsilon_p$: permanent axial strain, inch/inch (or mm/mm);
$\varepsilon_r$: resilient axial strain, inch/inch (or mm/mm);
*N*: number of loading cycles;
*T*: temperature of the asphalt mixture in °F;
$k_{r1}$, $k_{r2}$, *and* $k_{r3}$: experimentally determined coefficients;
$\beta_{r1}$, $\beta_{r2}$, *and* $\beta_{r3}$: laboratory-field calibration factors; and
$K_z$: AC layer thickness adjustment coefficient defined in Equation 3-8.

$$K_z = (C_1 + C_2 * depth) * 0.328196^{depth} \qquad \textbf{Equation 3-8}$$

$$C_1 = -0.1039 * h_{ac}^2 + 2.4868 * h_{ac} - 17.342 \qquad \textbf{Equation 3-9}$$

$$C_2 = 0.0172 * h_{ac}^2 - 1.7331 * h_{ac} + 27.428 \qquad \textbf{Equation 3-10}$$

Where;
$h_{ac}$: total AC layer thickness, inch;
$C_1, and\ C_2$ : regression constants defined as a function of $h_{ac}$ as expressed in Equation 3-9 and Equation 3-10, respectively; and
*depth*: distance between the top of the AC layer and the computational point, inch.

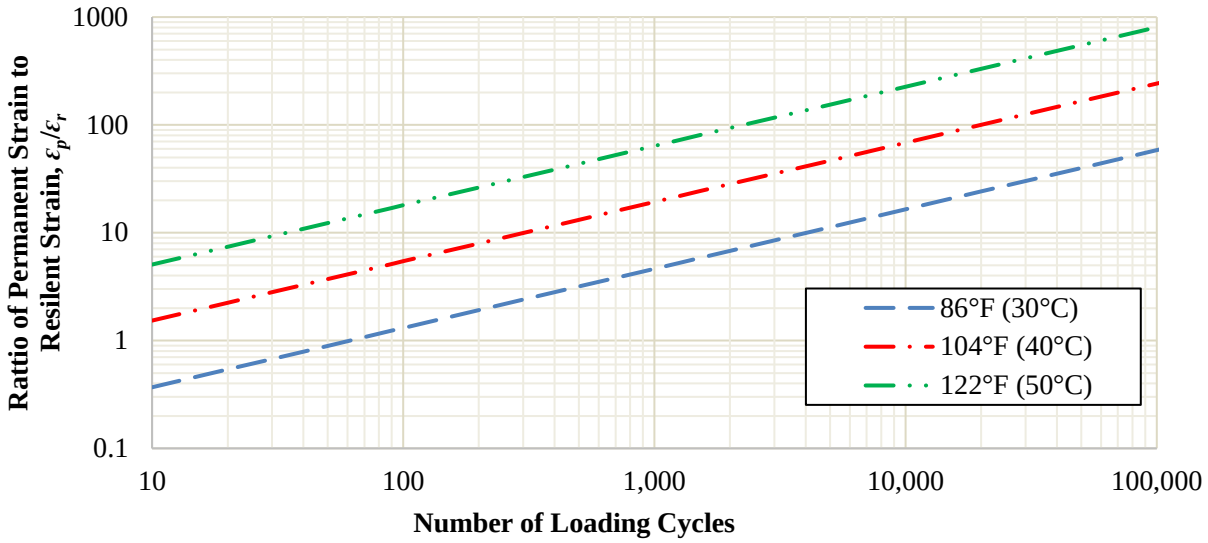


**Figure 3-14. Rutting curves for FL95_PMA(B) AC mix.**

### 3.3.3. Fatigue Cracking Performance Characteristic

Asphalt mixtures are expected to resist fatigue cracking after the first five years of their service life when the asphalt binder becomes brittle due to long-term aging. Fatigue cracking is typically caused by the repeated bending strains in the asphalt mix caused by heavy loads during moderate weather conditions. In this study, the resistance of the mixtures to fatigue cracking was evaluated using the flexural beam fatigue test according to ASTM D7460 *(75)* and AASHTO T321 *(35)*. The mixtures for the fatigue test were short-term aged followed by long-term aging since fatigue is a later pavement life distress. The 2×2×5 inch (51×51×381 mm) beam specimen is subjected to a 4-point bending with free rotation and horizontal translation at all load and reaction points. This produces a constant bending moment over the center portion of the specimen.

The constant strain-controlled tests were conducted at different strain levels using a repeated haversine load at a frequency of 10 Hz. Initial flexural stiffness is measured at the 50$^{th}$ load cycle. The normalized modulus (*NM*) is calculated as expressed in Equation 3-11 and plotted with respect to the number of loading cycles as shown in Figure 3-15. Fatigue life or failure is defined as the number of cycles at which the NM reaches its peak (i.e., maximum value).

$$NM = \frac{S_i * N_i}{S_0 * N_0} \qquad \textbf{Equation 3-11}$$

Where;
$NM$: normalized modulus;
$N_0$: initial loading cycle usually considered as 50;
$S_0$: initial flexural stiffness at initial loading cycle $N_0$;
$N_i$: i$^{th}$ loading cycle; and
$S_i$: flexural stiffness at i$^{th}$ loading cycle $N_i$.

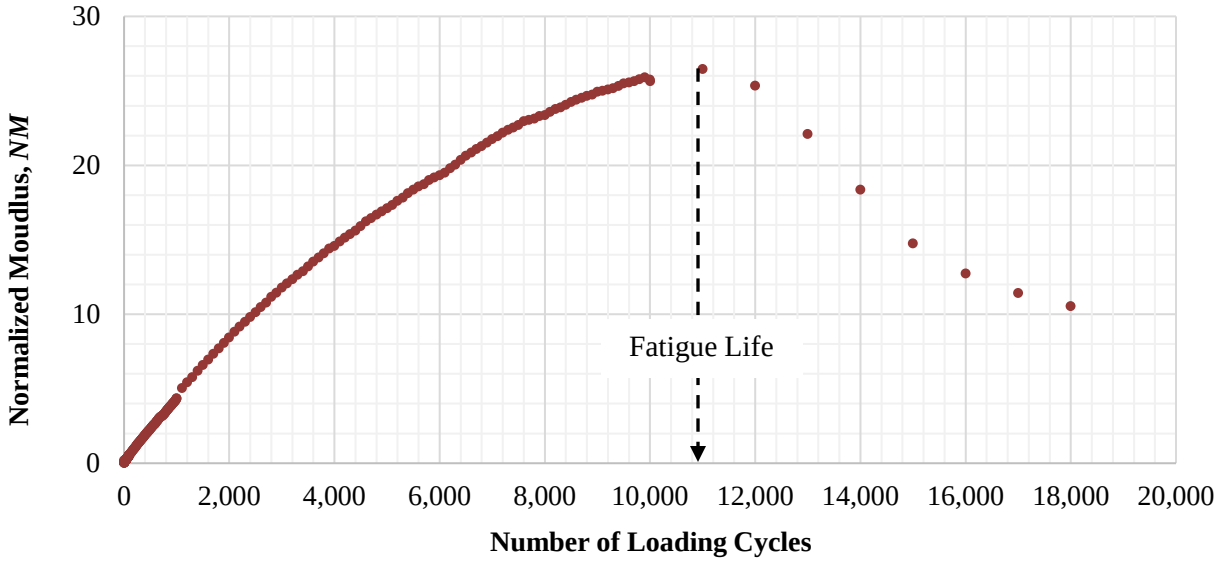


**Figure 3-15. NM curve for FL95_PMA(A) AC mix at 800 microstrain and 70°F (21.1°C).**

The flexural beam fatigue tests were conducted at three different temperatures: 55, 70, and 85°F (13, 21, and 30°C) for some mixes (all PMA mixes and FL95_HP(A)) and 40, 55, and 70°F (4.4, 13, and 21°C) for others (i.e., FL95_HP(B), FL125_HP(B) and all GA95 and GA125 HP AC mixes). The highest testing temperature (i.e., 70, or 85°F) was changed to ensure that the evaluated AC mixture is stiff enough to hold a constant strain during testing. A fatigue model for each mix was developed following Equation 3-12. Figure 3-16 shows fatigue curves at the three testing temperatures for an AC mix evaluated in this study.

$$N_f = \beta_{f1} * k_{f1} * \left(\frac{1}{\varepsilon_t}\right)^{\beta_{f2} * k_{f2}} * \left(\frac{1}{E_{AC}}\right)^{\beta_{f3} * k_{f3}} \qquad \textbf{Equation 3-12}$$

Where;
$N_f$: fatigue life, number of load repetitions to fatigue damage;
$\varepsilon_t$: applied tensile strain, inch/inch (or mm/mm);
$E_{AC}$: dynamic modulus of the asphalt mixture, psi;
$k_{f1}$, $k_{f2}$, *and* $k_{f3}$: experimentally determined coefficients; and
$\beta_{f1}$, $\beta_{f2}$, *and* $\beta_{f3}$: laboratory-field calibration factors.

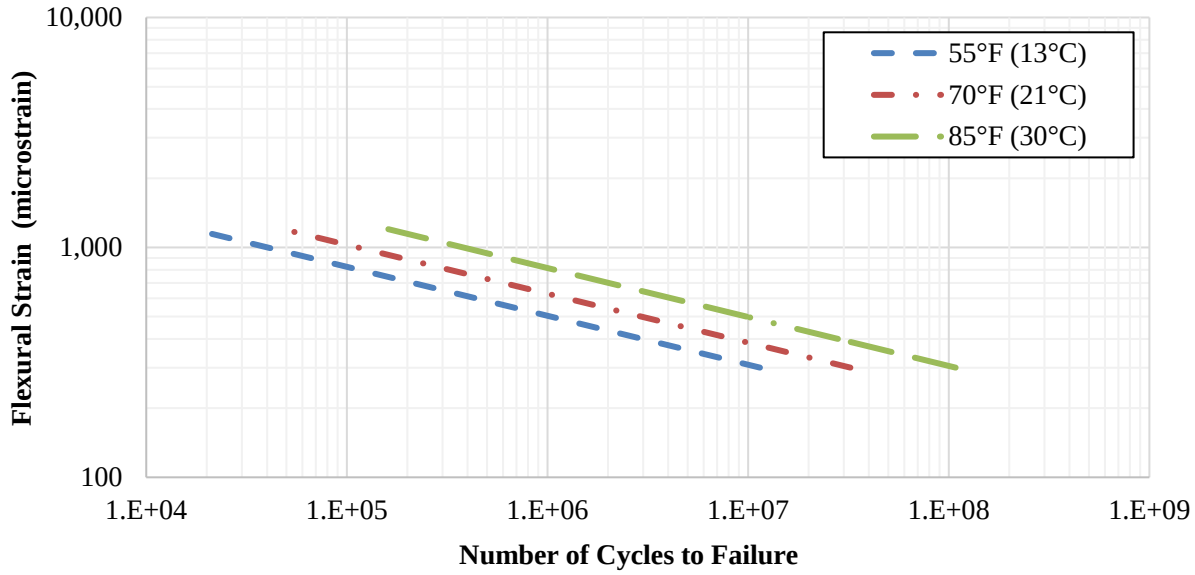


**Figure 3-16. Fatigue curves for FL95_PMA(A) AC mix.**

### 3.3.4. Top-Down Cracking Performance Characteristic

Top-down cracking mechanism can be defined as the combination of several basic factors including high surface horizontal tensile stresses at the tire-pavement interface, age hardening of the asphalt binder resulting in high thermal stresses in the HMA, etc. In this study, the resistance of the mixtures to top-down cracking was evaluated using the indirect tension test jig mounted into the AMPT-Pro machine in accordance with AASHTO T322 *(28)* and Appendix G of the NCHRP 9-57 study *(76)*. The mixtures for the IDT test were short-term aged followed by long-term aging in accordance with AASHTO R30 *(70)* since top-down cracking tends to occur after almost ~8 years of the pavement life in Florida.

The IDT test specimen consists of a 6.0 inch (150 mm) diameter by 1.5 inch (38 mm) height sample for an AC mix with a NMAS not exceeding ¾ inch (19 mm). The test specimen is trimmed from the middle part of a SGC sample of 6.0 inch (150 mm) diameter by 7.0 inch (175 mm) height. All test specimens were compacted to 7.0±1.0% air voids.

The top-down cracking evaluation of an AC mix consists of determining the tensile creep compliance and the tensile failure limit by conducting the tensile creep and tensile fracture tests, respectively. The tensile creep test is used to capture the permanent strain associated with the time-dependent response of an asphalt mixture. The tensile creep compliance parameters can be used to estimate the rate of damage accumulation of an asphalt mixture subjected to repeated loads. On the other hand, the tensile fracture test is used to determine the failure limit of an asphalt mixture. These material properties can be used for estimating the fracture tolerance of the asphalt mixture. The energy ratio *(ER)* will constitute the top-down cracking performance comparison parameter and the controlling failure criterion.

The tensile creep test applies a static step/ramp load of fixed magnitude rising from the seating load (i.e., 10 lbf (50 N)) for a duration of 1,000 seconds. The magnitude of the load is adjusted so

that the horizontal deformation at 100 seconds is between 0.0010 and 0.0015 inch (0.0254 and 0.0038 mm) and the horizontal deformation at 1,000 seconds does not exceed 0.0075 inches (0.0200 mm). The creep compliance *($D_t$)* at each recording time, t, is computed using Equation 3-13. The creep compliance values are fitted through a power-law as expressed in Equation 3-15 (Figure 3-17) and used to determine the mixture parameters $D_0$, $D_1$, and *m*-value.

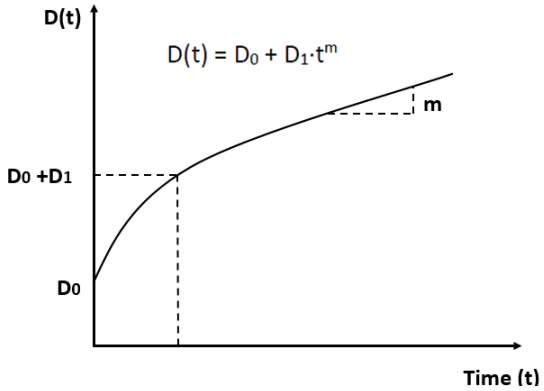


**Figure 3-17. Schematic representation of the mix creep compliance curve.**

$$D_t = \frac{\Delta H_{trim\ avg,t} * h_{avg} * \phi_{avg}}{P_{avg} * GL} * C_{compliance,t} \qquad \textbf{Equation 3-13}$$

$$C_{compliance,\ t} = 0.6354 * \frac{\Delta V_{trim\ avg,t}}{\Delta H_{trim\ avg,t}} - 0.332 \qquad \textbf{Equation 3-14}$$

$$D(t) = D_0 + D_1 t^m \qquad \textbf{Equation 3-15}$$

Where
$D(t)$: creep compliance at time t, psi$^{-1}$ (GPa$^{-1}$);
$\Delta H_{trim\ avg,t}$: mean absolute horizontal deformation of all specimens in test group, inch (mm);
$h_{avg}$: average thickness of the specimens in the test group, inch (mm);
$\phi_{avg}$: average diameter of the specimens in the test group, inch (mm);
$P_{avg}$: average creep load of the specimens in the test group, lbs. (N);
$GL$: gage length equal to 1.5 inch (38 mm);
$C_{compliance,t}$: creep compliance correction factor at *t* defined in Equation 3-14 (dimensionless);
$\Delta H_{trim\ avg,t}$: mean absolute horizontal deformation of all specimens in test group, inch (mm);
$\Delta V_{trim\ avg,t}$: mean absolute vertical deformation of all specimens in test group, inch (mm);
$D(t)$: creep compliance function, psi$^{-1}$ (GPa$^{-1}$);
$t$: recording time, second; and
$D_0, D_1, m$: creep compliance parameters.

On the other hand, the tensile fracture test is run immediately following the tensile creep test on the same specimen. The specimen is loaded with a constant rate of 2 inch (50 mm) of ram displacement per minute. The test is considered terminated when the load reaches a 20% reduction from the peak load value. The specimen tensile stress *($\sigma_t$)* at any recording time, *t*, is

determined using Equation 3-16. The specimen indirect tensile strength is defined as the tensile stress at the instant of fracture *($t_f$)*.

$$\sigma_t = \frac{2*P_t}{\pi*h*\phi} * C_{SX} \qquad \textbf{Equation 3-16}$$

$$C_{SX} = 0.984 - 0.01114 * \frac{h}{\phi} - 0.2693 * \upsilon + 1.436 * \left(\frac{h}{\phi}\right) * \upsilon \qquad \textbf{Equation 3-17}$$

$$\upsilon = -0.10 + [1.480 - 0.778 * \left(\frac{h}{\phi}\right)^2] * \left(\frac{\Delta H_{trim\ avg,0.5\ P_{tf}}}{\Delta V_{trim\ avg,0.5\ P_{tf}}}\right)^2 \qquad \textbf{Equation 3-18}$$

Where;
$\sigma_t$: tensile stress of tested specimen at time *t*, psi (Pa);
$P_t$: load for the tested specimen at time *t*, lbs. (N);
$h$: thickness of tested specimen, inch (mm);
$\phi$: diameter of tested specimen, inch (mm);
$C_{SX}$: stress correction factor for the tested specimen as defined in Equation 3-17;
υ: Poisson's ratio defined in Equation 3-18; and
$\Delta H_{trim\ avg,0.5\ P_{tf}}$ and $\Delta V_{trim\ avg,0.5\ P_{tf}}$: normalized absolute horizontal and vertical deformation at 50% of the peak load, inch (mm).

The specimen tensile strain *($\varepsilon_t$)* at any recording time t is determined using Equation 3-19. The specimen failure strain is defined as tensile strain at the instant of fracture *($t_f$)*.

$$\varepsilon_t = \frac{\Delta H_{norm,t}}{GL} * 1.072 * C_{BX} \qquad \textbf{Equation 3-19}$$

$$C_{BX} = 1.03 - 0.189 * \left(\frac{h}{\phi}\right) - 0.081 * \upsilon + 0.089 * \left(\frac{h}{\phi}\right)^2 \qquad \textbf{Equation 3-20}$$

Where;
$\varepsilon_t$: tensile strain of tested specimen at time *t*, inch/inch (mm/mm);
$GL$: gage length of 1.5 inch (38 mm);
$\Delta H_{norm,t}$: normalized absolute horizontal deformation of specimen at time *t*, inch (mm); and
$C_{BX}$: buldging correction factor for the tested specimen as defined in Equation 3-20.

The asphalt mixture failure limits are schematically defined in Figure 3-18. The fracture energy density failure limit is determined as the area under the stress-strain curve up to the instant of fracture. The elastic energy (EE) is then calculated using Equation 3-21.

$$EE = \frac{1}{2} * \frac{S_T^2}{E} \qquad \textbf{Equation 3-21}$$

Where;
$EE$: elastic energy of tested specimen, lbs. inch (KJ);
$S_T$: indirect tensile strength of tested specimen, psi (Pa); and
$E$: dynamic modulus at the testing temperature and a frequency of 10 Hz, psi (Pa).

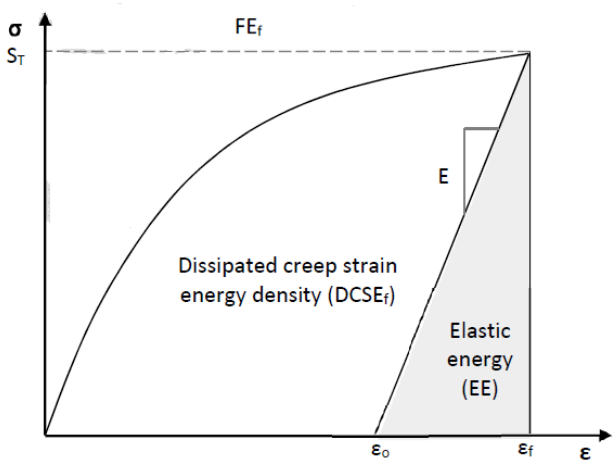


**Figure 3-18. Schematic representation of mixture failure limits ($FE_f$ and $DCSE_f$).**

The Dissipated Creep Strain Energy Density Failure Limit *($DSCE_f$)* is calculated as the difference between the fracture energy density failure limit *($FE_f$)* and elastic energy *(EE)*. The energy ratio *(ER)* is computed using Equation 3-22.

$$ER = \frac{DSCE_f}{DSCE_{min}} = \frac{DSCE_f}{\frac{m^{2.98} * D_1}{A}} \qquad \textbf{Equation 3-22}$$

Where;
*A*: parameter that takes into account the tensile strength of the asphalt mixture *($S_T$)* and the tensile stress *(σ)* in the pavement structure determined in the advanced pavement modeling section (Refer to Equation 3-23). It should be mentioned that Equation 3-23 is valid for stress and strength reported in psi, $DSCE_f$ in lbf-in/in$^3$, $D_1$ in psi$^{-1}$, and A in psi$^{-2}$. Equation 3-24 should replace Equation 3-21 for stress and strength reported in MPa, $DSCE_f$ in kJ/m$^3$, $D_1$ in GPa$^{-1}$, and A in MPa$^{-2}$.

$$A = 1.42 * 10^{-3} * \frac{(922.5 - S_T)}{\sigma^{3.1}} + 1.70 * 10^{-7} \qquad \textbf{Equation 3-23}$$

$$A = 8.64 * 10^{-4} * \frac{(6.36 - S_T)}{\sigma^{3.1}} + 3.57 * 10^{-3} \qquad \textbf{Equation 3-24}$$

### 3.3.5. Reflective Cracking Performance Characteristic

Reflective cracking is one of the primary forms of distresses in AC overlays of flexible and rigid pavements. It affects ride quality and allows the penetration of water and debris into the cracks which would accelerate the deterioration of the overlay and the underlying pavement, thus leading to a reduction in pavement serviceability. The Texas overlay test (OT) was used to evaluate the mixtures' resistance to reflective cracking in accordance with Tex-248-F procedure *(34)*. The horizontal opening and closing of joints and cracks that exist underneath a new AC overlay are specifically simulated. The Overlay test jig was recently designed to increase the functionality of the AMPT machine by enabling it to determine the susceptibility of asphalt mixtures to reflective cracking.

The OT specimens were only subjected to short-term aging. The OT specimen consists of a 6 inch (150 mm) long by 3 inch (75 mm) wide and 1.5 inch (37.5 mm) thick sample trimmed from a 6 inch (150 mm) diameter by 4.5 inch (115 mm) height SGC sample compacted to 7.0±1.0% air voids. Once prepared, each sample is glued on two metallic plates, and fixed on a mounting wide plate using epoxy. A photo of the overlay test setup and a specimen ready for testing is shown in Figure 3-19.

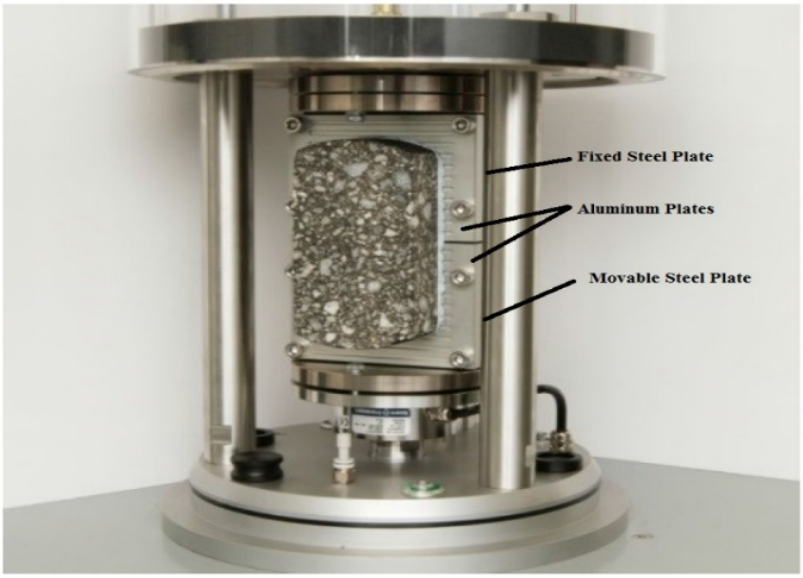


**Figure 3-19. AMPT overlay test setup.**

The test is conducted in a controlled displacement mode until failure occurs at a loading rate of one cycle per 10 seconds with a maximum displacement of 0.025 inch (0.6350 mm) at 77±1°F (25±0.5°C). Each cycle consists of 5 seconds of loading and 5 seconds of unloading. The number of cycles to failure is defined as the number of cycles to reach a 93% drop in initial load which is measured from the first opening cycle. If a 93% reduction in initial load is not reached within a certain specified maximum number of cycles, the test stops automatically. For this study, a total of 5,000 cycles is selected as a maximum number of cycles for stopping the test. The crack driving force is recorded at each loading cycle and a normalized load reduction curve is plotted as shown in Figure 3-20. The normalized load is defined as the load magnitude at each cycle divided by the initial load magnitude.

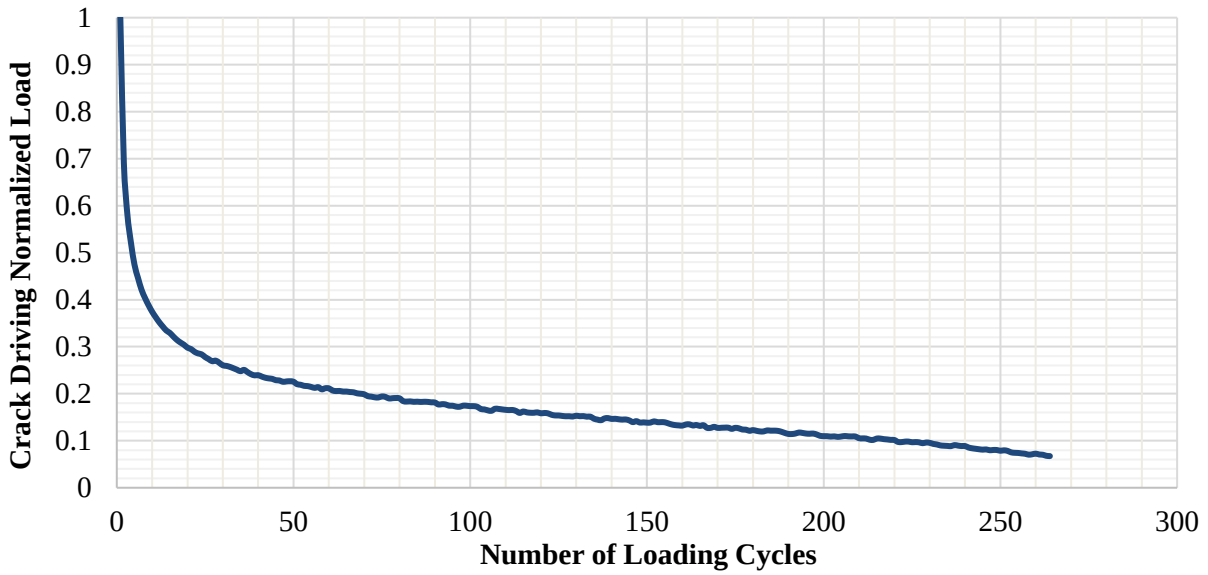


**Figure 3-20. Normalized load reduction curve for FL95_PMA(A) AC mix at a maximum displacement of 0.025 inch (0.6350 mm) and a temperature of 77°F (25°C).**

A power function expressed in Equation 3-25 is used to fit the load reduction versus number of loading cycles curve to determine the crack propagation rate (CPR) and the crack resistance index (CRI) *(77)*.

$$NL = N^{CPR} = N^{(0.0075*CRI-1)} \qquad \textbf{Equation 3-25}$$

Where;
$NL$: normalized crack driving force or load at each loading cycle, lb (kN);
$N$: loading cycles;
$CPR$: crack propagation rate; and
$CRI$: crack resistance index.

The critical fracture energy *($G_c$)* at the maximum peak load of the first loading cycle is considered as the energy required to initiate crack. Figure 3-21 illustrates the relationship between crack driving load and displacement during the first cycle. A negative load value indicates a tension load while a positive one indicates compression. The area under the hysteresis loop, limited for the tension phenomena (i.e., negative load), is considered essential to compute the fracture parameters (i.e., critical fracture energy, CPR, and CRI) that characterize the crack initiation stage of the OT. The critical fracture energy is calculated using Equation 3-26 *(77)*.

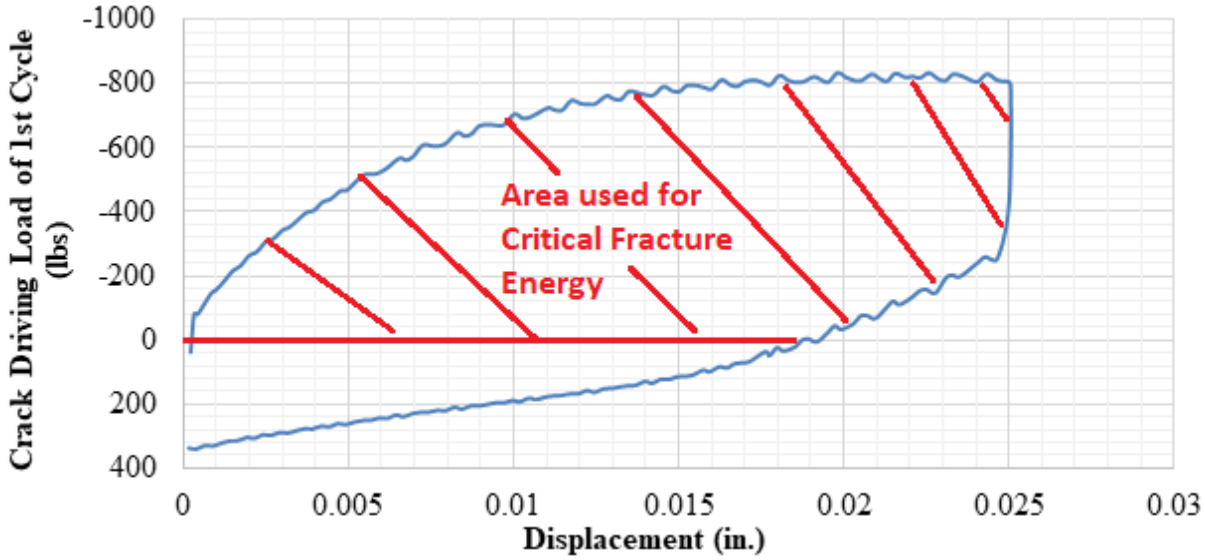


**Figure 3-21. Portion of hysteresis loop of the first loading cycle to calculate the critical fracture energy of FL95_PMA(A) AC mix.**

$$G_c = \frac{W_c}{b*h} \qquad \textbf{Equation 3-26}$$

Where;
$G_c$: critical fracture energy, lb.-in./in.$^2$ (kN-mm$^2$);
$W_c$: fracture area hatched in Figure 25, lb.-in. (kN-mm);
*b*: specimen width: 3 inch. (76.2 mm); and
*h*: specimen height: 1.5 inch. (38.1 mm).

The OT will also be used to determine the fracture properties of the evaluated mixtures assuming that Mode I (opening mode) and Mode II (shearing mode) share the same fracture mechanics properties (*A* and *n*). It should be mentioned that the first 100 cycles are only considered for fracture properties determination. The fracture parameters (*A* and *n*) will be determined in accordance with the "*Mechanistic-Empirical Asphalt Overlay Thickness Design and Analysis System*" *(78)*. The determined fracture properties *(A & n)* will be used in the advanced dynamic modeling of flexible pavements to predict crack propagation in AC overlays caused by both traffic loading and thermal effects.

# CHAPTER 4. MIX DESIGNS AND TEST RESULTS

As presented in Chapter 3, aggregates from Southeast Florida (FL) and Georgia Granite (GA), RAP material from Georgia Granite (GA), and highly and conventionally polymer modified asphalt binders, PG76-22 and HP binder, were identified for the development of laboratory AC mixes. This chapter presents the developed mix designs and provides the analysis of all test results generated from the performance evaluation of the laboratory AC mixes.

## 4.1. MIX DESIGNS

In this research, 16 types of AC mixtures (Table 4-1) were produced and evaluated in the laboratory based on the following guidelines and recommendations:

- The NMAS 9.5 mm mixes should be designed for traffic level C and the NMAS 12.5 mm mixes should be designed for traffic level D.
- The FL aggregate source should not include RAP materials.
- The HP AC mixes should not include RAP materials.
- All binders should include an approved liquid anti-strip agent at the dosage rate of 0.5% by weight of binder.

**Table 4-1. Summary of Mixtures for the Laboratory Evaluation.**

| Aggregate Source | Gradation NMAS | RAP (%) | Ergon (A) | | Vecenergy (B) | |
|---|---|---|---|---|---|---|
| | | | PG76-22PMA | HP Binder | PG76-22PMA | HP Binder |
| FL | 9.5 mm | 0 | FL95_PMA | FL95_HP | FL95_PMA | FL95_HP |
| | 12.5 mm | 0 | FL125_PMA | FL125_HP | FL125_PMA | FL125_HP |
| GA | 9.5 mm | 0 | – | GA95_HP | – | GA95_HP |
| | 12.5 mm | 0 | – | GA125_HP | – | GA125_HP |
| | 9.5 mm | 20 | GA95_PMA | – | GA95_PMA | – |
| | 12.5 mm | 20 | GA125_PMA | – | GA125_PMA | – |

–Not applicable.

As shown in Table 4-1, a total of 16 AC mixes were produced in the laboratory. These mixtures were designed following the FDOT Superpave mix design methodology (FDOT Specifications 2018 *(23)*). The heated aggregates were mixed with various amount of asphalt binder where at least two contents shall fall above/below the expected optimum binder content (OBC) for each mixture. After the samples are mixed and conditioned for 2 hours at the compaction temperature, the mixtures are compacted using the Superpave gyratory compactor (SGC) for a specified number of gyrations based on the NMAS and the targeted traffic level. The OBC for each mixture was determined by identifying the maximum asphalt content which provides 4% air voids and meeting all the applicable FDOT mix design specifications as summarized in Table 4-2.

**Table 4-2. FDOT Superpave Mix Design Specifications.**

| Aggregate Source | Gradation NMAS | Traffic Level | FDOT Specifications 2018 | | | | | |
|---|---|---|---|---|---|---|---|---|
| | | | $N_{init}$[1] | $N_{design}$[2] | Va[3] | VMA[4] | VFA[5] | DP[6] |
| FL | 9.5mm | C | 7 | 75 | 4% | ≥15% | 65-75% | 0.6-1.2 |
| | 12.5mm | D & E | 8 | 100 | 4% | ≥14% | 65-75% | 0.6-1.2 |
| GA | 9.5mm | C | 7 | 75 | 4% | ≥15% | 65-75% | 0.6-1.2 |
| | 12.5mm | D & E | 8 | 100 | 4% | ≥14% | 65-75% | 0.6-1.2 |

[1]$N_{init}$ stands for initial number of gyrations.
[2]$N_{design}$ stands for design number of gyrations.
[3]Va stands for air voids level.
[4]VMA stands for percentage of voids in mineral aggregate.
[5]VFA stands for percentage of voids filled with asphalt.
[6]DP stands for dust proportion

Table 4-3 to Table 4-6 summarize the mix design information for all AC mixes. The abbreviations in the provided tables are defined as follows: "twm" stands for total weight of mix, "$G_{mm}$" stands for theoretical maximum specific gravity of AC mixes, and "$P_{be}$" stands for percent of effective binder by volume. The details of the developed mix designs can be found in Appendix B Section 1 (B.1). Figure 4-1 compares the asphalt binder contents by twm of all developed PMA and HP AC mixes. It should be mentioned that for some mixes, an average OBC was selected between the two binder sources (i.e., A and B). This resulted in a slight variation in the target design air voids (i.e., 4%) while the other volumetric properties (i.e., VMA, VFA, and DP) remained within range in accordance with FDOT specifications 2018 *(23)*.

A review of the mix designs data reveals the following observations:

- The mixes manufactured using GA aggregates showed a lower OBC when compared with the AC mixes manufactured using FL aggregates. This can be attributed to the difference in absorption and mineralogy of the two aggregate sources. It should be reminded that the same asphalt binder sources, i.e., PMA(A/B) and HP(A/B), were used for both aggregate sources.
- For the mixes manufactured using FL aggregates; the 9.5 mm mix resulted in a higher asphalt binder content than the 12.5 mm gradations. This can be attributed to the lower design compaction effort for the 9.5 mm mixes ($N_{design}$ = 75).
- For the mixes manufactured using FL aggregates; the 9.5 mm and 12.5 mm HP mixes resulted in slightly lower binder contents than the 9.5 and 12.5 mm PMA mixes. It should be mentioned that same aggregate gradation was maintained for each of the 9.5 mm and 12.5 mm mixes when manufactured using PMA and HP asphalt binders for the FL aggregate source.
- For the PMA mixes manufactured using GA aggregates; the 12.5 mm mixes resulted in lower asphalt binder contents than the 9.5 mm mixes.
- The 9.5 and 12.5 mm HP mixes manufactured using GA aggregates resulted in similar OBC (i.e., 4.9%) which is higher than the OBC observed for their respective PMA control mixes. It should be mentioned that the 9.5 and 12.5 mm HP using the GA aggregates do not contain any RAP materials because RAP is not allowed in HP mixtures per FDOT specifications 2018 *(23)*.

**Table 4-3. Summary of Mix Designs for FL Aggregate, 9.5 mm NMAS, with PMA and HP Asphalt Binders.**

| Properties | Mix Design ID | | | |
|---|---|---|---|---|
| | **FL95_PMA(A)** | **FL95_PMA(B)** | **FL95_HP(A)** | **FL95_HP(B)** |
| Traffic Level ($N_{design}$) | C (75) | C (75) | C (75) | C (75) |
| OBC by twm (%) | 6.2 | 6.2 | 5.9* | 5.9* |
| RAP Binder Ratio, RBR | 0.00 | 0.00 | 0.00 | 0.00 |
| $G_{mm}$ at OBC | 2.368 | 2.362 | 2.356 | 2.370 |
| Va (%) | 4.0 | 4.0 | 3.7 | 4.3 |
| VMA (%), Min. 15% | 15.0 | 15.3 | 14.9 | 15.2 |
| VFA (%), 65 – 75% | 73.1 | 73.9 | 75.6 | 71.2 |
| $P_{be}$ at OBC (%) | 4.99 | 5.13 | 5.05 | 4.79 |
| DP, 0.6 – 1.2 | 0.8 | 0.8 | 0.8 | 0.8 |

*An average OBC was selected between the two binder sources.

**Table 4-4. Summary of Mix Designs for FL Aggregate, 12.5 mm NMAS, with PMA and HP Asphalt Binders.**

| Properties | Mix Design ID | | | |
|---|---|---|---|---|
| | **FL125_PMA(A)** | **FL125_PMA(B)** | **FL125_HP(A)** | **FL125_HP(B)** |
| Traffic Level ($N_{design}$) | D/E (100) | D/E (100) | D/E (100) | D/E (100) |
| OBC by twm (%) | 5.5* | 5.5* | 5.4 | 5.4 |
| RAP Binder Ratio, RBR | 0.00 | 0.00 | 0.00 | 0.00 |
| $G_{mm}$ at OBC | 2.372 | 2.378 | 2.360 | 2.369 |
| Va (%) | 3.8 | 4.4 | 4.0 | 4.0 |
| VMA (%), Min. 14% | 13.9 | 14.0 | 14.2 | 13.9 |
| VFA (%), 65 – 75% | 72.4 | 69.2 | 71.9 | 71.2 |
| $P_{be}$ at OBC (%) | 4.49 | 4.38 | 4.60 | 4.44 |
| DP, 0.6 – 1.2 | 0.8 | 0.8 | 0.8 | 0.8 |

* An average OBC was selected between the two binder sources.

**Table 4-5. Summary of Mix Designs for GA Aggregate, 9.5 mm NMAS, with PMA and HP Asphalt Binders.**

| Properties | Mix Design ID | | | |
|---|---|---|---|---|
| | **GA95_PMA(A)** | **GA95_PMA(B)** | **GA95_HP(A)** | **GA95_HP(B)** |
| Traffic Level ($N_{design}$) | C (75) | C (75) | C (75) | C (75) |
| OBC by twm (%) | 4.8* | 4.8 | 4.9 | 4.9 |
| RAP Binder Ratio, RBR | 0.23 | 0.23 | 0.00 | 0.00 |
| $G_{mm}$ at OBC | 2.558 | 2.571 | 2.551 | 2.547 |
| Va (%) | 3.8 | 4.0 | 4.0 | 4.0 |
| VMA (%), Min. 15% | 15.0 | 14.9 | 14.9 | 14.9 |
| VFA (%), 65 – 75% | 75.6 | 72.7 | 73.1 | 73.1 |
| $P_{be}$ at OBC (%) | 4.67 | 4.53 | 4.49 | 4.54 |
| DP, 0.6 – 1.2 | 1.2 | 1.2 | 1.2 | 1.2 |

* An average OBC was selected between the two binder sources.

**Table 4-6. Summary of Mix Designs for GA Aggregate, 12.5 mm NMAS, with PMA and HP Asphalt Binders.**

| Properties | Mix Design ID | | | |
|---|---|---|---|---|
| | GA125_PMA(A) | GA125_PMA(B) | GA125_HP(A) | GA125_HP(B) |
| Traffic Level ($N_{design}$) | D/E (100) | D/E (100) | D/E (100) | D/E (100) |
| OBC by twm (%) | 4.2* | 4.2 | 4.9* | 4.9* |
| RAP Binder Ratio, RBR | 0.32 | 0.32 | 0.00 | 0.00 |
| $G_{mm}$ at OBC | 2.555 | 2.545 | 2.574 | 2.574 |
| Va (%) | 4.4 | 4.0 | 3.8 | 4.6 |
| VMA (%), Min. 14% | 14.0 | 13.8 | 13.9 | 14.7 |
| VFA (%), 65 – 75% | 68.4 | 71.2 | 73.3 | 68.5 |
| $P_{be}$ at OBC (%) | 3.97 | 4.10 | 4.16 | 4.16 |
| DP, 0.6 – 1.2 | 0.8 | 0.8 | 1.2 | 1.2 |

* An average OBC was selected between the two binder sources.

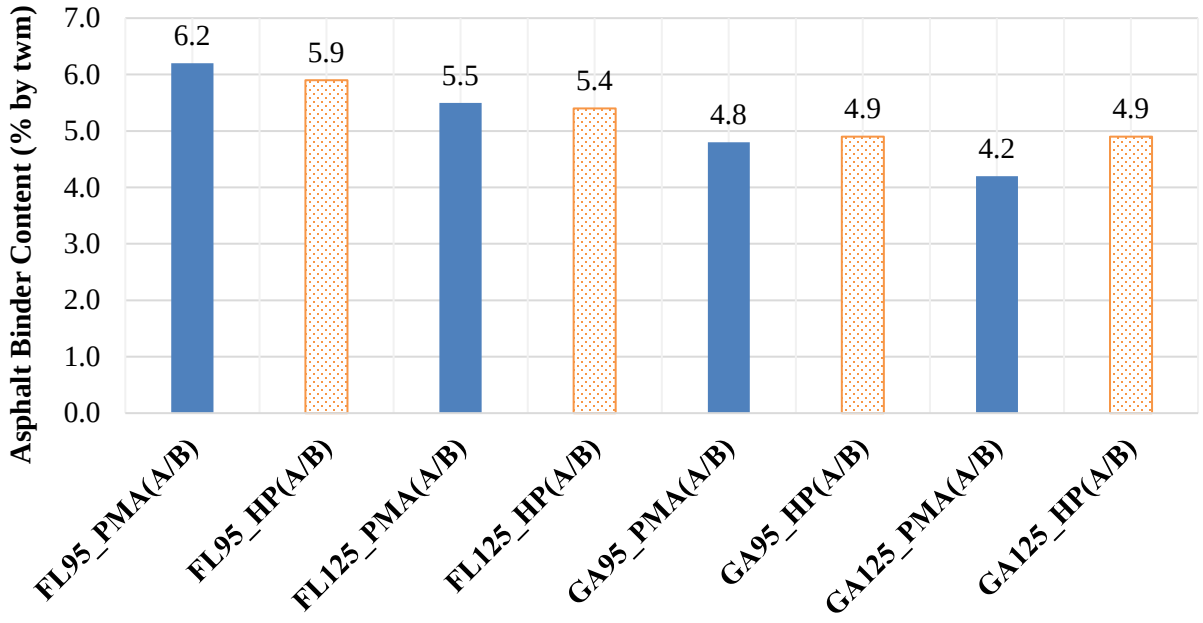


**Figure 4-1. Asphalt binder contents of all PMA and HP AC mixes.**

In addition to the specifications listed in Table 4-2, all designed mixtures were evaluated in terms of their resistance to moisture damage. Six to eight samples from each mix were prepared at OBC and short-term aged for two hours at the compaction temperature according to FM 1-T 283 *(79)* and AASHTO T283 *(49)*. The aged samples were compacted in the Superpave Gyratory Compactor to a target air void of 7±1%. The compacted samples were then split into two sets of 3-4 samples: one set was un-conditioned and the other set was moisture-conditioned. The samples in each set were selected to achieve similar average air voids. For the moisture-conditioned set, the samples were saturated between 70% and 80%, wrapped in plastic, and subjected to freezing at temperature of 0°F (-18°C) for 16 hours. Following the freezing cycle,

the samples were placed in a 140°F (60°C) water bath for 24 hours. This process constitutes one freeze-thaw cycle.

The un-conditioned and moisture-conditioned samples were placed in a 77°F (25°C) water bath for a minimum duration of 2 hours to reach the testing temperature for the indirect tension test. The indirect tension test applies a load at a constant rate of 2 in/min (50 mm/min) through the diametral direction of the sample. The tensile strength *(TS)* is calculated using Equation 4-1. The tensile strength ratio *(TSR)* is defined as the ratio of the average *TS* of the un-conditioned samples over the average *TS* of the moisture-conditioned samples. Following FDOT Specifications 2018 *(23),* all mixtures must achieve a minimum dry TS at 77°F (25°C) of 100 psi (690 kPa), and a minimum TSR of 80%.

$$TS = \frac{2*P}{\pi*t*D} \qquad \textbf{Equation 4-1}$$

Where;
*TS:* tensile strength, psi (kPa);
*P*: peak applied load, lbs (kN);
*t*: sample thickness, inch (mm); and
*D*: sample diameter, inch (mm).

Figure 4-2 to Figure 4-4 show the un-conditioned TS, the moisture-conditioned TS, and the TSR values of all evaluated AC mixes (i.e., eight PMA AC and eight HP AC mixes). The numerical values above the bars represent the average values while the whiskers represent the 95% confidence interval (CI). An overlap in the CI's indicates statistically similar properties of the mixtures. A review of the provided data reveals the following observations:

- Regardless of aggregate source (i.e., FL and GA) and asphalt binder type (i.e., PMA and HP), all evaluated mixtures met the FDOT criteria in terms of minimum TS and TSR for indicating a good resistance to moisture damage.
- Regardless of aggregate source, all HP mixes exhibited lower un-conditioned and moisture-conditioned TS values when compared with their corresponding control PMA AC mixes indicating a less stiff behavior of the HP mix at intermediate temperature of 77°F (25°C).
- Regardless of aggregate source, the HP AC mixes manufactured with binder source B exhibited slightly lower un-conditioned TS values when compared with HP AC mixes manufactured using HP binder from source A. The same observation can be made for the moisture-conditioned TS of all HP AC mixes except for the FL125_HP(B) mix that exhibited slightly higher moisture-conditioned TS.
- The PMA AC mixes manufactured using GA aggregates exhibited significantly higher un-conditioned and moisture-conditioned TS values than the PMA AC mixes manufactured using FL aggregates. This can be attributed to the stiffening effect from the RAP material used in the GA_PMA AC mixes.

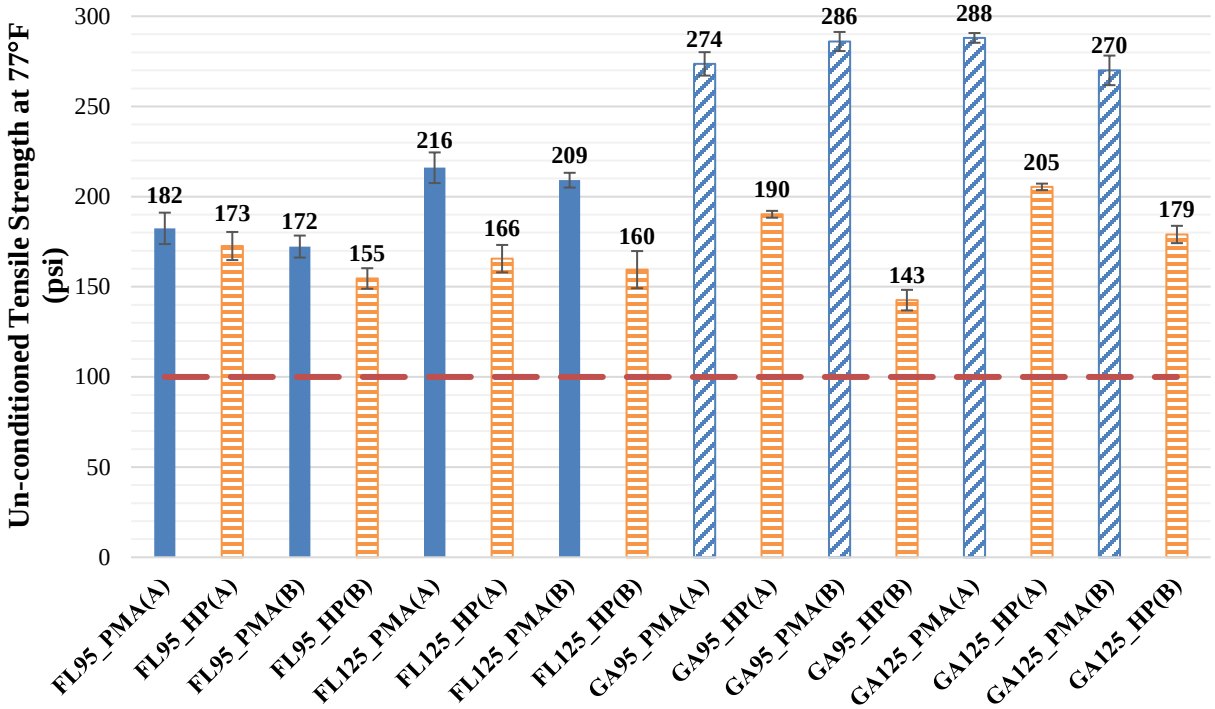


**Figure 4-2. Un-conditioned tensile strength properties of evaluated mixes.**

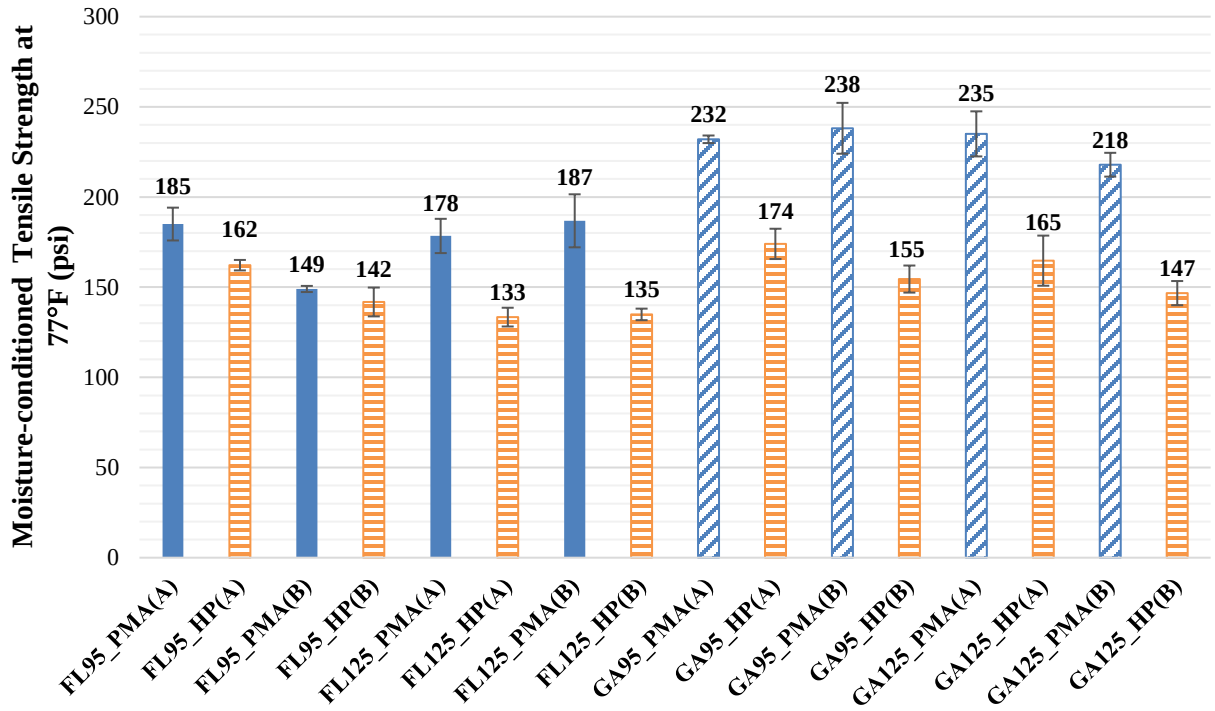


**Figure 4-3. Moisture-conditioned tensile strength properties of evaluated mixes.**

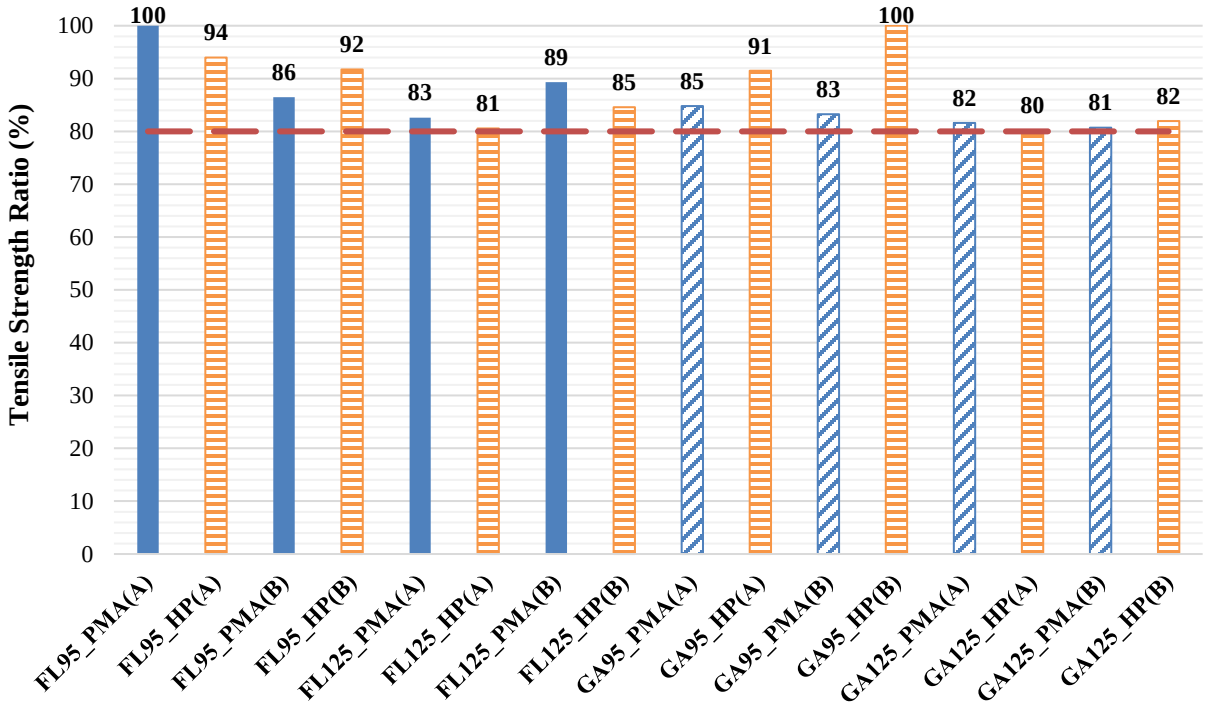


**Figure 4-4. Tensile strength ratios of evaluated mixes.**

## 4.2. TEST RESULTS AND ANALYSIS

The 16 designed mixtures (i.e., eight PMA and eight HP AC mixes) were evaluated at their respective OBC for their engineering properties in terms of the dynamic modulus property (*E**), rutting characteristics in terms of resistance to permanent strains in triaxial testing, fatigue cracking characteristics in terms of resistance to flexural bending strains, top-down cracking characteristics in terms of resistance to tensile strains, and reflective cracking characteristics in terms of resistance to crack propagation. Table 4-7 summarizes the laboratory tests that were conducted to evaluate the engineering properties and performance characteristics of the AC mixes listed in Table 4-1.

All engineering properties and performance characteristics were evaluated at the short-term aging condition except for the fatigue and top-down cracking since both are considered to be long-term distresses. Short-term aging consisted of curing loose mixtures at a temperature of 275°F (135°C) in a forced-draft laboratory oven for 4 hours prior to compaction in accordance with AASHTO R30 *(70)*. In the case of fatigue and top-down cracking, the compacted specimens were long-term aged at a temperature of 185°F (85°C) in a forced-draft oven for 5 days.

**Table 4-7. Summary of Laboratory Evaluation Program**

| Engineering Property/ Distress Mode | Standard Method/ Practice | Measured Property | Laboratory Conditioning | Number of Replicates |
|---|---|---|---|---|
| Dynamic Modulus | AASHTO T378 *(39)* AASHTO R84 *(40)* | E* Master Curve | Short-term oven aging | 2 |
| Rutting | AASHTO R83 *(71)* | ($\varepsilon_p/\varepsilon_r$) vs. ($N_r$, *T)* Rutting Model | Short-term oven aging | 2 per temperature |
| Shoving[1] | NA[2] | NA[2] | NA[2] | NA[2] |
| Fatigue Cracking | ASTM D7460 *(75)* AASHTO T321 (75)(71)*(35)* | $N_f$ vs. ($\varepsilon_t$, *E)* Fatigue Model | Long-term oven aging | Minimum of 3 strains per temperature |
| Top-Down Cracking | AASHTO T322 *(28)* NCHRP 9-57 Appendix G *(76)* | *DCSE, ER* | Long-term oven aging | 2 |
| Reflective Cracking | TxDOT Tex-248-F *(34)* | Cycles to Failure Fracture Parameters (*A*, *n*) | Short-term oven aging | 3 |

[1]will be evaluated through the mechanistic modeling of flexible pavements.
[2]Not applicable.

### 4.2.1. Engineering Properties

The E* property provides an indication on the overall quality of the asphalt mixture. The magnitude of the E* depends on several properties of the mixture including; aggregate properties, gradation, asphalt binder grade, mix volumetrics, and age. The magnitude of E* also depends on temperature and rate of loading (i.e., frequency). Figure 4-5 to Figure 4-12 show the E* master curves of all 16 evaluated mixes constructed at a reference temperature of 68°F (20°C) where each HP AC mix is compared to its respective control PMA AC mix. Figure 4-13 to Figure 4-16 show the E* master curves of PMA and HP AC mixes manufactured using same aggregate source (i.e., FL, and GA) and same NMAS (i.e., 9.5, and 12.5 mm). In addition, the values of E* were also compared at critical temperatures for fatigue (77°F (25°C)) and rutting (122°F (50°C)) at a loading frequency of 10 Hz which represents highway travel speed as shown in Figure 4-17 and Figure 4-18, respectively. Appendix C section 1 (C.1) presents in details the dynamic modulus data for all evaluated AC mixes. A review of the E* data reveals the following observations:

- The combination of aggregate source and asphalt binder type (i.e., PMA or HP) had a significant impact on the magnitude of the E* property. For all PMA AC mixes, higher E* values were observed for the mixes manufactured using GA aggregates when compared with the AC mixes manufactured using FL aggregate regardless of the binder content and the NMAS of the mix. This behavior can be partially attributed to the stiffening effect of the RAP material (i.e., 20%) added into the GA AC mixes. On the other hand, all HP mixes showed similar E* values at intermediate and high temperature regardless of the aggregate source, the NMAS of the AC mix, and the HP asphalt binder source (i.e., A or B).

- In the case of the FL95 AC mixes (i.e., FL95_HP(A) vs. FL95_PMA(A), and FL95_HP(B) vs. FL95_PMA(B)), lower E* values were observed for the HP AC mixes at intermediate frequencies and temperatures indicating a softer behavior under traffic loading. However, higher E* values were observed for the HP AC mixes at lower frequencies and higher temperature indicating a stable behavior and high rutting resistance under slow traffic loading.
- In the case of the FL125 AC mixes (i.e., FL125_HP(A) vs. FL125_PMA(A), and FL125_HP(B) vs. FL125_PMA(B)), lower E* values were observed for the HP AC mixes at intermediate frequency and temperature indicating a softer behavior under traffic loading. On the other hand, slightly lower E* values were observed for the HP AC mixes at much lower and higher frequencies simulating lower and higher temperatures, respectively.
- In the case of the GA95 and GA125 AC mixes, significantly lower E* values were observed for the HP mixes at all temperatures and frequencies when compared with their corresponding GA PMA AC control mixes. This can be partially attributed to the stiffer behavior of the GA PMA AC mixes containing 20% RAP.

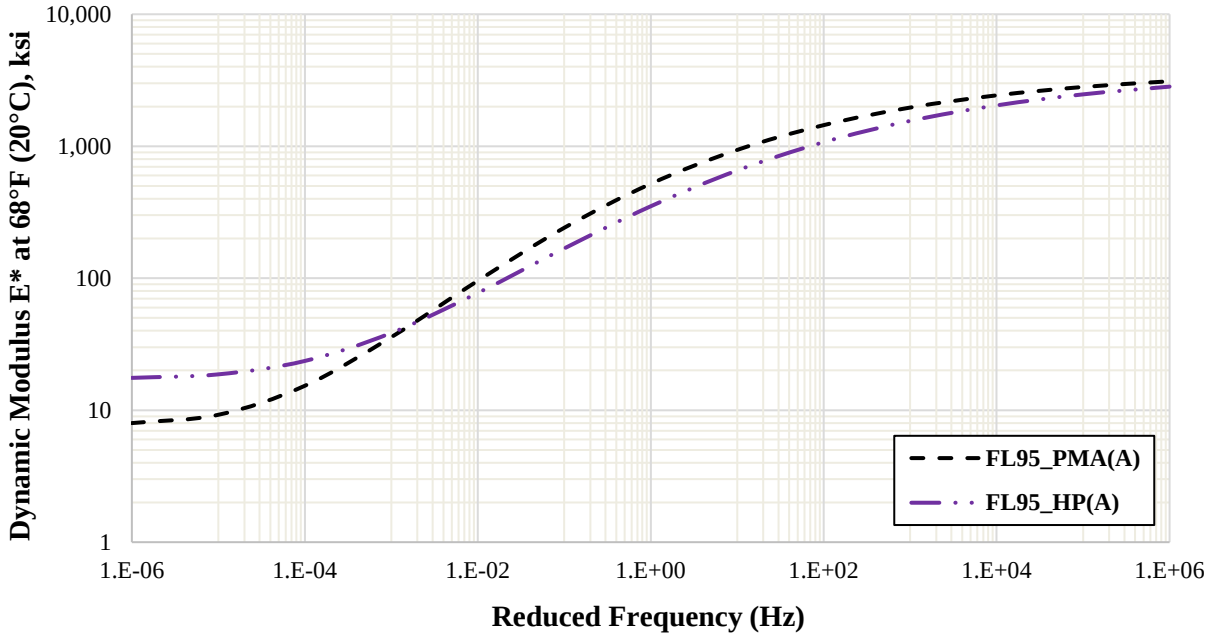


**Figure 4-5. E* master curves of FL95_PMA(A) and FL95_HP(A) at 68°F (20°C).**

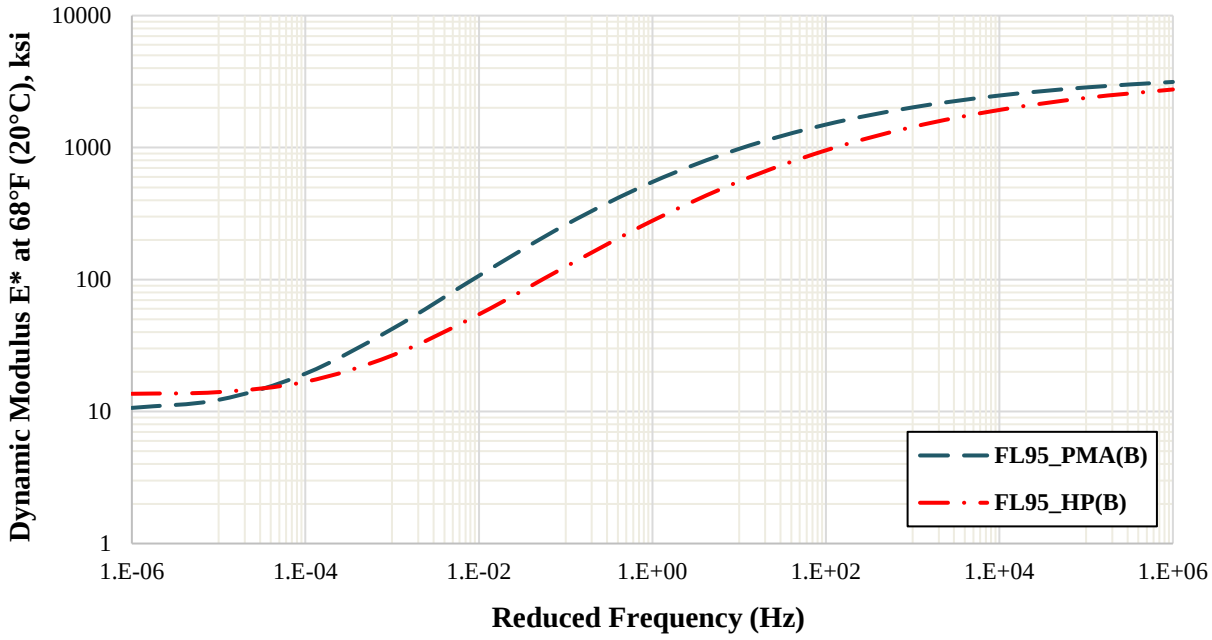


**Figure 4-6. E* master curves of FL95_PMA(B) and FL95_HP(B) at 68°F (20°C).**

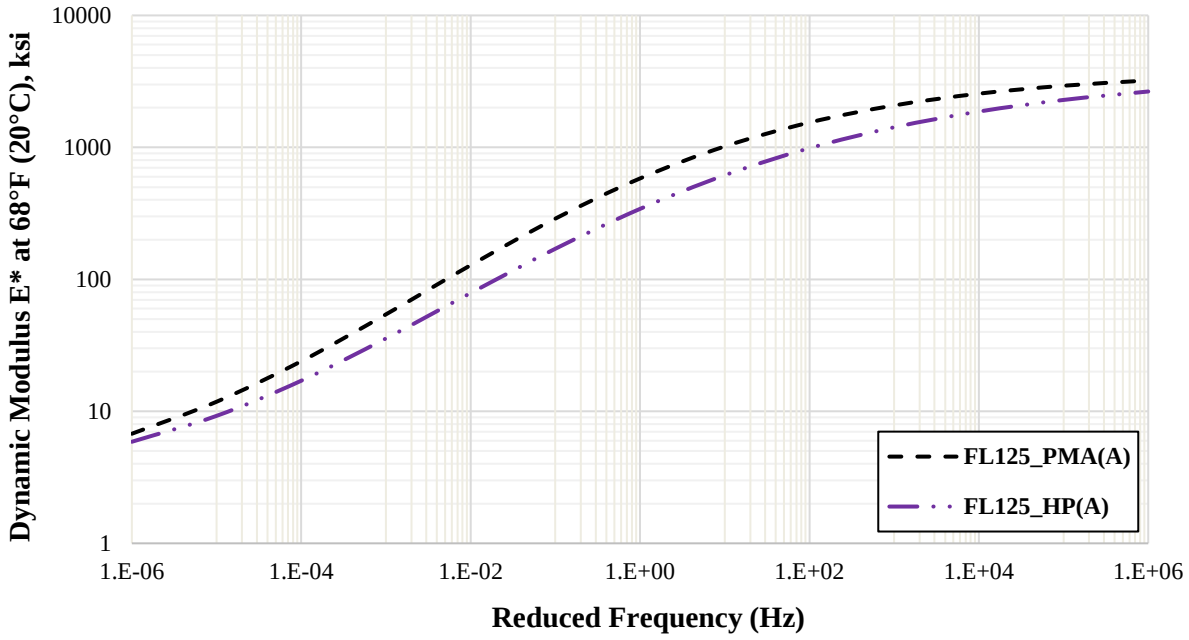


**Figure 4-7. E* master curves of FL125_PMA(A) and FL125_HP(A) at 68°F (20°C).**

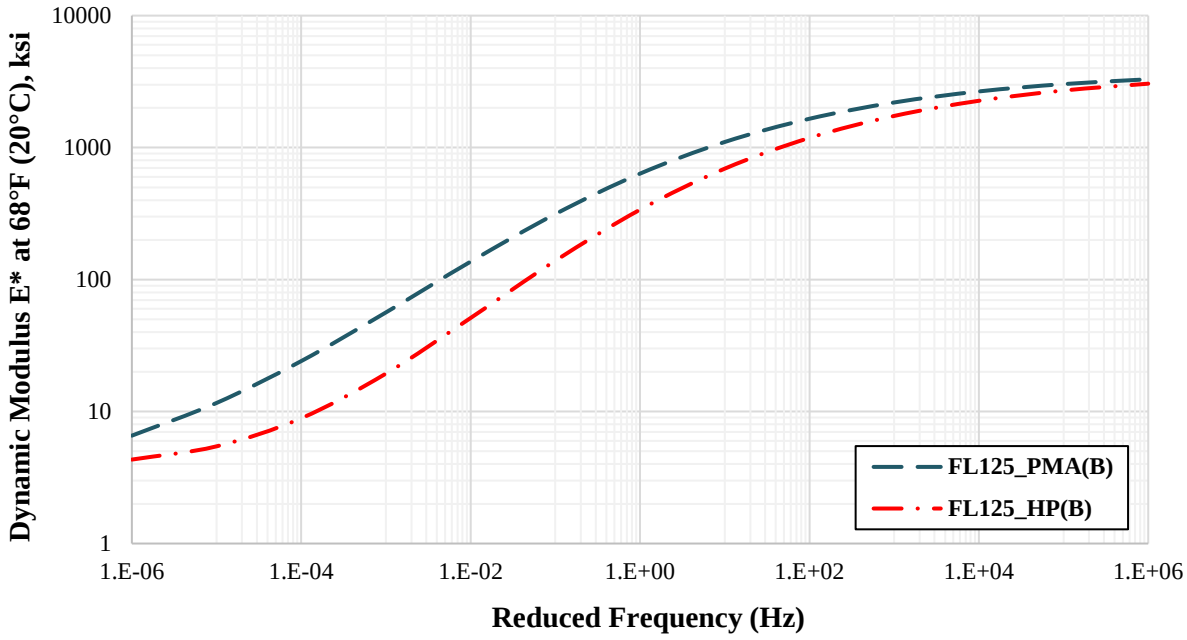


**Figure 4-8. E* master curves of FL125_PMA(B) and FL125_HP(B) at 68°F (20°C).**

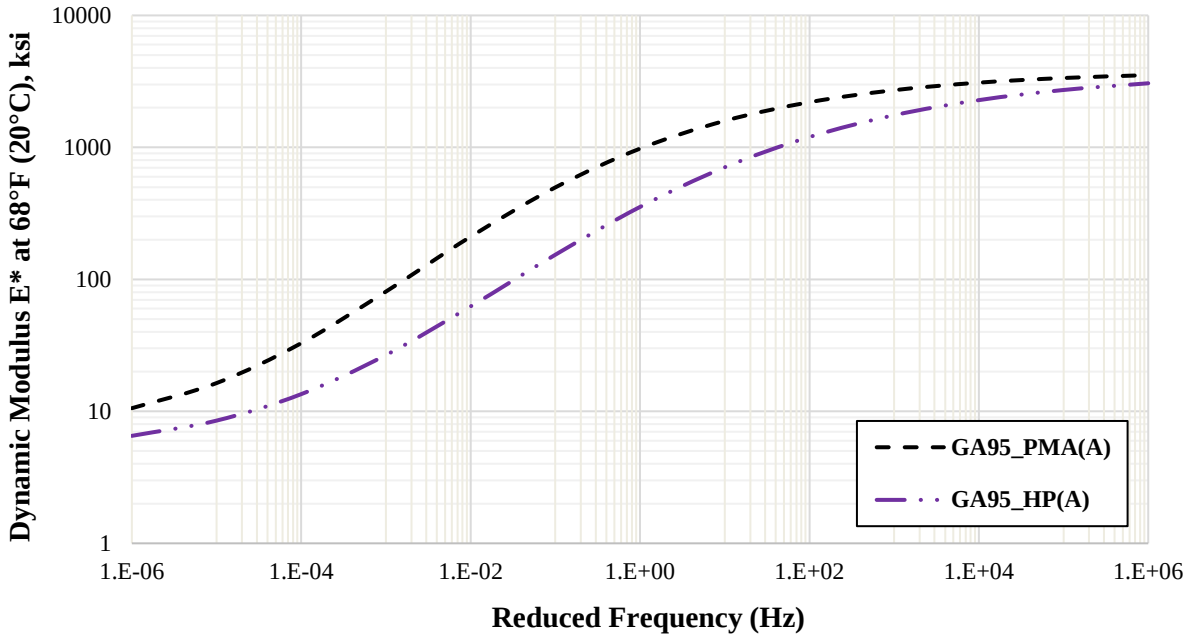


**Figure 4-9. E* master curves of GA95_PMA(A) and GA95_HP(A) at 68°F (20°C).**

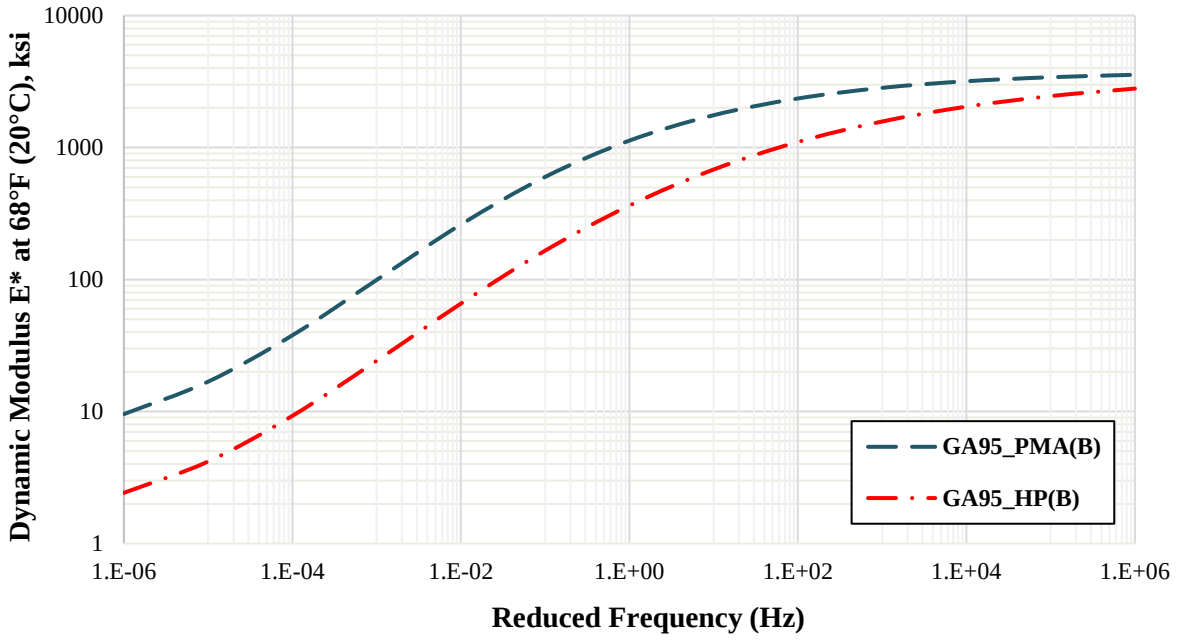


**Figure 4-10. E* master curves of GA95_PMA(B) and GA95_HP(B) at 68°F (20°C).**

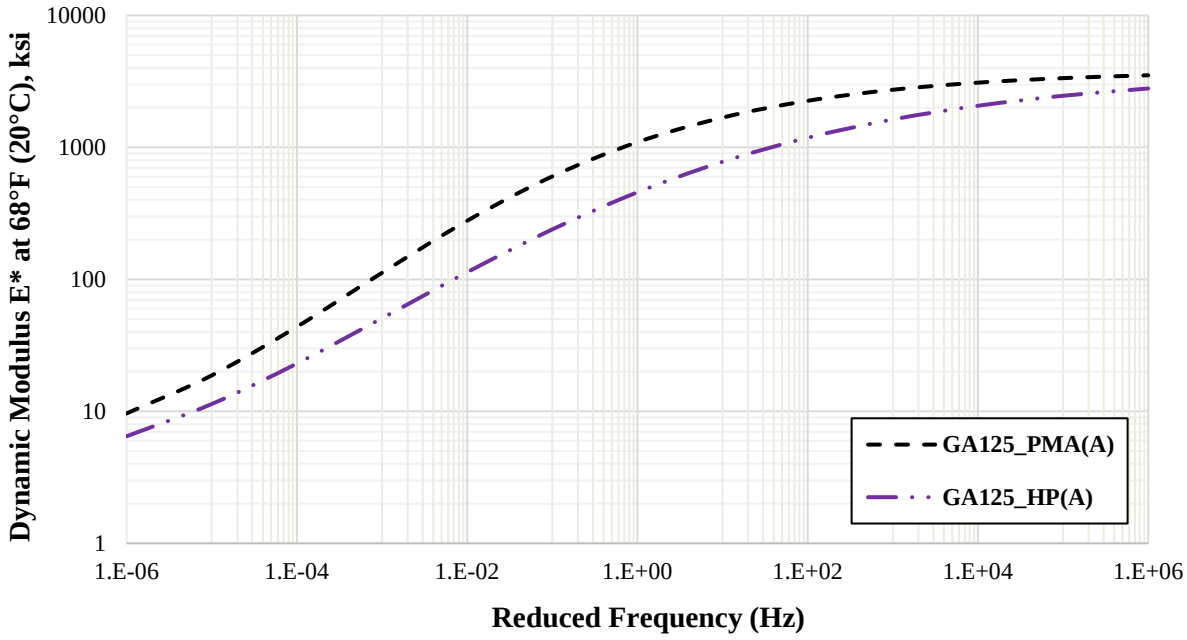


**Figure 4-11. E* master curves of GA125_PMA(A) and GA125_HP(A) at 68°F (20°C).**

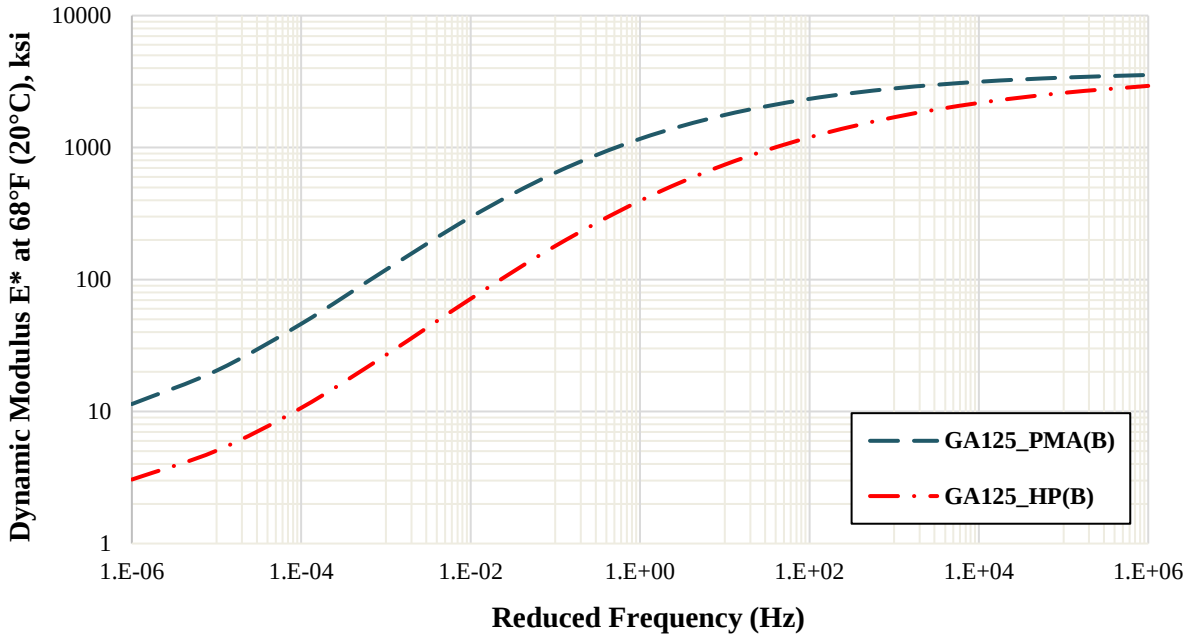


**Figure 4-12. E* master curves of GA125_PMA(B) and GA125_HP(B) at 68°F (20°C).**

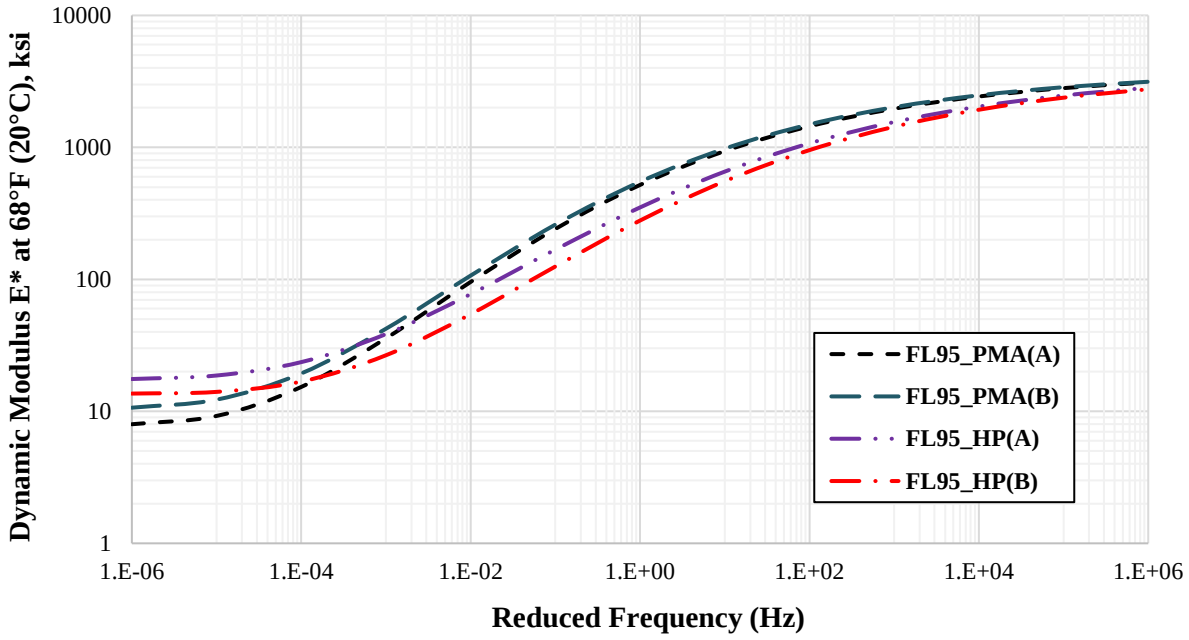


**Figure 4-13. E* master curves of all evaluated FL95 AC mixes at 68°F (20°C).**

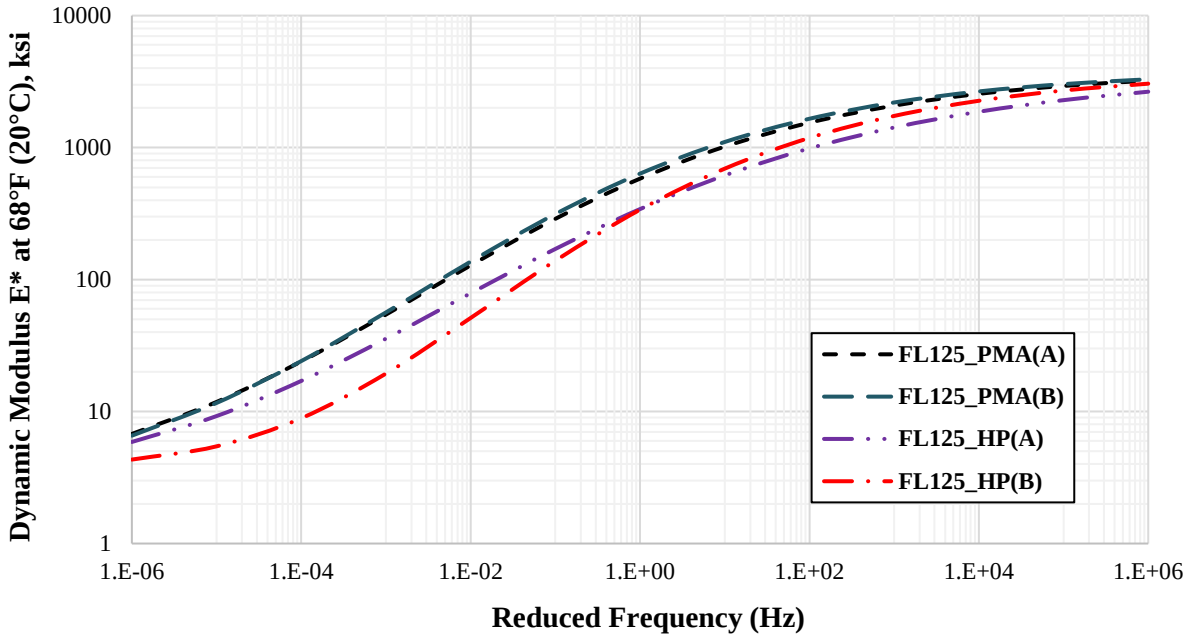


**Figure 4-14. E* master curves of all evaluated FL125 AC mixes at 68°F (20°C).**

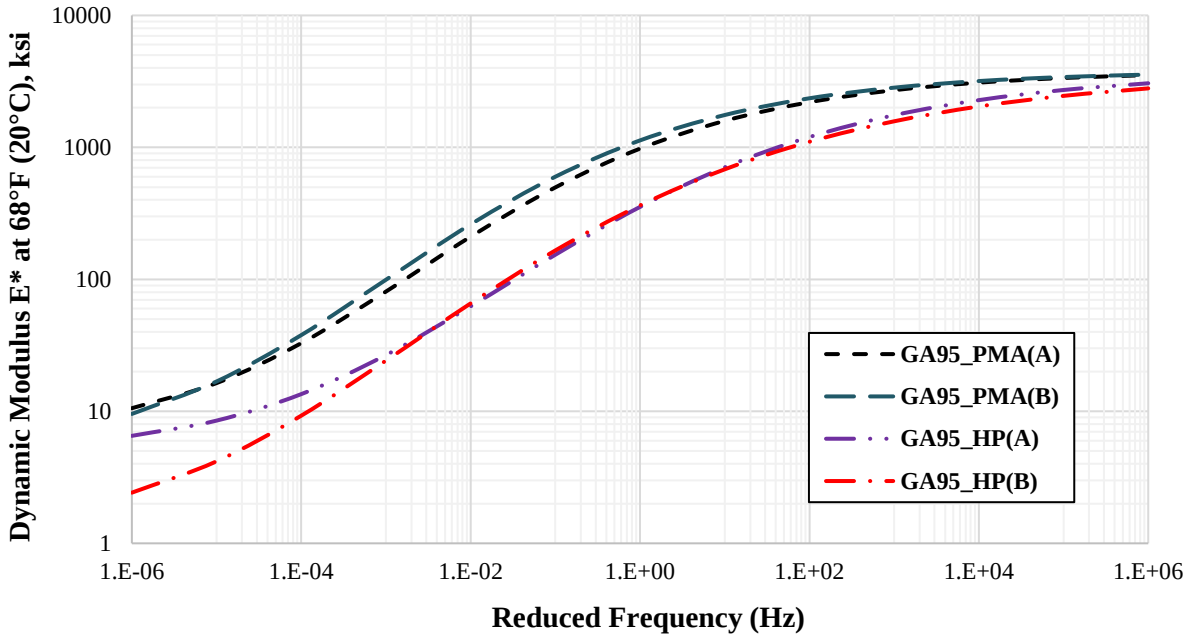


**Figure 4-15. E* master curves of all evaluated GA95 AC mixes at 68°F (20°C).**

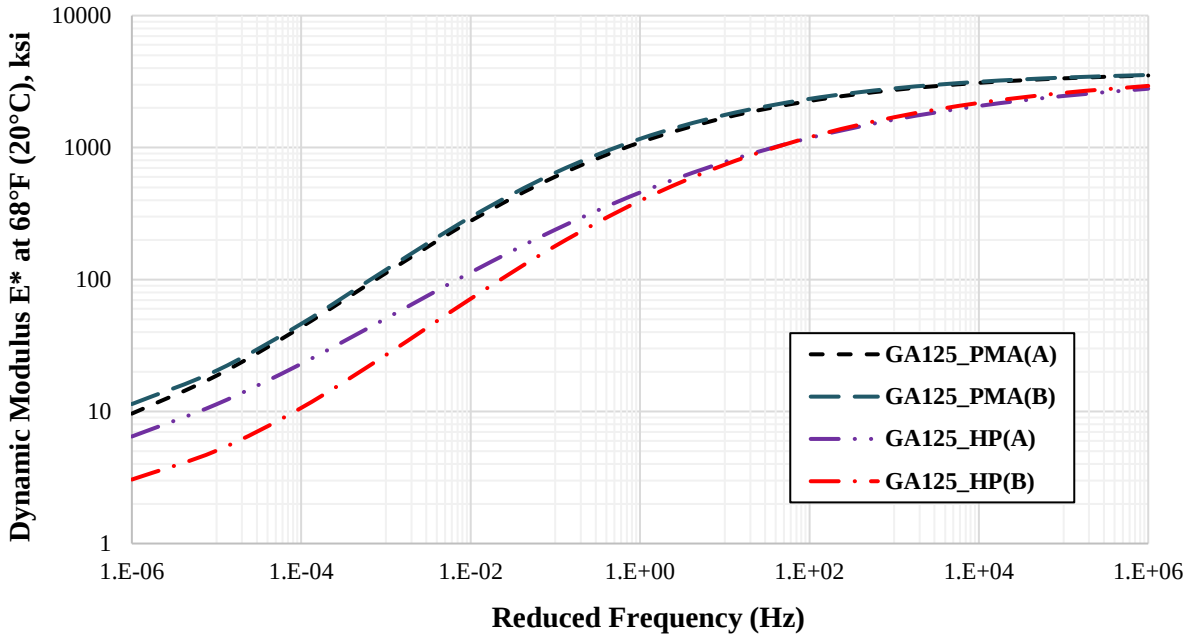


**Figure 4-16. E* master curves of all evaluated GA125 AC mixes at 68°F (20°C).**

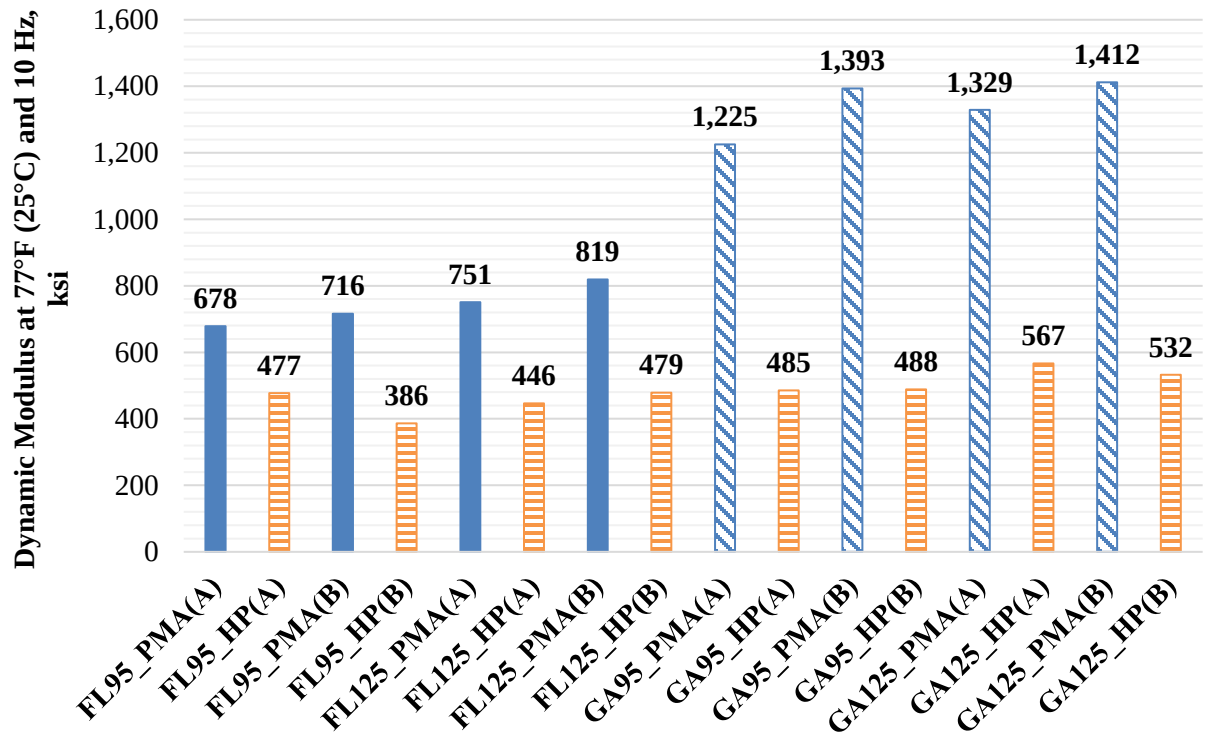


**Figure 4-17. E* values at 10 Hz and 77°F (25°C) of all evaluated mixes.**

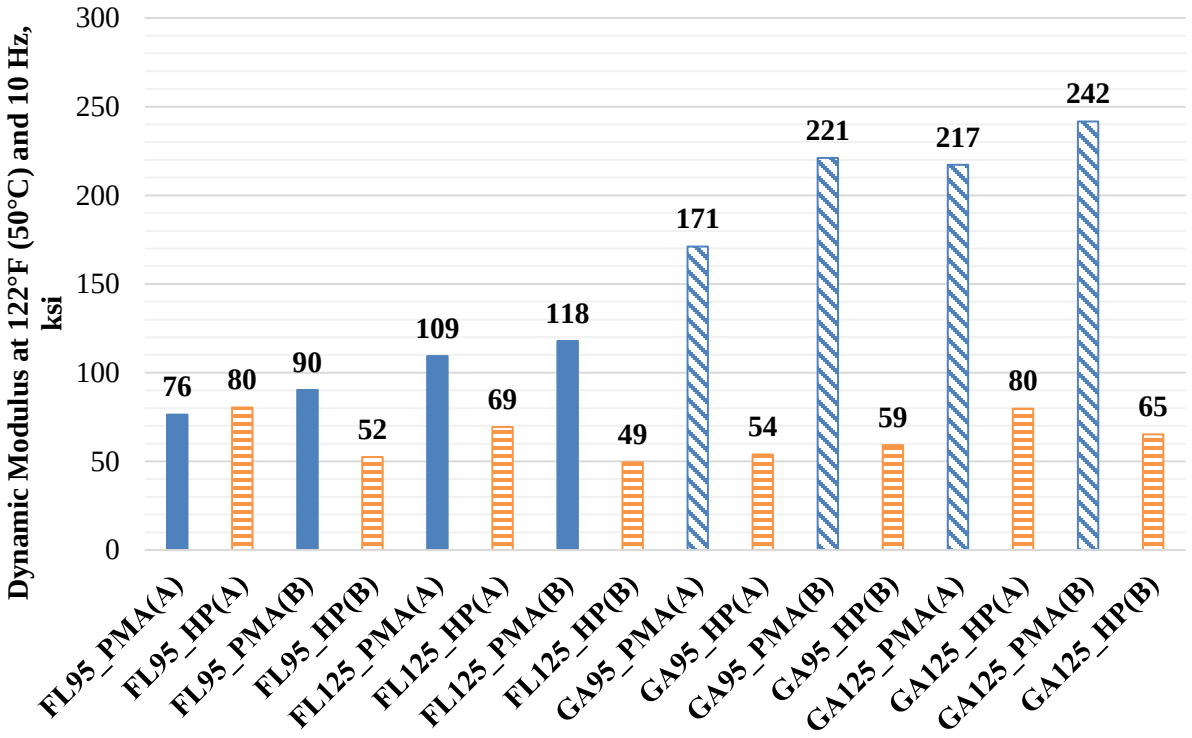


**Figure 4-18. E* values at 10 Hz and 122°F (50°C) of all evaluated mixes.**

### 4.2.2. Rutting Characteristics

The RLT test was used to evaluate the rutting characteristics of the 16 AC mixes under repeated loading. The permanent ($\varepsilon_p$) and resilient ($\varepsilon_r$) axial strains were measured during the RLT test as a function of the number of loading repetitions. The resulting cumulative permanent axial strain over the resilient strain ($\varepsilon_p/\varepsilon_r$) was plotted versus the number of load repetitions ($N$) to determine the rutting behavior of the evaluated asphalt mixtures at each of the three tested temperatures. The rutting relationship ($\varepsilon_p/\varepsilon_r$ versus $N$) indicates the response of the asphalt mixture to the repeated loading at high temperature. A lower relationship indicates lower accumulated permanent strains with loading, thus implying a better resistance to rutting. Furthermore, a flatter curve indicates a lower susceptibility of the asphalt mixture to repeated loading. Figure 4-19 to Figure 4-22 show the rutting relationships of the PMA control AC mixes versus the HP designed AC mixes for all FL95, FL125, GA95, and GA125 AC mixes at 122°F (50°C). In addition, the rutting relationships of all evaluated AC mixes manufactured using different aggregate source (i.e., FL, and GA), and same NMAS and binder type (i.e., PMA, and HP) are illustrated in Figure 4-23 and Figure 4-24. A review of the RLT data reveals the following observations:

- The combination of aggregate source and asphalt binder type (i.e., PMA or HP) had a significant impact on the rutting behavior of the 16 evaluated AC mixes. For all HP AC mixes, lower and flatter rutting relationships were observed when compared with the corresponding PMA AC control mixes. Thus, indicating a better resistance to rutting and a lower susceptibility of the evaluated HP AC mixes to repeated loading.

- For the AC mixes manufactured using PMA binder, the GA mixes showed a better rutting performance when compared with the FL mixes. This behavior can be partially attributed to the stiffening effect of the RAP material (i.e., 20% RAP content) added into the GA PMA AC mixes and their lower OBC.
- For the AC mixes manufactured using HP binder, the GA mixes showed a slightly better rutting performance when compared with the FL mixes which can be attributed to the lower OBC of the GA AC mixes. It should be mentioned that none of the HP AC mixes using both source of aggregate (i.e., FL or GA) contained any recycled material.
- In the case of the FL95 AC mixes, after 10,000 loading repetitions, the resulting cumulative $\varepsilon_p/\varepsilon_r$ of the FL95_PMA(A) and FL95_PMA(B) AC mixes were 6.2 and 18.9 times greater than the values of the FL95_HP(A) and FL95_HP(B) AC mixes, respectively.
- In the case of the FL125 AC mixes, after 10,000 loading repetitions, the resulting cumulative $\varepsilon_p/\varepsilon_r$ of the FL125_PMA(A) and FL125_PMA(B) AC mixes were 8.6 and 5.6 times greater than the values of the FL125_HP(A) and FL125_HP(B) AC mixes, respectively.
- In the case of the GA95 AC mixes, after 10,000 loading repetitions, the resulting cumulative $\varepsilon_p/\varepsilon_r$ of the GA95_PMA(A) and GA95_PMA(B) AC mixes were 2.6 and 2.7 times greater than the values of the GA95_HP(A) and GA95_HP(B) AC mixes, respectively. These ratios are lower than the ones corresponding to the FL95 mixes mainly because of the stiffer behavior of GA95 PMA AC mixes containing 20% RAP.
- Similarly, in the case of the GA125 AC mixes, after 10,000 loading repetitions, the resulting cumulative $\varepsilon_p/\varepsilon_r$ of the GA125_PMA(A) and GA125_PMA(B) AC mixes are 3.9 and 2.7 times greater than the values of the G125_HP(A) and GA125_HP(B) AC mixes, respectively. These ratios remain lower than the ones corresponding to the FL125 mixes given the stiffer behavior of the GA125 PMA AC mixes also containing 20% RAP.

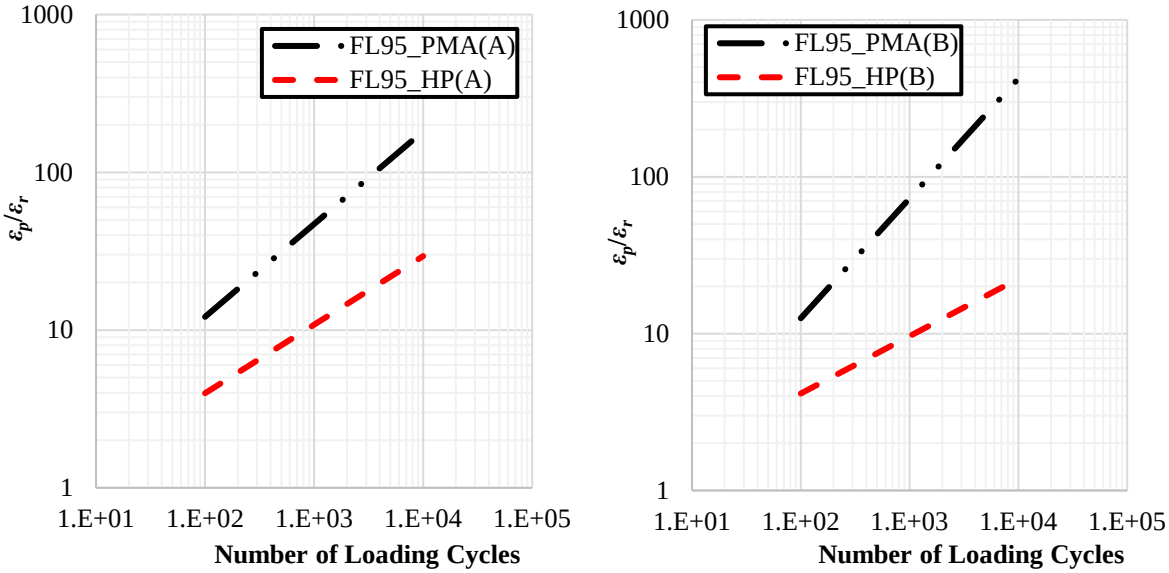


**Figure 4-19. Rutting behavior of FL95_PMA and HP AC mixes at 122°F (50°C).**

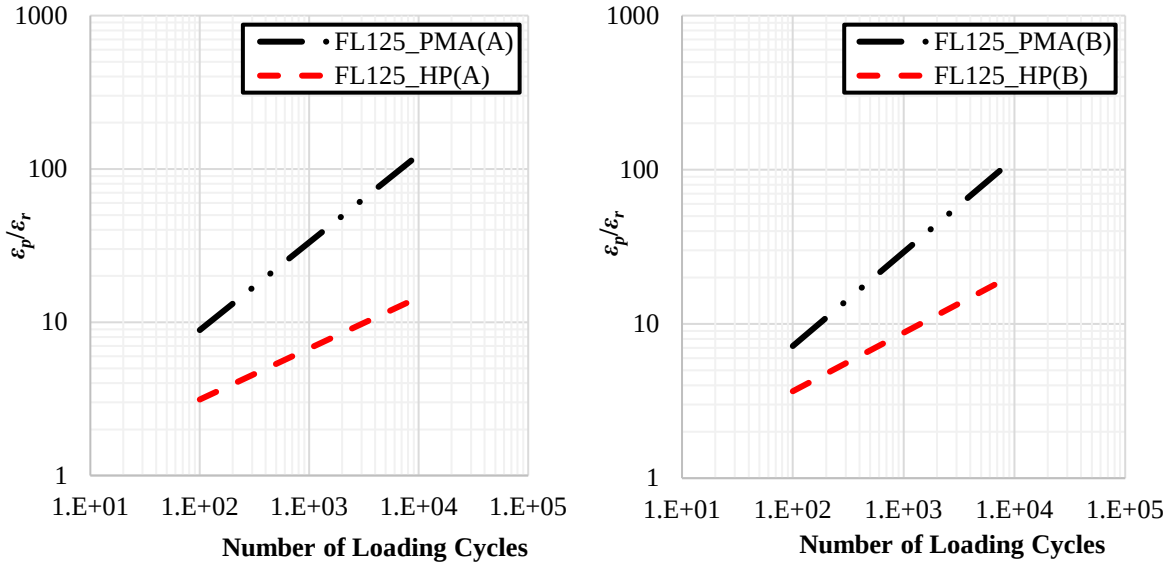


**Figure 4-20. Rutting behavior of FL125_PMA and HP AC mixes at 122°F (50°C).**

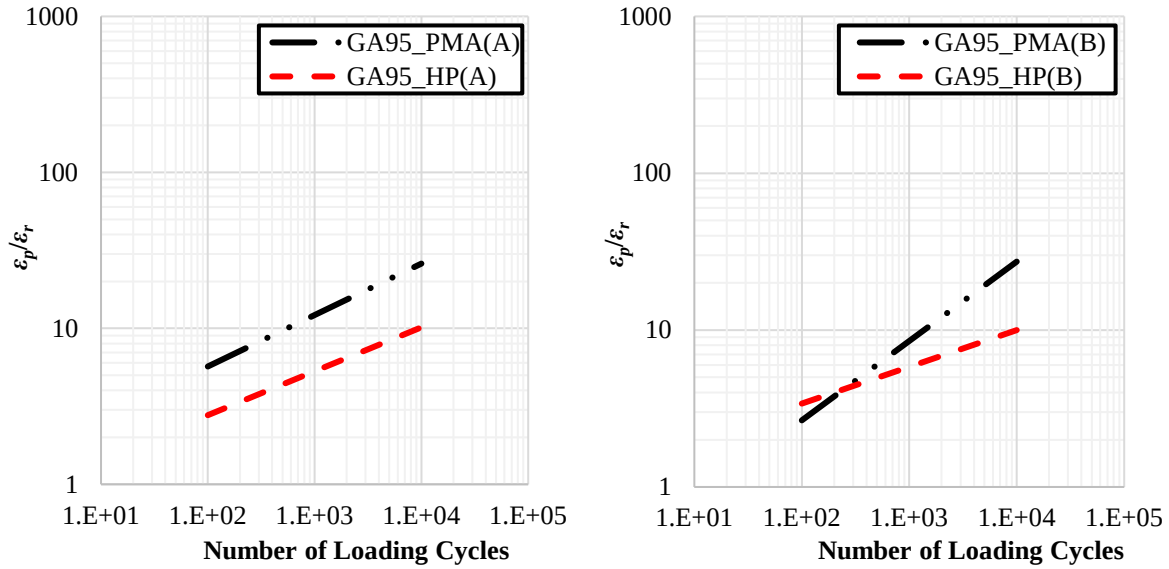


**Figure 4-21. Rutting behavior of GA95_PMA and HP AC mixes at 122°F (50°C).**

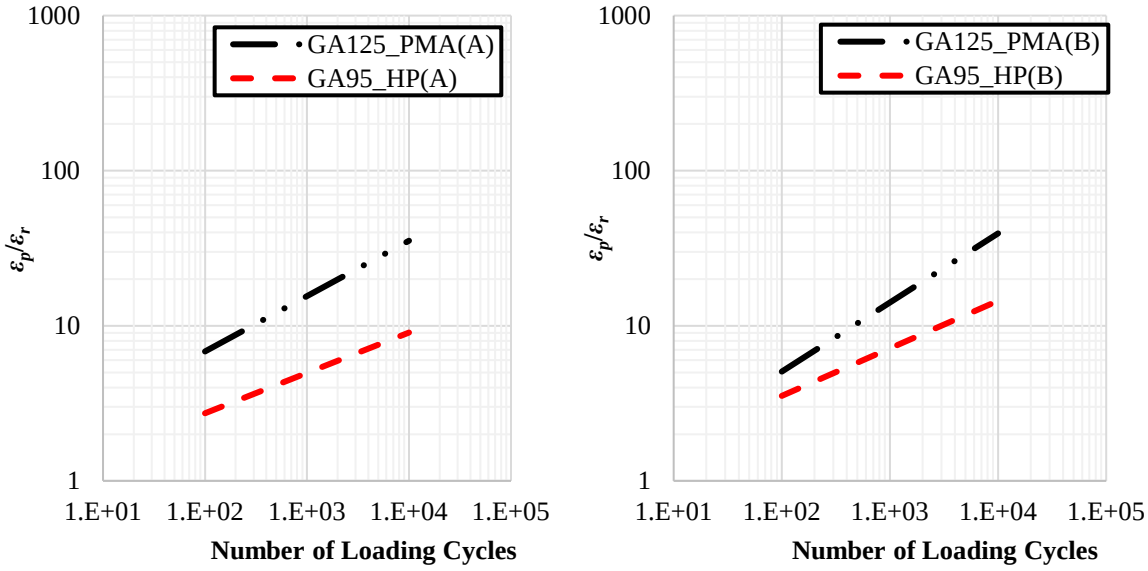


**Figure 4-22. Rutting behavior of GA125_PMA and HP AC mixes at 122°F (50°C).**

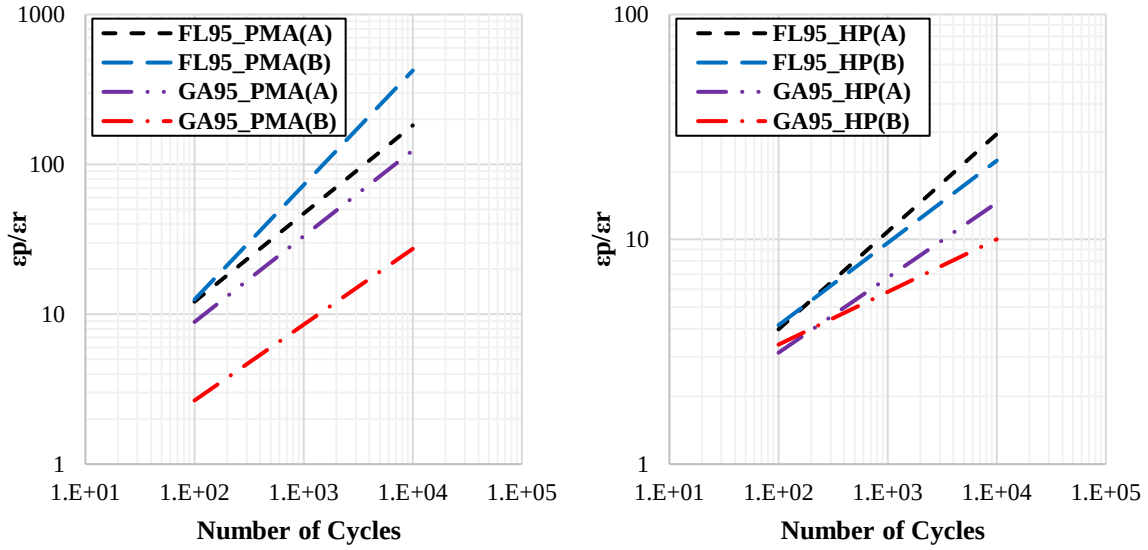


**Figure 4-23. Rutting behavior of all evaluated FL95 & GA95 AC mixes at 122°F (50°C).**

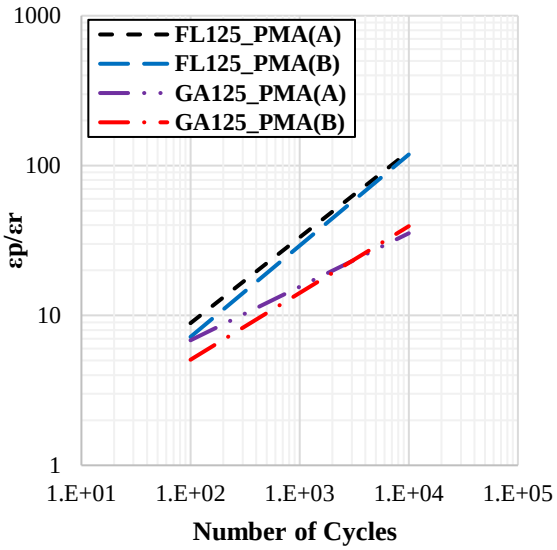


**Figure 4-24. Rutting behavior of all evaluated FL125 & GA125 AC mixes at 122°F (50°C).**

The improved behavior of the HP AC mixes was observed at all testing temperatures, thus indicating a better resistance to rutting and a lower susceptibility to repeated loading than the corresponding PMA AC mixes under different environmental conditions. The noticeably better rutting relationship of the HP AC mixes (i.e., lower and flatter curve) can be mainly attributed to the dominant behavior of the additional polymer. Appendix C section 2 (C.2) presents in details the RLT test data for the eight PMA and eight HP AC mixes. Table 4-8 summarizes the regression coefficients of the rutting models for the evaluated AC mixes based on the approach recommended in AASHTO Mechanistic-Empirical Pavement Design Guide (MEPDG).

It should be noted that, a significant difference in the laboratory rutting resistance will not necessarily translate into the same difference in rutting performance (i.e., rut depth) of the AC pavement in the field. Many factors may highly affect the rutting life of an AC pavement such as stiffness, the developed compressive strain in each of the AC sub-layers under field loading, the rutting characteristic of the evaluated asphalt mixture, and the interaction of all these factors. In a mechanistic pavement analysis, an AC layer with higher stiffness and lower laboratory rutting life (i.e. PMA AC mixes when compared with HP AC mixes) may experience lower compressive strains in the AC sub-layers under field loading conditions and result in a better pavement rutting life. Therefore, a full mechanistic analysis coupled with laboratory measured engineering and performance properties would be necessary to quantify and effectively evaluate the impact of HP binder on the rutting performance of the corresponding AC pavement.

**Table 4-8. Summary of Rutting Model Coefficients for All Evaluated AC Mixes.**

| Mix ID | Rutting Model Coefficients[1] | | |
|---|---|---|---|
| | $k_{r1}$ | $k_{f2}$ | $k_{f3}$ |
| FL95_PMA(A) | -12.4119 | 6.0735 | 0.4392 |
| FL95_PMA(B) | -15.4928 | 7.4574 | 0.5271 |
| FL125_PMA(A) | -14.2043 | 6.9175 | 0.4150 |
| FL125_PMA(B) | -10.7155 | 5.2287 | 0.4258 |
| GA95_PMA(A) | -18.8804 | 9.0534 | 0.3564 |
| GA95_PMA(B) | -13.7764 | 6.6140 | 0.3419 |
| GA125_PMA(A) | -11.4447 | 5.5212 | 0.3763 |
| GA125_PMA(B) | -21.5617 | 10.2064 | 0.4705 |
| FL95_HP(A) | -10.1818 | 4.8451 | 0.3992 |
| FL95_HP(B) | -6.1192 | 2.9910 | 0.2844 |
| FL125_HP(A) | -4.8104 | 2.4349 | 0.3113 |
| FL125_HP(B) | -12.8649 | 6.0716 | 0.3624 |
| GA95_HP(A) | -5.7850 | 2.6766 | 0.3280 |
| GA95_HP(B) | -6.3657 | 3.1349 | 0.2196 |
| GA125_HP(A) | -11.7157 | 5.5731 | 0.2401 |
| GA125_HP(B) | -9.0008 | 4.3241 | 0.2974 |

[1] $\frac{\varepsilon_p}{\varepsilon_r} = K_z * \beta_{r1} * 10^{k_{r1}} * (T)^{\beta_{r2} * k_{r2}} * (N)^{\beta_{r3} * k_{r3}}$

### 4.2.3. Fatigue Cracking Characteristics

The fatigue characteristics of the 16 AC mixes (i.e., eight PMA and eight HP AC mixes) were evaluated using the flexural beam fatigue test in accordance with ASTM D7460 *(75)* AASHTO T321 *(35)* at three temperatures and multiple strain levels. A fatigue curve at each testing temperature was developed for every AC mix (i.e., PMA and HP AC mix) by fitting a power regression function between the number of cycles to failure and the applied strain levels. Figure 4-25 to Figure 4-28 shows the fatigue relationships for all evaluated AC mixes at 77°F (25°C). A higher and flatter fatigue curve indicates a better resistance to fatigue cracking. A review of the fatigue data reveals the following observations:

- The combination of aggregate source and asphalt binder type (i.e., PMA or HP) had a significant impact on the fatigue behavior of the evaluated AC mixes. For all HP AC mixes, better fatigue relationships were observed when compared with the corresponding PMA AC control mixes at all strain levels and testing temperatures; thus, indicating increased flexibility and resistance to fatigue cracking of the HP AC mixes under different environmental conditions. The noticeably better fatigue relationship for the HP AC mixes can be mainly attributed to the dominant behavior of the additional polymer.
- For the AC mixes manufactured using PMA binder, the FL mixes showed a better fatigue performance when compared with the GA mixes. This behavior can be partially attributed to the stiffening effect of the RAP material added into the GA PMA AC mixes and their lower OBC.
- For the AC mixes manufactured using HP binder, the FL mixes showed a slightly better fatigue performance when compared with the GA mixes which can be attributed to the

higher OBC of the FL AC mixes. It should be mentioned that none of the HP AC mixes using both source of aggregate (i.e., FL or GA) contained any recycled material.

- In the case of the FL95 AC mixes, the number of cycles to failure for FL95_HP(A) and FL95_HP(B) mixes were about 6.4 and 9.0 times the number of cycles to failure for FL95_PMA(A) and FL95_PMA(B) mixes, respectively.
- In the case of the FL125 AC mixes, the number of cycles to failure for FL125_HP(A) and FL125_HP(B) mixes were about 4.1 and 24.5 times the number of cycles to failure for FL125_PMA(A) and FL125_PMA(B) mixes, respectively.
- In the case of the GA95 AC mixes, the number of cycles to failure for GA95_HP(A) and GA95_HP(B) mixes were about 16.1 and 20.2 times the number of cycles to failure for GA95_PMA(A) and GA95_PMA(B) mixes, respectively.
- In the case of the GA125 AC mixes, the number of cycles to failure for GA125_HP(A) and GA125_HP(B) mixes were about 320.5 and 13.7 times the number of cycles to failure for GA125_PMA(A) and GA125_PMA(B) mixes, respectively.

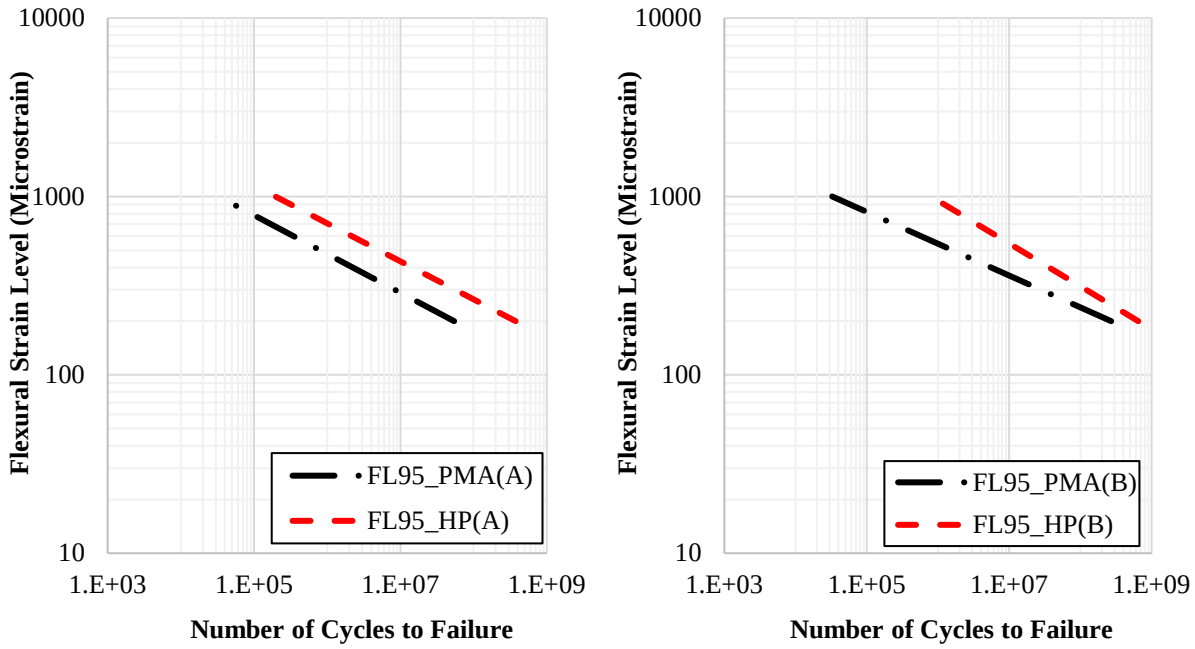


**Figure 4-25. Fatigue relationships of FL95 AC mixes at 77°F (25°C).**

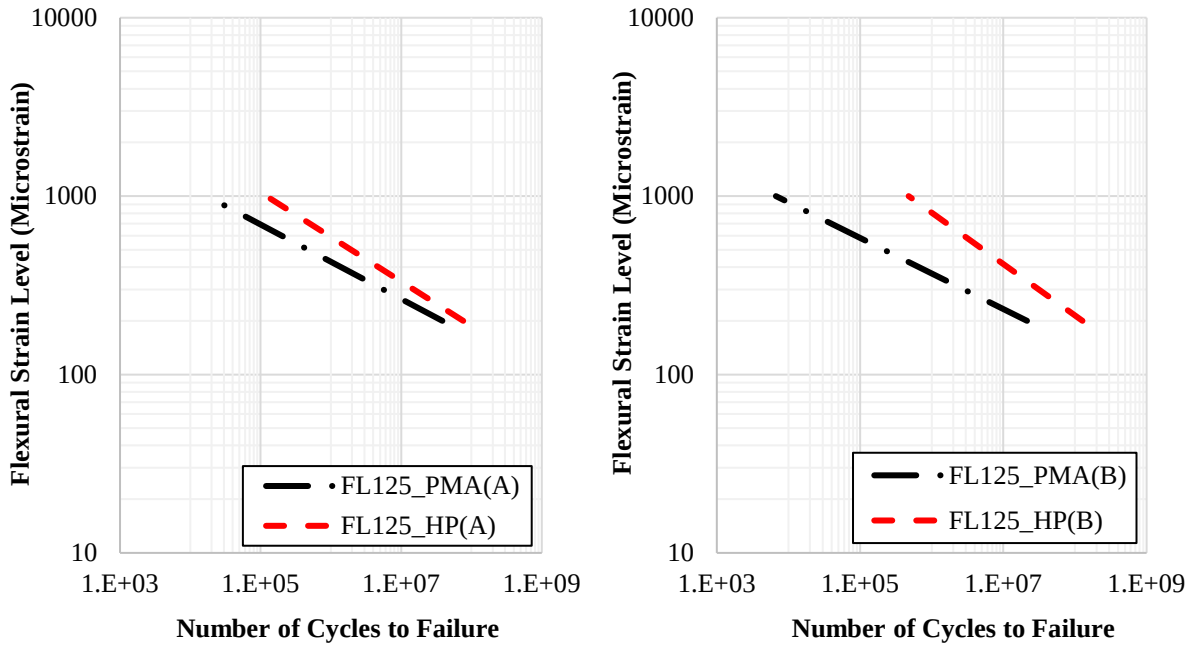


**Figure 4-26. Fatigue relationships of FL125 AC mixes at 77°F (25°C).**

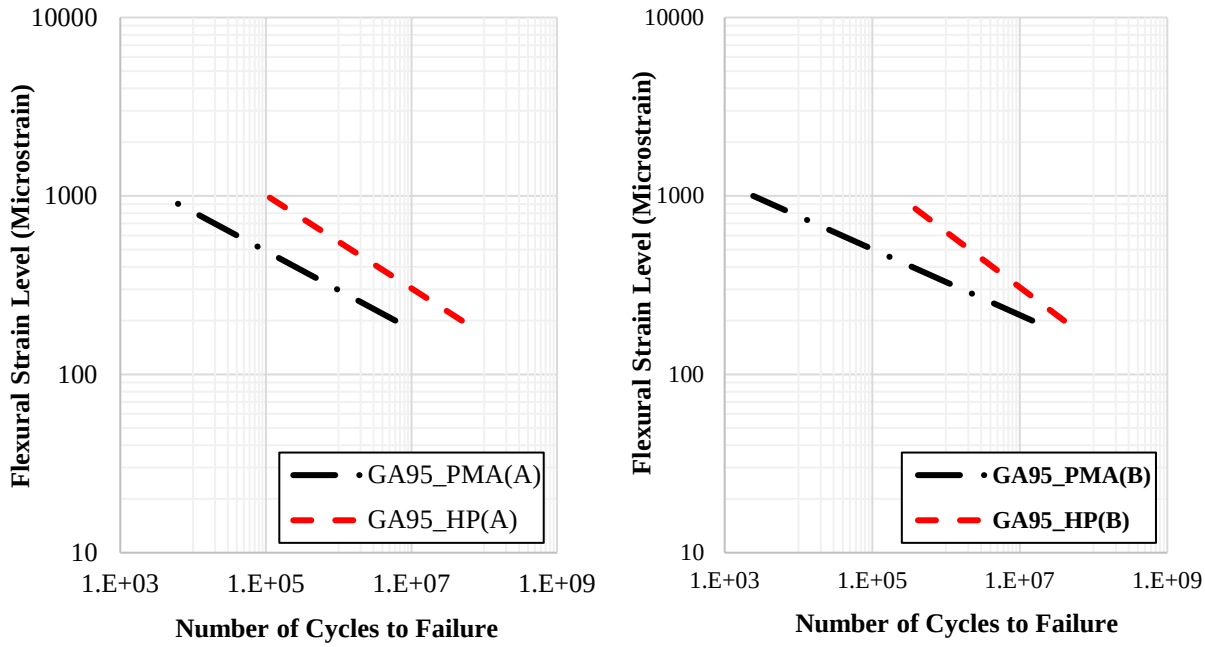


**Figure 4-27. Fatigue relationships of GA95 AC mixes at 77°F (25°C).**

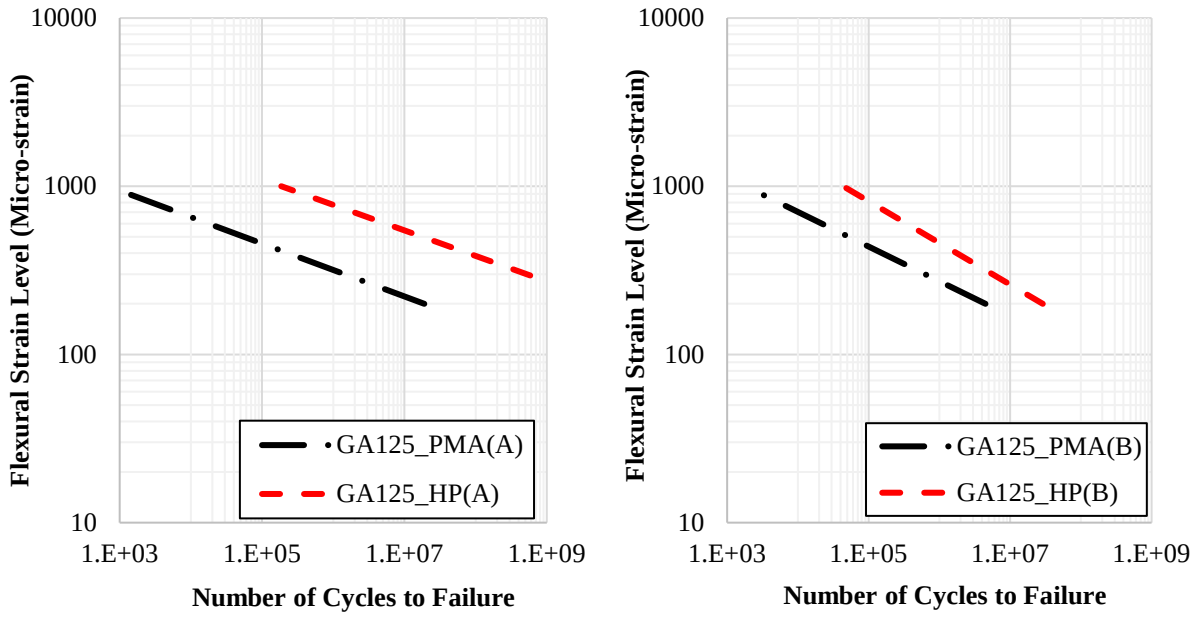


**Figure 4-28. Fatigue relationships of GA125 AC mixes at 77°F (25°C).**

Appendix C section 3 (C.3) presents in details the flexural beam fatigue data for the eight PMA and eight HP AC mixes. Table 4-9 summarizes the fatigue models regression coefficients for the evaluated AC mixes based on the approach recommended in AASHTO Mechanistic-Empirical Pavement Design Guide (MEPDG).

**Table 4-9. Summary of Fatigue Model Coefficients for All Evaluated AC Mixes.**

| Mix ID | Fatigue Model Coefficients[1] | | |
|---|---|---|---|
| | $k_{f1}$ | $k_{f2}$ | $k_{f3}$ |
| FL95_PMA(A) | 6.496E+10 | 4.6049 | 3.4488 |
| FL95_PMA(B) | 3.879E+08 | 5.6055 | 3.5679 |
| FL125_PMA(A) | 1.550E+11 | 4.7908 | 3.6296 |
| FL125_PMA(B) | 4.206E+10 | 5.0148 | 3.6938 |
| GA95_PMA(A) | 2.866E+11 | 4.5605 | 3.5392 |
| GA95_PMA(B) | 2.532E+06 | 5.4115 | 3.1332 |
| GA125_PMA(A) | 1.326E+14 | 6.3587 | 4.9585 |
| GA125_PMA(B) | 5.725E+14 | 4.8528 | 4.2370 |
| FL95_HP(A) | 4.441E+03 | 4.6965 | 2.1916 |
| FL95_HP(B) | 3.513E+11 | 4.1636 | 3.2456 |
| FL125_HP(A) | 1.512E+05 | 4.0043 | 2.1434 |
| FL125_HP(B) | 1.416E+19 | 3.4712 | 4.2054 |
| GA95_HP(A) | 1.961E+04 | 3.8268 | 1.8914 |
| GA95_HP(B) | 3.630E+12 | 3.2145 | 2.9618 |
| GA125_HP(A) | 4.822E+13 | 6.5922 | 4.8998 |
| GA125_HP(B) | 3.888E+09 | 4.0367 | 2.9792 |

[1] $N_f = \beta_{f1} * k_{f1} * \left(\frac{1}{\varepsilon_t}\right)^{\beta_{f2}*k_{f2}} * \left(\frac{1}{E_{AC}}\right)^{\beta_{f3}*k_{f3}}$

It should be noted that, a significant difference in the laboratory fatigue resistance will not necessarily translate into the same difference in fatigue performance of the AC pavement in the field. Many factors may highly affect the fatigue life of an AC pavement such as stiffness, the developed tensile strain under field loading, the fatigue characteristic of the evaluated asphalt mixture, and the interaction of all these factors. In a mechanistic pavement analysis, an AC layer with higher stiffness and lower laboratory fatigue life (in a strain-controlled mode of loading) may experience lower tensile strain under field loading and result in a longer pavement fatigue life. Therefore, a full mechanistic analysis would be necessary to effectively evaluate the impact of HP binder on fatigue performance of the corresponding AC pavement.

### 4.2.4. Top-Down Cracking Characteristics

The resistance to top-down cracking of the 16 AC mixes (i.e., eight PMA and eight HP AC mixes) were evaluated using the IDT test in accordance with AASHTO T322 *(28)* and Appendix G of the NCHRP 9-57 study *(76)* at 50°F (10°C). The IDT test specimens were short-term aged followed by long-term aging (AASHTO R30 *(70)*). The creep compliance parameters (i.e., $D_1$, and $m$) of the 16 AC mixes were determined using the tensile creep compliance test. In addition, the mixture failure strain $(\varepsilon_f)$ and the dissipated creep strain energy density failure limit $(DSCE_f)$ were determined using the tensile fracture test. Table 4-10 summarizes top-down cracking properties for the 16 AC mixes. The following are some of the challenges that were faced during testing which should be kept in mind when examining the test results:

- The Jig and associated instrumentations used for IDT testing which was mounted into the AMPT Pro is still under verification and improvement by the equipment supplier.
- The extensometers connected to the testing specimens were highly sensitive and susceptible to bending with the increase in load amplitude.
- The IDT creep compliance test and tensile fracture test had to be conducted as two separate tests for the software to properly record the required data.
- Some extensometers stopped working during testing of some test specimens. Thus, some of the test results were based on one extensometer and/or one face of the test specimen.

A review of the top-down cracking data in Table 4-10 reveals the following observations:

- The combination of aggregate source and asphalt binder type (i.e., PMA or HP) had an impact on the test results of the evaluated AC mixes. A lower $D_1$ is an indicator of a lower creep stiffness for the evaluated AC mix. A higher $m$ value is an indicator of a higher susceptibility of the mix to creep as a function of time. For all HP AC mixes, lower $m$ values were observed when compared with the respective PMA AC mixes.
- For the AC mixes manufactured using PMA binders, the FL mixes showed higher $D_1$ values when compared with the GA mixes. This behavior for the GA mixes can be attributed to both, the lower OBC and the stiffening of the mix as a result of the 20% RAP addition.
- For the AC mixes manufactured using HP binders and for a given aggregate source (i.e., FL, and GA), the mixes manufactured using asphalt binder from source (B) showed a greater $D_1$ value than the ones manufactured using asphalt binder from source (A).

**Table 4-10. Summary of Top-Down Cracking Coefficients for All Evaluated AC Mixes.**

| Mix ID | Creep Compliance Parameters | | E*[1] (psi) | $\varepsilon_f$ (micro-strain) | $S_T$ (psi) | $DSCE_f$ (lbf-in/in$^3$) |
|---|---|---|---|---|---|---|
| | $D_1$ (psi$^{-1}$) | m | | | | |
| FL95_PMA(A) | 6.26E-07 | 0.4396 | 1,564,815 | 841 | 243.8 | 0.1279 |
| FL95_PMA(B) | 3.70E-07 | 0.5262 | 1,553,067 | 959 | 232.1 | 0.1459 |
| FL95_HP(A) | 3.41E-07 | 0.4376 | 1,129,991 | 796 | 165.5 | 0.0827 |
| FL95_HP(B) | 1.13E-06 | 0.4288 | 1,026,289 | 859 | 81.1 | 0.1542 |
| FL125_PMA(A) | 7.31E-08 | 0.6490 | 1,659,670 | 934 | 267.3 | 0.1689 |
| FL125_PMA(B) | 4.39E-07 | 0.4641 | 1,769,174 | 507 | 199.0 | 0.0667 |
| FL125_HP(A) | 9.45E-08 | 0.6349 | 1,070,090 | 723 | 185.7 | 0.0830 |
| FL125_HP(B) | 1.08E-06 | 0.4357 | 1,267,922 | 437 | 137.4 | 0.0342 |
| GA95_PMA(A) | 5.34E-08 | 0.7298 | 2,326,119 | 675 | 270.5 | 0.1235 |
| GA95_PMA(B) | 5.45E-08 | 0.6111 | 2,467,531 | 660 | 272.8 | 0.1293 |
| GA95_HP(A) | 9.24E-08 | 0.6601 | 1,309,838 | 1,112 | 204.1 | 0.1400 |
| GA95_HP(B) | 6.19E-07 | 0.4199 | 1,279,090 | 513 | 206.5 | 0.0593 |
| GA125_PMA(A) | 1.98E-08 | 0.7104 | 2,383,554 | 220 | 177.9 | 0.0184 |
| GA125_PMA(B) | 2.03E-09 | 1.0050 | 2,458,249 | 261 | 245.1 | 0.0274 |
| GA125_HP(A) | 2.80E-08 | 0.7681 | 1,318,540 | 933 | 225.6 | 0.1252 |
| GA125_HP(B) | 1.19E-06 | 0.3987 | 1,284,311 | 862 | 198.9 | 0.1033 |

[1]E* determined at testing temperature of 50°F (10°C) and a frequency of 10 Hz.

### 4.2.5. Reflective Cracking Characteristics

The mixtures' resistance to reflective cracking were evaluated in accordance with Tex-248-F procedure using the AMPT machine *(34)*. Figure 4-29 shows the number of cycles at 77°F (25°C) at which each evaluated AC mix reached 93% drop in initial load. A higher number of OT cycles to failure indicates a better resistance to reflective cracking. The numerical values above the bars represent the average values while the whiskers represent the 95% CI. An overlap in the CI's indicates statistically similar properties of the mixtures.

In general, the combination of aggregate source and asphalt binder type (i.e., PMA or HP) had a significant impact on the reflective cracking behavior of the evaluated AC mixes. For all HP AC mixes, statistically similar or higher number of OT cycles to failure were observed when compared with the respective PMA AC control mixes. Thus, indicating an increased flexibility and resistance to reflective cracking of the HP AC mixes under different environmental conditions. In addition, significantly higher number of OT cycles to failure were observed for AC mixes manufactured using FL aggregate when compared with the mixes manufactured using GA aggregates. Furthermore, GA mixes manufactured using PMA binder exhibited very low number of OT cycles which can be attributed to the observed increase in mixture stiffness with the use of 20% RAP.

The OT test data were further analyzed to quantify the resistance of the evaluated mixes to cracking initiation and cracking propagation following Garcia et al. approach *(77)*. The crack initiation is represented and evaluated using the critical fracture energy *($G_c$)*, and the resistance to cracking during the propagation of the crack is evaluated using the crack propagation rate *(CPR)*.

Figure 4-30 and Figure 4-31 show $G_c$ and *CPR* of all evaluated AC mixes, respectively. A greater $G_c$ value indicates that the evaluated AC mix is tough and requires high initial energy to initiate a crack. On the other hand, a greater *CPR* value indicates that the evaluated AC mix is more susceptible to cracking (a fast crack propagation indicates shorter reflective cracking live). The reflective cracking data reveal the following observations:

- No consistent trends were observed for the generated $G_c$ values of evaluated AC mixes as a function of the aggregate mineralogy and asphalt binder type. For FL aggregate, the PMA AC mixes showed statistically similar or greater $G_c$ values when compared with the respective HP mixes. For GA aggregate, the PMA AC mixes showed statistically similar $G_c$ values when compared with the respective HP mixes. In addition, all HP AC mixes manufactured using GA aggregate showed statistically similar or greater $G_c$ values when compared with the respective HP AC mixes manufactured using FL aggregate. No consistent behavior was observed for the PMA AC mixes as a function of aggregate sources.
- In general, higher *CPR* values were observed for PMA AC mixes when compared with their corresponding HP AC mixes, thus, indicating a lower susceptibility to cracking for HP mixes. Higher *CPR* values were observed for PMA mixes manufactured using GA aggregate which can be attributed to the observed increase in mixture stiffness with the inclusion of RAP material (i.e., 20%). In addition, the HP AC mixes manufactured using FL aggregate source showed slightly lower *CPR* values when compared with the respective mixes manufactured using GA aggregate.

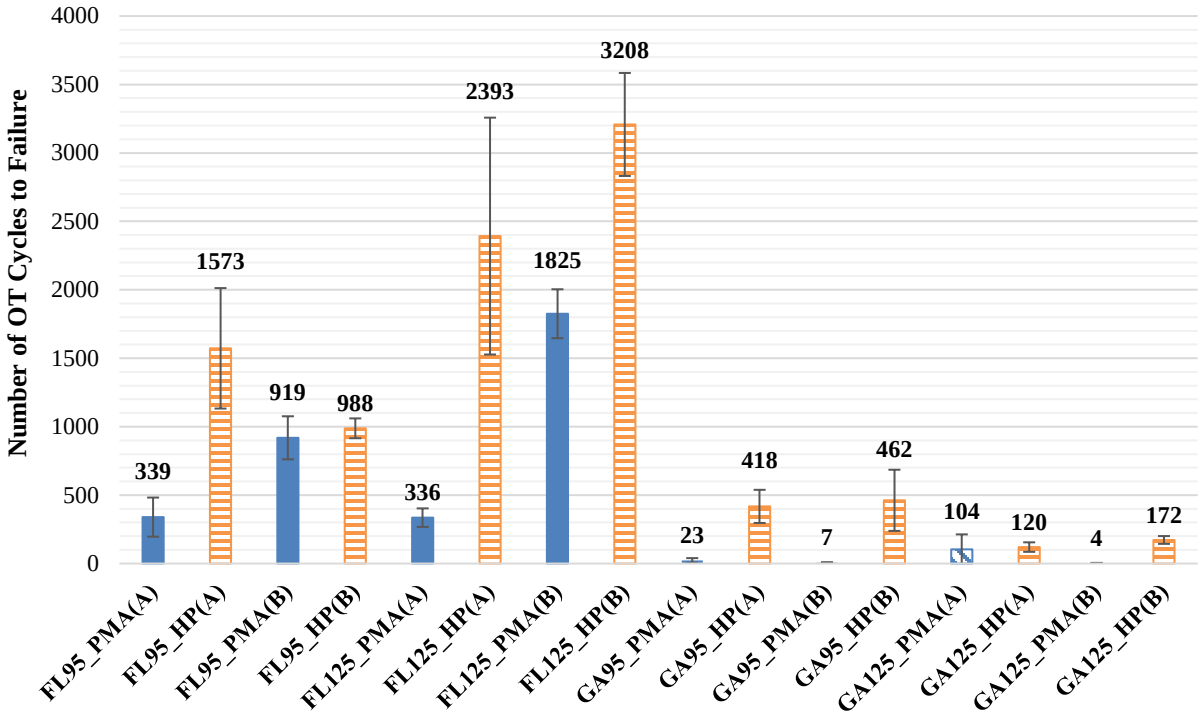


**Figure 4-29. Number of OT cycles to failure of all evaluated AC mixes at 77°F (25°C) (Whiskers represent the 95% CI).**

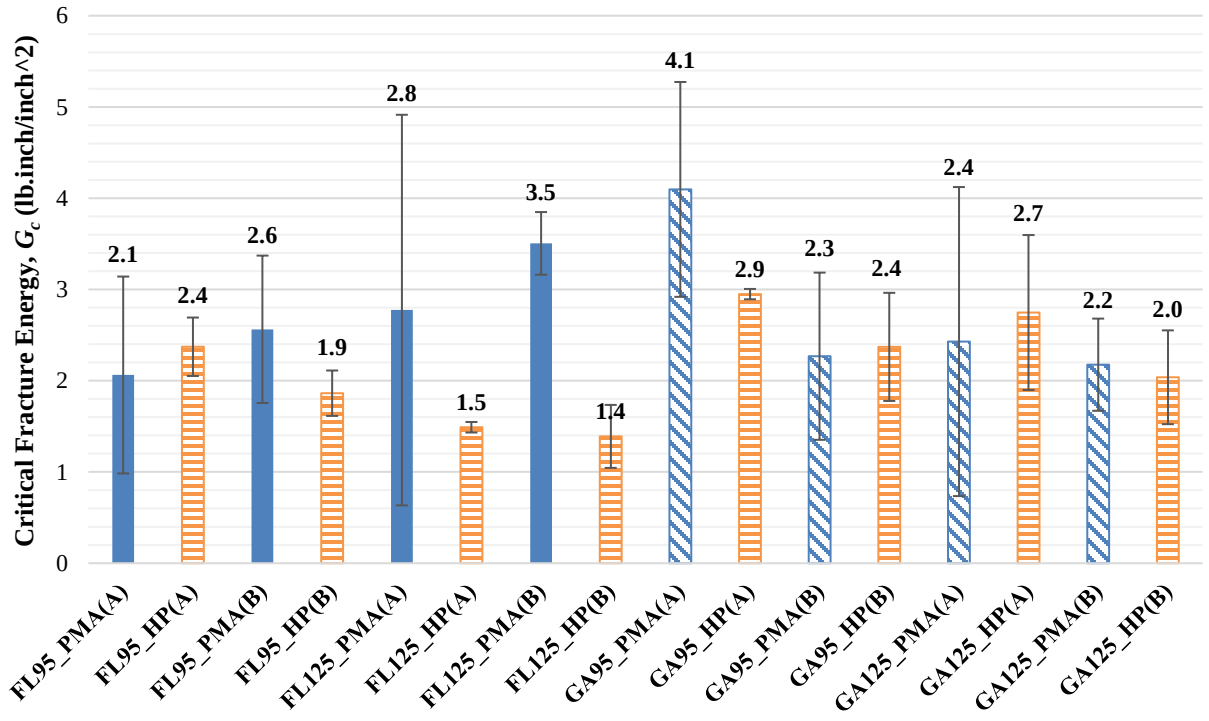


**Figure 4-30. Critical fracture energy at the first OT cycle of all evaluated AC mixes at a temperature 77°F (25°C) (Whiskers represent the 95% CI).**

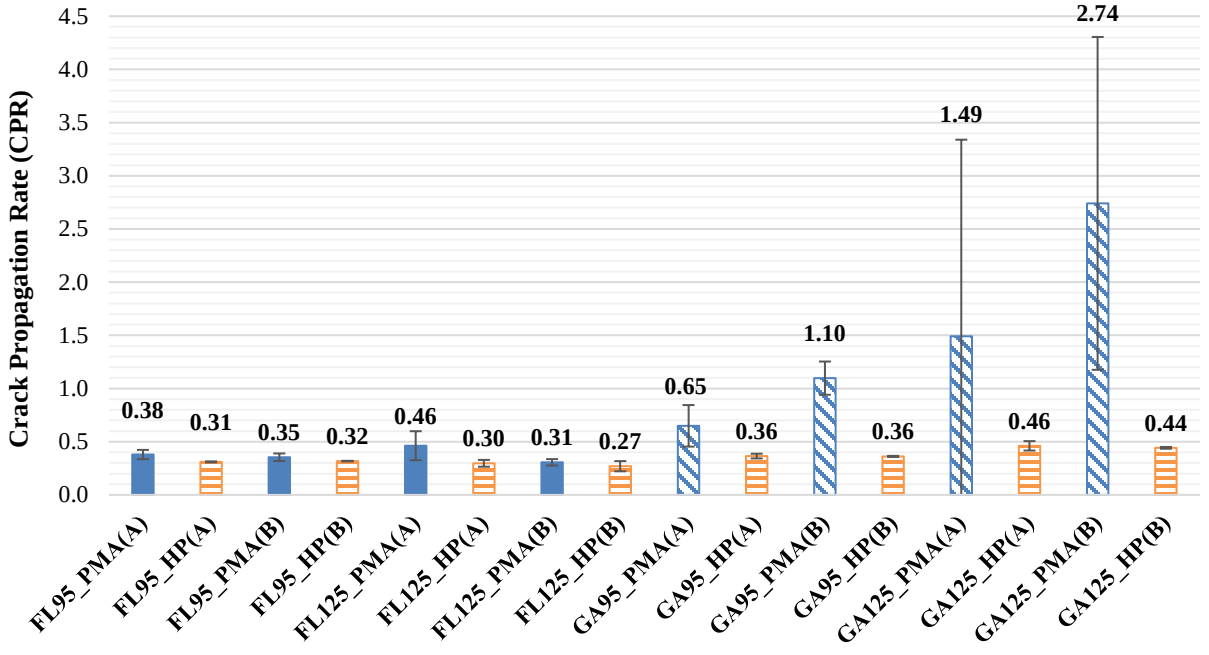


**Figure 4-31. Crack propagation rate of all evaluated AC mixes at a temperature of 77°F (25°C) (Whiskers represent the 95% CI).**

To better understand the cracking properties of all evaluated AC mixes, a design interaction graph plotting $G_c$ versus *CPR* was established. This interaction plot, illustrated in Figure 4-32, includes the following four categories *(77)*:

- ***Tough-Crack Resistant***: simulating a good resistance in both crack initiation (i.e., higher $G_c$ values) and crack propagation (flexible or crack resistance) (i.e., lower *CPR* values).
- ***Tough-Crack Susceptible***: simulating a good resistance in crack initiation (i.e., higher $G_c$ values) but susceptible to crack propagation (brittle) (i.e., higher *CPR* values).
- ***Soft-Crack Resistant***: simulating softness and susceptibility to crack initiation (i.e., lower $G_c$ values) but slow-down the propagation of the crack (flexible) (i.e., lower *CPR* values).
- ***Soft-Crack Susceptible***: simulating a significantly poor resistance to both crack initiation (i.e., lower $G_c$ values) and crack propagation (Brittle) (i.e., higher *CPR* values).

According to Garcia et al. *(77)*, a preliminary threshold for *CPR* of 0.5 was proposed based on the current criterion of 93% reduction in initial OT load. Preliminary limits for the $G_c$ were selected based on the correction between the tensile strength and $G_c$ measured from the IDT and OT tests, respectively. The upper limit (UL) was selected as 3 to screen the evaluated AC mixes with high brittleness potential. Meanwhile, the lower limit (LL) was selected at a value of 1.

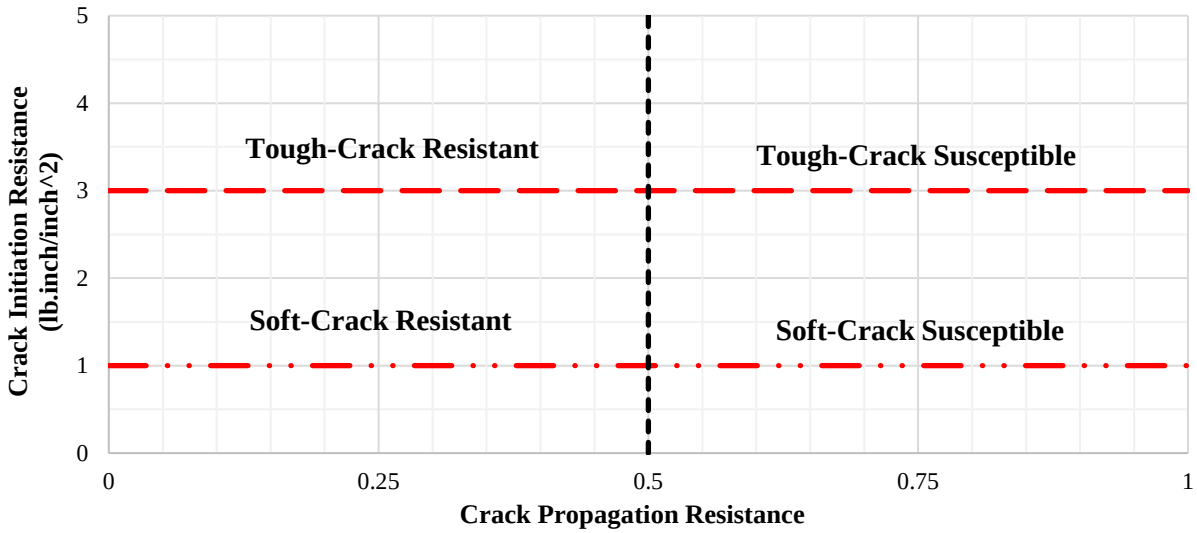


**Figure 4-32. Cracking resistance of AC mixes: a sketch of the design interaction plot.**

Figure 4-33 shows the cracking resistance interaction plot for all PMA and HP AC mixes manufactured using FL aggregates. All FL AC mixes showed a *CPR* value lower than 0.5 indicating a good cracking resistance. All FL mixes, except for FL125_PMA(B), showed a *CPR* value between 1 and 3 indicating a good resistance to crack initiation. FL125_PMA(B) mix was the only mix that showed tough-crack resistant mix. Figure 4-34 shows the cracking resistance interaction plot for all PMA and HP AC mixes manufactured with GA aggregates. All GA PMA AC mixes showed a *CPR* value greater than 0.5 indicating a brittle behavior and a low resistance to crack propagation. These mixes, except for GA95_PMA(A), showed $G_c$ values between 1 and 3 indicating a good resistance to crack initiation. On the other hand, all GA HP mixes show *CPR* values lower than 0.5 and $G_c$ values between 1 and 3 indicating soft-crack resistant mixes.

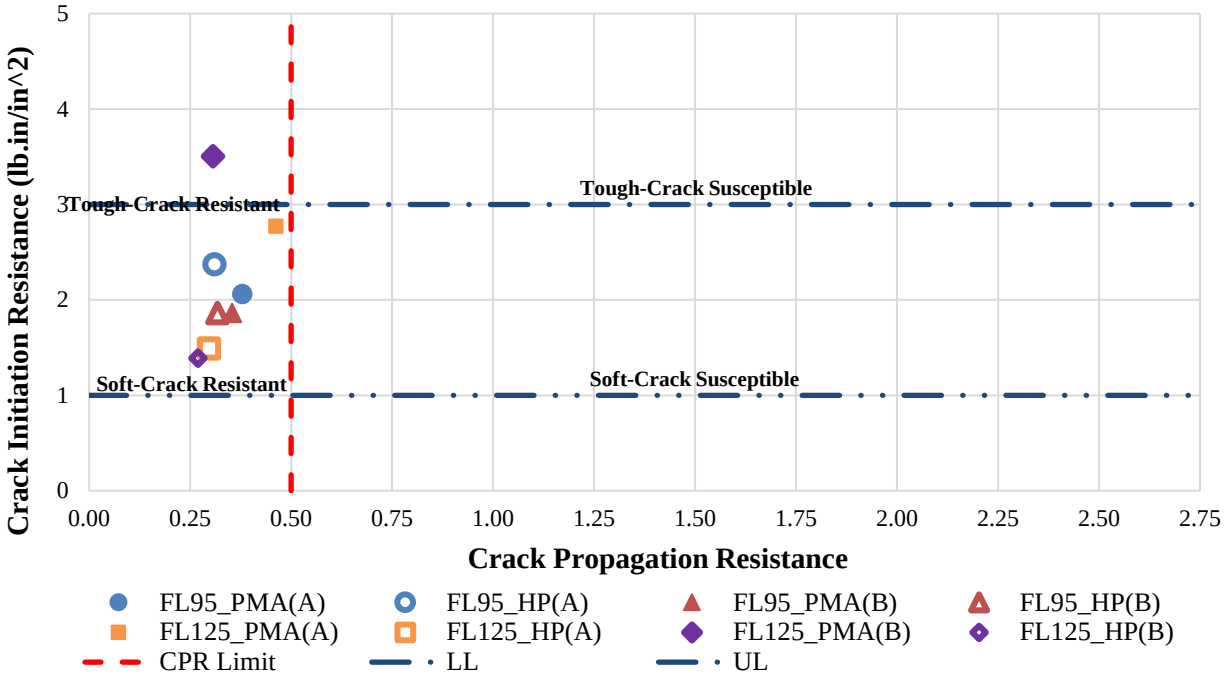


**Figure 4-33. Cracking resistance interaction plot for FL PMA and HP AC mixes.**

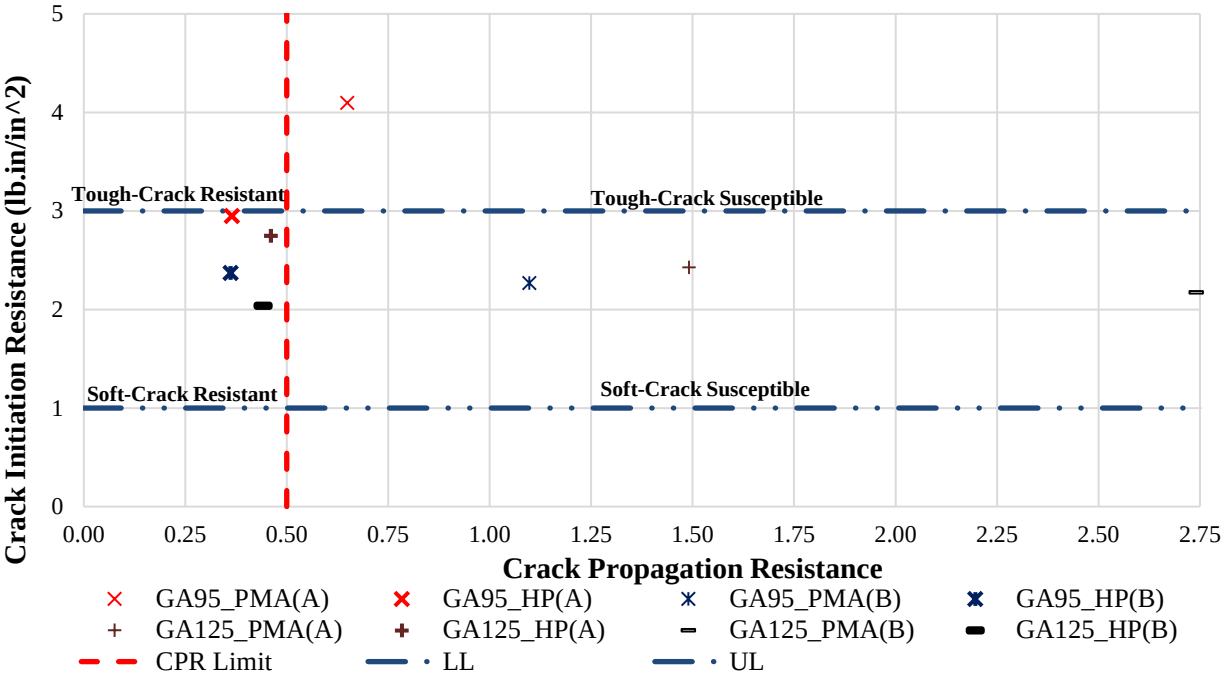


**Figure 4-34. Cracking resistance interaction plot for GA PMA and HP AC mixes.**

# CHAPTER 5. FLEXIBLE PAVEMENT MODELING

The objective of this chapter is to incorporate the measured engineering properties and performance characteristics of the evaluated PMA and HP AC mixes into mechanistic modeling of flexible pavements responses to traffic loads. Accordingly, several input parameters are defined and selected, and output critical responses are determined for evaluated distress modes (e.g., rutting, bottom-up fatigue, etc.). Figure 5-1 describes the overall approach implemented in the mechanistic analysis approach for flexible pavement modeling.

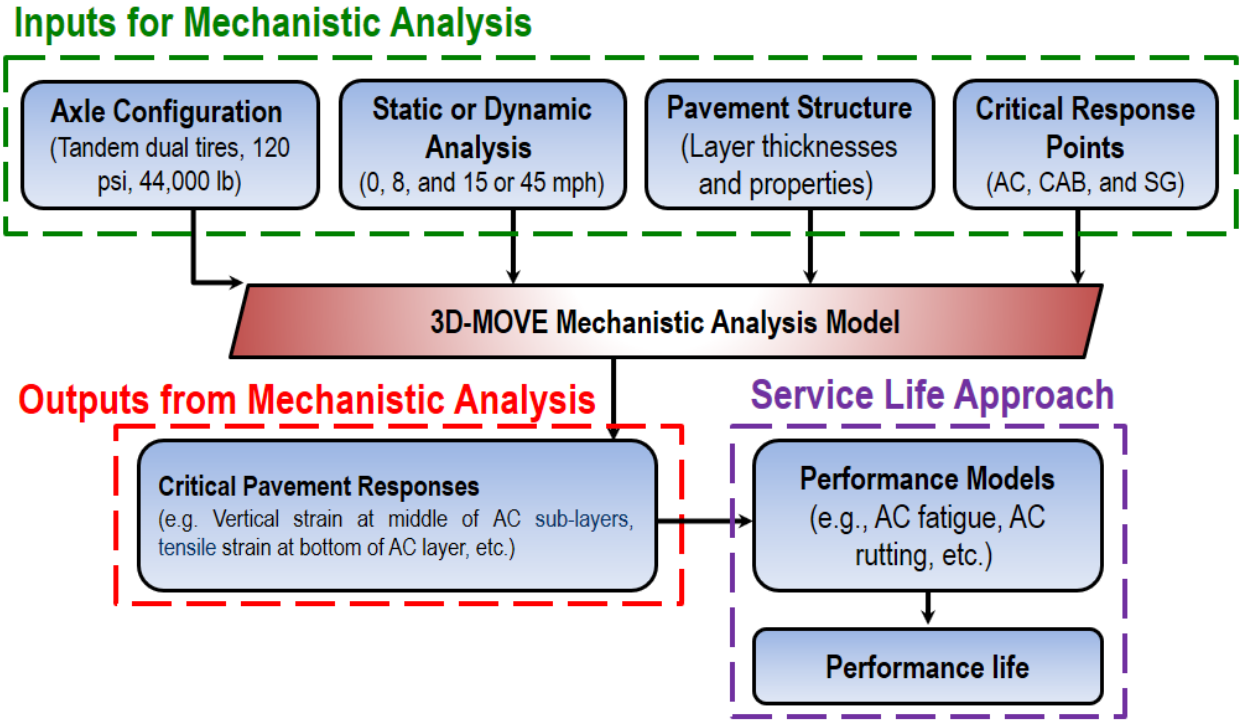


**Figure 5-1. Flow chart of the mechanistic approach.**

## 5.1. INPUTS FOR MECHANISTIC ANALYSIS

The mechanistic approach for the determination of the structural coefficient of HP AC mixes requires the determination of flexible pavement responses under traffic loads that are critical to the identified distresses of: rutting in AC, base (CAB), and subgrade (SG); AC fatigue cracking including bottom-up and top-down; and reflective cracking for AC overlays on rehabilitation projects only. The inputs for the mechanistic analysis includes; axle configuration, type of analyses (i.e., static or dynamic), pavement structures and corresponding layer properties, and the selection of critical response points.

### 5.1.1. Axle Configuration and Type of Analyses

The responses of the mixes in the AC pavements were evaluated under a tandem axle/dual tires loading configuration with 120 psi (828 kPa) tire pressure. Referring to the commercial motor

vehicle manual 9th edition published by Florida Highway Patrol in July 2016 *(80)*, the maximum weight for a tandem axle was selected as 44,000 lbs (195.8 kN) resulting in a 5,500 lbs (24.5 kN) load per tire. By definition, a tandem axle is described as any two axles whose centers are more than 40 inches (1,016 mm) but not more than 96 inches (2,438 mm) apart and are individually attached to or articulated from, or both, a common attachment to the vehicle, including a connecting mechanism designed to equalize the load between axles. Typical distances of 48 to 54 inches (1.22 to 1.37 m) are usually used between both axles of a typical tandem configuration. For this study, a value of 48 inches (1.22 m) is selected as the distance center to center between both axles of the tandem configuration. No specific definition was provided concerning the dual tires in accordance with Florida DOT. Typical values of 12 to 14 inches (305 to 356 mm) are usually used. For this study, a value of 14 inch (356 mm) is used as the distance center to center between dual tires. Figure 5-2 shows a 3-Dimensions (3D) configuration and a plan illustration of the applied loading. Two types of analysis were evaluated in this study for each distress mode; static analysis representing a speed of 0 mph (0 km/hr) and simulating traffic reaching a full-stop at an intersection, and dynamic analysis considering multiple speeds of 8, 15, and/or 45 mph (13, 24, and 72 km/h) with and without braking effect.

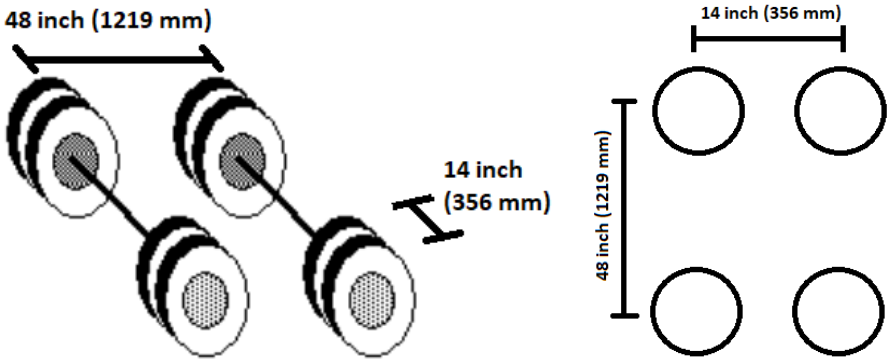


**Figure 5-2. Applied loading configuration: a) 3D configuration, and b) Plan illustration of a quarter axle.**

### 5.1.2. Braking Effect in Dynamic Analysis

By definition, shoving is described as a form of plastic movement characterized by an abrupt wave along the pavement surface. The distortion is usually perpendicular to the traffic direction and usually occurs at locations where traffic starts and stops such as traffic intersections. In order to simulate the actual loading conditions on pavements subjected to shoving, a dynamic mechanistic analysis was performed at a speed of 15 mph (24 km/h) and a temperature of 122°F (50°C) (which is the effective high analysis temperature for rutting and shoving) under braking conditions. The user needs to specify a braking friction coefficient *($f_{Br}$)* when specifying the axle/tire configuration. A braking friction coefficient *($f_{Br}$)* of 0.623 was calculated considering a tractor-semi trailer truck on a sloped pavement structure as illustrated in Figure 5-3 and based on the following assumptions *(54)*:

- The vehicle speed at brake initiation is 40 mph (64 km/h) and the stopping distance (SD) is 100 ft (30.48 m) with a pavement slope of 0 degree.

- The loading configuration consists of a tractor-semi trailer with a steering single tires, driving dual tires, and trailer dual tires axle.
- The tractor total weight, $W_1$, is considered 16,000 lbs (71.2 kN) and the semitrailer total weight $W_2$ is considered 64,000 lbs. (284.7 kN) resulting in a gross weight of 80,000 lbs. (355.9 kN). It should be mentioned that the same configuration of tandem axle/dual tires at the driving and trailer axle was considered as previously defined in section 5.1.1.

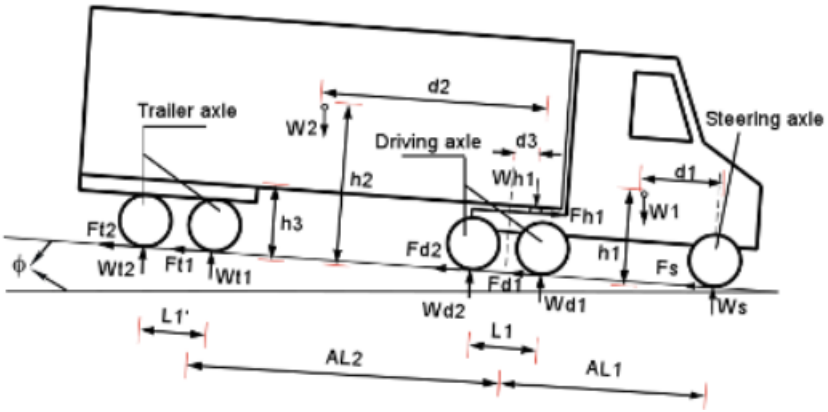


**Figure 5-3. Sketch a tractor- semi trailer truck considered for the determination of the braking friction coefficient *(54)*.**

### 5.1.3. Pavement Structures and Layers Properties

FDOT recently updated and published a manual for designing flexible pavements in Florida (September 2016) *(4)*. This manual provides guidance for conducting new and rehabilitated flexible pavement designs according to the AASHTO 1993 Guide *(2)*. The accumulated 18-kip (80 kN) Equivalent Single Axle Loads ($ESAL_D$) is the traffic load information used for pavement thickness design. Table **5-1** summarizes the Traffic Levels for $ESAL_D$ ranges for Superpave AC structural courses *(4)*. In this study, a design $ESAL_D$ of 7 and 20 million were considered for Traffic Levels C and D, respectively.

**Table 5-1. Summary Table of Traffic Level and Their Corresponding Design ESALs.**

| $ESAL_D$ (Million) | Traffic Level |
|---|---|
| < 0.3 | A |
| 0.3 to < 3 | B |
| 3 to < 10 | C |
| 10 to < 30 | D |
| >= 30 | E |

The following defines the general pavement layers in a flexible pavement system in accordance with the FDOT Pavement Design Manual (2016) *(4)*. The structural AC course is designed to distribute the traffic loadings to the base course. Two types of structural AC courses, typically used by FDOT, were considered in this study: a) structural course Type SP-9.5 which uses a 3/8 inch (9.5 mm) NMAS (i.e., FL95 and GA95 PMA and HP AC mixes) used for Traffic Level C,

and b) structural course Type SP-12.5 which uses a 1/2 inch (12.5 mm) NMAS (i.e., FL125 and GA125 PMA and HP AC mixes) used for Traffic Level D. The FDOT structural coefficient of 0.44 was used to design the PMA AC layer in a new flexible pavement structure.

By definition, the base course is a layer of specified material and design thickness, which supports the structural AC course and distribute the traffic loads to the subbase or subgrade. FDOT manual *(4)* presents the concept of an optional base group: different base course materials that may have different thickness, but are structurally equivalent are grouped together to form an optional base group. In this study, two base options were considered: a) a graded aggregate base with a Limerock Bearing Ratio (LBR) of 100 and a structural layer coefficient of 0.15 (i.e., referred to as low base strength), and b) a Limerock base material with a LBR of 100 with a structural coefficient of 0.18 (i.e., referred to as high base strength).

FDOT mandates the use of 12 inch (305 mm) thick stabilized subgrade structural layer. It serves as a working platform to permit the efficient construction of the base material. It is generally bid as Type B Stabilization with a LBR of 40 and a structural layer coefficient of 0.08. At the bottom, the subgrade or known as roadbed soil constitutes the natural in-situ material upon which the pavement structure is constructed. The strength of subgrade material is expressed using the 90% LBR values. LBR are then converted into resilient modulus ($M_r$) values using the FDOT relationship shown in Equation 5-1. In Florida, typical 90% LBR values for subgrade material range between 10 and 40 *(4)*. In this study, two extreme cases for subgrade material were considered: a) weak subgrade strength that corresponds to a 90% LBR value of 14 resulting in a $M_r$ value of 5,500 psi (37.9 MPa), and b) strong subgrade strength that corresponds to a 90% LBR value of 36 resulting in a $M_r$ value of 11,500 psi (79.3 MPa).

$$M_R = 10^{[0.7365*\log(LBR)]} * 809 \qquad \textbf{Equation 5-1}$$

Where;
$M_R$: resilient modulus, psi; and
*LBR*: limerock bearing ratio, %.

As mentioned before, FDOT uses the AASHTO 1993 design guide and methodology to conduct new and rehabilitated flexible pavement designs *(4)*. Equation 1-1 is used to design flexible pavements. The desired level of design reliability increases with the increase in design traffic. The empirical relationship among design traffic, pavement structure, and pavement performance for flexible pavements is solved to determine the required structural capacity of the pavement section, known as the structural number *(SN)*. The total pavement SN is defined as the summation of the layer thicknesses times the corresponding structural layers and drainage coefficients as expressed in Equation 1-2. For new construction project, once the SN value is calculated using Equation 1-1 and having the structural coefficient of the PMA AC layer and the thickness and structural coefficient of the base and stabilized subgrade, the thickness of the PMA AC layer is determined using Equation 5-2. For rehabilitation projects, the structural number of the designed overlay *($SN_0$)* is calculated as the difference between the required structural number ($SN_R$) for a newly constructed pavement structure calculated using Equation 1-2 and the structural number of the existing damaged pavement structure after any milling *($SN_E$)*. *$SN_E$* is calculated using the reduced layer coefficients taking into account the milling thickness of the

existing pavement. In this study, the design of AC overlays is based on existing pavement condition of "Fair". For that, a reduced structural coefficient of existing PMA AC mixes of 0.25 is used to compute $SN_E$. It should be mentioned that the structural coefficient of the base, and stabilized subgrade remain the same as already used for the design of new pavement structures. The thickness of the required structural overlay is then computed using Equation 5-2.

$$D_{OL} = SN_{OL}/0.44 \qquad \textbf{Equation 5-2}$$

Where;
$D_{OL}$: required thickness of the AC overlay, inch.
$SN_{OL}$: structural number of the AC overlay.

Table 5-2 summarizes the structural designs for new and rehabilitated flexible pavement structures. It should be noted that no valid FDOT structural designs could be determined for the case of weak subgrade under low base layer strength; therefore, this combination was eliminated. In addition, the AC overlay designs are determined considering a 2.5 inch (63.5 mm) milling for all existing pavement structures. A summary of the material properties for the mechanistic analysis is provided in Table 5-3.

**Table 5-2. Structural Designs for Flexible Pavements.[1, 2]**

| FDOT $ESAL_D$ | Base Type | Subgrade Strength $M_r$ (psi) | Label | New Pavement | | Rehabilitated Pavement with 2.5 inch milling | | |
|---|---|---|---|---|---|---|---|---|
| | | | | AC Layer (inch) | Base Layer (inch) | AC Overlay (inch) | Existing AC Layer (inch) | Base Layer (inch) |
| Traffic Level C: 7 million | Graded Aggregate $a_3$ = 0.15 | 11,500 | C1 | 3.0 | 12.0 | 3.5 | 0.5 | 12.0 |
| | Limerock $a_3$ = 0.18 | 5,500 | C2 | 5.0 | 11.0 | 4.5 | 2.5 | 11.0 |
| | | 11,500 | C3 | 3.0 | 10.0 | 3.5 | 0.5 | 10.0 |
| Traffic Level D: 20 million | Graded Aggregate $a_3$ = 0.15 | 11,500 | D1 | 4.5 | 12.0 | 4.0 | 2.0 | 12.0 |
| | Limerock $a_3$ = 0.18 | 5,500 | D2 | 6.0 | 12.5 | 5.5 | 3.5 | 12.5 |
| | | 11,500 | D3 | 4.5 | 10.0 | 4.0 | 2.0 | 10.0 |

[1]Designs were conducted following the FDOT Flexible Pavement Design Manual 2016.
[2]1 inch = 25.4 mm.

**Table 5-3. Material Properties for Mechanistic Analysis.[(1)]**

| Pavement Layer | Modulus | Poisson's Ratio | Characterization |
|---|---|---|---|
| Asphalt Concrete | Laboratory-determined Dynamic Modulus Master Curve | 0.35 | Viscoelastic |
| Aggregate Base | Low $M_r$ = 33,500 psi[(2)]<br>High $M_r$ = 44,300 psi | 0.38 | Linear Elastic |
| Stabilized Subgrade | $M_r$ = 12,250 psi[(3)] | 0.38 | Linear Elastic |
| Subgrade | Weak $M_r$ = 5,500 psi<br>Strong $M_r$ = 11,500 psi | 0.40 | Linear Elastic |

[(1)]1 psi = 6.9 kPa.
[(2)]determined using the AASHTO 1993 design guide recommended equation of structural coefficient for untreated base $a_3$=0.249*log($E_{base}$)-0.977; $a_3$=0.15 and $a_3$ =0.18.
[(3)]determined using Equation 4.1 at a 90% LBR of 40.

## 5.2. 3D-MOVE MECHANISTIC ANALYSIS MODEL

Mechanistic procedures to calculate pavement responses under loading have been evolving since 1960s to account for the changes in: characteristics of vehicle loading, pavement materials, and method of pavement construction. An important task in developing a successful mechanistic procedure is how realistically it can model the actual tire-pavement interaction loading and pavement material behavior. The 3D-Move model described in this section and used in this research considers a moving vehicle loading with all components of contact stress distributions (normal and shear) being of any shape *(54)*. It takes advantage of the horizontally-layered nature of the pavement structure in the formulation and it is more computer efficient than the three-dimensional finite element based models.

The 3D-Move model is based on finite-layer approach that uses the Fourier transform technique to evaluate the responses of the layered medium subjected to a moving load traveling along the x-axis at a constant speed. The properties for the AC layer can be either linear elastic (i.e., for static analyses) or viscoelastic (i.e., for dynamic analyses), while the properties of the unbound layers are linear elastic. Material properties are assumed to be uniform and constant within the layer. Frequency-domain solutions are adopted in the 3D-Move model which enables the direct use of dynamic modulus test data of the viscoelastic material (e.g., AC mix) in the analysis.

The 3D-Move model can handle any number of layers with the complex loading at the surface and any number of response evaluation points. Since the contact area can be of any shape, this approach is suitable to analyze any tire imprints, including those generated by wide-base tires. A study completed by Hajj et al. *(81)* showed that the effect of non-uniform stress distribution at the tire-pavement interface on pavement responses and performance is significant and should be considered in pavement analysis and design. Additionally, the effect of vehicle braking on pavement responses should be considered when designing pavements that are to be placed at intersections and stopping areas *(81)*.

Furthermore, since 3D-Move has the capability of modeling moving load and the resulting dynamic pavement responses, it is well-suited to evaluate and compare pavement responses measured using traffic speed deflection devices that move at high-speeds (e.g., Traffic Speed

Deflectometer, TSD, and Rolling Wheel Deflectometer, RWD, devices). Since rate-dependent material properties (viscoelastic) can be accommodated by the approach, it is an ideal tool to model the behavior of asphalt concrete layer and also to study pavement response as a function of vehicle speed.

Multiple analytical and field verification were undertaken to evaluate and confirm the applicability of the 3D-Move model. Both analytical and field based validations under variety of pavement conditions (i.e., layer configurations, material properties, and loading) demonstrated the applicability of the 3D-Move model relative to its consideration of appropriate procedures to account for moving vehicle loading and pavement material characterization *(82)*.

The research team used the 3D-Move model in this research to determine pavement critical responses and to estimate the structural layer coefficients of HP AC mixes due to the following unique features:

- The speed of the load can be varied from 0 to 100 mph (0 to 161 km/h). This feature becomes very critical as this research moves towards the validation phase under Accelerated Pavement Test (APT) loading. The 3D-Move model has been incorporated into a public domain software with highly efficient computational speed which distinguishes it from the non-public domain commercial 3D Finite Element software which have significantly longer computational time. FDOT will be able to download and implement the public domain 3D-Move software to analyze the PMA and HP AC pavements under APT loading. The variable speed feature of the 3D-Move model will facilitate the implementation of the APT results under low speed loading to highway loading at higher speeds.
- The pressure at the tire-pavement interface is non-uniform and can be applied in the vertical and horizontal directions. The horizontal pressure is used to simulate slow moving vehicles and braking on urban pavements, at intersections, and off-ramps.
- The AC layer is modeled as a viscoelastic material where vehicle speed ad loading frequency have a significant impact on flexible pavement response to loads.

## 5.3. CRITICAL RESPONSES AND ANALYSIS TEMPERATURES

Table 5-4 summarizes the selected critical responses along with their locations within the designed flexible pavement structures. These responses were computed at different locations depending on the type of analysis (i.e., static or dynamic) and at different depths according to the distress mode as illustrated in Figure 5-4.

**Table 5-4. Pavement Responses from 3D-Move Analysis.**

| Distress Mode | Pavement Responses | Location within Structure | Performance Model | Analysis Temperature |
|---|---|---|---|---|
| Fatigue Cracking | Tensile Strain ($\varepsilon_t$) | Bottom of AC layer | Equation 3.10 from laboratory evaluation | Effective Intermediate Pavement Temperature ($T_{eff\text{-}Int}$) |
| Rutting in AC Layer | Vertical Strain ($\varepsilon_r$) | Middle of AC sub-layers | Equation 3.7 from laboratory evaluation | Effective High Pavement Temperature ($T_{eff\text{-}High}$) |
| Total Rutting | Vertical Strain ($\varepsilon_r$) | Middle of AC sub-layers, Middle of base sub-layers, and 6 inch into Subgrade | AASHTO M-E Design | Effective High Pavement Temperature ($T_{eff\text{-}High}$) |
| Shoving | Shear Strain ($\gamma_{YZ}$) | Top 0.5 inch of AC layer | --- | Effective High Pavement Temperature ($T_{eff\text{-}High}$) |
| Top-Down Cracking | Horizontal Tensile Stress ($\sigma_t$) | Top 0.5 inch of AC layer | --- | Effective Intermediate Pavement Temperature ($T_{eff\text{-}Int}$) |

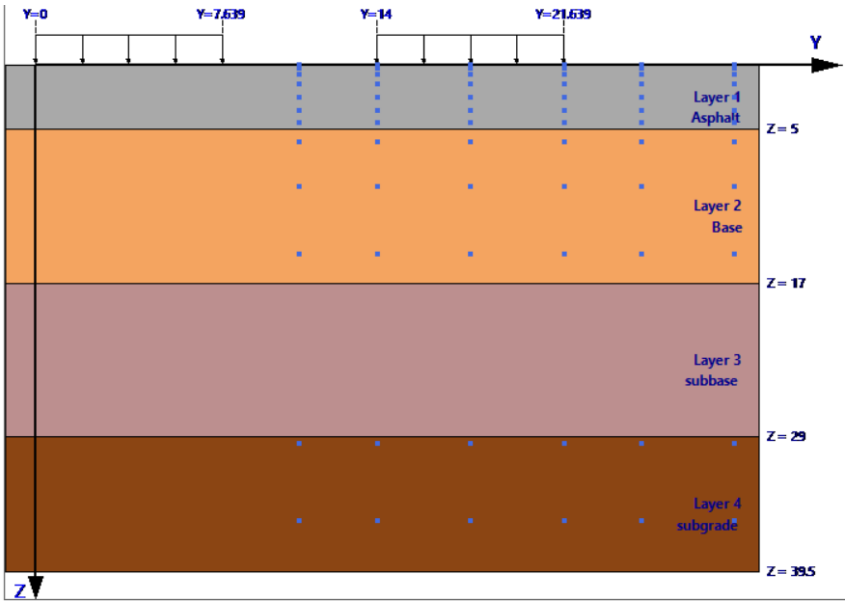


**Figure 5-4. Sketch of a newly constructed pavement section with the locations of the selected response points.**

The effective intermediate and high pavement temperatures were determined using Equation 5-3 and Equation 5-4, respectively, in accordance with National Corporation Highway Research Program (NCHRP 09-22) Report 704 "*A Performance-Related Specification for Hot-Mix Asphalt*" *(83)*. The climatic stations in Gainesville and Marathon were selected to compute the

effective pavement temperatures for the mechanistic analysis. Table 5-5 summarizes all the necessary climatic inputs for Equation 5-3 and Equation 5-4.

$$T_{eff-Int} = -13.995 - 2.332(Freq)^{0.5} + 1.006(MAAT) + 0.876(\sigma_{MAAT}) - 1.186(Wind) + 0.549(Sunshine) + 0.071(Rain) \quad \textbf{Equation 5-3}$$

$$T_{eff-high} = 14.62 - 3.361Ln(Freq) - 10.940(z) + 1.121(MAAT) + 1.718(\sigma_{MAAT}) - 0.431(Wind) + 0.333(Sunshine) + 0.08(Rain) \quad \textbf{Equation 5-4}$$

Where;
$T_{eff\text{-}Int/high}$: modified Witczak temperature, °F;
*z*: critical depth, inch (considered as 1 inch from the top of the AC layer);
*Freq*: loading frequency, Hz;
*MAAT*: mean annual air temperature, °F;
$\sigma_{MAAT}$: standard deviation of the mean monthly air temperature, °F;
*Rain*: annual cumulative rainfall depth, inches;
*Sunshine*: mean annual percentage sunshine, %; and
*Wind*: mean annual wind speed, mph.

**Table 5-5. Inputs Properties at the Selected Climatic Stations in Florida.**

| Property | Location of the Selected Climatic Station | |
|---|---|---|
| | Gainesville | Marathon |
| MAAT (°F) | 68.1 | 78.1 |
| $\sigma_{MAAT}$ (°F) | 9.7 | 6.0 |
| Rain (inch) | 45.9 | 34.0 |
| Sunshine (%) | 69.3 | 75.6 |
| Wind (mph) | 5.0 | 7.0 |

The Mechanistic-Empirical Pavement Design Guide (MEPDG) *(5)* recommends using a procedure based on stress distributions to estimate the traffic-induced loading time which determines the corresponding frequency at any depth in the pavement structure (i.e., AC, base, stabilized subgrade, and subgrade). In order to calculate the effective duration at the depth of interest, the MEPDG uses Odemark's method of equivalent thickness to transform the pavement structure into a single subgrade layer system, assuming that the stress distribution is developed at 45 degrees in the equivalent layer system as illustrated in Figure 5-5 and expressed in Equation 5-5. As presented in the MEPDG, the loading time of a haversine waveform in AC layer under moving traffic load is estimated using Equation 5-6. In the case of tandem axle configuration, an overlap of the stress distribution may occur at deeper depths from the surface; therefore, the effective length of the stress pulse *($L_{eff}$)* at these depths needs to be adjusted to account for the overlapping.

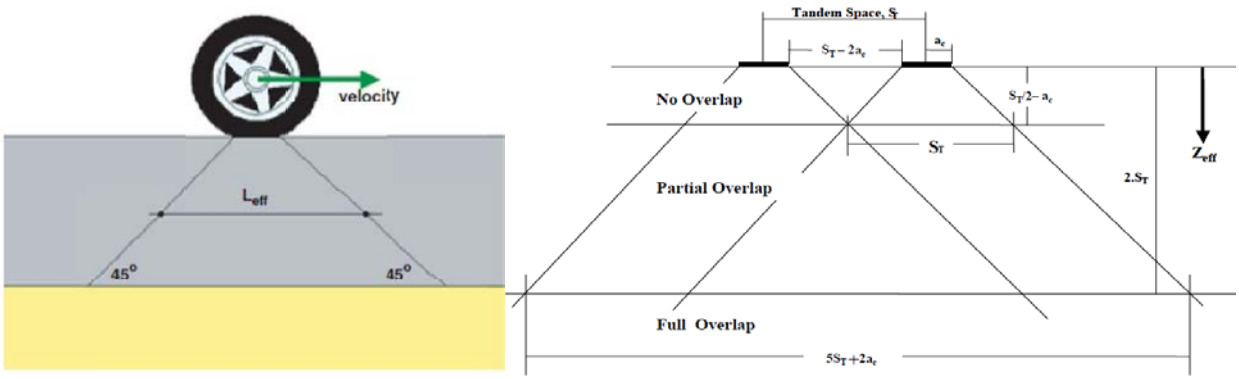


**(a)** **(b)**

**Figure 5-5. Schematic of load pulse frequency determination by MEPDG: a) single axle load, and b) tandem axle.**

$$Z_{eff} = \sum_{i=1}^{n-1}\left(h_i \sqrt[3]{\frac{E_i}{E_{SG}}}\right) \qquad \textbf{Equation 5-5}$$

Where;
$Z_{eff}$: determined depth in the transformed single subgrade layer pavement structure, inch (mm);
$h_i$: depth/thickness of the i$^{th}$ layer, inch (mm);
$E_i$: Young modulus of the i$^{th}$ layer, psi (MPa); and
$E_{SG}$: Young modulus of the subgrade layer, psi (MPa).

$$t = \frac{L_{eff}}{17.6 * S} \qquad \textbf{Equation 5-6}$$

Where;
$t$: time of loading, seconds;
$L_{eff}$: effective length of stress pulse at a given depth, inch; and
$S$: speed of the moving load, mph.

Having all the climatic inputs and the dynamic modulus master curve of any given mix, trial and errors computations are executed using the solver feature in Microsoft Excel to determine the frequency at any given depth (in this case z = 1 inch (25.4 mm)), any given speed, and any associated analysis temperature. Table 5-6 summarizes the determined high and intermediate analysis temperatures at the two selected locations (i.e., Gainesville and Marathon). The pavement analysis temperature for rutting and shoving evaluations in the 3D-Move model was selected as 122°F (50°C). However, the resistance to fatigue, top-down, and reflective cracking was evaluated at an intermediate pavement analysis temperature of 77°F (25°C).

**Table 5-6. Computations of High and Intermediate Pavement Analysis Temperatures.**

| **Climatic Station in Gainesville** | **Target Distress and Location** | |
|---|---|---|
| | **Rutting at z = 1 inch (25.4 mm)** | **Fatigue at z = 1 inch (25.4 mm)** |
| Mean Effective Temperature, °F (°C) | 109.4 (43.0) | 85.5 (29.7) |
| Standard Deviation (stdv), °F (°C) | 2.2 (1.2) | 4.0 (2.2) |
| Mean ± 2 stdv (95% CI) | 113.8 (45.4) | ***77.5 (25.3)*** |
| Mean ± 3 stdv (99% CI) | 116.0 946.7) | 73.5 (23.1) |
| **Climatic Station in Marathon** | **Target Distress and Location** | |
| | **Rutting at z = 1 inch (25.4 mm)** | **Fatigue at z = 1 inch (25.4 mm)** |
| Mean Effective Temperature, ° (°C) | 117.1 (47.3) | 97.0 (36.1) |
| Standard Deviation (stdv), °F (°C) | 3.0 (1.7) | 5.0 (2.8) |
| Mean ± 2 stdv (95% CI) | ***123.1 (50.6)*** | 87.0 (30.6) |
| Mean ± 3 stdv (99% CI) | 126.1 (52.3) | 82.0 (27.8) |

# CHAPTER 6. DETERMINATION OF STRUCTURAL COEFFICIENT OF HP AC MIXES

The objectives of this part of the research are; a) determine the critical responses of the designed pavement structures for the identified distresses of AC pavements including; fatigue cracking, AC rutting, total rutting, top-down cracking, and reflective cracking using the 3D-Move model, and b) determine the structural coefficient for HP AC mixes. First, the determined critical responses are used to estimate the fatigue performance life of the designed pavement structures followed by the development of the initial structural coefficient for HP AC mixes based on the equal fatigue performance life approach. Finally, the fatigue-based initial structural coefficients are verified for the other modes of distress. Figure 6-1 illustrates a step by step flowchart summary of these analyses.

## 6.1. FATIGUE CRACKING PERFORMANCE LIFE

The fatigue characteristics of the 16 different AC mixes were evaluated using the flexural beam fatigue test in accordance with AASHTO T321 *(35)* at three temperatures and multiple strain levels. Using the fatigue models developed for each AC PMA mix (Table 4-9) and the corresponding critical tensile strains *($\varepsilon_t$)* determined from the 3D-Move mechanistic analyses at the bottom of the AC layer, the number of cycles to fatigue failure was determined for each new pavement section (Table 5-2). It should be mentioned that the performance life of the PMA pavements were evaluated under stop-static traffic—0 mph (0 km/h)—simulating full-stop trucks at intersections, slow traffic—8 mph (13 km/h)—simulating the speed of HVS at FDOT facilities in Gainesville, and the fast-highway—45 mph (72 km/h)—traffic.

The dynamic modulus *(E)* term in the fatigue model was determined at the effective intermediate temperature (i.e., 77° (25°C)) using the laboratory determined dynamic modulus master curves (refer to Section 4.2.1). The frequency at which *E* was computed was determined based on the MEPDG stress distribution concept using Odemark's equivalent thickness method explained previously in Section 4.3. The matching performance life approach was then used to determine the required AC layer thickness for the HP pavement sections as expressed in Equation 6-1 to Equation 6-3. The HP pavement sections were then determined in a way to achieve the same fatigue service life (i.e., number of cycles to fatigue failure) as the corresponding PMA control pavement sections. It should be recognized that the same fatigue performance life does not translate into the same tensile strain value at the bottom of the AC layer. Using this approach, the target tensile strain at the bottom of the AC HP layer can be determined as expressed in Equation 6-4.

$$N_{f-PMA} = \beta_{f1} * k_{f1-PMA} * \left(\frac{1}{\varepsilon_{t-PMA}}\right)^{k_{f2-PMA}} * \left(\frac{1}{E_{AC-PMA}}\right)^{k_{f3-PMA}} \qquad \textbf{Equation 6-1}$$

$$N_{f-HP} = \beta_{f1} * k_{f1-HP} * \left(\frac{1}{\varepsilon_{t-HP}}\right)^{k_{f2-HP}} * \left(\frac{1}{E_{AC-HP}}\right)^{k_{f3-HP}} \qquad \textbf{Equation 6-2}$$

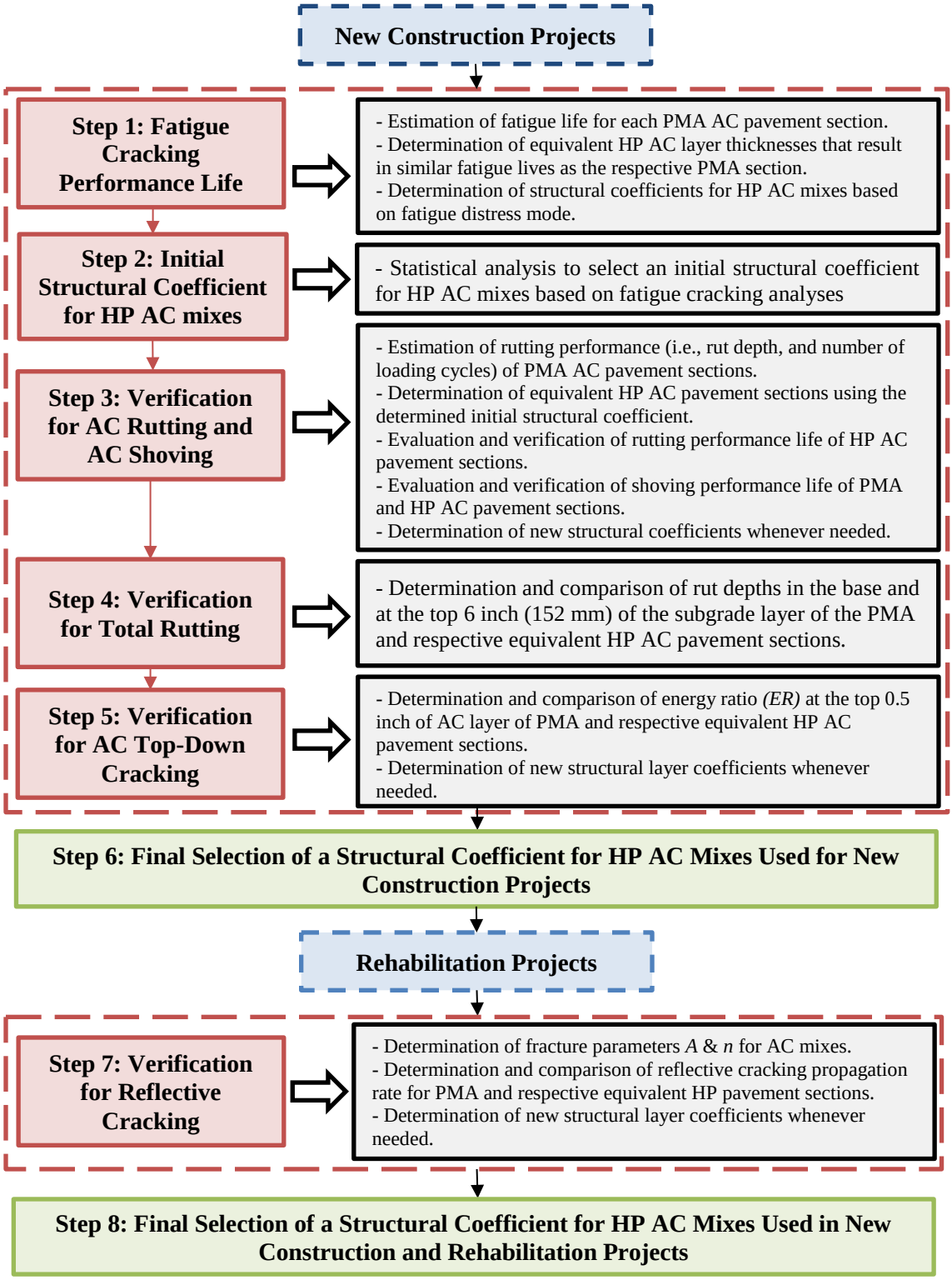


**Figure 6-1. Flowchart of the mechanistic analyses to determine an initial structural coefficient for HP AC mixes in Florida.**

$$N_{f-PMA} = N_{f-HP}$$ **Equation 6-3**

$$\varepsilon_{t-HP} = 10^{\left(\frac{-1}{k_{f2-HP}}\right)*\log[\left(\frac{k_{f1-PMA}}{k_{f1-HP}}\right)*\left(\frac{1}{\varepsilon_{t-PMA}}\right)^{k_{f2-PMA}}*\left(\frac{(\frac{1}{E_{AC-PMA}})^{k_{f3-PMA}}}{(\frac{1}{E_{AC-HP}})^{k_{f3-HP}}}\right)]}$$ **Equation 6-4**

Where;
$N_{f-PMA}$, and $N_{f-HP}$: fatigue life, number of load repetitions to fatigue damage for PMA and HP pavement sections;
$\varepsilon_{t-PMA}$, and $\varepsilon_{t-HP}$: applied tensile strain at the bottom of PMA and HP AC layers, inch/inch (or mm/mm);
$E_{AC-PMA}$, and $E_{AC-HP}$: dynamic modulus of PMA and HP AC asphalt mixtures, psi;
$k_{f1\text{-}PMA}$, $k_{f2\text{-}PMA}$, $k_{f3\text{-}PMA}$, $k_{f1\text{-}HP}$, $k_{f2\text{-}HP}$, *and* $k_{f3\text{-}HP}$: experimentally determined coefficients for PMA and HP AC mixes; and
$\beta_{f1\text{-}PMA}$, *and* $\beta_{f1\text{-}HP}$: mix-specific laboratory to field calibration factors ($\beta_{f1\text{-}PMA}$ assumed to be equal to $\beta_{f1\text{-}HP}$).

It should be mentioned that in this analysis mix-specific fatigue performance models were used. Thus, the calibration parameters $\beta_{f2\text{-}PMA}$, $\beta_{f2\text{-}HP}$, $\beta_{f3\text{-}PMA}$, *and* $\beta_{f3\text{-}HP}$ were set equal to 1 (refer to Equation 3-12.

Previous research showed that there might be a level of stress or strain below which no fatigue damage originating from the bottom of the AC layer occurs to the pavement section. This stress or strain has been termed as fatigue endurance limit *(84)*. In other words, if a pavement is designed and constructed so that under repeated traffic loads no fatigue damage occurs, then the pavement should last indefinitely without a structural fatigue failure. Multiple approaches exist to estimate a fatigue endurance limit of an evaluated AC mixture at a given temperature and loading frequency. The Strategic Highway Research Program (SHRP) suggested that an AC mix laboratory fatigue life of 50 million load cycles in a strain controlled test is equivalent to 500 MSA in the field. Therefore, any strain value which can result in a laboratory fatigue life of 50 million loading cycles can be considered as the fatigue endurance limit. Due to the impracticality of conducting laboratory fatigue test for 50 million cycles which would take more than 50 days per specimen per temperature, multiple extrapolation techniques including exponential model, power model, logarithmic model, single-stage Weibull function, and three stage Weibull function can be used to predict high fatigue life under low fatigue strain *(84)*. Using the fatigue relationships developed for the 16 evaluated AC mixes (i.e., eight PMA and eight HP), a tensile strain ($\varepsilon_{t\text{-}50\ million\ cycles}$) at a given temperature and loading frequency is estimated for 50 million loading cycles as expressed in Equation 6-5.

$$\varepsilon_{t-50\ million\ cycles} = 10^{\left(\frac{-1}{k_{f2}}\right)*\log[\left(\frac{50*10^6}{k_{f1}}\right)*(\frac{1}{E_{AC}})^{k_{f3}}]}$$ **Equation 6-5**

Currently, there is a draft AASHTO standard of practice to predict the endurance limit of AC mixes for long-life pavement design *(84)*. The standard specifies that the difference between the logs of the fatigue lives (i.e., log sample 1 – log sample 2) of two properly conducted test at a given temperature should not exceed 0.69 in the same laboratory. Using the fatigue relationship,

a difference between the logs of the tensile strains (i.e., $\Delta\log\varepsilon_t$ = log sample 1 – log sample 2) is then calculated using Equation 6-6. Finally, the fatigue strain endurance limits are calculated using Equation 6-7. For each pavement, the fatigue strain endurance limit of the PMA mix *($\varepsilon_{t\text{-}EL}$)* is calculated and compared to the critical tensile strain determined from the 3D-Move analysis. If the mechanistic analysis determined a strain lower than the $\varepsilon_{t\text{-}EL}$, it means that the pavement section will not experience a fatigue failure under the evaluated loading magnitude and configuration. In this case, the $\varepsilon_{t\text{-}EL}$ is considered in the analysis to determine the HP section with similar fatigue performance life of the PMA pavement one.

$$\Delta log N_f = 0.69 = -k_{f2} * \Delta log \varepsilon_t \qquad \textbf{Equation 6-6}$$

$$log\varepsilon_{t-EL} = log\varepsilon_{t-50\ million\ cycles} - \frac{\Delta log\varepsilon_t}{2} = log\varepsilon_{t-50\ million\ cycles} + \frac{0.69}{k_{f2}} \qquad \textbf{Equation 6-7}$$

The structural coefficient for each HP mix for fatigue *($SC_{AC\text{-}HP\text{-}Fat}$)* is calculated under each of the two traffic loading conditions as the ratio of the AC layer thickness of the PMA pavement section over the AC layer thickness of the HP pavement section multiplied by the conventional structural coefficient of PMA AC mixes in Florida (i.e., 0.44) as shown in Equation 6-8. It should be noted that HP pavements were only compared with the respective PMA pavements within each traffic category, binder source, and aggregate type.

$$SC_{AC-HP-Fat} = \left(\frac{AC\ layer\ thickness\ of\ PMA\ pavement\ for\ fatigue\ in\ AC}{AC\ layer\ thickness\ of\ HP\ pavement\ for\ fatigue\ in\ AC}\right) * 0.44 \qquad \textbf{Equation 6-8}$$

Table 6-1 to Table 6-6 summarize the output of the fatigue mechanistic analyses conducted at traffic levels C and D, respectively. A review of the data reveals the following observations:

- The combination of pavement structure (i.e., AC and base thickness), layer properties, applied traffic, loading speed, and performance characteristics of the evaluated mixes had an impact on the resultant structural coefficients for the evaluated HP AC mixes. Values lower and higher than the PMA AC structural coefficient (i.e., 0.44) were observed for the same pavement structure under the same traffic.
- For pavement section C1 (i.e., 3.00 inch (76 mm) PMA AC on top of 12.00 inch (305 mm) low strength base and strong subgrade), the number of cycles to fatigue failure decreased with the increase in loading speed for the evaluated 95 mm PMA AC mixes except for GA95_PMA(B). The four evaluated mixes exhibited critical tensile strains higher than their respective endurance limits irrespective of loading speed. The resultant structural coefficient decreased with the increase of speed for FL95_PMA(B) and GA95_PMA(B) mixes; while, an increasing and a constant structural coefficient were observed for FL95_HP(A) and GA95_HP(A) mixes, respectively.
- For pavement section C2 (i.e., 5.00 inch (127 mm) PMA AC on top of 11.00 inch (279 mm) high strength base and weak subgrade), The three evaluated AC mixes FL95_PMA(A), FL95_PMA(B), and GA95_PMA(B) exhibited critical tensile strains lower than their respective endurance limit at the effective intermediate temperature and analysis frequency irrespective of the loading speed. The number of cycles to fatigue failure for GA95_PMA(A) AC mix under a loading speed of 8 mph was observed slightly higher than the one evaluated under a loading speed of 0 mph (0 km/h); much lower

value was observed under a loading speed of 45 mph (72 km/h). Constant resultant structural coefficient was determined for FL95_HP(A) mix irrespective of the loading speed. High structural coefficient values were observed for FL95_HP(B) mix. GA95_HP(A) mix shows an increase in the structural coefficient with the increase of the speed, meanwhile the structural coefficient for GA95_HP(B) mix decreases with the increase of the loading speed.

- For pavement section C3 (i.e., 3.00 inch (76 mm) PMA AC on top of 10.00 inch (254 mm) high strength base and strong subgrade), all evaluated AC mixes showed critical tensile strains at the bottom of the AC layer lower than their respective endurance limit except for FL95_PMA(B) mix under static conditions regardless of the evaluated mix, and loading speed. The number of cycles to fatigue failure decreased with the increase of the speed for all evaluated PMA AC mixes except for GA95_PMA(B) mix. Higher structural coefficient was observed under a loading speed of 8 mph (13 km/h) for FL95_HP(A), and FL95_HP(B) mixes when compared with the coefficients determined at 0 and 45 mph (0 and 72 km/h). GA95_HP(A) AC mix shows a lower structural value under static conditions, and the same coefficient at speed 8 and 45 mph (13 and 72 km/h). GA95_HP(B) AC mix shows a decreasing HP structural coefficient with the increase of the loading speed.
- For pavement section D1 (i.e., 4.50 inch (114 mm) PMA AC on top of 12.00 inch (305 mm) low strength base and strong subgrade), all evaluated AC mixes showed critical tensile strains at the bottom of the AC layer higher than their respective endurance limit except for GA125_PMA(A) AC mix regardless of the evaluated mix, and loading speed. In addition, the number of cycles to fatigue failure decreased with the increase of the speed for all evaluated PMA AC mixes except for GA125_PMA(A) mix. Similarly, all HP mixes except GA125_HP(A) mix showed an increase in the structural coefficient with the increase of the loading speed. GA125_HP(A) mix showed a similar structural coefficient under static conditions and at speed of 8 mph (13 km/h); much higher when compared with the one determined at a speed of 45 mph (72 km/h).
- For pavement section D2 (i.e., 6.00 inch (152 mm) PMA AC on top of 12.50 inch (317 mm) high strength base and weak subgrade), all evaluated AC mixes showed critical tensile strains at the bottom of the AC layer lower than their respective endurance limit regardless of the evaluated mix, and loading speed. In addition, all evaluated mixes showed a structural coefficient for HP mixes higher than 0.44 with a maximum value of 1.32 for GA125_HP(A) mix and a minimum value of 0.46 for FL125_HP(A) and GA125_HP(B) mixes. It should be mentioned that the AC layer of pavement section D2 is the thickest among all the AC layers of the remaining five PMA pavement sections.
- For pavement section D3 (i.e., 4.50 inch (114 mm) PMA AC on top of 10.00 inch (254 mm) high strength base and strong subgrade), all evaluated PMA AC mixes showed critical tensile strains at the bottom of the AC layer lower than their endurance limit irrespective of the loading speed resulting in a number of cycles to fatigue failure of around 110 million. On the other side, FL125_PMA(B) and GA125_PMA(B) AC mixes showed a number of cycles to fatigue failure decreasing with the increase of the loading speed. An increase in the determined structural coefficient was observed with the increase of the loading speed for the evaluated AC HP 125 mm mixes except for FL125_HP(B) mix.

## Table 6-1. Mechanistic Fatigue Analyses of Pavement Section C1.

| PMA Mix ID | Speed (mph) | Thickness of PMA Layer (inch) | 3D-MOVE PMA Strain (ms) | PMA EL (ms) | Cycles to Failure (million) | HP Mix ID | Speed (mph) | Equivalent Max HP Strain | HP EL (ms) | Thickness of HP Layer (inch) | SC of AC HP |
|---|---|---|---|---|---|---|---|---|---|---|---|
| FL95_PMA(A) | 0 | 3.00 | 473 | 346 | 26.1 | FL95_HP(A) | 0 | 541 | 398 | 2.75 | 0.48 |
| | 8 | 3.00 | 333 | 210 | 13.3 | | 8 | 445 | 283 | 2.25 | 0.59 |
| | 45 | 3.00 | 273 | 152 | 7.5 | | 45 | 403 | 226 | 1.75 | 0.75 |
| FL95_PMA(B) | 0 | 3.00 | 460 | 419 | 66.1 | FL95_HP(B) | 0 | 757 | 669 | 2.00 | 0.66 |
| | 8 | 3.00 | 329 | 279 | 43.7 | | 8 | 456 | 365 | 2.25 | 0.59 |
| | 45 | 3.00 | 270 | 213 | 29.3 | | 45 | 349 | 253 | 2.50 | 0.53 |
| GA95_PMA(A) | 0 | 3.00 | 352 | 198 | 8.1 | GA95_HP(A) | 0 | 537 | 270 | 3.00 | 0.44 |
| | 8 | 3.00 | 248 | 130 | 5.8 | | 8 | 406 | 188 | 3.00 | 0.44 |
| | 45 | 3.00 | 207 | 97 | 3.6 | | 45 | 359 | 147 | 3.00 | 0.44 |
| GA95_PMA(B) | 0 | 3.00 | 322 | 213 | 11.9 | GA95_HP(B) | 0 | 709 | 354 | 2.50 | 0.53 |
| | 8 | 3.00 | 231 | 160 | 15.0 | | 8 | 358 | 192 | 3.25 | 0.41 |
| | 45 | 3.00 | 196 | 131 | 12.5 | | 45 | 253 | 128 | 3.75 | 0.35 |

## Table 6-2. Mechanistic Fatigue Analyses of Pavement Section C2.

| PMA Mix ID | Speed (mph) | Thickness of PMA Layer (inch) | 3D-MOVE PMA Strain (ms) | PMA EL (ms) | Cycles to Failure (million) | HP Mix ID | Speed (mph) | Equivalent Max HP Strain | HP EL (ms) | Thickness of HP Layer (inch) | SC of AC HP |
|---|---|---|---|---|---|---|---|---|---|---|---|
| FL95_PMA(A) | 0 | 5.00 | 285 | 346 | 110.1 | FL95_HP(A) | 0 | 398 | 398 | 3.75 | 0.59 |
| | 8 | 5.00 | 203 | 239 | 110.5 | | 8 | 306 | 306 | 3.75 | 0.59 |
| | 45 | 5.00 | 166 | 169 | 110.6 | | 45 | 248 | 248 | 3.75 | 0.59 |
| FL95_PMA(B) | 0 | 5.00 | 276 | 419 | 111.0 | FL95_HP(B) | 0 | 669 | 669 | 2.75 | 0.80 |
| | 8 | 5.00 | 199 | 310 | 110.7 | | 8 | 374 | 374 | 2.00 | 1.10 |
| | 45 | 5.00 | 165 | 232 | 111.9 | | 45 | 275 | 276 | 3.25 | 0.68 |
| GA95_PMA(A) | 0 | 5.00 | 206 | 198 | 92.4 | GA95_HP(A) | 0 | 284 | 270 | 6.00 | 0.37 |
| | 8 | 5.00 | 150 | 146 | 98.7 | | 8 | 214 | 208 | 5.25 | 0.42 |
| | 45 | 5.00 | 125 | 107 | 54.3 | | 45 | 191 | 158 | 4.75 | 0.46 |
| GA95_PMA(B) | 0 | 5.00 | 187 | 213 | 111.4 | GA95_HP(B) | 0 | 353 | 354 | 4.50 | 0.49 |
| | 8 | 5.00 | 139 | 173 | 111.5 | | 8 | 221 | 219 | 5.00 | 0.44 |
| | 45 | 5.00 | 117 | 139 | 112.5 | | 45 | 147 | 145 | 6.00 | 0.37 |

## Table 6-3. Mechanistic Fatigue Analyses of Pavement Section C3.

| PMA Mix ID | Speed (mph) | Thickness of PMA Layer (inch) | 3D-MOVE PMA Strain (ms) | PMA EL (ms) | Cycles to Failure (million) | HP Mix ID | Speed (mph) | Equivalent Max HP Strain | HP EL (ms) | Thickness of HP Layer (inch) | SC of AC HP |
|---|---|---|---|---|---|---|---|---|---|---|---|
| FL95_PMA(A) | 0 | 3.00 | 396 | 346 | 59.3 | FL95_HP(A) | 0 | 454 | 398 | 2.50 | 0.53 |
| | 8 | 3.00 | 293 | 210 | 24.1 | | 8 | 390 | 282 | 2.00 | 0.66 |
| | 45 | 3.00 | 244 | 152 | 12.6 | | 45 | 365 | 230 | 2.75 | 0.48 |
| FL95_PMA(B) | 0 | 3.00 | 387 | 419 | 111.0 | FL95_HP(B) | 0 | 669 | 669 | 2.75 | 0.48 |
| | 8 | 3.00 | 288 | 279 | 93.0 | | 8 | 382 | 366 | 2.25 | 0.59 |
| | 45 | 3.00 | 242 | 213 | 53.6 | | 45 | 308 | 258 | 2.75 | 0.48 |
| GA95_PMA(A) | 0 | 3.00 | 310 | 198 | 14.5 | GA95_HP(A) | 0 | 460 | 270 | 2.50 | 0.53 |
| | 8 | 3.00 | 225 | 130 | 9.1 | | 8 | 349 | 181 | 2.25 | 0.59 |
| | 45 | 3.00 | 189 | 97 | 5.4 | | 45 | 313 | 142 | 2.25 | 0.59 |
| GA95_PMA(B) | 0 | 3.00 | 286 | 213 | 22.6 | GA95_HP(B) | 0 | 581 | 354 | 2.50 | 0.53 |
| | 8 | 3.00 | 210 | 160 | 25.5 | | 8 | 302 | 191 | 3.25 | 0.41 |
| | 45 | 3.00 | 180 | 131 | 19.8 | | 45 | 220 | 129 | 3.75 | 0.35 |

## Table 6-4. Mechanistic Fatigue Analyses of Pavement Section D1.

| PMA Mix ID | Speed (mph) | Thickness of PMA Layer (inch) | 3D-MOVE PMA Strain (ms) | PMA EL (ms) | Cycles to Failure (million) | HP Mix ID | Speed (mph) | Equivalent Max HP Strain | HP EL (ms) | Thickness of HP Layer (inch) | SC of AC HP |
|---|---|---|---|---|---|---|---|---|---|---|---|
| FL125_PMA(A) | 0 | 4.50 | 333 | 308 | 76.5 | FL125_H(A) | 0 | 318 | 290 | 6.00 | 0.33 |
| | 8 | 4.50 | 233 | 209 | 65.6 | | 8 | 252 | 221 | 5.50 | 0.36 |
| | 45 | 4.50 | 188 | 151 | 39.4 | | 45 | 225 | 174 | 5.00 | 0.40 |
| FL125_PMA(B) | 0 | 4.50 | 320 | 272 | 49.5 | FL125_HP(B) | 0 | 987 | 783 | 2.50 | 0.79 |
| | 8 | 4.50 | 224 | 187 | 45.0 | | 8 | 384 | 296 | 3.00 | 0.66 |
| | 45 | 4.50 | 180 | 137 | 28.1 | | 45 | 253 | 170 | 3.75 | 0.53 |
| GA125_PMA(A) | 0 | 4.50 | 229 | 266 | 109.9 | GA125_HP(A) | 0 | 693 | 693 | 2.00 | 0.99 |
| | 8 | 4.50 | 166 | 194 | 110.0 | | 8 | 441 | 441 | 2.00 | 0.99 |
| | 45 | 4.50 | 137 | 148 | 109.1 | | 45 | 341 | 340 | 2.50 | 0.79 |
| GA125_PMA(B) | 0 | 4.50 | 219 | 191 | 57.6 | GA125_HP(B) | 0 | 344 | 293 | 5.50 | 0.36 |
| | 8 | 4.50 | 159 | 135 | 50.8 | | 8 | 233 | 192 | 5.25 | 0.38 |
| | 45 | 4.50 | 132 | 101 | 29.5 | | 45 | 187 | 135 | 5.00 | 0.40 |

## Table 6-5. Mechanistic Fatigue Analyses of Pavement Section D2.

| PMA Mix ID | Speed (mph) | Thickness of PMA Layer (inch) | 3D-MOVE PMA Strain (ms) | PMA EL (ms) | Cycles to Failure (million) | HP Mix ID | Speed (mph) | Equivalent Max HP Strain | HP EL (ms) | Thickness of HP Layer (inch) | SC of AC HP |
|---|---|---|---|---|---|---|---|---|---|---|---|
| FL125_PMA(A) | 0 | 6.00 | 219 | 308 | 111.4 | FL125_HP(A) | 0 | 289 | 290 | 5.75 | 0.46 |
| | 8 | 6.00 | 161 | 228 | 109.7 | | 8 | 227 | 226 | 5.25 | 0.50 |
| | 45 | 6.00 | 131 | 163 | 110.3 | | 45 | 179 | 179 | 5.25 | 0.50 |
| FL125_PMA(B) | 0 | 6.00 | 210 | 272 | 111.0 | FL125_HP(B) | 0 | 782 | 783 | 3.00 | 0.88 |
| | 8 | 6.00 | 155 | 203 | 111.0 | | 8 | 312 | 311 | 2.75 | 0.96 |
| | 45 | 6.00 | 128 | 147 | 109.8 | | 45 | 188 | 188 | 4.25 | 0.62 |
| GA125_PMA(A) | 0 | 6.00 | 152 | 266 | 109.9 | GA125_HP(A) | 0 | 693 | 693 | 2.00 | 1.32 |
| | 8 | 6.00 | 118 | 209 | 109.5 | | 8 | 442 | 441 | 2.00 | 1.32 |
| | 45 | 6.00 | 98 | 157 | 109.0 | | 45 | 332 | 331 | 2.00 | 1.32 |
| GA125_PMA(B) | 0 | 6.00 | 145 | 191 | 111.6 | GA125_HP(B) | 0 | 292 | 293 | 5.50 | 0.48 |
| | 8 | 6.00 | 114 | 147 | 111.0 | | 8 | 201 | 201 | 5.25 | 0.50 |
| | 45 | 6.00 | 96 | 107 | 112.0 | | 45 | 143 | 143 | 5.75 | 0.46 |

## Table 6-6. Mechanistic Fatigue Analyses of Pavement Section D3.

| PMA Mix ID | Speed (mph) | Thickness of PMA Layer (inch) | 3D-MOVE PMA Strain (ms) | PMA EL (ms) | Cycles to Failure (million) | HP Mix ID | Speed (mph) | Equivalent Max HP Strain | HP EL (ms) | Thickness of HP Layer (inch) | SC of AC HP |
|---|---|---|---|---|---|---|---|---|---|---|---|
| FL125_PMA(A) | 0 | 4.50 | 293 | 308 | 111.4 | FL125_HP(A) | 0 | 289 | 290 | 5.75 | 0.34 |
| | 8 | 4.50 | 211 | 209 | 105.0 | | 8 | 224 | 151 | 5.50 | 0.36 |
| | 45 | 4.50 | 153 | 151 | 104.3 | | 45 | 178 | 175 | 5.50 | 0.36 |
| FL125_PMA(B) | 0 | 4.50 | 283 | 272 | 91.3 | FL125_HP(B) | 0 | 827 | 783 | 2.50 | 0.79 |
| | 8 | 4.50 | 203 | 187 | 72.1 | | 8 | 327 | 289 | 2.75 | 0.72 |
| | 45 | 4.50 | 167 | 137 | 41.3 | | 45 | 230 | 173 | 3.75 | 0.53 |
| GA125_PMA(A) | 0 | 4.50 | 209 | 266 | 109.9 | GA125_HP(A) | 0 | 693 | 693 | 2.50 | 0.79 |
| | 8 | 4.50 | 153 | 194 | 110.0 | | 8 | 426 | 426 | 2.00 | 0.99 |
| | 45 | 4.50 | 130 | 148 | 109.1 | | 45 | 322 | 321 | 2.00 | 0.99 |
| GA125_PMA(B) | 0 | 4.50 | 201 | 191 | 86.9 | GA125_HP(B) | 0 | 311 | 293 | 5.25 | 0.38 |
| | 8 | 4.50 | 149 | 135 | 69.4 | | 8 | 214 | 199 | 5.00 | 0.40 |
| | 45 | 4.50 | 126 | 101 | 37.2 | | 45 | 175 | 134 | 4.75 | 0.42 |

## 6.2. INITIAL STRUCTURAL COEFFICIENT FOR HP AC MIXES

### 6.2.1. Introduction

Multiple factors including design traffic level, pavement structure, layer properties, and performance characteristics of the evaluated PMA and HP AC mixes resulted in different structural coefficients for HP AC mixes based on fatigue cracking analysis as summarized in Table 6-7 and Table 6-8. Some of the determined coefficients were lower than 0.44 with a minimum value of 0.33 for FL125_HP(A) AC mix under static conditions (i.e., under full stop at an intersection) when evaluated in pavement section D1. On the other hand, the highest value (i.e., 1.32) was observed for GA125_HP(A) AC mix at the three considered loading speeds when evaluated in pavement section D2.

**Table 6-7. Summary of Determined HP AC Structural Coefficient for Pavement Sections under Traffic Level C.**

| Pavement Section ID | Speed (mph) | Mix / Binder ID | | | |
|---|---|---|---|---|---|
| | | FL95 | | GA95 | |
| | | HP(A) | HP(B) | HP(A) | HP(B) |
| C1 | 0 | 0.48 | 0.66 | 0.44 | 0.53 |
| | 8 | 0.59 | 0.59 | 0.44 | 0.41 |
| | 45 | 0.75 | 0.53 | 0.44 | 0.35 |
| C2 | 0 | 0.59 | 0.80 | 0.37 | 0.49 |
| | 8 | 0.59 | 1.10 | 0.42 | 0.44 |
| | 45 | 0.59 | 0.68 | 0.46 | 0.37 |
| C3 | 0 | 0.53 | 0.48 | 0.53 | 0.53 |
| | 8 | 0.66 | 0.59 | 0.59 | 0.41 |
| | 45 | 0.48 | 0.48 | 0.59 | 0.35 |

**Table 6-8. Summary of Determined HP AC Structural Coefficient for Pavement Sections under Traffic Level D.**

| Pavement Section ID | Speed (mph) | Mix / Binder ID | | | |
|---|---|---|---|---|---|
| | | FL125 | | GA125 | |
| | | HP(A) | HP(B) | HP(A) | HP(B) |
| D1 | 0 | 0.33 | 0.79 | 0.99 | 0.36 |
| | 8 | 0.36 | 0.66 | 0.99 | 0.38 |
| | 45 | 0.40 | 0.53 | 0.79 | 0.40 |
| D2 | 0 | 0.46 | 0.88 | 1.32 | 0.48 |
| | 8 | 0.50 | 0.96 | 1.32 | 0.50 |
| | 45 | 0.50 | 0.62 | 1.32 | 0.46 |
| D3 | 0 | 0.34 | 0.79 | 0.79 | 0.38 |
| | 8 | 0.36 | 0.72 | 0.99 | 0.40 |
| | 45 | 0.36 | 0.53 | 0.99 | 0.42 |

Considering all these factors, a statistical analysis was needed to evaluate the distribution of the structural coefficient for AC HP mixes determined under different conditions. The purpose of this analysis was to determine a representative initial structural coefficient for the evaluated cases. Thus, three major analyses were carried out: a) by considering all 72 determined structural

coefficients, b) after dissecting the data into two separate groups based on the aggregate source (i.e., Limestone FL vs. Granite GA), and c) after dissecting the data into two separate groups based on the NMAS (i.e., 9.5 mm vs. 12.5 mm). The following section describes the findings from all three statistical analyses.

### 6.2.2. Statistical Analyses of Structural Coefficients

*6.2.2.1 Evaluation of all data combined*

The statistical distribution of the determined 72 structural coefficients did not follow a normal distribution. In statistics, a Q-Q plot ("Q" stands for quantile) is a probability plot used to compare the probability distributions by plotting their quantiles against each other. If the points in the Q-Q plot approximately lie on the equality line, the two distributions that are being compared are considered similar. Moreover, if the points in the Q-Q plot lie on a line but not necessarily the equality line, the two distributions are considered linearly related. Figure 6-2 illustrates the sample versus theoretical quantiles (Q-Q plot) of the statistical distribution representing the determined 72 structural coefficients. The theoretical quantiles represent a perfect normal distribution. As shown in Figure 6-2, the evaluated data set (i.e., 72 structural coefficient) is skewed from both sides and did not follow a normal distribution.

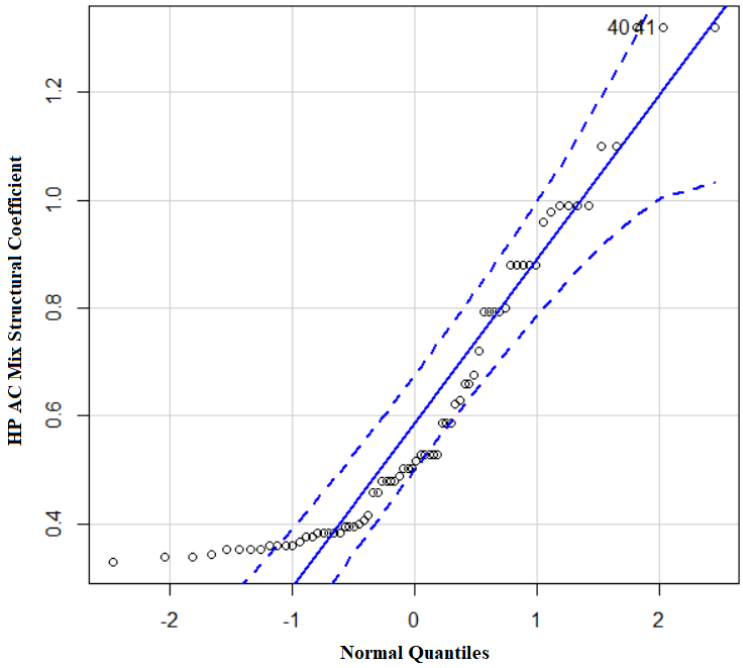


**Figure 6-2. Normal Q-Q plot of the 72 determined structural coefficients (original data).**

In addition, multiple tests exist in statistics to evaluate the normality of a given distribution. In this study, the Shapiro_Wilk test was used to evaluate and conform the non-normality of the evaluated 72 structural coefficients. The *p*-value stands for the probability of having an element lower than the *W*-value determined as output of the normality test. If the determined p-value is less than the alpha level (i.e., selected allowable error), then the null hypothesis that the data set

is normally distributed is rejected. The observation of having a p-value greater than the selected alpha level leads to the statement that the null hypothesis that the data are normally distributed is accepted.

For this study, the *W*- and *p*-values were determined as 0.85974 and 1.04E-06, respectively. An alpha level of 0.05 (i.e. 5%) was selected. The determined *p*-value (i.e., 1.04E-06) was observed to be significantly lower than 0.05 indicating that the 72 structural coefficients data do not follow a normal distribution. Normality tests and verification were implemented and multiple data transformations such as Box-Cox and multiple linear/non-linear transformations were attempted to make the data set distribution normal. All these attempts were unsuccessful and requested the need for a different methodology that can deal with complicated data set and unknown statistic.

It should be noted that, the 72 cases evaluated in this study would not exist in practice at all times throughout the pavement design life. These cases are dependent on various factors such as traffic level, pavement structure, loading speed, AC mix property and performance characteristics, and will not all occur at the same time. Furthermore, different strengths of base and subgrade material, as well as different AC mixes (i.e., different asphalt binders and aggregate sources) not evaluated in this study may exist. Therefore, a probabilistic type of analysis remains needed to effectively determine a representative structural coefficient for HP AC mixes in Florida.

In statistics, bootstrapping is any test or metric that relies on random sampling with replacement *(85)*. It allows assigning measures of accuracy defined in terms of bias, variance, confidence intervals, or prediction error to sample estimates. In this study, the bootstrapped method is considered adequate for the analysis of the 72 structural coefficients for HP AC mixes. It is used for estimating the distribution of mean statistic without using normal theory. The bootstrapping algorithm for case resampling consists of the following steps: a) data are resampled with replacement, and the size of the resample must be equal to the size of the original set of data (i.e., 72 in this case); b) the statistic of interest (i.e., in this case mean of the 72 determined structural coefficients for HP AC mixes) is computed for the resampled data from step a; c) this scenario is repeated many times to get a more precise estimate of the mean structural coefficient values. When the sample size is insufficient for straightforward statistical inference, if the underlying distribution is well-known, bootstrapping provides a way to account for the distortions caused by the specific sample that may not be fully representative of the population (e.g., in this case having different strengths of base and subgrade material, as well as different evaluated AC mixes).

In this study, the bootstrapping scenario was repeated 2,000 times to guarantee an accurate convergence of the bootstrapped mean of the 72 determined structural coefficients. Figure 6-3 illustrates the density distribution of the bootstrapped structural coefficient mean. The convergence of the bootstrapped mean can be explained by the observed bell-shape of the density curve. Moreover, a Q-Q plot of the bootstrapped data is provided in Figure 6-4. As all the points fall approximately along the reference line, a normal distribution can be assumed. In addition, the Shapiro_Wilk test was performed on the bootstrapped data. A *p*-value of 0.28 (>0.05) was determined implying that the distribution of the bootstrapped mean data of the 72 determined structural coefficients combined is normal.

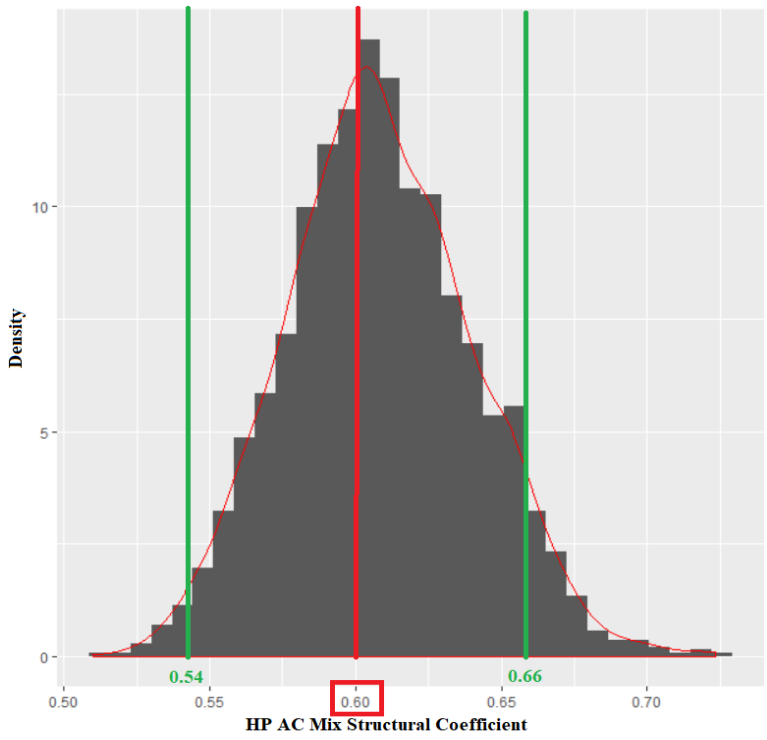


**Figure 6-3. Density of the bootstrapped mean values of determined structural coefficients.**

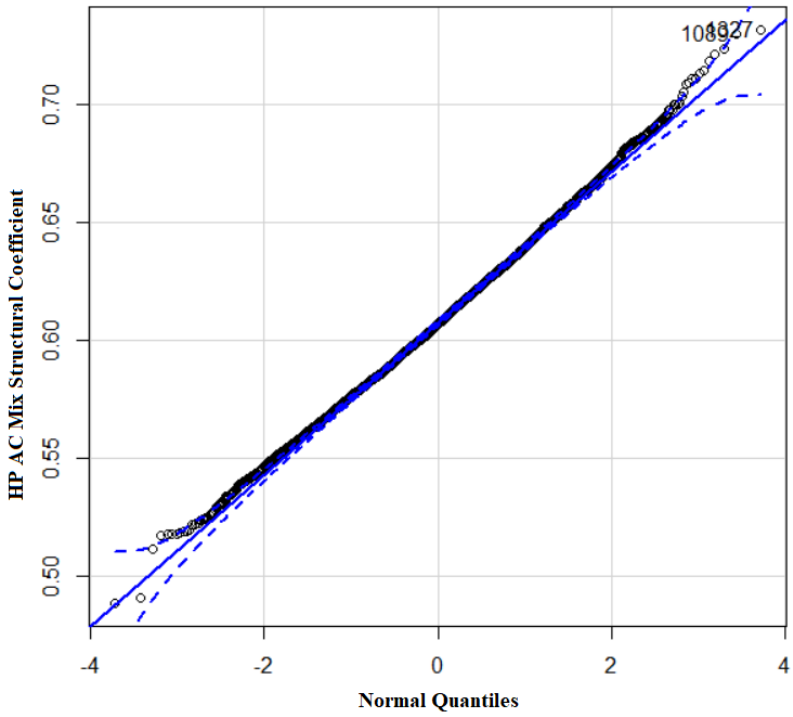


**Figure 6-4. Normal Q-Q Plot of the bootstrapped mean of the 72 determined structural coefficients.**

Finally, a bootstrapped structural coefficient mean value of 0.60 with a standard error of 0.03 resulted from this analysis. Using the mean value minus two times the standard error (corresponding to about 95% confidence interval), a value of 0.54 was estimated for the structural coefficient of HP AC mixes based on fatigue analyses.

*6.2.2.2 Evaluation of Data based on Aggregate Sources: FL vs. GA*

As mentioned before, two different aggregate sources were used in this study: Southeast Florida limestone labeled "FL," and Georgia Granite labeled "GA". The use of different aggregate source and mineralogy contributed to observed differences in the performance evaluation of the designed PMA and HP AC mixes, which resulted in a wide range of HP AC structural coefficients. Therefore, the 72 determined structural coefficients were subdivided into two major data sets based on the aggregate sources with each set included 36 coefficients. Figure 6-5 illustrates the Q-Q plots of the HP structural coefficients determined for FL and GA AC mixes. In the case of FL AC mixes, the structural coefficients fell approximately along the reference line, thus indicating that the data set is likely to have a normal distribution. However, the GA data set showed a skewed trend from both sides and all the points fell approximately outside the reference line indicating a non-normal distribution. The Shapiro_Wilk normality test performed on the FL data set showed a *p*-value of 0.074 that is slightly greater than the chosen alpha level of 0.05; thus, confirming the normality of the evaluated data set. However, the Shapiro_Wilk normality test performed on the GA data set showed a *p*-value of 1.64E-06 that is significantly lower than 0.05, confirming the rejection of normality for the GA data set.

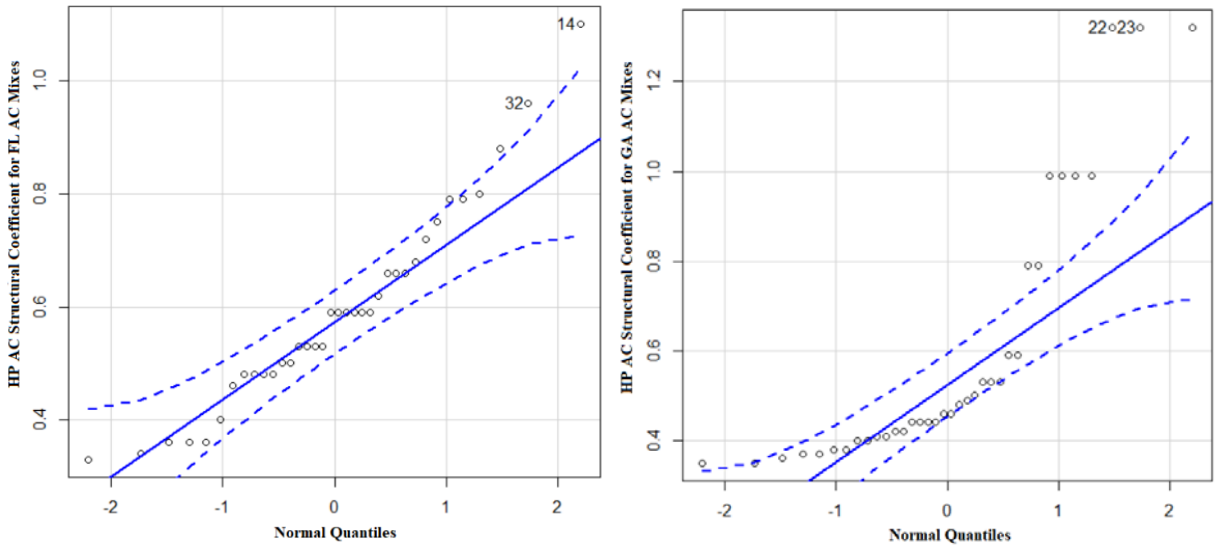


**(a)** **(b)**

**Figure 6-5. Normal Q-Q Plot of the determined structural coefficients for: (a) FL AC mixes, and (b) GA AC mixes.**

Similar to the analyses performed in section 6.2.2.1, the bootstrapping scenario was repeated 2,000 times on each data set separately to guarantee an accurate convergence of their bootstrapped means. It should be noted that, while the FL data set followed a normal distribution, bootstrapping was still applied for achieving a better estimate of the mean structural coefficient while considering multiple scenarios that might be encountered in practice. Figure 6-6 illustrates the density distribution of the bootstrapped structural coefficient mean for each of the FL and GA data sets. The convergence of the bootstrapped mean can be explained by the observed bell-shape of the density curve for each evaluated data set. Moreover, a Q-Q plot of the bootstrapped mean for each data set is provided in Figure 6-7. As all the points fall approximately along the reference line, a normal distribution can be assumed for each of the evaluated data set. In addition, the Shapiro_Wilk test was performed on the bootstrapped data. A *p*-value of 0.228 (>0.05) and 0.162 (>0.05) were determined for FL and GA data sets, respectively, confirming that the data sets are normally distributed. As a result, a bootstrapped structural coefficient mean value of 0.59 with a standard error of 0.029, and a bootstrapped structural coefficient mean value of 0.59 with a standard error of 0.047 were determined for the FL and GA data sets, respectively. Using the mean value minus two times the standard error (corresponding to about 95% confidence interval), values of 0.53 and 0.50 were estimated for the structural coefficient of HP AC mixes (based on fatigue analyses) from FL and GA aggregate sources, respectively.

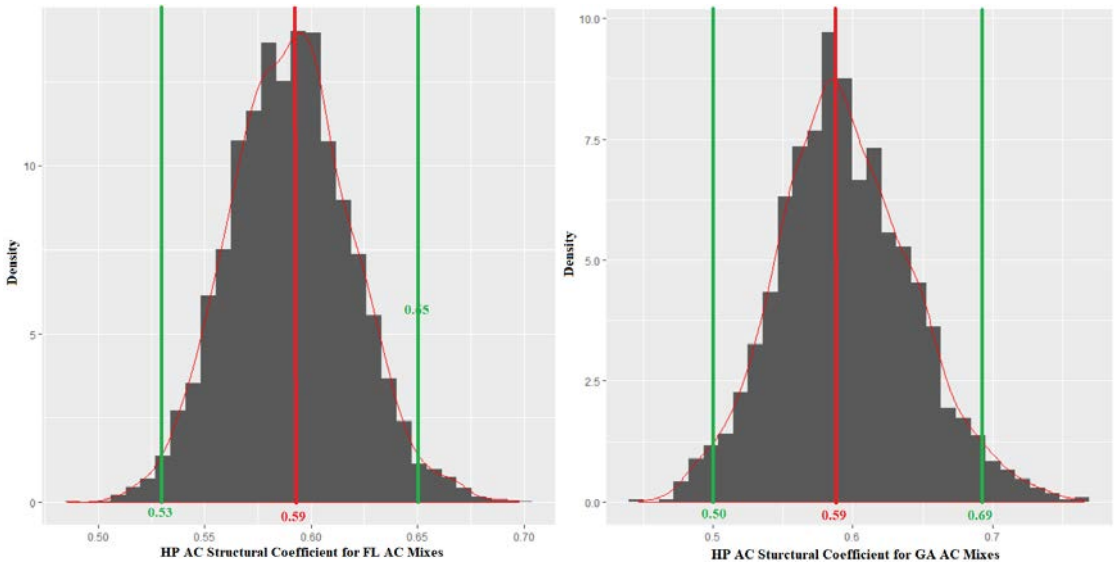


**(a)** **(b)**

**Figure 6-6. Density of the bootstrapped mean values of determined structural coefficients for: (a) FL AC mixes, and (b) GA AC mixes.**

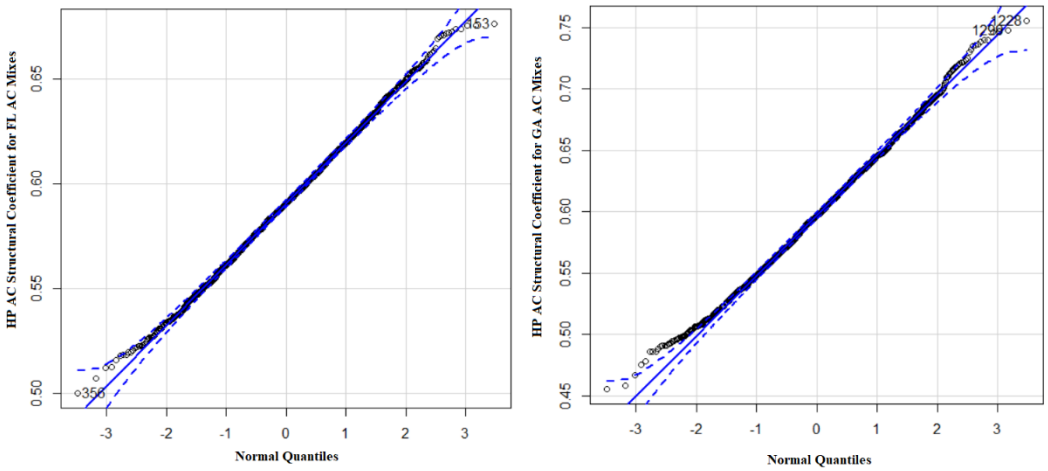


**(a)** **(b)**

**Figure 6-7. Normal Q-Q Plot of the bootstrapped mean of the determined structural coefficients for: (a) FL AC mixes, and (b) GA AC mixes.**

*6.2.2.3 Evaluation of Data based on NMAS: 9.5 vs. 12.5 mm*

As mentioned before, two aggregate gradations were evaluated from each aggregate source with NMAS of 9.5 mm and 12.5 mm. The difference in NMAS contributed to some of the differences in the performance evaluation of the designed PMA and HP AC mixes, which resulted in a wide range of HP AC structural coefficients. Therefore, the 72 determined structural coefficients were subdivided into two major data sets based on the NMAS with each set included 36 coefficients.

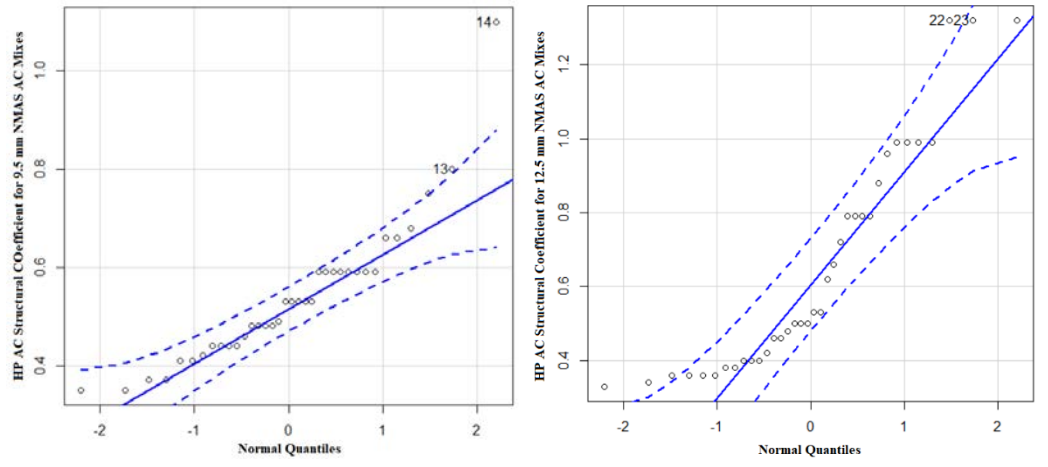


**(a)** **(b)**

**Figure 6-8. Normal Q-Q Plot of the determined structural coefficients for: (a) 9.5 mm NMAS AC mixes, and (b) 12.5 mm NMAS AC mixes.**

Figure 6-8 illustrates the Q-Q plots of the HP structural coefficients determined for 9.5 and 12.5 mm NMAS AC mixes. The majority of the structural coefficients of each of the data sets (i.e., 9.5 and 12.5 mm NMAS) fell approximately outside the reference line indicating that the data sets are not normally distributed. The Shapiro_Wilk normality test performed on the 9.5 mm and 12.5 mm NMAS data sets showed *p*-values of 3.19E-4 and 3.57E-4, respectively, which are significantly lower than the chosen alpha level of 0.05. Thus, rejecting the null hypothesis and providing evidence that the data tested are not normally distributed.

Similar to the analyses performed in Section 6.2.2.1 and Section 6.2.2.2, the bootstrapping scenario was repeated 2,000 times on each data set to guarantee an accurate convergence of their bootstrapped means. Figure 6-9 illustrates the density distribution of the bootstrapped structural coefficient means for the 9.5 and 12.5 mm NMAS data sets. The convergence of the bootstrapped mean can be explained by the observed bell-shape of the density curve for each evaluated data set. Moreover, a Q-Q plot of the bootstrapped mean for each data set is provided in Figure 6-10. As all the points fell approximately along the reference line, a normal distribution can be assumed for both data sets. In addition, the Shapiro_Wilk test was performed on the bootstrapped data. A *p*-value of 0.051 (>0.05) and 0.486 (>0.05) were determined providing evidence that that each of the data set tested is normally distributed. Resulting from these analyses, a bootstrapped structural coefficient mean value of 0.53 with a standard error of 0.023 and a bootstrapped structural coefficient mean value of 0.65 with a standard error of 0.049 that can be attributed for the 9.5 and 12.5 NMAS data sets, respectively. Using the mean value minus two times standard error (corresponding to about 95% confidence interval), values of 0.48 and 0.55 were estimated for the structural coefficient of HP AC mixes (based on fatigue analyses) with 9.5 and 12.5 NMAS, respectively.

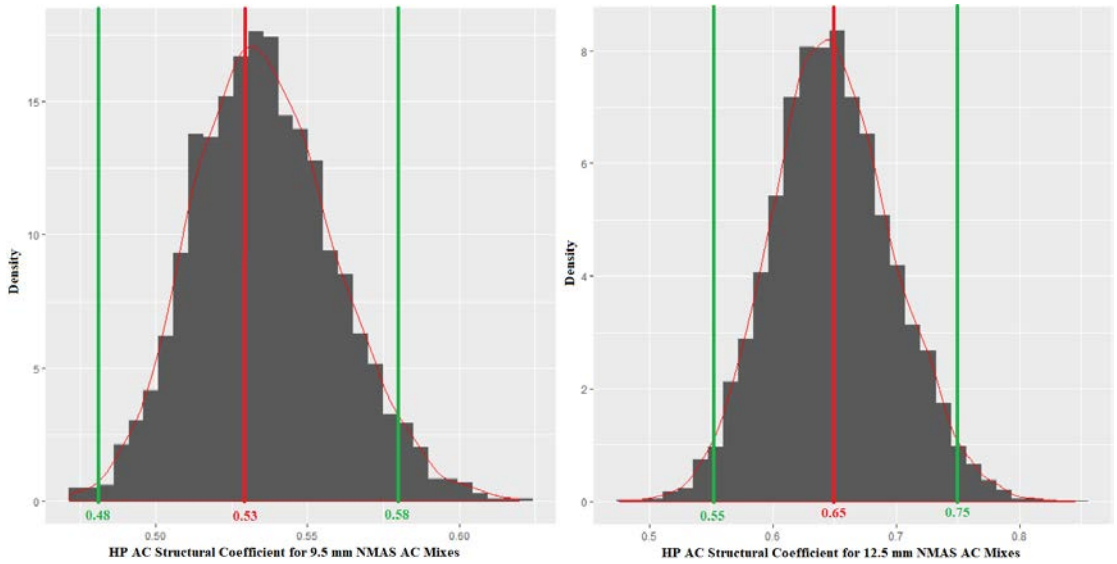


**(a)** **(b)**

**Figure 6-9. Density of the bootstrapped mean values of determined structural coefficients for: (a) 9.5 mm NMAS AC mixes, and (b) 12.5 mm NMAS AC mixes.**

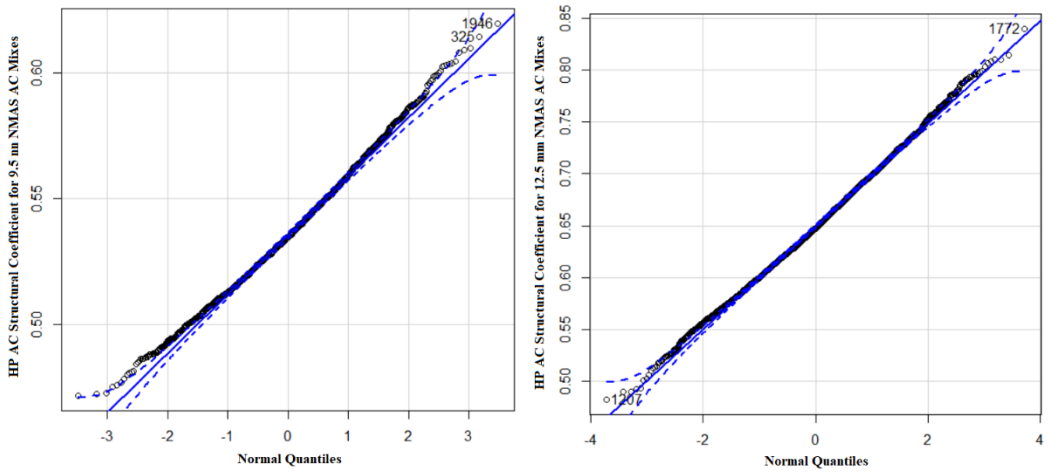


**(a)** **(b)**

**Figure 6-10. Normal Q-Q Plot of the bootstrapped mean of the determined structural coefficients for: (a) FL AC mixes, and (b) GA AC mixes.**

### 6.2.3. Summary

Table 6-9 summarizes the outcomes of the three statistical analyses. Based on the findings from the statistical analyses, the following observations can be made:

- A bootstrapped structural coefficient mean value of 0.60 with a standard error of 0.03 resulted from the analysis of all determined 72 structural coefficients combined as one set. Therefore, a fatigue-based SC of 0.54 was recommended for HP AC mixes in Florida.
- After dissecting the data into two separate groups based on the aggregate source (i.e., FL vs. GA), a similar bootstrapped structural coefficient mean value of 0.59 was obtained for each group. However, a higher standard error of 0.047 was observed for the mixes with GA aggregates irrespective of aggregate NMAS.
- After dissecting the data into two separate groups based on the NMAS (i.e., 9.5 mm vs. 12.5 mm), the mixes with 12.5 mm NMAS had a higher bootstrapped structural coefficient mean value than the mixes with 9.5 mm NMAS (0.65 vs. 0.53). The mixes with 12.5 mm NMAS had also a higher standard error than the mixes with 9.5 mm NMAS (0.049 vs. 0.023).

**Table 6-9. Summary of Statistical Analyses.**

| Analysis | Description | Factor | Mean ($\mu$) | Standard Error (SE) | $\mu$–2*SE (95% Confidence Interval) |
|---|---|---|---|---|---|
| I | Considering all 72 determined structural coefficients as one set. | All data combined | 0.60 | 0.030 | 0.54 |
| II | After dissecting the data into two separate groups based on the aggregate source (FL vs. GA). | FL aggregate source | 0.59 | 0.029 | 0.53 |
| | | GA aggregate source | 0.59 | 0.047 | 0.50 |
| III | After dissecting the data into two separate groups based on the NMAS (9.5 mm vs. 12.5 mm). | 9.5 mm NMAS | 0.53 | 0.023 | 0.48 |
| | | 12.5 mm NMAS | 0.65 | 0.049 | 0.55 |

## 6.3. VERIFICATION FOR RUTTING PERFORMANCE

### 6.3.1. AC Rutting

The RLT test was used to evaluate the rutting behavior of the 16 AC mixes under repeated loading. The permanent ($\varepsilon_p$) and resilient ($\varepsilon_r$) axial strains were measured during the RLT test as a function of the number of loading repetitions at three different temperatures including the effective high temperature for mechanistic analysis 122°F (50°C). The resulting cumulative permanent axial strain over the resilient strain ($\varepsilon_p/\varepsilon_r$) versus the number of load repetitions ($N$) at 122°F (50°C) is expressed in Equation 6-9.

$$\frac{\varepsilon_p}{\varepsilon_r} = K_z * 10^{k_{r1}} * (N)^{\beta_{r3} * k_{r3}} \qquad \textbf{Equation 6-9}$$

$$K_z = (C_1 + C_2 * depth) * 0.328196^{depth} \qquad \textbf{Equation 6-10}$$

$$C_1 = -0.1039 * h_{ac}^2 + 2.4868 * h_{ac} - 17.342 \qquad \textbf{Equation 6-11}$$

$$C_2 = 0.0172 * h_{ac}^2 - 1.7331 * h_{ac} + 27.428 \qquad \textbf{Equation 6-12}$$

Where;
$\varepsilon_p$: permanent axial strain, inch/inch (mm/mm);
$\varepsilon_r$: resilient axial strain, inch/inch (mm/mm);
$N$: number of loading cycles;
$K_z$: AC layer thickness adjustment coefficient defined in Equation 6-10];
$k_{r1}$ *and* $k_{r3}$: experimentally determined coefficients;

$\beta_{r3}$: traffic loading calibration factors;
$h_{ac}$: total AC layer thickness, inch;
$C_1, and\ C_2$ : regression constants defined as a function of $h_{ac}$; and
*depth*: distance between the top of the AC layer and the computational point, inch.

The MEPDG approach *(5)* was followed to sub-divide each layer of the pavement cross-section into sub-layers as illustrated in Figure 6-11. The critical responses were then computed at the middle of each sub-layer. Using the rutting model developed for each evaluated AC mix (i.e., PMA and HP) with the determined resilient strain ($\varepsilon_r$) from 3D-Move mechanistic analyses, the permanent strain ($\varepsilon_p$) within each AC sub-layer was calculated under three loading speeds of 0, 8, and 15 mph (0, 13, and 24 km/h). It should be mentioned that for the 15 mph (24 km/h) dynamic case, a braking friction coefficient *($f_{Br}$)* of 0.623 was considered for a tractor-semi trailer truck on a sloped pavement structure as described previously in Section 5.1.2. The rut depth generated in the AC layer is then determined for each pavement structure following the relationship in Equation 6-13.

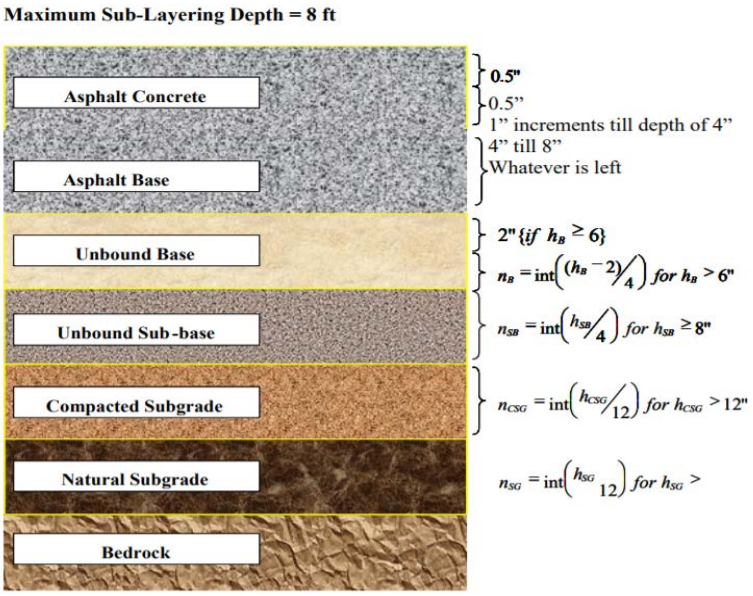


**Figure 6-11. MEPDG sub-layering of pavement cross-section for flexible pavements.**

$$RD = \sum \varepsilon_p * h_{ACi} \qquad \textbf{Equation 6-13}$$

Where;
$RD$: rut depth generated in the AC layer, inch (mm);
$\varepsilon_p$: permanent axial strain, inch/inch (mm/mm); and
$h_{ACi}$: thickness of the AC sub-layer i, inch (mm).

Preliminary traffic loading calibration factors $\beta_{r3}$ (refer to Table 6-10) were estimated for the purpose of this effort based on the following assumptions:

- The rut depth generated in the AC layer in a PMA designed pavement-cross section was fixed to its maximum allowable value of 0.25 inch (6.4 mm).
- The number of loading cycles was determined function of the traffic level. Referring to the AASHTO Guide 1993 *(2)*, one pass of a tandem axle loaded with 44,000 lbs. (196 kN) on a pavement section characterized with a structural number (SN) of 5.0 is equivalent to three equivalent single axle load (ESAL). Therefore, for a traffic level C (i.e., 7 million ESALs) and traffic level D (i.e., 20 million ESALs), the number of passes *(N)* is equal to 2.3 and 6.7 million tandem axles passes, respectively.

Three factors were taken into consideration including the PMA AC mixes, traffic level, and loading speed. An average βr3 factor was determined for each PMA AC mix at a given traffic level (i.e., C and D) under static conditions (i.e., 0 mph) as summarized in Table 6-10. These factors were then used for the corresponding HP AC mixes (e.g., FL95_PMA(A) vs. FL95_HP(A)) at the same traffic level under all loading speeds (i.e.,0, 8, and 15 mph (0, 13, and 24 km/h)).

**Table 6-10. Summary of $\beta_{r3}$ Factors.**

| Traffic Level | Section ID | FL95_PMA(A) | FL95_PMA(B) | GA95_PMA(A) | GA95_PMA(B) |
|---|---|---|---|---|---|
| C | C1 | 0.273355 | 0.295698 | 0.565351 | 0.615320 |
| | C2 | 0.257956 | 0.284580 | 0.544226 | 0.594831 |
| | C3 | 0.272963 | 0.267898 | 0.565633 | 0.615800 |
| | **Average** | ***0.268091*** | ***0.282725*** | ***0.558403*** | ***0.608651*** |
| **Traffic Level** | **Section ID** | **FL125_PMA(A)** | **FL125_PMA(B)** | **GA125_PMA(A)** | **GA125_PMA(B)** |
| D | D1 | 0.325921 | 0.349975 | 0.505013 | 0.511321 |
| | D2 | 0.329058 | 0.352872 | 0.508767 | 0.514225 |
| | D3 | 0.324395 | 0.348519 | 0.502157 | 0.508985 |
| | **Average** | ***0.326458*** | ***0.350455*** | ***0.505313*** | ***0.511510*** |

The initial structural coefficient of HP AC mixes determined based on the fatigue performance life section (i.e., 0.54) was used to determine the thickness of the HP AC layer in the various HP pavement structures (refer to Equation 6-14). It should be mentioned that the base, stabilized subgrade, and subgrade layers were maintained the same in both PMA and respective HP pavement structures.

$$h_{AC-HP} = \frac{0.44}{0.54} * h_{AC-PMA} \qquad \textbf{Equation 6-14}$$

Where;
$h_{AC-PMA}$: thickness of the AC layer in PMA pavement section, inch (mm); and
$h_{AC-HP}$: thickness of the AC layer in corresponding HP pavement section, inch (mm).

Table 6-11 to Table 6-16 summarize the rutting performance data of the AC layers in the PMA and HP pavement sections. A review of the presented data reveals the following observations:

- For traffic level C and under static conditions, all HP AC mixes except for GA95_HP(B) showed lower AC rut depths (i.e., a 16 to 40 % decrease in AC rut depths) when compared with their corresponding PMA AC layers. Thus, indicating a better rutting performance for the HP AC mixes.
- For traffic level C and under dynamic loading (i.e., 8 and 15 mph (13, and 24 km/h)), all rut depths of HP AC mixes were observed to be lower than the respective PMA AC mixes. Thus, indicating a better rutting performance for HP AC mixes.
- For traffic level D and under static conditions, all HP AC mixes except for the ones manufactured using HP asphalt binder from source B showed lower AC rut depths (i.e., a 32 to 52 % decrease in the rut depths) when compared with their corresponding PMA AC layers.
- For traffic level D and under dynamic loading (i.e., 8 and 15 mph (13, and 24 km/h)), all rut depths of HP AC were observed to be lowered than the control PMA ones.

It should be mentioned that for the case of AC mixes manufactured using HP asphalt binders from source B, the rut depths generated in the AC layers were higher than the ones generated in the corresponding PMA control and did not meet the criterion of 0.25 inch (6.4 mm) as a maximum allowable rut depth in the AC layer. However, this should not be of a concern since in reality, the design traffic will not be static (i.e., full stop) during the entire design life of the pavement. The traffic would typically comprise static and dynamic loads. It should also be noted that the static analysis considered in this study used a modulus for the AC layer that was selected at a very low loading frequency (i.e., 0.5 Hz) to represent heavy vehicles approaching a full stop condition at an intersection. This resulted in a relatively low modulus for the AC layer ranging between 22,116 and 71,067 psi (152.5 and 490 MPa) for PMA AC mixes and between 14,524 and 33,269 psi (100 and 229 MPa) for HP AC mixes.

**Table 6-11. Rutting Data for Traffic Level C under Static Conditions.**

| Section ID | PMA Mix ID | Rut Depths (inch) | | | HP Mix ID | Rut Depths (inch) | | |
|---|---|---|---|---|---|---|---|---|
| | | AC | Base | Subgrade | | AC | Base | Subgrade |
| C1 | FL95_PMA(A) | 0.25 | 0.34 | 0.13 | FL95_HP(A) | 0.15 | 0.35 | 0.13 |
| | FL95_PMA(B) | 0.25 | 0.33 | 0.13 | FL95_HP(B) | 0.17 | 0.36 | 0.13 |
| | GA95_PMA(A) | 0.25 | 0.31 | 0.12 | GA95_HP(A) | 0.14 | 0.37 | 0.13 |
| | GA95_PMA(B) | 0.25 | 0.30 | 0.12 | GA95_HP(B) | 0.20 | 0.37 | 0.13 |
| C2 | FL95_PMA(A) | 0.25 | 0.19 | 0.16 | FL95_HP(A) | 0.17 | 0.21 | 0.16 |
| | FL95_PMA(B) | 0.25 | 0.18 | 0.16 | FL95_HP(B) | 0.19 | 0.22 | 0.16 |
| | GA95_PMA(A) | 0.25 | 0.17 | 0.15 | GA95_HP(A) | 0.16 | 0.22 | 0.16 |
| | GA95_PMA(B) | 0.25 | 0.17 | 0.15 | GA95_HP(B) | ***0.26*** | 0.22 | 0.17 |
| C3 | FL95_PMA(A) | 0.25 | 0.25 | 0.14 | FL95_HP(A) | 0.16 | 0.26 | 0.14 |
| | FL95_PMA(B) | 0.25 | 0.25 | 0.14 | FL95_HP(B) | 0.11 | 0.26 | 0.14 |
| | GA95_PMA(A) | 0.25 | 0.23 | 0.13 | GA95_HP(A) | 0.14 | 0.27 | 0.14 |
| | GA95_PMA(B) | 0.25 | 0.23 | 0.13 | GA95_HP(B) | 0.21 | 0.27 | 0.14 |

**Table 6-12. Rutting Data for Traffic Level C under a Loading Speed of 8 mph.**

| Section ID | PMA Mix ID | Rut Depths (inch) | | | HP Mix ID | Rut Depths (inch) | | |
|---|---|---|---|---|---|---|---|---|
| | | AC | Base | Subgrade | | AC | Base | Subgrade |
| C1 | FL95_PMA(A) | 0.11 | 0.31 | 0.14 | FL95_HP(A) | 0.09 | 0.33 | 0.15 |
| | FL95_PMA(B) | 0.10 | 0.30 | 0.14 | FL95_HP(B) | 0.10 | 0.35 | 0.15 |
| | GA95_PMA(A) | 0.11 | 0.28 | 0.14 | GA95_HP(A) | 0.07 | 0.35 | 0.14 |
| | GA95_PMA(B) | 0.11 | 0.26 | 0.14 | GA95_HP(B) | 0.09 | 0.35 | 0.15 |
| C2 | FL95_PMA(A) | 0.12 | 0.19 | 0.16 | FL95_HP(A) | 0.10 | 0.19 | 0.18 |
| | FL95_PMA(B) | 0.11 | 0.16 | 0.18 | FL95_HP(B) | 0.11 | 0.20 | 0.19 |
| | GA95_PMA(A) | 0.11 | 0.15 | 0.17 | GA95_HP(A) | 0.08 | 0.20 | 0.19 |
| | GA95_PMA(B) | 0.11 | 0.14 | 0.17 | GA95_HP(B) | 0.11 | 0.20 | 0.19 |
| C3 | FL95_PMA(A) | 0.11 | 0.23 | 0.15 | FL95_HP(A) | 0.09 | 0.25 | 0.15 |
| | FL95_PMA(B) | 0.10 | 0.22 | 0.15 | FL95_HP(B) | 0.10 | 0.26 | 0.15 |
| | GA95_PMA(A) | 0.11 | 0.21 | 0.15 | GA95_HP(A) | 0.07 | 0.26 | 0.15 |
| | GA95_PMA(B) | 0.10 | 0.20 | 0.14 | GA95_HP(B) | 0.09 | 0.25 | 0.15 |

**Table 6-13. Rutting Data for Traffic Level C under a Loading Speed of 15 mph.**

| Section ID | PMA Mix ID | Rut Depths (inch) | | | HP Mix ID | Rut Depths (inch) | | |
|---|---|---|---|---|---|---|---|---|
| | | AC | Base | Subgrade | | AC | Base | Subgrade |
| C1 | FL95_PMA(A) | 0.08 | 0.31 | 0.15 | FL95_HP(A) | 0.07 | 0.33 | 0.15 |
| | FL95_PMA(B) | 0.08 | 0.30 | 0.14 | FL95_HP(B) | 0.08 | 0.35 | 0.15 |
| | GA95_PMA(A) | 0.08 | 0.27 | 0.14 | GA95_HP(A) | 0.05 | 0.35 | 0.15 |
| | GA95_PMA(B) | 0.08 | 0.25 | 0.14 | GA95_HP(B) | 0.07 | 0.35 | 0.15 |
| C2 | FL95_PMA(A) | 0.09 | 0.17 | 0.18 | FL95_HP(A) | 0.08 | 0.20 | 0.17 |
| | FL95_PMA(B) | 0.08 | 0.17 | 0.18 | FL95_HP(B) | 0.08 | 0.21 | 0.19 |
| | GA95_PMA(A) | 0.08 | 0.15 | 0.16 | GA95_HP(A) | 0.06 | 0.21 | 0.19 |
| | GA95_PMA(B) | 0.08 | 0.14 | 0.16 | GA95_HP(B) | 0.08 | 0.20 | 0.19 |
| C3 | FL95_PMA(A) | 0.08 | 0.23 | 0.15 | FL95_HP(A) | 0.07 | 0.25 | 0.15 |
| | FL95_PMA(B) | 0.08 | 0.22 | 0.15 | FL95_HP(B) | 0.08 | 0.26 | 0.15 |
| | GA95_PMA(A) | 0.10 | 0.20 | 0.15 | GA95_HP(A) | 0.05 | 0.26 | 0.16 |
| | GA95_PMA(B) | 0.08 | 0.19 | 0.14 | GA95_HP(B) | 0.07 | 0.26 | 0.16 |

**Table 6-14. Rutting Data for Traffic Level D under Static Conditions.**

| Section ID | PMA Mix ID | Rut Depths (inch) | | | HP Mix ID | Rut Depths (inch) | | |
|---|---|---|---|---|---|---|---|---|
| | | AC | Base | Subgrade | | AC | Base | Subgrade |
| D1 | FL125_PMA(A) | 0.25 | 0.26 | 0.13 | FL125_HP(A) | 0.17 | 0.31 | 0.14 |
| | FL125_PMA(B) | 0.25 | 0.26 | 0.13 | FL125_HP(B) | ***0.44*** | 0.33 | 0.14 |
| | GA125_PMA(A) | 0.25 | 0.24 | 0.13 | GA125_HP(A) | 0.12 | 0.31 | 0.14 |
| | GA125_PMA(B) | 0.25 | 0.24 | 0.13 | GA125_HP(B) | ***0.31*** | 0.32 | 0.14 |
| D2 | FL125_PMA(A) | 0.25 | 0.17 | 0.16 | FL125_HP(A) | 0.17 | 0.20 | 0.17 |
| | FL125_PMA(B) | 0.25 | 0.17 | 0.21 | FL125_HP(B) | ***0.44*** | 0.21 | 0.18 |
| | GA125_PMA(A) | 0.25 | 0.16 | 0.15 | GA125_HP(A) | 0.12 | 0.20 | 0.17 |
| | GA125_PMA(B) | 0.25 | 0.15 | 0.20 | GA125_HP(B) | ***0.30*** | 0.21 | 0.18 |
| D3 | FL125_PMA(A) | 0.25 | 0.20 | 0.14 | FL125_HP(A) | 0.17 | 0.23 | 0.14 |
| | FL125_PMA(B) | 0.25 | 0.19 | 0.14 | FL125_HP(B) | ***0.45*** | 0.23 | 0.15 |
| | GA125_PMA(A) | 0.25 | 0.18 | 0.13 | GA125_HP(A) | 0.12 | 0.23 | 0.14 |
| | GA125_PMA(B) | 0.25 | 0.18 | 0.13 | GA125_HP(B) | ***0.32*** | 0.23 | 0.15 |

**Table 6-15. Rutting Data for Traffic Level D under a Loading Speed of 8 mph.**

| Section ID | PMA Mix ID | Rut Depths (inch) | | | HP Mix ID | Rut Depths (inch) | | |
|---|---|---|---|---|---|---|---|---|
| | | AC | Base | Subgrade | | AC | Base | Subgrade |
| D1 | FL125_PMA(A) | 0.12 | 0.23 | 0.15 | FL125_HP(A) | 0.09 | 0.28 | 0.16 |
| | FL125_PMA(B) | 0.12 | 0.23 | 0.15 | FL125_HP(B) | 0.21 | 0.30 | 0.16 |
| | GA125_PMA(A) | 0.14 | 0.22 | 0.14 | GA125_HP(A) | 0.06 | 0.28 | 0.15 |
| | GA125_PMA(B) | 0.11 | 0.20 | 0.14 | GA125_HP(B) | 0.14 | 0.29 | 0.16 |
| D2 | FL125_PMA(A) | 0.11 | 0.15 | 0.18 | FL125_HP(A) | 0.09 | 0.18 | 0.20 |
| | FL125_PMA(B) | 0.11 | 0.15 | 0.24 | FL125_HP(B) | 0.20 | 0.19 | 0.20 |
| | GA125_PMA(A) | 0.10 | 0.14 | 0.17 | GA125_HP(A) | 0.06 | 0.18 | 0.19 |
| | GA125_PMA(B) | 0.11 | 0.14 | 0.22 | GA125_HP(B) | 0.13 | 0.19 | 0.20 |
| D3 | FL125_PMA(A) | 0.12 | 0.17 | 0.16 | FL125_HP(A) | 0.09 | 0.21 | 0.16 |
| | FL125_PMA(B) | 0.12 | 0.17 | 0.16 | FL125_HP(B) | 0.21 | 0.22 | 0.16 |
| | GA125_PMA(A) | 0.11 | 0.15 | 0.15 | GA125_HP(A) | 0.06 | 0.21 | 0.16 |
| | GA125_PMA(B) | 0.11 | 0.15 | 0.15 | GA125_HP(B) | 0.14 | 0.21 | 0.16 |

**Table 6-16. Rutting Data for Traffic Level D under a Loading Speed of 15 mph.**

| Section ID | PMA Mix ID | Rut Depths (inch) | | | HP Mix ID | Rut Depths (inch) | | |
|---|---|---|---|---|---|---|---|---|
| | | AC | Base | Subgrade | | AC | Base | Subgrade |
| D1 | FL125_PMA(A) | 0.09 | 0.23 | 0.15 | FL125_HP(A) | 0.07 | 0.28 | 0.16 |
| | FL125_PMA(B) | 0.09 | 0.23 | 0.15 | FL125_HP(B) | 0.15 | 0.30 | 0.16 |
| | GA125_PMA(A) | 0.11 | 0.21 | 0.15 | GA125_HP(A) | 0.05 | 0.28 | 0.15 |
| | GA125_PMA(B) | 0.08 | 0.19 | 0.14 | GA125_HP(B) | 0.10 | 0.29 | 0.16 |
| D2 | FL125_PMA(A) | 0.09 | 0.15 | 0.18 | FL125_HP(A) | 0.07 | 0.19 | 0.19 |
| | FL125_PMA(B) | 0.08 | 0.15 | 0.23 | FL125_HP(B) | 0.15 | 0.19 | 0.21 |
| | GA125_PMA(A) | 0.07 | 0.14 | 0.16 | GA125_HP(A) | 0.05 | 0.18 | 0.19 |
| | GA125_PMA(B) | 0.08 | 0.14 | 0.20 | GA125_HP(B) | 0.09 | 0.19 | 0.20 |
| D3 | FL125_PMA(A) | 0.09 | 0.17 | 0.16 | FL125_HP(A) | 0.07 | 0.21 | 0.16 |
| | FL125_PMA(B) | 0.09 | 0.17 | 0.16 | FL125_HP(B) | 0.15 | 0.22 | 0.17 |
| | GA125_PMA(A) | 0.08 | 0.15 | 0.15 | GA125_HP(A) | 0.05 | 0.21 | 0.16 |
| | GA125_PMA(B) | 0.08 | 0.15 | 0.15 | GA125_HP(B) | 0.10 | 0.22 | 0.17 |

### 6.3.2. Total Rutting

The total rutting represents the accumulation of rut depths generated from all pavement layers (i.e., AC, base, and subgrade). The previous section covered in details the rut depth generated in the AC layers. The analysis of rutting generated in the base and subgrade layers is presented in this section. It should be mentioned that no rutting is assumed to occur in the 12 inch (25.4 mm) stabilized subgrade layer. In this study, the nationally calibrated rutting performance models recommended in the AASHTO M-E Design method *(5)* were used for the rutting evaluation of the base and subgrade layers.

Equation 6-15 to Equation 6-22 show the national field-calibrated mathematical model and parameters used to calculate plastic vertical deformation within the unbound pavement layers (i.e., base layer in this case).

$$\delta_A(N) = \beta_1(\frac{\varepsilon_0}{\varepsilon_r})e^{-(\frac{\rho}{N})^{\beta}}\varepsilon_v h \qquad \textbf{Equation 6-15}$$

$$Log\beta = -0.61119 - 0.017638(W_c) \quad \textbf{Equation 6-16}$$

$$W_c = 51.712 * [(\frac{M_r}{2555})^{1/0.64}]^A \quad \textbf{Equation 6-17}$$

$$A = -0.3586 * GWT^{0.1192} \quad \textbf{Equation 6-18}$$

$$\rho = 10^9(\frac{C_0}{(1-(10^9)^\beta)})^{\frac{1}{\beta}} \quad \textbf{Equation 6-19}$$

$$\left(\frac{\varepsilon_0}{\varepsilon_r}\right) = [(0.15 * e^x) + (20 * e^y)]/2 \quad \textbf{Equation 6-20}$$

$$x = \rho^\beta \quad \textbf{Equation 6-21}$$

$$y = (\rho/10^9)^\beta \quad \textbf{Equation 6-22}$$

Where;
$\delta_a$: permanent or plastic deformation for each layer/sub-layer, inch;
*N*: number of axle-load repetitions;
$\varepsilon_0$, $\beta$, and $\rho$: material properties;
$\varepsilon_r$: resilient strain imposed in laboratory test to obtain material properties $\varepsilon_0$, β, and $\rho$, inch/inch;
$\varepsilon_v$: average vertical resilient or elastic strain in the layer/sub-layer and determined using the mechanistic analyses in 3D-Move software, inch/inch;
*h*: thickness of the unbound layer/sublayer (inch);
$\beta_1$: laboratory to field adjustment and calibration factor;
$W_c$: water content, %;
$M_r$: resilient modulus of the unbound layer or sublayer, psi;
*GWT*: ground water table depth, ft; and
$\beta_1$: 1.673 for granular base, and 1.350 for subgrade.

The plastic strains within the subgrade layer follow the model expressed in Equation 6-23 to estimate the total permanent strain of the subgrade. The compressive strains *($\varepsilon_v$)* were computed at the top of the subgrade layer and at a depth of 6 inch (152 mm) below the top of the subgrade using the 3D-Move mechanistic model. The material parameters *($\varepsilon_0/\varepsilon_r$), ($\beta$)*, and *($\rho$)* are then computed at the same locations (i.e., z = 0 and 6 inch (0 and 152 mm)). The plastic strain at both depths is estimated using Equation 6-24. Using the exponential decay function shown in Equation 6-25 and the two plastic strains determined at 0 and 6 inch (0 and 152 mm) below the top of the subgrade, the regression constant *(k)* is determined using Equation 6-25. The total permanent deformation of the subgrade layer is determined using Equation 6-26.

$$\varepsilon_p(z) = \left(\varepsilon_{p,z=0}\right) * e^{-k*z} \quad \textbf{Equation 6-23}$$

$$\varepsilon_p = (\frac{\varepsilon_0}{\varepsilon_r}) e^{-(\frac{\rho}{N})^{\beta}} \varepsilon_v \qquad \textbf{Equation 6-24}$$

$$k = \left(\frac{1}{6}\right) * Ln\left(\varepsilon_{p,z=0} / \varepsilon_{p,z=6}\right) \qquad \textbf{Equation 6-25}$$

$$RD_{SG} = \int_0^{h_{bedrock}} \varepsilon_p(z) dz = \left( \frac{1-e^{-k*h_{bedrock}}}{k} \right) * \varepsilon_{p,z=0} \quad \textbf{Equation 6-26}$$

Where;
$\varepsilon_p(z)$: plastic vertical strain at depth z (measured from top of subgrade), inch/inch;
$\varepsilon_{p,z=0}$: plastic vertical strain at top of subgrade, inch/inch;
*k*: regression constant;
$\varepsilon_0$ and $\beta$: material properties;
$\varepsilon_r$: resilient strain imposed in laboratory test to obtain material properties $\varepsilon_0$, β, and $\rho$, inch/inch;
$\varepsilon_v$: average vertical resilient or elastic strain in the layer/sub-layer and determined using the mechanistic analyses in 3D-Move software, inch/inch;
$RD_{SG}$: total plastic deformation of the subgrade layer, inch (mm); and
$h_{hedrock}$: depth to bedrock from top of the subgrade, inch (mm).

Table 6-11 to Table 6-16, and Figure 6-12 to Figure 6-17 summarize and illustrate the rutting performance data of the base and subgrade layers for the PMA and HP pavement sections. A review of the presented data reveals the following observations:

- Greater rut depths were generated in base layers of the HP pavement structures when compared with the ones calculated in the PMA pavement structures. It should be mentioned that thinner AC layers exist on top of the base layers in the HP pavement structures when compared with the PMA ones leading to a stress distribution of a higher magnitude into the base layer.
- Similar rut depths were observed in the subgrade layers of both PMA and HP pavement structures under the same loading conditions (i.e., static vs. dynamic). It should be mentioned that the pavement structures designed in accordance with FDOT design manual *(4)* are characterized by a thick base, and 12 inch (305 mm) stabilized layer on top of the subgrade which may make the subgrade insensitive to the decrease in the AC thickness.
- The total rutting criterion was limited to 0.75 inch (19 mm) for all the layers in the evaluated structure. Since 0.25 inch (6.4 mm) is only allowed in the AC layer, a value of 0.50 inch (12.5 mm) is only allowed as a total permanent deformation generated in all unbound layers (i.e., in this case base, and subgrade). All evaluated cases met this criterion indicating no excessive rutting in unbound materials over the design life of the pavement when a structural coefficient value of 0.54 for HP AC mixes is used.

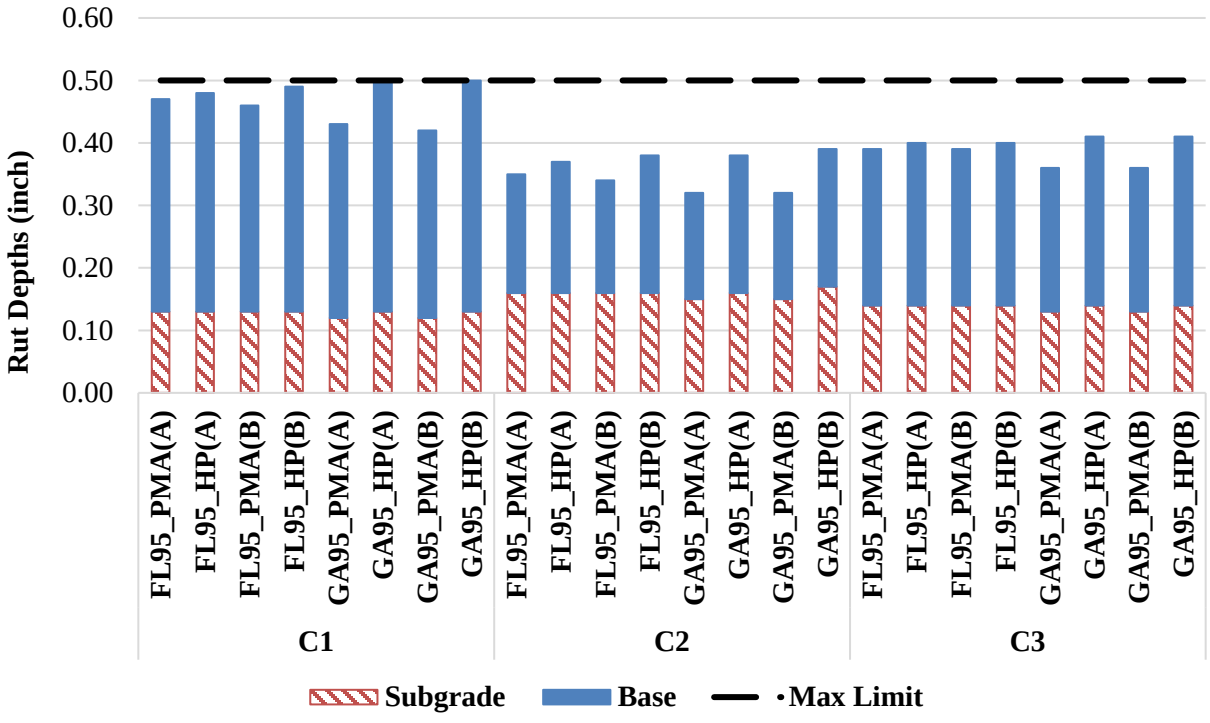


**Figure 6-12. Rutting data for traffic level C under static conditions.**

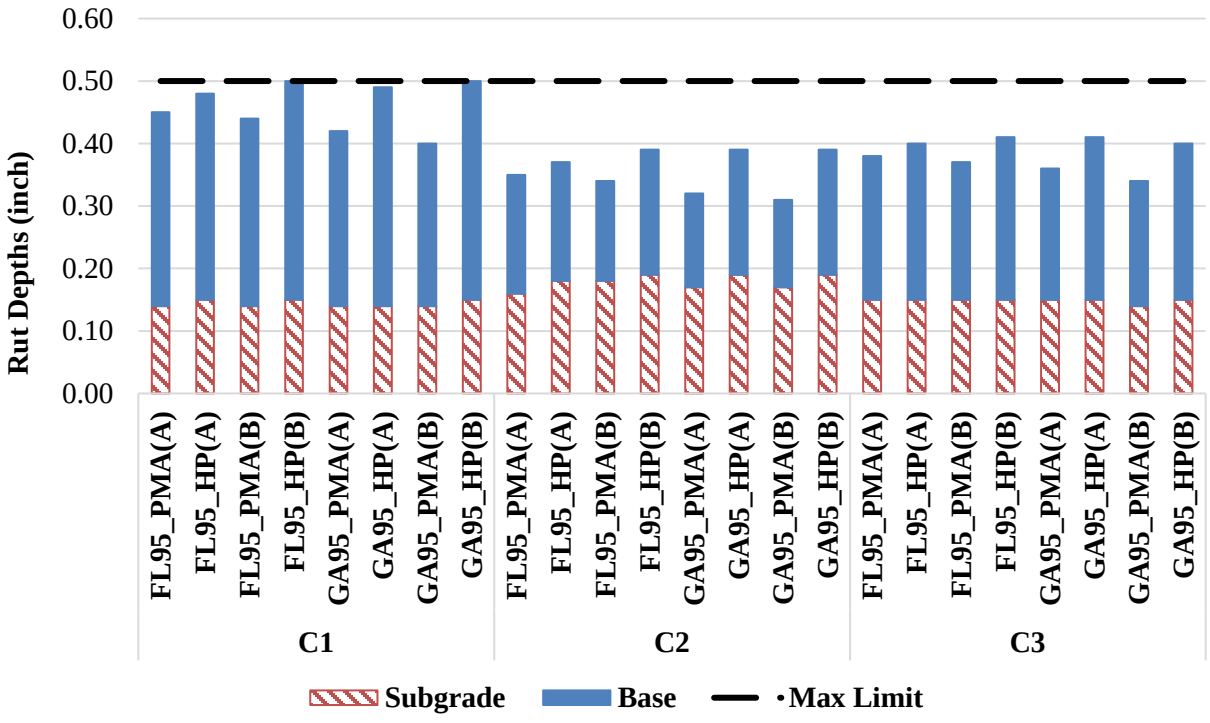


**Figure 6-13. Rutting data for traffic level C under loading speed of 8 mph.**

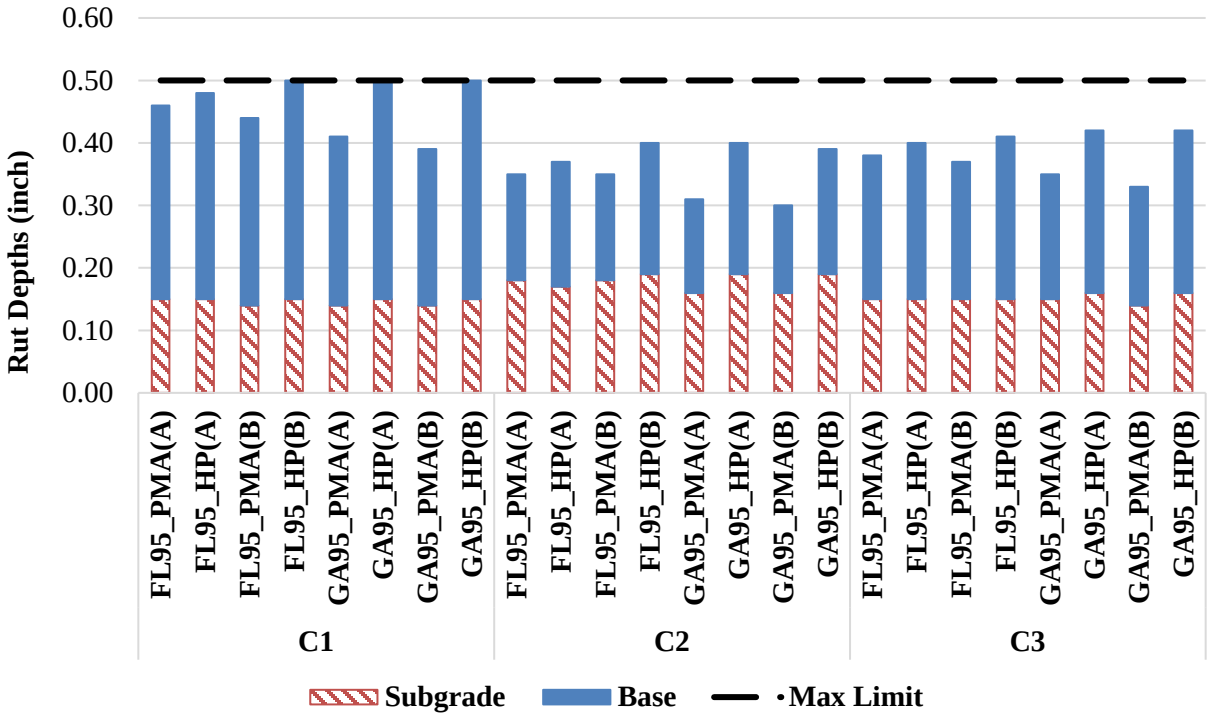


**Figure 6-14. Rutting data for traffic level C under loading speed of 15 mph.**

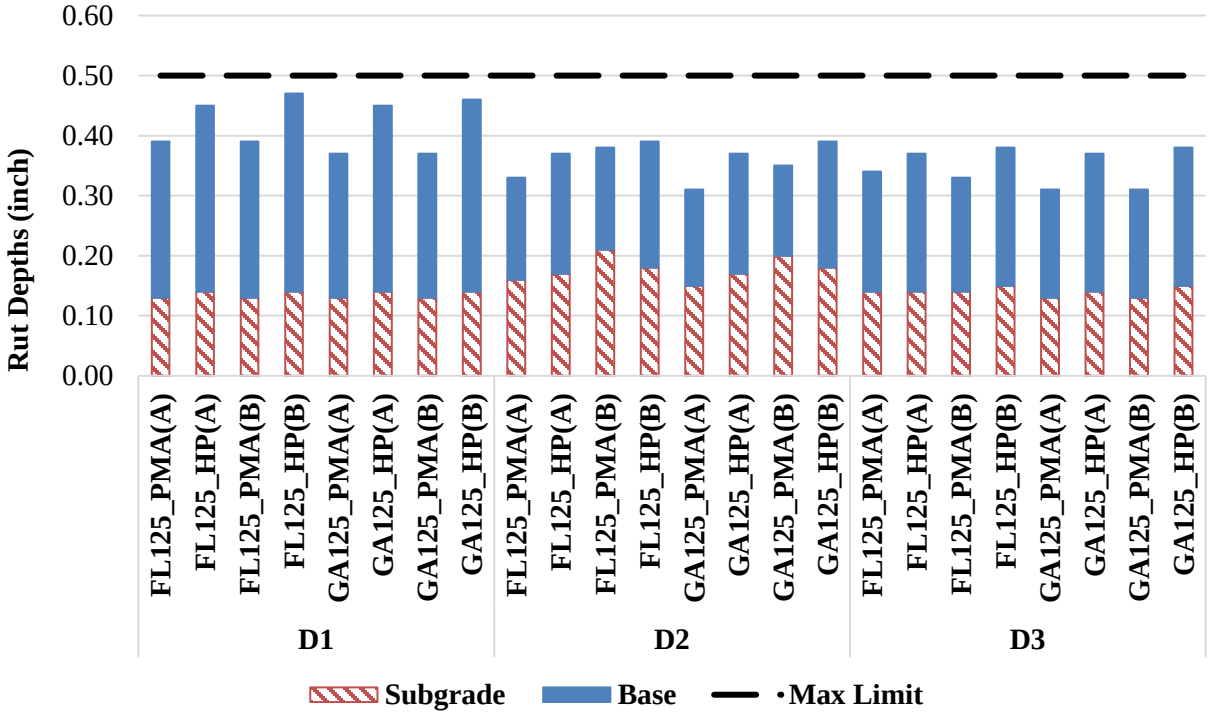


**Figure 6-15. Rutting data for traffic level D under static conditions.**

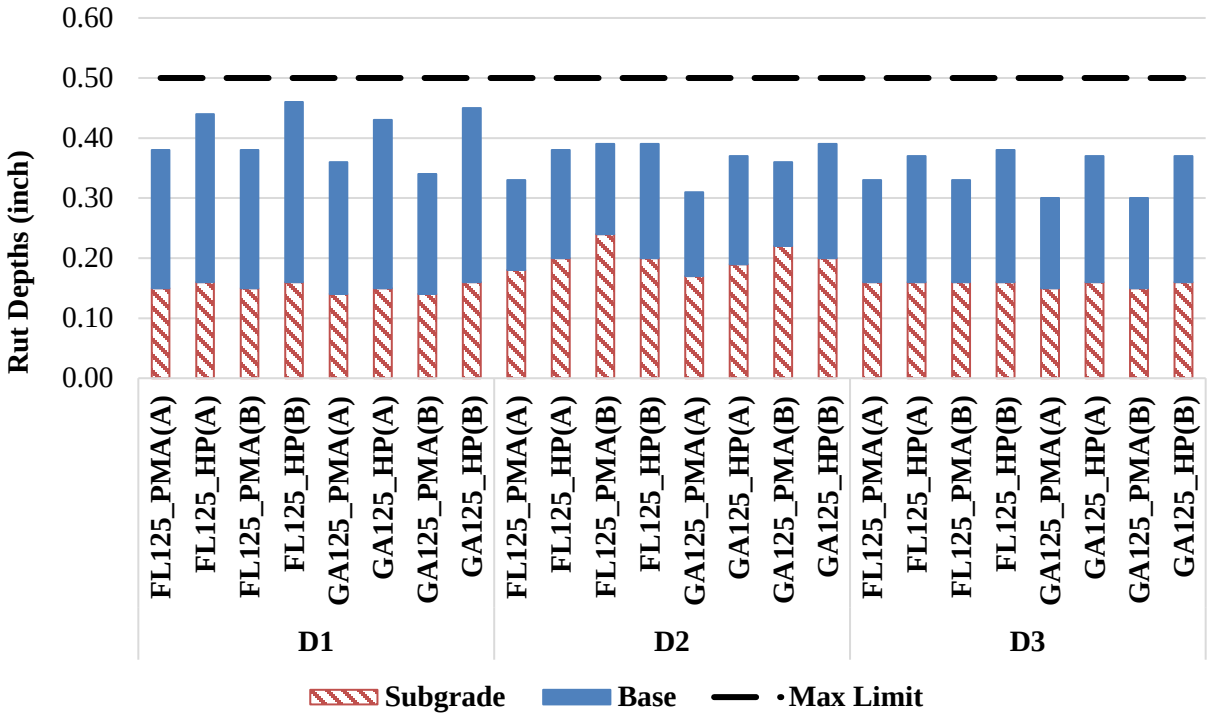


**Figure 6-16. Rutting data for traffic level D under loading speed of 8 mph.**

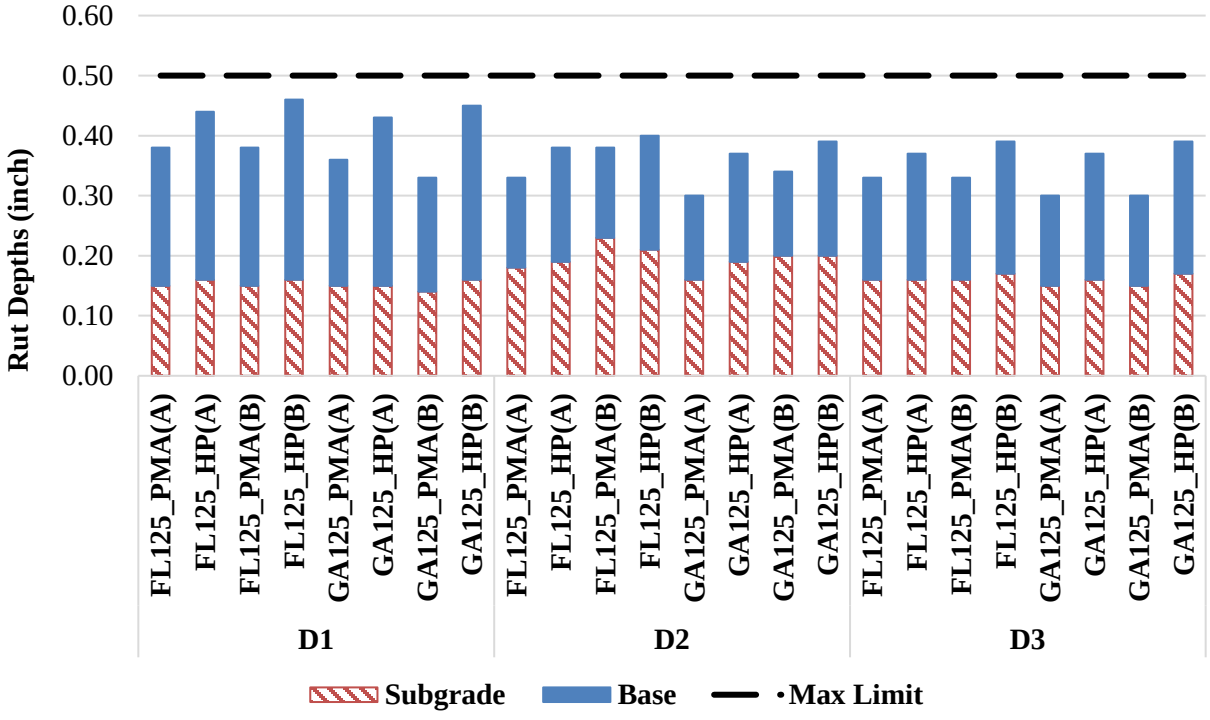


**Figure 6-17. Rutting data for traffic level D under loading speed of 15 mph.**

## 6.4. VERIFICATION OF AC SHOVING PERFORMANCE

As mentioned earlier, shoving is a form of horizontal plastic movement that occurs at locations where traffic starts and stops such as intersections *(74)*. Since HP AC mixes can also be used at this type of locations, the fatigue-based initial structural coefficient for HP AC mixes should be verified for shoving within the AC layer. Since no standard laboratory test exists to determine the shoving characteristics of AC mixes, the critical responses (e.g., shear strains and shear stresses) computed using the 3D-Move mechanistic analyses were used to complete this verification check. It should be reminded that shoving was verified by applying a braking friction coefficient *($f_{Br}$)* of 0.623 for the axle loading configuration at a speed of 15 mph (km/h) and a temperature of 122°F (50°C). The selected analysis temperature consists of the effective high analysis pavement temperature.

The shoving analysis was completed by conducting a relative comparison between the maximum shear strains determined from the mechanistic analysis within the top 0.50 inch (12.5 mm) of HP and PMA AC layers. Thus, a maximum allowable ratio between the maximum shear strain in a HP AC layer and the maximum shear in a PMA AC layer was developed. This maximum ratio between the estimated pavement responses was implemented to verify that an acceptable resistance to shoving is achieved in the HP AC mixes relative to their respective PMA AC mixes while giving due consideration to the various mixtures' properties. In this analysis, it was assumed that the resistance of the AC mix to shoving is proportional to its resistance to rutting. Accordingly, the HP and PMA mix specifics rutting relationships developed in the laboratory and provided in Table 4-8 were used to develop the maximum allowable ratio as a function of permanent axial strains. The ratio between the maximum resilient axial strains of a HP and its respective PMA AC mix, $R_{per}$ (Equation 6-27), was related to an allowable ratio between their corresponding shear strains using Hooke's law for resilient responses. The established shoving criterion for resilient shear strains ratio is shown in Equation 6-28.

$$R_{per} = \frac{\varepsilon_{r-HP}}{\varepsilon_{r-PMA}} \leq \frac{\varepsilon_{p-HP}}{\varepsilon_{p-PMA}} * \frac{a_{HP}}{a_{PMA}} * N^{(\beta_{PMA} * b_{PMA} - \beta_{HP} * b_{HP})} \qquad \textbf{Equation 6-27}$$

$$\frac{\gamma_{xz-HP}}{\gamma_{xz-PMA}} \leq \ Shoving\ Criterion = R_{per} * \frac{\tau_{xz-HP}}{\tau_{xz-PMA}} * \frac{[\sigma_{z-PMA} - \upsilon * (\sigma_{x-PMA} + \sigma_{y-PMA})]}{[\sigma_{z-HP} - \upsilon * (\sigma_{x-HP} + \sigma_{y-HP})]} \qquad \textbf{Equation 6-28}$$

Where;
$\varepsilon_p$: permanent axial strain, inch/inch (mm/mm);
$\varepsilon_r$: resilient axial strain in the top 0.50 inch (12.5 mm) of AC layer, inch/inch (mm/mm);
$\gamma_{xz}$: maximum resilient shear strain in the top 0.50 inch (12.5 mm) of AC layer, inch/inch (mm/mm);
*N*: number of loading cycles;
*a*, *and b*: experimentally determined coefficients;
$\beta_{r3}$: traffic loading calibration factors;
$\sigma_x$, $\sigma_y$, and $\sigma_z$: normal stresses in the top 0.50 inch (12.5 mm) of AC layer determined using 3D-Move, psi (Pa);
$\tau_{xz}$: maximum shear stress in the top 0.50 inch (12.5 mm) of AC layer determined using 3D-Move, psi (Pa); and $\upsilon$: Poisson's ratio.

Table 6-17 to Table 6-22 summarize the input stresses and strains used for the shoving verification. The shoving resistance analysis leads to the following observations:

- No issues regarding the shoving distress (Equation 6-28 verified) are expected in the HP AC layer in pavement sections C1, C2, and C3 (i.e., traffic level C).
- For traffic level D, the shoving criterion was met for all cases except for mix GA125_HP(A) in pavement sections C2 and C3. It should me mentioned that the corresponding control mix GA125_PMA(A) contains 20% of stiff RAP material which may jeopardize the relative comparison between a HP AC mix where no RAP material is allowed (as per FDOT specifications 2018 *(23)*) and its respective PMA AC mix. In addition, the degree of violations of the shoving criterion is insignificant in both cases, therefore, a revision of the structural coefficient is not warranted.

**Table 6-17. Shoving Data for Pavement Section C1 under a Loading Speed of 15 mph.**

| Mix ID | $\varepsilon_p$ (ms) | $\tau_{xz}$ (psi) | $\sigma_z$ (psi) | $\sigma_x$ (psi) | $\sigma_y$ (psi) | $\gamma_{xz}$ (ms) | Ratio | Shoving Criterion | Pass/ Fail |
|---|---|---|---|---|---|---|---|---|---|
| FL95_PMA (A) | 5.70E+03 | 26.2 | 25.0 | 95.0 | 43.1 | 974.6 | 0.9 | 2.5 | Pass |
| FL95_HP(A) | 3.75E+03 | 29.3 | 35.7 | 105.1 | 49.3 | 925.6 | | | |
| FL95_PMA(B) | 5.31E+03 | 26.3 | 25.0 | 101.6 | 46.4 | 812.4 | 1.7 | 28.4 | Pass |
| FL95_HP(B) | 4.44E+03 | 28.7 | 35.7 | 90.4 | 42.9 | 1424.7 | | | |
| GA95_PMA(A) | 4.16E+03 | 27.4 | 24.9 | 127.3 | 58.9 | 413.0 | 3.4 | 8.6 | Pass |
| GA95_HP(A) | 3.11E+03 | 28.7 | 35.7 | 90.9 | 42.8 | 1391.7 | | | |
| GA95_PMA(B) | 3.82E+03 | 27.5 | 24.9 | 141.5 | 67.0 | 324.4 | 4.0 | 636.8 | Pass |
| GA95_HP(B) | 3.64E+03 | 29.1 | 35.7 | 92.2 | 42.9 | 1306.8 | | | |

**Table 6-18. Shoving Data for Pavement Section C2 under a Loading Speed of 15 mph.**

| Mix ID | $\varepsilon_p$ (ms) | $\tau_{xz}$ (psi) | $\sigma_z$ (psi) | $\sigma_x$ (psi) | $\sigma_y$ (psi) | $\gamma_{xz}$ (ms) | Ratio | Shoving Criterion | Pass/ Fail |
|---|---|---|---|---|---|---|---|---|---|
| FL95_PMA (A) | 6.10E+03 | 24.6 | 25.1 | 87.4 | 42.5 | 965.5 | 0.9 | 2.4 | Pass |
| FL95_HP(A) | 3.75E+03 | 28.0 | 35.7 | 97.0 | 49.5 | 918.8 | | | |
| FL95_PMA(B) | 6.24E+03 | 24.7 | 25.1 | 92.4 | 45.4 | 805.3 | 1.7 | 22.5 | Pass |
| FL95_HP(B) | 4.48E+03 | 23.5 | 35.8 | 85.0 | 42.7 | 1414.7 | | | |
| GA95_PMA(A) | 4.38E+03 | 25.0 | 25.0 | 110.4 | 55.6 | 412.2 | 3.4 | 9.1 | Pass |
| GA95_HP(A) | 3.12E+03 | 27.8 | 35.8 | 84.8 | 42.2 | 1382.5 | | | |
| GA95_PMA(B) | 4.27E+03 | 28.1 | 35.7 | 121.9 | 64.1 | 327.1 | 4.0 | 429.9 | Pass |
| GA95_HP(B) | 3.66E+03 | 28.0 | 35.7 | 85.4 | 42.1 | 1298.7 | | | |

**Table 6-19. Shoving Data for Pavement Section C3 under a Loading Speed of 15 mph.**

| Mix ID | $\varepsilon_p$ (ms) | $\tau_{xz}$ (psi) | $\sigma_z$ (psi) | $\sigma_x$ (psi) | $\sigma_y$ (psi) | $\gamma_{xz}$ (ms) | Ratio | Shoving Criterion | Pass/ Fail |
|---|---|---|---|---|---|---|---|---|---|
| FL95_PMA (A) | 5.86E+03 | 25.8 | 25.1 | 90.1 | 41.3 | 978.9 | 0.9 | 2.6 | Pass |
| FL95_HP(A) | 3.80E+03 | 28.9 | 35.7 | 99.6 | 47.6 | 928.3 | | | |
| FL95_PMA(B) | 5.47E+03 | 25.9 | 25.0 | 96.2 | 44.3 | 816.4 | 1.7 | 30.8 | Pass |
| FL95_HP(B) | 4.51E+03 | 28.3 | 35.7 | 86.1 | 41.7 | 1427.6 | | | |
| GA95_PMA(A) | 5.52E+03 | 27.0 | 25.0 | 119.9 | 55.4 | 417.1 | 3.3 | 7.3 | Pass |
| GA95_HP(A) | 3.16E+03 | 28.4 | 35.7 | 86.5 | 41.5 | 1394.6 | | | |
| GA95_PMA(B) | 3.91E+03 | 27.1 | 24.9 | 133.1 | 62.9 | 327.7 | 4.0 | 497.9 | Pass |
| GA95_HP(B) | 3.73E+03 | 23.7 | 34.1 | 87.6 | 41.6 | 1310.6 | | | |

**Table 6-20. Shoving Data for Pavement Section D1 under a Loading Speed of 15 mph.**

| Mix ID | $\varepsilon_p$ (ms) | $\tau_{xz}$ (psi) | $\sigma_z$ (psi) | $\sigma_x$ (psi) | $\sigma_y$ (psi) | $\gamma_{xz}$ (ms) | Ratio | Shoving Criterion | Pass/ Fail |
|---|---|---|---|---|---|---|---|---|---|
| FL95_PMA (A) | 6.02E+03 | 25.1 | 28.2 | 101.8 | 49.4 | 659.3 | 1.6 | 4.0 | Pass |
| FL95_HP(A) | 3.42E+03 | 28.2 | 35.7 | 94.6 | 46.2 | 1081.4 | | | |
| FL95_PMA(B) | 5.78E+03 | 28.3 | 35.7 | 106.7 | 53.3 | 541.0 | 2.8 | 17.4 | Pass |
| FL95_HP(B) | 7.70E+03 | 28.1 | 35.7 | 84.4 | 40.5 | 1534.3 | | | |
| GA95_PMA(A) | 6.09E+03 | 25.4 | 25.0 | 115.6 | 56.8 | 408.3 | 0.5 | 0.7 | Pass |
| GA95_HP(A) | 2.42E+03 | 7.6 | 2.1 | 26.6 | 21.2 | 204.9 | | | |
| GA95_PMA(B) | 4.55E+03 | 28.4 | 35.6 | 132.3 | 68.2 | 295.8 | 3.7 | 10.0 | Pass |
| GA95_HP(B) | 4.42E+03 | 25.4 | 25.1 | 88.4 | 40.5 | 1101.2 | | | |

**Table 6-21. Shoving Data for Pavement Section D2 under a Loading Speed of 15 mph.**

| Mix ID | $\varepsilon_p$ (ms) | $\tau_{xz}$ (psi) | $\sigma_z$ (psi) | $\sigma_x$ (psi) | $\sigma_y$ (psi) | $\gamma_{xz}$ (ms) | Ratio | Shoving Criterion | Pass/ Fail |
|---|---|---|---|---|---|---|---|---|---|
| **FL95_PMA (A)** | 6.19E+03 | 27.6 | 35.7 | 95.6 | 49.2 | 664.0 | 1.6 | 2.7 | Pass |
| **FL95_HP(A)** | 3.44E+03 | 27.6 | 35.7 | 88.0 | 44.6 | 1082.0 | | | |
| **FL95_PMA(B)** | 5870 | 27.6 | 35.7 | 97.1 | 49.9 | 614.0 | 2.5 | 18.9 | Pass |
| **FL95_HP(B)** | 7880 | 27.6 | 35.8 | 79.4 | 39.2 | 1532.5 | | | |
| **GA95_PMA(A)** | 4860 | 27.7 | 35.7 | 113.1 | 59.5 | 332.3 | 2.8 | 2.0 | ***Fail*** |
| **GA95_HP(A)** | 2420 | 27.7 | 35.7 | 91.2 | 53.8 | 949.0 | | | |
| **GA95_PMA(B)** | 5320 | 27.7 | 35.7 | 113.0 | 59.3 | 330.5 | 3.3 | 7.5 | Pass |
| **GA95_HP(B)** | 4790 | 24.6 | 25.1 | 82.5 | 39.2 | 1099.9 | | | |

**Table 6-22. Shoving Data for Pavement Section D3 under a Loading Speed of 15 mph.**

| Mix ID | $\varepsilon_p$ (ms) | $\tau_{xz}$ (psi) | $\sigma_z$ (psi) | $\sigma_x$ (psi) | $\sigma_y$ (psi) | $\gamma_{xz}$ (ms) | Ratio | Shoving Criterion | Pass/ Fail |
|---|---|---|---|---|---|---|---|---|---|
| **FL95_PMA (A)** | 6.15E+03 | 28.2 | 35.7 | 99.7 | 49.8 | 663.8 | 1.6 | 2.9 | Pass |
| **FL95_HP(A)** | 3.50E+03 | 28.1 | 35.7 | 90.1 | 44.2 | 1086.1 | | | |
| **FL95_PMA(B)** | 5.91E+03 | 28.2 | 35.7 | 101.8 | 50.8 | 613.5 | 2.5 | 19.9 | Pass |
| **FL95_HP(B)** | 7.93E+03 | 27.9 | 35.8 | 80.7 | 38.9 | 1539.5 | | | |
| **GA95_PMA(A)** | 4.69E+03 | 28.4 | 35.7 | 122.1 | 62.5 | 329.6 | 2.9 | 2.7 | ***Fail*** |
| **GA95_HP(A)** | 2.45E+03 | 28.1 | 35.7 | 93.8 | 46.1 | 952.1 | | | |
| **GA95_PMA(B)** | 4.71E+03 | 28.3 | 35.6 | 126.4 | 65.1 | 298.8 | 3.7 | 10.3 | Pass |
| **GA95_HP(B)** | 4.67E+03 | 25.1 | 25.1 | 84.3 | 38.7 | 1106.3 | | | |

## 6.5. VERIFICATION OF TOP-DOWN CRACKING PERFORMANCE

Top-down cracking can be a critical mode of distress for asphalt pavements in Florida. Therefore, it is important to evaluate any designed asphalt mixture and/or pavement structure for its resistance to top-down cracking. The resistance to top-down cracking of all 16 AC mixes were evaluated using the IDT test in accordance with AASHTO T322 *(28)* and Appendix G of the NCHRP 9-57 study *(76)* at 50°F (10°C). Using the measured creep compliance and tensile strength, the threshold dissipated creep strain energy *($DSCE_{min}$)* and energy ratio (ER) were calculated using Equation 3-21. The ER compares the failure DSCE *($DSCE_f$)* to *$DSCE_{min}$*. It should be mentioned that *$DSCE_{min}$* takes into consideration the critical maximum tensile stress developed in the AC layer of a designed pavement structure under traffic loading. Table 6-23 and

Table 6-24 summarize the critical tensile stresses developed at the bottom of the PMA and HP AC layers of all designed pavement structures under the evaluated traffic speeds (i.e., 0, 8, and 45 mph), respectively.

**Table 6-23. Critical Tensile Stress at the Bottom of PMA AC Layer for all Pavement Sections under Different Loading Speeds.**

| PMA AC Mixes | | | | | |
|---|---|---|---|---|---|
| Pavement Section ID | Speed (mph) | Tensile Stress (psi) | | | |
| | | FL_PMA(A) | FL_PMA(B) | GA_PMA(A) | GA_PMA(B) |
| C-1 | 0 | 155 | 165 | 256 | 285 |
| | 8 | 238 | 244 | 336 | 360 |
| | 45 | 307 | 336 | 402 | 423 |
| C-2 | 0 | 91 | 97 | 149 | 166 |
| | 8 | 130 | 134 | 187 | 202 |
| | 45 | 171 | 175 | 227 | 242 |
| C-3 | 0 | 123 | 133 | 221 | 250 |
| | 8 | 205 | 211 | 300 | 325 |
| | 45 | 273 | 279 | 369 | 389 |
| D-1 | 0 | 135 | 142 | 200 | 207 |
| | 8 | 177 | 184 | 238 | 279 |
| | 45 | 217 | 224 | 273 | 244 |
| D-2 | 0 | 87 | 51 | 133 | 138 |
| | 8 | 114 | 120 | 160 | 165 |
| | 45 | 146 | 148 | 191 | 194 |
| D-3 | 0 | 116 | 123 | 182 | 189 |
| | 8 | 159 | 167 | 222 | 227 |
| | 45 | 200 | 209 | 258 | 264 |

**Table 6-24. Critical Tensile Stress at the Bottom of HP AC Layer for all Pavement Sections under Different Loading Speeds.**

| HP AC Mixes | | | | | |
|---|---|---|---|---|---|
| Pavement Section ID | Speed (mph) | Tensile Stress (psi) | | | |
| | | FL_HP(A) | FL_HP(B) | GA_HP(A) | GA_HP(B) |
| C-1 | 0 | 105 | 81 | 105 | 115 |
| | 8 | 214 | 184 | 213 | 227 |
| | 45 | 293 | 273 | 298 | 316 |
| C-2 | 0 | 77 | 53 | 69 | 75 |
| | 8 | 128 | 109 | 126 | 134 |
| | 45 | 176 | 161 | 178 | 188 |
| C-3 | 0 | 83 | 51 | 72 | 80 |
| | 8 | 173 | 146 | 173 | 187 |
| | 45 | 247 | 230 | 256 | 273 |
| D-1 | 0 | 104 | 90 | 132 | 111 |
| | 8 | 159 | 161 | 184 | 177 |
| | 45 | 206 | 224 | 233 | 234 |
| D-2 | 0 | 65 | 55 | 85 | 70 |
| | 8 | 99 | 101 | 119 | 112 |
| | 45 | 134 | 144 | 153 | 155 |
| D-3 | 0 | 80 | 67 | 108 | 87 |
| | 8 | 134 | 138 | 161 | 153 |
| | 45 | 181 | 197 | 207 | 211 |

The maximum tensile stress at the bottom of PMA AC layer ranged between 91.3 and 422.6 psi (0.63 and 2.91 MPa) for traffic level C, and between 51.1 and 278.8 psi (0.35 and 1.92 MPa) for traffic level D. The maximum tensile stress at the bottom of the HP AC layer ranged between 50.6 and 315.7 psi (0.35 and 2.17 MPa) for traffic level C, and between 55.4 and 234.4 psi (0.38 and 1.62 MPa) for traffic level D. Therefore, it can be observed that the maximum tensile stress at the bottom of the HP AC layer was on average 20% lower than the stress determined at the bottom of the PMA AC layer as illustrated in Figure 6-18. This indicates that the HP AC mixes have the potential to reduce top-down cracking when compared with the PMA AC mixes evaluated in this research.

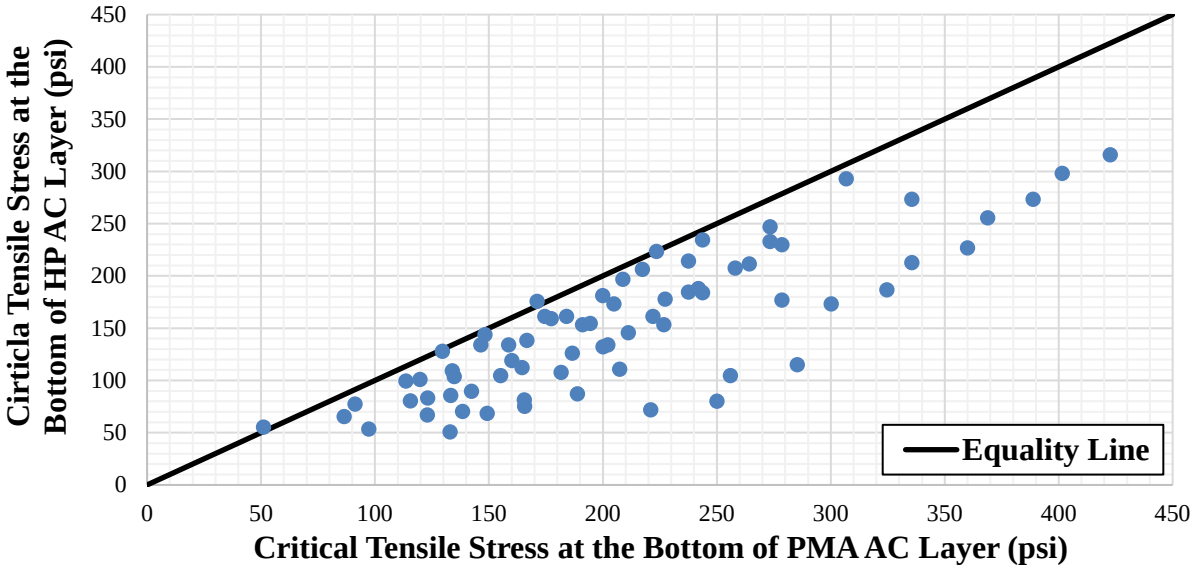


**Figure 6-18. Comparison of critical tensile stress at the bottom of PMA and HP AC layer for the same designed pavement structure and under the same loading speed.**

While no threshold limits have been set to assess the resistance to top-down cracking of PMA and HP AC mixes in Florida, the criteria recommended in earlier FDOT research at the University of Florida *(86)* were used for comparison purposes. It should be mentioned that for the purpose of this study, the resistance to top-down cracking of HP AC mixes were assessed relative to their respective PMA AC mixes in order to verify the recommended SC for HP AC mixes. The optimum ER *($ER_{opt}$)* for each traffic level was determined using $ESAL_D$ and design reliability level as summarized in Table 6-25. The FDOT criteria for top-down cracking for the PMA and HP pavement structures at traffic levels C and D are summarized in Table 6-26.

**Table 6-25. Energy Ratios Linear Regression Models Function of Design Number of ESALs for Different Reliability Levels.**

| Reliability (%) | ER = f($ESAL_D$ in 10 millions) |
|---|---|
| 99 | $ER = 0.4224*ESAL_D+0.9105$ |
| 95 | $ER = 0.2957*ESAL_D+0.8496$ |
| 90 | $ER = 0.2461*ESAL_D+0.8161$ |
| 85 | $ER = 0.2191*ESAL_D+0.8017$ |
| 80 | $ER = 0.1995*ESAL_D+0.7928$ |
| 75 | $ER = 0.1832*ESAL_D+0.7809$ |
| 70 | $ER = 0.1716*ESAL_D+0.7710$ |
| 50 | $ER = 0.1331*ESAL_D+0.7470$ |

**Table 6-26. FDOT Preliminary Criteria for Top-Down Cracking.**

| Type of Design | Reliability | Traffic Level | $ER_{opt}$ |
|---|---|---|---|
| New Construction | 85% | C: 7 MESALs[1] | 0.96 |
| | | D: 20 MESALs | 1.24 |

[1]M stands for million.

Table 6-27 and Table 6-28 summarizes the calculated energy ratio *(ER)* for all evaluated PMA and HP AC mixes using the IDT test results along with the maximum tensile stress ($\sigma_{max}$) at the bottom of the AC layer determined from the mechanistic analysis of the various pavement structures designed for traffic level C and level D, respectively. In general, all calculated energy ratios were found within the range of the determined $ER_{opt}$. However, it should be mentioned that the $ER_{opt}$ values may not be applicable for top-down cracking of lab produced PMA and HP AC mixes since they were developed based on aged and damaged core samples collected approximately 12 years after construction.

The next step of the analysis was to apply the limitations specified in the Roque et al. (2004) study *(87)* as stated below:

- *Limitation 1: ER values for AC mixes with excessively low compliance rate (m-values) are not considered reliable (relative to the change used in the calculation: 0.23 to 6.16E-03).*
- *Limitation 2: The ER concept should not be used to evaluate AC mixes characterized by a $DSCE_f$ lower than 0.1053 lbf-in./in.$^3$ (0.75 kJ/m$^3$).*

**Table 6-27. *ER* Values of Top-Down Cracking in PMA Pavement Sections under Different Loading Speeds.**

| Pavement Section ID | Speed (mph) | Energy Ratio *(ER)* | | | |
|---|---|---|---|---|---|
| | | FL_PMA(A) | FL_PMA(B) | GA_PMA(A) | GA_PMA(B) |
| C-1 | 0 | 0.7710 | 0.8015 | 1.1975 | 1.9779 |
| | 8 | 0.5010 | 0.5591 | 1.0904 | 1.8586 |
| | 45 | 0.4471 | 0.4933 | 1.0558 | 1.8145 |
| C-2 | 0 | 2.3123 | 2.2575 | 2.0116 | 2.9949 |
| | 8 | 1.0468 | 1.1222 | 1.5103 | 2.4208 |
| | 45 | 0.6748 | 0.7490 | 1.2810 | 2.1325 |
| C-3 | 0 | 1.1582 | 1.1395 | 1.3058 | 2.0945 |
| | 8 | 0.5582 | 0.6177 | 1.1240 | 1.9013 |
| | 45 | 0.4665 | 0.5236 | 1.0698 | 1.8347 |
| D-1 | 0 | 3.3766 | 0.5788 | 0.6379 | 3.1032 |
| | 8 | 4.4281 | 0.4010 | 0.5520 | 2.5977 |
| | 45 | 1.8694 | 0.3346 | 0.5137 | 2.7709 |
| D-2 | 0 | 9.1449 | 8.0309 | 1.1437 | 5.2084 |
| | 8 | 4.7418 | 0.8087 | 0.8369 | 3.9861 |
| | 45 | 2.9360 | 0.5410 | 0.6683 | 2.6579 |
| D-3 | 0 | 4.5756 | 0.7652 | 0.7078 | 3.3845 |
| | 8 | 2.6018 | 0.4535 | 0.5826 | 2.8991 |
| | 45 | 2.0006 | 0.3536 | 0.5286 | 2.6579 |

**Table 6-28. *ER* Values of Top-Down Cracking in HP Pavement Sections under Different Loading Speeds.**

| Pavement Section ID | Speed (mph) | Energy Ratio *(ER)* | | | |
|---|---|---|---|---|---|
| | | FL_HP(A) | FL_HP(B) | GA_HP(A) | GA_HP(B) |
| C-1 | 0 | 2.1623 | 2.7140 | 3.8135 | 0.7462 |
| | 8 | 2.0554 | 2.4172 | 3.7781 | 0.7316 |
| | 45 | 0.5486 | 0.3387 | 1.0006 | 0.2387 |
| C-2 | 0 | 4.5133 | 8.0612 | 11.5747 | 2.1423 |
| | 8 | 1.3284 | 1.1449 | 2.5110 | 0.5362 |
| | 45 | 0.7993 | 0.5449 | 1.4461 | 0.3286 |
| C-3 | 0 | 3.6789 | 9.5806 | 10.2064 | 1.7874 |
| | 8 | 0.8125 | 0.6405 | 1.4923 | 0.3308 |
| | 45 | 0.5937 | 0.3742 | 1.0692 | 0.2513 |
| D-1 | 0 | 2.5892 | 0.4378 | 4.2399 | 0.8604 |
| | 8 | 1.1111 | 0.1243 | 2.5833 | 0.3768 |
| | 45 | 0.8166 | 0.0859 | 2.1108 | 0.2899 |
| D-2 | 0 | 8.9885 | 1.7174 | 11.5685 | 2.8079 |
| | 8 | 2.8717 | 0.3226 | 5.2416 | 0.8362 |
| | 45 | 0.9342 | 0.0966 | 2.3032 | 0.3133 |
| D-3 | 0 | 5.0084 | 0.9854 | 6.5249 | 1.5616 |
| | 8 | 1.4839 | 0.1608 | 3.0578 | 0.4586 |
| | 45 | 0.9342 | 0.0966 | 2.3032 | 0.3133 |

Table 4-10 shows that all the PMA and HP AC mixes satisfied limitation 1 regarding the creep compliance rate by showing m-values within the acceptable range. However, many of the AC mixes such as; FL95_HP(A), GA95_HP(B), FL125_HP(A), FL125_PMA(B), FL125_HP(B), GA125_PMA(A), GA125_PMA(B), and GA125_HP(B) failed limitation 2 with $DSCE_f$ values lower than 0.1053 lbf-in./in.$^3$ (0.75 kJ/m$^3$). Therefore, the cases involving the use of these AC mixes were excluded from the mechanistic analysis for top-down cracking.

As mentioned previously, the purpose of this analysis is to verify the recommended SC for HP AC mixes based on top-down cracking. Therefore, after removing the mixes that failed limitation 2, only FL95_HP(B) and GA95_HP(A) AC mixes can be compared to their PMA control FL95_PMA(B) and GA95_PMA(A) AC mixes. Table 6-29 shows the variation in terms of percentage of $ER_{HP\text{-}AC\ mix}$ when compared with $ER_{PMA\text{-}AC\ mix}$. A positive value denotes an increase in the *ER* value. An increase of the *ER* of the HP AC mixes when compared with their respective PMA AC mixes was observed for the majority of the cases provided in Table 6-29 indicating a better performance in terms of resistance to top-down cracking.

**Table 6-29. Variation of $ER_{HP\text{-}AC}$ mix with respect to $ER_{PMA\text{-}AC}$ mix—$\Delta ER$ (%) for mixes FL95_PMA/HP(B) and GA95_PMA/HP(A).**

| Pavement Structure | C-1 | | | C-2 | | | C-3 | | |
|---|---|---|---|---|---|---|---|---|---|
| Speed (mph) | 0 | 8 | 45 | 0 | 8 | 45 | 0 | 8 | 45 |
| FL95_HP(B) vs. FL95_PMA(B) | 70.5% | 76.9% | -45.6% | 72.0% | 2.0% | -37.5% | 88.1% | 3.6% | -39.9% |
| GA95_HP(A) vs. GA95_PMA(A) | 68.6% | 71.1% | -5.5% | 82.6% | 39.9% | 11.4% | 87.2% | 24.7% | -0.1% |

## 6.6. VERIFICATION OF REFLECTIVE CRACKING PERFORMANCE LIFE

Over the last 35 years, state highway agencies (SHAs) shifted their emphasis from the construction of new roads to the maintenance and rehabilitation of existing infrastructure. Florida DOT uses various maintenance and rehabilitation repair strategies to improve the overall condition of the state's road network. AC overlays have been one of the most commonly used methods for rehabilitating aged and deteriorated asphalt pavements caused by the combined effect of traffic loading and climate. Consequently, reflection of cracks from existing pavements becomes a major type of distress influencing the life of an AC overlay and controlling its long-term performance. Once the AC overlay is cracked, it allows moisture to penetrate into the mix and to the supporting layers promoting the stripping of the asphalt binder from aggregates. It can also reduce the strength of the base and subgrade materials, which would lead to the total failure of the flexible pavement structure. Multiple factors can significantly influence the long-term performance of these techniques including the specific conditions of the existing pavement and the combination of materials, traffic, and environmental conditions under which the overlay has been applied *(88)*.

### 6.6.1. Reflective Cracking Model

The basic mechanism for reflective cracking is strain concentration in the AC overlay due to the movement in the existing pavement at the vicinity of joints and/or cracks. In fact, the majority of

reflective cracking is caused by the combination of bending, shearing, and thermal mechanisms resulting from traffic loads or daily and seasonal temperature changes. The comprehensive ME asphalt overlay system developed by Texas Transportation Institute (TTI) was used to evaluate the resistance to reflective cracking of PMA and HP AC mixes when used in AC overlay rehabilitation projects *(78)*.

Various models have been developed to analyze and/or predict reflective cracking. The TTI system consider the Paris' law-based fracture mechanics model expressed in Equation 6-29 for the evaluation of reflective cracking propagation *(78)*. The use of Paris' law for assessing the crack growth process in viscoelastic materials such as AC mixtures, has been theoretically justified in multiple studies *(78)*. This model requires the calculation of stress intensity factor (SIF) and the determination of AC mixes fracture properties (i.e., *A* and *n*). These calculations have been recently accomplished through the development of the *SA-CrackPro* program specifically tailored for pavement SIF analysis and the Texas overlay test for the asphalt mixes fracture properties *(78)*.

$$\frac{dc}{dN} = A * (SIF)^n \qquad \textbf{Equation 6-29}$$

Where;
$c$: crack length, inch (mm).
$N$: number of loading cycles.
$SIF$: stress intensity factor amplitude.

The recommended reflective cracking model includes three main components: reflective crack propagation model expressed in Equation 6-30 based on Paris' law with the combination of bending, shearing, and thermal loading; reflective cracking damage model expressed in Equation 6-31; and reflective cracking amount model expressed in Equation 6-32 to describe the development of the reflective cracking amount using a sigmoidal function *(78)*.

$$\Delta C = k_1 * A * (K_{bendig})^n * \Delta N_i + k_2 * A * (K_{shearing})^n * \Delta N_i + k_3 * A * (K_{thermal})^n * \Delta N_i \qquad \textbf{Equation 6-30}$$

$$D = \sum \Delta C / h \qquad \textbf{Equation 6-31}$$

$$RCR = \frac{100}{1+e^{C_1 * logD}} \qquad \textbf{Equation 6-32}$$

Where;
$\Delta C$: daily crack length increment, inch (mm);
$\Delta N$: daily load repetitions;
$A$ & $n$: asphalt mix fracture properties;
$K_{bending}, K_{shearing}, and\ K_{thermal}$: SIF caused by bending, shearing, and thermal loading;
$k_1, k_2, and\ k_3$: calibration factors;
$D$: damage ratio;
$h$: overlay thickness, inch (mm);
$\sum \Delta C$: total crack length;
$RCR$: reflective cracking rate, %; and
$C_1$: model constant equal to -7.0.

### 6.6.2. Determination of Fracture Parameters A and n

The determination of fracture parameters (i.e., *A* & *n*) for the PMA and HP AC mixes requires the accomplishment of the following five steps.

***Step 1: Determination of SIF as a Function of Crack Length, c:*** Zhou et al. *(78)* analyzed *SIF* values with the OT testing using a two-dimensional (2D) finite element (FE) program named *2D-CrackPro*. The *SIF* was found to be proportional to the dynamic modulus (*E*) of the evaluated AC mix and the maximum opening displacement (*MOD*) as expressed in Equation 6-33.

$$SIF = 0.2911 * E * MOD * c^{-0.4590} \qquad \textbf{Equation 6-33}$$

Where;
$SIF$: Stress Intensity Factor, MPa*mm$^{0.5}$;
$E$: dynamic modulus of evaluated AC mix at testing temperature and loading frequency (i.e., in this case T=77°F (25°C) and f = 0.1 Hz), MPa;
$MOD$: maximum opening displacement, mm; and
$c$: crack length, mm.

In this study, Equation 6-33 was implemented to determine the relationship between SIF and *c* for all evaluated AC mixes. The dynamic modulus was determined for each respective mix from the laboratory measured data at 77°F (25°C) and loading frequency of 0.1 Hz (refer to section 4.2.1 and Appendix C.1). Figure 6-19 illustrates, as an example, the calculated *SIF* versus *c* for FL95_PMA(A) mix. A modulus, *E*, of 142,686 psi (984 MPa) and a *MOD* of 0.025 inch (0.6350 mm) were used. The data in Figure 6-19 show a rapid decrease in *SIF* at low crack lengths indicating the importance of the initial crack propagation stage to determine reasonable fracture parameters (i.e., *A* & *n*).

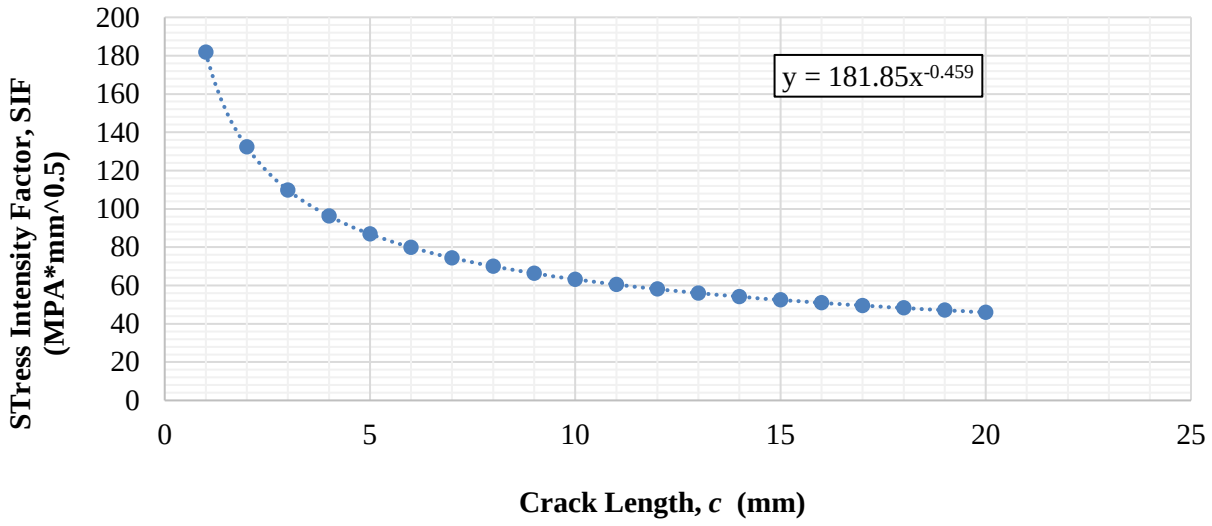


**Figure 6-19. Calculated SIF vs. Crack Length c for FL95_PMA(A) AC mix.**

***Step 2: Determination of normalized maximum load (NM) using OT test function of c***: In previous studies *(89)(90)*, different techniques (e.g., Digital Image Correlation (DIC)) have been used to monitor the crack length growth. However, such techniques can be difficult and costly to run and analyze. Accordingly, a backcalculation approach has been successfully used to backcalculate crack length from recorded load or displacements in an OT test *(89)(91)*. Equation 6-34 expresses the relationship between *NM* and *c* (refer to Figure 6-20).

$$NM = 3.10^{-5} * c^4 - 0.0012 * c^3 + 0.0189 * c^2 - 0.155 * c^1 + 1.0043 \qquad \textbf{Equation 6-34}$$

Where;
$NM$: normalized maximum load; and
$c$: crack length, mm.

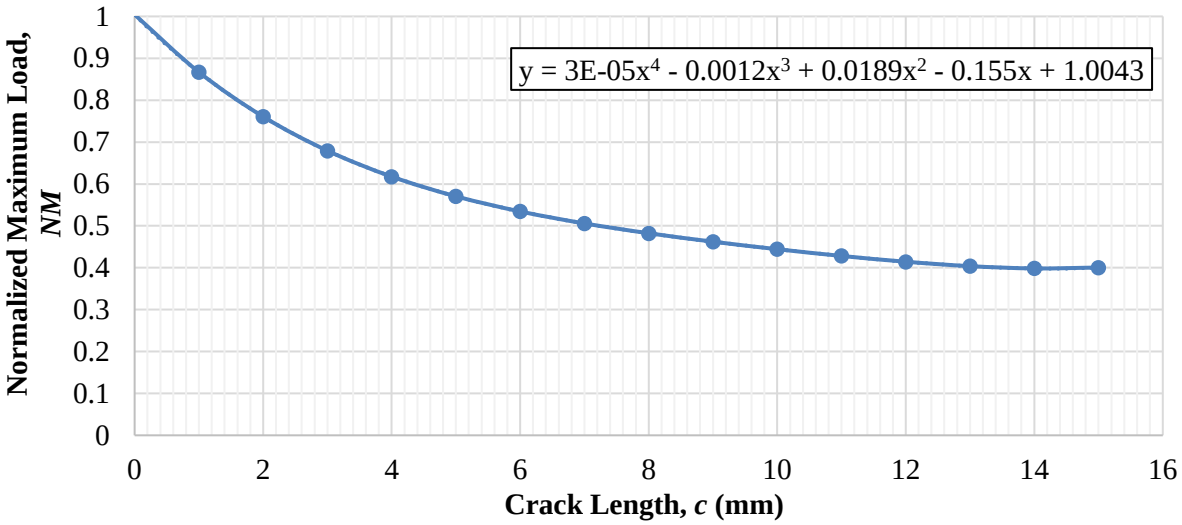


**Figure 6-20. NM vs. c characteristic plot.**

***Step 3: Determination of NM as a function of number of cycles (N) using the OT test:*** The *NM* is determined using the output of the OT test by normalizing the recorded applied load at each loading cycle to the maximum load applied at first cycle. As an example, Figure 6-21 illustrates the *NM* function of the first 100 loading cycles for FL95_PMA(A) mix.

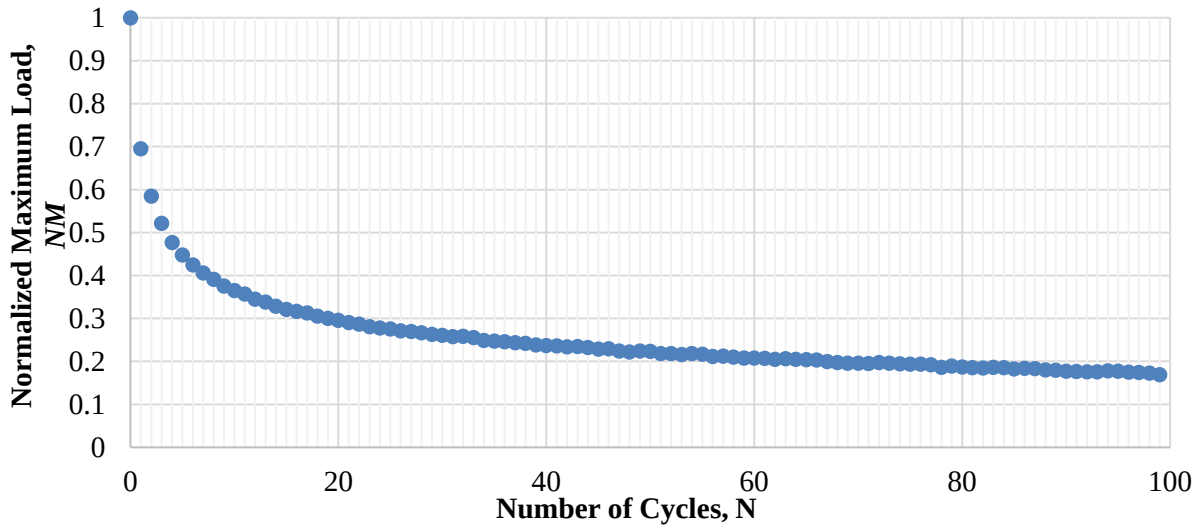


**Figure 6-21. NM vs. N plot for FL95_PMA(A) AC mix.**

***Step 4: Determination of c as a function of N:*** Using the outcomes of step 2 and step 3, the plot of *c* as a function of *N* is developed. Figure 6-22 illustrates a *c* versus *N* sample plot for FL95-PMA(A) mix for the first few cycles.

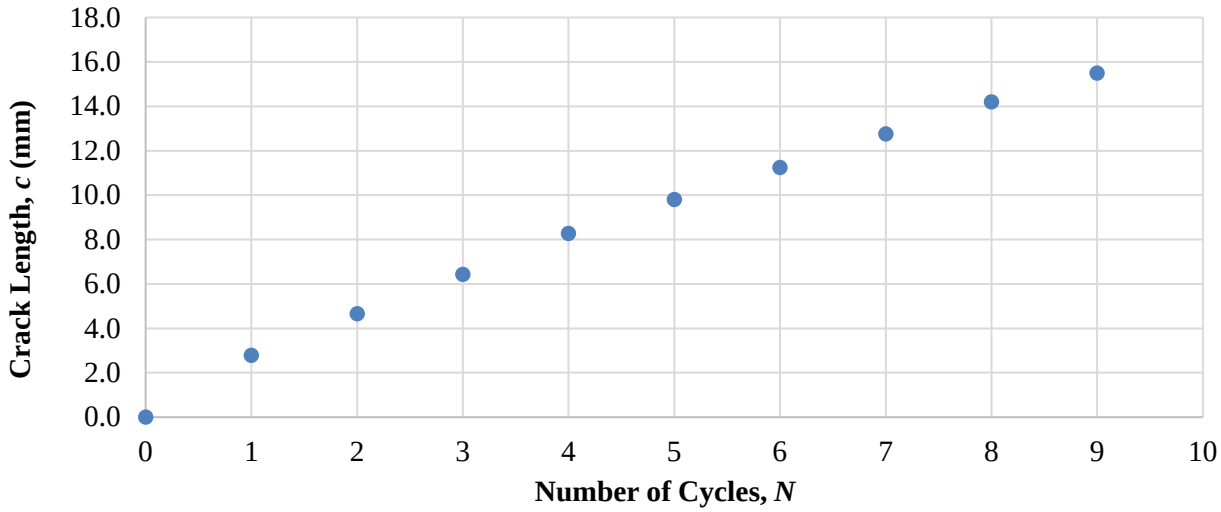


**Figure 6-22. c vs. N plot for FL95_PMA(A) AC mix.**

***Step 5: Determination of SIF function of N:*** Once *c* versus *N* is determined, *SIF* is computed at each loading cycle as a function of *c* using Equation 6-33. The crack length variation rate (d*c*/d*N*) is then determined function of *SIF*. The fracture parameters *A* and *n* are then determined as the corresponding intercept and slope of d*c*/d*N* vs. *N*, respectively (Refer to Figure 6-23 for an example; *A* = 8.40E-02, and *n* = 6.77E-01).

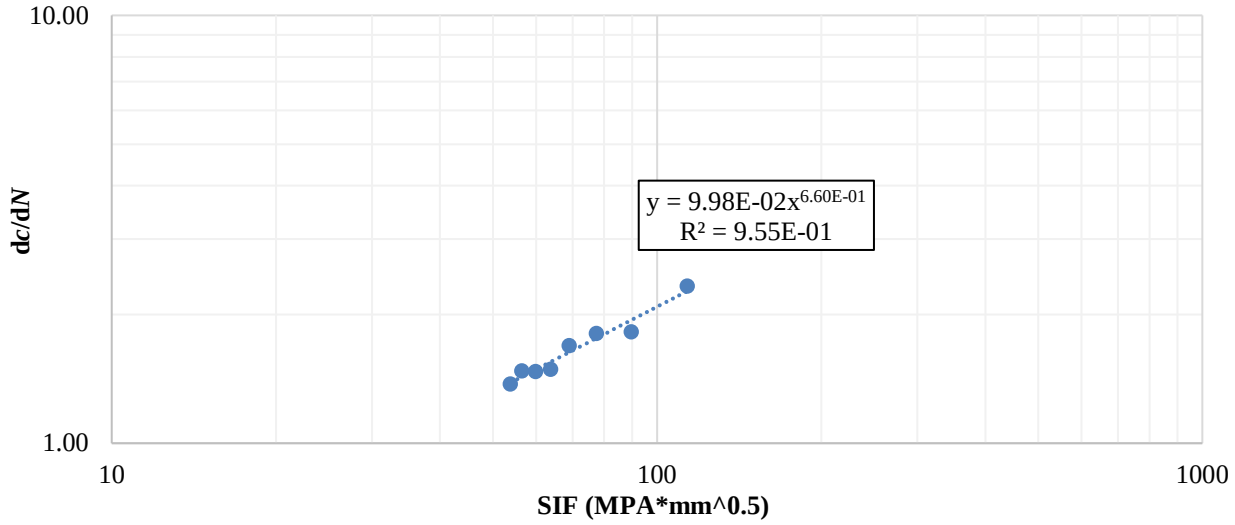


**Figure 6-23. Determination of A and n from crack length rate vs. N plot for FL95_PMA(A) AC mix.**

Table 6-30 summarizes the fracture parameters *A* and *n* values for the 16 evaluated AC mixes at a temperature of 77°F (25°C). In general, the *n* value is characteristic of the asphalt binder, meanwhile the *A* value is characteristic of the AC mixture (i.e., aggregate gradation and asphalt binder). Lower *A* values were observed for the PMA AC mixes when compared to their corresponding HP AC mixes. Meanwhile, higher *n* values were observed for the HP AC mixes when compared with their corresponding PMA AC mixes. It should be mentioned that *A* and *n* values could not be calculated for GA125_PMA(B) mix due to the low number of loading cycles to failure (i.e., $N = 4$ cycles). It should be reminded that this mix is the stiffest among all evaluated AC mixes since it contains 20% of RAP material. Accordingly, a mechanistic analysis for this mix could not be conducted.

**Table 6-30. Fracture Parameters A and n for 16 AC Mixes at 77°F (25°C).**

| Mix ID | E at 77°F (25°C) and 0.1 Hz (psi, MPa) | *A* | *n* |
|---|---|---|---|
| FL95_PMA(A) | 142,686 (984) | 9.98E-02 | 6.60E-01 |
| FL95_PMA(B) | 157,959 (1,089) | 7.15E-02 | 6.62E-01 |
| FL95_HP(A) | 110,974 (765) | 3.81E-03 | 1.36E+00 |
| FL95_HP(B) | 78,819 (543) | 1.71E-02 | 1.16E+00 |
| FL125_PMA(A) | 182,650 (1,259) | 2.90E-02 | 1.02E+00 |
| FL125_PMA(B) | 197,354 (1,361) | 5.58E-04 | 1.46E+00 |
| FL125_HP(A) | 110,467 (762) | 2.30E-03 | 1.49E+00 |
| FL125_HP(B) | 80,898 (558) | 6.17E-04 | 1.93E+00 |
| GA95_PMA(A) | 307,493 (2,120) | 6.14E-01 | 2.02E-01 |
| GA95_PMA(B) | 380,369 (2,623) | 2.70E-01 | 5.56E-01 |
| GA95_HP(A) | 91,930 (634) | 4.92E-02 | 8.79E-01 |
| GA95_HP(B) | 100,010 (690) | 7.94E-02 | 7.62E-01 |
| GA125_PMA(A) | 388,389 (2,677.8) | 6.30E-01 | 1.11E-01 |
| GA125_PMA(B) | 418,945 (2,888.5) | – | – |
| GA125_HP(A) | 151,620 (1,045.4) | 2.87E-01 | 4.48E-01 |
| GA125_HP(B) | 108,756 (749.8) | 2.47E-01 | 5.44E-01 |

–No data because of instantaneous failure.

### 6.6.3. Reflective Cracking Mechanistic Analysis

This section provides a detailed mechanistic analysis for reflective cracking to verify the adequacy of the developed initial structural coefficient of 0.54 for HP AC mixes when used in a rehabilitation design. The AC overlay designs were determined considering a 2.5 inch (63.5 mm) milling for all existing pavement structures. The thickness of the AC overlays for PMA pavements were designed following the FDOT Flexible Pavement Design Manual *(4)*.The calculation details can be found in Section 5.1.3. The thickness of the AC overlays for the HP pavement sections were reduced according to the initial structural coefficient determined previously (i.e., 0.54). The structural designs of all PMA and HP rehabilitated pavement sections are summarized in Table 6-31.

The Texas Asphalt Concrete Overlay Design and Analysis System (TxACOL) software developed by Zhou et al. *(78)* was used to estimate the reflective cracking rate in the PMA and HP AC overlays. Figure 6-25 summarizes the overall approach implemented in this study. The mechanistic analysis for reflective cracking considers multiple factors such as traffic loading and speed, environment, existing pavement condition, and characteristics of AC overlay material. Two traffic levels were evaluated for this study; traffic level C with 7 million ESALs for the 9.5 mm AC mixes, and traffic level D with 20 million ESALS for the 12.5 mm AC mixes. A speed of 45 mph (72 km/h), similar to the highest speed considered for the fatigue mechanistic analysis, was considered for the reflective cracking mechanistic analysis. A higher speed induces a higher loading frequency, which makes the AC layer stiffer and more susceptible to cracking. The climatic station in Gainesville was selected to simulate environmental conditions. It should be mentioned that the mechanistic analysis for reflective cracking was performed at the effective intermediate pavement temperature of 77°F (25°C).

**Table 6-31. Structural Designs for Rehabilitated Flexible Pavements.**

| FDOT $ESAL_D$ | Base Type | Subgrade Strength $M_r$ (psi) | Label | Rehabilitated Pavement with 2.5 inch milling | | | | | |
|---|---|---|---|---|---|---|---|---|---|
| | | | | PMA Section | | | HP Section | | |
| | | | | PMA AC Overlay (inch) | Existing PMA AC Layer (inch) | Base Layer (inch) | HP AC Overlay (inch) | Existing PMA AC Layer (inch) | Base Layer (inch) |
| Traffic Level C: 7 million | Graded Aggregate $a_3$ = 0.15 | 11,500 | R-C1 | 3.50 | 0.50 | 12.00 | 3.00 | 0.50 | 12.00 |
| | Limerock $a_3$ = 0.18 | 5,500 | R-C2 | 4.50 | 2.50 | 11.00 | 3.75 | 2.50 | 11.00 |
| | | 11,500 | R-C3 | 3.50 | 0.50 | 10.00 | 3.00 | 0.50 | 10.00 |
| Traffic Level D: 20 million | Graded Aggregate $a_3$ = 0.15 | 11,500 | R-D1 | 4.00 | 2.00 | 12.0 | 3.25 | 2.00 | 12.00 |
| | Limerock $a_3$ = 0.18 | 5,500 | R-D2 | 5.50 | 3.50 | 12.5 | 4.50 | 3.50 | 12.50 |
| | | 11,500 | R-D3 | 4.00 | 2.00 | 10.0 | 3.25 | 2.00 | 10.00 |

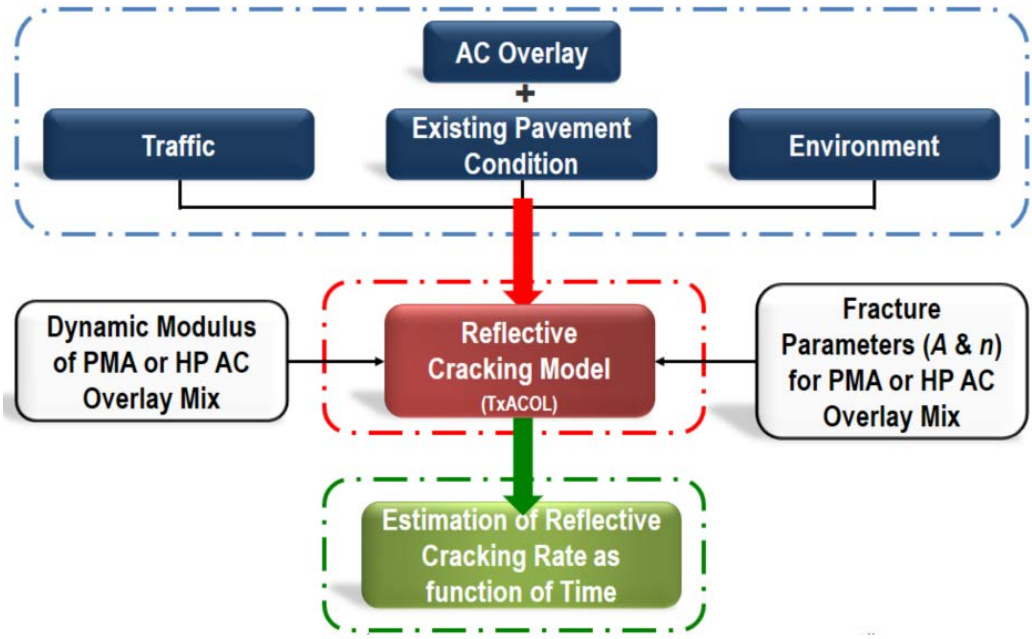


**Figure 6-24. Overall flowchart of the mechanistic analysis approach for reflective cracking.**

In order to simulate the deteriorated condition of an existing AC layer due to fatigue cracking before rehabilitation, a reduction in the stiffness of the existing PMA AC layer was applied. A damaged dynamic modulus master curve was calculated following the approach used in AASHTOWare Pavement ME *(5)*. The undamaged master curves of the evaluated PMA AC mixes, determined previously in Section 4.2.1 and Appendix D Section 1 (D.1), were used to determine the damaged master curve of the existing AC layer after milling (Equation 6-35) *(5)*. The damage accumulation in the AC layer was estimated to be 0.6 representing a fair condition of the existing AC layer over its service life *(5)*.

$$E_{AC-damaged} = 10^{\delta} + \frac{E_{AC-undamaged} - 10^{\delta}}{1+e^{-0.3+5*logd_{AC}}} \qquad \textbf{Equation 6-35}$$

$$\log(E_{AC-undamaged}) = \delta + \frac{\alpha}{1+e^{\beta+\gamma[\log(t)-c(\log(\eta)-\log(\eta_{T_r}))]}} \qquad \textbf{Equation 6-36}$$

Where;
$E_{AC-damaged}$: damaged dynamic modulus of existing AC layer, psi (MPa);
$E_{AC-undamaged}$: undamaged dynamic modulus of existing AC layer, psi (MPa);
$\delta$: undamaged dynamic modulus master curve fitting parameter (Equation 6-35);
$d_{AC}$: damage accumulation in AC from the bottom-up fatigue cracking (assumed equal to 0.6);
$t$: time of loading, sec;
$\eta$: viscosity of temperature of interest, CPoise;
$\eta_{T_r}$: viscosity at reference temperature, CPoise; and
$\alpha, \beta, \delta, \gamma, and\ c$: mix specific fitting parameters.

It should be mentioned that all existing AC layers before rehabilitation were assumed to be constructed with PMA AC mixes. Only the new AC overlay was considered as an undamaged PMA or HP AC mix. Appendix E presents in details the damaged dynamic modulus data for all evaluated PMA AC mixes. Table 6-32 summarizes the undamaged and damaged dynamic moduli determined at a temperature of 77° (25°C) and a frequency of 33.3 Hz.

**Table 6-32. Undamaged and Damaged E* of existing PMA AC Layer at 77°F (25°C) and 33.3 Hz.**

| Mix ID | Undamaged E*, psi (MPa) | Damaged E*, psi (MPa) |
|---|---|---|
| FL95_PMA(A) | 878,877 (6,060) | 706,802 (4,873) |
| FL95_PMA(B) | 906,153 (6,248) | 728,890 (5,026) |
| GA95_PMA(A) | 1,505,243 (10,378) | 1,210,944 (8,349) |
| GA95_PMA(B) | 1,656,232 (11,419) | 1,331,862 (9,183) |
| FL125_PMA(A) | 949,233 (6,545) | 763,289 (5,263) |
| FL125_PMA(B) | 1,014,891 (6,997) | 816,058 (5,627) |
| GA125_PMA(A) | 1,589,929 (10,962) | 1,278,362 (8,814) |
| GA125_PMA(B) | 1,662,822 (11,465) | 1,336,965 (9,218) |

The reflective cracking analysis criterion was selected to be 50% as recommended by Zhou et al. *(78)*. No distress survey and field performance data exist at the moment to calibrate the reflective cracking models expressed previously in Equation 6-30 and Equation 6-32. Therefore, the calibration factors ($k_1$, $k_2$, $k_3$, and $\beta$) for the PMA AC overlay mixes were selected based on the following assumptions: (1) reflective cracks in a PMA AC overlay over a PMA existing AC will start showing up at the surface approximately 3 to 5 years (36 to 60 months) after rehabilitation, and (2) PMA AC overlay does not reach the failure criterion (i.e., 50%) before approximately 8 to 10 years (96 to 120 months) after rehabilitation. The same calibration factors were used for the HP AC overlay mixes. However, mix specifics dynamic modulus and fracture parameters ($A$ and $n$) were used in the analysis to estimate the performance of the HP and PMA AC overlay mixes. These imposed assumptions are considered reasonable especially that the analysis focused at the relative comparison between HP and PMA mixes.

As an example, Figure 6-25 illustrates the reflective cracking propagation rate *(RCR)* for pavement section R-C1 for two cases: FL95_PMA(A) AC overlay (3.5 inch) on top of an existing damaged FL95_PMA(A) AC layer (0.5 inch), and FL95_HP(A) AC overlay (3.0 inch) on top of an existing damaged FL95_PMA(A) AC layer (0.5 inch). Based on the data presented in Figure 6-25 the following observations can be made:

- For the case of the PMA AC overlay, the cracks started to reflect in the overlay (i.e., *RCR* >0%) at an initial time (i.e., $t_{initial}$) of approximately 58 months (4.8 years) after construction. The *RCR* reached its failure criterion (i.e., 50%) after 96 months (8.0 years) ($t_{RCR=50\%}$) from construction. Thus it took 38 months (3.1 years) for the PMA AC overlay to reach failure after initial cracking has occurred.
- For the case of HP AC overlay, the cracks started reflecting on top of the AC overlay after 86 months (7.1 years) from construction. The *RCR* reached its failure criterion after 137 months (11.4 years). Thus, it took 51 months (4.3 years) for the HP AC overlay to reach failure after initial cracking has occurred.

- In summary, the illustrative example showed that, for the same traffic and environmental conditions, a 3.0 inch of HP AC overlay is expected to perform better than a 3.5 inch PMA AC overlay as demonstrated with the observed 41 month delay in reaching failure criterion.

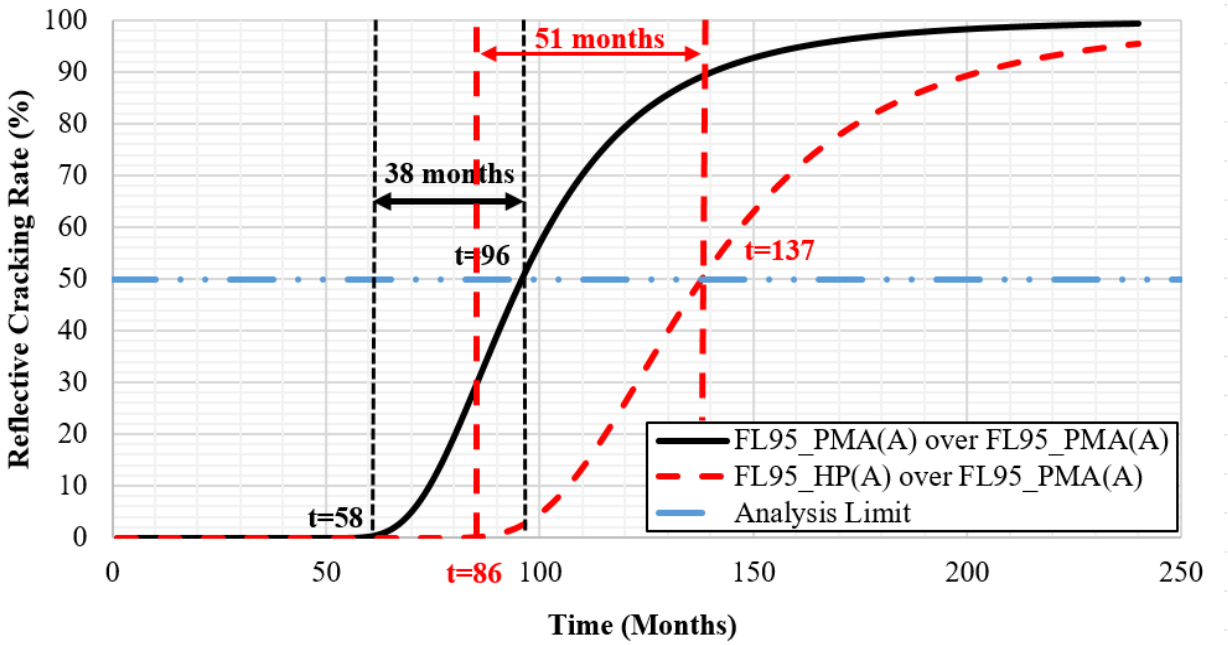


**Figure 6-25. RCR along time for pavement section R-C1: PMA/HP Ac mix on top of PMA AC layer.**

Table 6-33 and Table 6-34 summarize the results from the ME analysis of reflective cracking in terms of percent increase in time to reach initial cracking after construction, and percent of increase in performance life. The performance life is determined as the duration between the time of construction (i.e., 0 months) and the time to reach the failure criterion of 50% *RCR*. It should be noted that a ME analysis could not be conducted for the GA125_PMA(B) and GA125_HP(B) since the fracture parameters for the GA125_PMA(B) mix could not be determined because of an observed early brittle failure of the mix in the OT testing.

Based on the data presented in Table 6-33 and Table 6-34, the HP AC overlay mixes resulted in an increase in, both, time to reach initial cracking and performance life of the AC overlay. Thus, the structural coefficient of 0.54 used to design the HP AC overlay is expected to result in an acceptable or better reflective cracking performance for the HP AC overlay mix when compared to the respective PMA AC overlay mix.

**Table 6-33. Results of Reflective Cracking ME Analysis of Pavement Sections Designed for Traffic Level C (i.e., R-C1, R-C2, and R-C3).**

| Existing AC Layer | PMA AC Overlay | HP AC Overlay | % increase in time to reach initial cracking | % increase in performance life |
|---|---|---|---|---|
| ***Pavement Section R-C1*** | | | | |
| FL95_PMA(A) | FL95_PMA(A) | FL95_HP(A) | 48.3 | 42.7 |
| FL95_PMA(B) | FL95_PMA(B) | FL95_HP(B) | 31.1 | 32.7 |
| GA95_PMA(A) | GA95_PMA(A) | GA95_HP(A) | 76.3 | 59.2 |
| GA95_PMA(B) | GA95_PMA(B) | GA95_HP(B) | 375.0 | 312.9 |
| ***Pavement Section R-C2*** | | | | |
| FL95_PMA(A) | FL95_PMA(A) | FL95_HP(A) | 130.3 | 162.6 |
| FL95_PMA(B) | FL95_PMA(B) | FL95_HP(B) | 239.2 | 205.9 |
| GA95_PMA(A) | GA95_PMA(A) | GA95_HP(A) | 173.5 | 178.8 |
| GA95_PMA(B) | GA95_PMA(B) | GA95_HP(B) | 360.0 | 366.0 |
| ***Pavement Section R-C3*** | | | | |
| FL95_PMA(A) | FL95_PMA(A) | FL95_HP(A) | 57.9 | 57.1 |
| FL95_PMA(B) | FL95_PMA(B) | FL95_HP(B) | 43.9 | 39.5 |
| GA95_PMA(A) | GA95_PMA(A) | GA95_HP(A) | 37.1 | 52.6 |
| GA95_PMA(B) | GA95_PMA(B) | GA95_HP(B) | 293.3 | 296.0 |

**Table 6-34. Results of Reflective Cracking ME Analysis of Pavement Sections Designed for Traffic Level D (i.e., R-D1, R-D2, and R-D3).**

| Existing AC Layer | PMA AC Overlay | HP AC Overlay | % increase in time to reach initial cracking | % increase in performance life |
|---|---|---|---|---|
| ***Pavement Section R-D1*** | | | | |
| FL125_PMA(A) | FL125_PMA(A) | FL125_HP(A) | 195.5 | 201.2 |
| FL125_PMA(B) | FL125_PMA(B) | FL125_HP(B) | 18.6 | 14.3 |
| GA125_PMA(A) | GA125_PMA(A) | GA125_HP(A) | 58.5 | 80.3 |
| GA125_PMA(B) | GA125_PMA(B) | GA125_HP(B) | – | – |
| ***Pavement Section R-D2*** | | | | |
| FL125_PMA(A) | FL125_PMA(A) | FL125_HP(A) | 168.0 | 187.3 |
| FL125_PMA(B) | FL125_PMA(B) | FL125_HP(B) | 13.2 | 22.8 |
| GA125_PMA(A) | GA125_PMA(A) | GA125_HP(A) | 18.4 | 87.3 |
| GA125_PMA(B) | GA125_PMA(B) | GA125_HP(B) | – | – |
| ***Pavement Section R-D3*** | | | | |
| FL125_PMA(A) | FL125_PMA(A) | FL125_HP(A) | 189.8 | 201.8 |
| FL125_PMA(B) | FL125_PMA(B) | FL125_HP(B) | 25.2 | 20.7 |
| GA125_PMA(A) | GA125_PMA(A) | GA125_HP(A) | 70.8 | 92.7 |
| GA125_PMA(B) | GA125_PMA(B) | GA125_HP(B) | – | – |

–No data because of early brittle failure in OT testing.

## 6.7. SUMMARY OF MECHANISTIC ANALYSES

This chapter presented the determination of a structural coefficient for HP AC mixes that can be used in new and rehabilitated pavement projects in Florida. This was accomplished by combining laboratory measured properties for HP and PMA AC mixes with mechanistic analyses of pavement structures designed for traffic levels C and D. The structural coefficient of HP AC mixes was first estimated based on a comprehensive ME fatigue cracking analysis. The statistical

analysis of the data led to the selection of a structural coefficient of 0.54 for HP AC mixes in comparison with a value of 0.44 for PMA AC mixes.

The determined structural coefficient of 0.54 was used to verify the performance of HP AC mixes in new pavements in terms of their performance against rutting, including both rutting in the AC layer and total rutting in the pavement structure, shoving, and top-down cracking of the AC layer. The ME analysis resulted in most of the cases in a better rutting performance for the HP AC mixes when compared with their respective PMA AC mixes. The rut depths determined in the unbound layers were observed to be lower than the maximum allowable rut depth of 0.50 inch (12.6 mm) indicating an acceptable performance for the HP pavement sections which had a thinner AC layer thickness. The ME analysis for shoving in the AC layer showed, in general, acceptable performance for the HP AC mixes. The top-down cracking analysis showed acceptable performance for the HP AC mixes and exhibited *ER* values much greater than $ER_{opt}$ irrespective of traffic level. In summary, the verification efforts supported the use of a structural coefficient of 0.54 for HP AC mixes in new pavements.

In the case of rehabilitation projects, the adequacy of the selected structural coefficient was verified for HP AC overlay mixes using a ME analysis for reflective cracking. The analysis took into consideration the existing pavement condition in terms of damaged modulus for the existing AC layer, mix-specific material properties, traffic condition, and Florida climate. The HP AC overlay mixes resulted in an increase in both time to reach initial cracking and performance life of the AC overlay. Thus, the structural coefficient of 0.54 used to design the HP AC overlay is expected to result in an acceptable or better reflective cracking performance when compared to the respective PMA AC overlay mix.

As an overall summary, the various analyses conducted in this chapter supported the selection of a structural coefficient of 0.54 for HP AC mixes to be used in the design of new and rehabilitated pavements in Florida.

# CHAPTER 7. VERIFICATION OF STRUCTURAL COEFFICIENT FOR HP AC MIXES USING FULL-SCALE PAVEMENT TESTING

As part of the laboratory evaluation (Chapter 3 and Chapter 4), typical local materials from Florida were assessed and used for the development of 16 AC mixes using PMA and HP asphalt binders (i.e., eight PMA and eight HP AC mixes) for new construction and rehabilitation projects. The mix designs were conducted following the Superpave methodology to determine the OBC for each of the 16 evaluated AC mixes. Different OBC values were determined depending on the aggregate source, aggregate gradation, asphalt binder type (i.e., PMA or HP), and design traffic level. The viscoelastic properties of the 16 AC mixes were evaluated using the dynamic modulus. The mixes were also evaluated in terms of their resistance to rutting, fatigue cracking, top-down cracking, and reflective cracking. In general, it was found that the combination of aggregate source and asphalt binder type (i.e., PMA or HP) impacted the performance characteristics of the evaluated AC mixes. A structural coefficient for HP AC mixes from Florida was determined by incorporating the measured engineering property and performance characteristics of the evaluated PMA and HP AC mixes into mechanistic modeling of flexible pavement responses to traffic loads using the 3D-MOVE software. Based on the data generated in Chapter 6 and the accompanied analyses, it was recommended that HP AC mixes with a structural coefficient of 0.54 be evaluated in the FDOT APT facility. This represents a 19% reduction in the thickness of the AC layer when using a HP AC mix in place of a PMA AC mix while designing a flexible pavement under all similar conditions of traffic, environment, and properties of base and SG layers.

Prior to full implementation in the APT experiment, the developed structural coefficient for HP AC mixes (i.e., 0.54) was checked through full-scale laboratory testing of asphalt pavements. The following section describes the executed experimental plan under this part (i.e., Part IV) of this research project. The main objective of this effort is to verify the structural coefficient determined through laboratory testing and computer modeling in two instrumented full-scale asphalt pavements subjected to stationary dynamic loadings.

## 7.1. EXPERIMENTAL PLAN FOR FULL-SCALE PAVEMENT TESTING

Two experiments were conducted at the UNR full-scale pavement testing facility. For each experiment, a pavement structure was built and tested in the full-scale square box (PaveBox):

- Experiment No. 1 (referred to as PaveBox_PMA): pavement structure 1 consisted of a PMA AC layer on top of a CAB and a SG.
- Experiment No. 2 (referred to as PaveBox_HP): pavement structure 2 consisted of an HP AC layer with a reduced thickness on top of the same CAB and SG.

Both pavement structures were subjected to the same loading protocol. Dynamic loads simulating the FWD loading conditions, were applied at the surface of the pavement in the PaveBox for each experiment. The pavement surface deflections along with critical pavement responses at different locations in the pavement layers (i.e., stresses and strains) were monitored during testing through embedded instrumentations. Linear variable differential transformers (LVDTs) were used to record pavement surface deflections. Total earth pressure cells (TEPCs)

were used to capture the stresses induced in the CAB and SG due to surface loading. Strain gauges were attached to the bottom of the AC layer to measure the load-induced tensile strains. At the end of each PaveBox experiment, cores were cut from the AC layer for bulk specific gravity and air voids measurements.

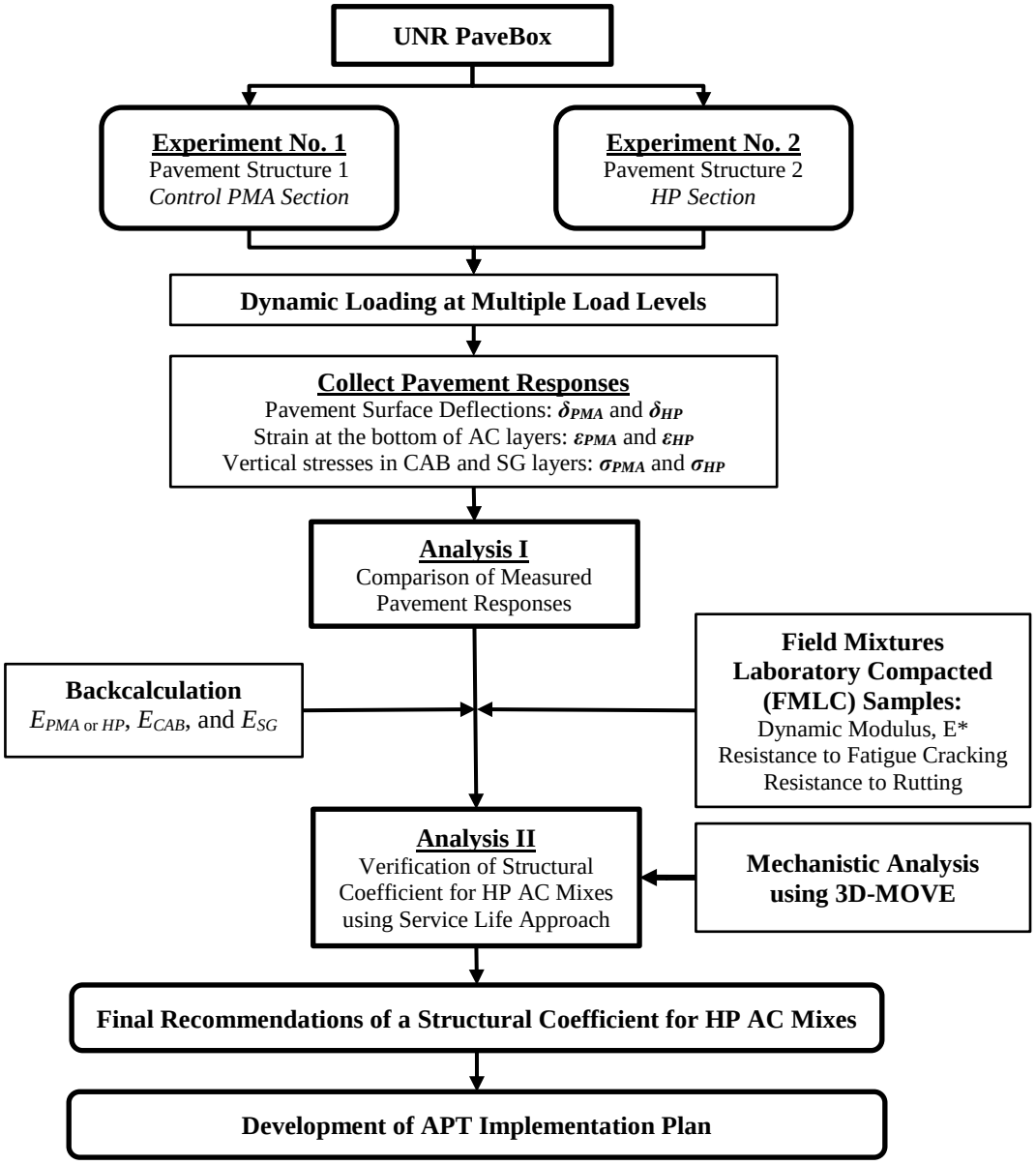


**Figure 7-1. Flowchart of the verification of structural coefficient based on full-scale pavement testing.**

The main objective of this effort is to verify the structural coefficient for HP AC mixes determined previously in Chapter 6. Thus, two major analyses were carried out. Analysis I consisted of a comparison of measured pavement responses under dynamic loadings, while analysis II verified the HP structural coefficient through mechanistic-empirical analyses using

the service life approach. Figure 7-1 illustrates the flowchart of the experimental plan for the verification of the recommended structural coefficient based on full-scale pavement testing in the PaveBox.

Analysis I assessed the impact of the reduced HP AC layer thickness on the measured pavement responses under different levels of surface loads. This was achieved through a direct comparison of the measured pavement responses collected from both experiments (PMA and HP sections).

Analysis II verified the structural coefficient for HP AC mixes using the service life approach. PMA and HP AC mixes produced for both experiments were collected and compacted in the laboratory. The compacted specimens were evaluated in terms of engineering property (i.e., E*), and performance characteristics (i.e., resistance to fatigue cracking and rutting). The measured properties and performance characteristics were implemented into an advanced flexible pavement modeling process to determine the responses and performance at multiple loading levels.

Finally, the findings from analysis I and analysis II of the PaveBox experiments were used to make any necessary modifications to the structural coefficient determined for HP AC mixes in Florida.

## 7.2. ELEMENTS OF EXPERIMENTAL PROGRAM

A full-scale experimental program was carried out to verify the determined structural coefficient for HP AC mixes. A total of two full-scale pavement structures were constructed and subjected to dynamic loadings. This section summarizes the specific characteristics of the two experiments including properties of the used materials, construction techniques, and instrumentation plans.

### 7.2.1. Description of PaveBox

The PaveBox consisted of a square box with internal dimensions of 124 by 124 by 72 inch (315 by 315 by 183 cm). The box is made of a steel base plate, H-shaped steel columns infilled with 4- by 6 by 30 inch (102 by 152 by 762 mm) wood beams and braced at two levels with steel beams and tension rods to act as lateral bracing system. Figure 7-2 and Figure 7-3 show the drawings of the PaveBox.

The steel base plate is grouted to the laboratory floor, and 20 steel columns are appropriately aligned and welded to the base plate. A total of 224 4- by 6- by 30-inch wood beams (102 by 152 by 762 mm) are fitted between the columns. Polyvinyl chloride (PVC) foam boards are used as filler between the gap inside the web of the columns and the wood beams. A screw/nut fastening method is used to install the bracing system, which consisted of eight steel beams and four tension rods.

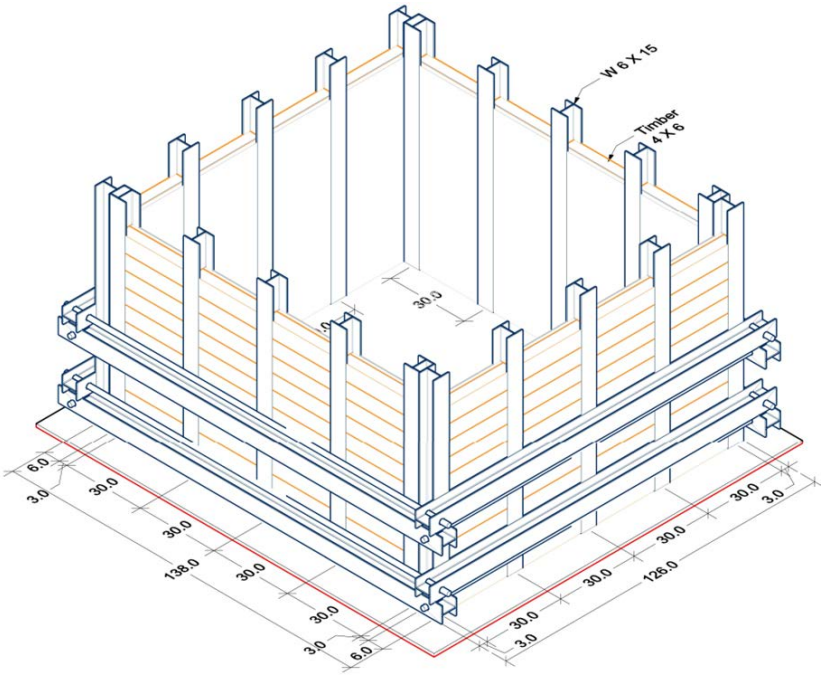


Note: All dimensions are in inches.

**Figure 7-2. Three-dimensional (3D) schematic of the PaveBox.**

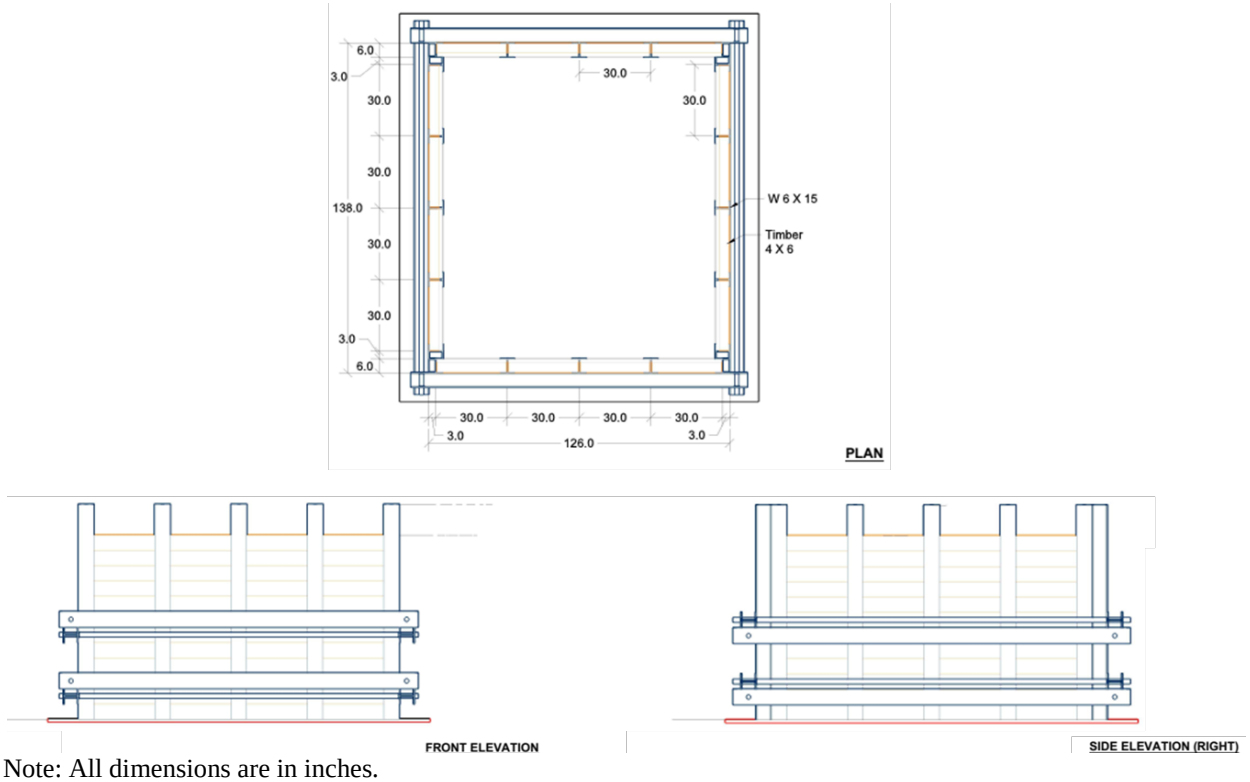


Note: All dimensions are in inches.

**Figure 7-3. Plan view and front and side elevations of the PaveBox.**

Since the experimental program included dynamic loading applied to a pavement structure contained within the PaveBox, there was a concern about introducing measurement errors in the data collected from the sensors due to the reflection of the waves at the boundaries. A common technique to minimize such error is to install wave-absorbing material on the inside walls of the PaveBox. Accordingly, the floor and the inner walls of the PaveBox were covered by a fiberglass material (with paper-vapor-retarder side facing inside) that is commercially available for use as insulation *(92)*. The PVC foam boards acted as an additional wave absorber at the boundaries during the dynamic tests.

A plastic sheet was placed all around the inside of the completed PaveBox. This sheet was intended to provide a frictionless boundary for vertical deformation similar to what is expected in the field.

### 7.2.2. Characteristics of SG Material

The SG material in the PaveBox experiments was procured from a local source. The following sections provide details of the SG material characterization.

*7.2.2.1 Soil Classification*

The results of sieve analysis test, undertaken in accordance AASHTO T11 *(93)* and AASHTO T27 *(61)* are shown in Figure 7-4. The Atterberg limits were determined in accordance with AASHTO T89 *(94)* and AASHTO T90 *(95)* and the results are summarized in Table 7-1. The subgrade soil was classified as A-2-7 according to the AASHTO system (AASHTO M145 *(96)*) and as clayey sand with gravel (group symbol: SC) according to the Unified Soil Classification System (USCS) (ASTM D2487 *(97)*).

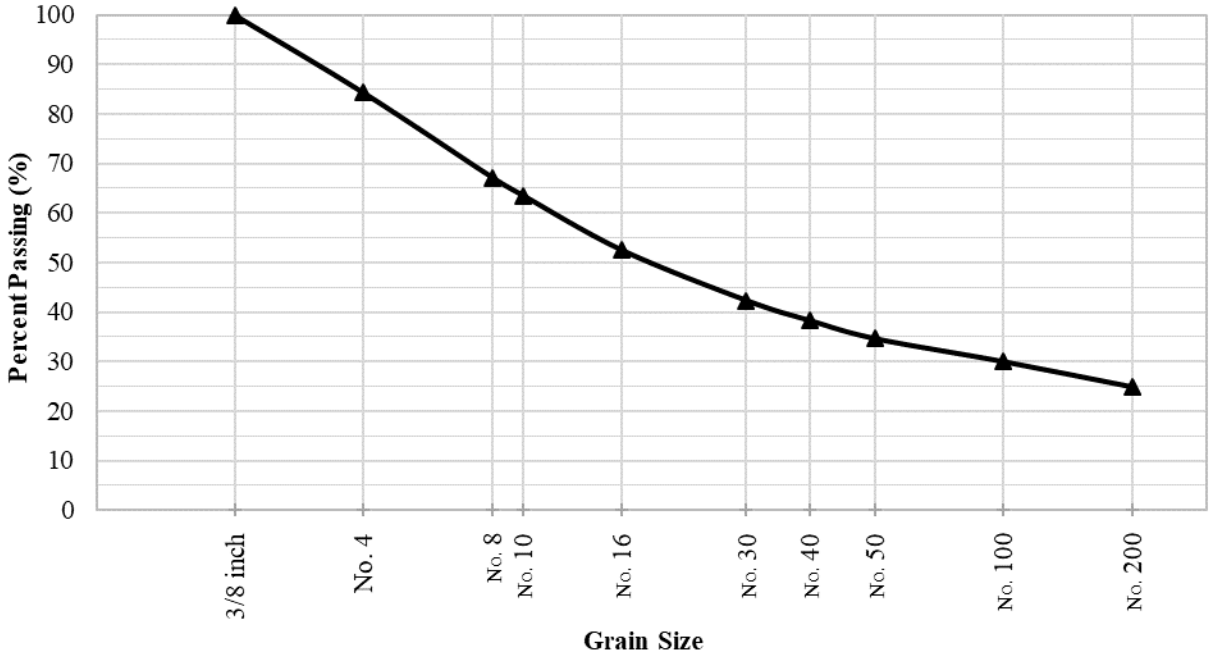


**Figure 7-4. Gradation of SG material.**

**Table 7-1. Atterberg Limits of SG Material.**

| Atterberg Limits | Value (%) |
|---|---|
| Liquid Limit | 43 |
| Plastic Limit | 23 |
| Plasticity Index | 20 |

The quality of a soil as a highway SG material is typically estimated based on the group index *(GI)*. In general, the quality of performance of a soil as an SG material is inversely proportional to the GI. The GI is calculated for A-2-7 material using Equation 7-1, where $P_{200}$ is the percentage passing through the number (No.) 200 sieve and *PI* is plasticity index. A GI of 1 was calculated for the tested SG material, and the SG was classified as A-2-7(1).

$$GI = 0.01 * (P_{200} - 15)(PI - 10) \qquad \textbf{Equation 7-1}$$

*7.2.2.2 Resilient Modulus*

The resilient modulus ($M_R$) represents the stiffness of a material under control confinement condition and repeated vertical loading. The $M_R$ test aims at simulating stress conditions that occur in the pavement structure. The $M_R$ test for the SG material used in the full-scale experiments was conducted in accordance with AASHTO T307 *(98)*. The moisture–density relation (compaction curve) for the SG material was developed in accordance with AASHTO T99 *(99)* (Figure 7-5). A maximum dry density ($\gamma_{d,max}$) of 125.5 pcf (2010 kg/m$^3$) was achieved at an optimum moisture content ($W_{opt}$) of 11.8%. A summary of specimen preparation, testing, and test results for $M_R$ is presented next.

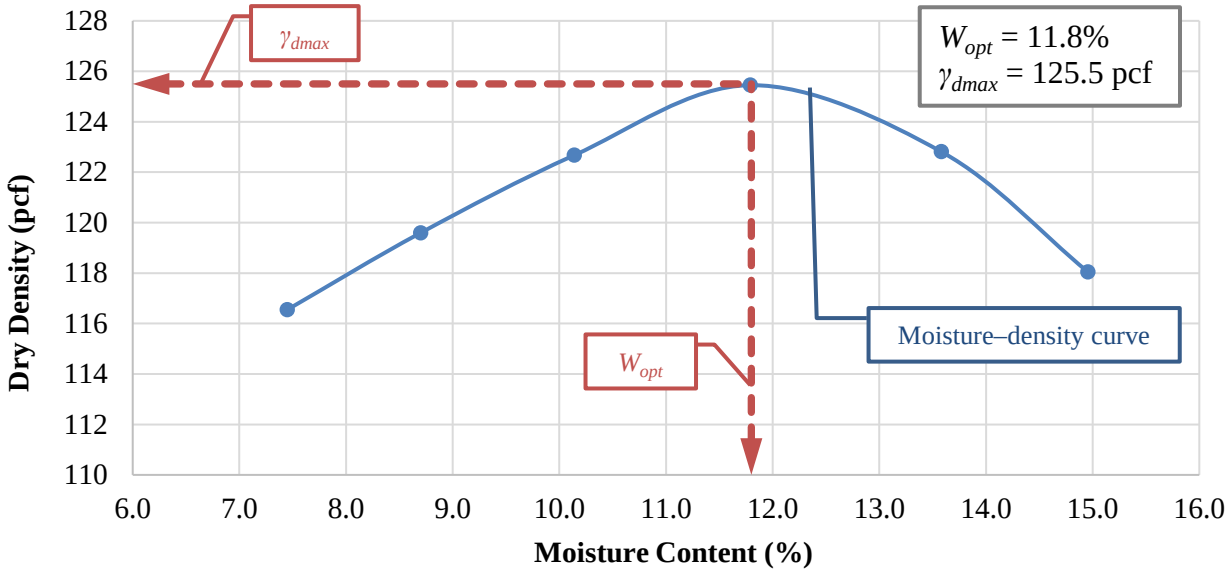


**Figure 7-5. Moisture-density curve of the A-2-7(1) SG material.**

The required amount of water based on the moisture–density curve results was added to the dry SG material to bring it to $W_{opt}$. The SG material and water were mechanically mixed until the

soil got uniform color and consistency (approximately 4 minutes). The prepared soil was cured in sealed buckets with thick plastic covers for a period of 16–24 hours.

After curing, soil specimens were fabricated to 12 inch (304.8 mm) in height and 6-inch (152.4 mm) diameter (Figure 7-6a) cylinders. Figure 7-6b shows a heavy duty mechanical drill with a 6-inch (152.4 mm) cap employed for the purpose of compaction. Each specimen was compacted in 15 lifts that resulted in a relative compaction of about 91%. It may be noted that the surface of each compacted lift was scarified to a depth about 1/8 inch (3.2 mm) to avoid de-bonding between the lifts (refer to Figure 7-6c).

The test specimen surrounded by a latex membrane was secured with top and bottom porous stone caps with moist paper filters placed in between porous stone and specimen. The membrane was carefully sealed with caps by using 'O' rings (Figure 7-7a). The specimen assembly secured within the triaxial cell is shown in Figure 7-7b. The load sequences in accordance with AASHTO T307 *(98)* were applied. Axial deformation and rebound of the specimen were monitored using LVDTs. The resilient modulus for each sequence was calculated from the average of the last 5 loading cycles of the applied 100 cycles. After completion of the $M_R$ test, the testing program was continued with quick shear test. Figure 7-7c and Figure 7-7d display a SG specimen before the resilient modulus test and after the quick shear test, respectively.

**(a)** **(b)** **(c)**

**Figure 7-6. Preparation of $M_R$ test specimen: (a) cylindrical mold, (b) drill hammer, and (c) scarifying tool.**

**(a)** **(b)** **(c)** **(d)**

**Figure 7-7. $M_R$ test specimen: (a) surrounded by latex membrane, (b) assembled in triaxial cell, (c) before test, and (d) after quick shear test.**

It is well accepted that an increase in $M_R$ resulting from an increase in bulk stress ($\theta$) is commonly referred to as "stress hardening" behavior. On the other hand, "stress softening" behavior exhibits a decrease in the $M_R$ with an increase in deviator stress ($\sigma_d$). Constitutive models are generally used to estimate $M_R$ of the material as a function of stress state. Three constitutive models that represent hardening behavior (referred to as Theta model or $K$-$\theta$), softening behavior (referred to as log-log model or $K$-$\sigma_d$), and hardening–softening behavior (referred to as Uzan model) were considered to describe the behavior of the tested SG material under the $M_R$ testing condition (Equation 7-2 through Equation 7-4), where $K$ is the regression constant of $M_R$ model. In these models, the exponents of $\theta$ and $\sigma_d$ (i.e., $n$ and $m$) are expected to have a positive and a negative value, respectively.

$$M_R = K\theta^n \qquad \textbf{Equation 7-2}$$

$$M_R = K\sigma_d^m \qquad \textbf{Equation 7-3}$$

$$M_R = K\theta^n\sigma_d^m \qquad \textbf{Equation 7-4}$$

In order to identify the parameters of the models, the method of lest squares in Microsoft® Excel™ Solver was employed. The calculated parameters for the evaluated models are presented in Table 7-2. These parameters are for $M_R$, $\theta$, and $\sigma_d$ given in pounds per square inch. Figure 7-8 through Figure 7-10 depict the comparison between the measured and calculated $M_R$ using the constitutive models and associated model parameters. It can be seen that the calculated $M_R$ using Uzan model that considers both hardening and softening behavior, show the best agreement with the measured values. The results of $M_R$ tests on the SG material revealed that the increase in $\sigma_d$ at a constant confining pressure resulted in the increase in $M_R$ value. The log-log model reflects the softening characteristics of an unbound material. Such a model did not properly capture the behavior of the tested SG material indicated by a positive value for the $m$ parameter.

**Table 7-2. Calculated Parameters of SG Constitutive Models.**

| Model | Stress-Dependent Behavior | *K* Parameter | *n* Parameter | *m* Parameter |
|---|---|---|---|---|
| Theta model | Hardening | 1,140.40 | 0.704 | — |
| Log-log model | Softening | 4,677.35 | — | 0.483 |
| Uzan model | Hardening–softening | 1,011.28 | 0.808 | −0.106 |

—Not applicable.

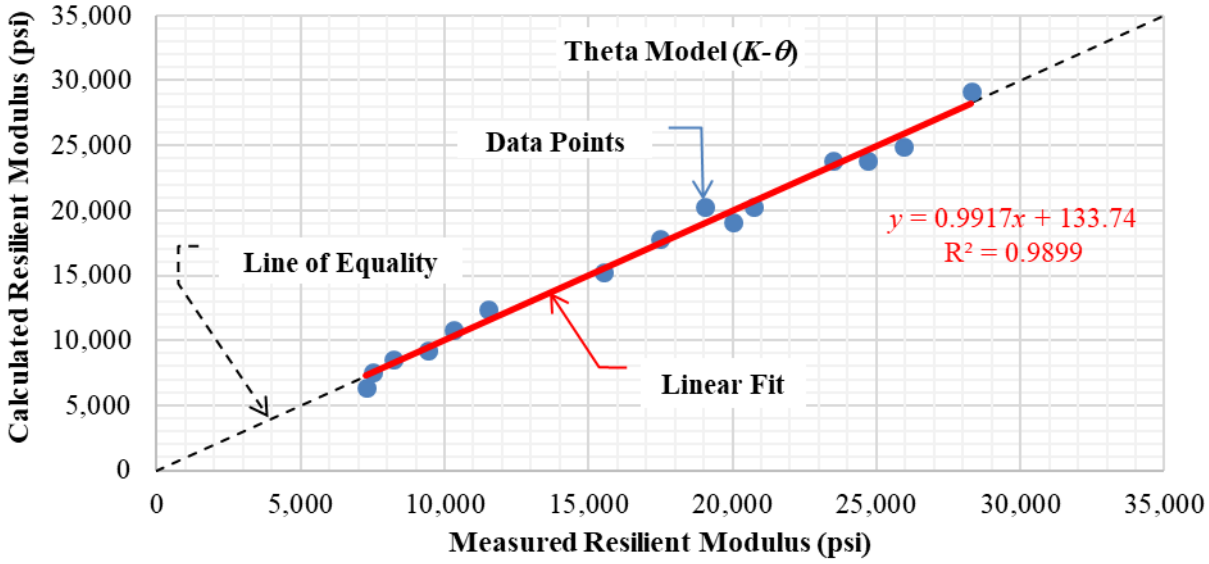


**Figure 7-8. Measured versus calculated SG $M_R$ using the Theta-model.**

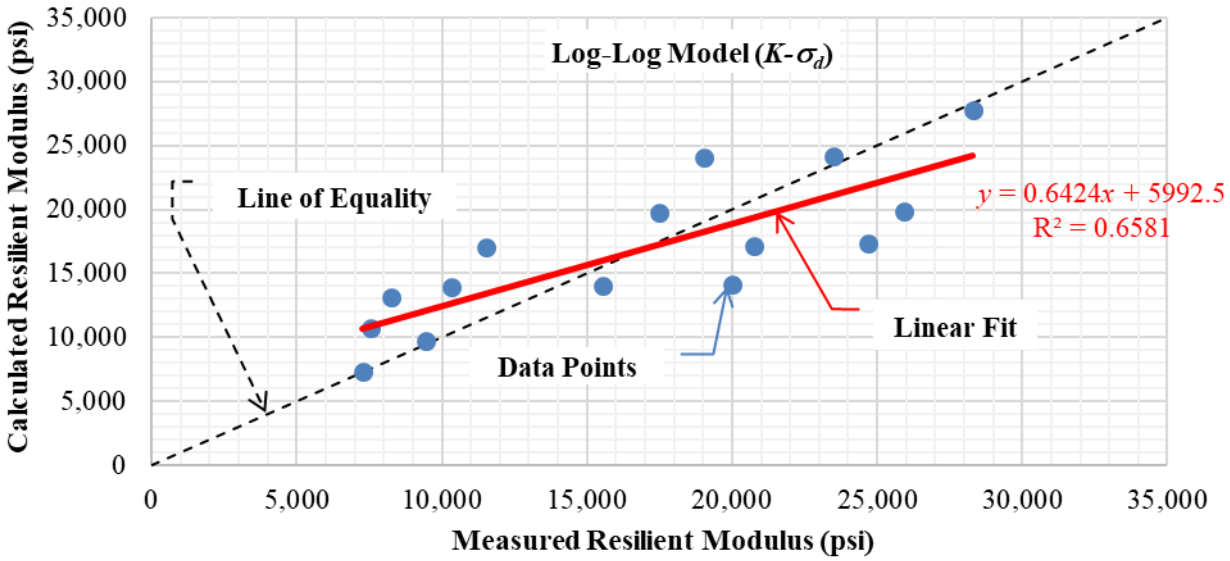


**Figure 7-9. Measured versus calculated SG $M_R$ using the log-log.**

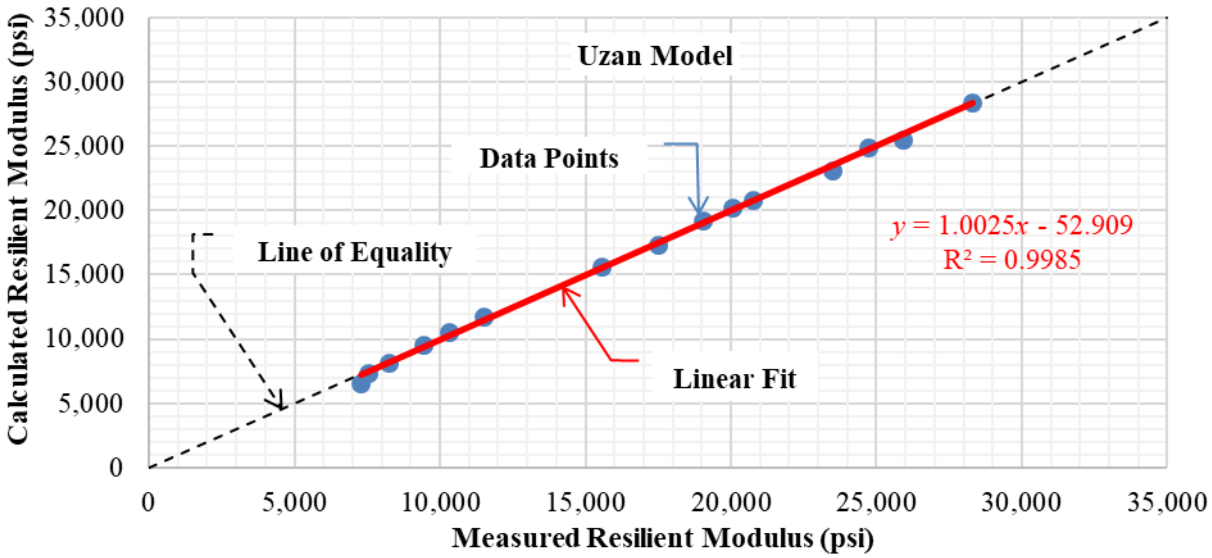


**Figure 7-10. Measured versus calculated SG $M_R$ using the Uzan model.**

### 7.2.3. Characteristics of Base Material

A typical local CAB layer was used in the full-scale PaveBox experiments. The CAB material was selected following the NDOT materials' specification for dense-graded CAB (Type 2, Class B) *(100)*. Table 7-3 summarizes the requirements for the CAB material typically used in Nevada (i.e., Type 2, Class B base) in comparison to the CAB used in Florida (i.e., Graded aggregate and Limerock bases). Overall, the requirements for the CAB materials from NDOT and FDOT were comparable and the CAB material used in the PaveBox experiments was considered acceptable for the purpose of this task. A structural coefficient of 0.18 that is consistent with the value imposed by FDOT for graded aggregate base was assumed for the CAB material used in the PaveBox *(23)*.

The CAB material used in both PaveBox experiments, was sampled from a local supplier in northern Nevada in accordance with AASHTO T2 *(67)* protocol. The sampled materials were blended and reduced to testing size following AASHTO T248 *(101)*. AASHTO T27 *(61)* and AASHTO T180 *(102)* protocols were followed to determine the gradation, $\gamma_{dmax}$, and $W_{opt}$. Figure 7-11 illustrates the moisture–density compaction curve for the CAB material. The $\gamma_{dmax}$ for the evaluated CAB material was 135.1 pcf (2164 kg/m$^3$), maximum wet density was 147.0 pcf (2,354 kg/m$^3$), and $W_{opt}$ was 8.8%.

**Table 7-3. NDOT and FDOT Requirements for CAB Materials.**

| Property | NDOT Type II, Class B Base | FDOT Graded Aggregate Base | FDOT Limerock Base |
|---|---|---|---|
| Soundness Loss | — | ≤ 15% | — |
| Percent of Carbonates | — | — | ≥ 70% |
| PI | 3 ≤ PI ≤ 15 (function of percent passing No. 200 sieve) | G1: PI ≤ 4 for passing No. 40 material | Non-Plastic (NP) |
| Liquid Limit (LL) | LL ≤ 35 | G1: LL ≤ 25 for passing No. 40 material | LL ≤ 35 |
| Sand Equivalent (SE) | — | G2: SE ≤ 28 for passing No.10 material | — |
| Lime Bearing Ratio (LBR) | — | LBR ≥ 100 | LBR ≥ 100 |
| R-Value | R ≥ 70 | — | — |
| Gradation<br>Percent Passing Sieve: | | | |
| 3.5 inch (87.5 mm) | 100 | 100 | ≥ 97% |
| 2 inch (50 mm) | 100 | 100 | — |
| 1.5 inch (37.5 mm) | 100 | 95–100 | — |
| 1 inch (25 mm) | 80–100 | — | — |
| 0.75 inch (19 mm) | — | 65–90 | — |
| 0.375 inch (9.5 mm) | — | 45–75 | — |
| No. 4 (4.75 mm) | 30–65 | 35–60 | — |
| No. 10 (2 mm) | — | 25–45 | — |
| No. 16 (1.18 mm) | 15–40 | — | — |
| No. 50 (0.3 mm) | — | 5–25 | — |
| No. 200 (0.075 mm) | 2–12 | 0–10 | — |

—Not applicable.

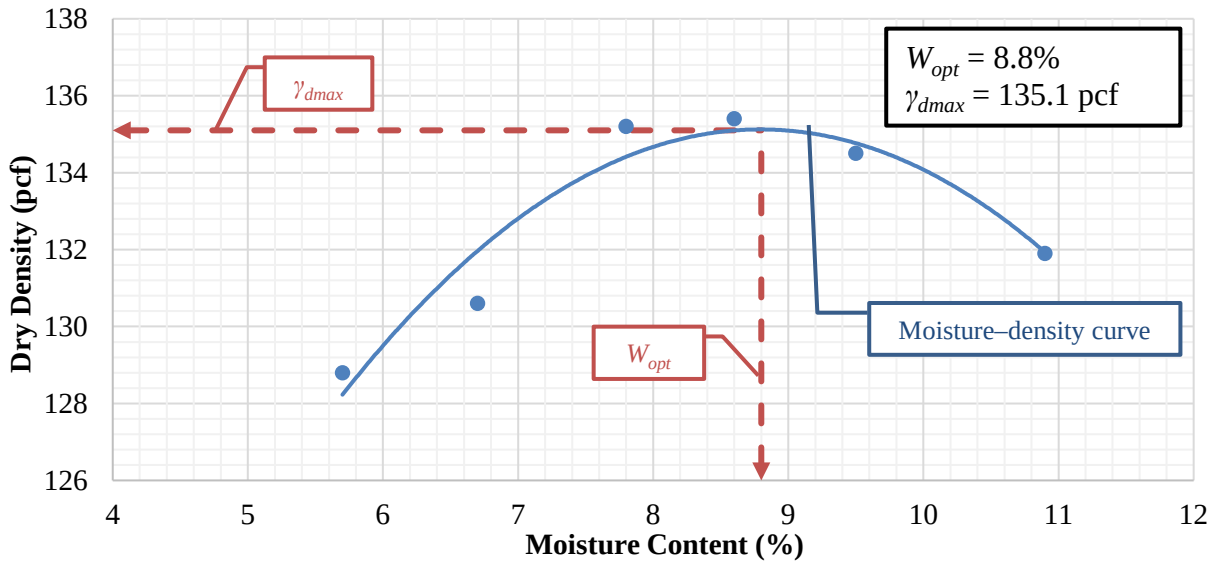


**Figure 7-11. Moisture-density curve of the CAB material.**

### 7.2.4. Characteristics of AC Material

This section summarizes the materials used in the fabrication of PMA and HP AC mixes for the PaveBox experiments. The Superpave mix designs that were developed in accordance with FDOT specifications 2018 *(23)* are also presented. The PMA and HP asphalt binders were sampled from Vecenergy of Rivera Beach in Florida, while the aggregates were sampled from Lockwood pit; a common source of aggregates in the greater Reno area. The AC mixes were produced on site using a half-ton asphalt mixer. Loose mixtures were collected in five-gallon steel pails during production for deposition in PaveBox. The produced mixtures were evaluated for their engineering properties in terms of dynamic modulus (E*) master curve, fatigue cracking characteristics in terms of resistance to flexural bending strains, and rutting characteristic in terms of resistance to permanent strains in triaxial testing. In addition, field cores from both experiments were collected after testing was completed for determination of as-constructed density and thickness values.

#### *7.2.4.1 Asphalt Binders*

Two asphalt binders were used in this task: a PG76-22PMA and an HP Binder. A total of fifteen 5-gallon buckets were obtained for each grade from the selected source. The PMA and HP binders were reported by the supplier to have 3.0%, and 8.0% SBS polymer by weight of binder, respectively. Thus, meeting the definition set forth in this research for PMA and HP asphalt binders. The grade and source of the base binder and the SBS content for each binder were provided by the supplier. Table 7-4 and Table 7-5 summarize the properties of the sampled PMA and HP asphalt binders, respectively. Both binders met the corresponding FDOT specifications 2018 *(23)*.

**Table 7-4. Properties of the PG76-22PMA Asphalt Binder Sampled from Vecenergy.**

| Test and Method | Condition | Measurement | FDOT Specification 2018 |
|---|---|---|---|
| Source of base binder | — | PG67-22 Marathon | — |
| Modifier | Polymer | SBS, 3.0% by weight of binder[(a)] | — |
| Additive | Anti-Strip Agent | — | — |
| Original Binder | | | |
| Flash Point, AASHTO T48-06 *(56)* | Cleveland Open Cup | 603°F | 450°F Min. |
| Rotational Viscosity, AASHTO T316-13 *(57)* | 275°F | 2.245 Pa.s | 3.000 Pa.s Max. |
| Dynamic Shear Rheometer, AASHTO T315-12 *(24)* | G*/sin $\delta$ at 76°C | 1.21 kPa | 1.00 kPa Min. |
| | Phase Angle, $\delta$ at 76°C | 74.0 degrees | 75 degrees Max. |
| Rolling Thin Film Oven Test Residues (AASHTO T240-13) *(58)* | | | |
| Rolling Thin Film Oven, AASHTO T240-13 *(58)* | Mass Change | 0.32% | 1.00% Max. |
| Multiple Stress Creep Recovery AASHTO M332-14 *(59)* | $J_{nr,\ 3.2}$ at 67°C | 0.62 $kPa^{-1}$ | 1.00 $kPa^{-1}$ Max. |
| | $J_{nr,diff}$ at 67°C | 19.8% | — |
| | $\%R_{3.2}$ at 67°C | 54.3% | $\%R_{3.2} \geq 29.37(J_{nr,\ 3.2})^{-0.2633} \geq 25.9\%$ |
| Pressure Aging Vessel Residue @ 100°C (AASHTO R 28-12) *(60)* | | | |
| Dynamic Shear Rheometer, AASHTO T315-12 *(24)* | G*sin $\delta$ at 26.5°C, 10 rad/sec. | 3,155 kPa | 5,000 kPa Max. |
| Creep Stiffness, AASHTO T313-12 *(30)* | S (Stiffness) at −12°C, 60 sec.[(b)] | 148 MPa | 300 MPa Max. |
| | m-value at −12°C, 60 sec.[(b)] | 0.328 | 0.300 Min. |

—Not applicable.
[(a)]%SBS was provided by the supplier.
[(b)]Testing temperature is 10°C warmer than the actual low PG.

**Table 7-5. Properties of the HP Asphalt Binder Sampled from Vecenergy.**

| Test and Method | Condition | Measurement | FDOT Specification 2018 |
|---|---|---|---|
| Source of base binder | — | PG58-28 Marathon | — |
| Modifier | Polymer | SBS, 8.0% by weight of binder[(a)] | — |
| Additive | Anti-Strip Agent | — | — |
| Original Binder | | | |
| Flash Point, AASHTO T48-06 *(56)* | Cleveland Open Cup | 604°F | 450°F Min. |
| Rotational Viscosity, AASHTO T316-13 *(57)* | 275°F | 3.401 Pa.s | 3.000 Pa.s Max.[(b)] |
| Dynamic Shear Rheometer, AASHTO T315-12 *(24)* | G*/sin $\delta$ at 76°C | 2.28 kPa | 1.00 kPa Max. |
| | Phase Angle, $\delta$ at 76°C | 47.1 degrees | 65 degrees Max. |
| Rolling Thin Film Oven Test Residues (AASHTO T240-13) *(58)* | | | |
| Rolling Thin Film Oven, AASHTO T240-13 *(58)* | Mass Change | 0.67% | 1.00% Max. |
| Multiple Stress Creep Recovery AASHTO M332-14 *(59)* | $J_{nr,\ 3.2}$ at 76°C | 0.03 $kPa^{-1}$ | 0.10 $kPa^{-1}$ Max. |
| | $J_{nr,diff}$ at 76°C | 8.6% | — |
| | $\%R_{3.2}$ at 76°C | 97.5% | $\%R_{3.2} \geq 90.0\%$ |
| Pressure Aging Vessel Residue @ 100°C (AASHTO R 28-12) *(60)* | | | |
| Dynamic Shear Rheometer, AASHTO T315-12 *(24)* | G*sin $\delta$ at 26.5°C, 10 rad/sec. | 1,150 kPa | 5,000 kPa Max. |
| Creep Stiffness, AASHTO T313-12 *(30)* | S (Stiffness) at −12°C, 60 sec.[(c)] | 85 MPa | 300 MPa Max. |
| | m-value at −12°C, 60 sec.[(c)] | 0.389 | 0.300 Min. |

—Not applicable.
[(a)]%SBS was provided by the supplier.
[(b)]Binders with values higher than 3 Pa.s should be used with caution and only after consulting with the supplier as to any special handling procedures, including pumping capabilities *(23)*.
[(c)]Testing temperature is 10°C warmer than the actual low PG.

*7.2.4.2 Aggregates*

The aggregates were sampled from Lockwood pit in the northern part of Nevada. An aggregate gradation with a NMAS of 0.5 inch (12.5 mm) following FDOT specifications *(23)* was targeted for the experiment. It should be mentioned that the same gradation was targeted for both PMA and HP AC mixes. Gradation analyses were conducted for all aggregate stockpiles. Table 7-6 presents the gradations of all the individual stockpiles. Figure 7-12 presents the aggregates JMF gradation for the AC mixes. It should be mentioned that no recycled material was used in any of the AC mixes.

Table 7-7 summarizes the requirements for the aggregates typically used in Nevada and Florida for AC mixes. Overall, the requirements for the aggregates from NDOT and FDOT were

comparable and the selected aggregates for the AC mixes used in the PaveBox experiments was considered acceptable for the purpose of this task. A structural coefficient of 0.44 that is consistent with the value imposed by FDOT was assumed for the PMA AC mix used in the PaveBox *(23)*.

**Table 7-6. Gradations and JMF for the 12.5 mm NMAS PMA and HP AC Mixes.**

| Sieve Size | Percentage Passing | | | | | | JMF Gradation |
|---|---|---|---|---|---|---|---|
| | 0.75 inch (19 mm) AGG Crushed | 0.5 inch (12.5 mm) AGG Crushed | 0.375 inch (9.5 mm) AGG Crushed | No. 4 (4.75 mm) Crusher Fines | Concrete Sand | No. 4 (4.75 mm) Natural Fines | |
| 1.5 inch (37.5 mm) | 100.0 | 100.0 | 100.0 | 100.0 | 100 | 100 | 100.0 |
| 1 inch (25 mm) | 100.0 | 100.0 | 100.0 | 100.0 | 100 | 100 | 100.0 |
| 0.75 inch (19 mm) | 100.0 | 100.0 | 100.0 | 100.0 | 100 | 100 | 100.0 |
| 0.5 inch (12.5 mm) | 36.8 | 100.0 | 100.0 | 100.0 | 100 | 100 | 93.7 |
| 0.375 inch (9.5 mm) | 5.5 | 55.3 | 100.0 | 100.0 | 100 | 100 | 85.2 |
| No. 4 (4.75 mm) | 1.1 | 0.9 | 21.2 | 98.0 | 99.3 | 99.6 | 65.7 |
| No. 8 (2.36 mm) | 0.9 | 0.8 | 1.3 | 64.4 | 90 | 98.7 | 51.9 |
| No. 16 (1.18 mm) | 0.8 | 0.7 | 0.7 | 40.4 | 62.2 | 96.5 | 38.8 |
| No. 30 (0.6 mm) | 0.8 | 0.6 | 0.5 | 26.8 | 39.8 | 84.1 | 28.3 |
| No. 50 (0.3 mm) | 0.7 | 0.6 | 0.5 | 19.6 | 19.7 | 45.6 | 16.2 |
| No. 100 (0.15 mm) | 0.7 | 0.5 | 0.4 | 15.4 | 7.5 | 11.7 | 7.5 |
| No. 200 (0.075 mm) | 0.7 | 0.5 | 0.4 | 12.6 | 4.1 | 3.2 | 4.8 |
| **Bin Percentages** | **10.0%** | **12.0%** | **15.0%** | **25.0%** | **24.0%** | **14.0%** | **100.0%** |

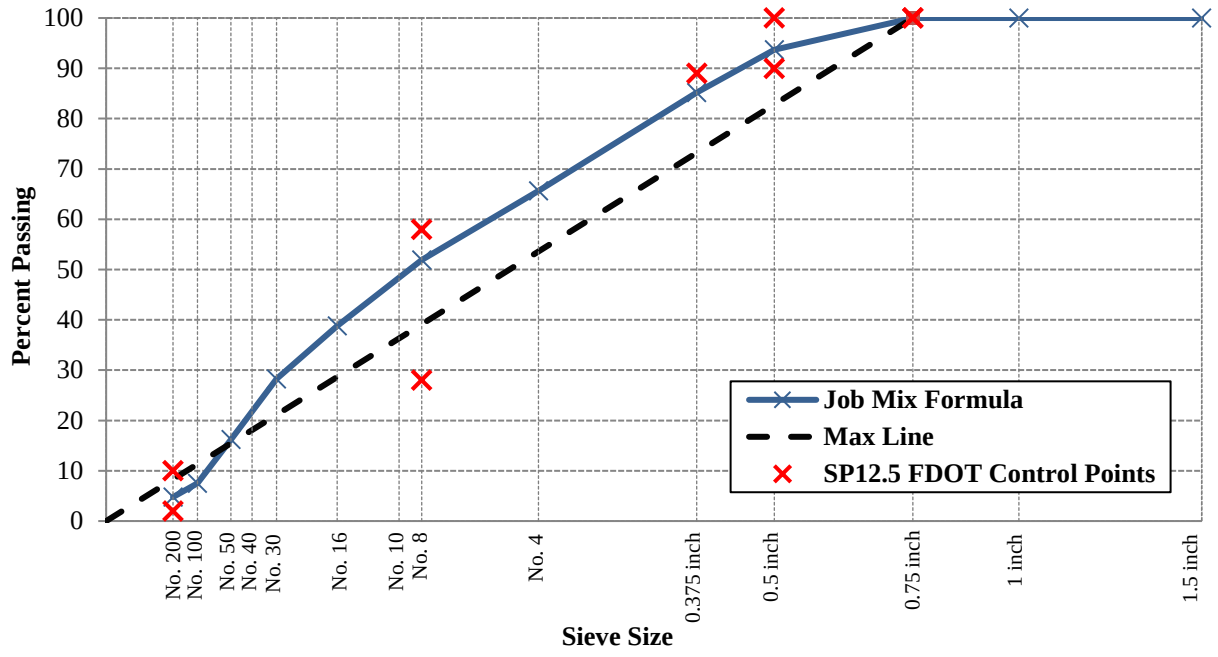


**Figure 7-12. JMF gradation for the 12.5 mm NMAS PMA and HP AC mixes.**

**Table 7-7. NDOT and FDOT Aggregates Specifications for Bituminous Courses.**

| Property | NDOT | | FDOT | |
|---|---|---|---|---|
| | **Test Method** | **Requirement** | **Test Method** | **Requirement** |
| Fractured Faces | Nev. T230 | 80% Min., 2 Fractures Min. | ASTM D5821 | 95/90% for Traffic Level D |
| Fine Aggregate Angularity | — | — | AASHTO T304 | 10% Max. |
| Flat and Elongated Particles | — | — | ASTM D4791 | 10% Max. |
| PI | Nev. T212 | 10 Max. | — | — |
| LL | Nev. T210 | 35 Max. | — | — |
| Sand Equivalent | — | — | AASHTO T176 | 45% Min. |
| Absorption of Coarse Aggregate | Nev. T111 | 4% Max. | — | — |
| Percentage of Wear | AASHTO T96 | 37% Max. | FM 1-T096 | 45% Max. |
| Soundness (Coarse Aggregate) (5 Cycles, Sodium Sulfate) | AASHTO T104 | 12% Max. Loss | AASHTO T104 | 12% Max. Loss |
| Soundness (Fine Aggregate) (5 Cycles, Sodium Sulfate) | AASHTO T104 | 15% Max. Loss | — | — |
| Specific Gravity (Fine Aggregate) | Nev. T493 | 2.95 Max. | — | — |
| Specific Gravity (Coarse Aggregate) | Nev. T111 | 2.95 Max. | — | — |

—Not applicable.

*7.2.4.3 Asphalt Mix Designs*

Two AC mixtures, one PMA labeled as “PaveBox_PMA” and one HP labeled “PaveBox_HP” were designed in the laboratory for use in the PaveBox. Both mixtures were designed following the FDOT Superpave mix design methodology *(23)*. The heated aggregates were mixed with various amount of asphalt binder so at least two were above and two were below the expected OBC for each mixture. After the samples were mixed and conditioned for 2 hours at the compaction temperature, the mixtures were compacted using the Superpave gyratory compactor for 100 gyrations based on the NMAS (i.e., 12.5 mm) and the targeted traffic level D. The OBC for each mixture was determined by identifying the asphalt content that provided 4% air voids and meeting all the applicable FDOT mix design specifications as summarized in Table 7-8. The mixtures for the PaveBox experiments were produced at the mix design OBCs: 5.6% for PaveBox_PMA and 5.7% for PaveBox_HP.

**Table 7-8. Summary of Mix Designs for 12.5 mm NMAS, Lockwood aggregates, with PMA and HP Asphalt Binders.**

| Property | PaveBox_PMA AC Mix | PaveBox_HP AC Mix | FDOT SP Mix Design Specifications 2018 *(23)* |
|---|---|---|---|
| Traffic Level | D | D | — |
| Design Number of Gyrations, $N_{design}$ | 100 | 100 | 100 |
| OBC by twm[(a)] (%) | 5.6 | 5.7 | — |
| Theoretical Maximum SG, $G_{mm}$ | 2.442 | 2.414 | — |
| Air Voids, *Va* (%) | 4.0 | 4.0 | 4.0 |
| Voids in Mineral Aggregates, *VMA* (%) | 14.0 | 14.9% | 14.0% Min. |
| Voids Filled with Asphalt, *VFA* (%) | 70.9 | 73.1 | 65–75% |
| Percent of Effective Binder by Volume, $P_{be}$ (%) | 4.2 | 4.9 | — |
| Dust Proportion, *DP* | 1.1 | 1.0 | 0.6–1.2 |

—Not applicable.
[(a)]Total weight of mix.

*7.2.4.4 Performance Testing*

Loose asphalt mixtures were collected from the outlet of the half-ton asphalt mixer during production. The mixtures were evaluated for their engineering property in terms of E*, and for performance characteristics in terms of their resistance to fatigue cracking and rutting. The E* and rutting were evaluated at the short-term aging condition while fatigue cracking was evaluated after long-term oven aging. Short-term aging consisted of reheating the loose mixtures at the compaction temperature in a force-draft laboratory oven for three hours prior to splitting, followed by an additional hour prior to compaction. In the case of the fatigue cracking, the compacted specimens were long-term aged at a temperature of 185°F (85°C) in a forced-draft oven for 5 days. It should be mentioned that test specimens were compacted to an air void level similar to the as-constructed air voids of the AC layer in the PaveBox. In-place density was determined using field cores sampled from each AC layer after completing the experiment (refer to section 2.9 for further details).

Fatigue and rutting testing were evaluated at the respective effective intermediate and high temperatures, 77°F (25°C) and 122°F (50°C), repsetcively. These temepratrues were determined for the state of Florida using the data of the climatic stations in Gainesville and Marathon. More information regarding this part can be found in Section 5.3.

Engineering Properties

The *E** property of each of the two AC mixes was determined in accordance with AASHTO T378 *(39)*. This test is described in details in Section 3.3.1. *E** provides an indication on the overall quality of the AC mixture. The magnitude of *E** depends on several properties of the

mixture including aggregate properties, gradation, asphalt binder grade, mix volumetrics, and mix age. Figure 7-13 and Figure 7-14 show the *E** and *δ(w)* master curves of both PaveBox_PMA and PaveBox_HP AC mixes at a reference temperature ($T_r$) of 68°F (20°C), respectively. In addition, Figure 7-15 compares the values of *E** at the effective intermediate and high temperatures for fatigue (i.e., 77°F (25°C)) and rutting (i.e., 122°F (50°C)) at a loading frequency of 10 Hz.

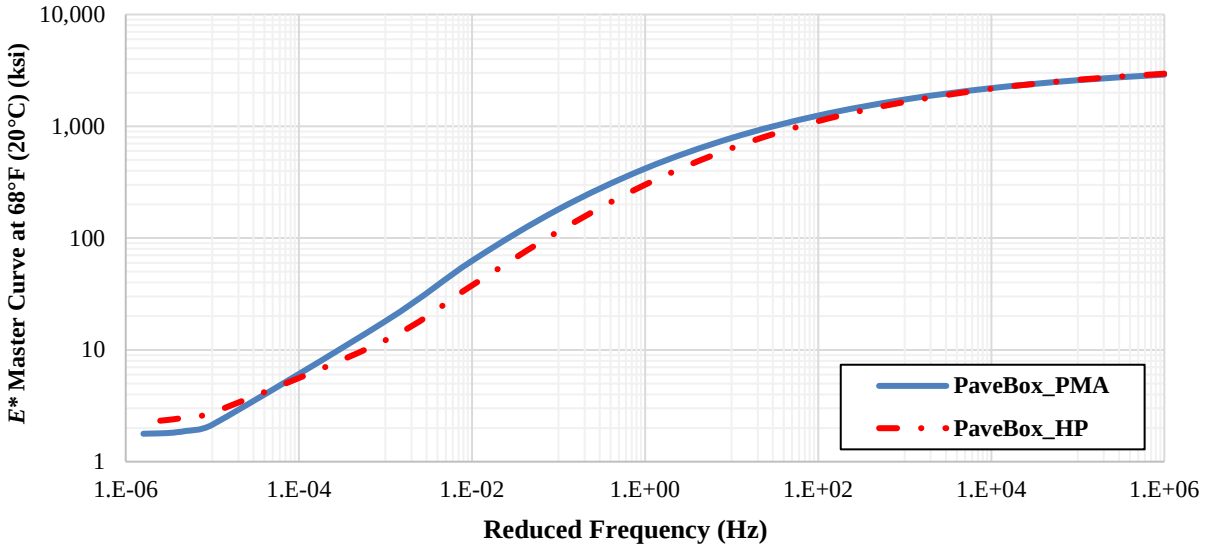


**Figure 7-13. *E** master curve of AC mixes at 68°F (20°C).**

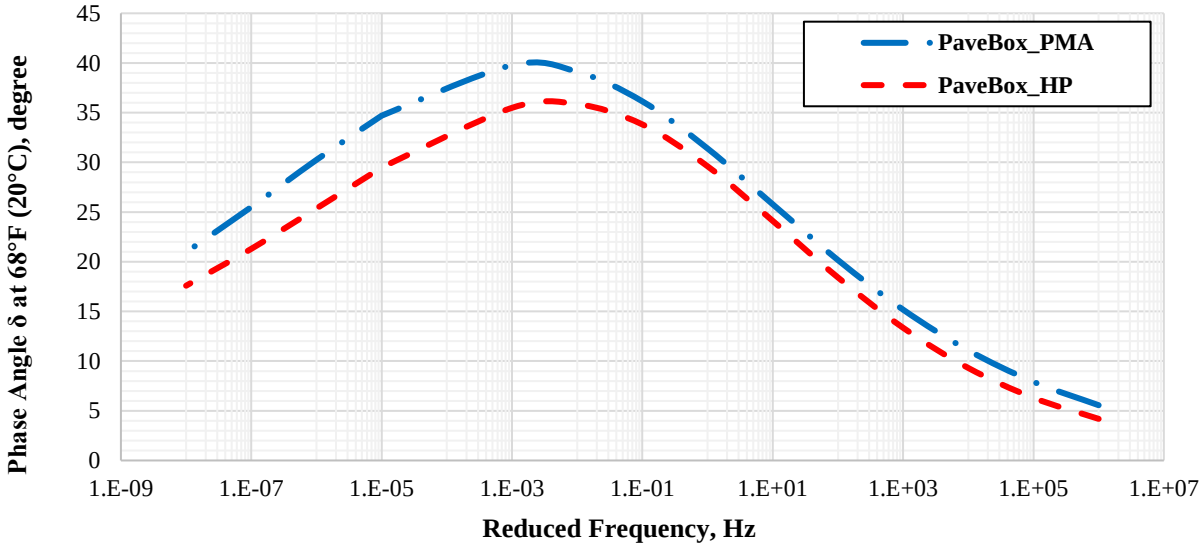


**Figure 7-14. Phase angle master curve of AC mixes at 68°F (20°C).**

Overall, the asphalt binder type (i.e., PMA or HP) had an impact on the magnitude of *E** and phase angle. Lower *E** values were observed for the PaveBox_HP mix at intermediate

frequencies and temperatures indicating a more flexible behavior under traffic loading. It should be mentioned that similar *E** values were observed for both mixes at higher frequencies and lower temperatures. In addition, lower phase angle values were observed for the PaveBox_HP AC mix at all frequencies and corresponding temperatures.

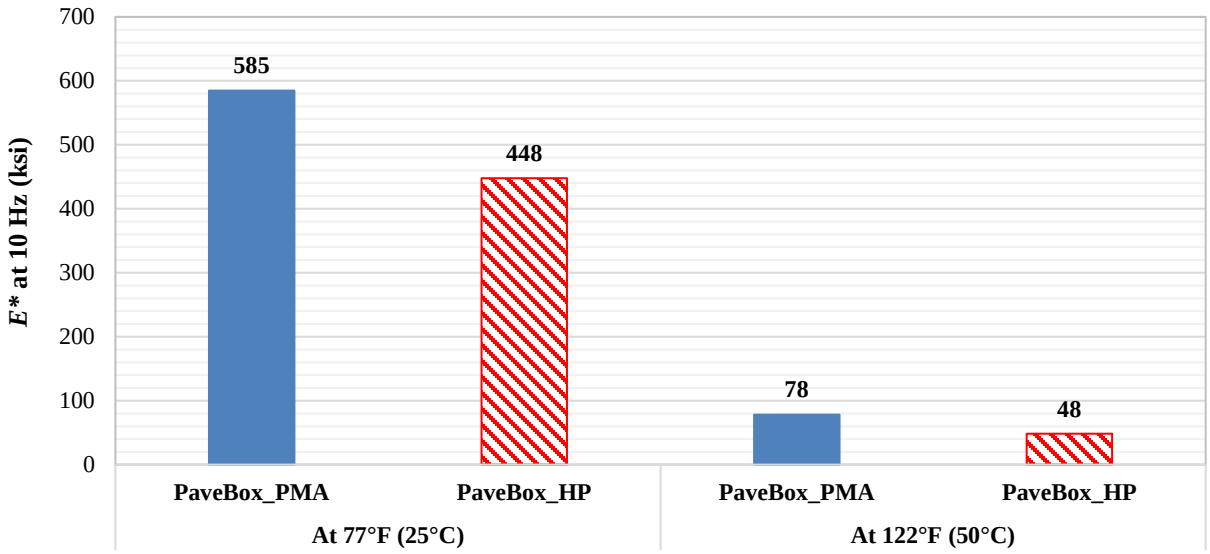


**Figure 7-15. *E** values at 10 Hz.**

Fatigue Cracking

The fatigue characteristics of the two AC mixes were evaluated using the flexural beam fatigue test according to AASHTO T321 *(35)* at three temperatures and multiple strain levels. The mixtures for the fatigue test were short-term aged followed by long-term oven aging since fatigue is a later pavement life distress. This performance test is described in details in Section 3.3.3. The flexural beam fatigue tests were conducted at 55, 70, and 85°F (13, 21, and 30°C) for the PaveBox_PMA AC mix and at 40, 55, and 70°F (4.4, 13, and 21°C) for the PaveBox_HP AC mix. The highest testing temperature was adjusted to ensure the evaluated AC mix was stiff enough to hold a constant strain during testing. The generalized MEPDG fatigue model, expressed in Equation 3-12, was develped for each AC mix (i.e., PaveBox_PMA and PaveBox_HP).

Figure 7-16 and Figure 7-17 show the fatigue relationships developed at all testing temperatures for the PaveBox_PMA and PaveBox_HP AC mixes, respectively. In addition, Figure 7-18 shows the fatigue relationships for the two evaluated AC mixes at 77°F (25°C). These relationships were interpolated using the measured data at the three testing temperatures (i.e. 55, 70, and 85°F for PMA AC mix and 40, 55, and 70°F for HP AC mix). A higher and flatter curve indicates a better resistance to fatigue cracking. The asphalt binder type (i.e., PMA or HP) had a significant impact on the fatigue behavior of the evaluated AC mixes. The PaveBox_HP AC mix showed better fatigue relationships when compared with the PaveBox_PMA AC mix at all strain levels and testing temperatures. Thus, indicating an increased flexibility and resistance to fatigue cracking for the HP AC mix under different environmental conditions. For example, at 500

micro-strain, the number of cycles to failure for PaveBox_HP AC mix was 4.5 times the number of cycles to failure for PaveBox_PMA AC mix. It should be mentioned that the noticeably better fatigue relationship for the HP AC mix can be mainly attributed to the dominant behavior of the additional polymer.

Table 7-9 summarizes the regressions coefficients of the developed fatigue models for the two evaluated AC mixes (i.e., PaveBox_PMA vs. PaveBox_HP). It should be noted that, a significant difference in the laboratory fatigue resistance will not necessarily translate into the same difference in fatigue performance of the AC pavement in the field. Many factors may highly affect the fatigue life of an AC pavement such as stiffness, the developed tensile strain under field loading, the fatigue characteristic of the evaluated asphalt mixture, and the interaction of all these factors. In a mechanistic pavement analysis, an AC layer with higher stiffness and lower laboratory fatigue life (in a strain-controlled mode of loading) may experience lower tensile strain under field loading and resulting in a longer pavement fatigue life. Therefore, a full mechanistic analysis would be necessary to effectively evaluate the impact of HP binder on fatigue performance of an AC pavement.

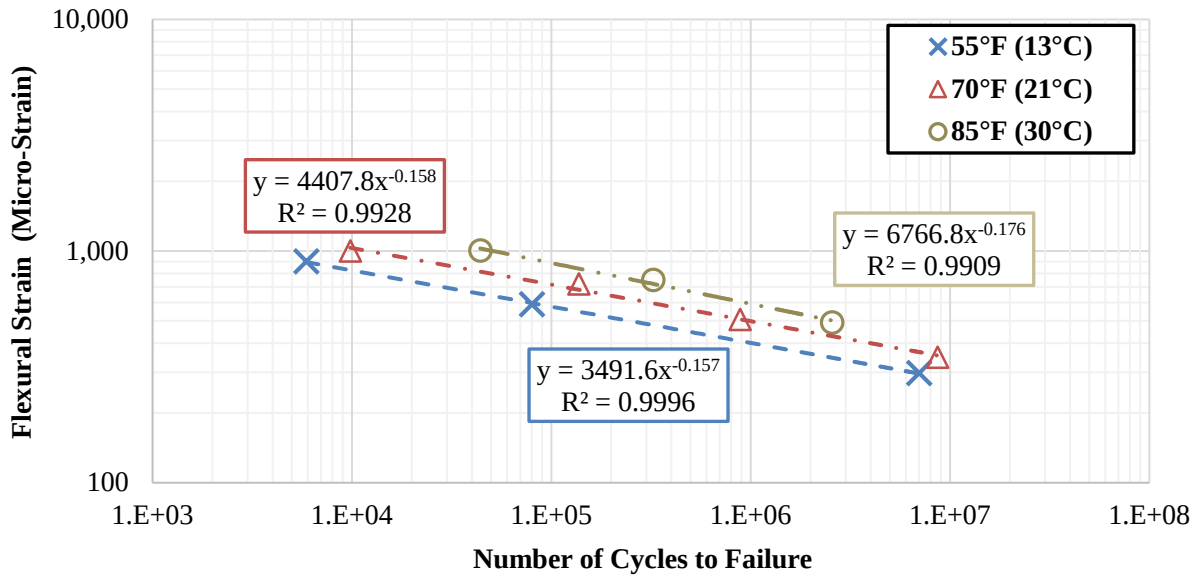


**Figure 7-16. Beam fatigue data at three temperatures of PaveBox_PMA AC mix.**

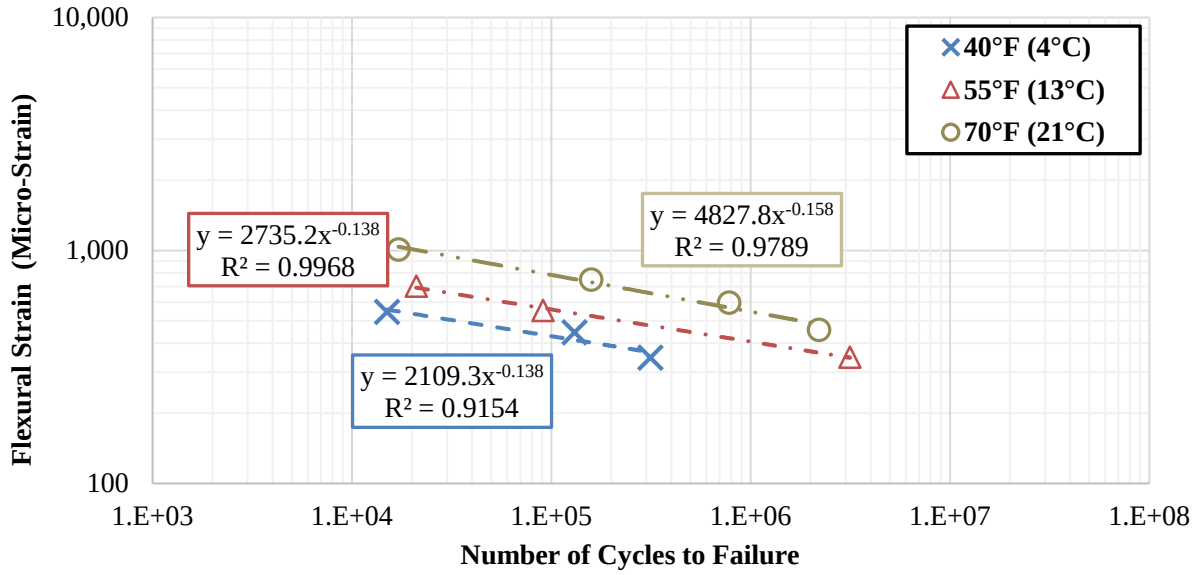


**Figure 7-17. Beam fatigue data at three temperatures of PaveBox_HP AC mix.**

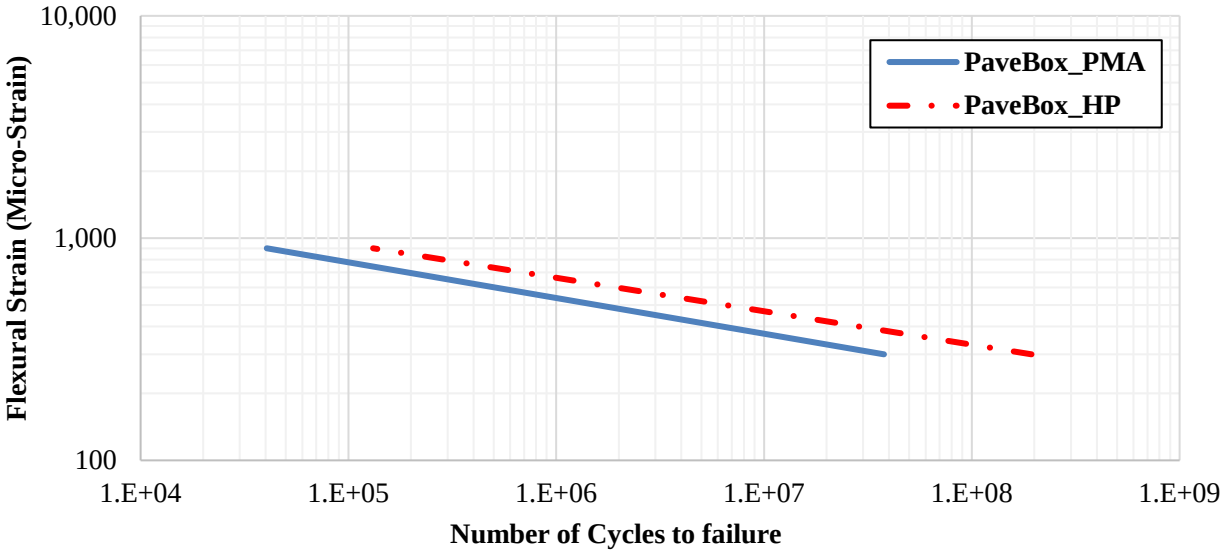


**Figure 7-18. Fatigue relationships of PaveBox_PMA and PaveBox_HP AC mixes at 77°F (25°C).**

**Table 7-9. Summary of Fatigue Model Coefficients for the Two Evaluated AC Mixes.**

| Mix ID | Fatigue Model Coefficients | | |
|---|---|---|---|
| | $k_{f1}$ | $k_{f2}$ | $k_{f3}$ |
| PaveBox_PMA | 1.1973E+01 | 6.2248E+00 | 2.6756E+00 |
| PaveBox_HP | 2.7552E+09 | 6.6407E+00 | 4.3438E+00 |

Rutting

The rutting characteristic of the two AC mixes were evaluated using the RLT setup *(72)*. Mixtures were evaluated at the short-term aging condition. The RLT test was conducted at 104, 122, and 140°F (40, 50, and 60°C). The generalized MEPDG rutting model, expressed in Equation 3-7, was developed for each of the two AC mixes.

Figure 7-19 and Figure 7-20 show the rutting curves for the evaluated PaveBox_PMA and PaveBox_HP AC mixes at the three testing temperatures, respectively. The rutting relationship describes the response of the AC mixture to the repeated loading at a high temperature. A lower relationship indicates lower accumulated permanent strains with loading, thus predicting a better resistance to rutting. Furthermore, a flatter curve indicates a lower susceptibility of the asphalt mix to repeated loading. Overall, the asphalt binder type (i.e., PMA or HP) had an impact on the rutting behavior of the two evaluated AC mixes. The PaveBox_HP AC mix showed a lower and flatter rutting relationship when compared with the corresponding PaveBox_PMA AC mix at all testing temperatures. Thus, indicating a better resistance to rutting and a lower susceptibility of the evaluated HP AC mix to repeated loading. The noticeably better relationship of the HP AC mix can be mainly attributed to the dominant behavior of the additional polymer.

Figure 7-21 shows the rutting relationship of the PaveBox_HP AC mix along with the PaveBox_PMA AC mix at 122°F (50°C). For example, after 10,000 loading repetitions, the resulting cumulative $\varepsilon_p/\varepsilon_r$ of the PaveBox_PMA AC mix was about 2.2 times greater than the value of the PaveBox_HP AC mix.

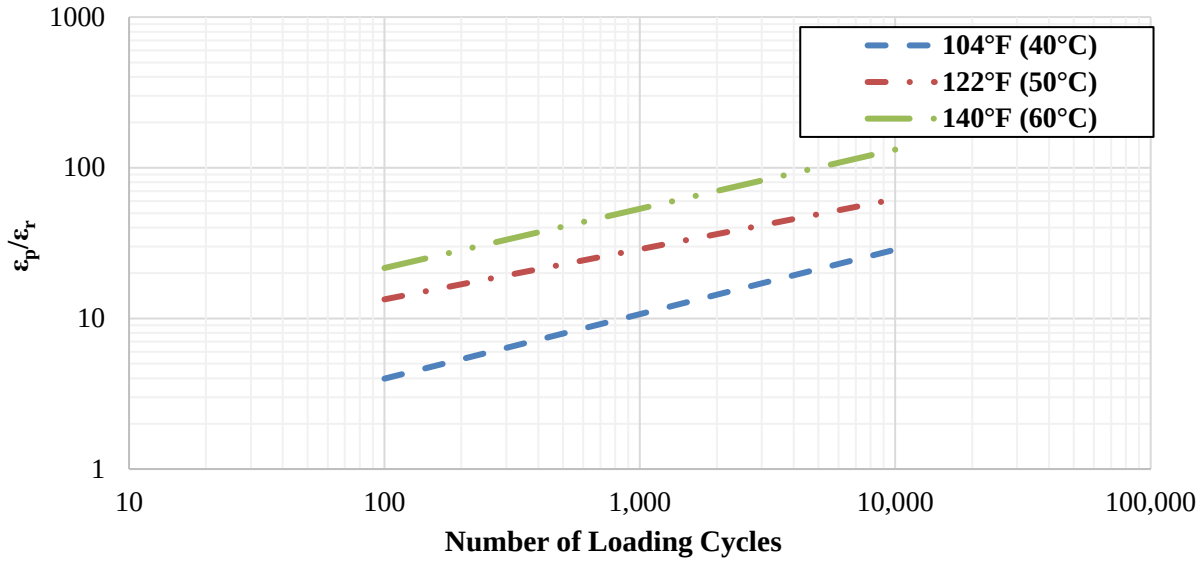


**Figure 7-19. Rutting curves for PaveBox_PMA AC mix.**

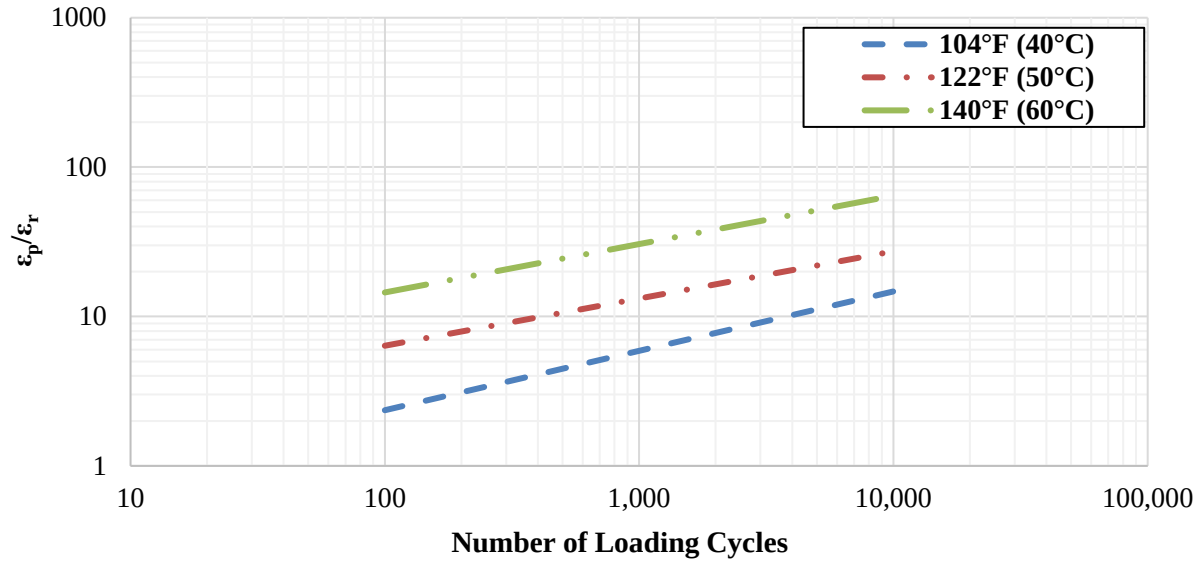


**Figure 7-20. Rutting curves for PaveBox_HP AC mix.**

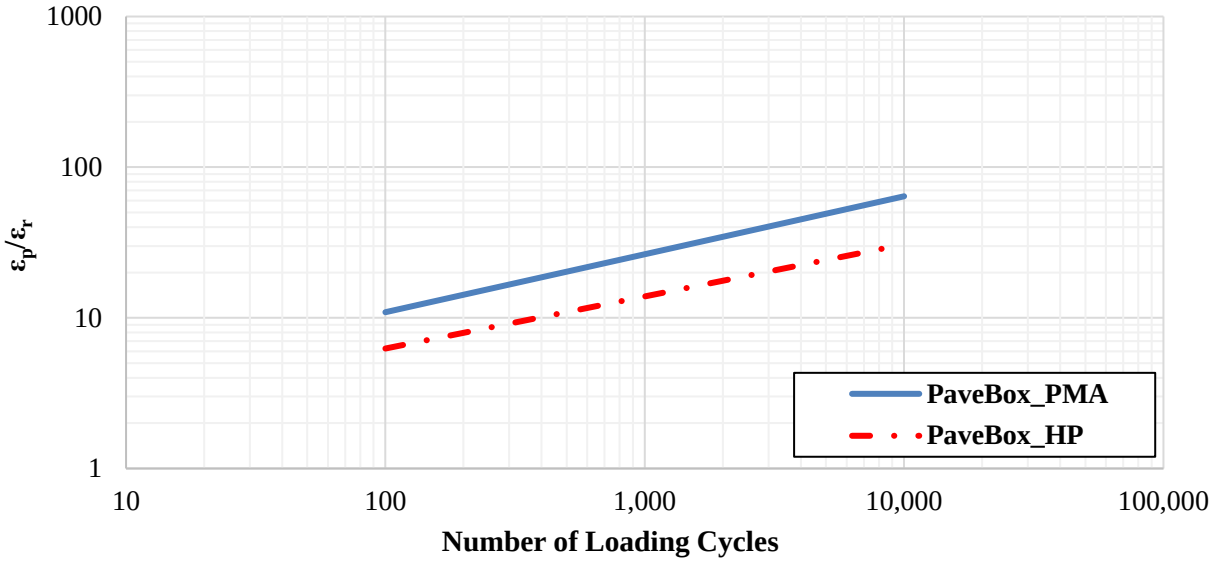


**Figure 7-21. Rutting behavior of PaveBox_PMA and PaveBox_HP AC mixes at 122°F (50°C).**

Table 7-10 summarizes the regression coefficients of the rutting models for the two evaluated AC mixes. It should be noted that, a significant difference in the laboratory rutting resistance will not necessarily translate into the same difference in rutting performance (i.e., rut depth) of the AC layer in the field. Many factors may highly affect the rutting life of an AC pavement such as stiffness, the developed compressive strain in each of the AC sub-layers under field loading, the rutting characteristic of the evaluated asphalt mixture, and the interaction of all these factors. Therefore, a full mechanistic analysis coupled with laboratory measured engineering and

performance properties would be necessary to quantify and effectively evaluate the impact of HP binder on the rutting performance of the corresponding AC pavement.

**Table 7-10. Summary of Rutting Model Coefficients for the Two Evaluated AC Mixes.**

| Mix ID | Rutting Model Coefficients | | |
|---|---|---|---|
| | $k_{r1}$ | $k_{r2}$ | $k_{r3}$ |
| PaveBox_PMA | -10.8922 | 5.3491 | 0.3847 |
| PaveBox_HP | -11.0584 | 5.3505 | 0.3458 |

### 7.2.5. Pavement Structures

The FDOT flexible pavement design manual *(4)* was used to design the PMA pavement structure for the PaveBox experiment. The manual provides guidance for designing new and rehabilitated flexible pavements according to the AASHTO 1993 Guide *(5)*. The accumulated 18-kip (80 kN) ESAL is the traffic load information used for pavement thickness design. A structural coefficient of 0.44 was used for the PMA AC layer and 0.18 was used for the CAB layer. All the properties and characteristics of the used AC and CAB materials were provided in details in Sections 7.2.3 and 7.2.4.

FDOT mandates the use of a 12 inch (305 mm) thick stabilized SG layer. This layer serves as a working platform to permit the efficient construction of the base layer. In this task, a stabilized SG layer was not used in the PaveBox and only a typical SG layer was implemented. This was considered acceptable for the purpose of this task that aimed for a relative comparison of responses between the PMA and HP pavement sections. A material classified as A-2-7(1) was used to build the SG layer in the PaveBox. An $M_R$ value of approximately 6,500 psi (45 MPa) was used for the computation of the pavement section structural number. The representative $M_R$ value (i.e., 6,500 psi) was determined through an iterative process using the 3D-Move calculated stresses in the SG layer at a depth of 18 inches (457 mm) below the top of the SG and the developed Uzan model for the tested SG material (Table 7-2). This approach is consistent with the MEPDG approach employed in the AASHTOWare® Pavement ME software *(5)*. All the properties and characteristics of the employed SG material were provided in details in Section 7.2.2. As mentioned earlier, FDOT uses the AASHTO 1993 design guide and methodology to design pavements for new construction and rehabilitation projects. Equation 1-1 is used to design flexible pavements. More information regarding the design of flexible pavement structures can be found in Section 1.2. The reduced equivalent thickness of the HP AC layer ($H_{AC\text{-}HP}$) is then determined using Equation 7-5 and a structural coefficient of 0.54 as previously determined in Chapter 6. It should be mentioned that the two pavement structures have the same CAB and SG layer thicknesses and material properties. Table 7-11 and Figure 7-22 show the designed pavement sections for the PMA and HP pavement structures.

$$H_{AC-HP} = H_{AC-PMA} \times \left(\frac{0.44}{0.54}\right) \qquad \textbf{Equation 7-5}$$

Where:
$H_{AC-PMA}$ = required thickness of the PMA AC layer, inch; and
$H_{AC-HP}$ = required thickness of the HP AC layer, inch.

**Table 7-11. Pavement Sections for PMA and HP PaveBox Experiments.**

| Layer Type | Design Thickness (inch) | |
|---|---|---|
| | PMA Pavement Section | HP Pavement Section |
| AC Layer | 4.25 | 3.50 |
| CAB Layer | 9.0 | 9.0 |
| SG Layer | 61.0 | 61.0 |

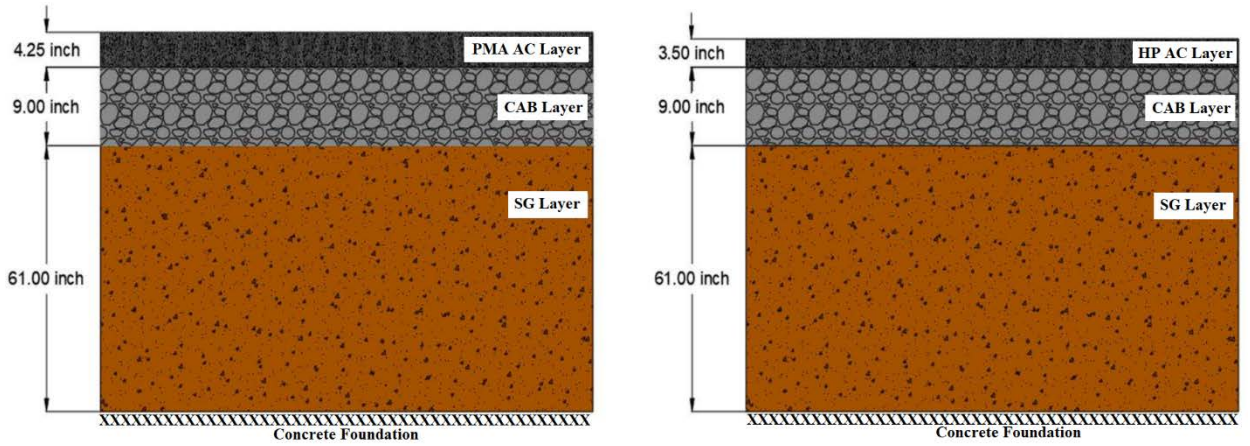


**Figure 7-22. PMA and HP pavement sections in the PaveBox experiments.**

### 7.2.6. Data Acquisition System

A National Instrument (NI) data acquisition system comprises of two 12 slot SCXI-1001 chassis populated with 18 NI SCXI-1320 conditioners were used to acquire the sensor data in the full-scale PaveBox experiments. This 72 data channel system is capable of sampling data at frequencies that range from 1 to 3,000 Hz. Such system is applicable for acquiring data from a wide range of sensors including strain gauges, displacement transducers, load cells, pressure cells, and accelerometers. Data from experiments involving dynamic loading were acquired at 1,024 Hz to accommodate the requirements for double integration algorithm for assessing the displacements. Data from experiments with static loading were acquired at 32 Hz. Once the data was acquired, it was stored locally on the computer hard drive in comma separated values (*CSV*) files that could be imported and utilized by most software packages for data analysis.

### 7.2.7. PaveBox Tests Preparation

*7.2.7.1 SG Deposition in the PaveBox*

The goal was to place the SG material at 11% moisture content and at a 90% $\gamma_{d,max}$ to a depth of 61 inches (155 cm). The SG material was shoveled from the stockpile into five-gallon buckets, placed in a concrete mixer, and mixed for less than a minute (10 to 30 seconds). The moist SG material was then transported and placed via a laboratory-fabricated shoot and distributed within PaveBox area.

A gasoline-powered vibratory plate compactor was used to achieve the required in-place compaction. Three to four passes lasting approximately 5 to 8 minutes each were needed to arrive at a 4-inch (10.2 cm) compacted lift. Nuclear density gauge readings were taken after each lift in the PaveBox, to confirm the required compaction had been reached (90% of $\gamma_{d,max}$). Figure 7-23 and Figure 7-24 show the various construction stages of placing the SG material into the PaveBox.

While nuclear density gauge was used to ensure the target density during the placement of the SG lifts, dynamic cone penetrometer (DCP) testing was also used to assess the density of the SG layer as a function of depth. Two DCP tests, at two different locations, were conducted on the finished SG, after placement of all the SG lifts. Figure 7-25 shows the readings of the two DCP tests. In general, the results indicated similar densities for the SG layer in both locations.

**(a)** **(b)**

**Figure 7-23. SG deposition: (a) soil mixing in the mechanical mixer, and (b) placement of moist soil in PaveBox.**

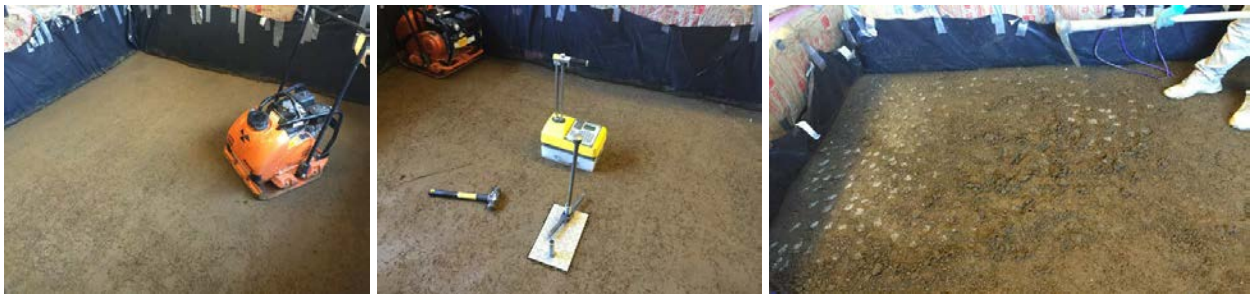

**(a)** **(b)** **(c)**

**Figure 7-24. SG compaction in PaveBox: (a) vibratory plate compactor, (b) nuclear density gauge measurements on top of compacted lift of SG soil, and (c) scarification of the SG lift surface using a pickaxe to ensure bonding between compacted lifts.**

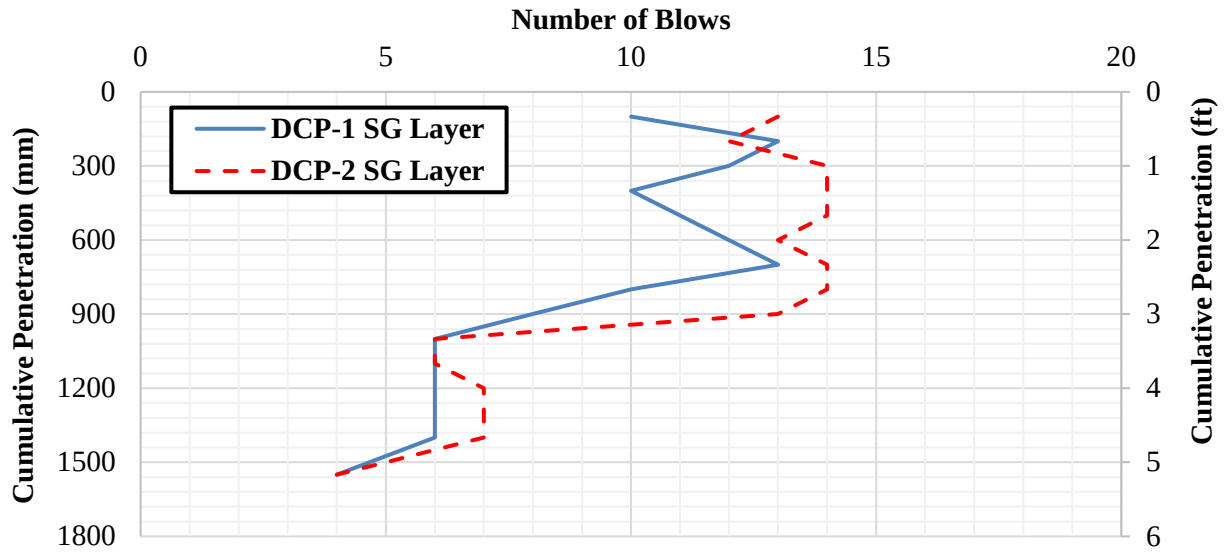


**Figure 7-25. DCP test results for SG layer at two locations in PaveBox.**

*7.2.7.2 CAB Deposition in the PaveBox*

The target in-place moisture content of the CAB material was 8.8% with a target in-place density of 92 to 95% of $\gamma_{d,max}$. The total thickness of the CAB layer was 9 inches (228 mm) constructed in three 3-inch (76 mm) lifts, in a manner similar to the SG material deposition process described in Section 2.7.1. However, the CAB material required more compaction effort to arrive at a 3-inch (76 mm) compacted lift. Nuclear density gauge readings were taken after each lift to confirm the required compaction had been reached.

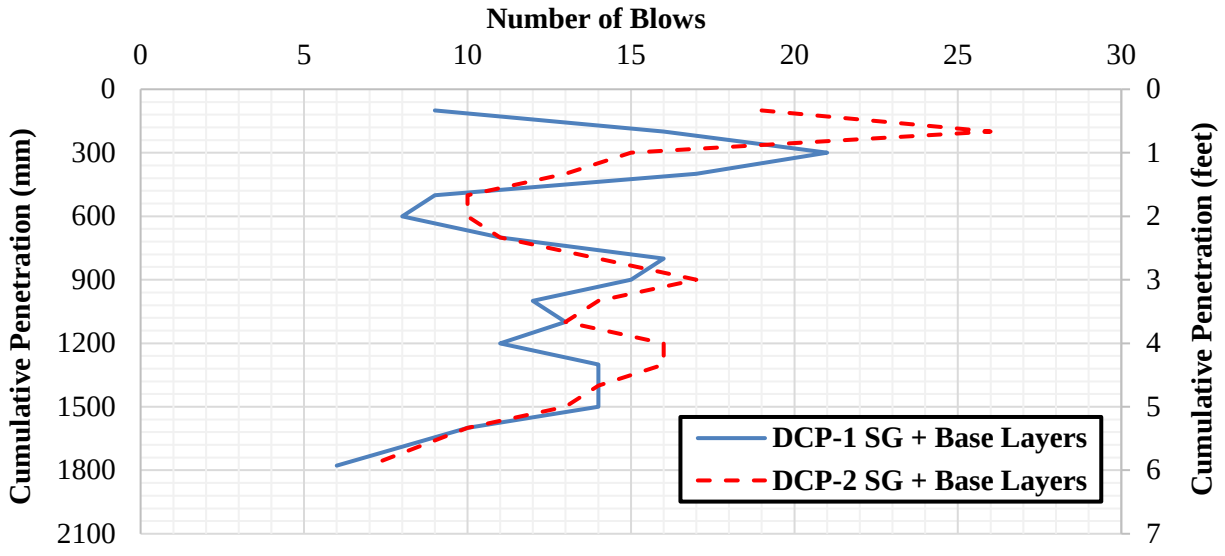


**Figure 7-26. DCP test results for CAB layer at two locations in PaveBox.**

DCP testing was also used to assess the density of the CAB layer as a function of depth. Two DCP tests, at two different locations, were conducted on the finished CAB layer, after placement of all the lifts. Figure 7-26 shows the readings of the two DCP tests. In general, the results showed similar densities for the CAB layer at both locations.

*7.2.7.3 AC Production and Deposition in PaveBox*

The target Both the PMA and HP asphalt mixes for PaveBox experiments were mixed in a half-ton asphalt mixer using asphalt binders sampled from Florida and local aggregates sampled from Nevada. Figure 7-27 shows the asphalt mixer used to produce the AC mixes for the PaveBox experiments. The aggregate stockpiles were sampled, brought to laboratory, and organized into different bins as shown in Figure 7-28. The aggregates are proportioned out of each bin onto a feeder belt according to the percentages given by the mix design. The feeder belt transported the proportioned aggregates to the mixing pug mill. The aggregates were heated in the pug mill at the mixing temperature for a minimum duration of 15 minutes. Approximate temperatures of 325°F (163°C) and 340°F (175°C) were used for the PMA and HP AC mixes, respectively. After drying the aggregates, the heated liquid asphalt binder was added into the pug mill on top of the heated aggregates. The mixing process continued for an additional duration of 15 minutes to ensure uniformity and proper coating of aggregates within the AC mix.

**Figure 7-27. Half-ton asphalt mixer used to mix and produce PMA and HP AC mixes for PaveBox.**

It should be mentioned that the moisture content of every stockpile was measured prior to each experiment and proper adjustments were made for the amount of asphalt binder to be added. The produced AC mix was discharged from the back of the asphalt mixer in a big steel bucket mounted to the front of a forklift. The discharged AC mix was then deposited into the PaveBox for compaction. The temperature of the discharged AC mix was monitored during the entire production process and the mixing temperature was adjusted to maintain the discharge temperatures as close as possible to 325°F (163°C) and 340°F (175°C) for the PMA and HP AC mixes, respectively. It should be mentioned that the asphalt mixer has a maximum capacity of

producing 1,000 lbs (453.6 kg) of ready AC mix within a duration of 30 to 40 minutes. Thus, five batches of AC mixes were needed to for each PaveBox experiment. This produced sufficient materials for both: constructing the full AC layer in the PaveBox and for the laboratory performance evaluation.


**Figure 7-28. Aggregate stockpiles organized and used to produce PMA and HP AC mixes.**

The produced AC mix was placed in 1.0 to 1.5-inch (25 to 38 mm) lifts. The lifts were compacted using a vibratory plate compactor to achieve a target in-place density of 92% to 96%. The produced AC mix was dumped directly into the PaveBox, spread uniformly over the entire area, and leveled to a thickness of approximately 2.5 inch (63.5 mm) of uncompacted material. A vibratory plate was then used for compaction of the lift by applying it around the perimeter of the PaveBox from the outside edge to the inside for better compaction. Upon achieving an acceptable compaction on the first lift, the same process was repeated for the second lift. A thin lift nuclear density gauge was used at several locations around the surface of the box to measure the in-place density of the compacted AC surface layer.

Loose AC mixtures were sampled into 5-gallon steel pails during placement of the material in PaveBox. These materials were brought to the laboratory and were tested for $G_{mm}$, $E^*$ property, and resistance to fatigue cracking and rutting. The results of the laboratory evaluation of the produced AC mixes were presented in Section 7.2.4.4.

The loading of the pavement structure was conducted 5-7 days after the placement of the AC layer. Cores were taken immediately after the completion of each of the experiments. Cores were used to measure the as-constructed AC layer thickness and in-place density. It should be noted that the laboratory specimens were compacted to a target density similar to the as-constructed density.

### 7.2.8. Loading Protocol and Instrumentation

A hydraulic ram capable of delivering 60,000 lb (267 kN) was used to apply the dynamic surface loads. The ram was modified by attaching a Moog-252 spool valve that can be electronically

controlled to provide the required flow to the ram to achieve the target dynamic load with the target pulse duration. The system was connected to a hydraulic pump along with accumulators to ensure adequate flow of hydraulic fluid necessary for the repeated cycles of loading. The ram was mounted onto a stiff horizontal steel beam connected between two vertical steel columns that comprised the reaction frame.

A computer running a real time operating system was connected to a National Instrument (NI) 4-slot SCXI-1001 chassis populated with two NI SCXI-1320 conditioners that were used to control the servo valve. A 100,000 lb (45 kN) interface pancake-type load cell along with a string pot were attached to the ram, which in turn were electronically connected to the controller. The controller design was a proportional-integral-derivative (PID) controller. This control loop feedback mechanism was used to control the ram in either force or displacement control mode depending on the mode selected for testing. Careful calibration of the gain was essential to ensure the proper operation of the entire loading system.

An FWD loading plate with 11.9 inch (300 mm) diameter (Figure 7-29) was used to apply the dynamic loads on top of the pavement structure to better simulate actual tire loading conditions. The ratio of the PaveBox dimensions to the diameter of the loading plate was deemed sufficient to minimize the interference from the PaveBox boundaries.

**Figure 7-29. Top view of the FWD loading plate used for dynamic loading.**

Various sensors were used in the experiments to capture the response of the pavement structure to surface loading. Non-vibrating wire TEPC (P) were used to measure the total vertical stresses at different locations within the domain. These cells were 4 inch (101.6 mm) in diameter with capacities that ranged between 36 psi (248 kPa) and 362 psi (2,496 kPa). LVDTs with a range between 0 and 4 inch (102 mm) were used to capture pavement surface deflections. Embedded strain gauges were also used to capture the tensile strain at the bottom of the AC layer under dynamic loadings.

*7.2.8.1 Experiment No. 1: PaveBox_PMA*

In this experiment, a full pavement structure was constructed with a total thickness of 74 inches (1,880 mm). The pavement structure consisted of 4.3 inch (109 mm) of PMA AC on top of 9 inch (229 mm) of CAB and 61 inch (1,550 mm) of SG. The dynamic loading was applied on top of the AC surface layer. In experiment No.1, the pavement structure was subjected to repeated dynamic loads with amplitudes between 6,000 and 16,000 lbs (27 and 71 kN). Twenty-five cycles were applied at each incremental dynamic load with a pulse duration of 0.1 sec followed by a rest period of 0.9 sec in each loading cycle. The pavement structure was subjected to a series of four loading levels with a sequentially higher load amplitudes. Table 7-12 summarizes the loading protocol for experiment No.1. All loads were applied on the loading plate positioned directly at the top of the AC layer and at the center of the PaveBox.

**Table 7-12. Loading Protocol for Experiment No.1 (PaveBox_PMA).**

| Load Type | Target Load Amplitude (lb) | No. of Loading Cycles | Load Plate Diameter (inch) | Rest Period Between Load Levels (min) |
|---|---|---|---|---|
| Dynamic load (0.1 sec. loading + 0.9 sec. rest period) | 6,000 | 25 | 11.9 (FWD loading plate) | 2 |
| Dynamic load (0.1 sec. loading + 0.9 sec. rest period) | 9,000 | 25 | 11.9 (FWD loading plate) | 2 |
| Dynamic load (0.1 sec. loading + 0.9 sec. rest period) | 12,000 | 25 | 11.9 (FWD loading plate) | 2 |
| Dynamic load (0.1 sec. loading + 0.9 sec. rest period) | 16,000 | 25 | 11.9 (FWD loading plate) | 2 |

The instrumentation for the pavement structure consisted of surface LVDTs installed diagonally to measure surface deflections at various radial distances of 0, 8, 12, 24, 36, 48, and 60 inch (0, 203, 305, 610, 914, 1,219, and 1,524 mm) from the center of the load. The moving tips of the surface LVDTs rested on top of the AC layer. Figure 7-30 shows the drawing of the experiment No.1 setup (PaveBox_PMA) at the top of the AC layer at an elevation (z) of 74 inches (188 cm) from the PaveBox floor. Ten 4-inch (101 mm) pressure cells were placed at three different locations: in the middle of the base—z = 65.5 inch (z = 166.4 cm), at 6 inch (15.2 cm) below the SG surface—z = 56.0 inch (z = 142.2 cm), and at 24 inches (61.0 cm) below the SG surface—z = 42 inch (z = 106.7 cm). These cells were located directly under the center of the loading plate and diagonally at each of the depth levels at various locations. At the first level (middle of the CAB layer), there were four sensors (refer to Figure 7-31), and at the second level, 6 inches (15.2 cm) below the SG surface, there were four sensors (refer to Figure 7-33). At the bottom level, 24 inches (61.0 cm) below the SG surface, there were two sensors (refer to Figure 7-34). The sensors were installed after compacting the SG and CAB to the level of the instruments. The pressure cells were then placed carefully on a leveled surface created by a thin layer of compacted fine material to ensure full contact with the cell and to facilitate a better bearing surface. After placement of the sensor, additional fine material was placed carefully on top of the cell and compacted by hand using a steel tamper plate to avoid any horizontal or vertical shifting of the measuring instrument.

AC strain gauges were also placed at the bottom of the AC layer to capture the strains of the pavement under dynamic loadings. A small amount of asphalt binder was placed over the CAB to ensure a proper support for the strain gauge and a good bond between the strain gauge and the AC layer. Asphalt mixture was then sieved through sieve No. 4 and placed in a thin layer on top of the strain gauge. Figure 7-35 shows a sketch of the pavement structure along with the installed instruments at different levels within the pavement structure. More details regarding the instrumentation plan for experiment No.1 (PaveBox_PMA) are available in Table 7-13. Figure 7-35 shows a picture after placement of all pavement layers and instruments.

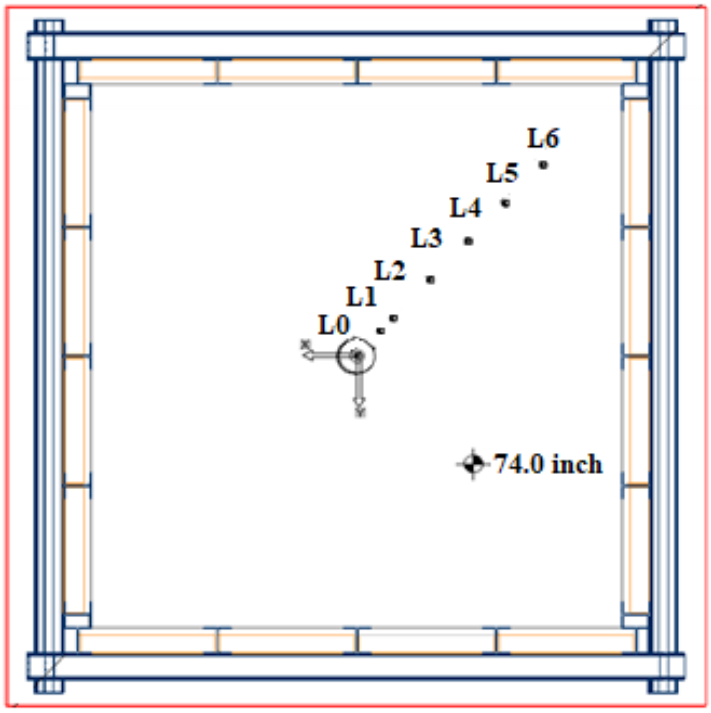


Note: L = LVDT.

**Figure 7-30. Plan view for PaveBox_PMA experiment No.1 at the AC surface.**

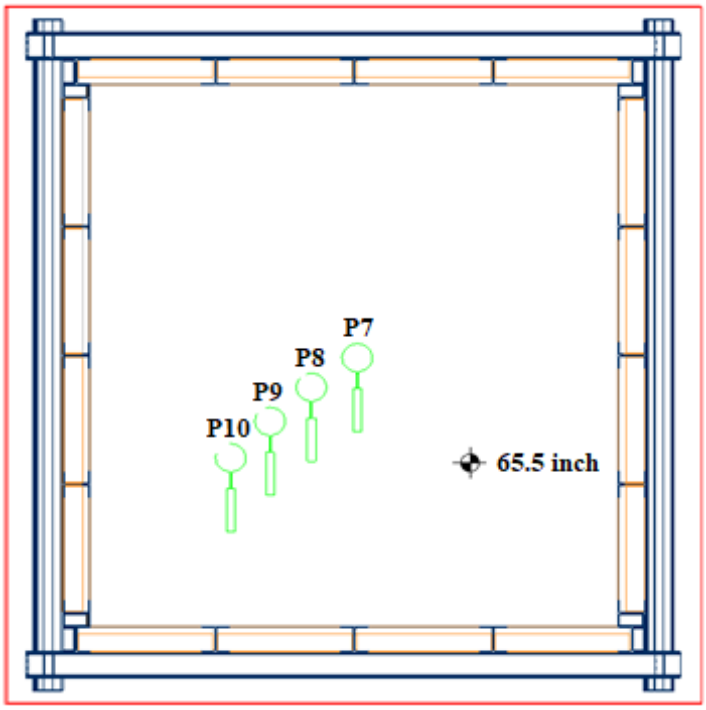


Note: P = TEPC.

**Figure 7-31. Section view for PaveBox_PMA experiment No.1 at the middle of CAB layer.**

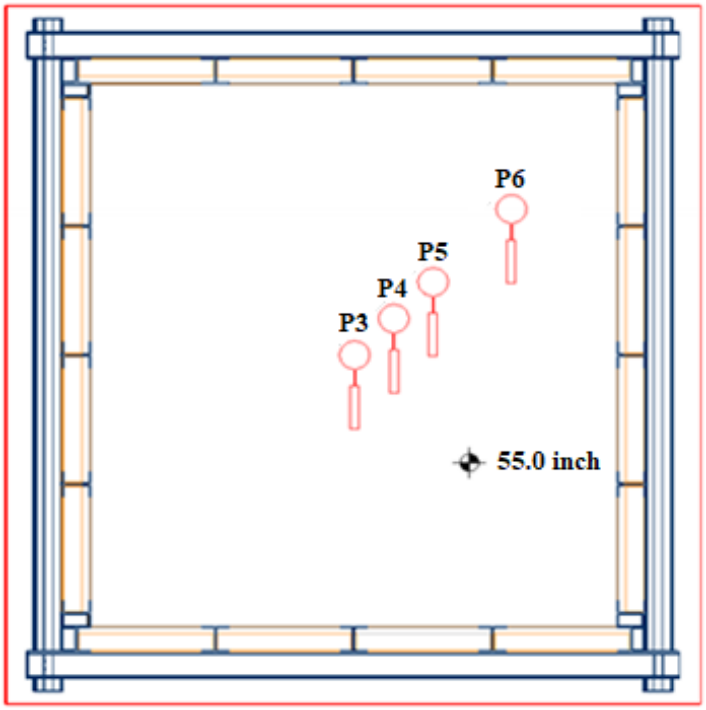


**Figure 7-32. Section view for PaveBox_PMA experiment No.1 at 6 inch below the top of SG.**

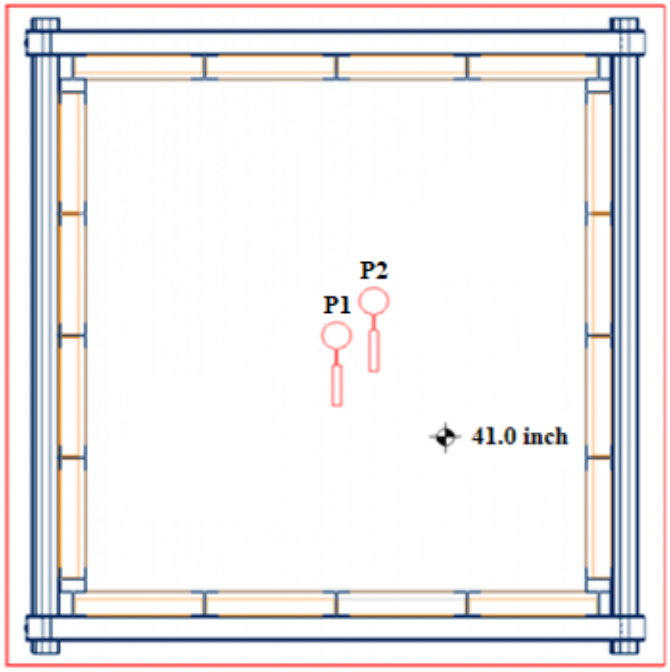


Note: P = TEPC.

**Figure 7-33. Section view for PaveBox_PMA experiment No.1 at 24 inch below the top of SG.**

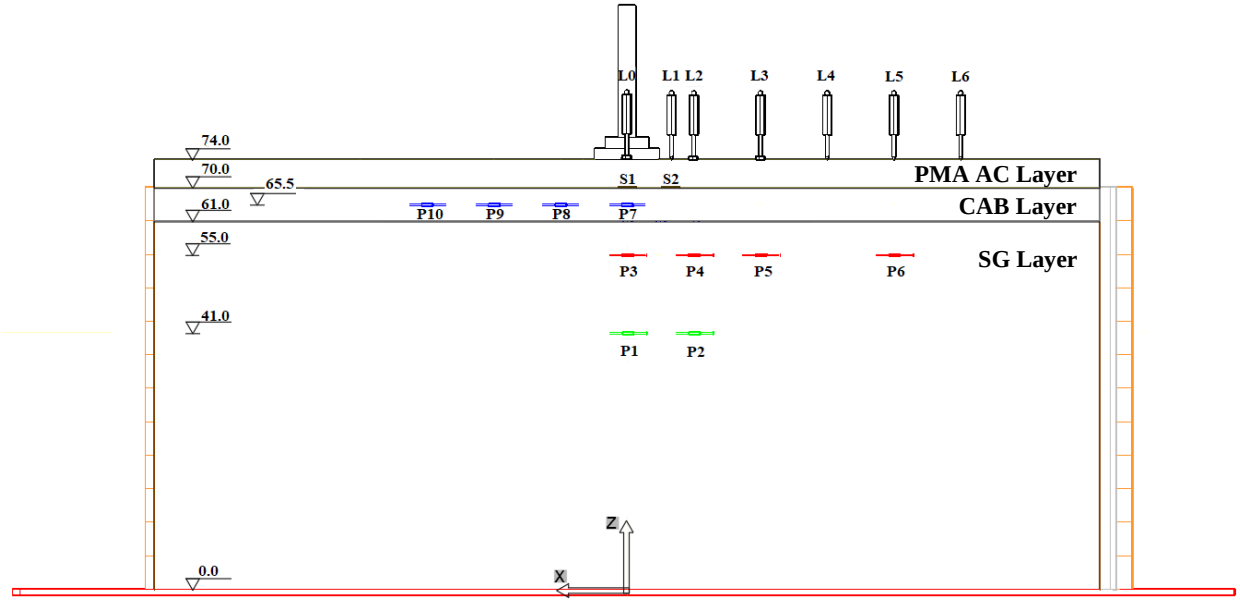


Note: L = LVDT.
P = TEPC,
S = strain gauge.

**Figure 7-34. Section view for PaveBox_PMA experiment No.1 at 24 inch below the top of SG.**

**Table 7-13. Details of Instrumentation Plan for Experiment No.1.**

| No. | Tag | Radial Distance (inch) | Angle (°) | Depth (inch) | X (inch) | Y (inch) | Z (inch) | Notes |
|---|---|---|---|---|---|---|---|---|
| 1 | L0 | 0.0 | 0.0 | 0.0 | 0.0 | 0.0 | 74.3 | LVDT |
| 2 | L1 | 8.0 | 228.0 | 0.0 | −5.3 | −6.0 | 74.3 | LVDT |
| 3 | L2 | 12.0 | 228.0 | 0.0 | −8.0 | −9.0 | 74.3 | LVDT |
| 4 | L3 | 24.0 | 228.0 | 0.0 | −15.9 | −17.9 | 74.3 | LVDT |
| 5 | L4 | 36.0 | 228.0 | 0.0 | −23.9 | −26.9 | 74.3 | LVDT |
| 6 | L5 | 48.0 | 228.0 | 0.0 | −31.9 | −35.9 | 74.3 | LVDT |
| 7 | L6 | 60.0 | 228.0 | 0.0 | −39.9 | −44.8 | 74.3 | LVDT |
| 8 | P1 | 0.0 | 0.0 | 37.3 | 0.0 | 0.0 | 65.5 | Pressure Cell |
| 9 | P2 | 12.0 | 48.0 | 37.3 | 8.0 | 9.0 | 65.5 | Pressure Cell |
| 10 | P3 | 0.0 | 0.0 | 19.3 | 0.0 | 0.0 | 65.5 | Pressure Cell |
| 11 | P4 | 12.0 | 48.0 | 19.3 | 8.0 | 9.0 | 65.5 | Pressure Cell |
| 12 | P5 | 24.0 | 48.0 | 19.3 | 15.9 | 17.9 | 55.0 | Pressure Cell |
| 13 | P6 | 48.0 | 48.0 | 19.3 | 23.9 | 26.9 | 55.0 | Pressure Cell |
| 14 | P7 | 0.0 | 0.0 | 8.8 | 0.0 | 0.0 | 55.0 | Pressure Cell |
| 15 | P8 | 12.0 | 228.0 | 8.8 | −8.0 | −9.0 | 55.0 | Pressure Cell |
| 16 | P9 | 24.0 | 228.0 | 8.8 | −15.9 | −17.9 | 41.0 | Pressure Cell |
| 17 | P10 | 36.0 | 228.0 | 8.8 | −23.9 | −26.9 | 41.0 | Pressure Cell |
| 18 | S1 | 0.0 | 0.0 | 4.3 | 0.0 | 0.0 | 70.0 | Strain Gauge |
| 19 | S2 | 8.0 | 228.0 | 4.3 | −5.3 | −6.0 | 70.0 | Strain Gauge |

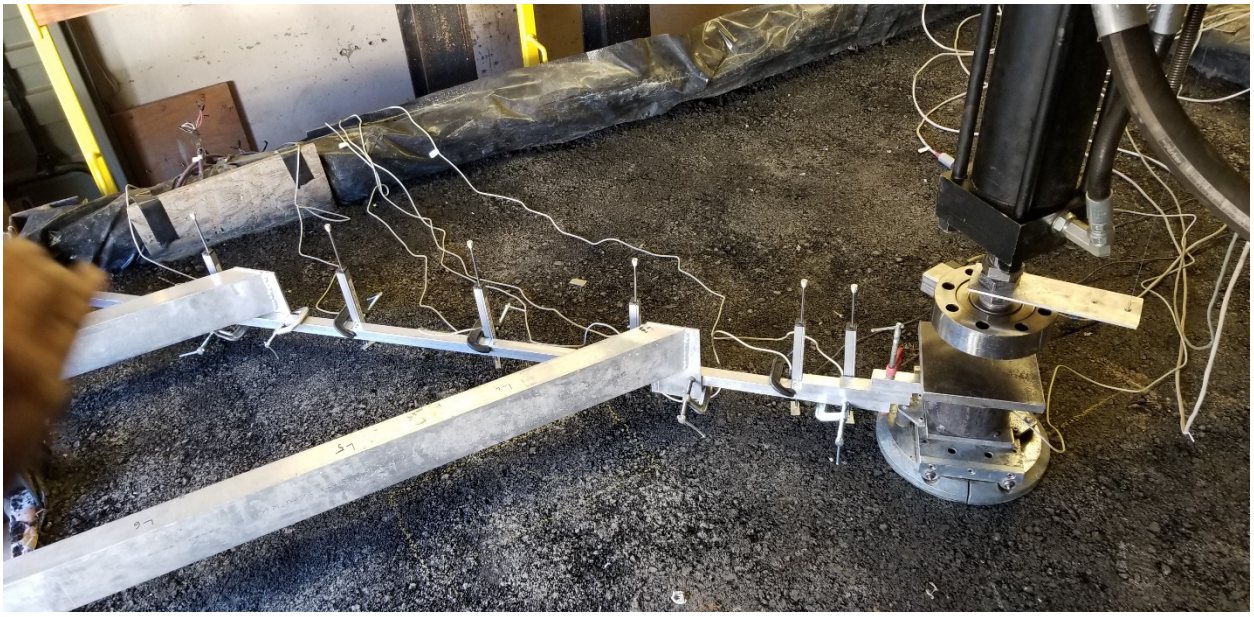

**Figure 7-35. Completed full-scale PaveBox test setup for experiment No. 1.**

*7.2.8.2 Experiment No. 2: PaveBox_HP*

In this experiment, a full pavement structure was constructed with a total thickness of 73.25 inch (186 cm). The pavement structure consisted of 3.5 inch (89 mm) of HP AC on top of 9.0 inch (229 mm) of CAB and 61.0 inch (1,550 mm) of SG. The loading protocol followed for experiment No. 2 (PaveBox_HP) was the same as the one followed for experiment No. 1 (PaveBox_PMA) (refer to Table 7-12). All loads were applied on the loading plate positioned directly at the top of the AC layer and at the center of the PaveBox.

The same instrumentations configurations followed for experiment No.1 (PaveBox_PMA) were also followed for experiment No. 2 (PaveBox_HP). The only difference remains that the HP AC layer in experiment No. 2 was 19% thinner than the PMA AC layer in experiment No. 1. More details regarding the instrumentation plan for experiment No. 2 (PaveBox_HP) are available in Table 7-14.

**Table 7-14. Details of Instrumentation Plan for Experiment No. 2.**

| No. | Tag | Radial Distance (inch) | Angle (°) | Depth (inch) | X (inch) | Y (inch) | Z (inch) | Notes |
|---|---|---|---|---|---|---|---|---|
| 1 | L0 | 0.0 | 0.0 | 0.0 | 0.0 | 0.0 | 73.5 | LVDT |
| 2 | L1 | 8.0 | 228.0 | 0.0 | −5.3 | −6.0 | 73.5 | LVDT |
| 3 | L2 | 12.0 | 228.0 | 0.0 | −8.0 | −9.0 | 73.5 | LVDT |
| 4 | L3 | 24.0 | 228.0 | 0.0 | −15.9 | −17.9 | 73.5 | LVDT |
| 5 | L4 | 36.0 | 228.0 | 0.0 | −23.9 | −26.9 | 73.5 | LVDT |
| 6 | L5 | 48.0 | 228.0 | 0.0 | −31.9 | −35.9 | 73.5 | LVDT |
| 7 | L6 | 60.0 | 228.0 | 0.0 | −39.9 | −44.8 | 73.5 | LVDT |
| 8 | P1 | 0.0 | 0.0 | 36.5 | 0.0 | 0.0 | 65.5 | Pressure Cell |
| 9 | P2 | 12.0 | 48.0 | 36.5 | 8.0 | 9.0 | 65.5 | Pressure Cell |
| 10 | P3 | 0.0 | 0.0 | 18.5 | 0.0 | 0.0 | 65.5 | Pressure Cell |
| 11 | P4 | 12.0 | 48.0 | 18.5 | 8.0 | 9.0 | 65.5 | Pressure Cell |
| 12 | P5 | 24.0 | 48.0 | 18.5 | 15.9 | 17.9 | 55.0 | Pressure Cell |
| 13 | P6 | 48.0 | 48.0 | 18.5 | 23.9 | 26.9 | 55.0 | Pressure Cell |
| 14 | P7 | 0.0 | 0.0 | 8.0 | 0.0 | 0.0 | 55.0 | Pressure Cell |
| 15 | P8 | 12.0 | 228.0 | 8.0 | −8.0 | −9.0 | 55.0 | Pressure Cell |
| 16 | P9 | 24.0 | 228.0 | 8.0 | −15.9 | −17.9 | 41.0 | Pressure Cell |
| 17 | P10 | 36.0 | 228.0 | 8.0 | −23.9 | −26.9 | 41.0 | Pressure Cell |
| 18 | S1 | 0.0 | 0.0 | 3.5 | 0.0 | 0.0 | 70.0 | Strain Gauge |
| 19 | S2 | 8.0 | 228.0 | 3.5 | −5.3 | −6.0 | 70.0 | Strain Gauge |

## 7.2.9. Loading Protocol and Instrumentation

Field core samples from each experiment were collected after completing testing of the pavement structures. Figure 7-36 shows the locations of the cores sampled from experiments No.1 and No.2. As noticed, the cores were sampled from different locations near and far from the loading area to account for all possible variabilities of the thickness and in-place density of the corresponding AC layer. The core samples were used to measure the as-constructed thickness and air voids of the PMA and HP AC layers. Figure 7-37 shows photos of core samples taken

from the PMA and HP AC layers. The photos clearly highlight the difference in the thickness of the AC layer between the two experiments (PaveBox_PMA and PaveBox_HP). Table 7-15 summarizes the measured in-place thicknesses and air voids for the various collected field core samples from each experiment. For both experiments, the designed and as-constructed thicknesses were similar and consistent throughout the entire AC layer. In addition, the in-place air voids for experiment No. 1 (PaveBox_PMA) and experiment No. 2 (PaveBox_HP) were within the desired air voids levels of 8±1%. The HP AC layer showed a slightly lower air voids level when compared with the PMA one.

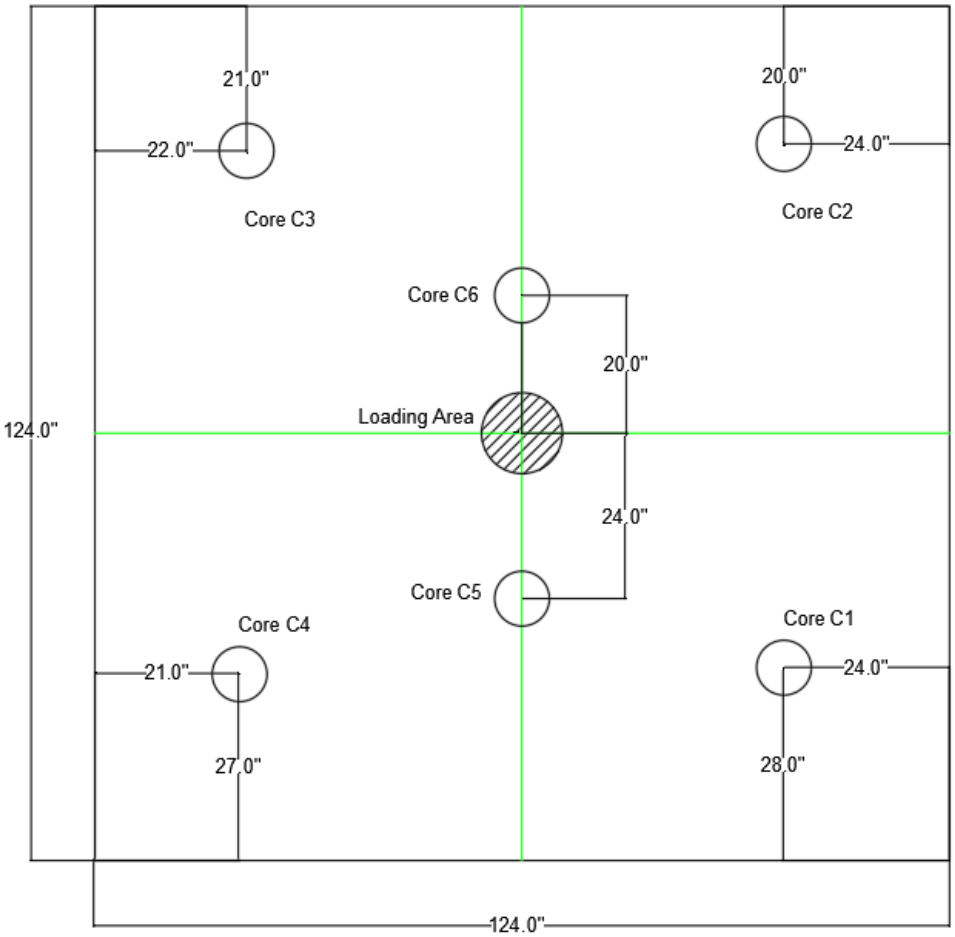


**Figure 7-36. Diagram showing the locations of the cores sampled from both experiments.**

**Table 7-15. As-Constructed AC Layer Thicknesses and Air Voids.**

| AC Layer Type | As-Constructed Layer Thickness (inch) | | | As-Constructed Air Voids (%) | |
|---|---|---|---|---|---|
| | Average | Target | 95% Confidence Interval | Average | 95% Confidence Interval |
| PMA (Experiment No. 1) | 4.30 | 4.25 | 0.19 | 8.1 | 1.3 |
| HP (Experiment No. 2) | 3.47 | 3.50 | 0.18 | 7.5 | 0.4 |

**(a)** **(b)**

**Figure 7-37. (a) PMA AC core sample from experiment No. 1, and (b) HP AC core sample from experiment No. 2.**

## 7.3. ANALYSIS OF MEASURED PAVEMENT RESPONSES

This section summarizes the measured pavement responses from each of the two PaveBox experiments. It also presents a comparison analysis for the measured pavement responses in the PMA and HP pavement structures (referred to as analysis I in Figure 7-1). First, the steps undertaken to preprocess the recordings from the various instruments are presented. Then the analysis of the preprocessed data from the instruments in the various pavement layers is presented and discussed.

### 7.3.1. Preprocessing

As mentioned earlier, the testing program for both experiments (i.e., experiment No. 1 PaveBox_PMA, and experiment No. 2 PaveBox_HP) involved a series of instruments. This included LVDTs, pressure cells, and strain gauges to measure vertical displacements, vertical stresses, and tensile strains at the installed locations, respectively.

The following preprocessing steps were undertaken for all recordings to identify and separate the appropriate load-induced response signals from the recorded data:

- Selection of the five representative consecutive cycles of loading: these cycles are selected after the application of the pulse load has been repeated many times (up to about 20 cycles).
- Removal of the noise: subtracting the average of the recorded measurements prior to the application of impulse load from all measurements.

- Computation of the magnitude of the load-induced responses at each instrumented location.

Figure 7-38 through Figure 7-41 show, as an example, preprocessed measured recordings at the center of the applied dynamic load of 16,000 lb for the load cell, the surface LVDT, the TEPC in the middle of the CAB layer, and the strain gauge at the bottom of the AC layer. By visually observing the data for 16,000 lb in Figure 7-38 to Figure 7-41, it can be inferred that the reduced thickness of the HP AC layer resulted in an increase in both, the center surface deflection and the vertical stress in the middle of the CAB layer. However, a lower tensile strain at the bottom of the AC layer under 16,000 lb was observed in the PaveBox_HP when compared to the PaveBox_PMA. Under the lower applied surface load levels (i.e., 6,000 to 12,000 lb), the measured tensile strain at the bottom of the HP AC layer was in general comparable to the corresponding strain measured at the bottom of the PMA AC layer.

While similar characteristics were observed for the recorded signals from the load cell, LVDTs, and TEPCs, the load-induced strain data recorded in the PaveBox_HP exhibited a different shape than the one observed in the PaveBox_PMA. In particular, the stain data recorded in the PaveBox_HP did not show a time strain recovery during the rest (i.e., unloading) period of the surface dynamic load. This same behavior was observed under all levels of surface load. It was also noted that the magnitude of the initial strain at the beginning of the PaveBox_HP experiment and before the application of the loading sequences was much higher than the one observed in the PaveBox_PMA experiment (around 500 microstrain compared to 100 microstrain).

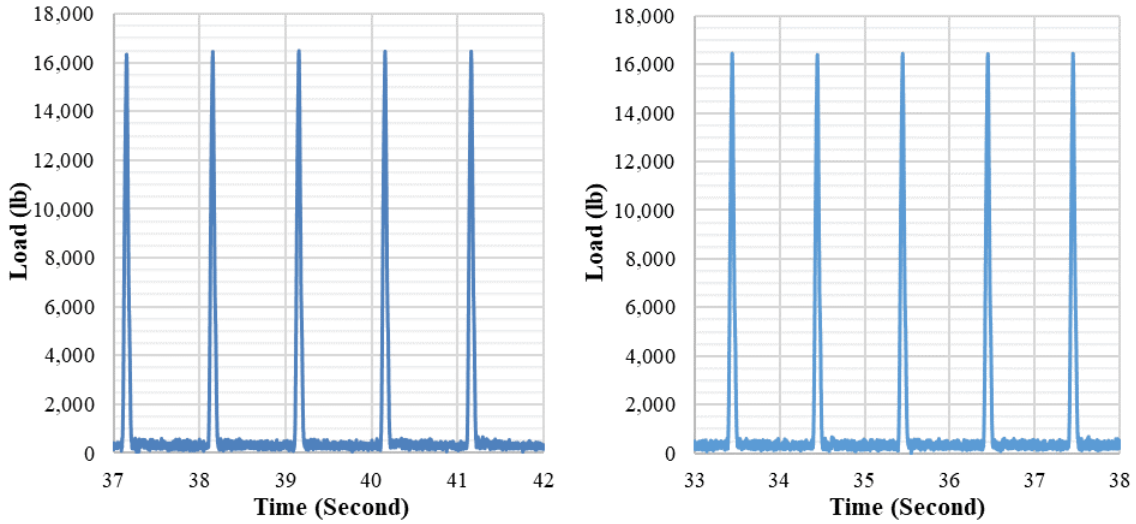


**Figure 7-38. Preprocessed recordings by load cell at a target load level of 16,000 lb: (a) PaveBox_PMA; and (b) PaveBox_HP.**

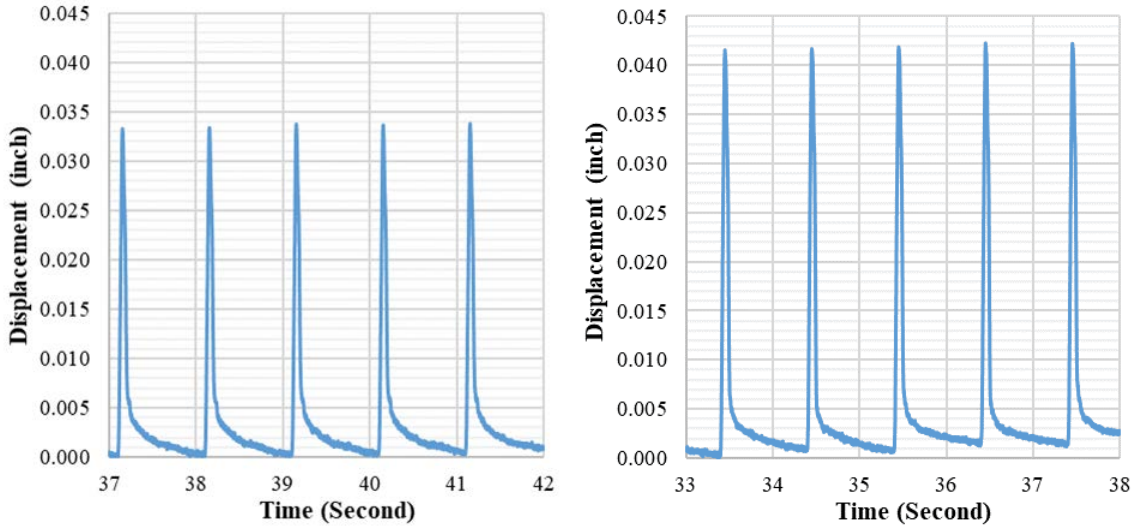


**(a)** **(b)**

**Figure 7-39. Preprocessed recordings by LVDT L0 at a target load level of 16,000 lb: (a) PaveBox_PMA; and (b) PaveBox_HP.**

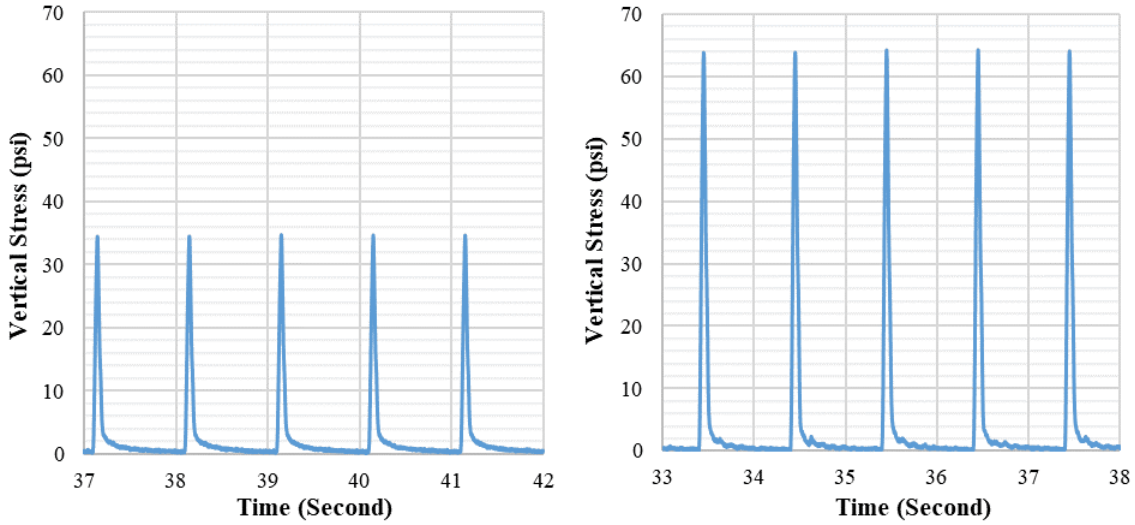


**(a)** **(b)**

**Figure 7-40. Preprocessed recordings by TEPC P7 at a target load level of 16,000 lb: (a) PaveBox_PMA; and (b) PaveBox_HP.**

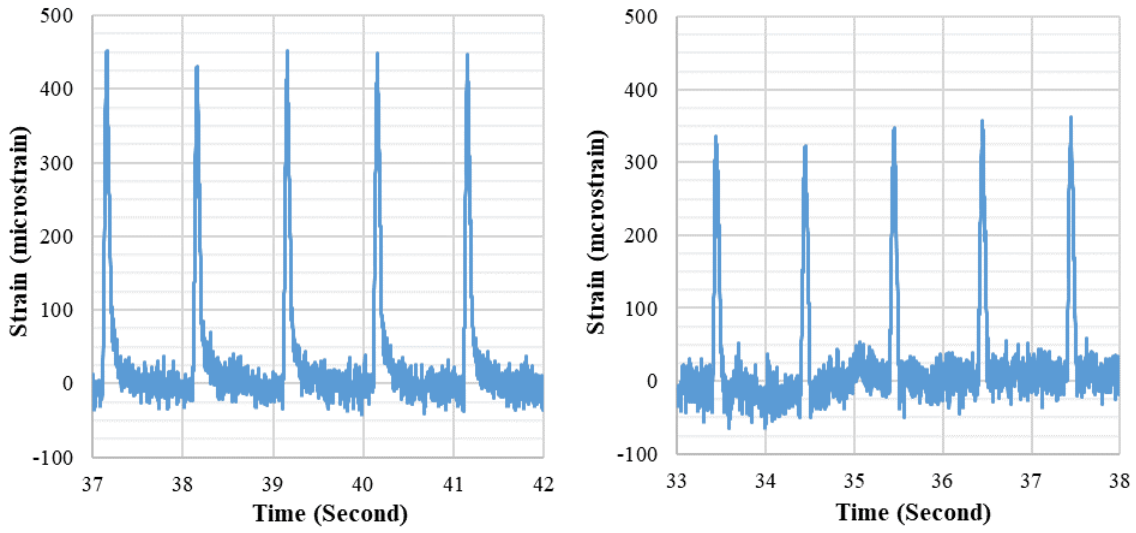


**(a)** **(b)**

**Figure 7-41. Preprocessed recordings by strain gauge S1 at a target load level of 16,000 lb: (a) PaveBox_PMA; and (b) PaveBox_HP.**

While the analysis focus was on the load-induced strain value (calculated as the difference between the initial strain and the peak strain value), it was not clear if the difference in the observed shape of the load-induced-strain is reflecting a true material behavior or it is a result of the high initial strain value, or a combination of the aforementioned. Thus, a certain degree of caution should be exercised when analyzing and comparing the measured strain data from the two PaveBox experiments.

### 7.3.2. Vertical Surface Deflections

The LVDT measurements for the vertical surface deflections on top of the PMA and HP AC layers as a function of surface load levels are presented in Figure 7-42 and Figure 7-43, respectively. Figure 7-45 to Figure 7-50 show, for each of the surface LVDTs (i.e., L0 through L6), the measured vertical surface deflections in the PaveBox_PMA and PaveBox_HP experiments as a function of surface load levels. Table 7-16 and Table 7-17 summarize the vertical surface deflections measured in experiment No. 1 and experiment No. 2, respectively. Based on the presented data, the following observations can be made:

- As expected, higher vertical surface deflections were observed in both experiments at the middle of the loading plate. The vertical surface deflections decreased with the increase in the radial distance from the center of the loading plate. It should be noted that the vertical surface deflections were minimal at the radial distance of 60 inches (152 cm).
- Regardless of the applied load level, a higher vertical surface deflection at the middle of the loading plate (i.e., L0) was observed in the case of the HP AC layer when compared with the PMA AC layer. This is demonstrated with vertical surface deflection measurements in the PaveBox_HP that are 22 to 76% higher than those observed in the PaveBox_PMA.

- In general, the vertical surface deflections were similar in the PaveBox_PMA and PaveBox_HP experiments at radial distances greater than 8 inches.
- Flatter deflection–load curves were observed at radial distances farther away from the load indicating less sensitivity of the measured vertical deflections to the magnitude of the applied surface load.

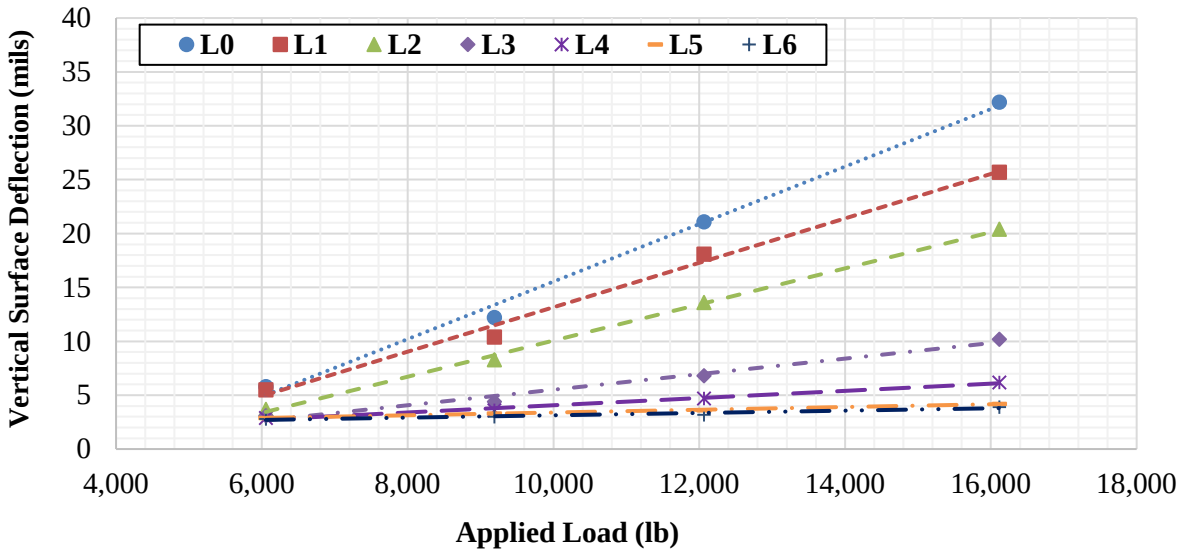


**Figure 7-42. Measured vertical surface deflections as a function of applied surface loads (experiment No. 1: PaveBox_PMA).**

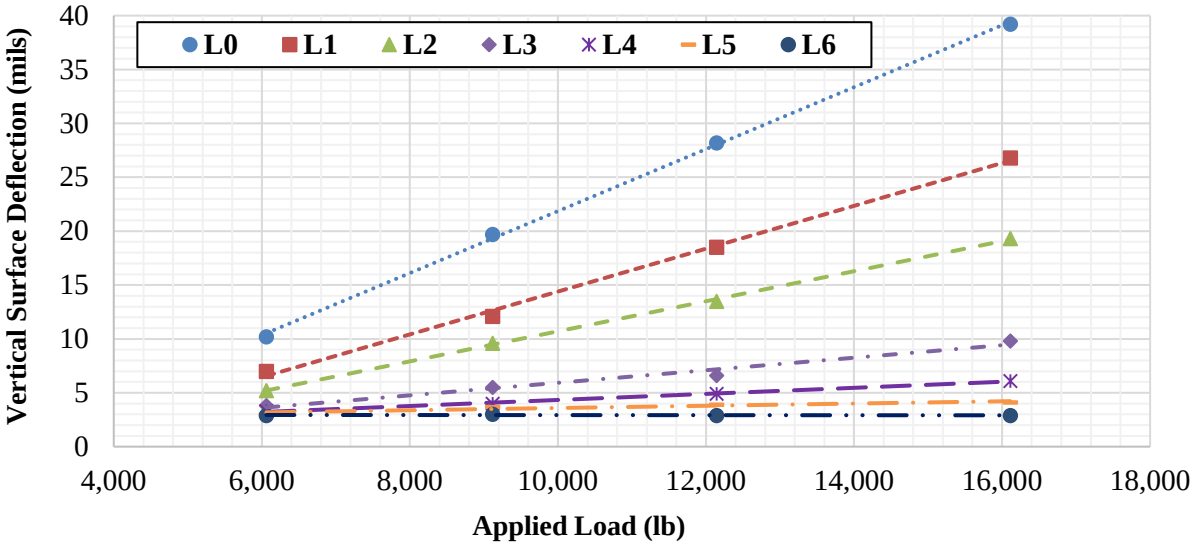


**Figure 7-43. Measured vertical surface deflections as a function of applied surface loads (experiment No. 2: PaveBox_HP).**

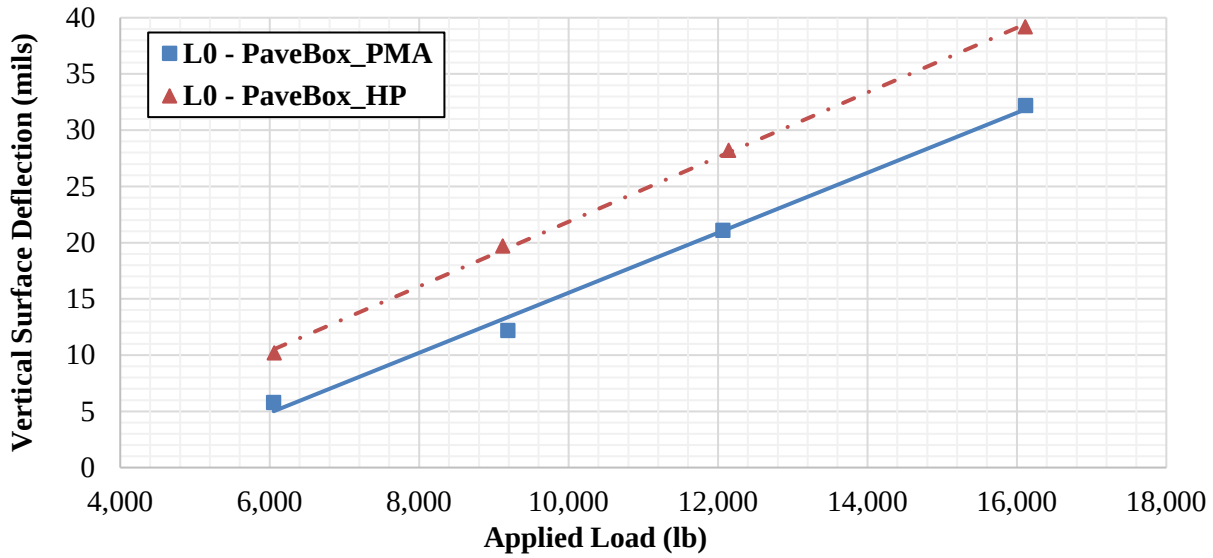


**Figure 7-44. Measured vertical surface deflections at the center of the loading plate (L0).**

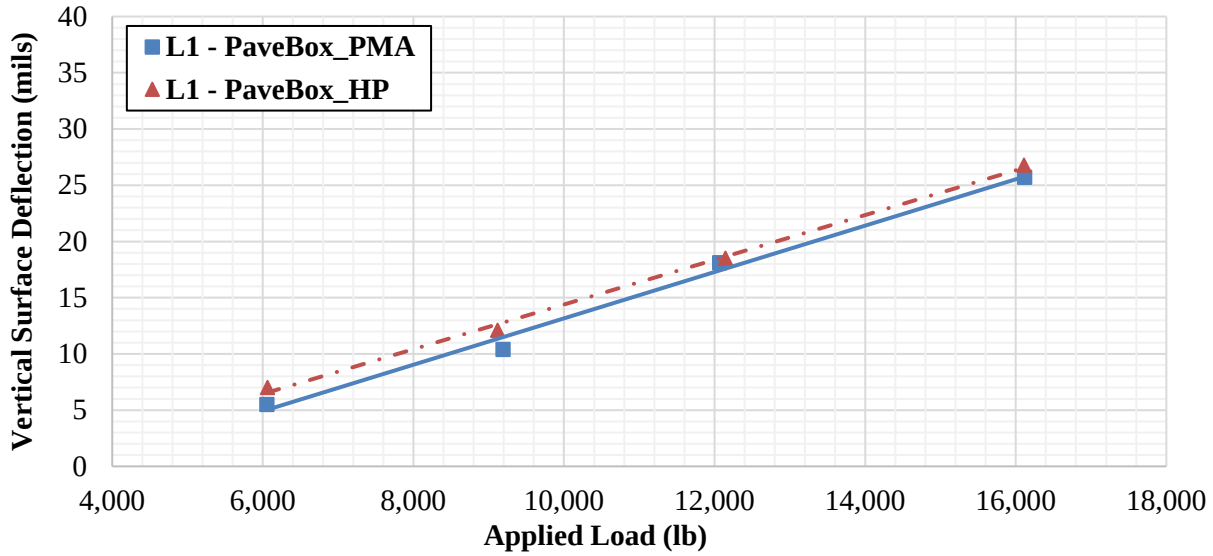


**Figure 7-45. Measured vertical surface deflections at 8 inches from the center of the loading plate (L1).**

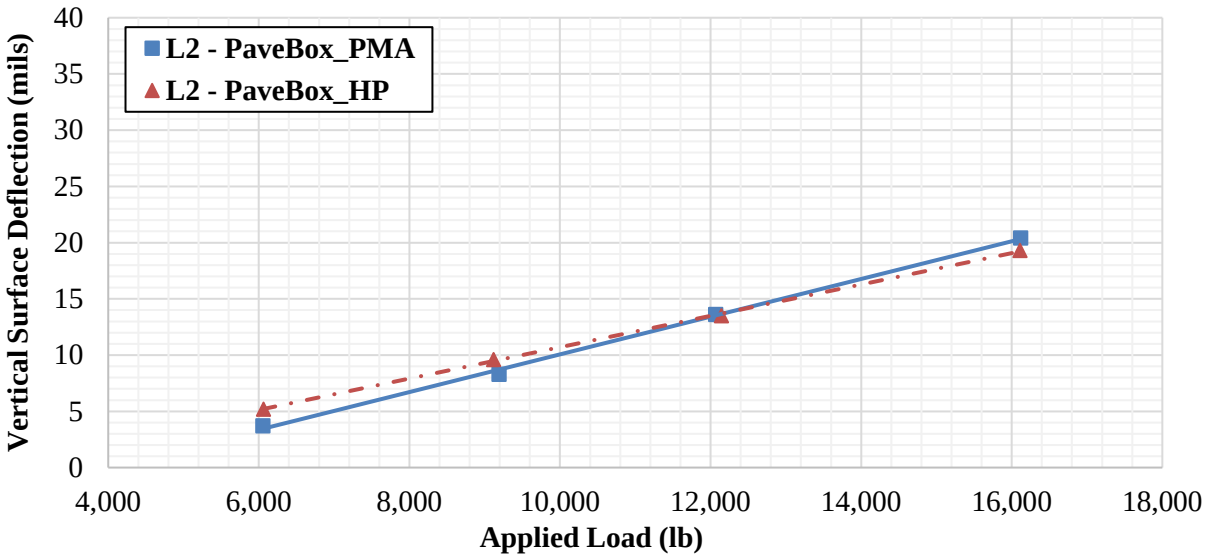


**Figure 7-46. Measured vertical surface deflections at 12 inches from the center of the loading plate (L2).**

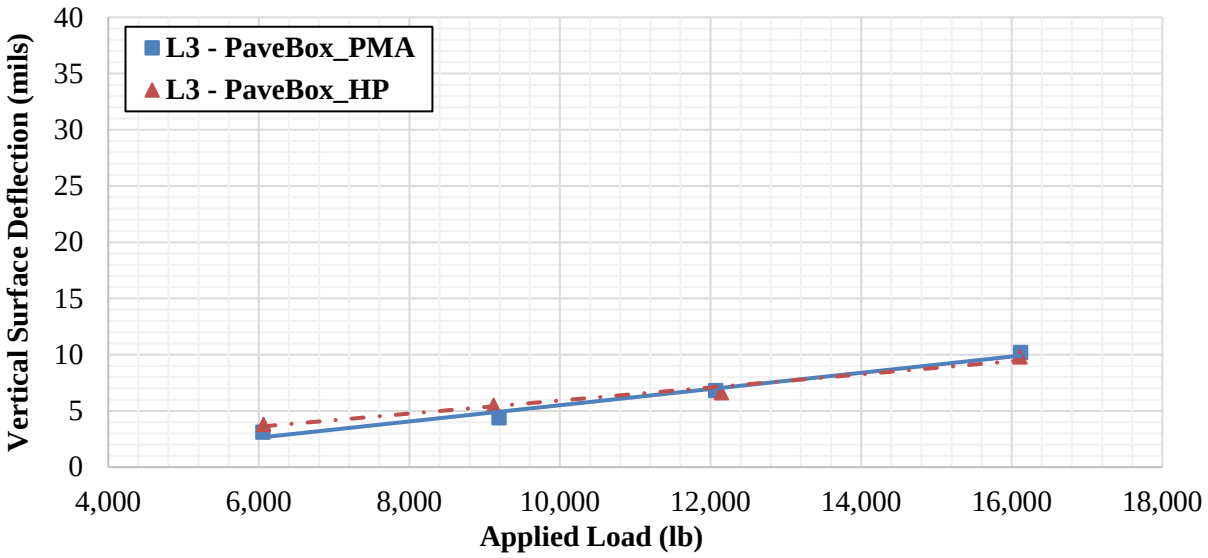


**Figure 7-47. Measured vertical surface deflections at 24 inches from the center of the loading plate (L3).**

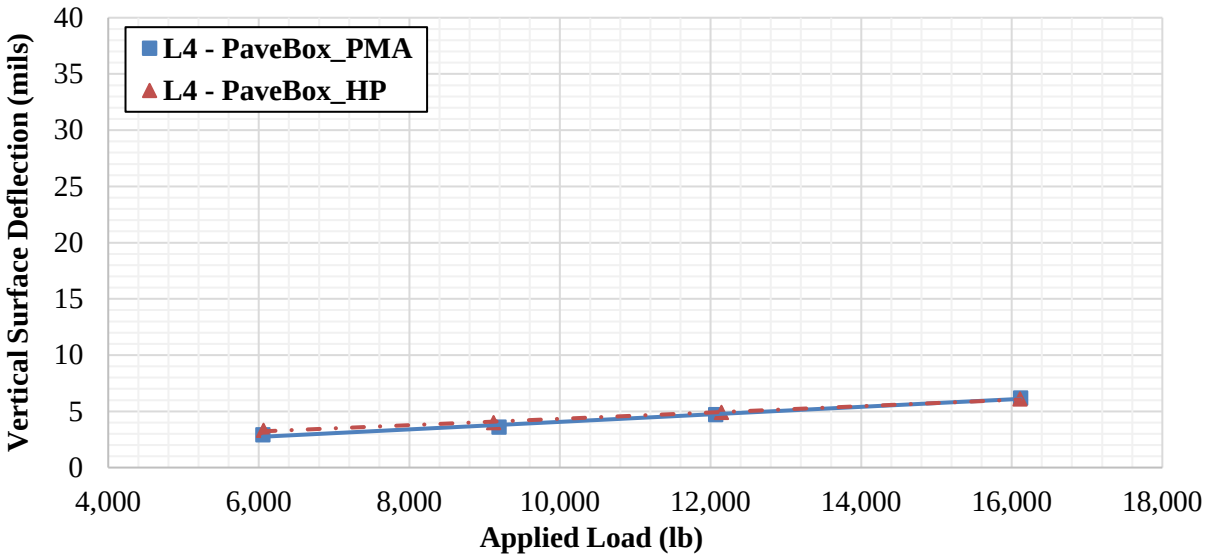


**Figure 7-48. Measured vertical surface deflections at 36 inches from the center of the loading plate (L4).**

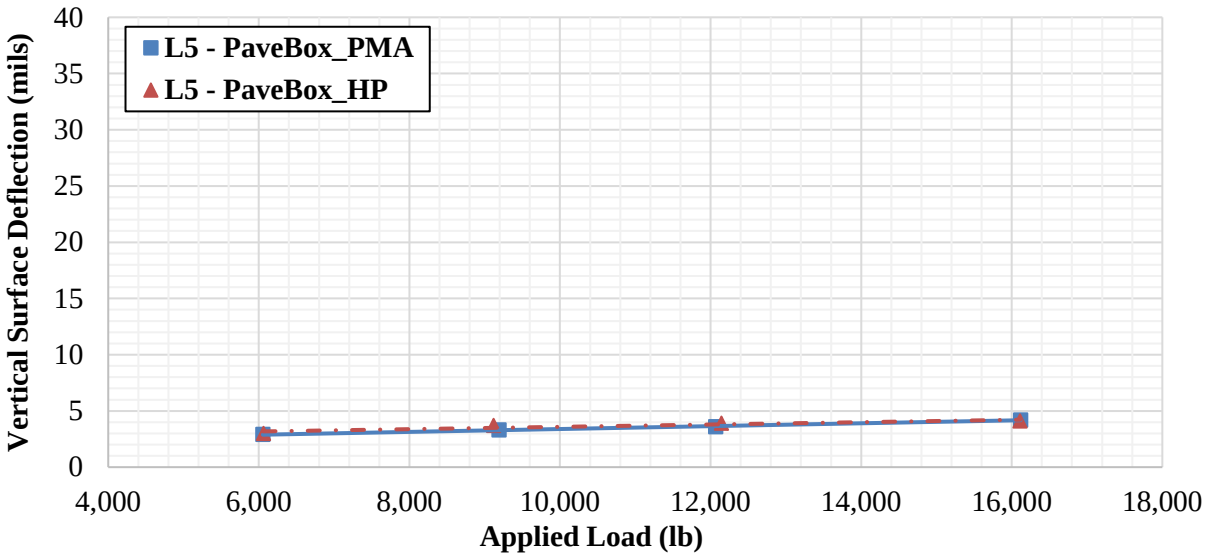


**Figure 7-49. Measured vertical surface deflections at 48 inches from the center of the loading plate (L5).**

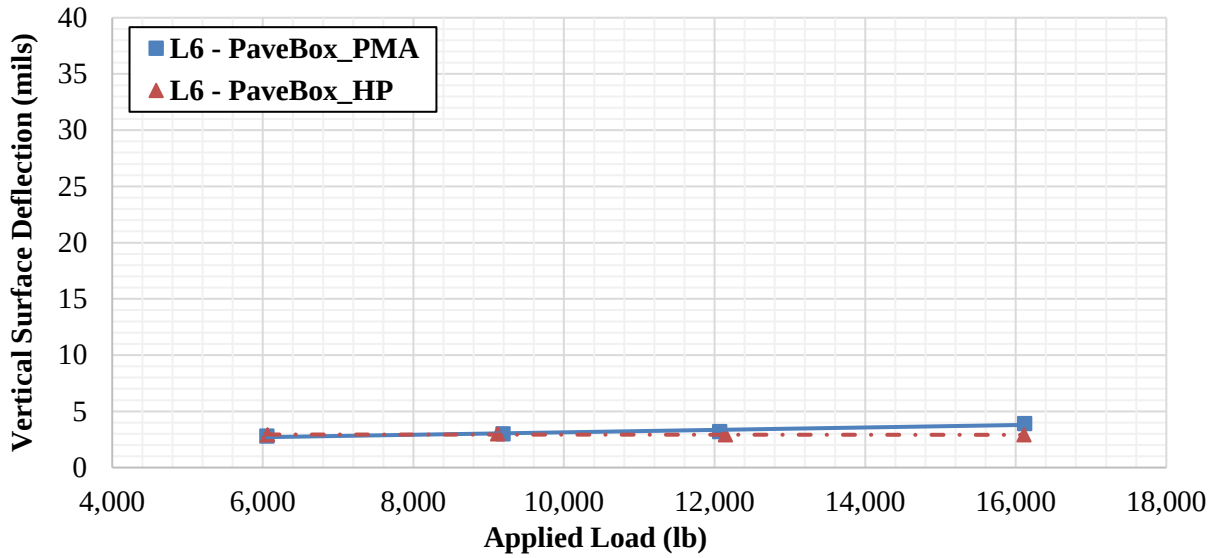


**Figure 7-50. Measured vertical surface deflections at 60 inches from the center of the loading plate (L6).**

**Table 7-16. Vertical Surface Deflections at Multiple Load Levels: Experiment No. 1 (PaveBox_PMA).**

| Target Load Level (lb) | Average Applied Load (lb) | L0 (mils) | L1 (mils) | L2 (mils) | L3 (mils) | L4 (mils) | L5 (mils) | L6 (mils) |
|---|---|---|---|---|---|---|---|---|
| 6,000 | 6,054 | 5.8 | 5.5 | 3.7 | 3.1 | 2.9 | 2.9 | 2.8 |
| 9,000 | 9,189 | 12.2 | 10.4 | 8.3 | 4.4 | 3.6 | 3.3 | 3.0 |
| 12,000 | 12,066 | 21.1 | 18.1 | 13.6 | 6.8 | 4.7 | 3.6 | 3.2 |
| 16,000 | 16,117 | 32.2 | 25.7 | 20.4 | 10.2 | 6.2 | 4.2 | 3.9 |

**Table 7-17. Vertical Surface Deflections at Multiple Load Levels: Experiment No. 2 (PaveBox_HP).**

| Target Load Level (lb) | Average Applied Load (lb) | L0 (mils) | L1 (mils) | L2 (mils) | L3 (mils) | L4 (mils) | L5 (mils) | L6 (mils) |
|---|---|---|---|---|---|---|---|---|
| 6,000 | 6,062 | 10.2 | 7.0 | 5.2 | 3.8 | 3.3 | 3.0 | 2.9 |
| 9,000 | 9,119 | 19.7 | 12.1 | 9.6 | 5.5 | 4.0 | 3.7 | 3.0 |
| 12,000 | 12,143 | 28.2 | 18.5 | 13.5 | 6.6 | 4.9 | 3.9 | 2.9 |
| 16,000 | 16,111 | 39.2 | 26.8 | 19.3 | 9.8 | 6.1 | 4.1 | 2.9 |

### 7.3.3. Vertical Stresses in the Middle of the CAB Layers

The TEPC measurements for the vertical stresses in the middle of the CAB layer in the PaveBox_PMA and PaveBox_HP experiments as a function of surface load levels are presented in Figure 7-51 and Figure 7-52, respectively. Figure 7-53 to Figure 7-56 show the measured

vertical stresses from each of the TEPCs (i.e., P7 through P10) in the PaveBox_PMA and PaveBox_HP experiments as a function of surface load levels. Table 7-18 and Table 7-19 summarize the vertical stresses measured in experiment No. 1 and experiment No. 2, respectively. Based on the presented data, the following observations can be made:

- The highest vertical stresses in the middle of the CAB layer were observed under the middle of the loading plate in each of the two experiments. The vertical stresses decreased with the increase in radial distance from the center of the loading plate. It should be noted that the vertical stresses were minimal at the radial distance of 36 inches (91.4 cm).
- Regardless of the surface loading level, higher vertical stresses under the middle of the loading plate (i.e., P7) were observed in the PaveBox_HP experiment when compared with the PaveBox_PMA experiment. This is demonstrated with vertical stress measurements in the PaveBox_HP experiment that are 85 to 100% higher than those observed in the PaveBox_PMA experiment.
- In general, the vertical stress measurements in the PaveBox_PMA experiment were slightly higher than or similar to the respective measurements in the PaveBox_HP experiment at radial distances greater than 8 inches (20.3 cm).
- Flatter stress–load curves were observed at radial distances farther away from the load indicating less sensitivity of the measured vertical stresses to the magnitude of the applied surface load.

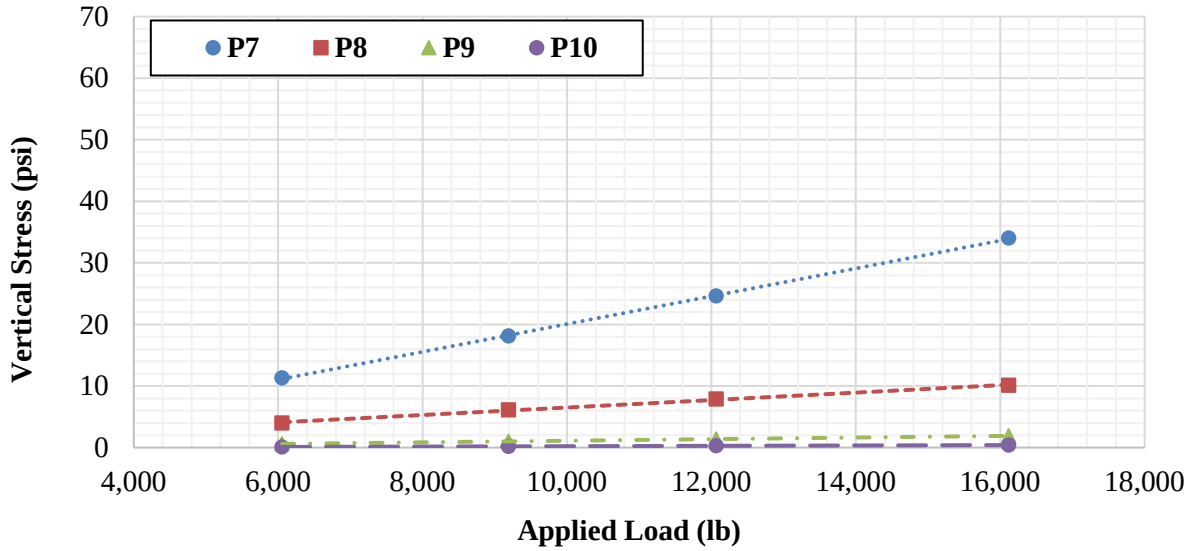


**Figure 7-51. Measured vertical stresses as a function of applied surface loads (experiment No. 1: PaveBox_PMA).**

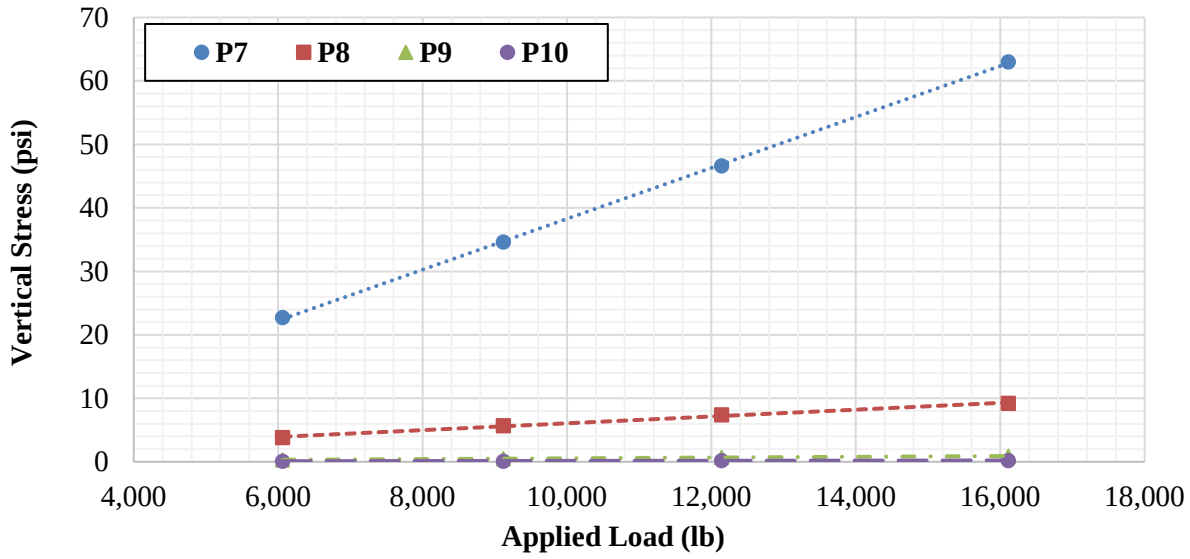


**Figure 7-52. Measured vertical stresses as a function of applied surface loads (experiment No. 2: PaveBox_HP).**

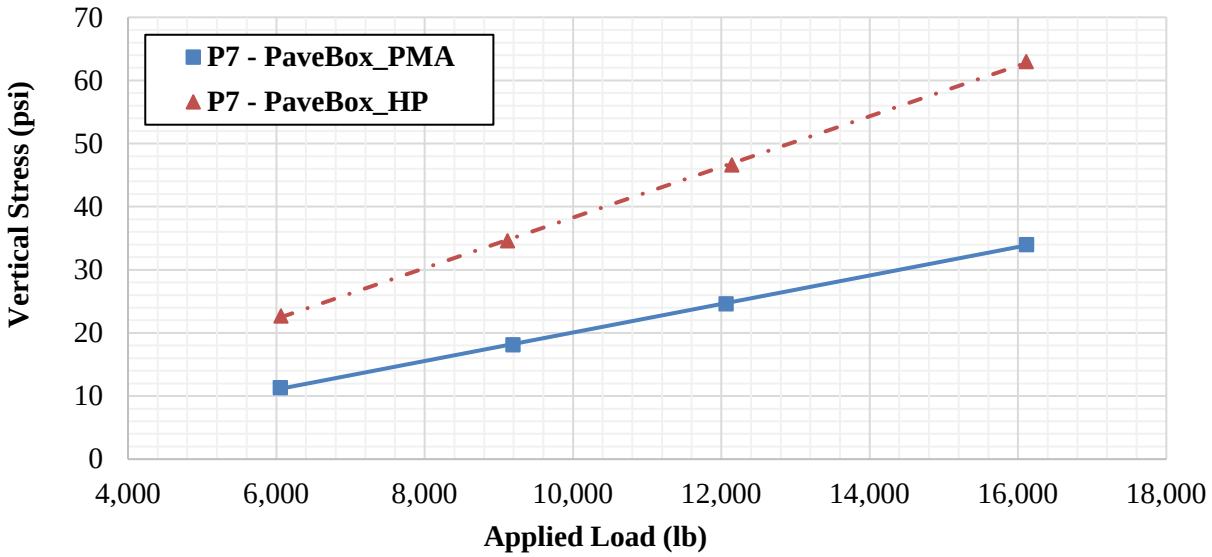


**Figure 7-53. Measured vertical stresses in the middle of the CAB layer and at the center of the loading plate (P7).**

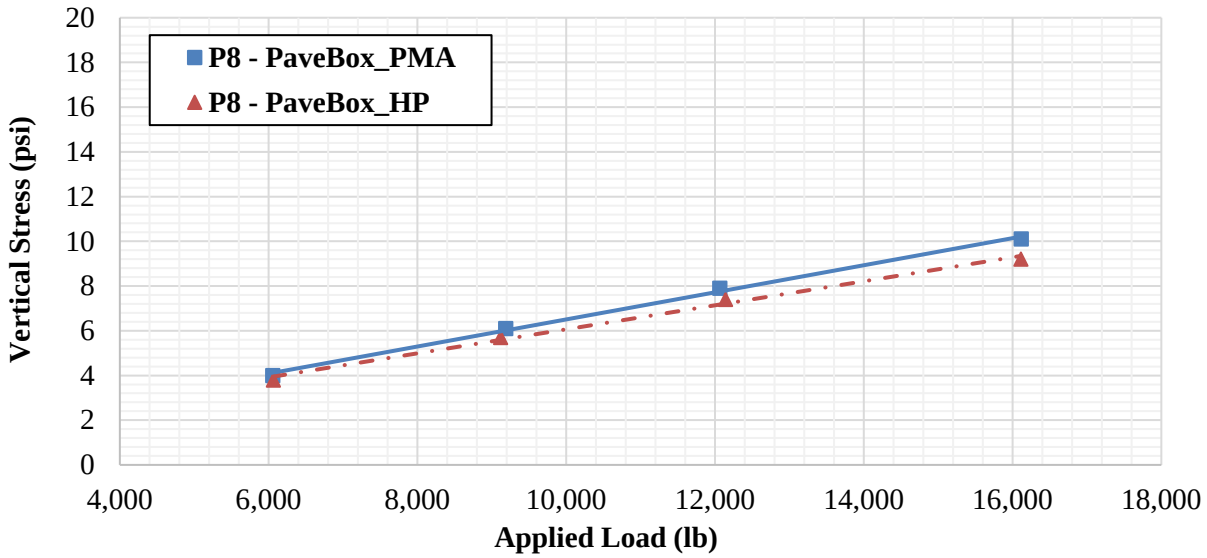


**Figure 7-54. Measured vertical stresses in the middle of the CAB layer and at 12 inches from the center of the loading plate (P8).**

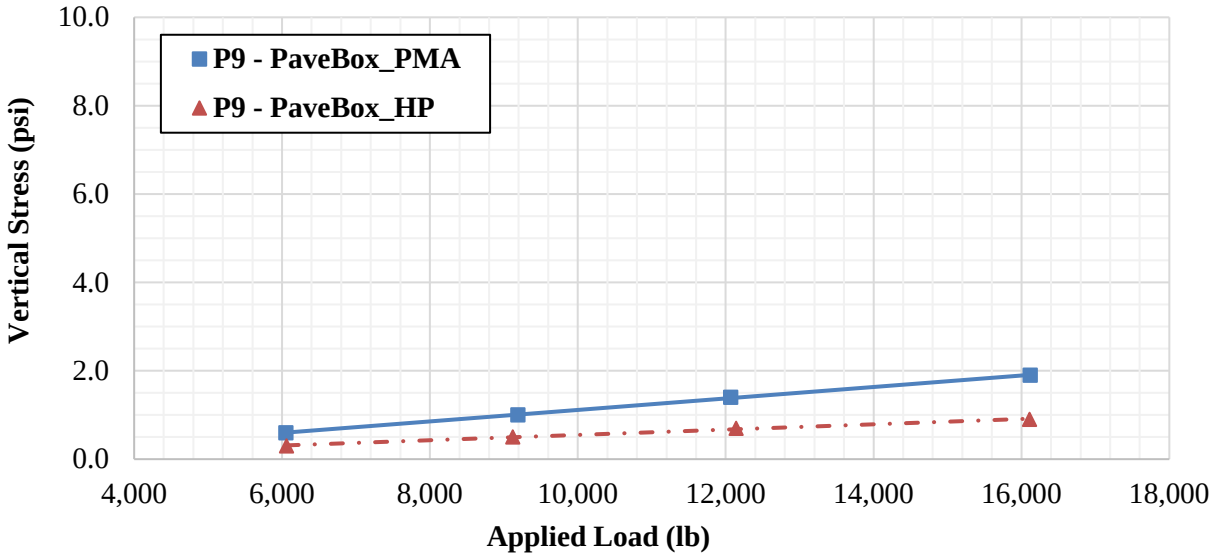


**Figure 7-55. Measured vertical stresses in the middle of the CAB layer and at 24 inches from the center of the loading plate (P9).**

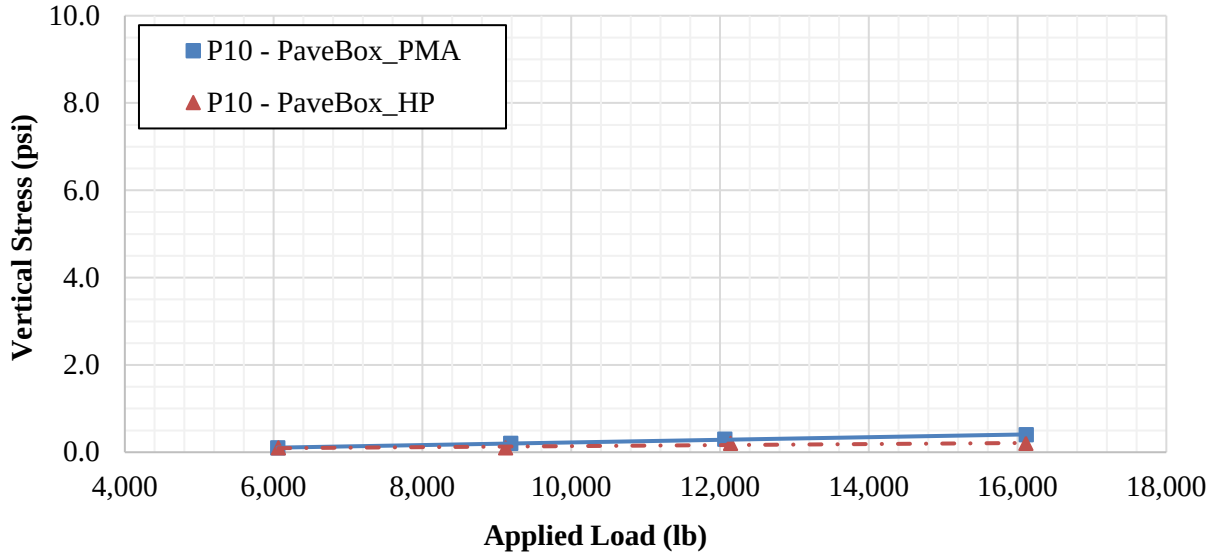


**Figure 7-56. Measured vertical stresses in the middle of the CAB layer and at 36 inches from the center of the loading plate (P10).**

**Table 7-18. Vertical Stress Measurements in the Middle of the CAB Layer at Multiple Load Levels: Experiment No. 1 (PaveBox_PMA).**

| Target Load Level (lb) | Average Applied Load (lb) | P7 (psi) | P8 (psi) | P9 (psi) | P10 (psi) |
|---|---|---|---|---|---|
| 6,000 | 6,054 | 11.3 | 4.0 | 0.6 | 0.1 |
| 9,000 | 9,189 | 18.1 | 6.1 | 1.0 | 0.2 |
| 12,000 | 12,066 | 24.6 | 7.9 | 1.4 | 0.3 |
| 16,000 | 16,117 | 34.0 | 10.1 | 1.9 | 0.4 |

**Table 7-19. Vertical Stress Measurements in the Middle of the CAB Layer at Multiple Load Levels: Experiment No. 1 (PaveBox_PMA).**

| Target Load Level (lb) | Average Applied Load (lb) | P7 (psi) | P8 (psi) | P9 (psi) | P10 (psi) |
|---|---|---|---|---|---|
| 6,000 | 6,062 | 22.7 | 3.8 | 0.3 | 0.1 |
| 9,000 | 9,119 | 34.6 | 5.7 | 0.5 | 0.1 |
| 12,000 | 12,143 | 46.6 | 7.4 | 0.7 | 0.2 |
| 16,000 | 16,111 | 63.0 | 9.2 | 0.9 | 0.2 |

### 7.3.4. Vertical Stresses in the SG Layers

The TEPC measurements for the vertical stresses in the SG layer at 6 inches (152 mm) and 24 inches (610 mm) below the top of the SG as a function of surface load levels, are presented in Figure 7-57 and Figure 7-58 for the PaveBox_PMA and PaveBox_HP experiments, respectively. Figure 7-59 to Figure 7-64 show the measured vertical stresses from each of the TEPC (i.e., P1 through P6) in the PaveBox_PMA and PaveBox_HP experiments as a function of surface load

levels. Table 7-20 and Table 7-21 summarize the vertical stresses in experiment No. 1 and experiment No. 2, respectively. Based on the presented data, the following observations can be made:

- Higher vertical stresses in the SG layer were observed under the center of the loading plate. The vertical stresses in the SG layer decreased with the increase in radial distance from the center of the loading plate. It should be noted that the vertical stresses were minimal at the radial distance of 48 inch (1,220 mm) at a distance of 6 inch (152 mm) below the SG surface.
- Regardless of the loading level, higher vertical stresses under the middle of the loading plate (i.e., P3) was observed at a distance of 6 inch (152 mm) below the top of the SG layer in the PaveBox_HP experiment when compared with the PaveBox_PMA experiment. This is demonstrated with vertical stress measurements in the PaveBox_HP experiment that are 43 to 46% higher than those observed in the PaveBox_PMA experiment.
- Regardless of the loading level, higher vertical stresses under the middle of the loading plate (i.e., P3) was observed at a distance of 24 inch (610 mm) below the top of the SG layer in the PaveBox_HP experiment when compared with the PaveBox_PMA experiment. This is demonstrated with vertical stress measurements in the PaveBox_HP that are 20 to 30% higher than those observed in the PaveBox_PMA.
- In general, the vertical stress measurements in the PaveBox_PMA experiment were slightly higher than or similar to the respective measurements in the PaveBox_HP experiment at both locations in the SG layer, i.e., 6 (152 mm) and 24 inch (610 mm) below the top of the SG layer) and at any radial distance greater than 8 inches (203 mm).
- Flatter stress–load curves were observed at both evaluated depths in the SG layer and at radial distances farther away from the load indicating less sensitivity of the measured vertical stresses to the magnitude of the applied surface load.

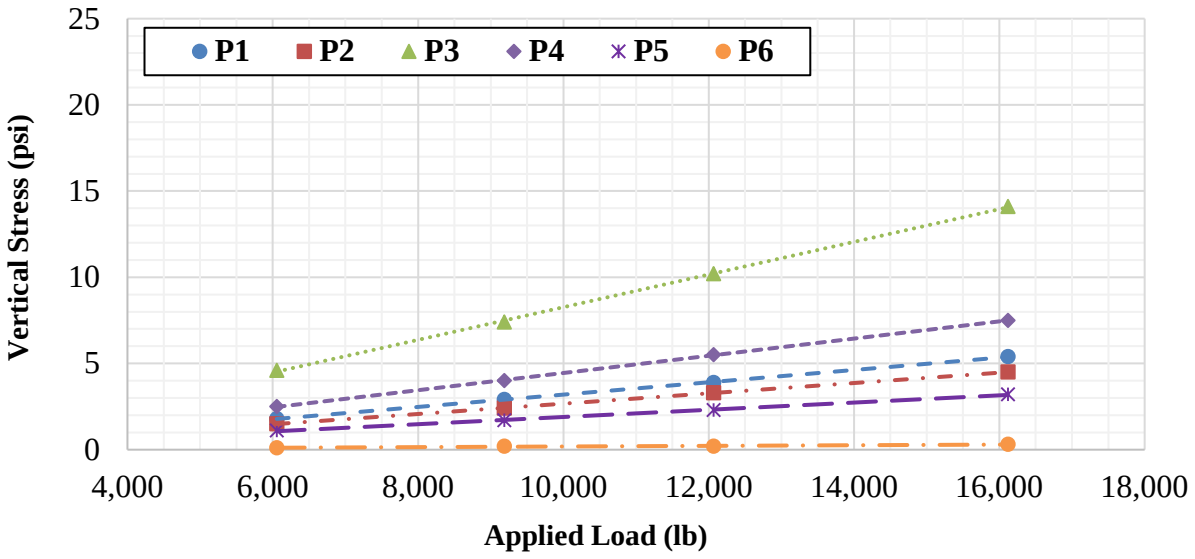


**Figure 7-57. Measured vertical stresses in the SG as a function of applied surface loads (experiment No. 1: PaveBox_PMA).**

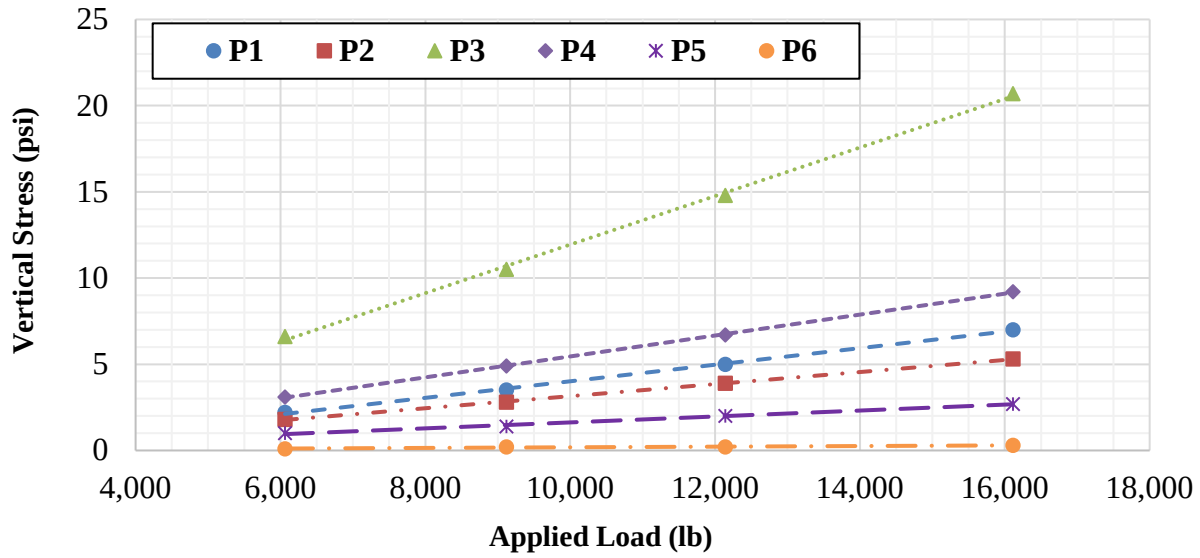


**Figure 7-58. Measured vertical stresses in the SG as a function of applied surface loads (experiment No. 2: PaveBox_HP).**

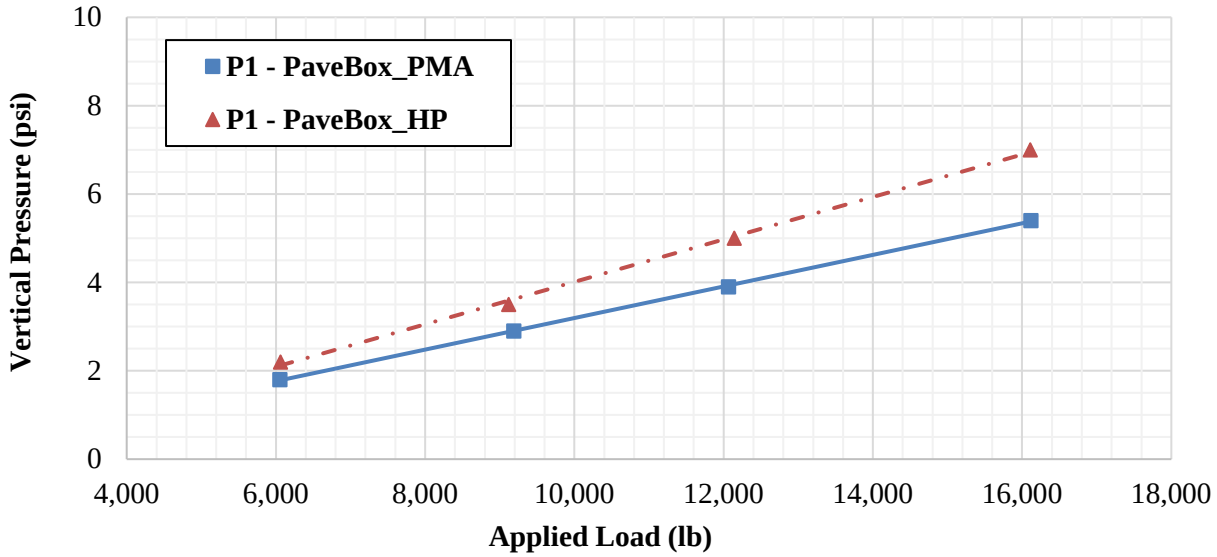


**Figure 7-59. Measured vertical stresses at 24 inches below the top of the SG and at the center of the loading plate (P1).**

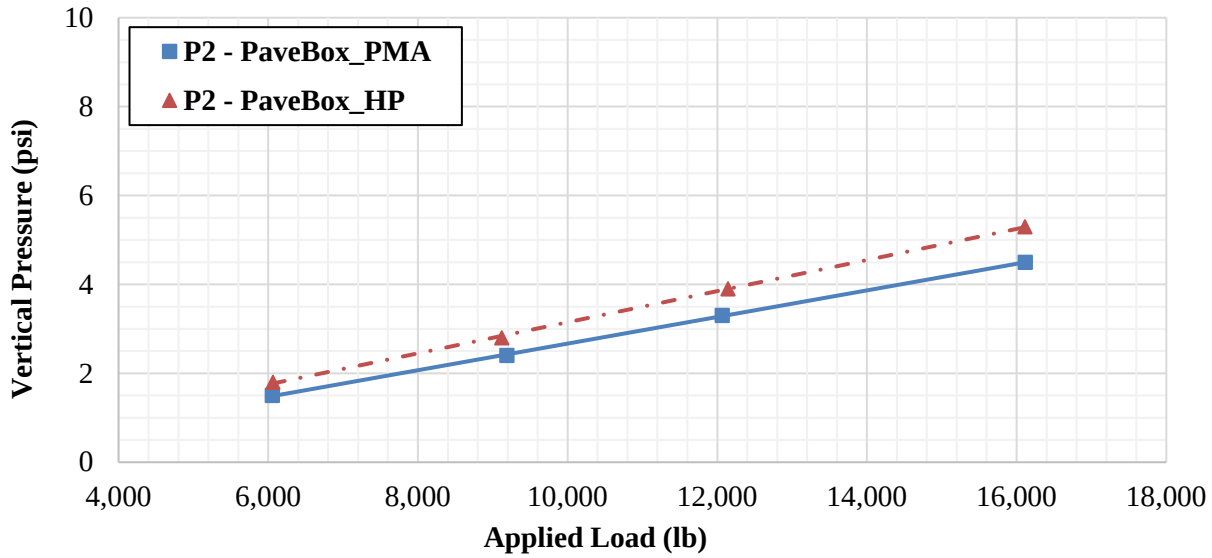


**Figure 7-60. Measured vertical stresses at 24 inches below the top of the SG and at a radial distance of 12 inches from the center of the loading plate (P2).**

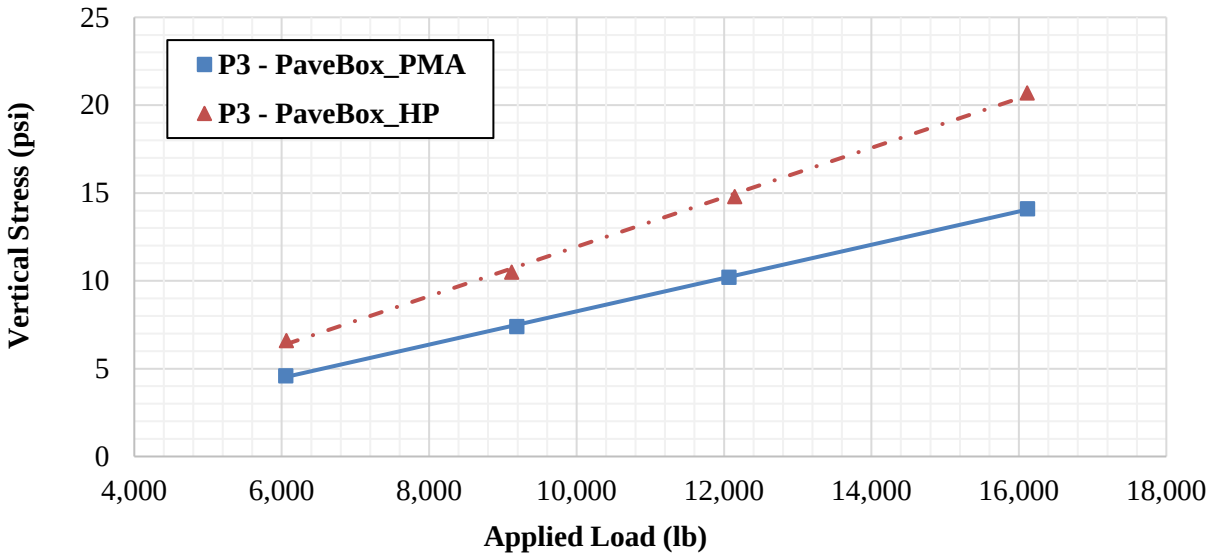


**Figure 7-61. Measured vertical stresses at 6 inches below the top of the SG and at the center of the loading plate (P3).**

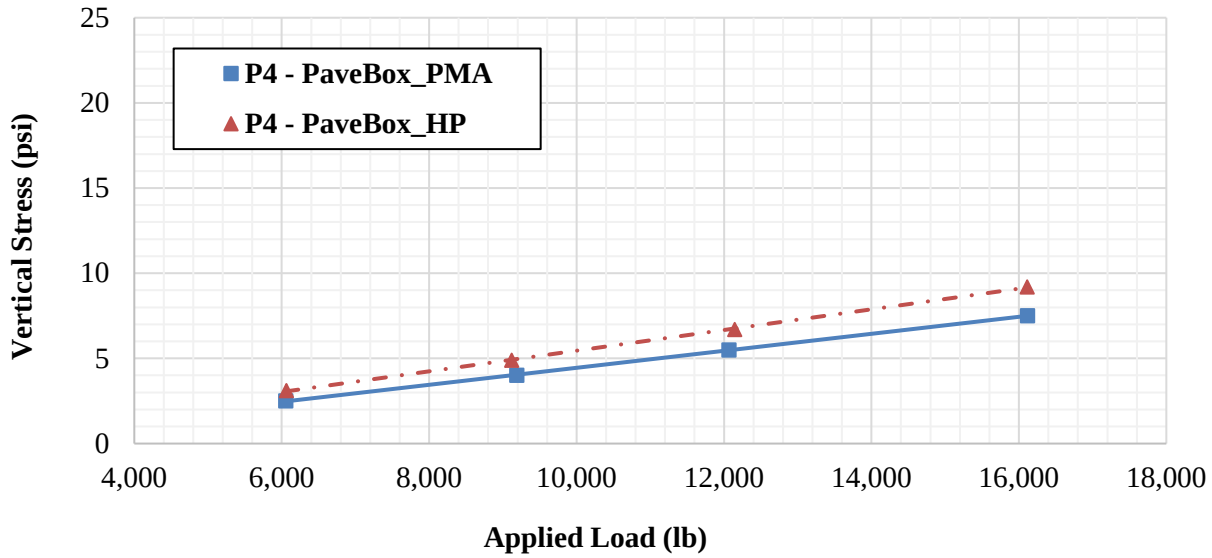


**Figure 7-62. Measured vertical stresses at 6 inches below the top of the SG and at a radial distance of 12 inches from the center of the loading plate (P4).**

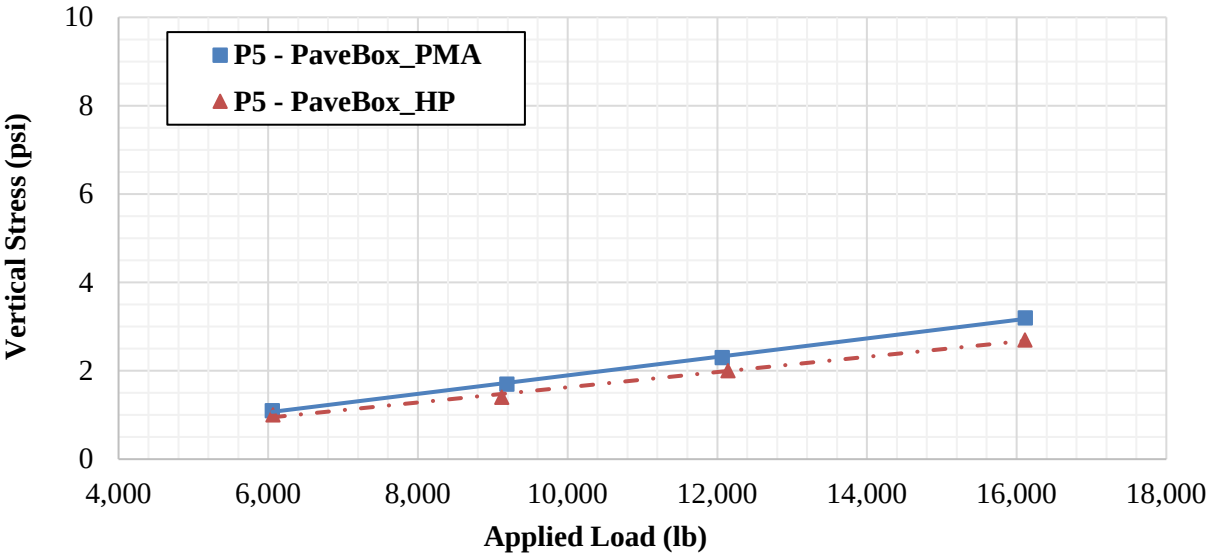


**Figure 7-63. Measured vertical stresses at 6 inches below the top of the SG and at a radial distance of 24 inches from the center of the loading plate (P5).**

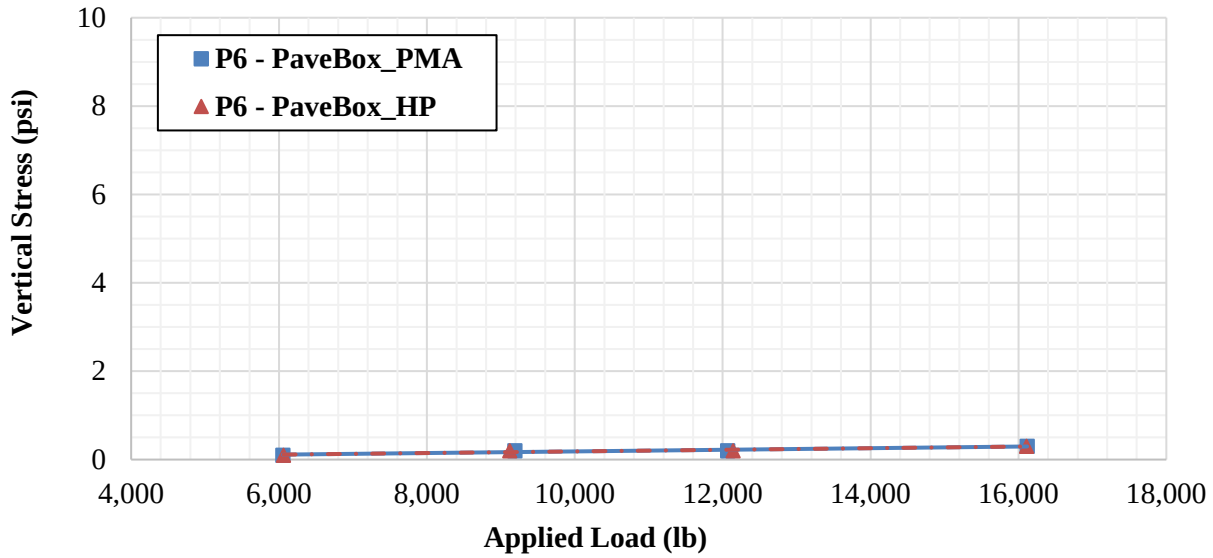


**Figure 7-64. Measured vertical stresses at 6 inches below the top of the SG and at a radial distance of 36 inches from the center of the loading plate (P5).**

**Table 7-20. Vertical Stress Measurements in the SG Layer at Multiple Load Levels: Experiment No. 1 (PaveBox_PMA).**

| Target Load Level (lb) | Average Applied Load (lb) | P1 (psi) | P2 (psi) | P3 (psi) | P4 (psi) | P5 (psi) | P6 (psi) |
|---|---|---|---|---|---|---|---|
| 6,000 | 6,054 | 1.8 | 1.5 | 4.6 | 2.5 | 1.1 | 0.1 |
| 9,000 | 9,189 | 2.9 | 2.4 | 7.4 | 4.0 | 1.7 | 0.2 |
| 12,000 | 12,066 | 3.9 | 3.3 | 10.2 | 5.5 | 2.3 | 0.2 |
| 16,000 | 16,117 | 5.4 | 4.5 | 14.1 | 7.5 | 3.2 | 0.3 |

**Table 7-21. Vertical Stress Measurements in the SG Layer at Multiple Load Levels: Experiment No. 2 (PaveBox_HP).**

| Target Load Level (lb) | Average Applied Load (lb) | P1 (psi) | P2 (psi) | P3 (psi) | P4 (psi) | P5 (psi) | P6 (psi) |
|---|---|---|---|---|---|---|---|
| 6,000 | 6,062 | 2.2 | 1.8 | 6.6 | 3.1 | 1.0 | 0.1 |
| 9,000 | 9,119 | 3.5 | 2.8 | 10.5 | 4.9 | 1.4 | 0.2 |
| 12,000 | 12,143 | 5.0 | 3.9 | 14.8 | 6.7 | 2.0 | 0.2 |
| 16,000 | 16,111 | 7.0 | 5.3 | 20.7 | 9.2 | 2.7 | 0.3 |

### 7.3.5. Tensile Strains at the Bottom of AC Layers

Figure 7-65 and Figure 7-66 show, respectively, the tensile strains measured by S1 and S2 at the bottom of the PMA (at a depth of 4.30 inches from the top of the pavement surface) and HP (at a depth of 3.47 inches from the top of the pavement surface) AC layers as a function of the surface load levels. S1 in both experiments is located under the center of the loading plate while S2 is located at a radial distance of 8 inches from the center of the loading plate. Table 7-22 and Table

7-23 summarize the tensile strains in experiment No. 1 and experiment No. 2, respectively. Based on the presented data, the following observations can be made:

- Regardless of the load level, higher tensile strains were observed below the middle of the loading plate when compared to the tensile strains measured at a radial distance of 12 inches (305 mm) from the center of the loading plate.
- In both experiments (i.e., PaveBox_PMA and PaveBox_HP), an increase in the tensile strain was observed with the increase in the applied surface load level.
- The tensile strain measurements in the PaveBox_PMA experiment were higher than or similar to the respective measurements in the PaveBox_HP experiment.

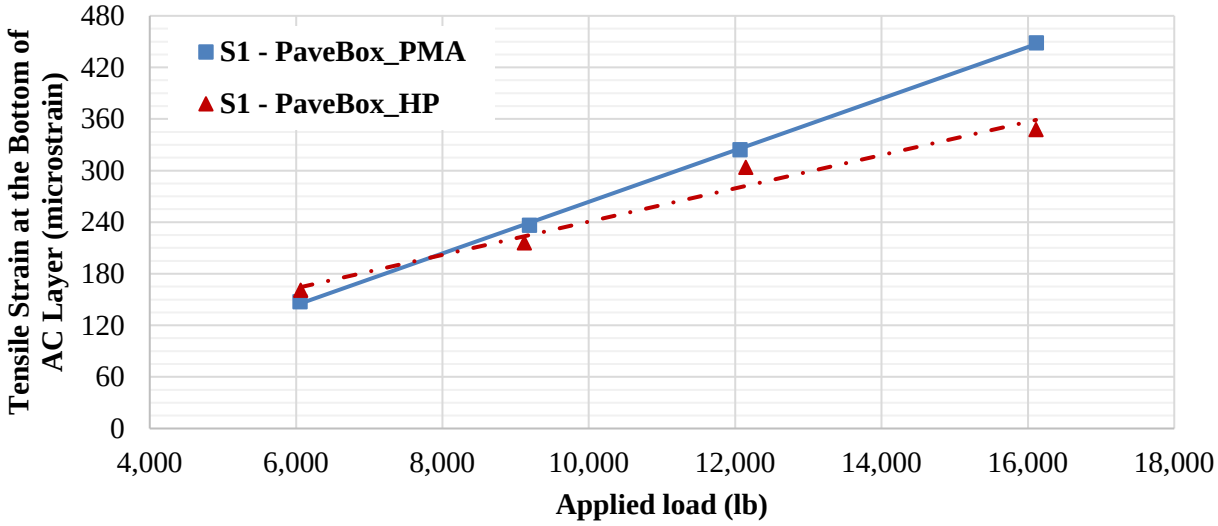


**Figure 7-65. Measured tensile strains at the bottom of the AC layer and at the center of the loading plate (S1).**

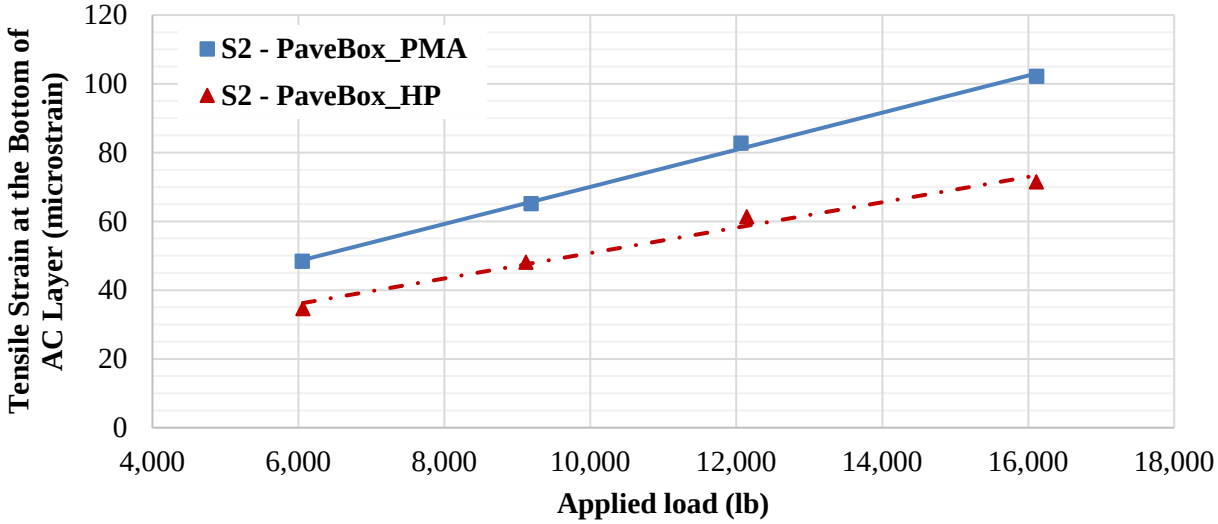


**Figure 7-66. Measured tensile strains at the bottom of the AC layer and 8 inches from the center of the loading plate (S2).**

**Table 7-22. Strain Measurements at the Bottom of the PMA AC Layer at Multiple Load Levels: Experiment No. 1 (PaveBox_PMA).**

| Target Load Level (lb) | Average Applied Load (lb) | S1 (microstrain) | S2 (microstrain) |
|---|---|---|---|
| 6,000 | 6,054 | 147.6 | 48.4 |
| 9,000 | 9,189 | 236.6 | 65.2 |
| 12,000 | 12,066 | 324.4 | 82.8 |
| 16,000 | 16,117 | 448.8 | 102.2 |

**Table 7-23. Strain Measurements at the Bottom of the HP AC Layer at Multiple Load Levels: Experiment No. 2 (PaveBox_HP).**

| Target Load Level (lb) | Average Applied Load (lb) | S1 (microstrain) | S2 (microstrain) |
|---|---|---|---|
| 6,000 | 6,062 | 161.0 | 34.7 |
| 9,000 | 9,119 | 216.2 | 48.2 |
| 12,000 | 12,143 | 303.8 | 61.4 |
| 16,000 | 16,111 | 348.0 | 71.5 |

### 7.3.6. Summary of Pavement Responses

This section presented the results of the preprocessed recordings measured by the embedded instrumentations in the PMA and HP pavement structures tested in the PaveBox experiments. A comparison of the pavement responses from the two experiments was conducted. In general, the reduced thickness of the HP AC layer resulted in the following observations: a) higher vertical surface deflections under the center of the loading plate, b) higher vertical stresses under the center of the loading plate at the middle of the CAB layer, c) similar vertical stresses at 6 inch (152 mm) and 24 inch (610 mm) below the SG surface, and d) similar or lower tensile strains at the bottom of the AC layer.

## 7.4. VERIFICATION OF STRUCTURAL COEFFICIENT USING FULL-SCALE PAVEMENT TESTING

This section presents the service life approach used to mechanistically verify the applicability of the $a_{HP\text{-}AC}$ of 0.54 that was implemented in the full-scale pavement experiments. An ME analysis was conducted using the backcalculated layers' moduli in conjunction with the laboratory developed performance models for the PMA and HP AC mixtures used in the PaveBox (Section 7.2.4). The verification of the $a_{HP\text{-}AC}$ was conducted based on AC fatigue cracking, AC rutting, and total pavement rutting. This effort is referred to as analysis II in Figure 7-1.

### 7.4.1. Introduction

As described in the previous section, seven LVDTs were used at the surface of the AC layer to measure the vertical deflections under four surface load levels. Figure 7-67 and Figure 7-68 illustrate the deflection basins measured in PaveBox_PMA and PaveBox_HP experiments, respectively.

MODULUS 6.1 *(103)* was used to backcalculate the moduli of the various pavement layers from the measured vertical surface deflection basins. The average thickness of the PMA and HP AC layers, as determined from the field core samples, were used in the backcalculation process. The AC layer temperature during testing was measured using an infrared temperature detector and was found to be 63.5°F (17.5°C) and 65.0°F (18.3°C) during the PaveBox_PMA and PaveBox_HP experiments, respectively. Table 7-24 summarizes the backcalculated moduli of the various pavement layers (i.e., AC, CAB, and SG) at the load levels of 9,000, 12,000, and 16,000 lb (40, 53, and 71 kN).

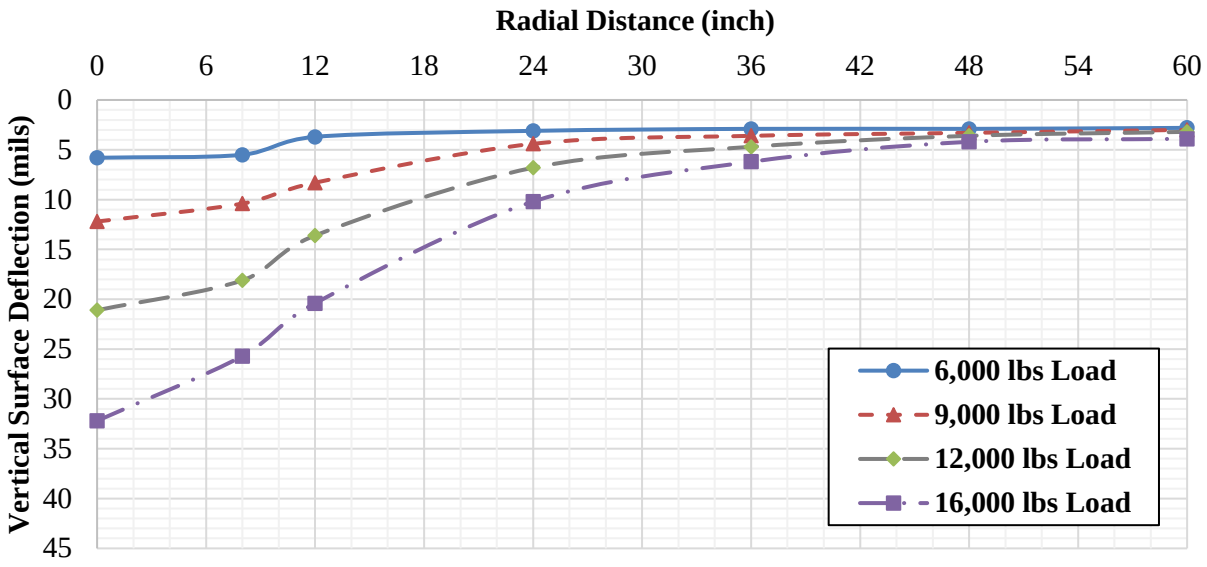


**Figure 7-67. Deflection basins at different load levels (experiment No. 1: PaveBox_PMA).**

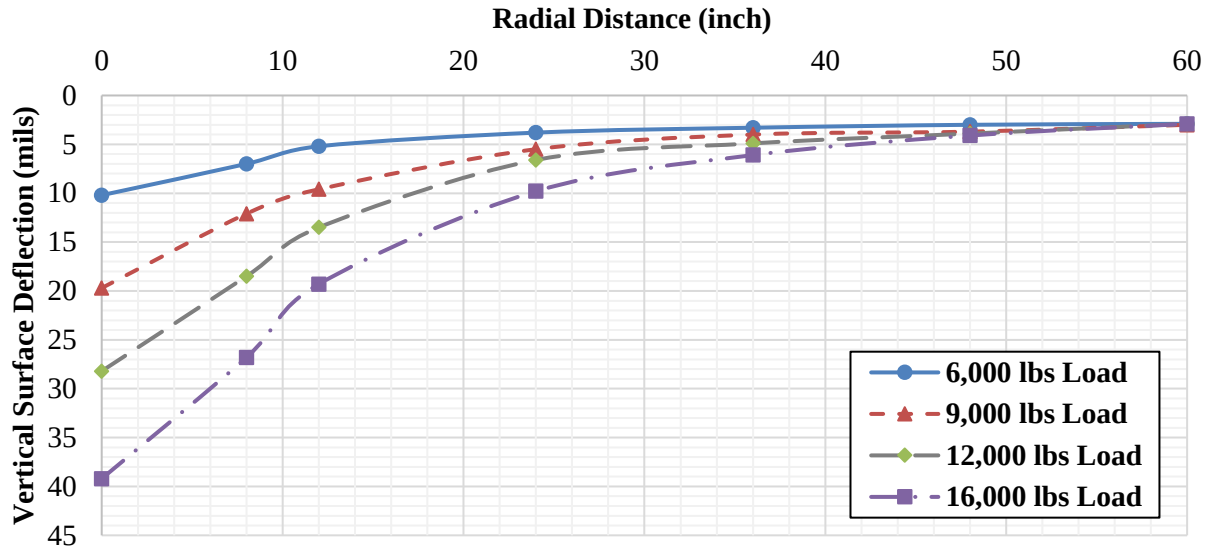


**Figure 7-68. Deflection basins at different load levels (experiment No. 2: PaveBox_HP).**

**Table 7-24. Backcalculated Moduli at Different Load Levels.**

| Experiment ID | Average AC Temperature (°F) | Average Applied Load (lb) | Backcalculated AC Modulus, $E_{AC}$ (ksi) | Backcalculated CAB Modulus, $E_{CAB}$ (ksi) | Backcalculated SG Modulus, $E_{SG}$ (ksi) |
|---|---|---|---|---|---|
| PaveBox_PMA | 63.5 | 9,189 | 555.0 | 39.2 | 11.1 |
| | | 12,066 | 524.2 | 40.8 | 14.8 |
| | | 16,117 | 553.9 | 25.9 | 14.7 |
| PaveBox_HP | 65.0 | 9,119 | 194.0 | 39.5 | 28.1 |
| | | 12,143 | 213.4 | 35.9 | 19.9 |
| | | 16,111 | 294.6 | 30.4 | 16.4 |

Based on the results of the backcalculation, the following observations can be made:

- Regardless of the applied load level, a higher $E_{AC}$ was observed for the PMA AC layer when compared with the HP AC layer. This is demonstrated with an average $E_{AC}$ for the PMA AC layer of 544 ksi (3,751 MPa) compared with 234 ksi (1,613 MPa) for the HP AC layer.
- In the case of the CAB layer, a decrease in $E_{CAB}$ was generally observed with the increase in the applied surface load level. $E_{CAB}$ ranged from 26 to 41 ksi (179 to 283 MPa), and from 30 to 40 ksi (207 to 276 MPa) for the PaveBox_PMA and PaveBox_HP experiments, respectively. The overall average of $E_{CAB}$ based on both experiments was 35.3 ksi (243 MPa).
- In general, higher $E_{SG}$ values were backcalculated for the PaveBox_HP experiment, 16 to 28 ksi (110 to 193 MPa), when compared with the PaveBox_PMA experiment, 11 to 15 ksi (76 to 104 MPa). The overall average of $E_{SG}$ based on both experiments was 17.5 ksi (121 MPa).

The measured surface deflections under the 9,000–16,000 lb (40–71 kN) load levels were compared to the corresponding calculated deflections from 3D-Move using the backcalculated layers' moduli associated with the load levels under consideration (Figure 7-69 and Figure 7-70). Overall, good agreement was observed between the measured and 3D-Move calculated surface deflections at different radial distances from the center of the applied surface load; 0–60 inches (0–152 cm).

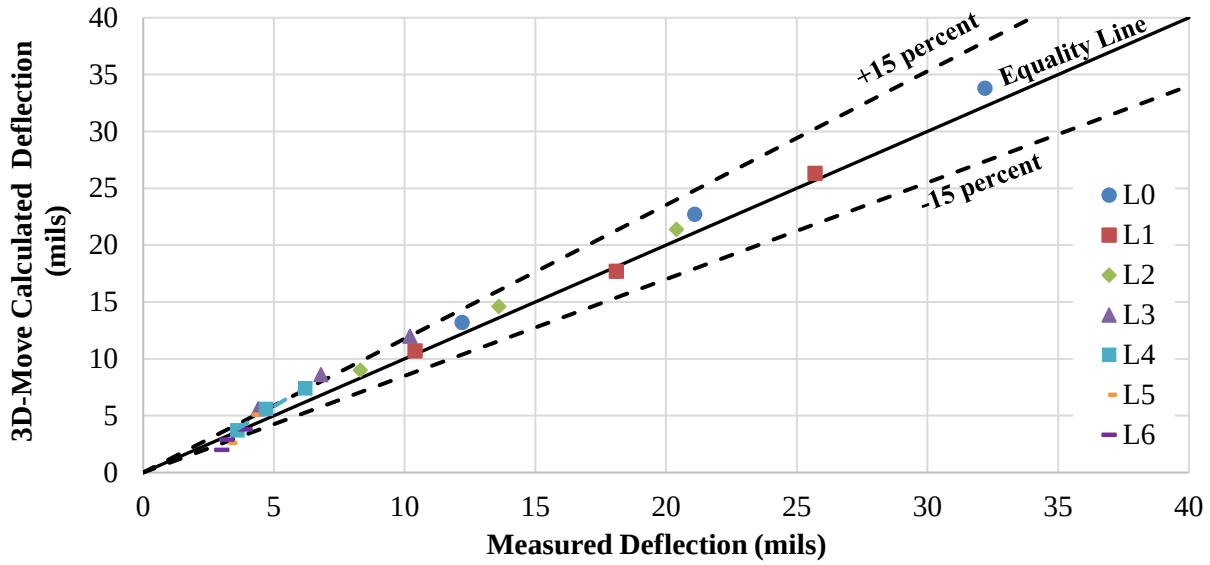


**Figure 7-69. Comparison between measured and 3D-Move calculated surface deflections (experiment No. 1: PaveBox_PMA).**

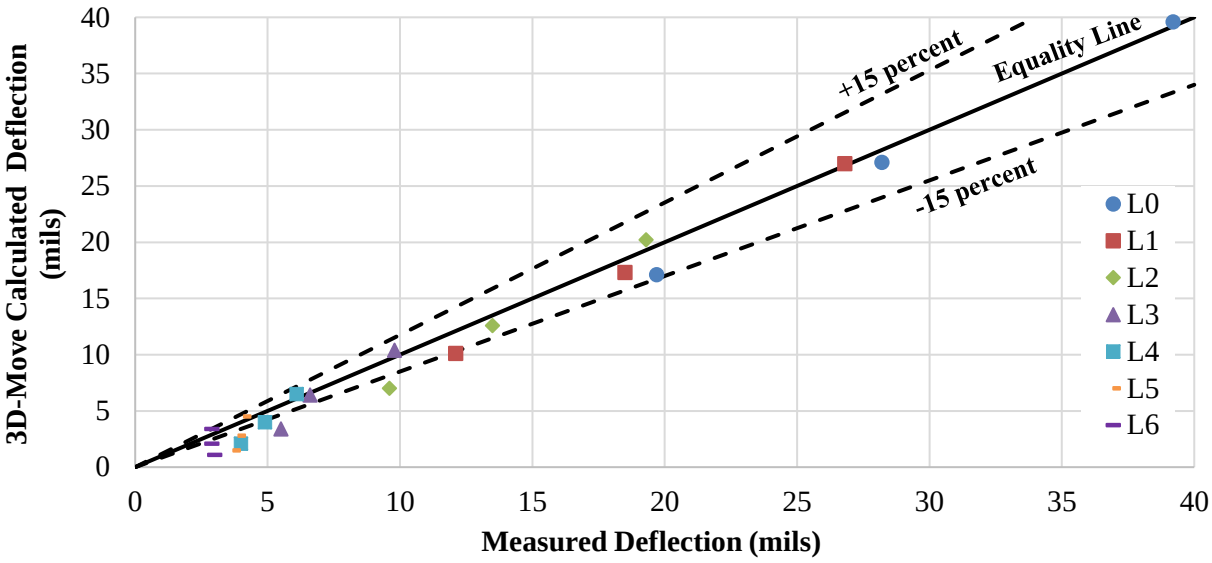


**Figure 7-70. Comparison between measured and 3D-Move calculated surface deflections (experiment No. 2: PaveBox_HP).**

Figure 7-71 and Figure 7-72 present the calculated versus measured tensile strains at the bottom of the AC layer under the center of the loading plate at load levels of 9,000–16,000 lb (40–71 kN) for the PaveBox_PMA and PaveBox_HP experiments, respectively.

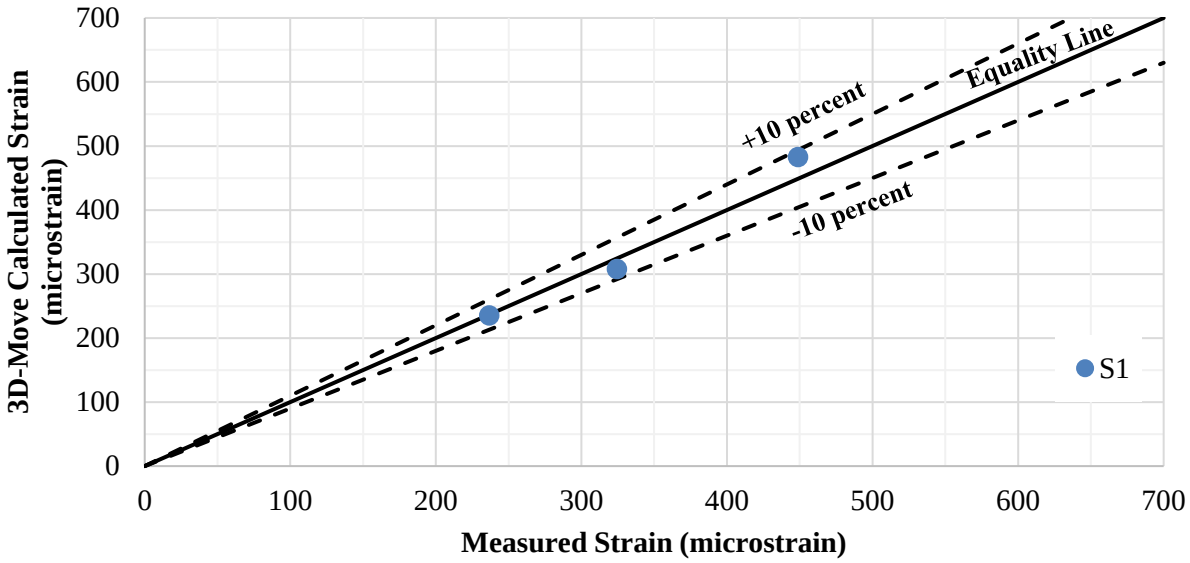


**Figure 7-71. Comparison between measured and 3D-Move calculated strains at the bottom of AC layer (experiment No. 1: PaveBox_PMA).**

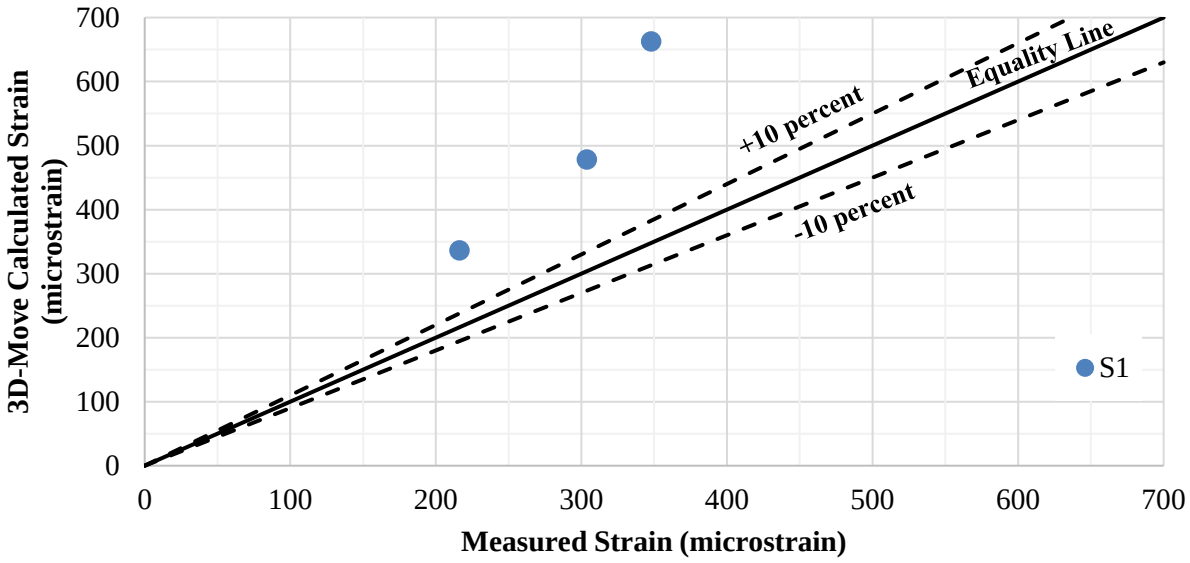


**Figure 7-72. Comparison between measured and 3D-Move calculated strains at the bottom of AC layer (experiment No. 2: PaveBox_HP).**

A very good agreement was observed between the measured and 3D-Move calculated strains at the bottom of the PMA AC layer (Figure 7-71). However, the 3D-Move calculated strains at the bottom of the HP AC layer were 21–90% higher than the corresponding strains measured in the PaveBox_HP experiment (Figure 7-72). Furthermore, the 3D-Move calculated strains at the bottom of the AC layer were higher in the case of the HP AC layer when compared to the PMA AC layer. The 3D-Move results are expected since the HP pavement structure had a reduced AC layer thickness along with lower values of $E_{AC}$ when compared to the PMA pavement structure.

As mentioned in Section 7.3.1, the load-induced strain data recorded in the PaveBox_HP exhibited a different shape than the one observed in the PaveBox_PMA. Accordingly, the measured strain data in the PaveBox_HP experiment should be used with caution. Thus, the verification of $a_{HP\text{-}AC}$ based on fatigue performance life was conducted in the following section using both measured and 3D-Move calculated strains.

### 7.4.2. Verification of $a_{HP\text{-}AC}$ Based on Fatigue Cracking

As noted in previous sections (Section 7.2.4.4), specimens of PMA and HP AC mixes were prepared and evaluated in terms of their resistance to fatigue cracking at three different temperatures using the flexural beam fatigue test. Equation 7-6 and Equation 7-7 show the developed fatigue models for the PMA and HP AC mixes used in the PaveBox experiments, respectively. In these equations, $\varepsilon_t$ is in inch/inch (or mm/mm) and $E_{AC}$ is the backcalculated modulus of the AC layer in psi.

$$N_f = (1.1973\text{E}+01)\left(\frac{1}{\varepsilon_t}\right)^{6.2248}\left(\frac{1}{E_{AC}}\right)^{2.6756} \qquad \textbf{Equation 7-6}$$

$$N_f = (2.7552\text{E}+09)\left(\frac{1}{\varepsilon_t}\right)^{6.6407}\left(\frac{1}{E_{AC}}\right)^{4.3438} \qquad \textbf{Equation 7-7}$$

The measured strains in the PaveBox experiments were used to estimate $N_f$ under different load levels. $N_f$ was also estimated using the 3D-Move calculated strains. Table 7-25 and Table 7-26 summarize the results of the fatigue analysis conducted using measured and 3D-Move calculated strains, respectively. It should be kept in mind while analyzing the data that the HP AC layer was 19% thinner than the PMA AC layer.

Regardless of the AC mix type, $N_f$ decreased with the increase in the applied surface load. Furthermore, higher $N_f$ values were calculated for the HP AC layer when compared to the PMA AC layer. The ratio of the HP to PMA fatigue lives ranged from 125–339 in the case of measured strains, and 2.7–17.4 in the case of 3D-Move calculated strains. A lower ratio was observed at the target load level of 16,000 lb (71 kN) when compared to 9,000 lb (40 kN).

In summary, the fatigue analysis of the two evaluated PMA and HP pavement structures indicated an increase in the fatigue life of the HP AC layer when compared to the PMA AC layer. The difference in AC layer fatigue life between the HP and PMA AC mixes was highest at the lower load levels and decreased with the increase in load level. Thus, the overall results of the fatigue analysis support the $a_{HP\text{-}AC}$ selection of 0.54.

**Table 7-25. Fatigue Analysis of PMA and HP Pavement Structures at Different Load Levels Using Measured Strains.**

| Target Load Level (lbs) | AC Mix ID | Measured Tensile Strain (microstrain) | $E_{AC}$ (psi) | $N_f$ (million) | Ratio of HP to PMA fatigue lives |
|---|---|---|---|---|---|
| 9,000 | PaveBox_PMA | 236.6 | 555,000 | 190.5 | 339.1 |
| | PaveBox_HP | 216.2 | 194,000 | 64,583.8 | |
| 12,000 | PaveBox_PMA | 324.4 | 524,200 | 31.1 | 143.3 |
| | PaveBox_HP | 303.8 | 213,400 | 4,459.4 | |
| 16,000 | PaveBox_PMA | 448.8 | 553,900 | 3.6 | 125.3 |
| | PaveBox_HP | 348.0 | 294,600 | 445.9 | |

**Table 7-26. Fatigue Analysis of PMA and HP Pavement Structures at Different Load Levels Using 3D-Move Calculated Strains.**

| Target Load Level (lbs) | AC Mix ID | Measured Tensile Strain (microstrain) | $E_{AC}$ (psi) | $N_f$ (million) | Ratio of HP to PMA fatigue lives |
|---|---|---|---|---|---|
| 9,000 | PaveBox_PMA | 235.2 | 555,000 | 197.6 | 17.4 |
| | PaveBox_HP | 336.2 | 194,000 | 3,442.1 | |
| 12,000 | PaveBox_PMA | 307.9 | 524,200 | 43.1 | 5.1 |
| | PaveBox_HP | 478.1 | 213,400 | 219.5 | |
| 16,000 | PaveBox_PMA | 482.8 | 553,900 | 2.3 | 2.7 |
| | PaveBox_HP | 662.5 | 294,600 | 6.2 | |

### 7.4.3. Verification of $a_{HP\text{-}AC}$ Based on Rutting

Since the PaveBox experiments were conducted at intermediate temperatures, the verification of $a_{HP\text{-}AC}$ based on rutting was conducted using the 3D-Move generated responses at the critical high temperature for Florida of 122°F (50°C). The verification was conducted for rutting in the AC layer and in the unbound layers (i.e., CAB and SG).

As notes in previous sections (Section 7.2.4.4), specimens of PMA and HP AC mixes were prepared and evaluated in terms of their resistance to rutting at three different temperatures using the RLT test. The permanent ($\varepsilon_p$) and resilient ($\varepsilon_r$) axial strains were measured during the RLT test as a function of the number of load repetitions ($N$). Equation 7-8 and Equation 7-9 show the developed rutting models for the PMA and HP AC mixes used in the PaveBox experiments, respectively. In these equations, $T$ is in °F and equals to 122°F, $\beta_{r3}$ is a laboratory-to-field calibration factor, and $K_z$ is determined using Equation 2.14. A $\beta_{r3}$ of 0.207915 was estimated for the purpose of this effort by assuming a maximum $RD_{AC}$ of 0.25 inch (6.4 mm) under 16,000 lb for the PMA AC layer.

$$\frac{\varepsilon_p}{\varepsilon_r} = K_z * 10^{-10.8922} * (T)^{5.3491} * (N)^{0.3847*\beta_{r3}} \qquad \textbf{Equation 7-8}$$

$$\frac{\varepsilon_p}{\varepsilon_r} = K_z * 10^{-11.0584} * (T)^{5.3505} * (N)^{0.3458*\beta_{r3}} \qquad \textbf{Equation 7-9}$$

The AASHTOWare® Pavement ME software *(5)* approach was followed to sub-divide each layer of the pavement cross-section into sub-layers. The maximum vertical compressive strains were then computed by 3D-Move at the middle of each of the sub-layers. Using the rutting model developed for each of the AC mixes (i.e., PMA and HP) along with the determined $\varepsilon_{ri}$ from 3D-Move, $\varepsilon_{pi}$ within each AC sub-layer was calculated under the considered loading conditions. The total rut depth in the AC layer is then determined. More details regarding these caluclations can be found in Section 6.3.1.

The Backcalculated moduli of the AC layers at the PaveBox testing temperatures (Table 7-27) along with the developed *E** master curves (Section 7.2.4.4) were used to estimate the modulus of the PMA and HP AC layers at 122°F (50°C). An average of modulus of 21.2 ksi (146 MPa) and 14.2 ksi (98 MPa) were estimated for the PMA and HP AC mixes, respectively. In the case of the unbound layers, average backcalculated moduli (between PaveBox_PMA and PaveBox_HP) for the CAB and SG layers at each of the loading levels were utilized in 3D-Move for the rutting analysis. Tab 28 summarizes the moduli of the various layers used in the 3D-Move analysis.

**Table 7-27. Moduli of Various Layers at 122°F (50°C).**

| Target Load Level Load (lb) | Average PMA AC Layer Modulus at 122°F (Ksi) | Average HP AC Layer Modulus at 122°F (Ksi) | Average CAB Layer Modulus (Ksi) | Average SG Layer Modulus (Ksi) |
|---|---|---|---|---|
| 9,000 | 21.2 | 14.2 | 39.4 | 19.6 |
| 12,000 | 21.2 | 14.2 | 38.4 | 17.4 |
| 16,000 | 21.2 | 14.2 | 28.2 | 15.6 |

Rutting in the CAB and SG layers were also estimated using the nationally calibrated rutting performance models recommended in the AASHTOWare® Pavement ME software. More details regarding these calculations can be found in Section 6.3.2.

Table 7-28 presents the calculated rut depths for the AC, CAB, and SG layers. Table 7-29 summarizes the percent change in the calculated rut depths of the HP pavement structure relative to the PMA pavement structure at different load levels. In general, a decrease in the $RD_{AC}$ was determined for the HP AC layer. The percent change in $RD_{AC}$ ranged between 12.0 and 17.6%. On the other hand, an increase in $RD_{CAB}$ and $RD_{SG}$ was determined for the CAB and SG layers in the HP pavement structure. The percent change in $RD_{CAB}$ was higher than that of $RD_{SG}$ and ranged between 8.0 and 10.2%. The percent change in $RD_{SG}$ ranged between 4.5 and 9.4%.

Table 7-28 also summarizes the combined rut depth for the CAB and SG layers as well as the total rut depth (i.e., summation of $RD_{AC}$, $RD_{CAB}$, and $RD_{SG}$). While an increase in the unbound material rut depth was observed, the total rut depth was found to be similar for the PMA and HP pavement structures. In other words, the increase in the unbound material rut depths was compensated by a decrease in the $RD_{AC}$ of the HP AC layer.

In summary, the rutting analysis of the two evaluated PMA and HP pavement structures at 122°F (50°C) indicated a decrease in the rut depth of the HP AC layer when compared to the PMA AC layer. However, a relative increase in the rut depths of the CAB and SG layers were observed. The percent change in rut depth of the unbound materials was limited to about +10% under the evaluated conditions. This is associated with the reduced AC layer along with a lower modulus for the HP AC mix. However, the total rut depths were similar between the HP and PMA pavement structures. Accordingly, the overall results of the rutting analysis support the $a_{HP\text{-}AC}$ selection of 0.54. However, a reduction in the value of the recommended $a_{HP\text{-}AC}$ might be warranted in cases where excessive stresses are induced into the unbound layers, in particular in the CAB layer. This aspect will need to be further evaluated as part of the FDOT APT experiment.

**Table 7-28. Rutting Analysis of PMA and HP Pavement Structures at Different Load Levels.**

| Target Load Level Load (lb) | Pavement Structure | $RD_{AC}$ (inch) | $RD_{CAB}$ (inch) | $RD_{SG}$ (inch) | $RD_{CAB} + RD_{SG}$ *(inch)* | Total Rut Depth, $RD_{total}$ (inch) |
|---|---|---|---|---|---|---|
| 9,000 | PMA | 0.17 | 0.25 | 0.15 | 0.40 | 0.57 |
| | HP | 0.14 | 0.27 | 0.16 | 0.43 | 0.57 |
| 12,000 | PMA | 0.23 | 0.34 | 0.22 | 0.56 | 0.79 |
| | HP | 0.20 | 0.37 | 0.23 | 0.60 | 0.80 |
| 16,000 | PMA | 0.25 | 0.59 | 0.32 | 0.91 | 1.16 |
| | HP | 0.22 | 0.65 | 0.35 | 1.00 | 1.22 |

**Table 7-29. Percent Change in Rut Depths at Different Load Levels.(a)**

| Target Load Level Load (lb) | Percent Change in $RD_{AC}$ | Percent Change in $RD_{CAB}$ | Percent Change in $RD_{SG}$ | Percent Change in $RD_{CAB} + RD_{SG}$ | Percent Change in $RD_{total}$ |
|---|---|---|---|---|---|
| 9,000 | –17.6 | +8.0 | +6.7 | +7.5 | +0.0 |
| 12,000 | –13.0 | +8.8 | +4.5 | +7.1 | +1.3 |
| 16,000 | –12.0 | +10.2 | +9.4 | +9.9 | +5.2 |

(a)Percent change calculated relative to PMA pavement structure.

### 7.4.4. Summary of Mechanistic Analyses

In Section 7.4, the service life approach was used to mechanistically verify the applicability of the $a_{HP\text{-}AC}$ of 0.54 that was implemented in the PaveBox experiments (referred to as analysis II in Figure 7-1). An ME analysis was conducted using the backcalculated layers' moduli in conjunction with the laboratory-developed performance models for the PMA and HP AC mixes. The ME analysis resulted in a better fatigue and rutting performance for the HP AC layer when compared with the PMA AC layer. Higher rut depths were observed in the unbound layers of the HP pavement structure, especially in the CAB layer. However, similar total rut depths were determined for the PMA and HP pavement structures. In general, the overall results of analysis II support the $a_{HP\text{-}AC}$ selection of 0.54. Though, a reduction in the recommended value might be warranted if the load-induced stresses in the unbound materials lead to permanent deformations that exceeds rut depth limits set by FDOT.

# CHAPTER 8. SUMMARY OF FINDINGS, CONCLUSIONS, AND DEVELOPMENT OF RECOMMENDATIONS: APT IMPLEMENTATION PLAN

The overall objective of this FDOT research study is to determine the structural coefficient for asphalt mixes manufactured using HP binder that contains approximately 7.5% SBS polymer. This chapter constitutes a summary and presents conclusions drawn based on the literature review, laboratory evaluation, advanced mechanistic modeling, and full-scale testing conducted in this research study. In addition, an implementation plan of the final recommended structural coefficient for HP AC mixes using the APT setup at FDOT facilities is provided in this chapter.

## 8.1. SUMMARY OF FINDINGS AND CONCLUSIONS

### 8.1.1. Literature Review

The objective of the literature review was to identify all currents and previous studies that have been conducted to evaluate the performance of HP AC mixes. In this research, HP AC mixes are defined as asphalt mixtures manufactured using asphalt binders modified with SBS or SB polymers at the approximate rate of 7.5% by weight of binder. The findings of the literature review were presented with respect to the three areas of interest that were defined in the Scope of the review as: a) laboratory evaluations of HP modified asphalt binders and mixtures, b) performance of pavement sections constructed with HP AC mixes, and c) techniques to determine structural coefficient of HP AC mixes.

*8.1.1.1 Laboratory Evaluations of HP Modified Asphalt Binders and Mixtures*

The review identified several studies that evaluated the engineering properties and performance characteristics of HP asphalt binders and mixtures. On the positive side, all the identified studies used the Superpave technology to evaluate the properties of the binders and mixtures which makes the generated data highly applicable to the current research. On the not so positive side, none of the identified studies conducted a complete experimental design that can lead to the evaluation of the performance of HP AC mixes with respect to all modes of distresses, i.e., rutting, fatigue, thermal, and reflective cracking. In addition, some of the studies did not incorporate the evaluation of a control binder or mixture in order to clearly define the contribution of the HP asphalt binder. Furthermore, some studies went directly into the evaluation of HP mixtures without providing sufficient information on the properties of the HP binders used in the manufacturing of the mixtures.

Table 8-1 summarizes the findings of the reviewed studies that evaluated the laboratory properties of HP binders and mixtures. The summary is presented in terms of the impact of HP modification on the performance properties of binders and mixtures. A review of the findings in Table 8-1 leads to the following observations:

- Increasing the SBS polymer content from 0, 3, 6, to 7.5% continues to improve the performance properties of the asphalt binder and mixture in terms of its resistance to the various modes of distresses, i.e. rutting, fatigue, thermal, and reflective cracking.

- A unique feature of the HP modification has been identified as its ability to slow down the oxidative aging of the asphalt binder. This feature is expected to positively impact the resistance of the HP AC mix to the various types of cracking.
- The HP asphalt binder should not be used to overcome the negative impact of RAP on the resistance of the AC mixture to various types of cracking. The properties of the RAP binder should be taken into consideration when designing HP AC mix with RAP content at or above 25% in order to optimize the benefits of the HP modification.

**Table 8-1. Summary of Laboratory Evaluations of HP Binders and Mixtures.**

| Study | Impact of High Polymer Modification | |
|---|---|---|
| | **Binder Properties** | **Mixture Properties** |
| Florida DOT[1]: Evaluation and Implementation of Heavy Polymer Modified Asphalt Binder through Accelerated Pavement Testing | - Increased resistance to rutting<br>- Increased resistance to fracture | - Reduced creep rate<br>- Increased resistance to cracking |
| University of Nevada: Evaluation of Thermal Oxidative Aging Effect on the Rheological Performance of Modified Asphalt Binders | - Increased resistance to long-term oxidative aging | - *NO MIX TESTING* |
| ORLEN Asfalt, Poland: Highly Modified Binders Orbiton HiMA | - Increased resistance to thermal cracking<br>- Increased resistance to fatigue cracking<br>- Increase resistance to rutting | - Increased resistance to thermal cracking<br>- Increased resistance to rutting |
| New Hampshire and Vermont DOTs: Development and Validation of Performance based Specifications for High Performance Thin Overlay Mix | - *NO BINDER TESTING* | - RAP content of 25% negatively impacted the resistance of the mixture to cracking<br>- HP binder could not overcome the negative impact of Rap on cracking |
| New Hampshire DOT: Materials and Mixture Test Results, New Hampshire DOT Highways for Life, 2011 Auburn-Candia Resurfacing | -*NO BINDER TESTING* | - Reduced dynamic modulus<br>- Increased resistance to rutting<br>- Increased resistance to fatigue cracking<br>- Increased resistance to reflective cracking<br>- Increased resistance to thermal cracking |
| National Center Asphalt for Asphalt Technology: Field and Laboratory Study of High-Polymer Mixtures at the NCAT Test Track | - Increased resistance to rutting | - Increased tensile strength<br>- Increased dynamic modulus<br>- Increased resistance to rutting<br>- Increased resistance to fatigue cracking |

[1] Not a true HP binder according to FDOT Specifications 2018

*8.1.1.2 Performance of Pavement Sections Constructed with HP AC Mixes*

Several field projects were constructed to evaluate the performance of HP modified asphalt mixtures as compiled in Section 2.3. Table 8-2 summarizes the review of seven field projects using HP AC mixes with limited and extensive performance data.

**Table 8-2. Summary of Laboratory Evaluations of HP Binders and Mixtures.**

| Location | Project Description | Key Findings |
|---|---|---|
| Brazil, 2011 | - Mill and AC overlay on highway PR-092<br>-Traffic up to 4,200 heavy agricultural trucks per day | - Good early performance<br>- Additional HP projects were constructed on Dutra road which runs between Sao Paulo and Rio de Janeiro |
| USA/ Advanced Material Services LLC, 2013 | - Designing for Corvette Museum Race Track in Bowling Green Nashville<br>- Raveling and bleeding remain the main concerns<br>- Evotherm WMA additive was used to improve workability | - A potentially high performance AC mix was delivered for the race track by using HP asphalt binder |
| USA / City of Bloomington, MN, 2012 | - Mill and AC overlay on Normandale Road, City of Bloomington<br>- Subjected to heavy traffic due to its location adjacent to the airport<br>- Two projects were constructed: Normandale Service Road at 84$^{th}$ Street and West 98$^{th}$ Street | - HP AC mix performed well and constituted a good way to place more cost-effective and durable asphalt pavements with reduced thicknesses.<br>- HP AC mix offered possibility of building pavement section on top of weak base and subgrade layers |
| USA / Georgia DOT, 2010 | - Thin AC overlay at junction of Routes 138 and 155<br>- Pavement rutting and shoving were the main concerns | - HP AC mix was observed to have similar workability as regular PMA mix based on general observations reported from the job site |
| USA/NCAT Test Track, 2009 | - HP test section designed with an AC layer thickness 18% less than the AC layer thickness of the PMA section | - HP section experienced lower rutting under the entire loading cycle of 8.9 million ESALs<br>- Both HP and PMA sections did not experience any fatigue cracking under the entire loading cycle of 8.9 million ESALs |
| USA / NHDOT and VTDOT, 2011 | - New Hampshire project on Route 202, AC overlay over existing pavement in bad conditions without pre-treatment<br>- Vermont project on US-7, AC overlay over existing pavement in bad conditions with some pre-treatment | - Minimal reflective cracking on the New Hampshire section containing RAP material<br>-No signs of environmental related cracking and no evidence of rutting were observed after 2 years of service |
| USA / Oklahoma DOT, 2012 | - Mill and overlay on I-40 west of Oklahoma city | - HP AC mix had a low enough viscosity making it workable and compactable when used in the field |
| USA / Oregon DOT, 2012 | - Thin overlay mix on I-5 in Oregon<br>- Existing pavement had some wearing ruts and raveling due to heavy trucks and high traffic volumes | - No special plant adjustments were made to accommodate the production of HP AC mix.<br>- No problems with viscosity were faced during the paving of the HP mix |

A review of the findings in Table 8-2 leads to the following observations:

- HP AC mixes have been used over a wide range of applications ranging from full depth AC layers to thin AC overlays under heavy traffic on interstates and slow-braking loads at intersections.
- HP AC mixes did not experience any construction issues in terms of mixing temperatures and in-place compaction. Standard construction practices and equipment were adequately used.
- All the identified HP field projects lack information on long-term performance, however, early performances are encouraging. In addition, the HP test section on the NCAT Test Track showed excellent performance under accelerated full-scale loading.

*8.1.1.3 Techniques to Determine Structural Coefficient of HP Modified AC Mixes*

None of the available studies calculated the structural coefficient of HP AC mixes *($a_{HP\text{-}AC}$)* mainly because of the unavailability of the required full performance characterizations of the mixtures. In some cases, a hypothetical structural coefficient may be identified as shown below:

- For the project in Brazil; the HP section replaced the standard section at a 45% reduction in the overall thickness indicating an $a_{HP\text{-}AC}$ that is 45% higher than the corresponding structural coefficient for the composite pavement (i.e., AC over cement-stabilized RAP).
- For the projects in Bloomington, MN and Oklahoma; the HP section replaced the standard section at a 25% reduction in the thickness of the AC layer indicating an $a_{HP\text{-}AC}$ that is 25% higher than the corresponding structural coefficient for the standard AC mix.

The performance data generated from the PMA and HP test sections at the NCAT Test Track offered some basis for the determination of an $a_{HP\text{-}AC}$. However, the fact that both sections did not show any fatigue cracking and only the minimal rutting was experienced by both sections (i.e., less than 0.25 inch) limits the applicability of the estimated $a_{HP\text{-}AC}$. Despite these limitations, the research team attempted to demonstrate the various methods to establish an $a_{HP\text{-}AC}$ based on the data from the NCAT test sections. Four approaches were examined; three empirical approaches based on the AASHTO 1993 Guide methodology and one mechanistic approach based on the analysis of fatigue performance. The three empirical approaches recommended an $a_{HP\text{-}AC}$ ranging from 0.54 to 0.57 while the mechanistic approach recommended an $a_{HP\text{-}AC}$ ranging between 0.82 and 0.88.

In summary, while several previous studies highlighted the positive impacts of the HP modification of asphalt binders and mixtures, there is still a serious lack of understanding on the structural value of the HP AC mix as expressed through the structural coefficient for the AASHTO 1993 Guide. The attempt by the research team to determine an $a_{HP\text{-}AC}$ based on the available information led to the conclusion that empirically-based $a_{HP\text{-}AC}$ can underestimate the structural value of the HP AC mix while determining the $a_{HP\text{-}AC}$ based on the mechanistic analysis of a single failure mode (i.e., fatigue cracking) may overestimate the structural value of the HP AC mix. This important and critical finding strongly supports the approach implemented in this research where the full evaluation of the performance characteristics of the HP AC mixes were conducted and the $a_{HP\text{-}AC}$ is determined based on the mechanistic analysis of all possible critical modes of failure.

### 8.1.2. Execution of the Experiment: Laboratory Evaluation and Advanced Modeling

Materials shipped from Florida were assessed and used for the development of 16 AC mixes using PMA and HP asphalt binders (i.e., eight PMA and eight HP AC mixes) for new construction and rehabilitation projects. The mix designs were conducted following the Superpave methodology to determine the optimal asphalt binder content (OBC) for each of the 16 evaluated mixes. Various OBC values were determined depending on the aggregate source, aggregate gradation, binder type (i.e., PMA or HP), binder source, and the possible use of any recycled material (i.e., RAP). The 16 AC mixes were evaluated in terms of their resistance to moisture damage, dynamic modulus, rutting, and multiple cracking distress modes (i.e., fatigue, top-down, and reflective). In general, the combination of aggregate source and asphalt binder type (i.e., PMA or HP) had significant impacts on the performance behavior of the evaluated AC mixes. The following bullets summarize the findings and recommendations from the laboratory evaluation and advanced modelling of HP AC mixes produced using materials from Florida:

- Overall, HP AC mixes showed better engineering property and performance characteristics when compared with the corresponding PMA control AC mixes which can be credited to the high polymer modification of the asphalt binder (i.e., HP binder). The true impact of the improvements in engineering property and performance characteristics of the HP AC mixes were evaluated through the mechanistic analysis of flexible pavements incorporating the two types of mixtures.
- The critical responses determined using the 3D-Move mechanistic model were used to evaluate the performance life of the designed pavement structures for several targeted distresses including; fatigue cracking, AC rutting, total rutting, top-down cracking, and reflective cracking. The critical responses were computed and determined at different locations within the structure depending on the distress mode. It should be mentioned that two temperatures were considered for the mechanistic analysis: 77°F (25°C) simulating an intermediate temperature for cracking analyses, and 122°F (50°C) simulating a high temperature for rutting/showing analyses. These temperatures were determined using the corresponding critical climatic stations in Florida (i.e., Gainesville and Marathon).
- Initial structural coefficient for HP AC mixes was determined based on the fatigue performance life of flexible pavements. An equivalent HP AC layer thickness was determined which resulted in a similar fatigue life as the respective PMA pavement section under static and dynamic loading conditions. Multiple factors including applied traffic level, pavement structure, layers properties, and performance characteristics of the evaluated PMA and HP AC mixes resulted in different structural coefficients for HP AC mixes based on the fatigue cracking analysis. The estimated initial fatigue-based structural coefficients ranged from 0.33 to 1.32. Using advanced statistical analyses and considering all factors and their interactions, an initial fatigue-based structural coefficient of 0.54 was determined for HP AC mixes.
- The initial fatigue-based structural coefficient for HP AC mixes of 0.54 was verified for the following distresses; rutting in AC layer, shoving in AC layer, total rutting, top-down cracking, and reflective cracking. In all cases, the thickness of the HP layer was reduced based on the fatigue-based structural coefficient of 0.54 and the resistance of the HP pavement to the specific distress was evaluated and compared to the resistance of its corresponding PMA pavement. The verification process concluded that the structural

coefficient of 0.54 for HP AC mixes would lead to the design of HP pavements that offer equal or better resistance to the various distresses as the designed PMA pavements with the structural coefficient of 0.44. This conclusion held valid for the design of both new and rehabilitation projects.

- Based on the data generated and the analyses conducted in this part of the research, it was recommended that HP AC mixes be incorporated into the current FDOT Flexible Pavement Design Manual with a structural coefficient of 0.54. This represents a 23% reduction in the thickness of the AC layer when using a HP AC mix in place of a PMA AC mix while designing a flexible pavement under all similar conditions of traffic, environment, and properties of base and subgrade layers.

### 8.1.3. Verification of Structural Coefficient for HP AC Mixes using Full-Scale Testing

A verification of the recommended $a_{HP\text{-}AC}$ of 0.54 was conducted using full-scale pavement testing prior to the full implementation in the FDOT APT experiment. The experimental plan comprised a PMA and an HP full-scale pavement structures that were fully instrumented and subjected to stationary dynamic loads. The two pavement structures had identical CAB and SG layers. The HP AC layer in the PaveBox_HP experiment was 19% thinner than the PMA AC layer in the PaveBox_PMA experiment (3.50 versus 4.25 inches AC layer thickness). While FDOT mandates the use of a 12 inch (305 mm) thick stabilized SG layer, only a typical SG layer was used in the two PaveBox experiments. This was considered acceptable for the purpose of this study that aimed for a relative comparison of responses between the PMA and HP pavement sections.

The two pavement structures were subjected to the same loading protocol. Dynamic loads simulating FWD loading, were applied at the surface of the AC pavements. Pavement surface deflections, vertical stresses, and strains at different depths and locations in the pavement layers were monitored during testing through embedded instrumentations. LVDTs were used to record surface pavement deflections. TEPC were used to capture the vertical stresses induced in the CAB and SG layers due to surface loading. Strain gauges were attached to the bottom of the AC layer to measure the load-induced strains. At the end of each experiment, cores were cut from the AC layer for thickness and air voids measurements. Two major analyses were carried out in this task. Analysis I consisted of a comparison of measured pavement responses under dynamic loadings, while analysis II verified the $a_{HP\text{-}AC}$ of 0.54 using a ME approach of the tested pavement structures. The following summarizes the findings and conclusions from the full-scale testing task:

- Overall, the HP AC mix showed better fatigue and rutting characteristics when compared with the PMA AC mix. This was demonstrated with higher fatigue and lower rutting relationships for the produced HP AC mix when compared with the PMA AC mix.
- A comparison of the measured pavement responses from the two experiments was conducted. The reduced thickness of the HP AC layer resulted in the following observations: a) higher vertical surface deflections under the center of the loading plate, b) higher vertical stresses under the center of the loading plate at the middle of the CAB layer, c) similar vertical stresses at 6 inch (152 mm) and 24 inch (610 mm) below the SG surface, d) similar or lower tensile strains at the bottom of the AC layer, and e)

comparable surface deflections and vertical stresses in the CAB and SG layers at radial distances farther away from the load, i.e. 8–60 inches (203–152 cm).

- An ME analysis was conducted using 3D-Move and the backcalculated layers' moduli in conjunction with the laboratory-developed performance models for the produced PMA and HP AC mixes. The ME analysis with the reduced thickness of the HP AC layer resulted in the following observations: a) better fatigue and rutting performance for the HP AC layer when compared with the PMA AC layer, b) higher rutting in the unbound layers of the HP pavement structure, especially in the CAB layer, and c) similar total rutting for the PMA and HP pavement structures.
- In general, the results and findings from this task supported the selection of $a_{HP\text{-}AC} = 0.54$. A reduction in the recommended $a_{HP\text{-}AC}$ value might be warranted if the load-induced stresses in the unbound materials (in the CAB layer in particular) lead to excessive permanent deformations that exceeds the rut depth limits set by FDOT. This aspect requires further evaluation in the FDOT APT experiment.

Based on these findings, an implementation plan was recommended for the APT experiment at FDOT facility for the validation of the recommended $a_{HP\text{-}AC}$ of 0.54. The recommended implementation plan is presented the following section.

## 8.2. APT IMPLEMENTATION PLAN

This section presents recommendations for FDOT to validate the recommended structural coefficient ($a_{HP\text{-}AC}$ of 0.54) through full scale testing under the APT facility. The main concept of the validation plan is to evaluate the performance of flexible pavement sections constructed with HP AC mixes at a reduced thickness of the AC layer relative to the performance of control pavement sections. The plan was developed based on the findings from the performance modeling of the flexible pavement sections and the full-scale pavement testing experiments conducted in the PaveBox. The factors proposed in the APT implementation plan stems from those that were considered in the previous tasks of this study (e.g., aggregate and asphalt binder sources, NMAS, traffic level, etc.).

### 8.2.1. Experimental Design

The comparison of the performance of an HP pavement section with that of a PMA pavement section is one of the main objectives of the recommended APT experiment. Table 8-3 summarizes the recommended APT experiments. The following factors were identified for consideration in the APT experimental plan:

- Asphalt binder type: a conventional PG76-22PMA and an HP asphalt binder from a common supplier in Florida. Two candidate suppliers are Ergon Asphalt and Emulsion and Vcenergy.
- Aggregate source: Southeast Florida limestone labeled as "FL," and Georgia Granite labeled as "GA."
- Recycled asphalt pavement (RAP): a single source of RAP to be used with GA aggregates and PMA asphalt binder at a rate of 20% following current FDOT standard of practice.

- Pavement structure: conventional pavement structures designed in accordance with the FDOT design manual including a CAB layer and a 12 inch (305 mm) stabilized SG layer on top of the existing SG. The CAB and SG layer will be the same across all pavement sections.
- AC layer thickness: the thickness of the PMA AC layer will be designed using a structural coefficient of 0.44. The thickness of the HP AC layer will be designed using the recommended structural coefficient of 0.54 and a lower structural coefficient of 0.50. The proposed structural coefficient of 0.50 is based on the results of the statistical analysis conducted in task 3 for the structural coefficients of AC mixes with GA aggregate source and 9.5 mm NMAS.
- Traffic Level: AC mixes with 9.5 and 12.5 mm NMAS designed for traffic levels C and D, respectively, were considered in task 3. The NMAS contributed to some of the differences in the performance evaluation of the designed PMA and HP AC mixes, which resulted in a wide range of HP AC structural coefficients. Thus, AC mixes designed for traffic levels C and D are recommended for the validation effort in the APT experiment.
- Pavement temperature: rutting was found to be most critical among the evaluated distresses. Thus, testing during the hot seasons at the temperatures typically observed at the APT facility is considered appropriate for the objectives of this experiment.

**Table 8-3. Proposed APT Experiments.**

| Experiment ID | Traffic Level | Aggregate Source | Pavement Structure | RAP (%) |
|---|---|---|---|---|
| HP1 | C | GA | Control PMA: $a_{PMA\text{-}AC}$ = 0.44<br>HP1A: $a_{HP\text{-}AC}$ = 0.54<br>HP1B: $a_{HP\text{-}AC}$ = 0.50 | 20<br>0<br>0 |
| HP2 | D | FL | Control PMA: $a_{PMA\text{-}AC}$ = 0.44<br>HP2A: $a_{HP\text{-}AC}$ = 0.54 | 0<br>0 |

### 8.2.2. Instrumentation Plan

The pavement test sections should be instrumented to provide a comprehensive picture of the system response. Strain gauges should be installed at the bottom of the AC layers to provide the strain history as a result of the surface loading. Strain gauges should be installed in the travel direction and perpendicular to the travel direction to capture both the longitudinal and traverse strains, respectively. TEPCs should be used to capture the stresses induced in the CAB and SG layers due to loading. The TEPCs should be installed under the centerline of the load and at different radial distances from the centerline of the load. Multi-depth deflectometers (MDD) should be installed to measure elastic vertical deflections and permanent vertical deformations at various depths within the pavement structure, relative to a reference depth located in the SG. Thus, allowing for the continuous monitoring of rutting under loading in the various pavement layers. Thermocouples should be used to measure temperatures at various depths within the AC layer. Time domain reflectometer can be used to monitor the changes in water content in the unbound layers just outside the trafficked area during testing of the pavement sections.

### 8.2.3. Pavement Design

The pavement structures for the PMA control sections will need to be designed in accordance with the FDOT manual for designing flexible pavements in Florida. The design thickness is based on a tested Lime Bearing Ratio (LBR) of the SG, the type of CAB material to be used, and the design traffic level. Consequently, the thickness of the AC layers in the HP pavement sections are reduced based on the structural coefficients shown in Table 8-3.

A mechanistic analysis should be conducted for the designed pavement structures to estimate the rutting level in the unbound layers, in particular the CAB layer. Based on this study, it is anticipated that the load-induced vertical stresses in the CAB layer of the HP pavement sections will be higher than the ones measured in the CAB layer of the PMA pavement structures. It is suggested that a localized shear failure analysis be conducted prior to finalizing the pavement structural designs to investigate the influence of the reduced HP AC layer on the rutting performance of unbound layers. The analysis will consist of comparing the load-induced stress level calculated at the middle of the CAB layer with the corresponding yield criterion of the material. It should be noted that the localized shear failure analysis can only focus on the CAB layer, since the12-inch stabilized layer will likely reduce the load-induced stresses in the SG layer.

Several failure criteria, such as Mohr–Coulomb, Drucker–Prager, Lade–Duncan, etc. have been proposed for evaluating shear failure of unbound materials. The Mohr–Coulomb yield criterion is one of the well-accepted criterion in soil plasticity that is determined using the shear strength parameters (cohesion and angle of internal friction) of the material. The concept of shear stress ratio (SSR) can be employed for assessing the potential for localized shear failure.
Previous studies examined the use of SSR to assess permanent deformation potential in unbound materials *(104)(107)*. As illustrated in Figure 8-1, the SSR is defined as the ratio of the applied (mobilized) shear stress ($\tau_{mobilized}$) to the material's shear strength ($\tau_{max}$). It has been concluded that an unbound material experiencing an SSR value greater than 0.70 will likely accumulate high permanent strains, thus resulting in excessive permanent deformation. Accordingly, the AC layer thickness should be increased to result in an acceptable level of SSR in the unbound layers. Depending on the findings from the SSR mechanistic analysis, considerations should be given for the possibility of including an additional pavement section, HP2 (traffic level D), to experiment with an $a_{HP\text{-}AC}$ lower than 0.54.

### 8.2.4. Pavement Construction

After accomplishing all needed structural designs and mechanistic analyses, the pavement structures should be constructed in accordance with the FDOT specifications *(23)*. Dynamic cone penetrometer (DCP) and falling weight deflectometer (FWD) testing should be carried out periodically on the individual layers during pavement construction to monitor the pavement strength, modulus, and stiffening rate.

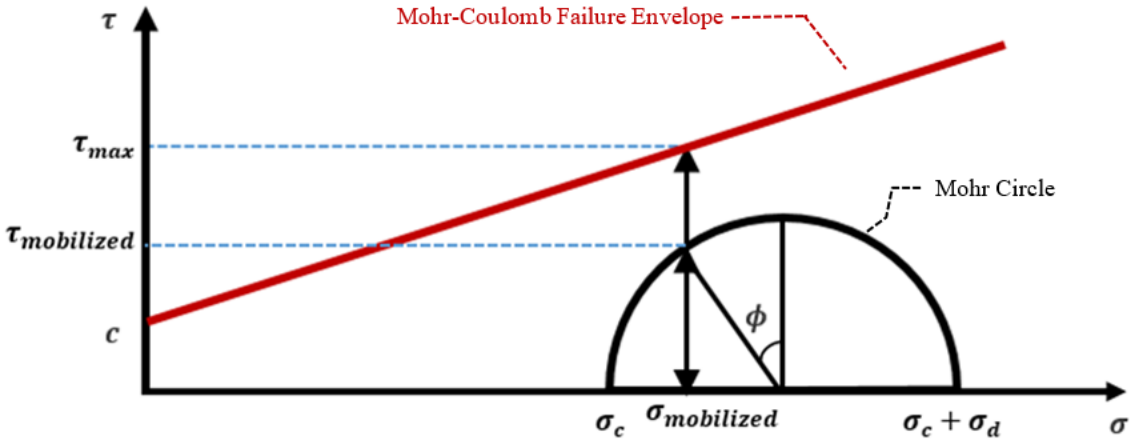


**Figure 8-1. Mohr-Coulomb Failure and SSR.**

# CHAPTER 9. REFERENCES


(1) IDOT (2005). *Polymer-Modified Hot Mix Asphalt*, Illinois Department of Transportation, Bureau of Materials and Physical Research, Pavement Technology Advisory, Design, Construction and Materials, PTA-B5.
(2) AASHTO (1993). *AASHTO Guide for Design of Pavement Structures*, American Association of State Highway and Transportation Officials, Washington, D.C.
(3) Timm D.H., and K. Peters-Davis (2009). *Recalibration of the Asphalt Layer Coefficient*, Report No. 09-03, National Center for Asphalt Technology, Auburn University.
(4) FDOT (2016). *Flexible Pavement Design Manual*, Florida Department of Transportation, Office of Design, Pavement Management Section.
(5) ARA, Inc. (2004). *Guide for Mechanistic-Empirical Design*, ERES Consultants Division, Transportation Research Board of the National Academies, National Cooperative Highway Research Program NCHRP, Project 1-37A, Washington DC.
(6) Habbouche, J., Hajj, E. Y., Sebaaly, P. E., and Piratheepan, M. (2018). *A Critical Review of High Polymer-Modified Asphalt Binders and Mixtures*, International Journal of Pavement Engineering, Taylor & Francis, DOI: 10.1080/10298436.2018.1503273.
(7) Zhu. C. (2015). *Evaluation of Thermal Oxidative Aging Effect on the Rheological Performance of Modified Asphalt Binders*, Thesis submitted in partial fulfillment of the requirements for the degree of Master of Science in Civil and Environmental Engineering, University of Nevada, Reno.
(8) Yildirim. Y. (2005). *Polymer Modified Asphalt Binders*, Construction and Building Materials, ELSEVIER.
(9) Thompson DC. Hoiberg AJ (1979), editor. Bituminous Materials: *Asphalt Tars and Pitches*, Robert Krieger Publishing Co.
(10) Terrel R, Walter J. (1986). *Modified Asphalt Pavement Materials: The European Experience*, Journal of Association of Asphalt Pavement Technologists (AAPT), 55:482.
(11) Bahia H.U., Perdomo D., and Turner P. (1997). *Applicability of Superpave Binder Testing Protocols to Modified Binders*, Transportation Research Record, 1586:16-23.
(12) Sargand S.M., Kim S.S. (2001). *Performance Evaluation of Polymer Modified and Unmodified Superpave Mixes*, In: Second International Symposium on Maintenance and Rehabilitation of Pavements and Technological Control, Auburn, AL.
(13) Sebaaly P.E., Bazi G.M., and Vivekanathan Y. (2003). *Evaluation of New Pavement Technologies in Nevada*, University of Nevada.
(14) Newcomb D. (2003), *Limit the Strain at the Bottom of an Asphalt Pavement, and What Do You Get? A Perpetual Pavement*, Hot Mix Asphalt Technology, 8(6): 30-2.
(15) Partl M. N., and Newman J. K. (2003). *Flexural Beam Fatigue Properties of Airfield Asphalt mixtures Containing Styrene-Butadiene Based Polymer Modifiers*, In: Proceedings of the Sixth International Rilem, Symposium, Zurich, Switzerland, P. 357-63.
(16) Becker Y., Mendez M. P., and Rodriguez Y. (2011). *Polymer Modified Asphalt*, Vis Technology, 9 (1):39-50.
(17) Bates R., and Worch R. (1987). *Styrene-Butadiene Rubber Later Modified Asphalt*, Engineering Brief No. 39, Federal Aviation Administration, Washington, DC. http://www.faa.gov/arp/engineering/briefs/eb39.htm.

(18)Roque R., Birgisson B., Tia M., Kim B., and Cui Z. (2004). *Guidelines for the Use of Modifiers in Superpave Mixtures: Executive Summary*, and Volume 1 of 3 volumes, *Evaluation of SBS Modifier*, State Job 9905279., Florida Department of Transportation, Tallahassee, FL.
(19)Mohammed L.N. et al. (2003). *Investigation of the Use of Recycled Polymer Modified Asphalt Binder in Asphalt Concrete Pavements* (with discussion and closure), Journal of the Association of Asphalt Paving Technologists, 72:551-94.
(20)Fournier P. (2010). *Georgia DOT Chooses Highly Modified Asphalt for Busy Intersection*, Dixie Contactor Edition, Volume 84, Number 10, kraton.com/products/hima/documents/DXC%20Oct2010_feature2%20(2).pdf.
(21)Timm D.H., Robbins M.M., Willis J.R., Tran N., and Taylor A. (2012). *Field and Laboratory Study of High-Polymer Mixtures at the NCAT Test Track*, Interim Report, Report No. 12-08, National Center for Asphalt Technology, Auburn University.
(22)Greene J., Chun S., and Choubane B. (2014). *Evaluation and Implementation of a Heavy Polymer Modified Asphalt Binder Through Accelerated Pavement Testing*, Florida Department of Transportation, State Materials Office, Research Report Number FL/DOT/SMO/14-564.
(23)FDOT (2018), *Standard Specifications for Road and Bridge Construction*, Florida Department of Transportation.
(24)AASHTO T315 (2013). *Standard Method of Test for Determining the Rheological Properties of Asphalt Binder Using a Dynamic Shear Rheometer (DSR)*, American Association of State Highway and Transportation Officials, Washington, D.C..
(25)AASHTO T350 (2013). *Standard Method of Test for Multiple Stress Creep Recovery (MSCR) Test of Asphalt Binder Using a Dynamic Shear Rheometer (DSR)*, American Association of State Highway and Transportation Officials, Washington, D.C..
(26)D'Angelo J. (2010). *New High-Temperature Binder Specifications Using Multistress Creep and Recovery*, Transportation Research Circular, Development in Asphalt Binder Specifications, No E-C147, pp.1-13.
(27)Roque R., Niu T., Lopp G., and Zou J. (2012). *Development of a Binder Fracture Test to Determine Fracture Energy*, Florida Department of Transportation, Contract BDK75 977-27, Tallahassee, FL.
(28)AASHTO T322 (2013). *Standard Method of Test for Determining the Creep Compliance and Strength of Hot-Mix Asphalt (HMA) Using the Indirect Tensile Test Device*, American Association of State Highway and Transportation Officials, Washington, D.C.
(29)Blazejowski K., Olszacki J., and Peciakowski H. (2015), *Highly Modified Binders Orbiton HiMA*, ORLEN Asfalt, Application Guide, Version 1e, Poland.
(30)AASHTO T313 (2012), *Standard Method of test for Determining the Flexural Creep Stiffness of Asphalt Binder Using the Bending Beam Rheometer (BBR)*, American Association of State Highway and Transportation Officials, Washington, D.C..
(31)AASHTO TP10 (1993), *Standard Test Method for Thermal Stress Restrained Specimen Tensile Strength*, American Association of State Highway and Transportation Officials, Washington, D.C..
(32)AASHTO (2012), Transportation System Preservation Technical Services Program (TSP2), *Kraton Ultra-thin HMA / WMA Overlay Study*, American Association for State Highway and

Transportation Officials, http://www.tsp2.org/pavement/other-information/research-pavement/, Accessed July 5th, 2012.
(33)Mogawer W. S., Austerman A. J., Kluttz R., and Mohammad L. N. (2014). *Development* and Validation of *Performance Based Specifications for High Performance Thin Overlay Mix*, Transportation research Board, Transportation Research Circular, Number E-C189, Page 52-68.
(34)Tex-248-F (2014). *Overlay Test*, Test Procedure for Texas Department of Transportation, Austin, TX.
(35)AASHTO T321 (2014). *Standard Method of Test for Determining the Fatigue Life of Compacted Asphalt Mixtures Subjected to Repeated Flexural Bending*, Association of State Highway and Transportation Officials, Washington, D.C.
(36)AASHTO T340 (2010). *Standard Method of Test for Determining Rutting Susceptibility of Hot Mix Asphalt (HMA) Using the Asphalt Pavement Analyzer (APA)*, American Association of State Highway and Transportation Officials, Washington, D.C..
(37)AASHTO T324 (2011). *Standard Method of Test for Hamburg Wheel-Track Testing of Compacted Hot Mix Asphalt (HMA)*, American Association of State Highway and Transportation Officials, Washington, D.C.
(38)Mogawer W. S. (2014). *Material and Mixture Test Results*, New Hampshire DOT Highways for Life Project, 2011 Auburn-Candia Resurfacing, University of Massachusetts, Highway Sustainability Research Center (HRSC).
(39)AASHTO T378 (2013). *Determining the Dynamic Modulus and Flow Number for Hot Mix Asphalt (HMA) Using the Asphalt Mixture Performance Tester (AMPT)*, American Association of State Highway and Transportation Officials, Washington, D.C.
(40)AASHTO R84 (2010). *Standard Practice for Developing Dynamic Modulus Master Curves for Hot Mix Asphalt (HMA) Using the Asphalt Mixture Performance Tester (AMPT)*, American Association of State Highway and Transportation Officials, Washington, D.C.
(41)Smith K. (2012). *Kraton's HiMA Trials in Brazil*, Asphalt Paving, Reproduced by kind permission of World Highways, Route One Publishing.
(42)Kuennen T. (2015). *Winning the Race Track Challenge*, Asphalt Pavement Magazine, Published by the National Asphalt Pavement Association, Volume 20, Number 6, p.18-23.
(43)Fournier P. (2013), *New Pavement Technologies Tried in Twin Cities*, Asphalt Review, Roads, published by the Australian Asphalt Pavement Association, Volume 103, Number 4.
(44)Kuennen T. (2012). *Oklahoma Anticipates I-40 Performance Gain with HMA*, www.theasphaltpro.com, Asphalt Pro, p.38-43.
(45)Fournier P. (2012). *Oregon Tries Advanced Pavement Overlay*, Asphalt Review, Roads, Pacific Builder and Engineer, Volume 118, Number 8.
(46)AASHTO T301 (2017). *Standard Method of Test for Elastic Recovery Test of Asphalt Materials by Means of a Ductilometer*, American Association of State Highway and Transportation Officials, Washington, D.C.
(47)AASHTO M320 (2010). *Standard Specification for Performance-Graded Asphalt Binder*, American Association of State Highway and Transportation Officials, Washington, D.C.
(48)AASHTO MP19 (2010). *Standard Specification for Performance-Graded Asphalt Binder Using Multiple Stress Creep Recovery*, American Association of State Highway and Transportation Officials, Washington, D.C., Inactive.

(49) AASHTO T283 (2014). *Standard Method of Test for Resistance of Compacted Asphalt Mixtures to Moisture-Induced Damage*, American Association of State Highway and Transportation Officials, Washington, D.C.
(50) Van Wyk A., Yoder E.J., and Wood L.E. (1983). *Determination of Structural Equivalency Factors for Recycled Layers by Using Field Data*, Transportation Research Record 898, Transportation Research Board, Washington, D.C.
(51) Hossain M., Habib A., and LaTorella T.M. (1997). *Structural Layer Coefficients of Crumb-Rubber Modified Asphalt Concrete Mixtures*, Transportation Research Record 1583, Transportation Research Board, Washington, D.C.
(52) Timm D. H., Design (2009). *Construction, and Instrumentation of the 2006 test Track Structural Study*, Report No. 09-01, National Center for Asphalt Technology, Auburn University.
(53) Al-Omari B., and Darter M. I. (1994). *Relationships between International Roughness Index and Present Serviceability Rating*, Transportation Research Record 1435, Transportation Research Board, Washington, D. C.
(54) Siddharthan R.V., Hajj E.Y., Sebaaly P.E., and Nitharsan R. (2015). *Formulation and Application of 3D-Move: A dynamic Pavement Analysis Program*, Report FHWA-RD-WRSC-UNR-201506, Western Regional Superpave Center, University of Nevada, Reno.
(55) Sebaaly P. E., Bazi G. M, and Vivekanathan Y. (2003). *Evaluation of New Pavement Technologies in Nevada*, Report No. RDT-03-034, Western Regional Superpave Center, university of Nevada, Reno.
(56) AASHTO T48 (2006). *Standard Method of Test for Flash and Fire Points by Cleveland Open Cup*, American Association of State Highway and Transportation Officials.
(57) AASHTO T316 (2013). *Standard Method of Test for Viscosity Determination of Asphalt Binder Using Rotational Viscometer*, American Association of State Highway and Transportation Officials.
(58) AASHTO T240 (2013). *Effect of Heat and Air on a Moving Film of Asphalt Binder (Rolling Thin-Film Oven Test)*, American Association of State Highway and Transportation Officials.
(59) AASHTO M332 (2014). *Standard Specification for Performance-Graded Asphalt Binder Using Multiple Stress Creep Recovery (MSCR) Test*, American Association of State Highway and Transportation Officials.
(60) AASHTO R28 (2012). *Standard Practice for Accelerated Aging of Asphalt Binder Using a Pressurized Aging Vessel (PAV)*, American Association of State Highway and Transportation Officials.
(61) AASHTO T27 (2014). *Standard method of Test for Sieve Analysis of Fine and Coarse Aggregates*, American Association of State Highway and Transportation Officials.
(62) FM 1-T011 (2015). *Florida Method of Test for Materials Finer Than 75µm (No. 200) Sieve in Mineral Aggregate by Washing*, Florida Department of Transportation, State Materials Office.
(63) ASTM D5821 (2017). *Standard Test Method for Determining the Percentage of Fractured Particles in Coarse Aggregate*, American Society for Testing and Materials.
(64) AASHTO T304 (2017). *Standard Method of Test for Uncompacted Void Content of Fine Aggregate*, American Association of State Highway and Transportation Officials.
(65) ASTM D4791 (2017). *Standard Test Method for Flat Particles, Elongated Particles, or Flat and Elongated Particles in Coarse Aggregate*, American Society for Testing and Materials.

(66) AASHTO T176 (2017). *Standard Method of Test for Plastic Fines in Graded Aggregates and Soils by Use of the Sand Equivalent Test*, American Association of State Highway and Transportation Officials.
(67) AASHTO T2 (1991-2015). *Standard Method of Test for Sampling of Aggregates*, American Association of State Highway and Transportation Officials.
(68) AASHTO T164 (2014). *Standard Method of Test for Quantitative Extraction of Asphalt Binder form Hot Mix Asphalt (HMA)*, American Association of State Highway and Transportation Officials.
(69) FM 3-D5404 (2000). *Florida Method of Test for Recovery of Asphalt From Solution Using The Rotavapor Apparatus*, Florida Department of Transportation, State Materials Office.
(70) AASHTO R30 (2002). *Standard Practice for Mixture Conditioning of Hot-Mix Asphalt (HMA)*, American Association of State Highway and Transportation Officials.
(71) AASHTO R83 (2017). *Standard Practice for Preparation of Cylindrical Performance Test Specimens Using the Superpave Gyratory Compactor (SGC)*, American Association of State Highway and Transportation Officials.
(72) NCHRP Project 719 (2012). *Calibration of Rutting Models for Structural and Mix Design*, National Cooperative Highway Research Program, a Synthesis of Highway Practice, Transportation Research Board, National Research Council.
(73) NCHRP Report 669 (2010), *Model for Predicting Reflection Cracking of Hot-mix Asphalt Overlays*, National Cooperative Highway Research Program and Transportation Research Board of the National Academies.
(74) Pavement Interactive (2008), *Rutting*, Flexible Pavement Distress, Pavement Distresses, Pavement Management.
(75) ASTM D7460 (2010). *Standard Test Method for Determining Fatigue Failure of Compacted Asphalt Concrete Subjected to repeated Flexural Bending*, American Society for Testing and Materials.
(76) NCHRP Project No. 09-57 (2016), *Experimental Design for Field Validation of Laboratory Tests to Assess Cracking Resistance of Asphalt Mixture*, National Cooperative Highway Research Program and Transportation Research Board of the National Academies.
(77) Garcia V., Miramontes A., Garibay J., Abdallah I. , and Nazarian S. (2016). *Improved Overlay Tester for Fatigue Cracking Resistance of Asphalt Mixtures*, Center for Transportation Infrastructure Systems, The University of Texas at El Paso, Research performed in cooperation with Texas Department of Transportation (TxDOT), Report No. TxDOT 0-6815-1.
(78) Zhou F., Hu S., Hu X., and Scullion T. (2008). *Mechanistic-Empirical Asphalt Overlay Thickness Design and Analysis System*, Texas Transportation Institute (TTI), Texas Department of Transportation, Technical Report 0-5123-3.
(79) FM 1-T 283 (2018). *Florida Method of Test for Resistance of Compacted Bituminous Mixture to Moisture-Induced Damage*, Florida Department of Transportation, State Materials Office.
(80) Florida Highway Patrol (2016). *Commercial Motor Vehicle Manual*, Office of Commercial Vehicle Enforcement. Ninth edition.
(81) Hajj E.Y., Thushanthan P., Sebaaly P., and Siddharthan R. (2014). *Influence of Tire-Pavement Stress Distribution, Shape, and Braking on Performance Predictions for Asphalt*

*Pavement*, Transportation Research Board, Transportation Research Record, Print ISSN 0361-1981, Washington D.C.
(82)Nabizadeh H. S. (2017). *Development of a Comprehensive Analysis Approach for Evaluating Superheavy Load Movement on Flexible Pavements*, Dissertation for fulffilemnt of doctorate degree, Civil and Environmental Engineering, University of Nevada Reno (UNR).
(83)NCHRP Project No. 09-22 (2011). *A Performance-Related Specification for Hot-Mixed Asphalt*, National Cooperative Highway research Program, Transportation research Board, NCHRP Report 704, Washington D.C..
(84)Prowell B.D., Brown E. R., Aderson R. M., Daniel J.S., Quintus H. V, Shen S., Carpenter S.H., Bhattacharjee S., and Maghsoodloo S. (2010). *Validating the Fatigue Endurance Limit for Hot Mix Asphalt*, National Cooperative Highway research Program, Transportation research Board, NCHRP Report 646, Washington D.C..
(85)Singh K., and Xie M. (2008). *Bootstrap: A Statistical Method*, Rutgers University.
(86)Birgisson B., Wang J., and Roque R. (2006). *Implementation of the Florida Cracking Model Into the Mechanistic-Empirical Pavement Design*, University of Florida, Florida Department of Transportation (FDOT), UF No.: 0003932, Contract No.: BD-545 #20.
(87)Roque R., Birgisson B., Drakos C., and Dietrich B. (2004). *Development and Field Evlaution of Energy-Based Criteria for Top-Down Cracking Performance of Hot Mix Asphalt*, Journal of the Association of Asphalt Paving Technologists, Vol. 73, pp. 229-260.
(88)Habbouche J., Hajj E.Y., Morian N. E., Sebaaly P.E., and Piratheepan M. (2017). *Reflective Cracking Relief Interlayer for Asphalt Pavement Rehabilitation: From Development to Demonstration*, Road Materials and Pavement Design, 18:sup4, 30-57, DOI: 10.1080/14680629.2017.1389080.
(89)Jacobs M. M. J. (1995). *Crack Growth in Asphaltic Mixes*, Ph.D. Dissertation, Delft University of Technology, Road Railroad Research Laboratory, The Netherlands.
(90)Seo Y., Kim Y., Schapery, Witczak M., and Bonaquist R. (2004). *A Study of Crack-Tip Deformation and Crack Growth in Asphalt Concrete Using Fracture Mechanics*, Journal of the Association of Asphalt Paving Technologists, Vol. 73, pp. 200-228.
(91)Roque R., Zhang Z., and Sankar B. (1999). *Determination of Crack Growth Rate Parameters of Asphalt Mixtures Using the Supeprave IDT*, Journal of the Association of Asphalt Paving Technologists, Vol. 68, pp. 404-433.
(92)Hajj E. Y., Siddharthan R. V., Nabizadeh H., Elfass S., Nimeri M., Kazemi S. F., batioja-Alvarez D. D., and Piratheepan M. (2018). *Analysis Procedures for Evaluating Superheavy Load Movement on Flexible Pavements*, Volume I: Final Report, Report No. FHWA-HRT-18-049, Federal Highway Administration, Washington D.C..
(93)AASHTO T11-05 (2005). *Standard Method of Test for Materials Finer Than 75-µm (No.200) Sieve in Mineral Aggregates by Washing*, American Association of State Highway and Transportation Officials, Washington, D.C.
(94)AASHTO T89-13 (2013). *Standard Method of Test for Determining the Liquid Limit of Soils*, American Association of State Highway and Transportation Officials, Washington, D.C.
(95)AASHTO T90-16 (2016). *Standard Method of Test for Determining the Plastic Limit and Plasticity Index of Soils*, American Association of State Highway and Transportation Officials, Washington, D.C.

(96) AASHTO M145 (2017). *Standard Specification for Classification of Soils and Soil-Aggregate Mixtures for Highway Construction Purposes*, American Association of State Highway and Transportation Officials, Washington, D.C.
(97) ASTM D2487 (2011). *Standard Practice for classification of Soils for Engineering Purposes (Unified Soil Classification System)*, Book of Standards 04.08, American Society for testing and Materials, ASTM International, West Conshohocken, PA.
(98) AASHTO T307 (2017), *Standard Method of Test for Determining the resilient Modulus of Soils and Aggregate Materials*, American Association of State Highway and Transportation Officials, Washington, D.C.
(99) AASHTO T99 (2017). *Standard Method of Test for Moisture-Density Relations of Soils Using a 2.5-kg (5.5-lb) Rammer and a 305-mm (12-inch) Drop*, American Association of State Highway and Transportation Officials, Washington, D.C.
(100) NDOT (2018). *Standard Specifications for Road and Bridge Construction*, Nevada Department of Transportation, Carson City, Nevada, July 6.
(101) AASHTO T248 (2014). *Standard Method of Test for Reducing Samples of Aggregate to Testing Size*, American Association of State Highway and Transportation Officials, Washington, D.C.
(102) AASHTO T180 (2017). *Standard Method of Test for Moisture-Density Relations of Soils Using a 4.54-kg (10-lb) Rammer and a 457-mm (18-inch) Drop*, American Association of State Highway and Transportation Officials, Washington, D.C.
(103) Liu, W., and T. Scullion (2001). *Modulus 6.0 for Windows: User's Manual*. FHWA/TX-05/0-1869-2. Texas Transportation Institute, The Texas A&M University System, Federal Highway Administration, Texas.
(104) Chow, L.C., Mishra, D., and Tutumluer, E. (2014), *Framework for Development of an Improved Unbound Aggregate Base Rutting Model for Mechanistic–Empirical Pavement Design*, Transportation Research Record, 2401, pp. 11–21, Transportation Research Board, Washington, DC.
(105) Kazmee, H. and Tutumluer, E. (2015), *Evaluation of Aggregate Subgrade Materials Used as Pavement Subgrade/Granular Subbase*, Report No. FHWA-ICT-15-013, Federal Highway Administration, Washington, DC.
(106) Seyhan, U. and Tutumluer, E. (2002), *Anisotropic Modular Ratios as Unbound Aggregate Performance Indicators*, Journal of Materials in Civil Engineering, 14(5), pp. 409–416, American Society of Civil Engineers, Reston, VA.
(107) Tutumluer, E., Kim, I.T., and Santoni, R.L. (2004), *Modulus Anisotropy and Shear Stability of Geofiber-Stabilized Sands*, Transportation Research Record, 1874, pp. 125–135, Transportation Research Board, Washington, DC.

# APPENDIX A. LABORATORY EVALUATION OF HP MODIFIED ASPHALT BINDERS AND MIXTURES – EXTENDED LITERATURE REVIEW

Polymer modification of asphalt binders is not a new concept and has become progressively more common over the past several decades. While several agencies utilize unmodified asphalt binders, many have increasingly become reliant upon polymer modified asphalt binders with a fair portion of those located in climatic regions that experience significantly wider temperature range conditions and higher levels of oxidation. Therefore, it is becoming ever more important to characterize the benefits afforded with the polymer modification process. The objectives of this appendix are to: a) present an overall background on the history of asphalt binder modification using polymers, and b) provide some detailed information about recent laboratory studies that evaluated the performance of HP asphalt binders and mixtures.

## A.1. HISTORY OF POLYMER MODIFIED ASPHALT BINDERS

The increase in traffic volume and axle loads coupled with reduced budgets of public agencies required better performance from the designed pavement structure. The modification of asphalt binders was identified as a suitable solution to provide the improved performance *(7)*. The processes providing the modification of asphalt binders using natural and synthetic polymers were patented as early as 1843 in Europe *(8), (9)*. The significantly higher costs of the early polymer modified asphalt binders limited their use in the United States till mid-1980s when newer and less expensive polymers were developed *(10)*. A survey conducted in 1997, indicated that 47 out of 50 states allowed the use of modified asphalt binders and some DOTs (35 out of 47) confirmed that their use is quickly increasing *(11)*. At that time, many research teams around the world focused on evaluating the benefits to pavement performance attributed to the use of polymer modified asphalt binders. A study done for Ohio DOT (OHDOT) showed that AC mixtures manufactured using modified asphalt binders performed much better in terms of resistance to fatigue cracking and permanent deformation when compared with mixtures manufactured using neat asphalt binders *(12)*. A significantly higher viscosity was observed for modified asphalt binders at 140°F (60°C) in accordance with a study done in Nevada in 2003 *(13)*. In a 2003 study discussing the concept of hot mix asphalt (HMA) perpetual pavements, Newcomb claimed the benefit of using a modified asphalt mixture in the bottom lift of the AC layer in increasing the fatigue life of the pavement structure *(14)*. Consequently, agencies estimated an addition of four to six years of life for a pavement structure when constructed using a modified asphalt binder.

A 2003 study by the US Army Corps of Engineers showed that the type of modifier may affect the performance of the asphalt binder in resisting multiple distresses such as rutting, fatigue, thermal cracking, and moisture damage *(15)*. In comparison to neat asphalt binders, modifiers typically invoke specific enhancements to the physical properties and rheological performance of asphalt binders, such as improving the ductility, expanding the relaxation spectra, and increasing its overall strength. For example, ductility and resistance to rutting can be improved by the use of natural rubber in asphalt binder despite its problems with compatibility and decomposition *(16)*. The use of tire rubber improved the resistance to rutting and reflective cracking but still required high mixing temperatures and long digestion times to prevent the separation of the modified asphalt binder *(16)*. Meanwhile, the addition of Styrene-Butadiene-Rubber modifier (SBR) to

asphalt binders helped in improving the low-temperature ductility, elastic recovering as well as the cohesive and adhesive properties of the binder *(16)*. Within the past 20 years, the SBS modifier replaced the SBR because of its wider compatibility and greater tensile strength property *(17)*. In general, improvement in asphalt binder ductility in conjunction with the improved elastic behavior due to polymer modification can have a positive influence on the cracking resistance of asphalt mixtures. Previous studies have shown the capability of polymer modifiers to lessen the deteriorative oxidative age hardening effects *(18)*. Accordingly, more durable asphalt pavements can be expected from the use of polymer modified AC mixtures.

Currently, SBS is a well-recognized elastomer which is commonly used in asphalt mixtures due to its elasticity and ability to be recycled. Asphalt binders modified with SBS polymers have shown improved performance at low temperatures when compared to un-modified binders and binders modified with chemically reactive polymers (e.g., Polyphosphoric Acid…). In 2003, Mohammed et al. evaluated the possibility of recycling SBS modified asphalt mixtures as part of the pavement rehabilitation process *(19)*. Cores were sampled from US-61 in Louisiana and the eight-year-old SBS modified binder was extracted and recovered. The recovered polymer modified asphalt binder was blended with virgin binder and evaluated at different range of temperatures. The blend was found to be much stiffer than anticipated at both low and high temperatures with a higher rutting resistance and a lower fatigue resistance. A 2004 FDOT study showed the use of SBS polymer in asphalt binder was able to reduce the rate of micro-damage accumulation and therefore benefited cracking resistance *(18)*. However, it was found that there is no effect for using SBS on healing or aging characteristics of the asphalt mixture.

The most commonly used polymer modified asphalt binders limit the SBS content to around 3% due to cost and construction issues. Recent studies showed that these issues can be overcome by modifying the conventional structure of the SBS polymer to produce a modified asphalt binder with increased durability and reduced costs. In 2010, researchers at Delft University developed a new SBS polymer structure that allowed the use of SBS at levels of 7 – 8% by weight of asphalt binder *(20)*.

Figure A.1 illustrates a typical polymer modified asphalt binder with 2.5% polymer where the polymer is not in continuous phase *(21)*. Increasing the polymer content up to 7.5% changes the structure from asphalt binder with a dispersed swollen polymer phase to a swollen polymer with a dispersed asphalt binder phase. At this stage, the HP asphalt binder is more like an asphalt-modified rubber rather than a rubber-modified asphalt where the rubber makes the continuous phase in the structure. The phase reversal achieved by the addition of high polymer content produces a more elastic asphalt binder with improved resistance to permanent deformations (i.e., rutting and shoving) and cracking (i.e., fatigue, thermal, and reflective).

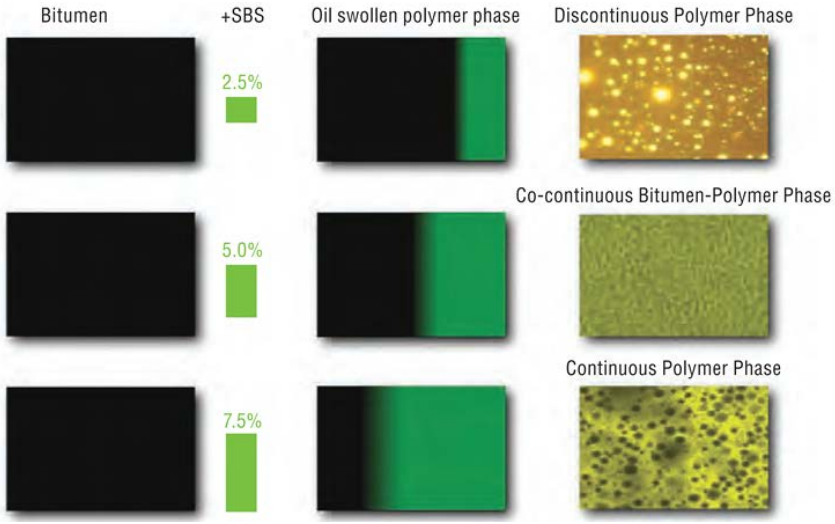


**Figure A.1. Effect of increasing SBS polymer content on asphalt binder/polymer morphology** *(21)***.**

## A.2. LABORATORY EVALUATION OF POLYMER MODIFIED ASPHALT BINDERS IN FLORIDA

In 2001, FDOT conducted a study to evaluate the effect of polymer modified PG76-22 asphalt binder on the rutting resistance of Superpave mixes through laboratory evaluations and Accelerated Pavement Testing (APT). Guidelines resulted from this study directed the use of polymer modified PG76-22 asphalt binder in the final structural course for traffic level D mixtures (10 to 30 million ESALs) and the top two structural courses for traffic level E mixtures (more than 30 million ESALs). At that time, FDOT did not have sufficient number of pavement sections with modified asphalt mixtures to fully quantify the additional life that can be expected, while an extension of five to ten years of service life was being estimated by other agencies when PMA AC mixes are used *(22)*.

Within the past five years, FDOT attempted to increase the rutting resistance of asphalt mixtures by increasing the polymer content of asphalt binders resulting in a grade of PG82-22PMA. The cost of the PG82-22PMA, in 2014, was approximately $100 and $250 per liquid metric ton more expensive than the PG76-22PMA and the neat PG67-22 asphalt binder, respectively. Therefore, such investment requires the assessment and quantification of additional benefits provided by the use of PG82-22PMA. In response, an extensive study was conducted to evaluate the performance of PG82-22PMA mixtures in terms of rutting and fatigue resistance in the laboratory and under APT loading *(22)*.

It should be noted that the PG82-22PMA asphalt binder and mixture evaluated in the FDOT study contained 6% SBS polymer by weight of binder. Therefore, the PG82-22PMA does not meet the requirement of a HP binder as defined in this current study (i.e., approximate SBS content of 7.5% by weight of binder). As discussed in the scope of the literature review, the FDOT study was included since it offers an insight on the impact of incrementally increasing the SBS content from 0, 3, to 6% by weight of binder.

### A.2.1. Properties of Evaluated Asphalt Binders

Three asphalt binders meeting the current FDOT specifications were evaluated in this study: a PG67-22 neat binder, a PG76-22PMA binder at 3% SBS content, and a PG82-22PMA binder at 6% SBS content. All asphalt binders were collected at the plant and laboratory tests such as dynamic shear rheometer (DSR), multiple stress creep recovery (MSCR), and binder fracture energy were conducted for analysis and characterization *(22)*.

*Dynamic Shear Rheometer*

The DSR is used to characterize the viscous and elastic behavior of asphalt binders at high to intermediate pavement temperatures (part of the in-service pavement temperature range) via measuring the complex modulus (G*) and phase angle (δ) *(24)*. This characterization is used in the Superpave Performance Grade (PG) asphalt binder specification. DSR tests were performed on original asphalt binders at the high temperature of each selected binder grade (i.e. 67, 76, and 82°C). Figure A.2 presents the DSR properties of the three evaluated binders. The results showed that the PG82-22PMA binder exhibited the greatest stiffness, elasticity, and rutting resistance, as shown by its high G*, low $\delta$, and high $G^*/\sin(\delta)$, respectively. It should be mentioned that FDOT specifies a minimum $G^*/\sin(\delta)$ of 1.0 kPa and a maximum phase angle (δ) of 75° and 65° for PG76-22PMA and PG82-22PMA asphalt binders, respectively.

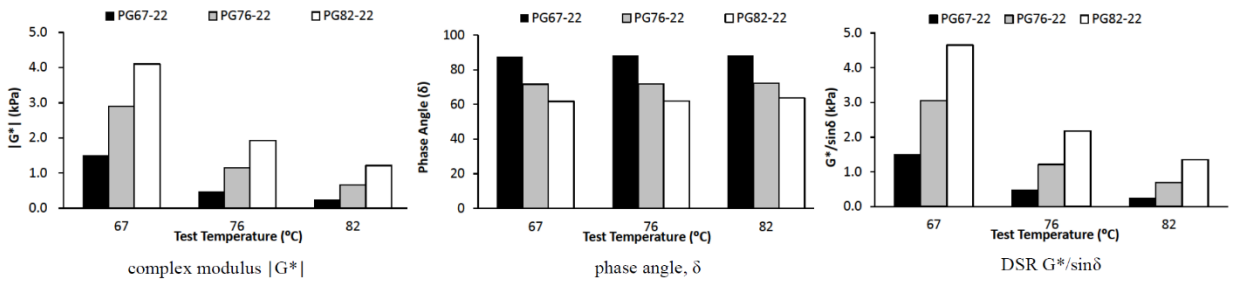


**Figure A.2. DSR properties of PG67-22, PG76-22PMA, and PG82-22PMA binders** *(22)*.

*Multiple Stress Creep Recovery*

The MSCR test provides additional properties on the asphalt binder at high pavement temperature to assess its resistance to rutting under the expected traffic level. The test consists of applying a stress level of 0.1 kPa or 3.2 kPa for ten consecutive cycles. Each cycle consists of a creep period loaded for 1 second followed by a 9 second recovery period *(25)*. The non-recoverable creep compliance *($J_{nr}$)* has been used as an indicator of the asphalt binder's resistance to rutting under repeated load. It is calculated as the average of non-recovered strain for the ten cycles divided by the applied stress level. The MSCR test was conducted on the rolling thin film oven (RTFO) residues at temperature of 64°C (147°F). Figure A.3 presents the MSCR test results of the three evaluated asphalt binders *(22)*.

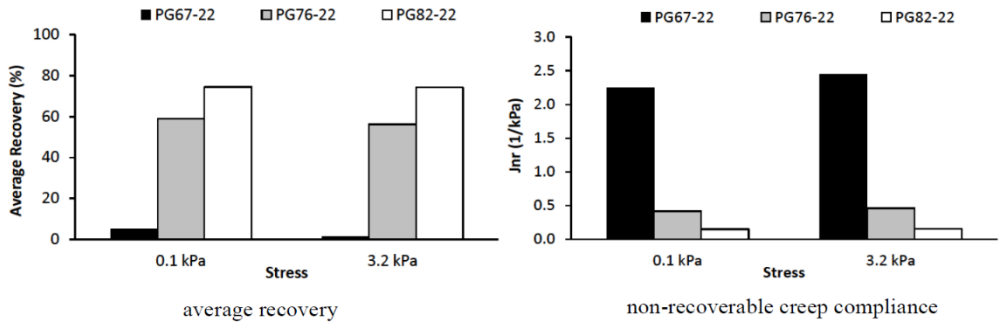


**Figure A.3. MSCR test results at 64°C (147°F) for PG67-22, PG76-22PMA and PG82-22PMA binders** *(22)*.

The MSCR test results indicate that the two polymer modified asphalt binders exhibit greater viscoelastic behavior than the neat binder shown by the higher recovery and lower non-recoverable creep compliance values accompanied with a lower sensitivity to the stress level. An earlier Federal Highway Administration (FHWA) study showed that a 50% reduction in $J_{nr}$ can reduce the rutting of actual pavement sections by 50% and the rutting of APT pavement sections by 30 to 40% *(26)*.

*Binder Fracture Energy*

A new binder fracture energy test procedure was developed by researchers at the University of Florida to predict the fracture energy of an asphalt binder at intermediate pavement temperatures *(27)*. It was shown that this fracture energy constitutes a fundamental property of the asphalt binder independent of the testing temperature and the loading rate. The test consists of applying a direct tensile stress on a binder specimen at relatively high loading rate (0.4-3.9 inch/min (10-100 mm/min)) and measures the stress versus strain curve. The average true stress versus strain curve is calculated on the central cross-sectional area of the specimen where fracture initiates and propagates. Fracture energy is calculated as the surface underneath the stress-strain curve from the beginning of the test to the highest stress level representing the point of initial fracture. The test was conducted at a temperature of 50°F (10°C) on RTFO residues subjected to long-term aging in the pressure aging vessel (PAV). A greater fracture energy was observed for the PG82-22PMA when compared with the PG76-22PMA and PG67-22 binders (Figure A.3) indicating a better fracture resistance for AC mixes manufactured with the PG82-22PMA binder *(22)*.

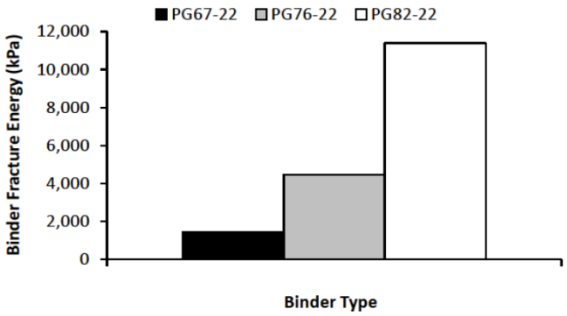


**Figure A.3. Binder fracture energy test results for PG67-22, PG76-22PMA and PG82-22PMA binders** *(22)*.

### A.2.2. Properties of AC Mixtures

The AC mixtures were designed with 0.5-inch (12.5 mm) nominal maximum aggregate size (NMAS) fine gradation using granite aggregate. The optimum asphalt binder contents were selected as 4.9, 4.8, and 4.7% by total weight of mix for mixtures manufactured using PG67-22, PG76-22PMA, and PG82-22PMA, respectively. Figure A.4 illustrates the aggregate gradations of the three mixes. During construction, there was a concern of achieving the required in-place density on the lane constructed using the PG82-22PMA AC mix because of the high percent of polymer and increased stiffness. A non-nuclear Pavement Quality Indicator (PQI) device was utilized to estimate the compacted AC mix in-place density after each pass of the static and vibratory rollers. The final density measurements were verified by cutting cores from each lane *(22)*.

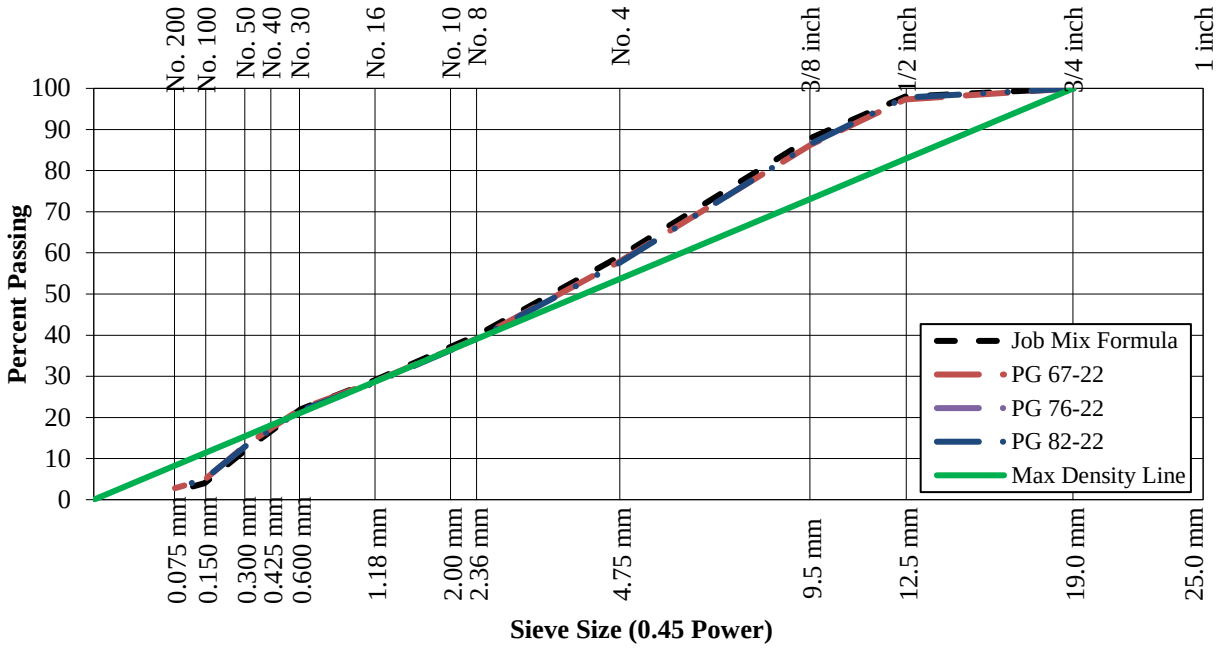


**Figure A.4. Aggregate gradations of PG67-22, PG76-22PMA, and PG82-22PMA mixes used on FDOT APT Test Track.**

*Superpave Indirect Tension*

The cracking resistance of the mixtures was evaluated using the Superpave indirect tension test (IDT) *(28)*. The test was conducted only on cores from the PG76-22PMA and PG82-22PMA sections at a temperature of 50°F (10°C) due to time limitations. The IDT applies a diametral creep load on a 6 inch (150 mm) diameter by 2.5 inch (64 mm) height sample to measure the creep compliance followed by the tensile strength. Using the measured creep compliance and tensile strength, the dissipated creep strain energy (DCSE) and energy ratio (ER) are calculated and used to assess the resistance of the evaluated asphalt mixture to top-down cracking. Figure A.5 shows the measured properties from the IDT in terms of fracture energy, creep rate, and energy ratio. These plots lead to the following observations:

- Slightly lower fracture energy was observed for the PG82-22PMA AC mix when compared with the PG76-22PMA AC mix. However, this minor difference in the measured fracture energy values may be due to the variability in the IDT test.
- A 66% reduction in the creep rate was observed for the PG82-22PMA AC mix as compared to the PG76-22PMA AC mix.
- Relatively higher energy ratio was exhibited by the PG82-22PMA AC mix indicating a better cracking resistance when compared with the PG76-22PMA AC mix.

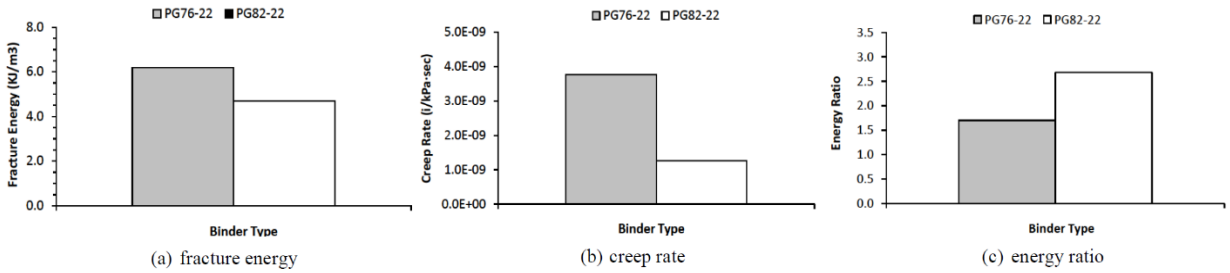


(a) fracture energy (b) creep rate (c) energy ratio

**Figure A.5. IDT fracture properties for PG76-22PMA and PG82-22PMA asphalt mixtures *(22)*.**

### A.2.3. APT Experiment: Design and Testing

In general, APT consists of applying repetitive full scale wheel loads to a pavement structure to simulate in-service loading conditions. The accelerated loading was performed using the FDOT Heavy Vehicle Simulator (HVS), electrically powered, mobile, and fully automated. The overall experiment evaluated the rutting and fatigue performance of the different mixtures *(22)*.

For the evaluation of rutting resistance, the AC layers of the existing three test lanes were milled to a depth of 4 inch (102 mm) leaving 1 inch (25 mm) of the existing AC layer in-place. The milled 4 inch (102 mm) AC mix was replaced by the PMA and neat asphalt mixtures as shown in Figure A.6-a. The mix designs were classified as Superpave fine-graded mixes manufactured using granite material with 5.1% asphalt binder content by total weight of mix. For rutting evaluation, the pavement test track lanes were heated to 122°F (50°C) and trafficked with a 9,000 pounds (4,082 Kg) load on dual tires with inflation pressure of 100 psi (690 kPa). Laser profiles were used to measure rut depths at various intervals of the HVS loading *(22)*.

For the evaluation of fatigue resistance, additional two test lanes were constructed consisting of two 1.5 inch (38 mm) lifts of the same PMA Superpave fine-graded AC mixes placed directly on the granular base layer (Refer to Figure A.6-b). The water table was raised to the bottom of the base to weaken the pavement structure. Longitudinal strains under dual tires load of 12,000 pounds (5,443 Kg) with inflation pressure of 110 psi (758 kPa) were measured by strain gauges installed at the bottom of the 3 inch (76 mm) AC layer *(22)*.

The rutting performance of the various mixes were evaluated through measuring the actual rut depth developed in the wheel path and by estimating the shear area at the edge of the rut relative to the area of wheel path. Figure A.7 illustrates the rut profiles (i.e., progression of rut depths) of the three test lanes as well as the transverse rut profiles after 100,000 passes. Table A.1 summarizes the rutting and shear area values of the various sections under the HVS loading. The data in Figure A.7 and Table A.1 indicate that both polymer modified mixtures (i.e., PG76-22PMA, and PG82-22PMA) significantly out-performed the neat mix (i.e., PG67-22) showing a rut depth reduction of 29% and 49% after 100,000 passes, respectively. Meanwhile the PG82-22PMA AC mix performed significantly better than the PG76-22PMA in both measured rut depth (reduction of 28%) and shear area (reduction of 40%) *(22)*.

In the fatigue resistance evaluation, FDOT researchers reported significant reductions in measured tensile strains at the bottom of AC layer for the two PMA AC mixes with the percent reduction increasing with the higher polymer content (i.e., PG82-22PMA). In addition, the predicted fatigue life of the PG82-22PMA AC mix was seven times higher than the fatigue life of the PG76-22PMA AC mix. On the other hand, the predicted fatigue lives of the two polymer modified mixes were more than 20 times higher than the predicted fatigue life of the neat PG67-22 mix *(22)*.

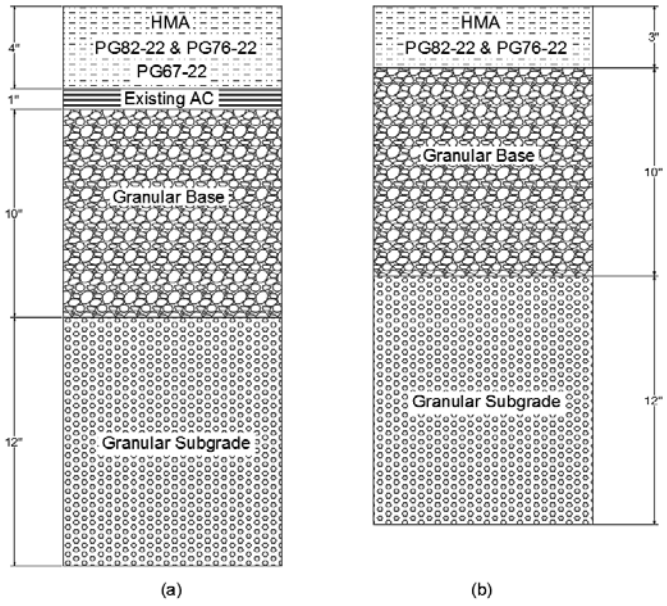


**Figure A.6. APT pavement structures for evaluating: (a0 rutting, and (b) fatigue.**

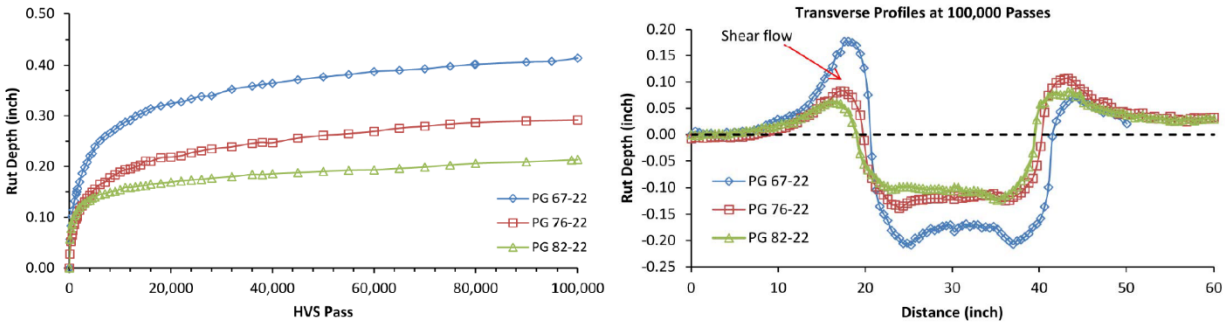


(a) (b)

**Figure A.7. APT rutting test results: (a) rut depth progression, and (b) Transverse profiles after 100,000 passes** *(22)***.**

**Table A.1. Summary of the Rutting Performance of the APT Sections** *(22)***.**

| Pass Number | PG67-22 | | PG76-22PMA | | PG82-22PMA | |
|---|---|---|---|---|---|---|
| | Rut, inch (mm) | Shear Area/ WP Area | Rut, inch (mm) | Shear Area/ WP Area | Rut, inch (mm) | Shear Area/ WP Area |
| 100 | 0.06 (1.52) | 0.21 | 0.03 (0.76) | 0.44 | 0.06 (1.52) | 0.23 |
| 5,000 | 0.24 (6.10) | 0.60 | 0.16 (4.06) | 0.50 | 0.14 (3.56) | 0.28 |
| 10,000 | 0.28 (7.11) | 0.63 | 0.19 (4.83) | 0.52 | 0.15 (3.81) | 0.20 |
| 20,000 | 0.32 (8.13) | 0.61 | 0.22 (5.59) | 0.49 | 0.17 (4.32) | 0.30 |
| 100,000 | 0.41 (10.41) | 0.72 | 0.29 (7.37) | 0.45 | 0.21 (5.34) | 0.27 |

### A.2.4. Conclusions and Implementation

The data presented in this FDOT research on the laboratory evaluations of the asphalt binders and mixtures and the APT evaluations indicated that the incremental addition of the SBS polymer from 0, 3, to 6% by weight of binder significantly improved the resistance of the materials to rutting and fatigue. Under all the evaluations, the data showed that the addition of 3% SBS improved the performance of the binder and mix relative to the 0% SBS while the addition of 6% SBS improved the performance of the binder and mix relative to the 3% SBS at a significantly higher rate. These observations lead to the belief that increasing the SBS content to the HP level of 7.5% would continue to improve the performance of the asphalt binder and mix.

Based on the findings of this study, FDOT allowed the use of the PG82-22PMA binder by increasing the mix compaction temperature from 331°F (166°C) to 340°F (171°C) along with a decrease of the phase angle criterion in the binder specification from 75° to 65°. FDOT

implemented the PG82-22PMA in two resurfacing projects during 2012: (a) SR 60 in Hillsborough County, and (b) the mainline pavement in Nassau County on SR 200. The latest comments received from FDOT personnel indicated that both projects are still showing good performance in terms of smoothness, rutting, and fatigue resistance *(22)*.

## A.3. EFFECT OF LONG-TERM AGING ON HP-MODIFIED ASPHALT BINDERS

In addition to improving the resistance of the AC mixtures to rutting and cracking, the high polymer content may improve the resistance of the asphalt binder to long-term aging. An asphalt binder with low susceptibility to long-term aging would significantly reduce the potential of the asphalt mixture to all types of cracking: bottom-up fatigue, top-down fatigue, thermal, reflective, and block. This phenomenon was evaluated in a recent research study by the Pavement Engineering and Science (PES) Program at University of Nevada, Reno (UNR) where the long-term aging susceptibility of three asphalt binders: neat, polymer modified with 3% SBS (PMA), and highly polymer modified with 7.5% SBS (HP) were evaluated *(7)*. The main objective of the study was to observe and quantify the influence of binder modification on the oxidative aging characteristics of asphalt binders.

The neat binder was used as the base for the two polymer modified binders. The evaluated asphalt binders were aged to measure the aging kinetics as a function of time and temperature when the binders were exposed to free-atmospheric air. The three asphalt binders were placed in 5.5 inch (140 mm) diameter PAV pan at 0.04 inch (1 mm) film thickness and subjected to long-term aging in forced draft ovens for various combinations of temperatures and aging durations as follows:

- 122°F (50°C) for 4, 8, 15, 30, 60, 120, 180, and 240 days;
- 140°F (60°C) for 2, 4, 8, 15, 30, 60, 100, and 160 days; and
- 185°F (85°C) for 0.5, 1, 2, 4, 8, 15, 25, and 40 days.

Rheological evaluations based upon master curve development can be a very useful method to evaluate the influence of oxidative aging on multiple physical characteristics of asphalt binders. The rheological indices utilized in this study were derived from the developed dynamic shear modulus master curve utilizing the time-temperature superposition principle to predict properties at the temperature and frequency combinations. Two asphalt binder replicates were tested in the DSR to determine the rheological parameters by conducting isothermal frequency sweeps at different temperatures ranging from 230°F (110°C) to 28.4°F (-2°C). The isotherms were then shifted into master curves of dynamic shear modulus *(G*)* and phase angle ($\delta$) utilizing the Rhea software package. Correspondingly, black space diagrams, defined as shear modulus versus phase angle plot, provides a robust evaluation methodology for the rheological evaluation of asphalt binders. The aging susceptibility of the asphalt binders were evaluated using the Glover-Row (G-R) parameter defined as function of G* and the corresponding $\delta$ as indicated in Equation A.1.

$$G - R = \frac{G^* cos^2 \delta}{\sin \delta} \qquad \textbf{[Equation A.1]}$$

Where;
$G^*$: dynamic shear modulus, psi (Pa); and

$\delta$: phase angle, degree.

Figure A.8 shows the measured properties of the aged binders plotted on the G-R parameter scale. Each data point plotted in this figure represents a specific asphalt binder condition in terms of temperature and time as defined earlier. It is anticipated that lower G* and lower δ represent lower susceptibility to long-term aging. In addition, a steeper slope between G* and δ represents lower susceptibility to long-term aging. In other words, a steep curve located closer to the left side of the chart indicates lower susceptibility to long-term aging. The data presented in Figure A.8 show that the HP asphalt binder is the least susceptible to long-term aging, followed by the PMA binder, while the neat asphalt binder is the most susceptible to long-term aging. Furthermore, the data show that the neat asphalt binder was the first binder to reach the G-R cracking criterion of 87 psi (600 kPa) after about 170 days of oven aging while the PMA and HP asphalt binders lasted for about 190 and 230 days before reaching the same failure criterion.

The advantages of the SBS polymer modification have been fairly distinct, consistent and directly evident as outcome of this study. In summary, the addition of SBS polymer in well formulated and consistently blended materials do provide clear benefits to the overall performance of asphalt binders and corresponding mixtures in terms of longevity and aging resistance.

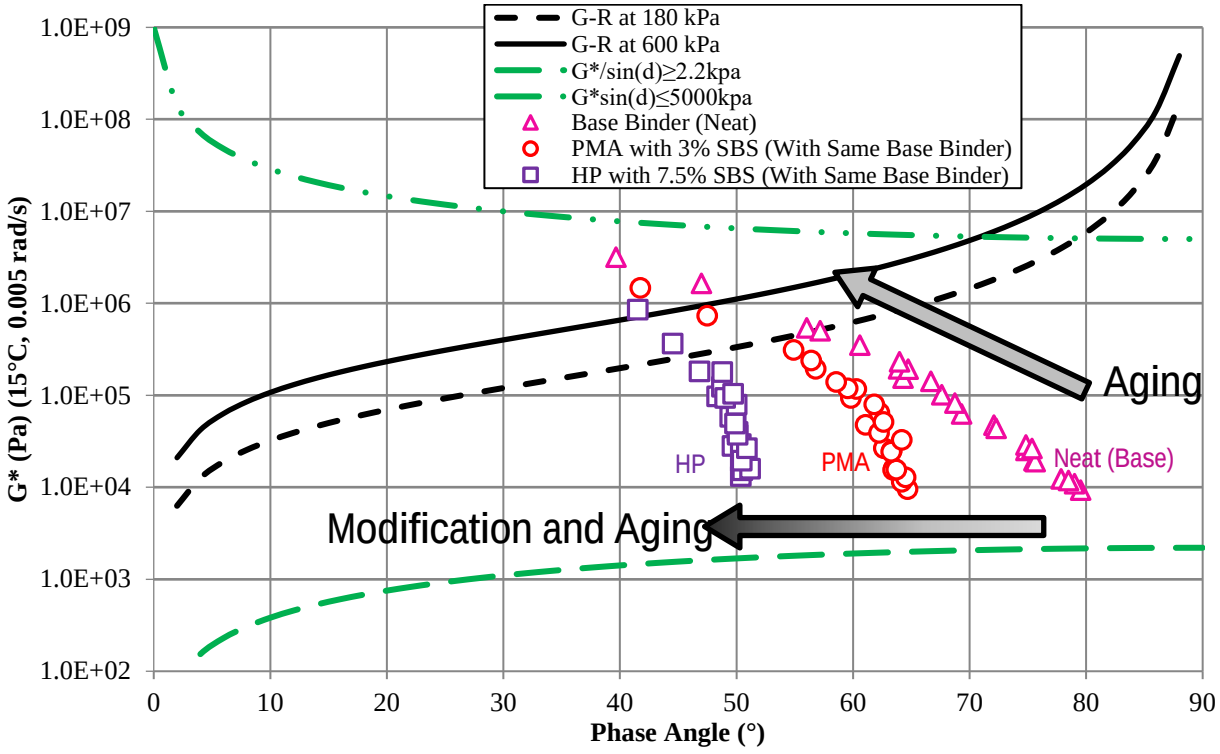


**Figure A.8. Comparison of Glover-Rowe (G-R) parameters for neat, PMA, and HP asphalt binders in a black space diagram *(7)*.**

## A.4. LABORATORY EVALUATION OF HP BINDERS IN POLAND: ORBITON HIMA

Researchers at ORLEN Asfalt in Poland hypothesized that a crack can pass through a conventionally modified asphalt binder by finding weak spots between the polymer network sections. Meanwhile, the crack passage through a highly modified asphalt binder is more difficult because of the barrier formed by the polymer network as depicted in Figure A.9 *(29)*. Limiting crack propagation in asphalt mixtures remains a clear example illustrating the benefits of a continuous polymer network acting in the asphalt binder and mixtures as an elastic reinforcement. In 2011, three new HP asphalt binders were developed by researchers at ORLEN Asfalt in Poland: (a) ORBITON 25/55-80 HiMA designated to be used for typical asphalt base courses of long-life pavements (i.e., perpetual) with slow traffic, (b) ORBITON 45/80-80 HiMA designated to be used for wearing and binder courses of pavements subjected to very heavy loads and/or low temperatures, and c) ORBITON 65/105-80 HiMA designed to be used for special technologies such as stress absorbing membrane interlayers (SAMI), and emulsion applications in slurry seals *(29)*. All three binders were modified with 7.5% SBS by weight of binder. The properties of the three HP binders and AC mixes were evaluated in the laboratory at the low, intermediate, and high temperatures.

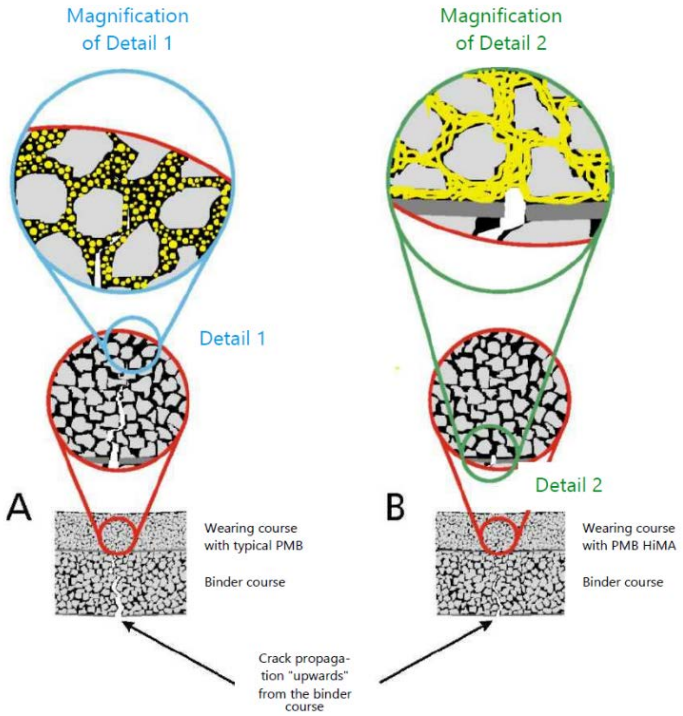


**Figure A.9. Crack propagation illustration through: (a) conventional PMA mixes and (b) HP mixes *(29)*.**

### A.4.1. Low Temperature Properties

As surrounding temperatures drop, pavements contract and build up internal stresses. The bending beam rheometer (BBR) test provides a measure of low temperature stiffness and

relaxation properties of asphalt binders *(30)*. The parameters give an indication of the asphalt binder's ability to resist low temperature cracking. The test is conducted on short and long-term aged binder condition (RTFO + PAV). A static load simulating the slow rate of thermal stresses is applied on the aged binder beam sample and the stiffness and coefficient of relaxation are measured after 60 seconds. It should be mentioned that the time – temperature superposition principle is applied to simulate a 2-hour stress rate in the field with 60 seconds in the laboratory at 18°F (10°C) warmer temperature. To ensure good resistance to thermal cracking, the Superpave PG system requires the long-term aged asphalt binder to maintain a creep stiffness *(S)* below 300 MPa and an m-value above 0.300.

As indicated earlier, the HiMA binders contained 7.5% SBS while the neat asphalt binders contained 0% SBS. The SBS content of the PMA binders could not be verified from the literature, however, it is believed to be approximately 3%.

In addition to testing the binders in the BBR, mixtures manufactured using neat, conventional PMA, and HP binders were evaluated in terms of thermal cracking resistance using the thermal stress restrained specimen test (TSRST) *(31)*. The test measures the tensile stress in a restrained AC specimen as it is cooled at a constant rate. As the temperature drops, the specimen is restrained from contracting thus inducing tensile stresses. The fracture strength and the fracture temperature are measured as part of this test. Figure A.10 parts a and b present the data of the low temperature evaluations on the neat, two PMA, and HP binders from the BBR and the corresponding mixes from the TSRST. It should be noted that the evaluated binders and mixes were originally labeled as follows: a) the neat binders and mixes were labeled by their Pen Grade, b) the conventional PMA binders and mixes were labeled with a "PMB" extension, and c) the HP binders and mixtures were labeled with a "HiMA" extension. The data in Figure A.10 are grouped into three parts where each part compares the properties of the corresponding neat, two PMA, and HP binders and mixtures. The data in Figure A.10-a are presented in terms of the temperatures at which the S(60) and m-value Superpave PG criteria are met while the data in Figure A.10-b are presented in terms of the TSRST fracture temperature. It should be noted that the lower the critical temperature of the S(60) and m-value the more resistant the binder is to thermal cracking. The lower the TSRST fracture temperature the more resistant is the asphalt mix to thermal carking.

The measured S(60) and m-value properties of the neat, two PMA, and HP binders show that the BBR critical low temperatures continue to decrease as the SBS content increases from 0, 3, to 7.5% except for the third HP binder designed for use in SAMI and slurry seals. In addition, the TSRST fracture temperature of the neat, two PMA, and HP mixtures continues to decrease as the SBS content increases from 0, 3, to 7.5%. These results clearly show the benefits of using HP binders towards improving the resistance of AC mixes to thermal cracking.

### A.4.2. Intermediate Temperature Properties

The asphalt binders were evaluated in terms of their resistance to fatigue cracking using the DSR test according to the Superpave PG system *(24)*. The long-term aged asphalt binder (RTFO + PAV) is tested in the DSR at a frequency of 10 rad/sec and the G* and δ are measured. To ensure good resistance to fatigue cracking, the Superpave PG system requires the long-term aged binder to maintain a G*sin(δ) less than 5,000 kPa. Figure A.11 presents the data of the intermediate

temperature evaluations on the neat, two PMA, and HP binders from the DSR. The data in Figure A.11 are presented in terms of the temperatures at which the G*sin(δ) Superpave PG criterion is met. It should be noted that the lower the temperature of the G*sin(δ) the more resistant the binder to fatigue cracking. The measured G*sin(δ) properties of the neat, two PMA, and HP binders show that the DSR critical intermediate temperature continues to decrease as the SBS content increases from 0, 3, to 7.5%. These results clearly show the increased resistance of the HP binders to fatigue cracking.

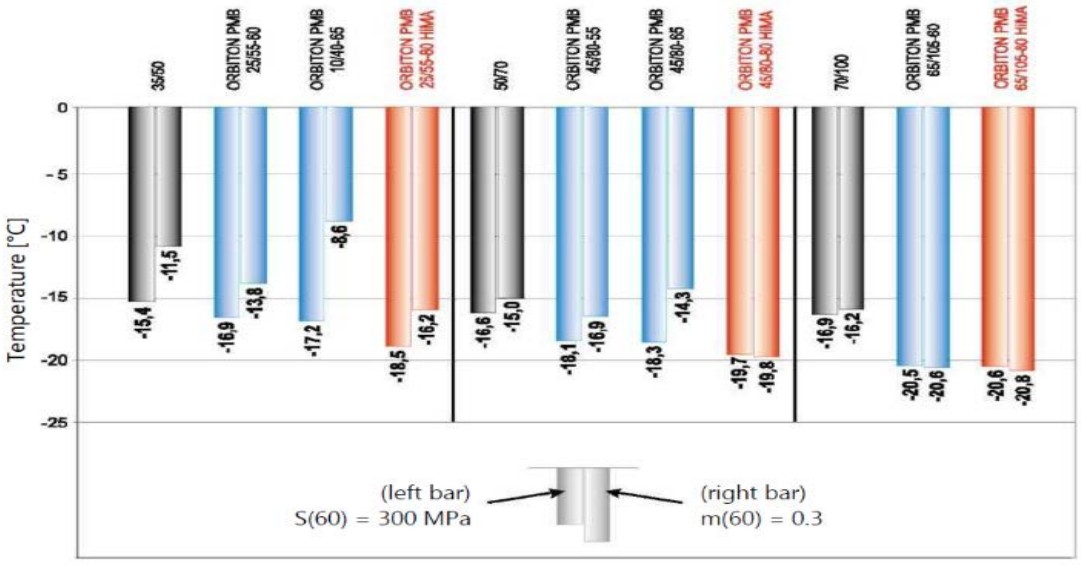


(a)

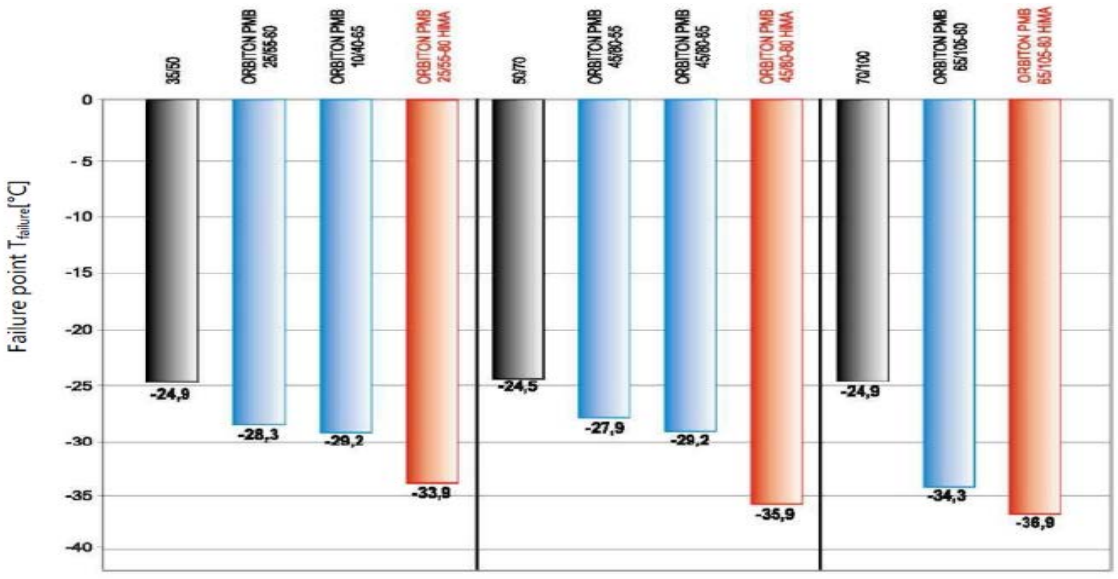


(b)

**Figure A.10. Low temperature properties for neat, PMA, and HP asphalt binders and mixtures** *(29)***.**

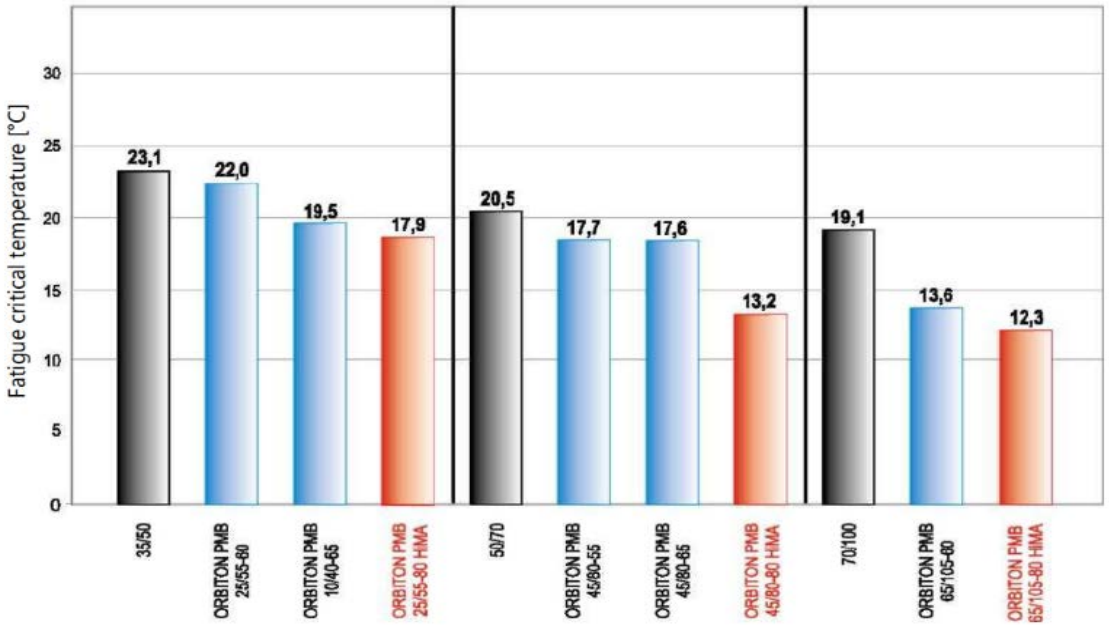


**Figure A.11. Intermediate temperature properties for neat, PMA, and HP asphalt binders *(29)*.**

### A.4.3. High Temperature Properties

The asphalt binders were evaluated in terms of their resistance to rutting using the DSR test according to the Superpave PG system *(24)*. Testing was conducted on original binders prior to aging and on short-term aged residues (i.e., RTFO aged). To ensure good resistance to rutting, the Superpave system requires a G*/sin(δ) higher than 1.00 and 2.20 kPa for original un-aged and short-term aged binders, respectively. Figure A.12 presents the data of the high temperature evaluations on the neat, two PMA, and HP binders from the DSR. The data in Figure A.12 are presented in terms of the temperatures at which the G*/sin(δ) Superpave PG criteria are met for the original and short-term aged binders. It should be noted that the higher the temperature of the G*/sin(δ) the more resistant the binder to rutting. The measured G*/sin($\delta$) properties of the neat, two PMA, and HP binders show the DSR critical temperatures continue to increase as the SBS content increases from 0, 3, to 7.5%. These results clearly show the increased resistance of the HP binders to rutting.

To further assess the rutting resistance of the binders, the MSCR test was performed at temperatures of 147 and 158°F (64 and 70°C). The MSCR test measures the creep compliance ($J_{nr}$) and the average percent recovery (R) of the binder at two stress levels (i.e., 0.1 kPa and 3.2 kPa). Figure A.13 presents the $J_{nr}$ and R properties of the neat, two PMA, and HP binders at the two testing temperatures. The lower the $J_{nr}$ and the higher the R the more resistant the binder will be to rutting. The data in Figure A.13 show the HP binders plotted at the upper right hand corner of the graph indicating lower $J_{nr}$ and higher R properties than the neat and PMA binders at both temperatures. In addition, the PMA binders also showed lower $J_{nr}$ and higher R properties than the neat binders at both temperatures. Again, the MSCR data show increased rutting resistance of the binders as the SBS content increases from 0, 3, to 7.5%.

In addition to binder testing, mixtures manufactured with neat, two PMA, and HP binders were evaluated for rutting resistance by applying 10,000 cycles using a small wheel tracker at a temperature of 140°F (60°C). Figure A.14 presents the measured rut depths of the various mixtures. Lower rut depths were observed for mixtures manufactured using the HP asphalt binders.

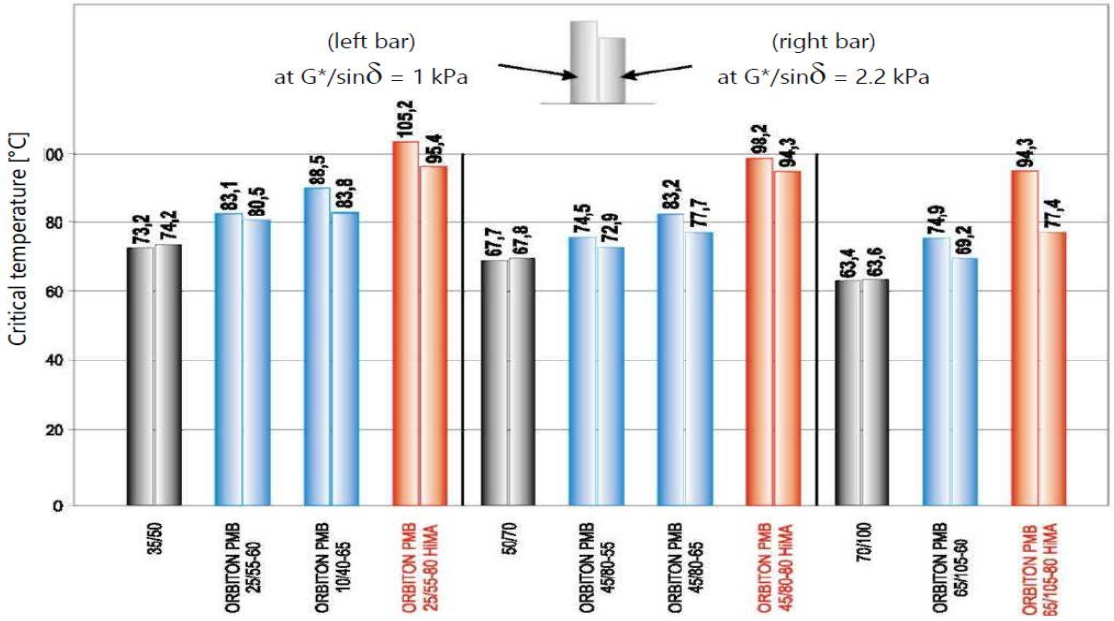


**Figure A.12. High temperature properties for neat, PMA, and HP binders based on DSR *(29)*.**

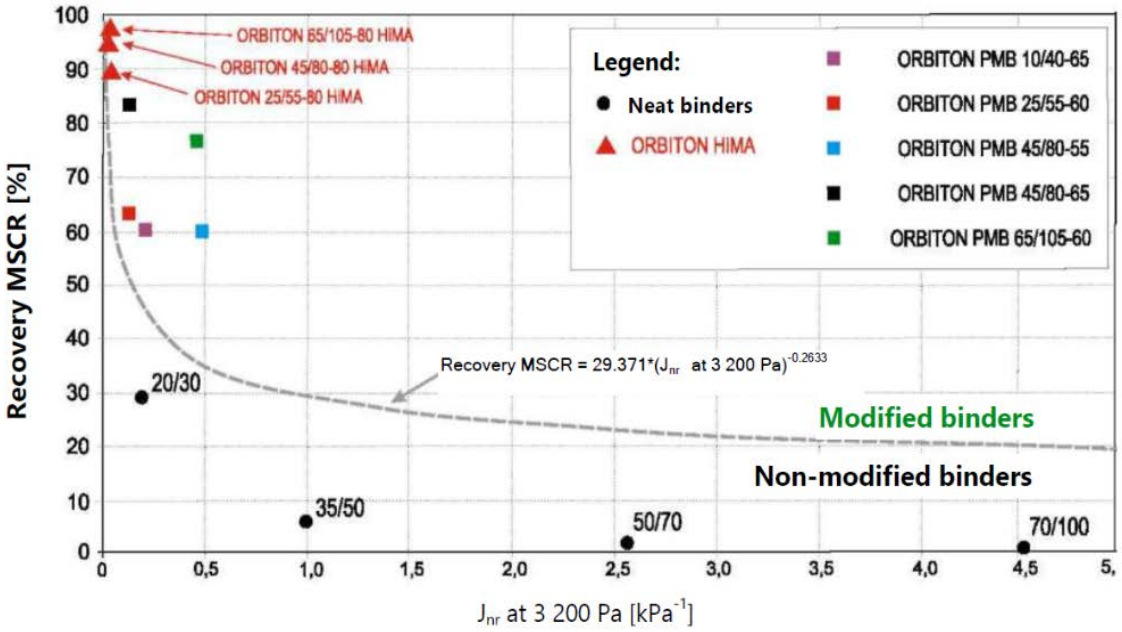


(a)

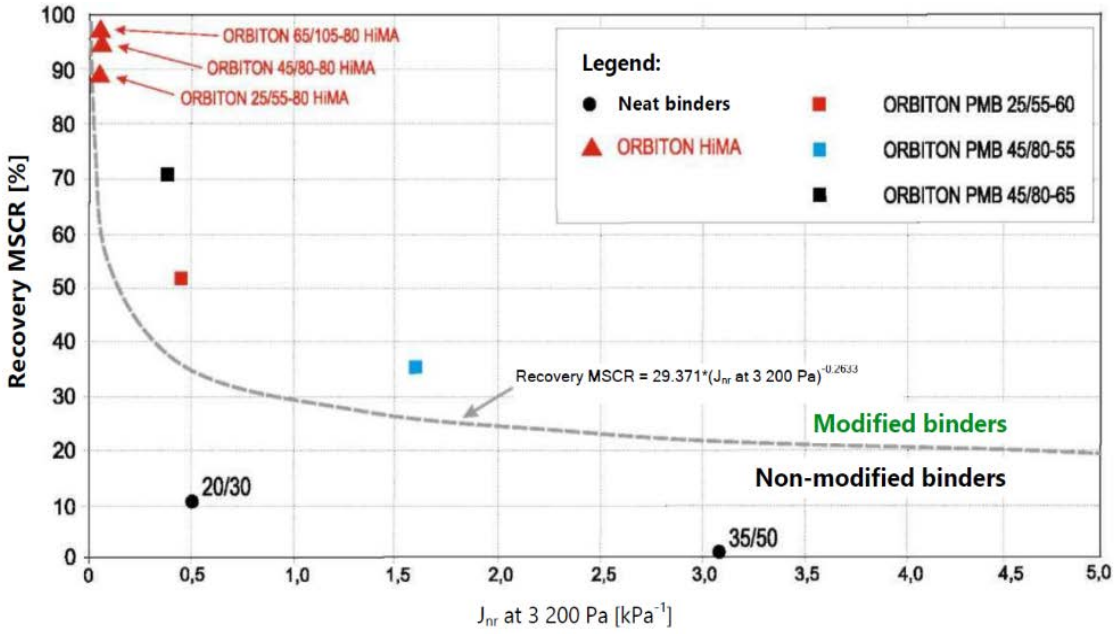


(b)

**Figure A.13. High temperature properties for neat, PMA, and HP binders based on the MSCR test at (a) 64°C, and (b) 70°C** *(29)***.**

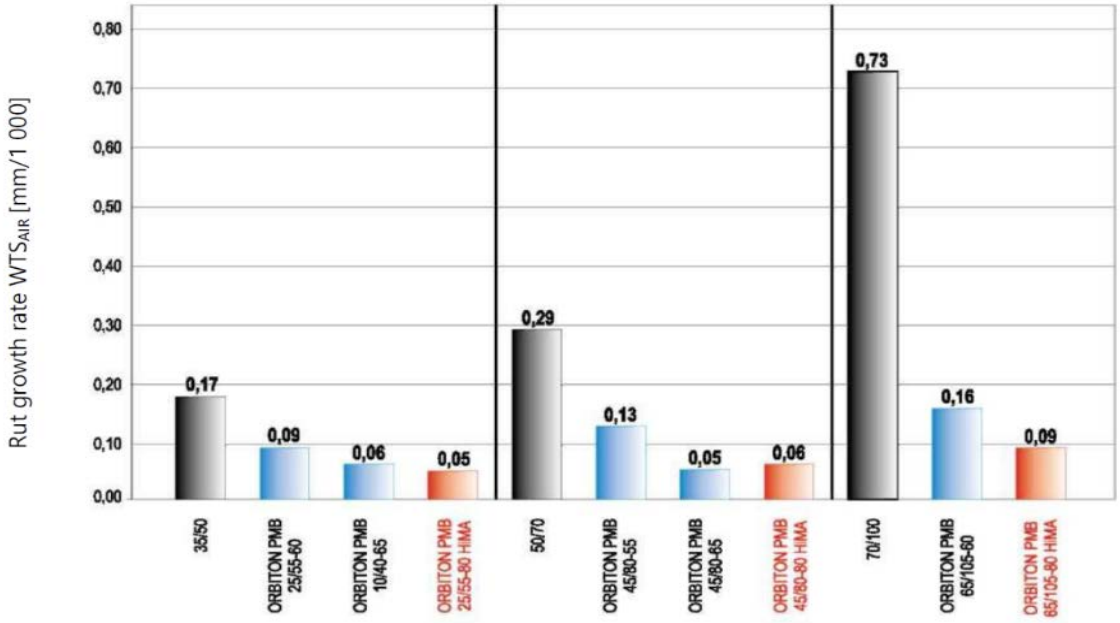


**Figure A.14. High temperature properties for neat, PMA, and HP mixtures** *(29)***.**

In summary, this study showed the positive impact of increasing the SBS content of asphalt binders on the performance of asphalt binders and mixtures in terms of resisting the three categories of asphalt pavement distresses: thermal cracking, fatigue cracking, and rutting.

## A.5. EVALUATION OF THIN OVERLAY MIXES USING HP ASPHALT BINDERS

Over the last 35 years, the focus of state DOTs changed from the construction of new roads to maintenance and rehabilitation of existing infrastructure by using several pavement preservation techniques. These techniques are defined as a set of cost-effective practices designed to extend pavement life, improve safety, and save public funds. Thin asphalt concrete overlay (thickness ≤ 1.5 inch (38 mm)) is considered a preservation treatment for AC pavements. State DOTs in the Northeast Pavement Preservation Partnership (NEPPP), the Pennsylvania Asphalt Pavement Association (PAPA), academia, and industry, developed a pilot specification for high-performance thin overlay (HiPO) mixtures manufactured using HP asphalt binders and reclaimed asphalt pavement (RAP). HiPO was intended as a mean to extend the available funds for pavement preservation and for essentially delaying future need for pavement rehabilitation. Several distresses and issues that shorten the service life of conventional overlays such as reflective cracking, thermal cracking, fatigue cracking, and rutting were addressed while developing the HiPO mixtures specifications. In 2012, the pilot specification was published by the National Center for Pavement Preservation (NCPP) and was posted on the AASHTO Transportation System Preservation Technical Services Program (TSP2) website *(32)*. Following the publication of the HiPO Specifications, the New Hampshire (NH), Vermont (VT), and Minnesota (MN) DOTs showed interest in using this specification for demonstration field projects. The main interest in the HiPO specification is that it allows the use of RAP up to 25% by dry weight of aggregate and a HP asphalt binder with 7.5 % of SBS polymer, graded as PG76-34 or PG82-28 *(33)*.

### A.5.1. Experimental Plan and Pilot Specification

The experimental plan, illustrated in Figure A.15, included work to develop a Superpave mix design with a NMAS of 3/8-inch (9.5 mm) based on input from interested DOTs following the pilot specification summarized in Table A.2. It should be mentioned that the Minnesota mixture did not meet the NMAS for a HiPO mixture and was excluded from further evaluations. The evaluations included performance tests to evaluate the plant-produced mixtures collected from the field projects in terms of resistance to reflective, thermal, and fatigue cracking as well as rutting. Additional tests, not mandated as part of the specifications, were conducted such as Hamburg wheel tracking device (HWTD) for further rutting evaluation as well as the semicircular bending (SCB) test for further evaluation of resistance to cracking.

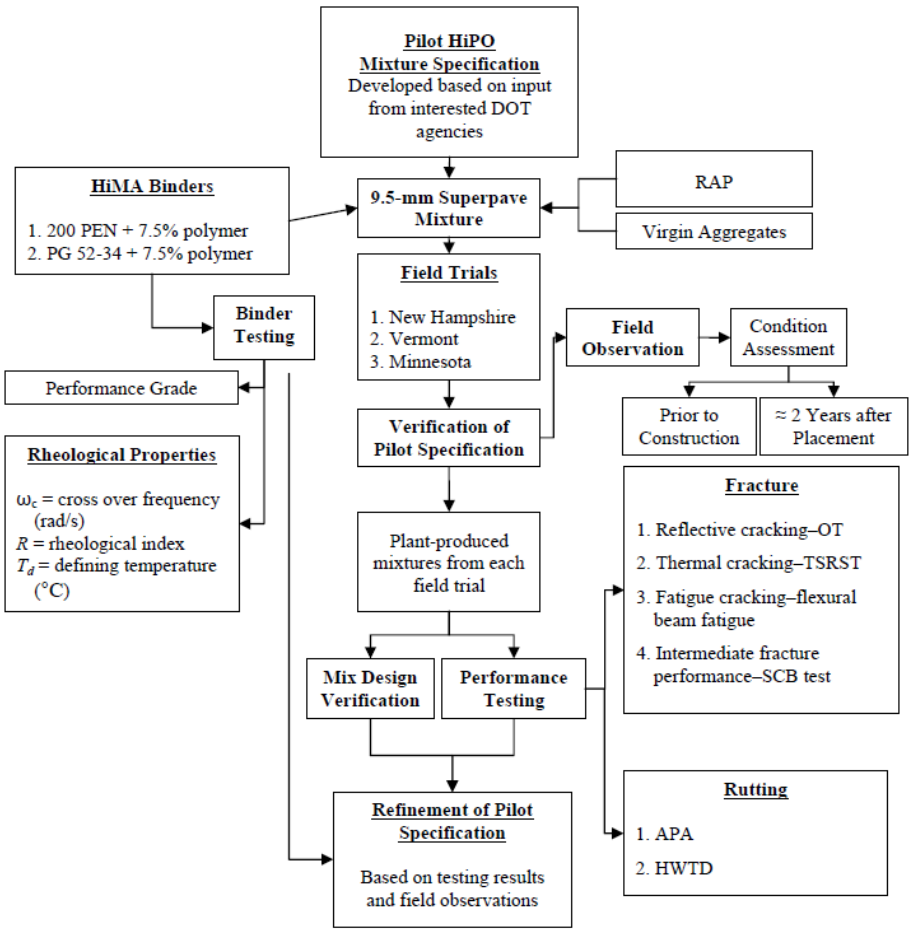


**Figure A.15. Experimental plan for evaluating HiPO mixtures *(33)*.**

**Table A.2. Pilot Specification for HiPO Mixture Performance Requirements.**

| HiPO Mixtures with no RAP | | |
|---|---|---|
| **Property** | **Device/Test** | **Criteria** |
| Thermal cracking temperature of mixture | TSRST: AASHTO TP 10-93 | ± 6°C from the low-temperature PG of the binder (minimum of 3 replicates per mixture) |
| Cracking | OT: Texas DOT: Tex-248-F | Minimum Number of OT cycles to failure > 300 (failure criteria: 93% load reduction). |
| Fatigue Life | Flexural Beam Fatigue Test AASHTO T321 | >100,000 cycles |
| Rutting | APA: AASHTO TP63 at the standard PG high temperature for each project location | Average rut depth for 6 specimens < 4 mm (0.16 inch) at 8,000 loading cycles |
| **HiPO Mixtures with RAP** | | |
| **Property** | **Device/Test** | **Criteria** |
| Cracking | OT: Texas DOT: Tex-248-F | OT cycles of Mixtures containing RAP shall be within ± 10% of the OT cycles of Mixtures without RAP |

### A.5.2. Test Results of Evaluated Binders and Mixtures

Figure A.16 presents the aggregate gradations for the HiPO mixtures used on the NH and VT projects. While the gradations of both the NH and VT mixtures met the HiPO specifications, the NH gradation seems to be coarser than the VT gradation.

Table A.3 summarizes some of the mix design information from the NH and VT projects. As shown in Table A.3, two base binders graded as PG52-34 were obtained from different sources and used on each of the NH and VT. The base binders were modified with 7.5% SBS polymer to produce the HP binders for each project. The HP binder used on the NH project graded as PG76-28 which did not meet the HiPO specification of PG76-34. However, the actual low temperature grade of the HP binder used on the NH project was -33°C. In order to assess the impact of slightly violating the HiPO specification on the PG grade, the shear modulus master curves were developed for the HP binders from the two projects. The Christensen-Anderson model (CAM) presented in Equation A.2 was used to develop the shear modulus master curves of the HP binders as illustrated in Figure A.17.

$$G^*(\omega) = G_g[1 + (\frac{\omega_c}{\omega_r})^{\frac{\log 2}{R}}]^{\frac{-R}{\log 2}} \qquad \textbf{[Equation A.2]}$$

Where;
$G^*(\omega)$: complex shear modulus, kPa;
$G_g$: glass modulus assumed equal to $10^6$, kPa;
$\omega_r$: reduced frequency at the defining temperature, rad/s;
$\omega_c$: cross over frequency at the defining temperature, rad/s;

$\omega$: loading frequency, rad/s; and
R: rheological index.

It was found that the shear modulus master curves of the two HP binders shown in Figure A.17 are very similar indicating that the overall rheological properties of the two HP binders are close. Therefore, it was concluded that the slight difference in the low temperature grade should not influence the overall performance of the two binders.

The available mix design information did not contain any reference on the use of an anti-strip additive in both mixtures, therefore, it can be reasonably assumed that no such additive was used. The optimum binder content of the NH mixture violated the HiPO mix specification by 0.2%. The impact of this minor violation will be taken into consideration when comparing the performance properties of the two mixtures.

The properties of the RAP materials used in the two mixtures were not documented in the available literature from this study. However, the available information provided the optimum binder content and the virgin binder content for each mixture as shown in Table A.3. Using this information, the research team calculated the RAP binder contents as presented in Table A.3. This calculation showed the binder content of the RAP material used in the VT mixture to be 0.2% higher than the binder content of the RAP material used in the NH mixture.

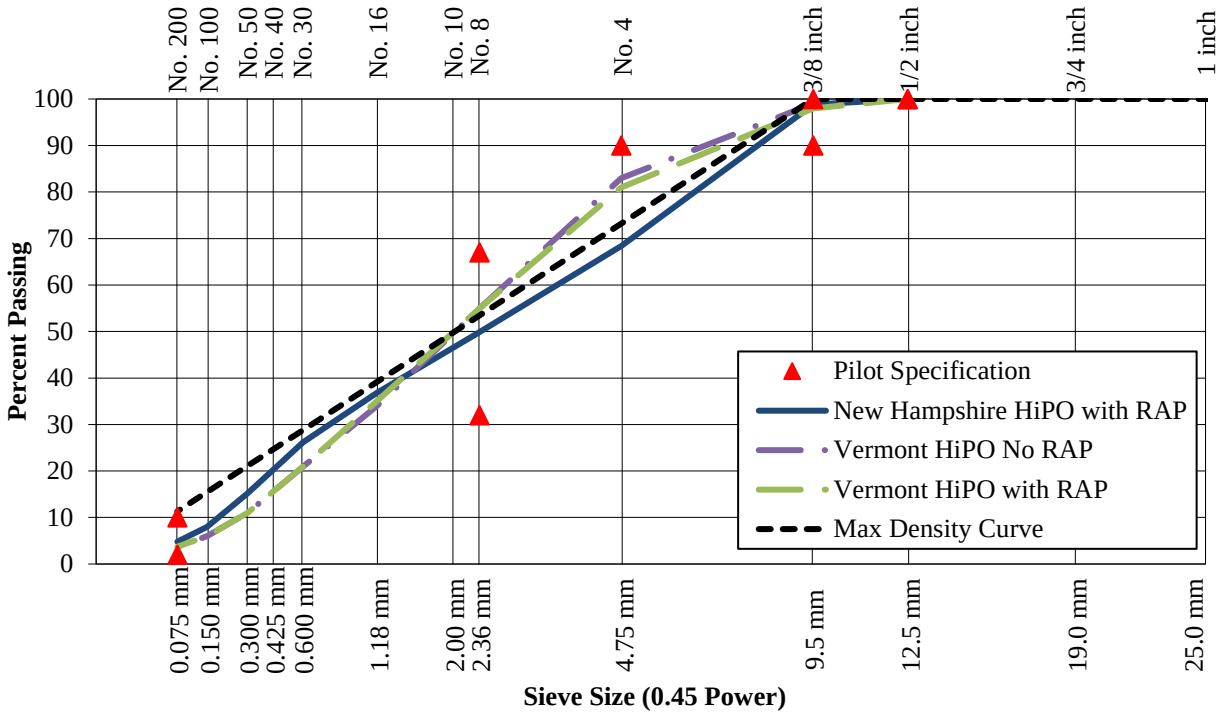


**Figure A.16. HiPO mixtures gradations for New Hampshire and Vermont projects.**

**Table A.3. Summary of HiPO Mix Design Details for the NH and VT Projects.**

| Property ID | New Hampshire (NH) HiPO | Vermont (VT) HiPO No-RAP | Vermont (VT) HiPO With-RAP | Pilot Specifications |
|---|---|---|---|---|
| RAP, % | 25 | 0 | 24 | 25 max. |
| Base Binder PG[1] | PG52-34[2] | PG52-34 | PG52-34 | PG52-34 |
| SBS Content, % | 7.5 | 7.5 | 7.5 | 7.5 |
| Virgin Binder PG | PG76-28 | PG76-34 | PG76-34 | PG76-34 or PG82-28 |
| Optimum Binder Content, % | 6.3 | 6.8 | 6.5 | 6.5 min. |
| Virgin Binder Content, % | 5.3 | 6.8 | 5.5 | -- |
| RAP Binder Content[3], % | 3.8 | -- | 4.0 | |
| Mixing Temperature | 340°F (171°C) | 311-351°F (155-177°C) | 311-351°F (155-177°C) | -- |
| Compaction Temperature | 300°C (149°F) | 291-310°F (144-154°C) | 291-310°F (144-154°C) | -- |
| $N_{design}$ | 75 | 65 | 65 | -- |

[1] different sources for NH and VT base binder
[2] actual low temperature is -33ºC
[3] calculated by the research team

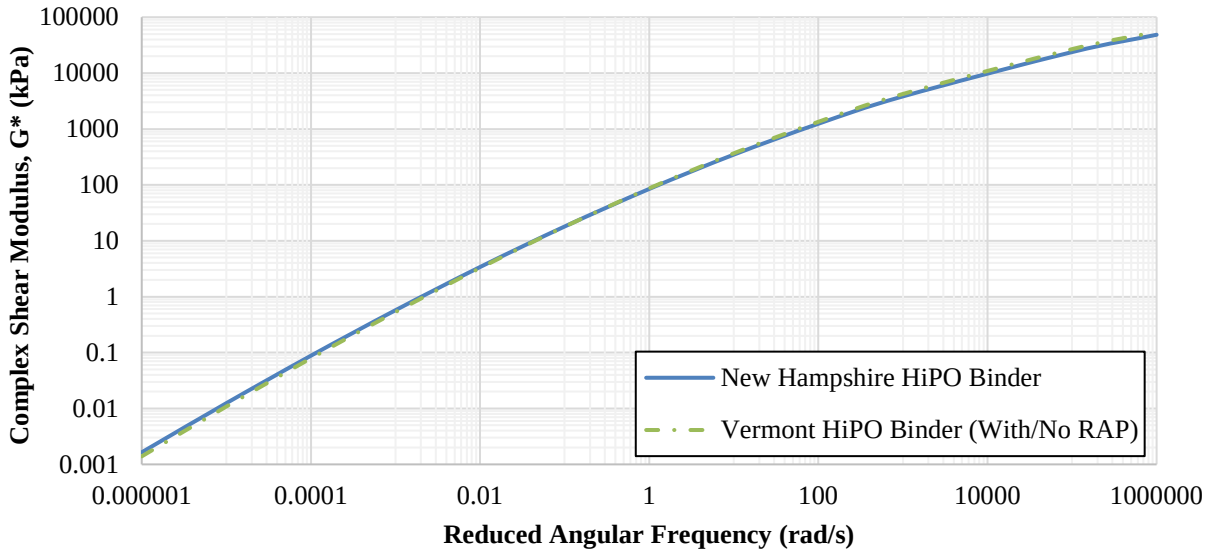


**Figure A.17. Shear modulus master curves for HP binders.**

*Reflective Cracking Properties*

The Texas Overlay Test (OT) was used to evaluate the resistance of the HiPO AC mixtures to reflective cracking *(34)*. The testing was conducted at a temperature of 59°F (15°C) on specimens compacted to an air void level of 7.0±1.0%. The test specimens consisted of 6.0 inch

(150 mm) long by 3.0 inch (75 mm) wide and 1.5 inch (38 mm) thick sample trimmed from a 6.0 inch (150 mm) diameter by 4.5 inch (115 mm) height sample prepared in the Superpave Gyratory Compactor (SGC). The maximum displacement (i.e., joint opening) was selected as 0.025 inch (0.635 mm). The test was stopped after 2,000 loading cycles if a 93% drop in initial load, measured from the first opening cycle, was not reached. Table A.4 summarizes the results from the various mixture performance tests. All evaluated mixtures exhibited an average OT cycles to failure greater than the minimum required 300 cycles. However, the Vermont with RAP mix did not exhibit cycles to failure within ±10% of the number of cycles exhibited by the corresponding mix without RAP indicating the need of assessing the applicability of using 24% RAP without changing the grade of the virgin binder.

**Table A.4. HiPO Mixtures Performance Test Results.**

| Mixture ID | New Hampshire HiPO with RAP | Vermont HiPO No RAP | Vermont HiPO with RAP |
|---|---|---|---|
| Reflective Cracking: Number of Cycles to Failure | 2,000 | 2,000 | 1,144 |
| Thermal Cracking: Fracture Temperature | -33.1°C | -30.1°C | -27.8°C |
| Fatigue Cracking: Number of Cycles to Failure | 348,266 | 794,790 | 383,065 |
| APA Rut Depth after 8,000 cycles | 0.20 inch (5.16 mm) | 0.08 inch (2.03 mm) | 0.11 inch (2.87 mm) |
| HWTD Rut Depth after 10,000 cycles | 0.17 inch (4.20 mm) | 0.10 inch (2.55 mm) | 0.05 inch (1.26 mm) |
| HWTD Rut Depth after 20,000 cycles | 0.51 inch (12.91 mm) | 0.35 inch (8.98 mm) | 0.11 inch (2.70 mm) |

*Thermal Cracking Properties*

The TSRST was used to evaluate the resistance of the HiPO AC mixtures to thermal cracking *(31)*. The fracture temperatures of the HiPO mixtures are presented in Table A.4. The addition of RAP decreased the thermal cracking resistance of the VT mixture as presented by the warmer thermal fracture temperature. The NH and VT with no RAP mixtures met the specification requirement of having a fracture temperature ±6°C from the low temperature PG of the asphalt binder. On the other hand, the VT mixture with RAP slightly violated the specification with a fracture temperature of 6.2°C warmer than the low temperature PG of the asphalt binder.

*Fatigue Cracking Properties*

The flexural beam fatigue test was used to evaluate the resistance of the HiPO AC mixes to fatigue cracking *(35)*. The beam specimens were compacted to an air void level of 7.0±1.0% and were tested at a temperature of 59°F (15°C) in strain control mode (i.e., a strain level of 750

micro-strain). The 50% reduction in initial stiffness computed at cycle 50 was considered as a failure criterion. The results of the fatigue cracking are summarized in Table A.4. The two mixtures with RAP (NH and VT) showed similar numbers of cycles to failure which is significantly lower than the number of cycles to failure for the VT mixture with no RAP. This data further question the applicability of using RAP without changing the PG of the virgin binder.

*Rutting Properties*

The asphalt pavement analyzer (APA) was used to evaluate the rutting resistance of the HiPO AC mixtures. The maximum high pavement temperature that mixtures may experience in the field was estimated to be 140°F (60°C). The APA rutting data are presented in Table A.4. The NH with RAP mixture did not meet the APA rutting criterion in the pilot specification of minimum 0.16 inch (4.0 mm) after 8,000 loading cycles. Both VT mixtures with and no RAP met the APA rutting criterion.

Additional rutting evaluations were conducted in the HWT *(37)*. The specimens, compacted to an air void level of 7.0±1.0%, were soaked for 30 minutes in a heated water bath at a temperature of 122°F (50°C) prior to testing. A continuous loading was applied to the submerged samples using a steel wheel. The HWTD rutting data are presented in Table A.4. The HWTD rutting data on the VT mixtures followed the expected trend where the addition of 24% RAP decreased the rut depth of the HiPO AC mixtures.

In summary, this study showed that HP binders can be used to design HiPO AC mixtures with and without RAP as per the pilot specifications for thin AC overlays to be used as a preservation treatment. However, the following observations were made from the measured mixtures properties:

- The use of 24-25% RAP without changing the PG of the virgin binder can have a negative impact on the resistance of the mixture to thermal and fatigue cracking. This impact was more obvious on the VT mixtures since both with and no RAP mixtures were evaluated.
- Even though the available literature from this study did not include information on the properties of the RAP materials used in each mix, the analysis of the performance data leads to the conclusion that the RAP material used in the NH mix is softer than the RAP material used in the VT mix. This is supported by the higher thermal fracture temperature and higher rutting observed in the APA and HWTD for the NH mix with RAP.
- One significant observation from this study is that the use of HP binder will improve the performance of the AC mixtures BUT will not make up for the deficiencies associated with the percent and properties of RAP materials used in the mixtures. Therefore, agencies should still assess the impact of these two important parameters on the performance of the AC mix even with the use of HP binders.

## A.6. NEW HAMPSHIRE DOT HIGHWAYS: 2011 AUBURN-CANDIA RESURFACING

### A.6.1. Introduction and Testing Plan

In 2011, FHWA awarded the New Hampshire DOT (NHDOT) a $2 million grant for new technologies as part of resurfacing NH Route 101 from Auburn to Candia. The evaluation of HP and neat AC mixes were incorporated into this project. The experiment evaluated the following mixtures: mix A (0.5-inch NMAS (12.5-mm)) and 35% RAP using neat PG52-34 with Evotherm, mix B (0.75-inch NMAS (19.0-mm)) and 20% RAP using neat PG64-28, and mix C (0.375-inch NMAS (9.5-mm)) and no RAP using a PG70-34HP binder with 7.5% SBS *(38)*. This study was incorporated into the literature review to examine the ability of the HP binder to produce an AC mix with comparable properties to other AC mixes from the same aggregate source with higher NMAS and RAP contents.

### A.6.2. Testing Description and Detailed Results

*Aggregate Gradation and Mix Designs*

Figure A.18 illustrates the aggregate gradation of the three evaluated mixtures. The three mixtures were designed using the Superpave mix design methodology with 75 design gyrations. The optimum asphalt binder content for mixes A, B, and C are 5.50%, 4.90%, and 6.50%, respectively.

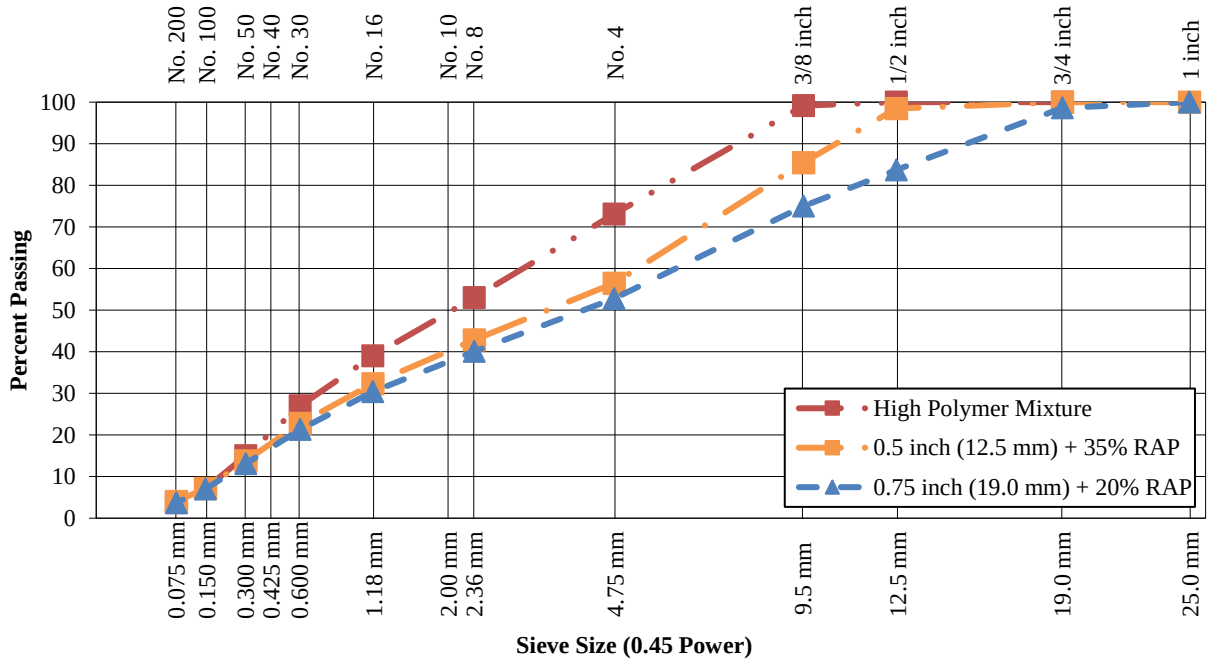


**Figure A.18. Aggregate gradations of NHDOT mixes A, B, and C.**

*Engineering Properties*

The Dynamic modulus (E*) represents the engineering property of the AC mix and provides an indication on its overall quality. Dynamic modulus testing was performed for the three mixes (A, B, and C) in accordance with AASHTO T378 *(39)* and R84 *(40)*. Mix B exhibited the highest E* property while mix C (HP) exhibited the lowest modulus. This indicates that the HP binder was unable to overcome the impact of RAP, higher NMAS with coarser gradation, and higher optimum binder content on the E* property of the AC mix.

*Rutting Properties*

The AMPT machine was used to determine the flow number (FN) of the three mixes (A, B, and C) according to AASHTO T378 *(39)*. The testing temperature was 122°F (50°C) selected as the design high temperature at 50% reliability as determined using the long-term pavement performance bind (LTPPBind) software version 3.1. This temperature was computed at a depth of 0.80 inch (20 mm) below the pavement surface. The Francken model was used to determine the tertiary flow. The highest FN was measured on the HP mix C at 346 followed by mix B at 237 and mix A at 128 cycles. This indicates that the HP binder was able to overcome the impact of RAP, higher NMAS with coarser gradation, and higher OBC on the FN property and produced an HP AC mix that is more resistant to rutting.

*Cracking Properties*

Fatigue Cracking: Flexural beam fatigue testing was performed in accordance with AASHTO T321 *(35)* to determine the fatigue characteristics of the three mixes. Beams were trimmed from slabs compacted using the IPC Global Pressbox slab compactor. In order to account for the relative locations of the various mixtures within the pavement structure, mixes A and B were tested at strains of 250, 500, and 750 micro-strain while higher strains of 750, 1000, 1,250 micro-strain were applied to test mix C. All tests were conducted at a loading frequency of 10Hz and a temperature of 59°F (15°C). The 50% reduction in initial beam stiffness (determined at cycle 50) was adopted as a failing criterion. Figure A.19 presents the beam fatigue results and fatigue relationship of the evaluated mixes *(38)*. A considerably better fatigue relationship was observed for the HP mix C when compared with mixes A and B.

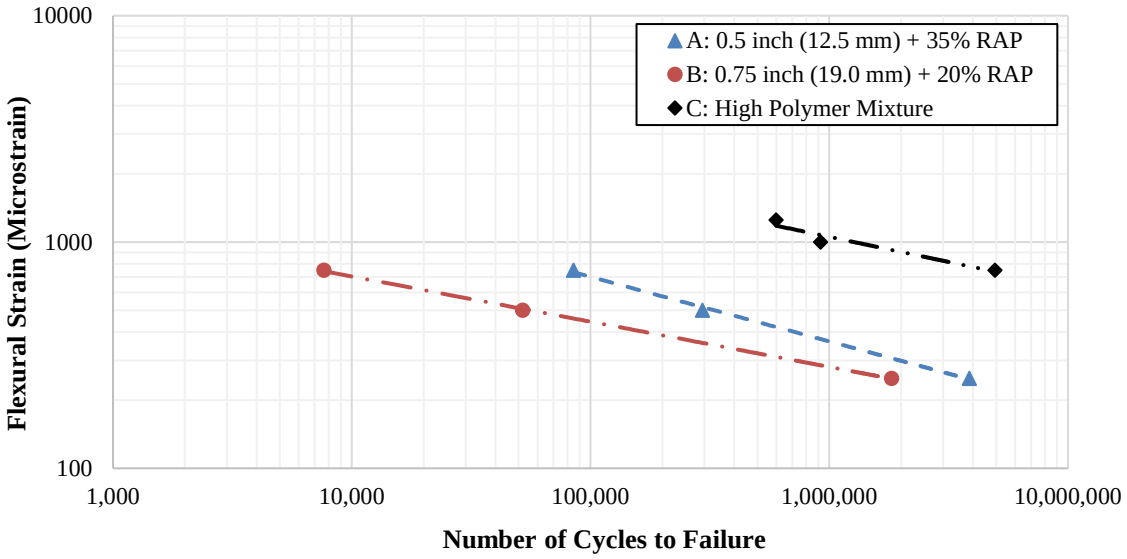


**Figure A.19. Fatigue characteristics of mixes A, B, and C at 59°F (15°C).**

It should be noted that, a significant difference in the laboratory fatigue resistance will not necessarily translate to the same difference in fatigue performance in the field. Many factors may highly affect the fatigue life of an asphalt pavement such as stiffness, tensile strain under field loading, the fatigue characteristic of the asphalt mixture, pavement structure, and the interaction of all these factors. In a mechanistic pavement analysis, an AC layer with a higher stiffness will show a lower laboratory fatigue life in a strain-controlled mode of loading, on the other hand, it will produce a lower tensile strain under field loading which may result in a longer fatigue life in the field. Therefore, a full mechanistic analysis would be necessary to effectively evaluate the impact of HP mixes on the fatigue performance of AC pavements.

Reflective Cracking: The Texas OT was used to evaluate the mixtures' resistance to reflective cracking in accordance with Tex-248-F *(34)* procedure at a testing temperature of 50°F (10°C). Failure was defined as the number of cycles to reach a 93% drop in initial load which is measured from the first opening cycle. The best performance was observed for the HP mix C with a number of cycles to failure of 968. Mixes A and B showed much lower resistance to reflective cracking with similar number of cycles to failures of 18 and 17, respectively *(38)*.

Thermal Cracking: The TSRST was used to evaluate the resistance of the mixes to thermal cracking *(31)*. The thermal fracture temperatures were observed to be -26, -22, and -37°C for mixes A, B, and C, respectively. The lowest fracture temperature was observed for the HP mix C followed by mix A while mix B showed the warmest fracture temperature. It should be noted that only the HP mix C exhibited a fracture temperature lower than the low temperature PG of the binder. Mixes A and B exhibited fracture temperatures that are significantly warmer than the low temperature PG of their respective binder.

In summary, it should be recognized that the presence of RAP in mixes A and B and the higher optimum binder content of mix C contributed to the increase in its resistance to all three modes

of cracking: fatigue, reflective and thermal. However, the fatigue life of the HP mix C at 750 micro-strain is over 600 times the fatigue life of mixes A and B, the reflective cracking life of the HP mix is 54 times the reflective cracking life of mixes A and B, and the thermal fracture temperature is 11 - 15°C lower than the thermal fracture temperature of mixes A and B. It is believed that a significant portion of this large increase in the resistance of the HP mix C to fatigue, reflective, and thermal cracking can be attributed to the properties of the HP binder. In addition to exhibiting a superior resistance to all modes of cracking, the HP mix C also exhibited higher resistance to rutting than mixes A and B with RAP.

# APPENDIX B. MIX DESIGNS AND RESISTANCE TO MOISTURE DAMAGE – DETAILED DATA

## B.1. MIX DESIGNS

### B.1.1. Definition of Terms

Mix Design IDs:

- “FL”: White Rock Quarries, Southeast Florida.
- “GA”: Junction City Mining, Georgia Granite.
- “95” and “125”: NMAS of 9.5 mm and 12.5 mm, respectively.
- “PMA”: polymer modified asphalt binder (modified with SBS at the approximate rate of 3% by weight of binder).
- “HP”: high polymer modified asphalt binder (modified with SBS at the approximate rate of 7.5% by weight of binder).
- “(A)”: binder from Ergon Asphalt and Emulsion.
- “(B)”: binder from Vecenergy.

### B.1.2. Mix Design 1: FL95_PMA(A)

**Type of Mix:** Fine SP-9.5
**Intended Use of Mix**: Structural
**Design Traffic Level:** C
**Gyrations @ $N_{des}$:** 75

| Product Description | Product Code | Producer Name | Product Name | Plant/Pit Number | Bin Percentage (%) |
|---|---|---|---|---|---|
| S1B Stone | C51 | White Rock Quarries | S1B Stone | 87339 | 44.25 |
| Screenings | F22 | White Rock Quarries | Screenings | 87339 | 54.25 |
| Generated Dust | -- | -- | FL P200 | -- | 1.50 |

***PERCENTAGE BY WEIGHT TOTAL AGGREGATE PASSING SIEVES***

| Blend | | 44.25% | 54.25% | 1.50% | Job Mix Formula | Control Points |
|---|---|---|---|---|---|---|
| Stockpile ID | | S1B Stone C51 | Screenings F22 | FL P200 | | |
| SIEVE SIZE | 3/4" (19.00 mm) | 100.0 | 100.0 | 100.0 | 100.0 | |
| | 1/2" (12.50 mm) | 99.7 | 99.9 | 100.0 | 99.8 | 100 |
| | 3/8" (9.50 mm) | 91.4 | 99.8 | 100.0 | 96.1 | 90 – 100 |
| | No.4 (4.75 mm) | 17.9 | 99.5 | 100.0 | 63.4 | ≤ 90 |
| | No.8 (2.36 mm) | 6.3 | 90.5 | 100.0 | 53.4 | 32 – 67 |
| | No.16 (1.18 mm) | 5.0 | 75.0 | 100.0 | 44.4 | |
| | No.30 (0.600 mm) | 4.4 | 60.7 | 100.0 | 36.4 | |
| | No.50 (0.300 mm) | 3.8 | 39.2 | 100.0 | 24.4 | |
| | No.100 (0.150 mm) | 2.8 | 9.1 | 100.0 | 7.7 | |
| | No.200 (0.075 mm) | 2.0 | 2.7 | 100.0 | 3.8 | 2 – 10 |
| | $G_{sb}$ | | | | 2.510 | |

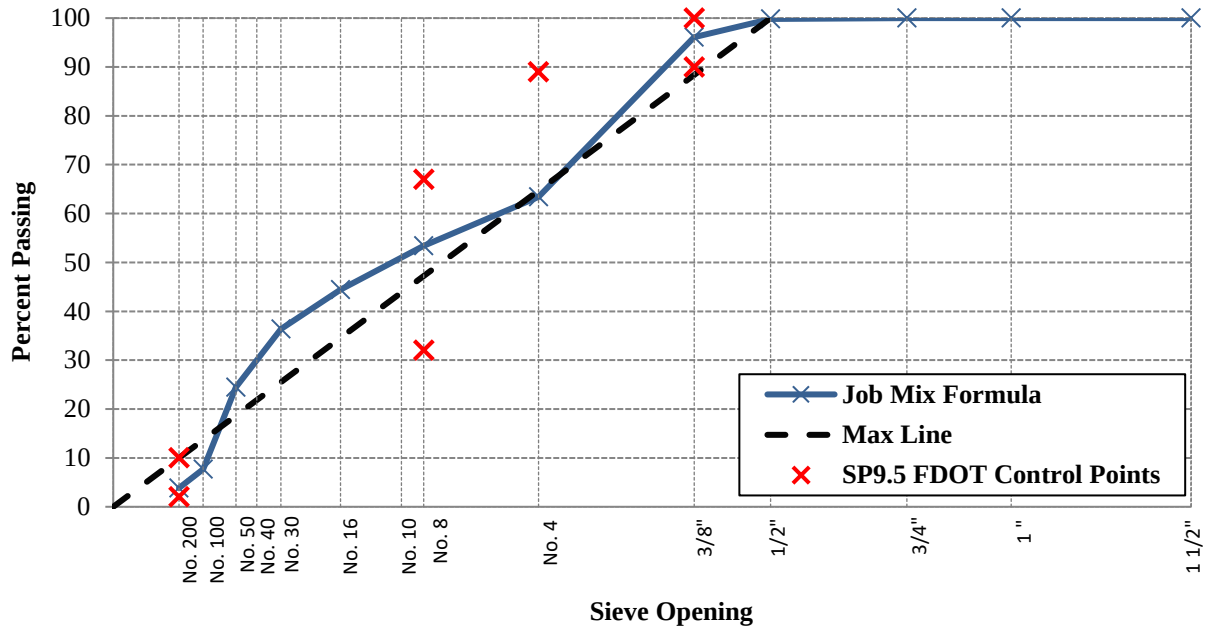


***AGGREGATE GRADATION CURVE***

## *HOT MIX DESIGN DATA*

| $P_b$ (%) | $G_{mb}$ @ $N_{des}$ | $G_{mm}$ | $V_a$ (%) | VMA (%) | VFA (%) | $P_{be}$ (%) | DP = $P_{0.075}/P_{be}$ |
|---|---|---|---|---|---|---|---|
| 5.0 | 2.245 | 2.407 | 6.8 | 15.1 | 55.1 | 3.8 | 1.0 |
| 5.5 | 2.262 | 2.391 | 5.4 | 14.8 | 63.9 | 4.3 | 0.9 |
| 6.0 | 2.269 | 2.374 | 4.4 | 15.1 | 70.5 | 4.8 | 0.8 |
| 6.5 | 2.279 | 2.358 | 3.3 | 15.1 | 78.0 | 5.3 | 0.7 |

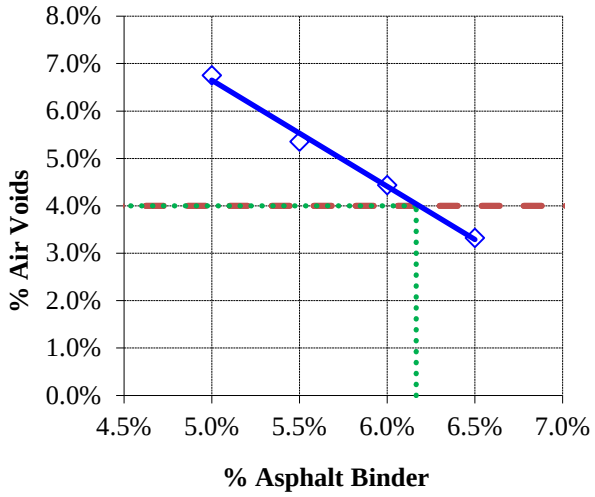


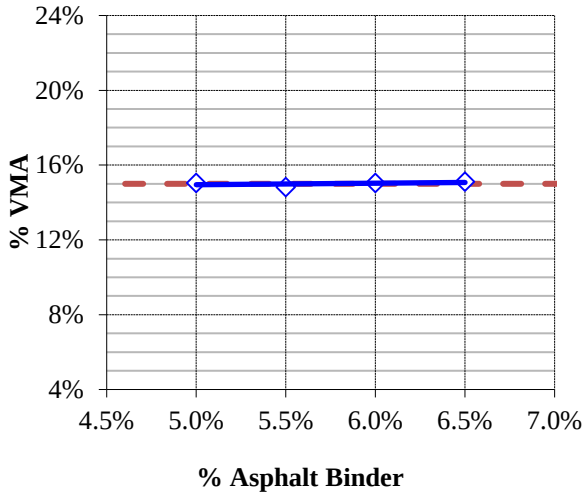


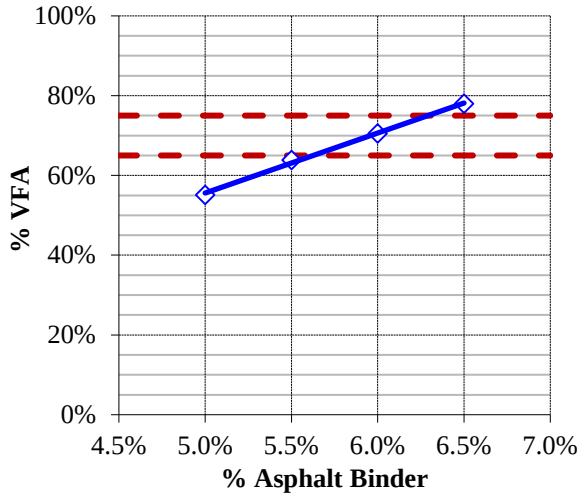


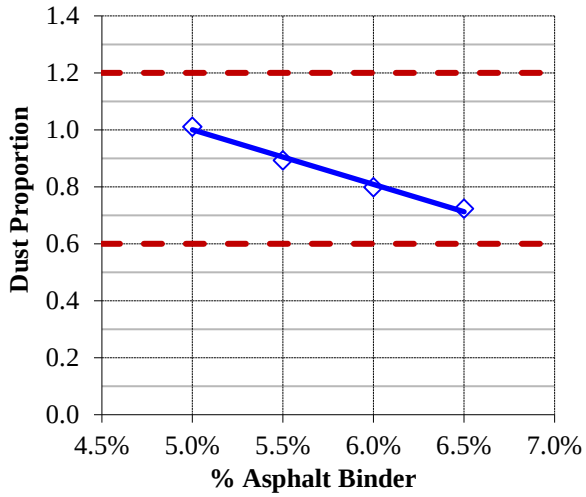


***Selected Optimum Total Binder Content (OBC):*** 6.2 %
***RAP Total Binder Content:*** No RAP was used
***RAP Binder Ratio (RBR) at OBC:*** 0.00
***VA at OBC:*** 4.0%
***VMA at OBC:*** 15.0%
***VFA at OBC:*** 73.1%
***DP at OBC:*** 0.8%
***Mixing Temperature:*** 325°F (163°C)
***Compaction Temperature:*** 310°F (155°C)
***Additives:*** Antistrip 0.5%

### B.1.3. Mix Design 2: FL95_PMA(B)

**Type of Mix:** Fine SP-9.5
**Intended Use of Mix**: Structural
**Design Traffic Level:** C
**Gyrations @ $N_{des}$:** 75

| Product Description | Product Code | Producer Name | Product Name | Plant/Pit Number | Bin Percentage (%) |
|---|---|---|---|---|---|
| S1B Stone | C51 | White Rock Quarries | S1B Stone | 87339 | 44.25 |
| Screenings | F22 | White Rock Quarries | Screenings | 87339 | 54.25 |
| Generated Dust | -- | -- | FL P200 | -- | 1.50 |

***PERCENTAGE BY WEIGHT TOTAL AGGREGATE PASSING SIEVES***

| Blend | | 44.25% | 54.25% | 1.50% | Job Mix Formula | Control Points |
|---|---|---|---|---|---|---|
| Stockpile ID | | S1B Stone C51 | Screenings F22 | FL P200 | | |
| SIEVE SIZE | 3/4" (19.00 mm) | 100.0 | 100.0 | 100.0 | 100.0 | |
| | 1/2" (12.50 mm) | 99.7 | 99.9 | 100.0 | 99.8 | 100 |
| | 3/8" (9.50 mm) | 91.4 | 99.8 | 100.0 | 96.1 | 90 – 100 |
| | No.4 (4.75 mm) | 17.9 | 99.5 | 100.0 | 63.4 | ≤ 90 |
| | No.8 (2.36 mm) | 6.3 | 90.5 | 100.0 | 53.4 | 32 – 67 |
| | No.16 (1.18 mm) | 5.0 | 75.0 | 100.0 | 44.4 | |
| | No.30 (0.600 mm) | 4.4 | 60.7 | 100.0 | 36.4 | |
| | No.50 (0.300 mm) | 3.8 | 39.2 | 100.0 | 24.4 | |
| | No.100 (0.150 mm) | 2.8 | 9.1 | 100.0 | 7.7 | |
| | No.200 (0.075 mm) | 2.0 | 2.7 | 100.0 | 3.8 | 2 – 10 |
| | $G_{sb}$ | | | | 2.510 | |

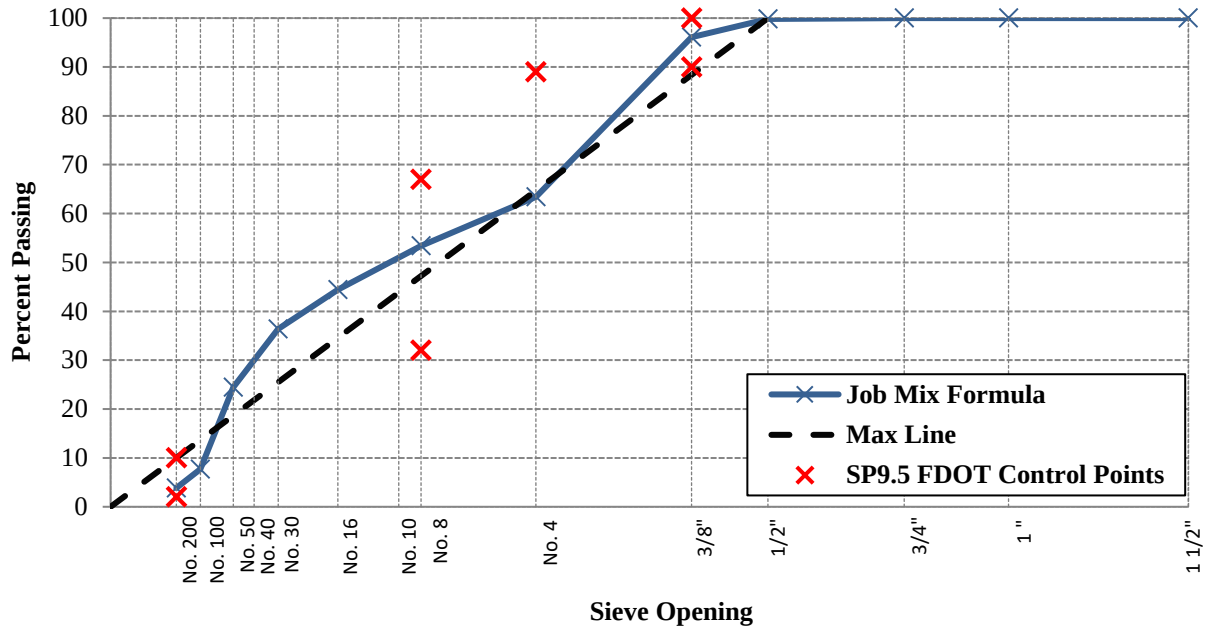


***AGGREGATE GRADATION CURVE***

## *HOT MIX DESIGN DATA*

| $P_b$ (%) | $G_{mb}$ @ $N_{des}$ | $G_{mm}$ | $V_a$ (%) | VMA (%) | VFA (%) | $P_{be}$ (%) | DP = $P_{0.075}/P_{be}$ |
|---|---|---|---|---|---|---|---|
| 5.5 | 2.241 | 2.385 | 6.0 | 15.6 | 61.5 | 4.4 | 0.9 |
| 6.0 | 2.255 | 2.368 | 4.8 | 15.5 | 69.4 | 4.9 | 0.8 |
| 6.5 | 2.284 | 2.352 | 2.9 | 14.9 | 80.6 | 5.4 | 0.7 |
| 7.0 | 2.303 | 2.336 | 1.4 | 14.7 | 90.5 | 5.9 | 0.6 |

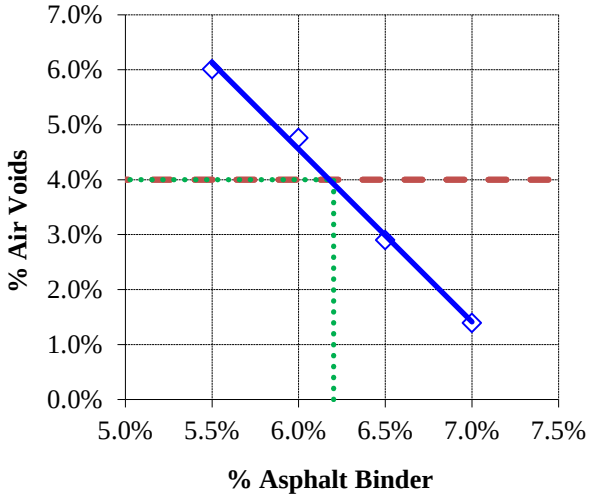


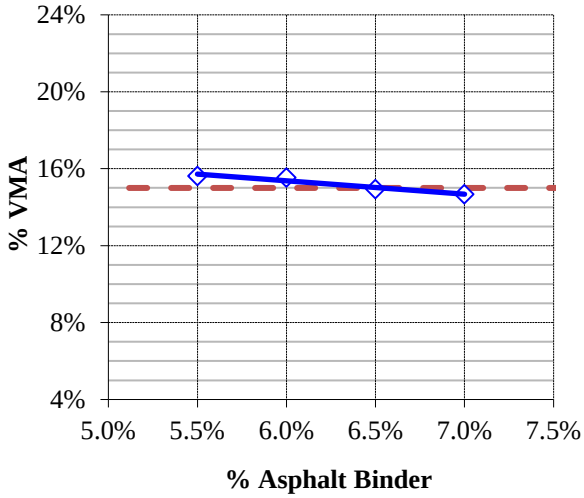


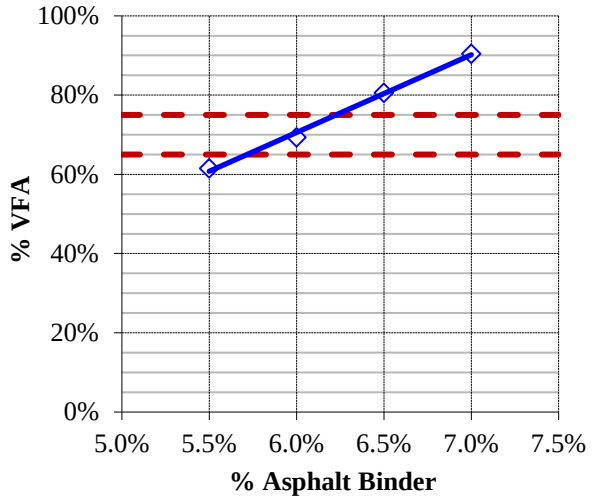


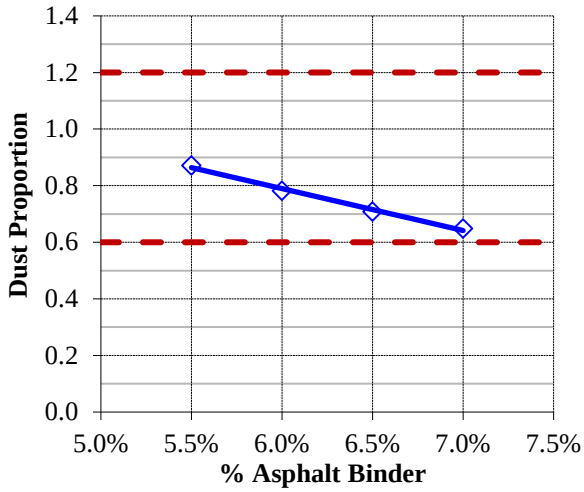


***Selected Optimum Total Binder Content (OBC):*** 6.2 %
***RAP Total Binder Content:*** No RAP was used
***RAP Binder Ratio (RBR) at OBC:*** 0.00
***VA at OBC:*** 4.0%
***VMA at OBC:*** 15.3%
***VFA at OBC:*** 73.9%
***DP at OBC:*** 0.8%
***Mixing Temperature:*** 325°F (163°C)
***Compaction Temperature:*** 310°F (155°C)
***Additives:*** Antistrip 0.5%

### B.1.4. Mix Design 3: FL95_HP (A)

**Type of Mix:** Fine SP-9.5
**Intended Use of Mix**: Structural
**Design Traffic Level:** C
**Gyrations @ $N_{des}$:** 75

| Product Description | Product Code | Producer Name | Product Name | Plant/Pit Number | Bin Percentage (%) |
|---|---|---|---|---|---|
| S1B Stone | C51 | White Rock Quarries | S1B Stone | 87339 | 44.25 |
| Screenings | F22 | White Rock Quarries | Screenings | 87339 | 54.25 |
| Generated Dust | -- | -- | FL P200 | -- | 1.50 |

***PERCENTAGE BY WEIGHT TOTAL AGGREGATE PASSING SIEVES***

| Blend | | 44.25% | 54.25% | 1.50% | Job Mix Formula | Control Points |
|---|---|---|---|---|---|---|
| Stockpile ID | | S1B Stone C51 | Screenings F22 | FL P200 | | |
| SIEVE SIZE | 3/4" (19.00 mm) | 100.0 | 100.0 | 100.0 | 100.0 | |
| | 1/2" (12.50 mm) | 99.7 | 99.9 | 100.0 | 99.8 | 100 |
| | 3/8" (9.50 mm) | 91.4 | 99.8 | 100.0 | 96.1 | 90 – 100 |
| | No.4 (4.75 mm) | 17.9 | 99.5 | 100.0 | 63.4 | ≤ 90 |
| | No.8 (2.36 mm) | 6.3 | 90.5 | 100.0 | 53.4 | 32 – 67 |
| | No.16 (1.18 mm) | 5.0 | 75.0 | 100.0 | 44.4 | |
| | No.30 (0.600 mm) | 4.4 | 60.7 | 100.0 | 36.4 | |
| | No.50 (0.300 mm) | 3.8 | 39.2 | 100.0 | 24.4 | |
| | No.100 (0.150 mm) | 2.8 | 9.1 | 100.0 | 7.7 | |
| | No.200 (0.075 mm) | 2.0 | 2.7 | 100.0 | 3.8 | 2 – 10 |
| | $G_{sb}$ | | | | 2.510 | |

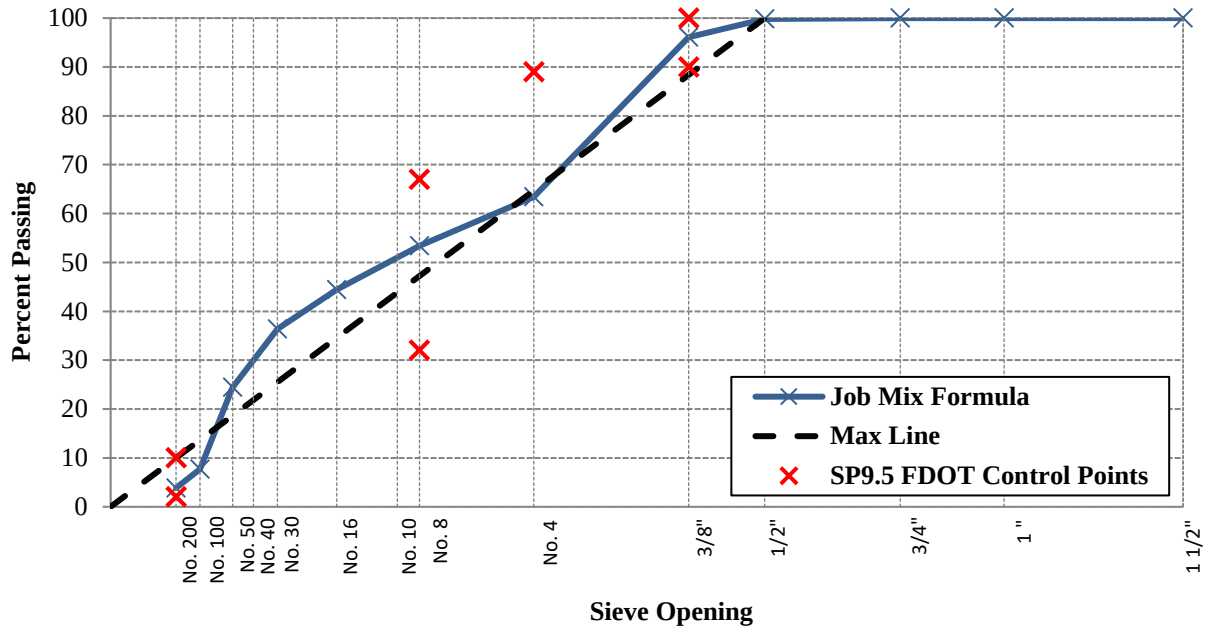


***AGGREGATE GRADATION CURVE***

## *HOT MIX DESIGN DATA*

| $P_b$ (%) | $G_{mb}$ @ $N_{des}$ | $G_{mm}$ | $V_a$ (%) | VMA (%) | VFA (%) | $P_{be}$ (%) | DP = $P_{0.075}/P_{be}$ |
|---|---|---|---|---|---|---|---|
| 5.0 | 2.242 | 2.386 | 6.0 | 15.2 | 60.2 | 4.1 | 0.9 |
| 5.5 | 2.256 | 2.369 | 4.8 | 15.1 | 68.3 | 4.6 | 0.8 |
| 6.0 | 2.275 | 2.353 | 3.3 | 14.8 | 77.6 | 5.1 | 0.7 |
| 6.5 | 2.290 | 2.337 | 2.0 | 14.7 | 86.5 | 5.7 | 0.7 |

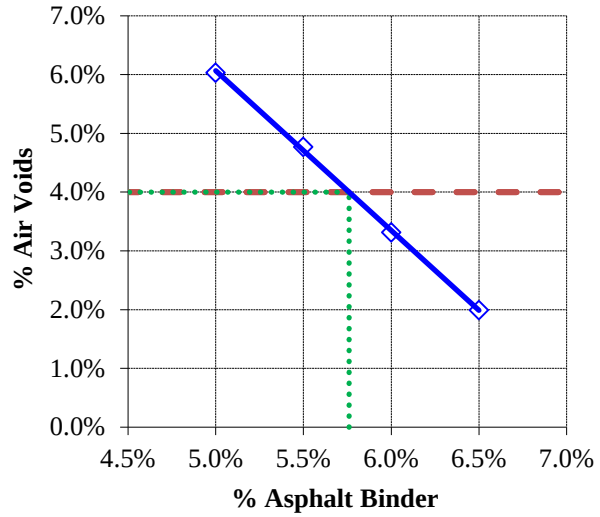


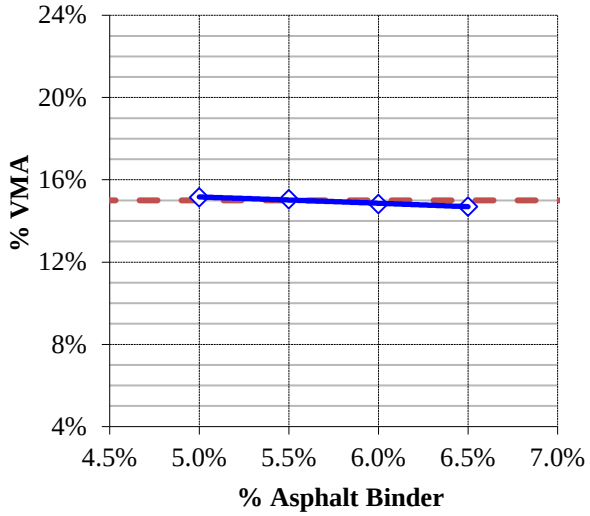


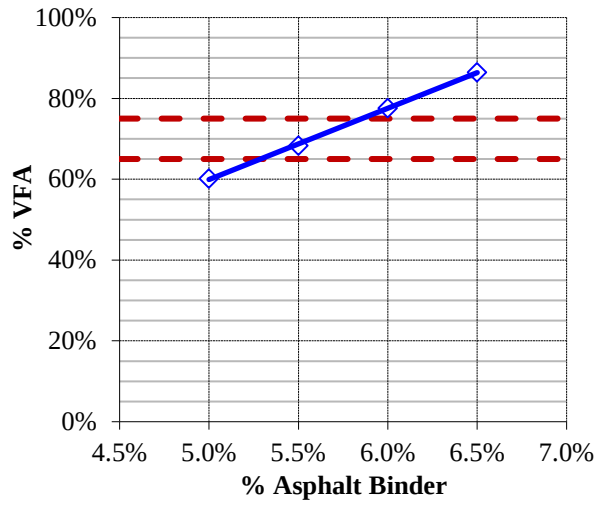


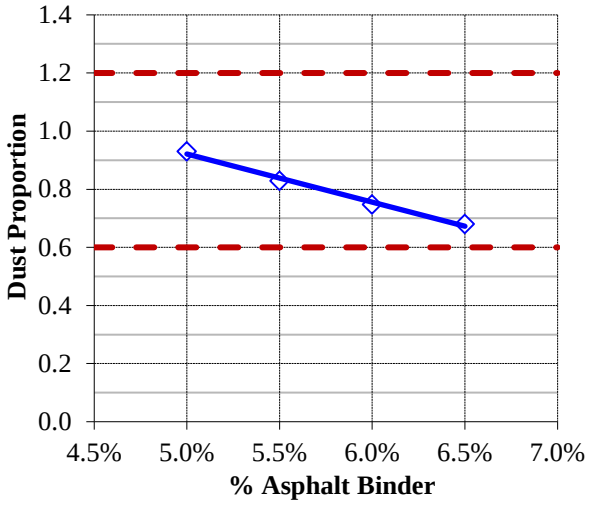


***Selected Optimum Total Binder Content (OBC):*** 5.8 %
***RAP Total Binder Content:*** No RAP was used
***RAP Binder Ratio (RBR) at OBC:*** 0.00
***VA at OBC:*** 4.0%
***VMA at OBC:*** 14.9%
***VFA at OBC:*** 73.2%
***DP at OBC:*** 0.8%
***Mixing Temperature:*** 340°F (171°C)
***Compaction Temperature:*** 325°F (163°C)
***Additives:*** Antistrip 0.5%

### B.1.5. Mix Design 4: FL95_HP(B)

**Type of Mix:** Fine SP-9.5
**Intended Use of Mix**: Structural
**Design Traffic Level:** C
**Gyrations @ $N_{des}$:** 75

| Product Description | Product Code | Producer Name | Product Name | Plant/Pit Number | Bin Percentage (%) |
|---|---|---|---|---|---|
| S1B Stone | C51 | White Rock Quarries | S1B Stone | 87339 | 44.25 |
| Screenings | F22 | White Rock Quarries | Screenings | 87339 | 54.25 |
| Generated Dust | -- | -- | FL P200 | -- | 1.50 |

***PERCENTAGE BY WEIGHT TOTAL AGGREGATE PASSING SIEVES***

| Blend | | 44.25% | 54.25% | 1.50% | Job Mix Formula | Control Points |
|---|---|---|---|---|---|---|
| Stockpile ID | | S1B Stone C51 | Screenings F22 | FL P200 | | |
| SIEVE SIZE | 3/4" (19.00 mm) | 100.0 | 100.0 | 100.0 | 100.0 | |
| | 1/2" (12.50 mm) | 99.7 | 99.9 | 100.0 | 99.8 | 100 |
| | 3/8" (9.50 mm) | 91.4 | 99.8 | 100.0 | 96.1 | 90 – 100 |
| | No.4 (4.75 mm) | 17.9 | 99.5 | 100.0 | 63.4 | ≤ 90 |
| | No.8 (2.36 mm) | 6.3 | 90.5 | 100.0 | 53.4 | 32 – 67 |
| | No.16 (1.18 mm) | 5.0 | 75.0 | 100.0 | 44.4 | |
| | No.30 (0.600 mm) | 4.4 | 60.7 | 100.0 | 36.4 | |
| | No.50 (0.300 mm) | 3.8 | 39.2 | 100.0 | 24.4 | |
| | No.100 (0.150 mm) | 2.8 | 9.1 | 100.0 | 7.7 | |
| | No.200 (0.075 mm) | 2.0 | 2.7 | 100.0 | 3.8 | 2 – 10 |
| | $G_{sb}$ | | | | 2.510 | |

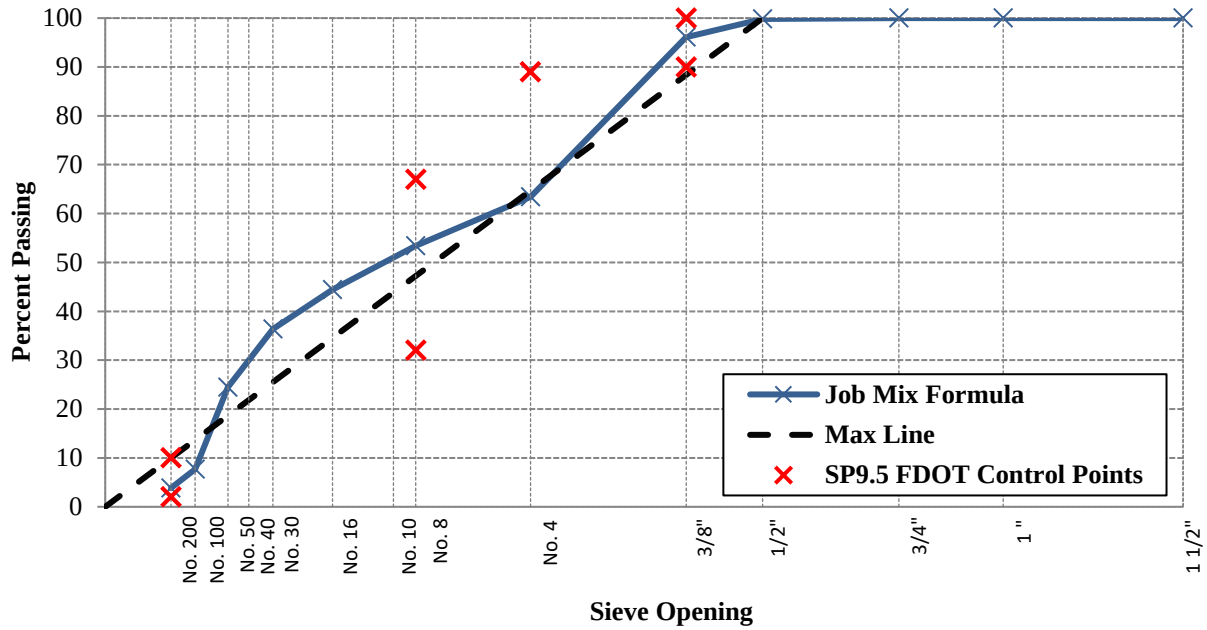


***AGGREGATE GRADATION CURVE***

## *HOT MIX DESIGN DATA*

| $P_b$ (%) | $G_{mb}$ @ $N_{des}$ | $G_{mm}$ | $V_a$ (%) | VMA (%) | VFA (%) | $P_{be}$ (%) | DP = $P_{0.075}/P_{be}$ |
|---|---|---|---|---|---|---|---|
| 5.5 | 2.237 | 2.383 | 6.2 | 15.8 | 61.0 | 4.4 | 0.9 |
| 6.0 | 2.279 | 2.367 | 3.7 | 14.7 | 74.7 | 4.9 | 0.8 |
| 6.5 | 2.288 | 2.350 | 2.6 | 14.8 | 82.3 | 5.4 | 0.7 |
| 7.0 | 2.306 | 2.334 | 1.2 | 14.6 | 92.0 | 5.9 | 0.7 |

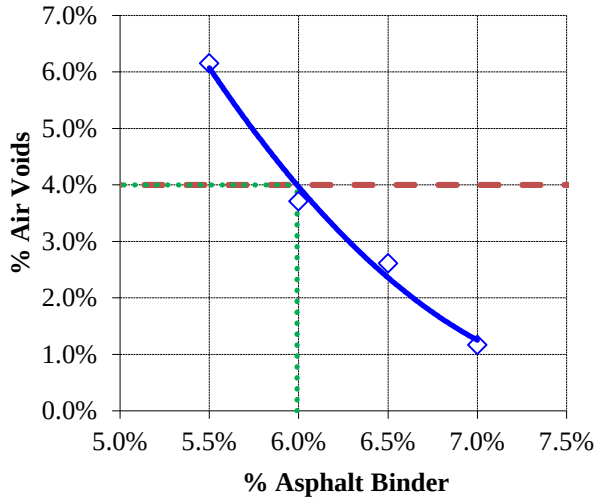


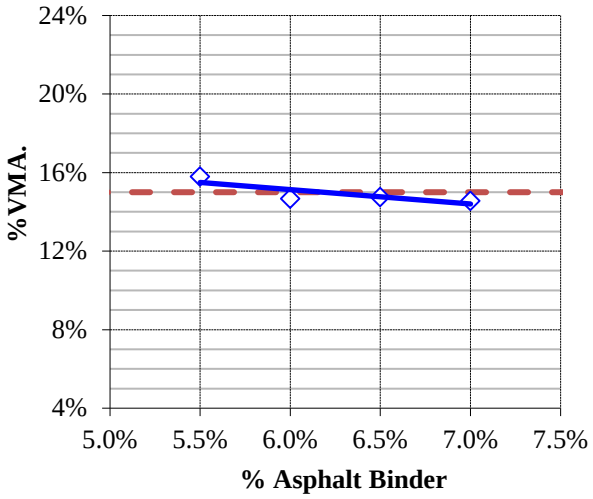


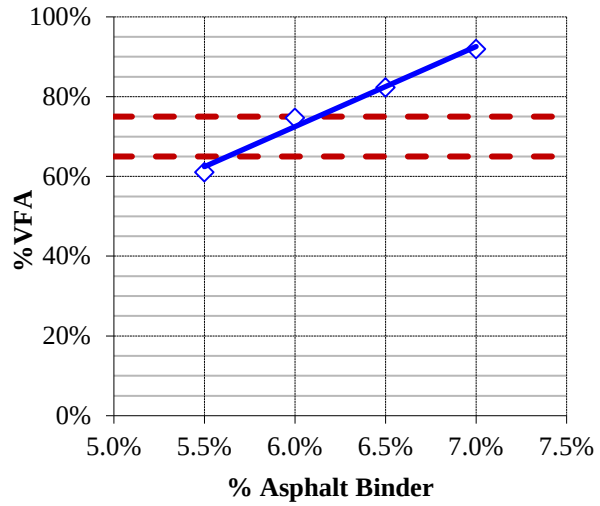


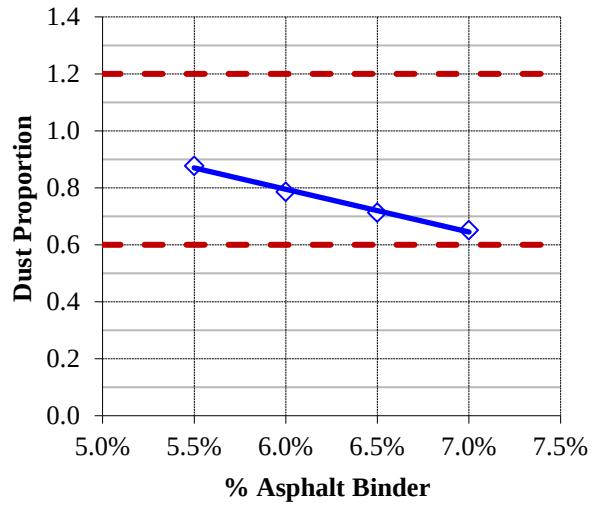


***Selected Optimum Total Binder Content (OBC):*** 6.0 %
***RAP Total Binder Content:*** No RAP was used
***RAP Binder Ratio (RBR) at OBC:*** 0.00
***VA at OBC:*** 4.0%
***VMA at OBC:*** 15.1%
***VFA at OBC:*** 73.3%
***DP at OBC:*** 0.8%
***Mixing Temperature:*** 340°F (171°C)
***Compaction Temperature:*** 325°F (163°C)
***Additives:*** Antistrip 0.5%

### B.1.6. Mix Design 5: FL125_PMA(A)

**Type of Mix:** Fine SP-12.5
**Intended Use of Mix**: Structural
**Design Traffic Level:** D/E
**Gyrations @ $N_{des}$:** 100

| Product Description | Product Code | Producer Name | Product Name | Plant/Pit Number | Bin Percentage (%) |
|---|---|---|---|---|---|
| S1A Stone | C41 | White Rock Quarries | S1A Stone | 87339 | 13.50 |
| S1B Stone | C51 | White Rock Quarries | S1B Stone | 87339 | 31.50 |
| Screenings | F22 | White Rock Quarries | Screenings | 87339 | 53.50 |
| Generated Dust | -- | -- | FL P200 | -- | 1.50 |

***PERCENTAGE BY WEIGHT TOTAL AGGREGATE PASSING SIEVES***

| Blend | | 13.50% | 31.50% | 53.50% | 1.50% | Job Mix Formula | Control Points |
|---|---|---|---|---|---|---|---|
| Stockpile ID | | S1A Stone C41 | S1B Stone C51 | Screenings F22 | FL P200 | | |
| SIEVE SIZE | 1” (25.0 mm) | 100.0 | 100.0 | 100.0 | 100.0 | 100.0 | |
| | 3/4” (19.00 mm) | 99.6 | 100.0 | 100.0 | 100.0 | 99.9 | 100 |
| | 1/2” (12.50 mm) | 60.8 | 99.7 | 99.9 | 100.0 | 94.6 | 90 – 100 |
| | 3/8” (9.50 mm) | 12.1 | 91.4 | 99.8 | 100.0 | 85.3 | ≤ 90 |
| | No.4 (4.75 mm) | 2.1 | 17.9 | 99.5 | 100.0 | 60.7 | |
| | No.8 (2.36 mm) | 2.0 | 6.3 | 90.5 | 100.0 | 52.2 | 28 – 58 |
| | No.16 (1.18 mm) | 2.0 | 5.0 | 75.0 | 100.0 | 43.5 | |
| | No.30 (0.600 mm) | 1.9 | 4.4 | 60.7 | 100.0 | 35.6 | |
| | No.50 (0.300 mm) | 1.7 | 3.8 | 39.2 | 100.0 | 23.9 | |
| | No.100 (0.150 mm) | 1.4 | 2.8 | 9.1 | 100.0 | 7.4 | |
| | No.200 (0.075 mm) | 1.0 | 2.0 | 2.7 | 100.0 | 3.7 | 2 – 10 |
| | $G_{sb}$ | | | | | 2.499 | |


***AGGREGATE GRADATION CURVE***

## *HOT MIX DESIGN DATA*

| $P_b$ (%) | $G_{mb}$ @ $N_{des}$ | $G_{mm}$ | $V_a$ (%) | VMA (%) | VFA (%) | $P_{be}$ (%) | DP = $P_{0.075}/P_{be}$ |
|---|---|---|---|---|---|---|---|
| 4.5 | 2.244 | 2.405 | 6.7 | 14.3 | 53.0 | 3.5 | 1.1 |
| 5.0 | 2.259 | 2.388 | 5.4 | 14.1 | 61.7 | 4.0 | 0.9 |
| 5.5 | 2.286 | 2.372 | 3.6 | 13.6 | 73.2 | 4.5 | 0.8 |
| 6.0 | 2.298 | 2.356 | 2.4 | 13.6 | 82.1 | 5.0 | 0.7 |

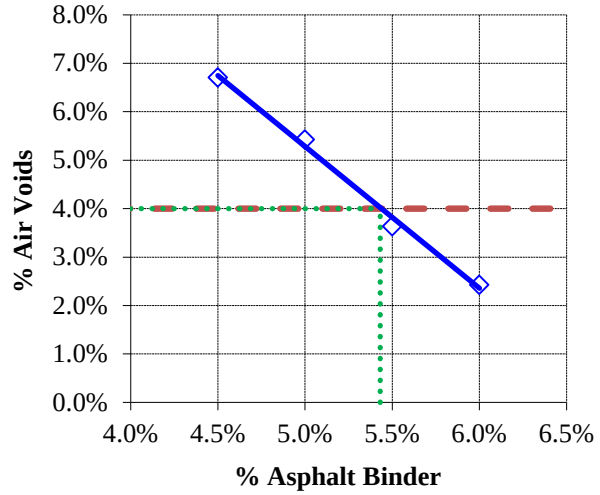


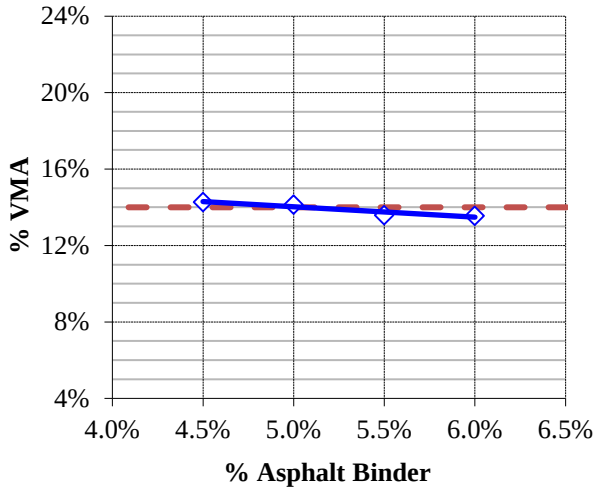


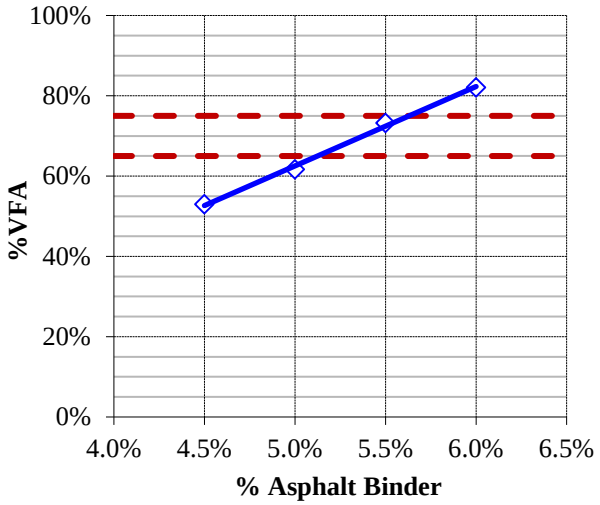


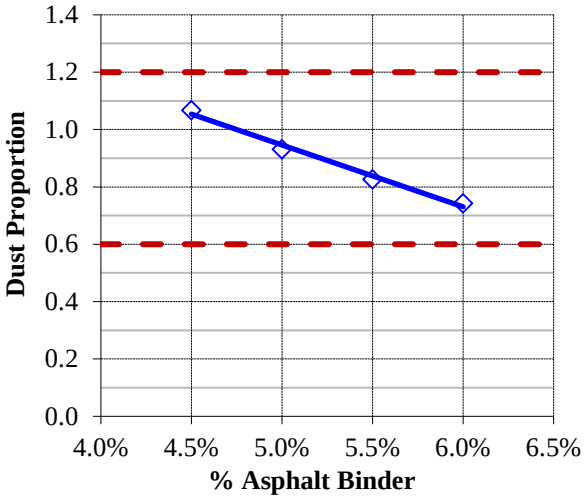


***Selected Optimum Total Binder Content (OBC):*** 5.4 %
***RAP Total Binder Content:*** No RAP was used
***RAP Binder Ratio (RBR) at OBC:*** 0.00
***VA at OBC:*** 4.0%
***VMA at OBC:*** 13.9%
***VFA at OBC:*** 71.2%
***DP at OBC:*** 0.8%
***Mixing Temperature:*** 325°F (163°C)
***Compaction Temperature:*** 310°F (155°C)
***Additives:*** Antistrip 0.5%

### B.1.7. Mix Design 6: FL125_PMA(B)

**Type of Mix:** Fine SP-12.5
**Intended Use of Mix**: Structural
**Design Traffic Level:** D/E
**Gyrations @ $N_{des}$:** 100

| Product Description | Product Code | Producer Name | Product Name | Plant/Pit Number | Bin Percentage (%) |
|---|---|---|---|---|---|
| S1A Stone | C41 | White Rock Quarries | S1A Stone | 87339 | 13.50 |
| S1B Stone | C51 | White Rock Quarries | S1B Stone | 87339 | 31.50 |
| Screenings | F22 | White Rock Quarries | Screenings | 87339 | 53.50 |
| Generated Dust | -- | -- | FL P200 | -- | 1.50 |

***PERCENTAGE BY WEIGHT TOTAL AGGREGATE PASSING SIEVES***

| Blend | | 13.50% | 31.50% | 53.50% | 1.50% | Job Mix Formula | Control Points |
|---|---|---|---|---|---|---|---|
| Stockpile ID | | S1A Stone C41 | S1B Stone C51 | Screenings F22 | FL P200 | | |
| SIEVE SIZE | 1” (25.0 mm) | 100.0 | 100.0 | 100.0 | 100.0 | 100.0 | |
| | 3/4” (19.00 mm) | 99.6 | 100.0 | 100.0 | 100.0 | 99.9 | 100 |
| | 1/2” (12.50 mm) | 60.8 | 99.7 | 99.9 | 100.0 | 94.6 | 90 – 100 |
| | 3/8” (9.50 mm) | 12.1 | 91.4 | 99.8 | 100.0 | 85.3 | ≤ 90 |
| | No.4 (4.75 mm) | 2.1 | 17.9 | 99.5 | 100.0 | 60.7 | |
| | No.8 (2.36 mm) | 2.0 | 6.3 | 90.5 | 100.0 | 52.2 | 28 – 58 |
| | No.16 (1.18 mm) | 2.0 | 5.0 | 75.0 | 100.0 | 43.5 | |
| | No.30 (0.600 mm) | 1.9 | 4.4 | 60.7 | 100.0 | 35.6 | |
| | No.50 (0.300 mm) | 1.7 | 3.8 | 39.2 | 100.0 | 23.9 | |
| | No.100 (0.150 mm) | 1.4 | 2.8 | 9.1 | 100.0 | 7.4 | |
| | No.200 (0.075 mm) | 1.0 | 2.0 | 2.7 | 100.0 | 3.7 | 2 – 10 |
| | $G_{sb}$ | | | | | 2.499 | |

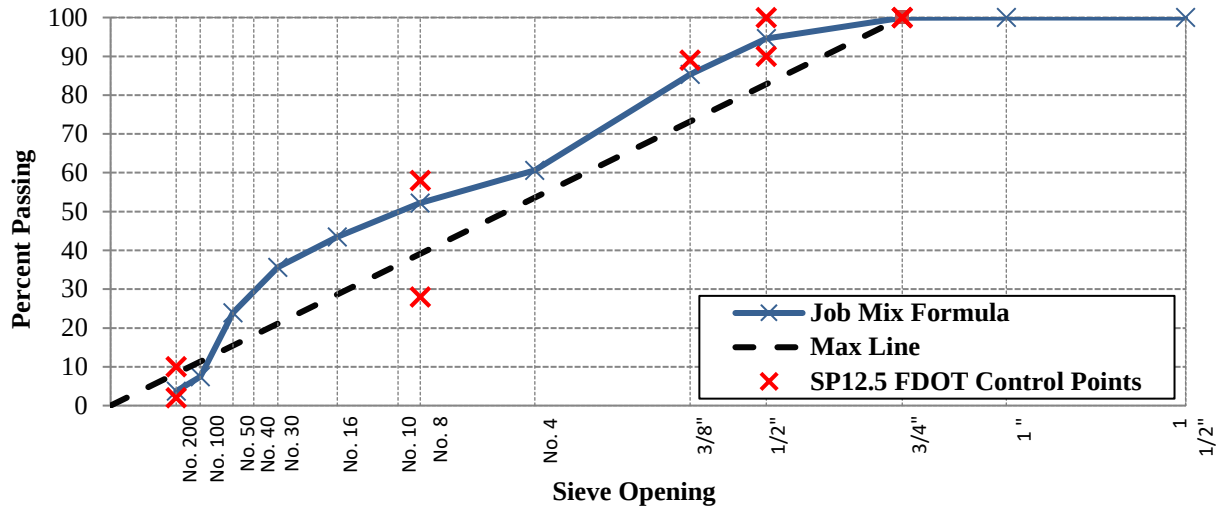


***AGGREGATE GRADATION CURVE***

## *HOT MIX DESIGN DATA*

| $P_b$ (%) | $G_{mb}$ @ $N_{des}$ | $G_{mm}$ | $V_a$ (%) | VMA (%) | VFA (%) | $P_{be}$ (%) | DP = $P_{0.075}/P_{be}$ |
|---|---|---|---|---|---|---|---|
| 5.0 | 2.255 | 2.394 | 5.8 | 14.3 | 59.4 | 3.9 | 1.0 |
| 5.5 | 2.275 | 2.378 | 4.3 | 14.0 | 69.0 | 4.4 | 0.8 |
| 6.0 | 2.290 | 2.361 | 3.0 | 13.9 | 78.3 | 4.9 | 0.8 |
| 6.5 | 2.299 | 2.345 | 2.0 | 14.0 | 86.0 | 5.4 | 0.7 |

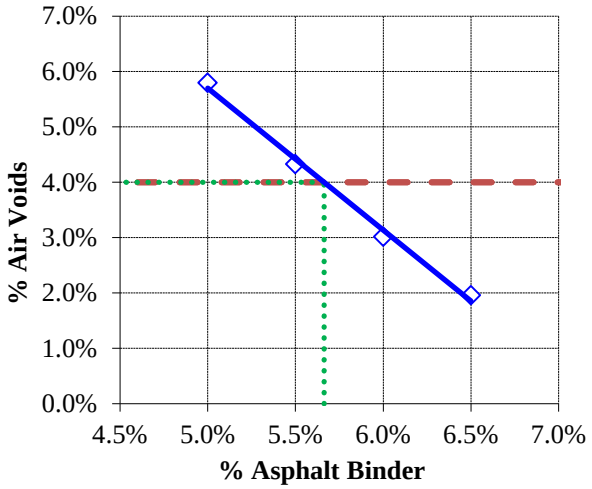


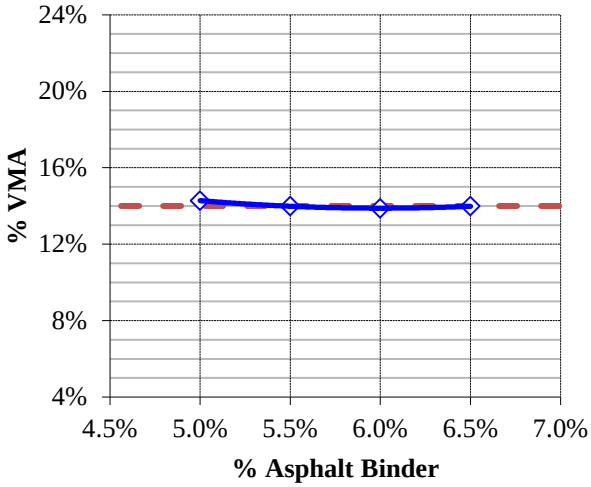


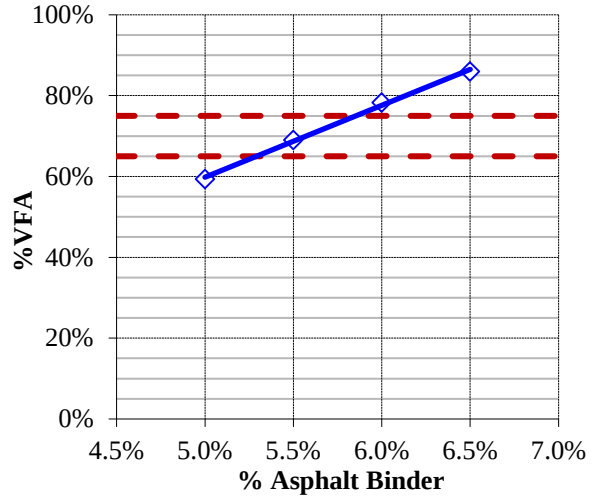


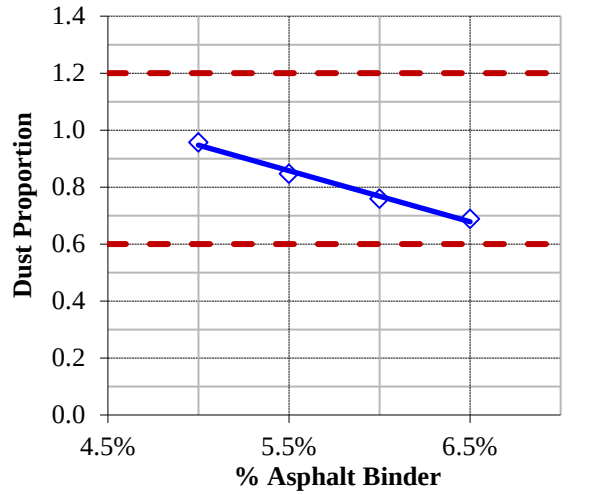


***Selected Optimum Total Binder Content (OBC):*** 5.7 %
***RAP Total Binder Content:*** No RAP was used
***RAP Binder Ratio (RBR) at OBC:*** 0.00
***VA at OBC:*** 4.0%
***VMA at OBC:*** 13.9%
***VFA at OBC:*** 72.2%
***DP at OBC:*** 0.8%
***Mixing Temperature:*** 325°F (163°C)
***Compaction Temperature:*** 310°F (155°C)
***Additives:*** Antistrip 0.5%

### B.1.8. Mix Design 7: FL125_HP (A)

**Type of Mix:** Fine SP-12.5
**Intended Use of Mix**: Structural
**Design Traffic Level:** D/E
**Gyrations @ $N_{des}$:** 100

| Product Description | Product Code | Producer Name | Product Name | Plant/Pit Number | Bin Percentage (%) |
|---|---|---|---|---|---|
| S1A Stone | C41 | White Rock Quarries | S1A Stone | 87339 | 13.50 |
| S1B Stone | C51 | White Rock Quarries | S1B Stone | 87339 | 31.50 |
| Screenings | F22 | White Rock Quarries | Screenings | 87339 | 53.50 |
| Generated Dust | -- | -- | FL P200 | -- | 1.50 |

***PERCENTAGE BY WEIGHT TOTAL AGGREGATE PASSING SIEVES***

| Blend | | 13.50% | 31.50% | 53.50% | 1.50% | Job Mix Formula | Control Points |
|---|---|---|---|---|---|---|---|
| Stockpile ID | | S1A Stone C41 | S1B Stone C51 | Screenings F22 | FL P200 | | |
| SIEVE SIZE | 1” (25.0 mm) | 100.0 | 100.0 | 100.0 | 100.0 | 100.0 | |
| | 3/4” (19.00 mm) | 99.6 | 100.0 | 100.0 | 100.0 | 99.9 | 100 |
| | 1/2” (12.50 mm) | 60.8 | 99.7 | 99.9 | 100.0 | 94.6 | 90 – 100 |
| | 3/8” (9.50 mm) | 12.1 | 91.4 | 99.8 | 100.0 | 85.3 | ≤ 90 |
| | No.4 (4.75 mm) | 2.1 | 17.9 | 99.5 | 100.0 | 60.7 | |
| | No.8 (2.36 mm) | 2.0 | 6.3 | 90.5 | 100.0 | 52.2 | 28 – 58 |
| | No.16 (1.18 mm) | 2.0 | 5.0 | 75.0 | 100.0 | 43.5 | |
| | No.30 (0.600 mm) | 1.9 | 4.4 | 60.7 | 100.0 | 35.6 | |
| | No.50 (0.300 mm) | 1.7 | 3.8 | 39.2 | 100.0 | 23.9 | |
| | No.100 (0.150 mm) | 1.4 | 2.8 | 9.1 | 100.0 | 7.4 | |
| | No.200 (0.075 mm) | 1.0 | 2.0 | 2.7 | 100.0 | 3.7 | 2 – 10 |
| | $G_{sb}$ | | | | | 2.499 | |

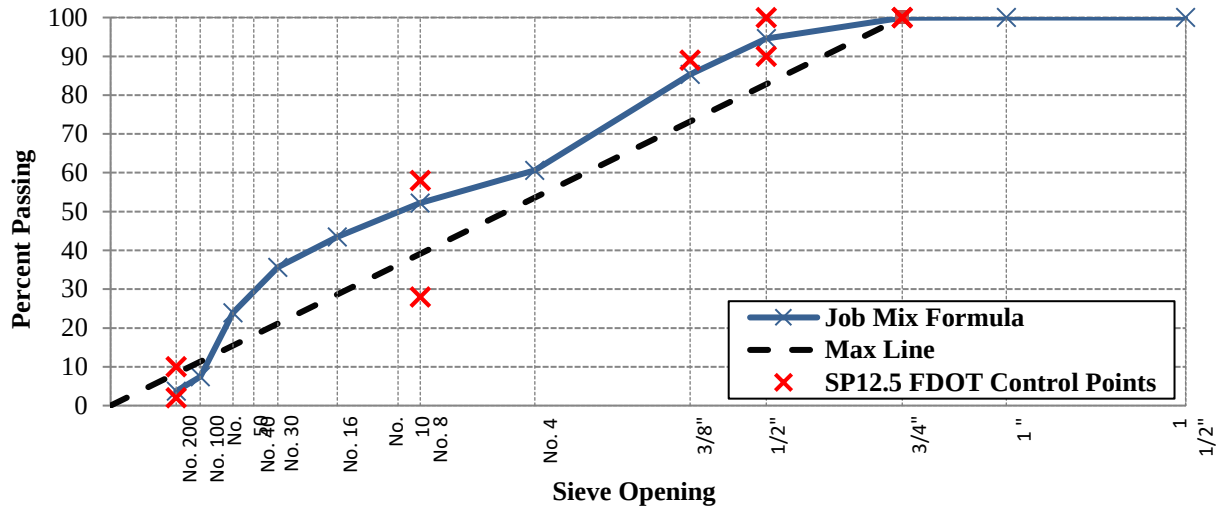


***AGGREGATE GRADATION CURVE***

## *HOT MIX DESIGN DATA*

| $P_b$ (%) | $G_{mb}$ @ $N_{des}$ | $G_{mm}$ | $V_a$ (%) | VMA (%) | VFA (%) | $P_{be}$ (%) | DP = $P_{0.075}/P_{be}$ |
|---|---|---|---|---|---|---|---|
| 4.5 | 2.246 | 2.389 | 6.0 | 14.2 | 57.9 | 3.7 | 1.0 |
| 5.0 | 2.256 | 2.372 | 4.9 | 14.2 | 65.7 | 4.2 | 0.9 |
| 5.5 | 2.269 | 2.356 | 3.7 | 14.2 | 74.0 | 4.7 | 0.8 |
| 6.0 | 2.286 | 2.340 | 2.3 | 14.0 | 83.8 | 5.2 | 0.7 |

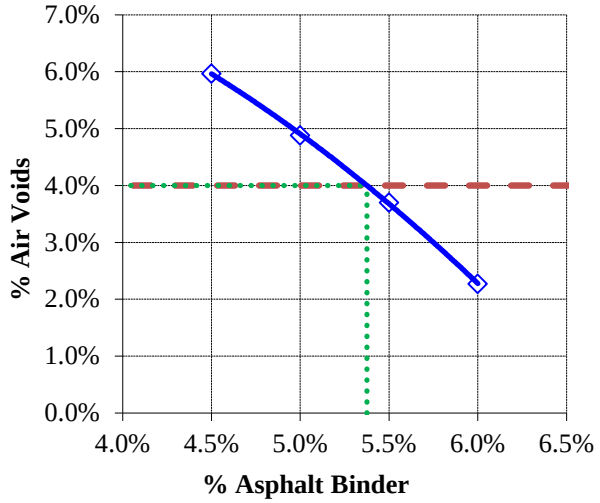


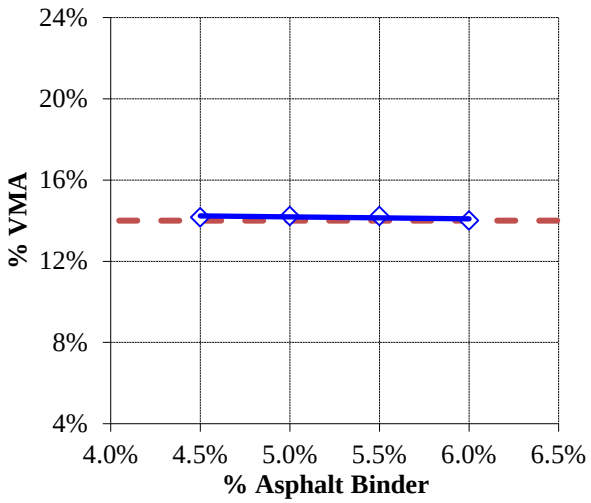


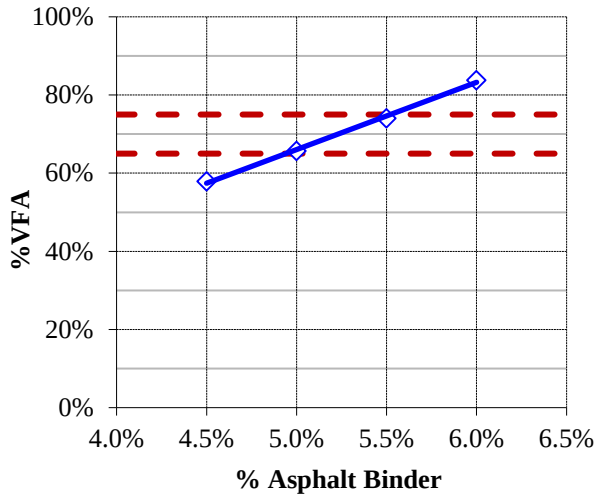


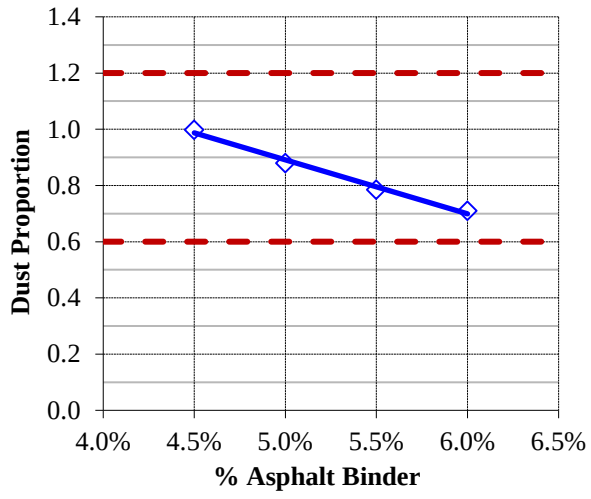


***Selected Optimum Total Binder Content (OBC):*** 5.4 %
***RAP Total Binder Content:*** No RAP was used
***RAP Binder Ratio (RBR) at OBC:*** 0.00
***VA at OBC:*** 4.0%
***VMA at OBC:*** 14.2%
***VFA at OBC:*** 71.9%
***DP at OBC:*** 0.8%
***Mixing Temperature:*** 340°F (171°C)
***Compaction Temperature:*** 325°F (163°C)
***Additives:*** Antistrip 0.5%

### B.1.9. Mix Design 8: FL125_HP(B)

**Type of Mix:** Fine SP-12.5
**Intended Use of Mix**: Structural
**Design Traffic Level:** D/E
**Gyrations @ $N_{des}$:** 100

| Product Description | Product Code | Producer Name | Product Name | Plant/Pit Number | Bin Percentage (%) |
|---|---|---|---|---|---|
| S1A Stone | C41 | White Rock Quarries | S1A Stone | 87339 | 13.50 |
| S1B Stone | C51 | White Rock Quarries | S1B Stone | 87339 | 31.50 |
| Screenings | F22 | White Rock Quarries | Screenings | 87339 | 53.50 |
| Generated Dust | -- | -- | FL P200 | -- | 1.50 |

***PERCENTAGE BY WEIGHT TOTAL AGGREGATE PASSING SIEVES***

| Blend | | 13.50% | 31.50% | 53.50% | 1.50% | Job Mix Formula | Control Points |
|---|---|---|---|---|---|---|---|
| Stockpile ID | | S1A Stone C41 | S1B Stone C51 | Screenings F22 | FL P200 | | |
| SIEVE SIZE | 1” (25.0 mm) | 100.0 | 100.0 | 100.0 | 100.0 | 100.0 | |
| | 3/4” (19.00 mm) | 99.6 | 100.0 | 100.0 | 100.0 | 99.9 | 100 |
| | 1/2” (12.50 mm) | 60.8 | 99.7 | 99.9 | 100.0 | 94.6 | 90 – 100 |
| | 3/8” (9.50 mm) | 12.1 | 91.4 | 99.8 | 100.0 | 85.3 | ≤ 90 |
| | No.4 (4.75 mm) | 2.1 | 17.9 | 99.5 | 100.0 | 60.7 | |
| | No.8 (2.36 mm) | 2.0 | 6.3 | 90.5 | 100.0 | 52.2 | 28 – 58 |
| | No.16 (1.18 mm) | 2.0 | 5.0 | 75.0 | 100.0 | 43.5 | |
| | No.30 (0.600 mm) | 1.9 | 4.4 | 60.7 | 100.0 | 35.6 | |
| | No.50 (0.300 mm) | 1.7 | 3.8 | 39.2 | 100.0 | 23.9 | |
| | No.100 (0.150 mm) | 1.4 | 2.8 | 9.1 | 100.0 | 7.4 | |
| | No.200 (0.075 mm) | 1.0 | 2.0 | 2.7 | 100.0 | 3.7 | 2 – 10 |
| | $G_{sb}$ | | | | | 2.499 | |

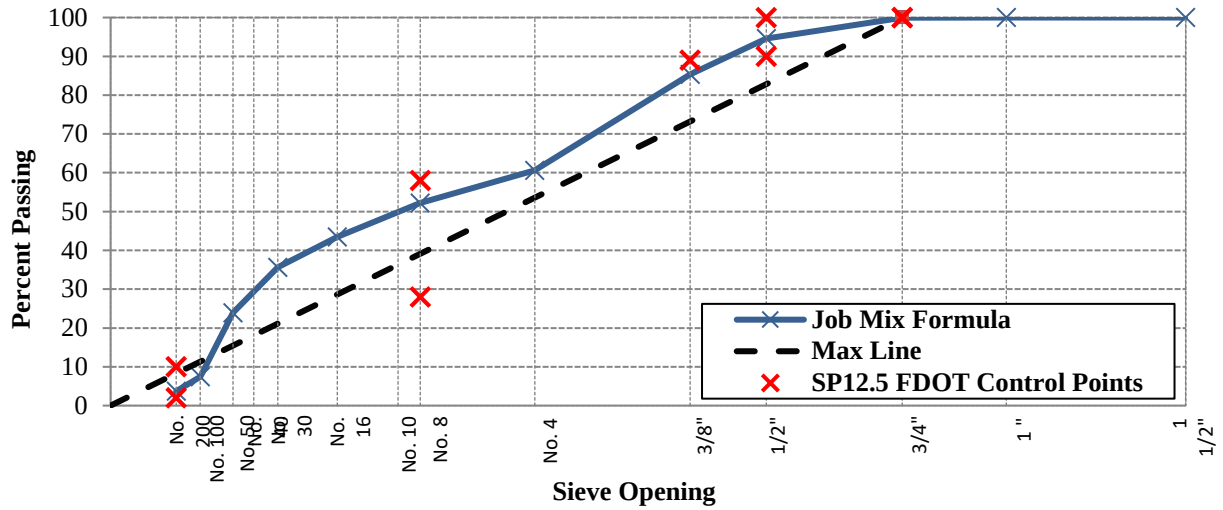


***AGGREGATE GRADATION CURVE***

## *HOT MIX DESIGN DATA*

| $P_b$ (%) | $G_{mb}$ @ $N_{des}$ | $G_{mm}$ | $V_a$ (%) | VMA (%) | VFA (%) | $P_{be}$ (%) | DP = $P_{0.075}/P_{be}$ |
|---|---|---|---|---|---|---|---|
| 4.5 | 2.254 | 2.400 | 6.1 | 13.9 | 56.2 | 3.5 | 1.1 |
| 5.0 | 2.266 | 2.383 | 4.9 | 13.9 | 64.8 | 4.0 | 0.9 |
| 5.5 | 2.275 | 2.366 | 3.8 | 14.0 | 72.6 | 4.5 | 0.8 |
| 6.0 | 2.296 | 2.349 | 2.3 | 13.6 | 83.3 | 5.0 | 0.7 |

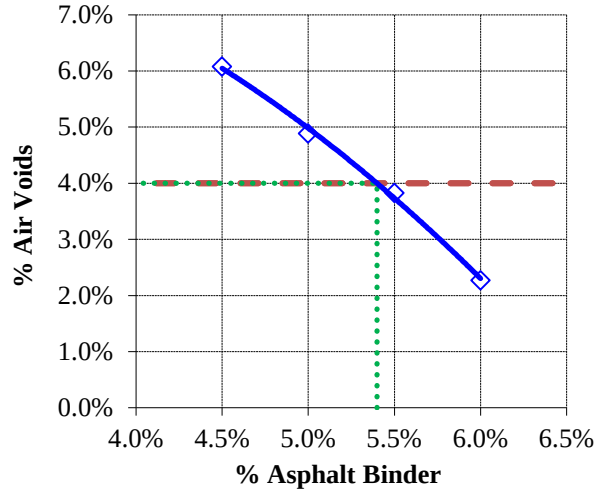


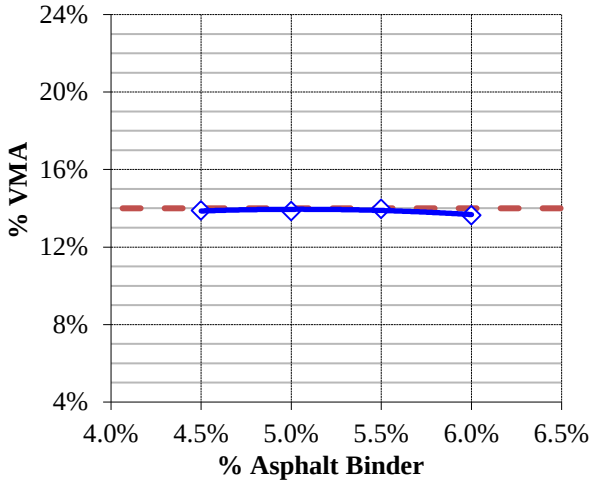


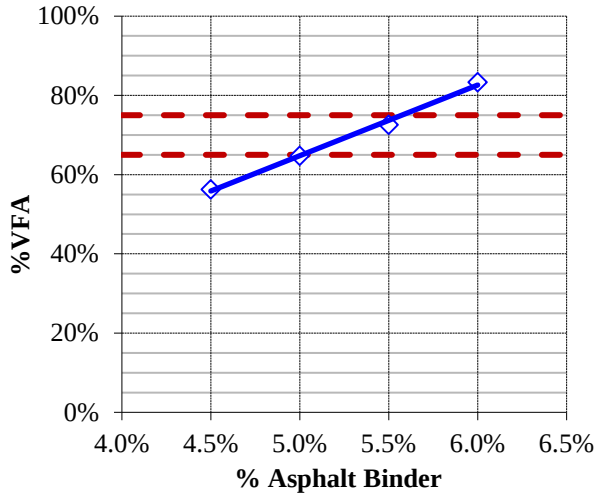


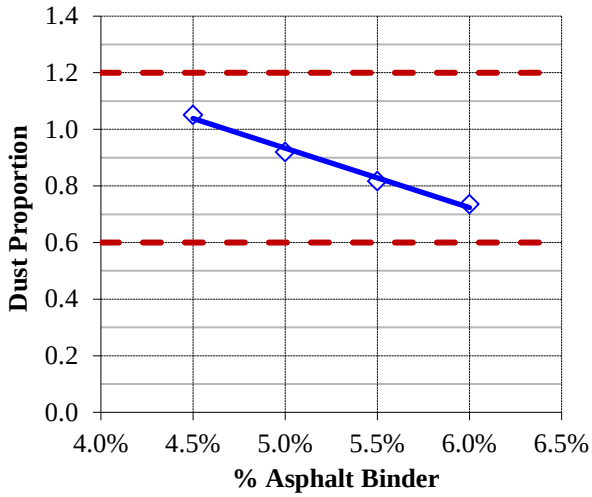


***Selected Optimum Total Binder Content (OBC):*** 5.4 %
***RAP Total Binder Content:*** No RAP was used
***RAP Binder Ratio (RBR) at OBC:*** 0.00
***VA at OBC:*** 4.0%
***VMA at OBC:*** 13.9%
***VFA at OBC:*** 71.2%
***DP at OBC:*** 0.8%
***Mixing Temperature:*** 340°F (171°C)
***Compaction Temperature:*** 325°F (163°C)
***Additives:*** Antistrip 0.5%

### B.1.10. Mix Design 9: GA95_PMA(A)

**Type of Mix:** Fine SP-9.5
**Intended Use of Mix**: Structural
**Design Traffic Level:** C
**Gyrations @ $N_{des}$:** 75

| Product Description | Product Code | Producer Name | Product Name | Plant/Pit Number | Bin Percentage (%) |
|---|---|---|---|---|---|
| Milled Material | 334-MM | Anderson Columbia Company Inc. | SR-8 | A0716 | 20.00 |
| S1B Stone | C53 | Junction City Mining | #89 Stone | GA553 | 31.95 |
| Screenings | F22 | | W-10 Screenings | GA553 | 11.95 |
| Screenings | F23 | | M-10 Screenings | GA553 | 21.95 |
| Sand | 334-MS | Mossy Head Sand Mine | Mossy Head | -- | 13.95 |
| Generated Dust | -- | -- | GA P200 | -- | 0.20 |

***PERCENTAGE BY WEIGHT TOTAL AGGREGATE PASSING SIEVES***

| Blend | | 20.00% | 31.95% | 11.95% | 21.95% | 13.95% | 0.20% | Job Mix Formula | Control Points |
|---|---|---|---|---|---|---|---|---|---|
| Stockpile ID | | SR-8_334 | S1B Stone C53 | Screenings F22 | Screenings F23 | Sand 334-MS | GA P200 | | |
| SIEVE SIZE | 3/4" (19.00 mm) | 100.0 | 100.0 | 100.0 | 100.0 | 100.0 | 100.0 | 100.0 | |
| | 1/2" (12.50 mm) | 97.8 | 100.0 | 100.0 | 100.0 | 100.0 | 100.0 | 99.6 | 100 |
| | 3/8" (9.50 mm) | 89.6 | 98.0 | 100.0 | 100.0 | 100.0 | 100.0 | 97.3 | 90 – 100 |
| | No.4 (4.75 mm) | 55.7 | 35.0 | 98.0 | 98.0 | 100.0 | 100.0 | 69.7 | ≤ 90 |
| | No.8 (2.36 mm) | 34.1 | 4.0 | 73.0 | 77.0 | 97.0 | 100.0 | 47.5 | 32 – 67 |
| | No.16 (1.18 mm) | 25.3 | 3.0 | 47.0 | 53.0 | 78.0 | 100.0 | 34.4 | |
| | No.30 (0.600 mm) | 20.1 | 2.0 | 32.0 | 38.0 | 40.0 | 100.0 | 22.6 | |
| | No.50 (0.300 mm) | 13.9 | 1.0 | 21.0 | 29.0 | 13.0 | 100.0 | 14.0 | |
| | No.100 (0.150 mm) | 8.5 | 1.0 | 13.0 | 20.0 | 1.0 | 100.0 | 8.3 | |
| | No.200 (0.075 mm) | 4.8 | 1.0 | 5.5 | 15.0 | 1.0 | 100.0 | 5.6 | 2 – 10 |
| | $G_{sb}$ | | | | | | | 2.759 | |

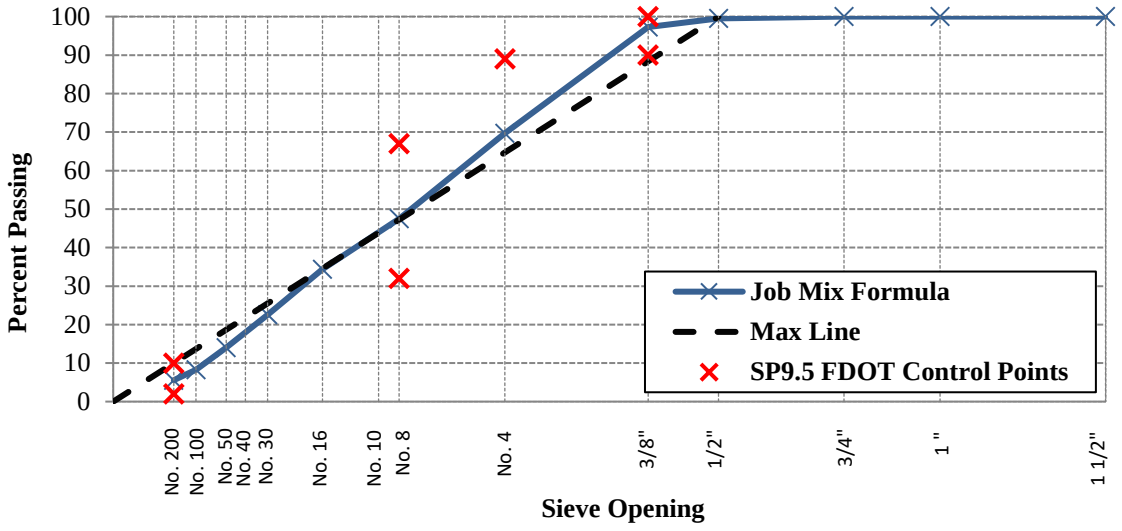


***AGGREGATE GRADATION CURVE***

## *HOT MIX DESIGN DATA*

| $P_b$ (%) | $G_{mb}$ @ $N_{des}$ | $G_{mm}$ | $V_a$ (%) | VMA (%) | VFA (%) | $P_{be}$ (%) | DP = $P_{0.075}/P_{be}$ |
|---|---|---|---|---|---|---|---|
| 4.0 | 2.426 | 2.591 | 6.4 | 15.6 | 59.2 | 3.8 | 1.4 |
| 4.5 | 2.445 | 2.570 | 4.9 | 15.4 | 68.4 | 4.3 | 1.3 |
| 5.0 | 2.478 | 2.550 | 2.8 | 14.7 | 80.7 | 4.8 | 1.1 |
| 5.5 | 2.490 | 2.531 | 1.6 | 14.7 | 89.1 | 5.3 | 1.0 |

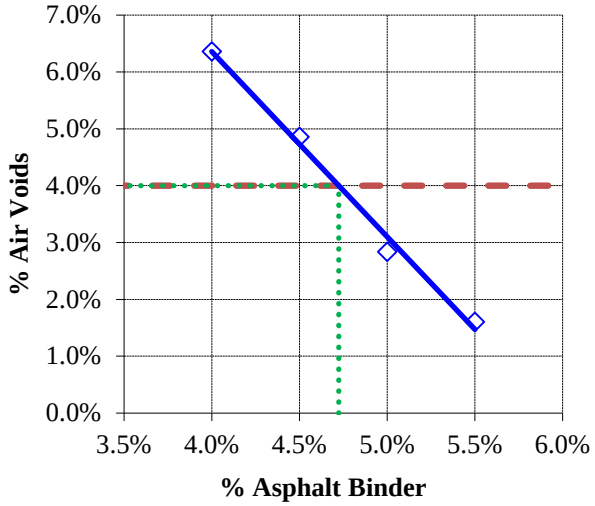


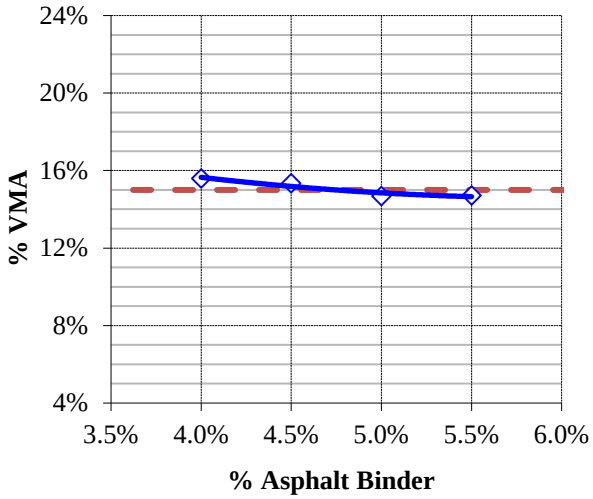


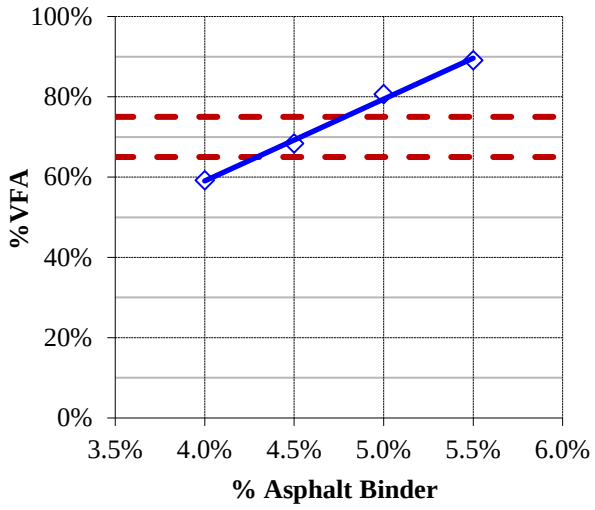


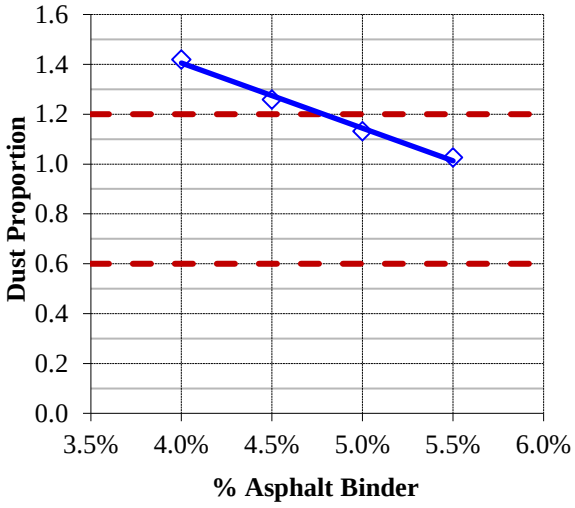


***Optimum Total Binder Content (OBC):*** 4.7 %
***RAP Total Binder Content:*** 5.63%
***RAP Binder Ratio (RBR) at OBC:*** 0.24
***VA at OBC:*** 4.0%
***VMA at OBC:*** 15.0%
***VFA at OBC:*** 74.0%
***DP at OBC:*** 1.2
***Mixing Temperature:*** 325°F (163°C)
***Compaction Temperature:*** 310°F (155°C)
***Additives:*** Antistrip 0.5%

### B.1.11. Mix Design 10: GA95_PMA(B)

**Type of Mix:** Fine SP-9.5
**Intended Use of Mix**: Structural
**Design Traffic Level:** C
**Gyrations @ $N_{des}$:** 75

| Product Description | Product Code | Producer Name | Product Name | Plant/Pit Number | Bin Percentage (%) |
|---|---|---|---|---|---|
| Milled Material | 334-MM | Anderson Columbia Company Inc. | SR-8 | A0716 | 20.00 |
| S1B Stone | C53 | Junction City Mining | #89 Stone | GA553 | 31.95 |
| Screenings | F22 | | W-10 Screenings | GA553 | 11.95 |
| Screenings | F23 | | M-10 Screenings | GA553 | 21.95 |
| Sand | 334-MS | Mossy Head Sand Mine | Mossy Head | -- | 13.95 |
| Generated Dust | -- | -- | GA P200 | -- | 0.20 |

***PERCENTAGE BY WEIGHT TOTAL AGGREGATE PASSING SIEVES***

| Blend | | 20.00% | 31.95% | 11.95% | 21.95% | 13.95% | 0.20% | Job Mix Formula | Control Points |
|---|---|---|---|---|---|---|---|---|---|
| Stockpile ID | | SR-8_334 | S1B Stone C53 | Screenings F22 | Screenings F23 | Sand 334-MS | GA P200 | | |
| SIEVE SIZE | 3/4" (19.00 mm) | 100.0 | 100.0 | 100.0 | 100.0 | 100.0 | 100.0 | 100.0 | |
| | 1/2" (12.50 mm) | 97.8 | 100.0 | 100.0 | 100.0 | 100.0 | 100.0 | 99.6 | 100 |
| | 3/8" (9.50 mm) | 89.6 | 98.0 | 100.0 | 100.0 | 100.0 | 100.0 | 97.3 | 90 – 100 |
| | No.4 (4.75 mm) | 55.7 | 35.0 | 98.0 | 98.0 | 100.0 | 100.0 | 69.7 | ≤ 90 |
| | No.8 (2.36 mm) | 34.1 | 4.0 | 73.0 | 77.0 | 97.0 | 100.0 | 47.5 | 32 – 67 |
| | No.16 (1.18 mm) | 25.3 | 3.0 | 47.0 | 53.0 | 78.0 | 100.0 | 34.4 | |
| | No.30 (0.600 mm) | 20.1 | 2.0 | 32.0 | 38.0 | 40.0 | 100.0 | 22.6 | |
| | No.50 (0.300 mm) | 13.9 | 1.0 | 21.0 | 29.0 | 13.0 | 100.0 | 14.0 | |
| | No.100 (0.150 mm) | 8.5 | 1.0 | 13.0 | 20.0 | 1.0 | 100.0 | 8.3 | |
| | No.200 (0.075 mm) | 4.8 | 1.0 | 5.5 | 15.0 | 1.0 | 100.0 | 5.6 | 2 – 10 |
| | $G_{sb}$ | | | | | | | 2.759 | |

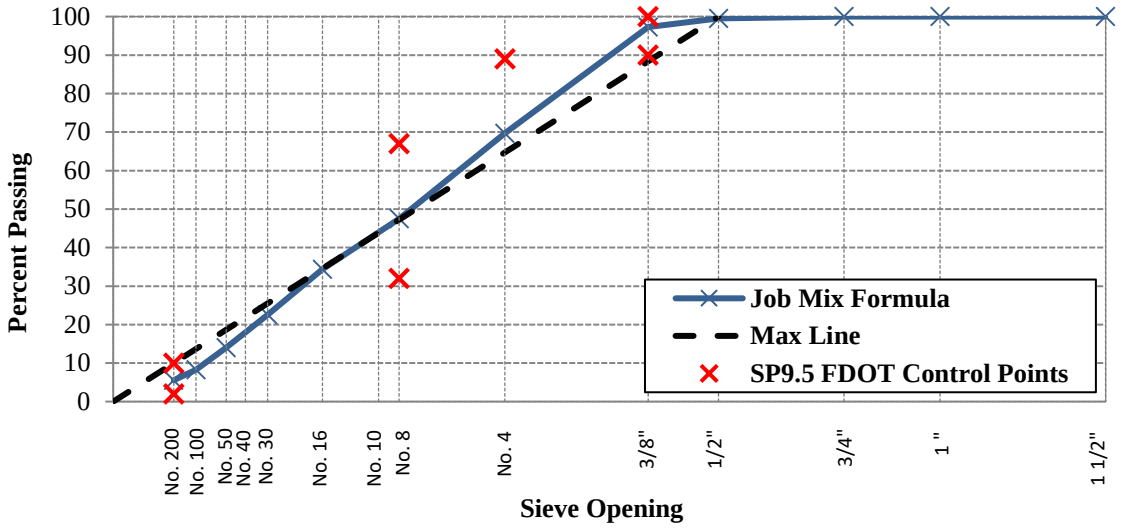


***AGGREGATE GRADATION CURVE***

## *HOT MIX DESIGN DATA*

| $P_b$ (%) | $G_{mb}$ @ $N_{des}$ | $G_{mm}$ | $V_a$ (%) | VMA (%) | VFA (%) | $P_{be}$ (%) | DP = $P_{0.075}/P_{be}$ |
|---|---|---|---|---|---|---|---|
| 4.0 | 2.443 | 2.603 | 6.2 | 15.0 | 59.0 | 3.7 | 1.5 |
| 4.5 | 2.460 | 2.583 | 4.8 | 14.9 | 68.0 | 4.2 | 1.3 |
| 5.0 | 2.470 | 2.562 | 3.6 | 15.0 | 75.9 | 4.7 | 1.2 |
| 5.5 | 2.492 | 2.542 | 2.0 | 14.6 | 86.5 | 5.2 | 1.1 |

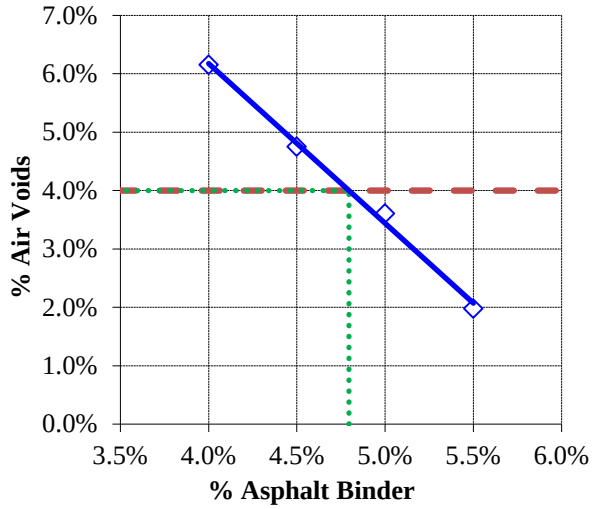


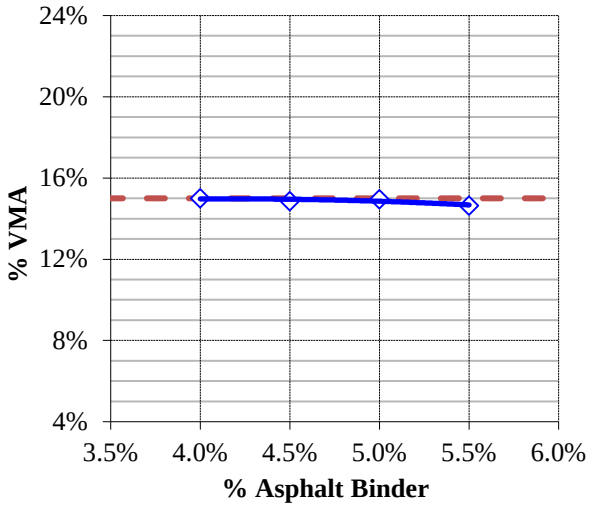


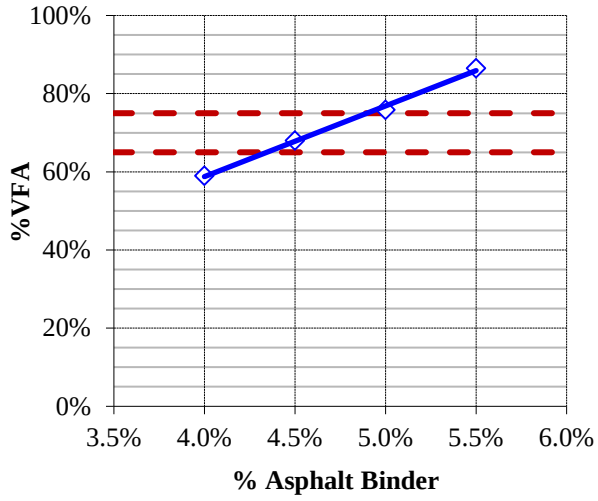


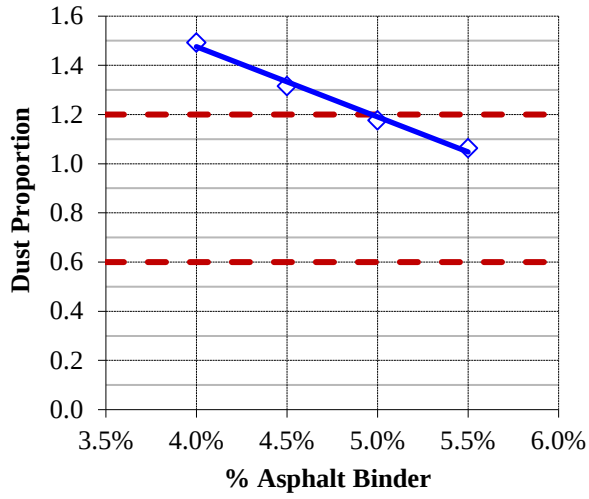


***Optimum Total Binder Content (OBC):*** 4.8 %
***RAP Total Binder Content:*** 5.63%
***RAP Binder Ratio (RBR) at OBC:*** 0.23
***VA at OBC:*** 4.0%
***VMA at OBC:*** 14.9%
***VFA at OBC:*** 72.7%
***DP at OBC:*** 1.2
***Mixing Temperature:*** 325°F (163°C)
***Compaction Temperature:*** 310°F (155°C)
***Additives:*** Antistrip 0.5%

### B.1.12. Mix Design 11: GA95_HP(A)

**Type of Mix:** Fine SP-9.5
**Intended Use of Mix**: Structural
**Design Traffic Level:** C
**Gyrations @ $N_{des}$:** 75

| Product Description | Product Code | Producer Name | Product Name | Plant/Pit Number | Bin Percentage (%) |
|---|---|---|---|---|---|
| S1B Stone | C51 | Junction City Mining | #89 Stone | GA553 | 37.95 |
| Screenings | F22 | | W-10 Screenings | GA553 | 33.95 |
| Screenings | F23 | | M-10 Screenings | GA553 | 15.95 |
| Sand | 334-LS | Anderson Columbia Company, Inc. | Blossom Loop | -- | 11.95 |
| Generated Dust | -- | -- | GA P200 | -- | 0.20 |

***PERCENTAGE BY WEIGHT TOTAL AGGREGATE PASSING SIEVES***

| Blend | | 37.95% | 33.95% | 15.95 | 11.95 | 0.20% | Job Mix Formula | Control Points |
|---|---|---|---|---|---|---|---|---|
| Stockpile ID | | S1B Stone C53 | Screenings F22 | Screenings F23 | Sand 334-LS | GA P200 | | |
| SIEVE SIZE | 3/4" (19.00 mm) | 100.0 | 100.0 | 100.0 | 100.0 | 100.0 | 100.0 | |
| | 1/2" (12.50 mm) | 100.0 | 100.0 | 100.0 | 100.0 | 100.0 | 100.0 | 100 |
| | 3/8" (9.50 mm) | 98.0 | 100.0 | 100.0 | 100.0 | 100.0 | 99.2 | 90 – 100 |
| | No.4 (4.75 mm) | 35.0 | 98.0 | 98.0 | 100.0 | 100.0 | 74.3 | ≤ 90 |
| | No.8 (2.36 mm) | 4.0 | 73.0 | 77.0 | 100.0 | 100.0 | 50.7 | 32 – 67 |
| | No.16 (1.18 mm) | 3.0 | 47.0 | 53.0 | 100.0 | 100.0 | 37.7 | |
| | No.30 (0.600 mm) | 2.0 | 32.0 | 38.0 | 88.0 | 100.0 | 28.4 | |
| | No.50 (0.300 mm) | 1.0 | 21.0 | 29.0 | 43.0 | 100.0 | 17.5 | |
| | No.100 (0.150 mm) | 1.0 | 13.0 | 20.0 | 9.0 | 100.0 | 9.3 | |
| | No.200 (0.075 mm) | 1.0 | 5.5 | 15.0 | 4.0 | 100.0 | 5.3 | 2 – 10 |
| | $G_{sb}$ | | | | | | 2.732 | |

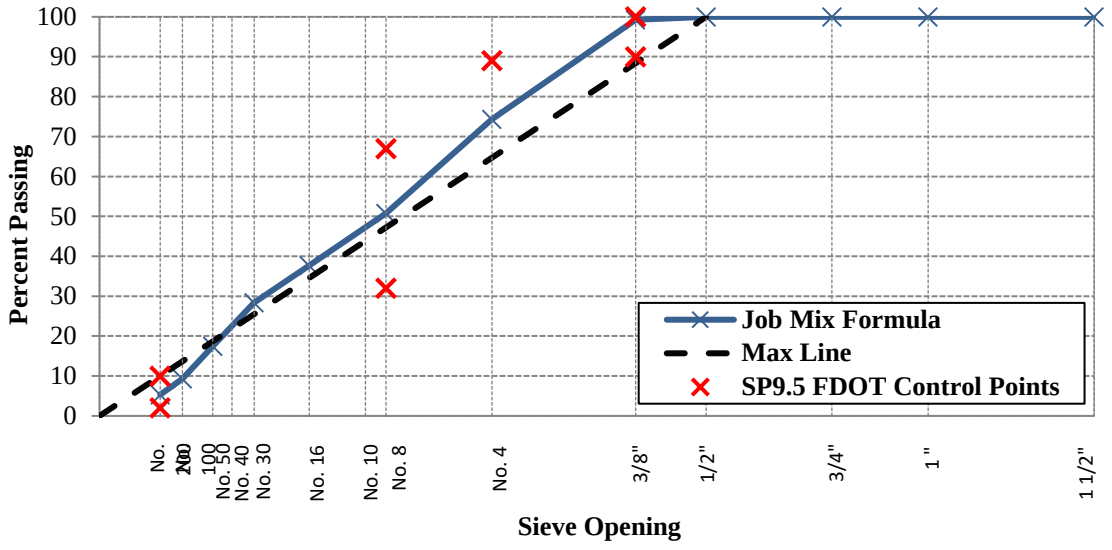


***AGGREGATE GRADATION CURVE***

## *HOT MIX DESIGN DATA*

| $P_b$ (%) | $G_{mb}$ @ $N_{des}$ | $G_{mm}$ | $V_a$ (%) | VMA (%) | VFA (%) | $P_{be}$ (%) | DP = $P_{0.075}/P_{be}$ |
|---|---|---|---|---|---|---|---|
| 4.5 | 2.429 | 2.569 | 5.5 | 15.1 | 63.9 | 4.0 | 1.3 |
| 5.0 | 2.450 | 2.549 | 3.9 | 14.8 | 73.9 | 4.5 | 1.2 |
| 5.5 | 2.466 | 2.529 | 2.5 | 14.7 | 83.2 | 5.0 | 1.1 |
| 6.0 | 2.472 | 2.509 | 1.5 | 14.9 | 90.2 | 5.5 | 1.0 |

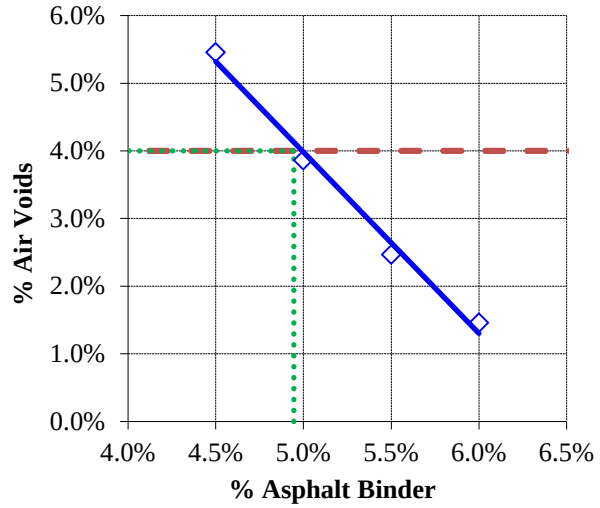


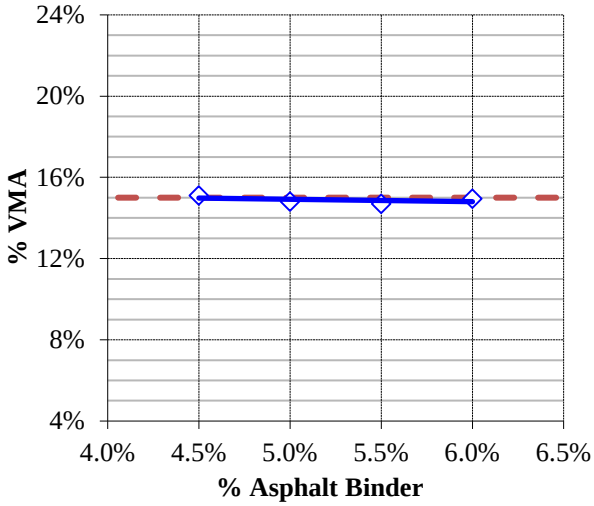


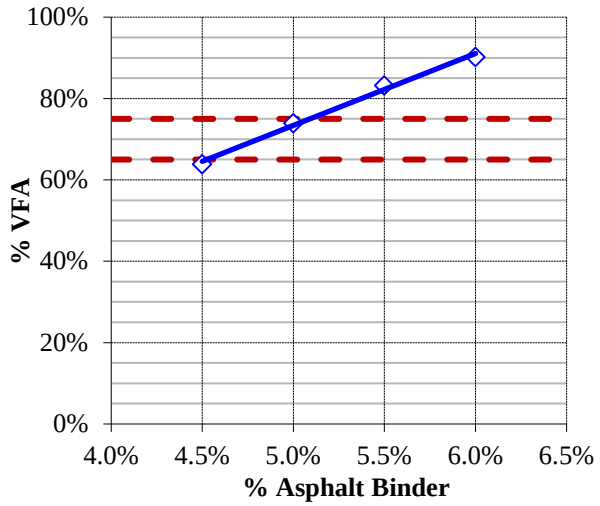


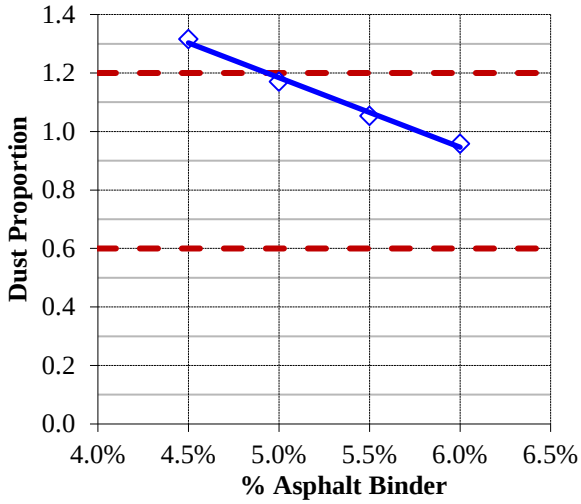


***Optimum Total Binder Content (OBC):*** 4.9 %
***RAP Total Binder Content:*** No RAP was used
***RAP Binder Ratio (RBR) at OBC:*** 0.00
***VA at OBC:*** 4.0%
***VMA at OBC:*** 14.9%
***VFA at OBC:*** 73.1%
***DP at OBC:*** 1.2
***Mixing Temperature:*** 340°F (171°C)
***Compaction Temperature:*** 325°F (163°C)
***Additives:*** Antistrip 0.5%

### B.1.13. Mix Design 12: GA95_HP (B)

**Type of Mix:** Fine SP-9.5
**Intended Use of Mix**: Structural
**Design Traffic Level:** C
**Gyrations @ $N_{des}$:** 75

| Product Description | Product Code | Producer Name | Product Name | Plant/Pit Number | Bin Percentage (%) |
|---|---|---|---|---|---|
| S1B Stone | C51 | Junction City Mining | #89 Stone | GA553 | 37.95 |
| Screenings | F22 | | W-10 Screenings | GA553 | 33.95 |
| Screenings | F23 | | M-10 Screenings | GA553 | 15.95 |
| Sand | 334-LS | Anderson Columbia Company, Inc. | Blossom Loop | -- | 11.95 |
| Generated Dust | -- | -- | GA P200 | -- | 0.20 |

***PERCENTAGE BY WEIGHT TOTAL AGGREGATE PASSING SIEVES***

| Blend | | 37.95% | 33.95% | 15.95 | 11.95 | 0.20% | Job Mix Formula | Control Points |
|---|---|---|---|---|---|---|---|---|
| Stockpile ID | | S1B Stone C53 | Screenings F22 | Screenings F23 | Sand 334-LS | GA P200 | | |
| SIEVE SIZE | 3/4" (19.00 mm) | 100.0 | 100.0 | 100.0 | 100.0 | 100.0 | 100.0 | |
| | 1/2" (12.50 mm) | 100.0 | 100.0 | 100.0 | 100.0 | 100.0 | 100.0 | 100 |
| | 3/8" (9.50 mm) | 98.0 | 100.0 | 100.0 | 100.0 | 100.0 | 99.2 | 90 – 100 |
| | No.4 (4.75 mm) | 35.0 | 98.0 | 98.0 | 100.0 | 100.0 | 74.3 | ≤ 90 |
| | No.8 (2.36 mm) | 4.0 | 73.0 | 77.0 | 100.0 | 100.0 | 50.7 | 32 – 67 |
| | No.16 (1.18 mm) | 3.0 | 47.0 | 53.0 | 100.0 | 100.0 | 37.7 | |
| | No.30 (0.600 mm) | 2.0 | 32.0 | 38.0 | 88.0 | 100.0 | 28.4 | |
| | No.50 (0.300 mm) | 1.0 | 21.0 | 29.0 | 43.0 | 100.0 | 17.5 | |
| | No.100 (0.150 mm) | 1.0 | 13.0 | 20.0 | 9.0 | 100.0 | 9.3 | |
| | No.200 (0.075 mm) | 1.0 | 5.5 | 15.0 | 4.0 | 100.0 | 5.3 | 2 – 10 |
| | $G_{sb}$ | | | | | | 2.732 | |

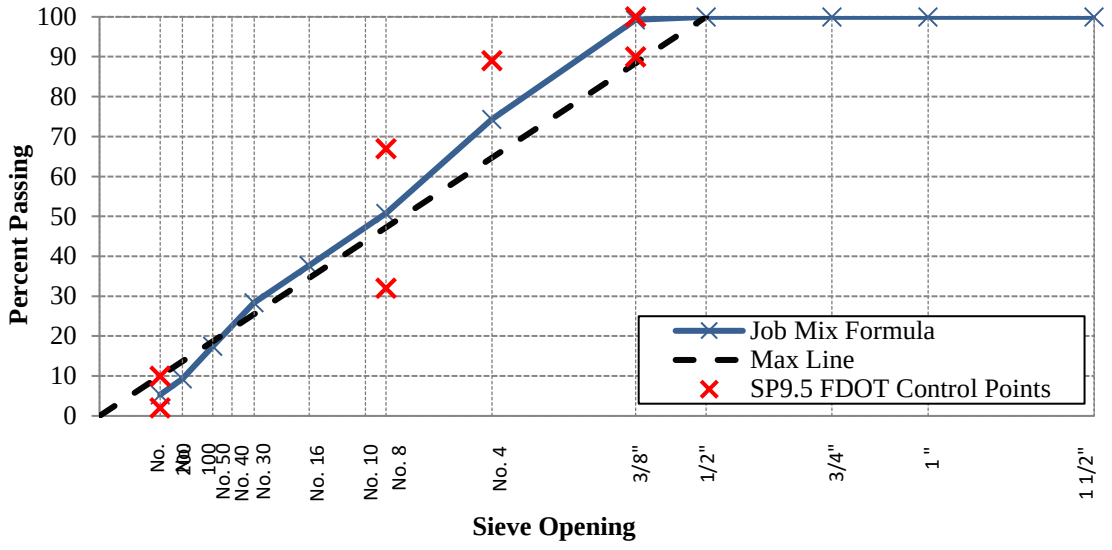


***AGGREGATE GRADATION CURVE***

## *HOT MIX DESIGN DATA*

| $P_b$ (%) | $G_{mb}$ @ $N_{des}$ | $G_{mm}$ | $V_a$ (%) | VMA (%) | VFA (%) | $P_{be}$ (%) | DP = $P_{0.075}/P_{be}$ |
|---|---|---|---|---|---|---|---|
| 4.5 | 2.436 | 2.563 | 5.0 | 14.9 | 66.7 | 4.1 | 1.3 |
| 5.0 | 2.442 | 2.542 | 4.0 | 15.1 | 73.8 | 4.6 | 1.1 |
| 5.5 | 2.466 | 2.523 | 2.2 | 14.7 | 84.7 | 5.1 | 1.0 |
| 6.0 | 2.476 | 2.503 | 1.1 | 14.8 | 92.7 | 5.6 | 0.9 |

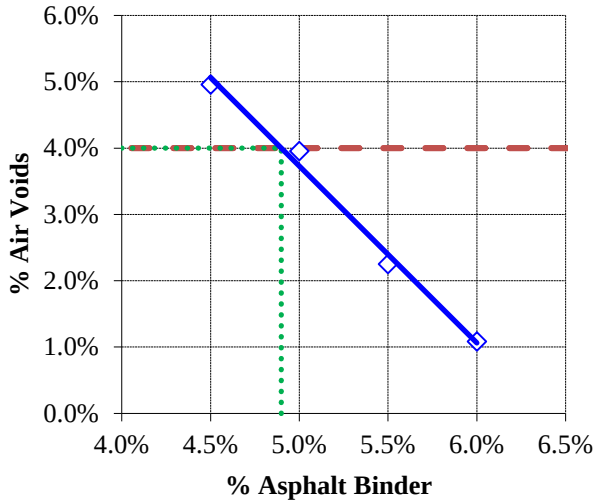


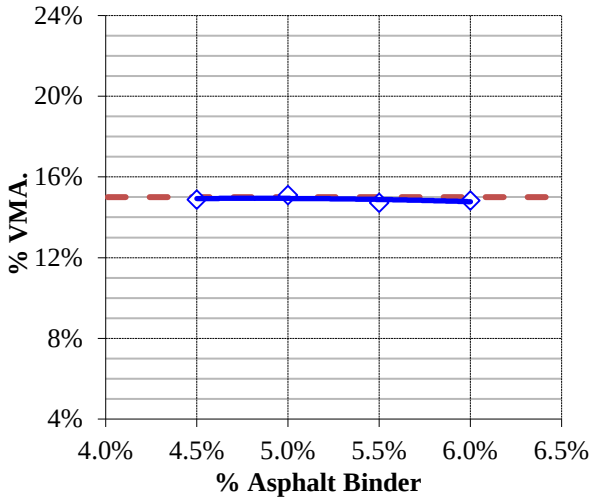


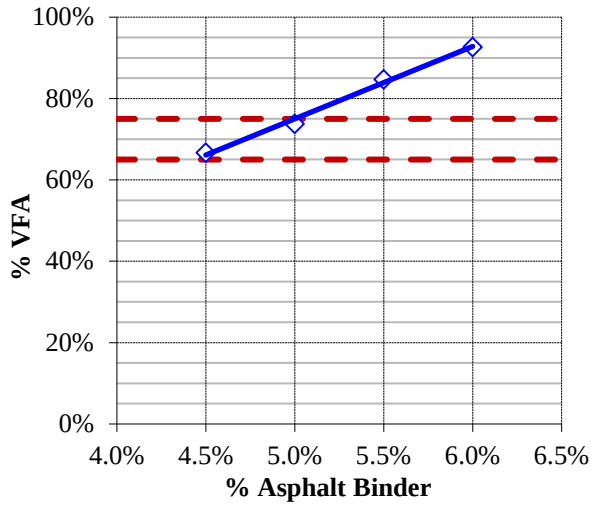


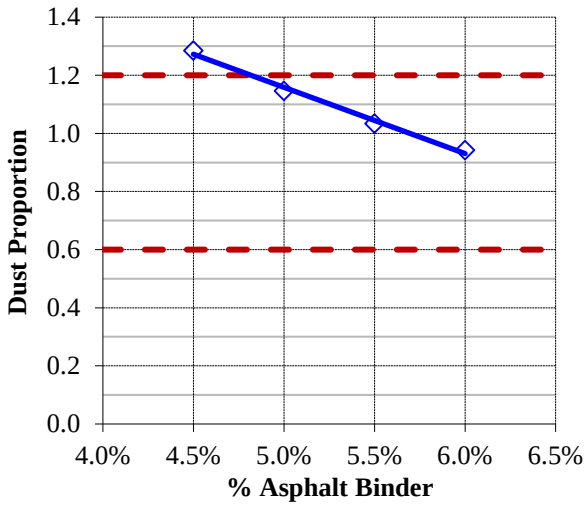


***Optimum Total Binder Content (OBC):*** 4.9 %
***RAP Total Binder Content:*** No RAP was used
***RAP Binder Ratio (RBR) at OBC:*** 0.00
***VA at OBC:*** 4.0%
***VMA at OBC:*** 14.9%
***VFA at OBC:*** 73.1%
***DP at OBC:*** 1.2
***Mixing Temperature:*** 340°F (171°C)
***Compaction Temperature:*** 325°F (163°C)
***Additives:*** Antistrip 0.5%

### B.1.14. Mix Design 10: GA125_PMA(A)

**Type of Mix:** Fine SP-12.5
**Intended Use of Mix**: Structural
**Design Traffic Level:** D/E
**Gyrations @ $N_{des}$:** 100

| Product Description | Product Code | Producer Name | Product Name | Plant/Pit Number | Bin Percentage (%) |
|---|---|---|---|---|---|
| Milled Material | 334-CR | Anderson Columbia Company Inc. | 1_15 | A0716 | 20.00 |
| S1A Stone | C47 | Junction City Mining | #78 Stone | GA553 | 22.95 |
| S1B Stone | C53 | | #89 Stone | GA553 | 14.95 |
| Screenings | F22 | | W-10 Screenings | GA553 | 29.95 |
| Sand | F01 | Vulcan Materials Company | Silica Sand | 11057 | 11.95 |
| Generated Dust | -- | -- | GA P200 | -- | 0.20 |

***PERCENTAGE BY WEIGHT TOTAL AGGREGATE PASSING SIEVES***

| Blend | | 20.00% | 22.95% | 14.95% | 29.95% | 11.95% | 0.20% | Job Mix Formula | Control Points |
|---|---|---|---|---|---|---|---|---|---|
| Stockpile ID | | Crushed RAP | S1A Stone C47 | S1B Stone C53 | Screenings F22 | Sand F01 | GA P200 | | |
| SIEVE SIZE | 1" (25.00 mm) | 100.0 | 100.0 | 100.0 | 100.0 | 100.0 | 100.0 | 100.0 | |
| | 3/4" (19.00 mm) | 100.0 | 100.0 | 100.0 | 100.0 | 100.0 | 100.0 | 100.0 | 100 |
| | 1/2" (12.50 mm) | 91.8 | 97.0 | 100.0 | 100.0 | 100.0 | 100.0 | 97.7 | 90 – 100 |
| | 3/8" (9.50 mm) | 85.5 | 60.0 | 100.0 | 100.0 | 100.0 | 100.0 | 87.6 | ≤ 90 |
| | No.4 (4.75 mm) | 61.2 | 15.0 | 98.0 | 98.0 | 100.0 | 100.0 | 62.4 | |
| | No.8 (2.36 mm) | 44.7 | 4.0 | 35.0 | 73.0 | 100.0 | 100.0 | 44.5 | 28 – 58 |
| | No.16 (1.18 mm) | 36.6 | 2.0 | 4.0 | 47.0 | 99.0 | 100.0 | 34.3 | |
| | No.30 (0.600 mm) | 29.1 | 1.0 | 3.0 | 32.0 | 87.0 | 100.0 | 26.5 | |
| | No.50 (0.300 mm) | 18.3 | 1.0 | 2.0 | 21.0 | 53.0 | 100.0 | 16.9 | |
| | No.100 (0.150 mm) | 8.1 | 1.0 | 1.0 | 13.0 | 17.0 | 100.0 | 8.1 | |
| | No.200 (0.075 mm) | 4.1 | 1.0 | 1.0 | 5.5 | 0.3 | 100.0 | 3.2 | 2 – 10 |
| | $G_{sb}$ | | | | | | | 2.718 | |

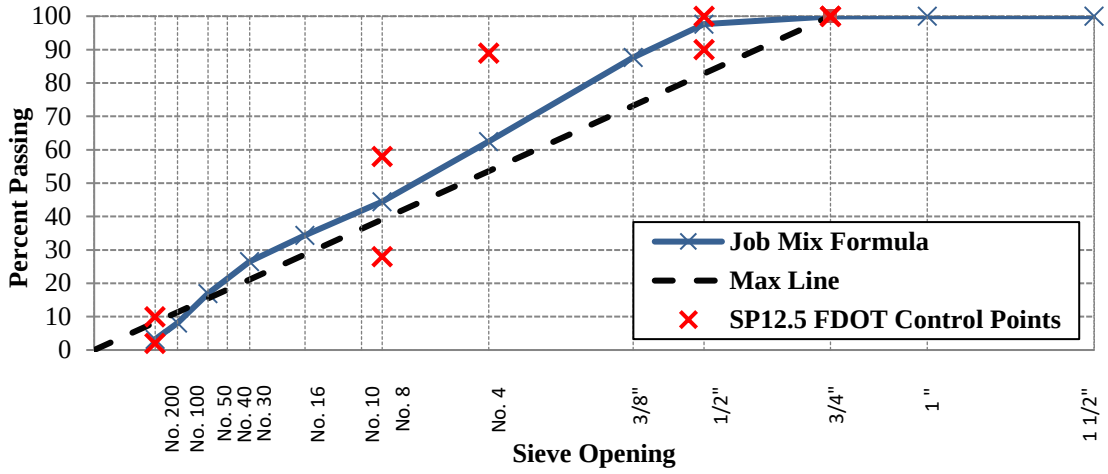


***AGGREGATE GRADATION CURVE***

## *HOT MIX DESIGN DATA*

| $P_b$ (%) | $G_{mb}$ @ $N_{des}$ | $G_{mm}$ | $V_a$ (%) | VMA (%) | VFA (%) | $P_{be}$ (%) | DP = $P_{0.075}/P_{be}$ |
|---|---|---|---|---|---|---|---|
| 4.0 | 2.425 | 2.563 | 5.4 | 14.4 | 62.5 | 3.8 | 0.9 |
| 4.5 | 2.463 | 2.543 | 3.1 | 13.5 | 76.8 | 4.3 | 0.8 |
| 5.0 | 2.475 | 2.523 | 1.9 | 13.5 | 86.0 | 4.8 | 0.7 |
| 5.5 | 2.485 | 2.503 | 0.7 | 13.6 | 94.5 | 5.3 | 0.6 |

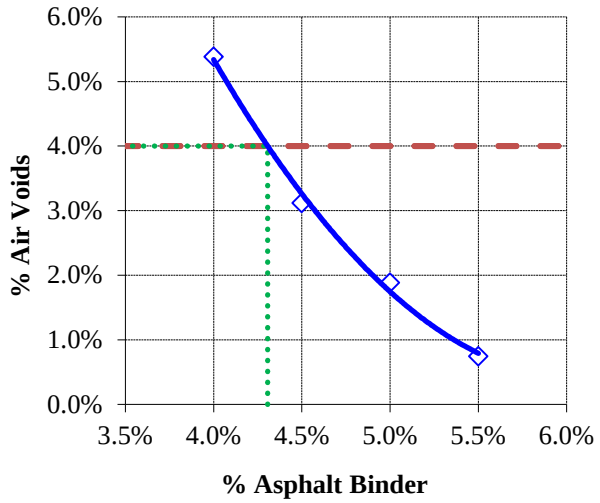


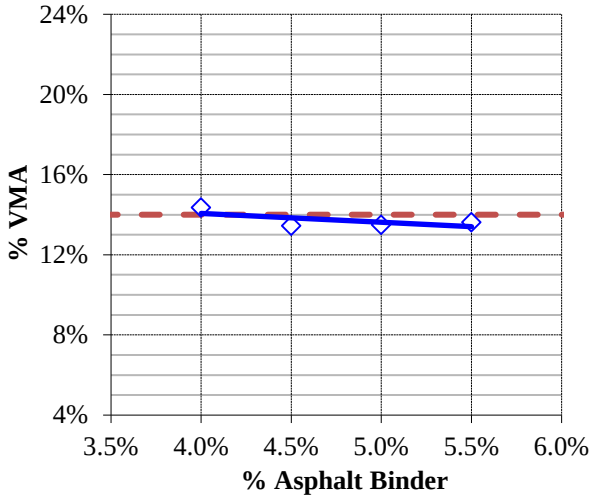


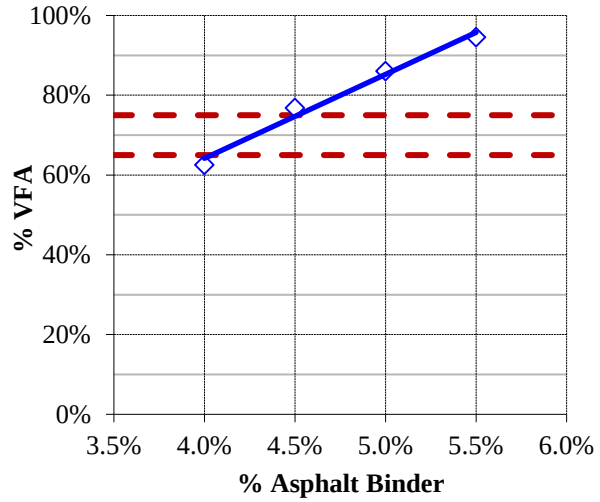


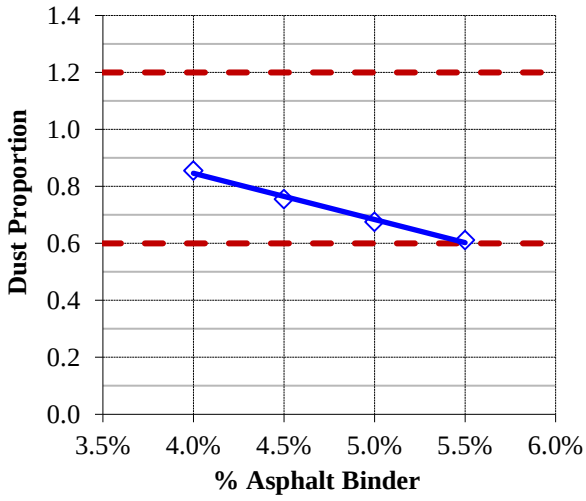


***Optimum Total Binder Content (OBC):*** 4.3 %
***RAP Total Binder Content:*** 6.68%
***RAP Binder Ratio (RBR) at OBC:*** 0.31
***VA at OBC:*** 4.0%
***VMA at OBC:*** 13.9%
***VFA at OBC:*** 71.3%
***DP at OBC:*** 0.8
***Mixing Temperature:*** 325°F (163°C)
***Compaction Temperature:*** 310°F (155°C)
***Additives:*** Antistrip 0.5%

### B.1.15. Mix Design 14: GA125_PMA(B)

**Type of Mix:** Fine SP-12.5
**Intended Use of Mix**: Structural
**Design Traffic Level:** D/E
**Gyrations @ $N_{des}$:** 100

| Product Description | Product Code | Producer Name | Product Name | Plant/Pit Number | Bin Percentage (%) |
|---|---|---|---|---|---|
| Milled Material | 334-CR | Anderson Columbia Company Inc. | 1_15 | A0716 | 20.00 |
| S1A Stone | C47 | Junction City Mining | #78 Stone | GA553 | 22.95 |
| S1B Stone | C53 | | #89 Stone | GA553 | 14.95 |
| Screenings | F22 | | W-10 Screenings | GA553 | 29.95 |
| Sand | F01 | Vulcan Materials Company | Silica Sand | 11057 | 11.95 |
| Generated Dust | -- | -- | GA P200 | -- | 0.20 |

***PERCENTAGE BY WEIGHT TOTAL AGGREGATE PASSING SIEVES***

| Blend | | 20.00% | 22.95% | 14.95% | 29.95% | 11.95% | 0.20% | Job Mix Formula | Control Points |
|---|---|---|---|---|---|---|---|---|---|
| Stockpile ID | | Crushed RAP | S1A Stone C47 | S1B Stone C53 | Screenings F22 | Sand F01 | GA P200 | | |
| SIEVE SIZE | 1" (25.00 mm) | 100.0 | 100.0 | 100.0 | 100.0 | 100.0 | 100.0 | 100.0 | |
| | 3/4" (19.00 mm) | 100.0 | 100.0 | 100.0 | 100.0 | 100.0 | 100.0 | 100.0 | 100 |
| | 1/2" (12.50 mm) | 91.8 | 97.0 | 100.0 | 100.0 | 100.0 | 100.0 | 97.7 | 90 – 100 |
| | 3/8" (9.50 mm) | 85.5 | 60.0 | 100.0 | 100.0 | 100.0 | 100.0 | 87.6 | ≤ 90 |
| | No.4 (4.75 mm) | 61.2 | 15.0 | 98.0 | 98.0 | 100.0 | 100.0 | 62.4 | |
| | No.8 (2.36 mm) | 44.7 | 4.0 | 35.0 | 73.0 | 100.0 | 100.0 | 44.5 | 28 – 58 |
| | No.16 (1.18 mm) | 36.6 | 2.0 | 4.0 | 47.0 | 99.0 | 100.0 | 34.3 | |
| | No.30 (0.600 mm) | 29.1 | 1.0 | 3.0 | 32.0 | 87.0 | 100.0 | 26.5 | |
| | No.50 (0.300 mm) | 18.3 | 1.0 | 2.0 | 21.0 | 53.0 | 100.0 | 16.9 | |
| | No.100 (0.150 mm) | 8.1 | 1.0 | 1.0 | 13.0 | 17.0 | 100.0 | 8.1 | |
| | No.200 (0.075 mm) | 4.1 | 1.0 | 1.0 | 5.5 | 0.3 | 100.0 | 3.2 | 2 – 10 |
| | $G_{sb}$ | | | | | | | 2.718 | |

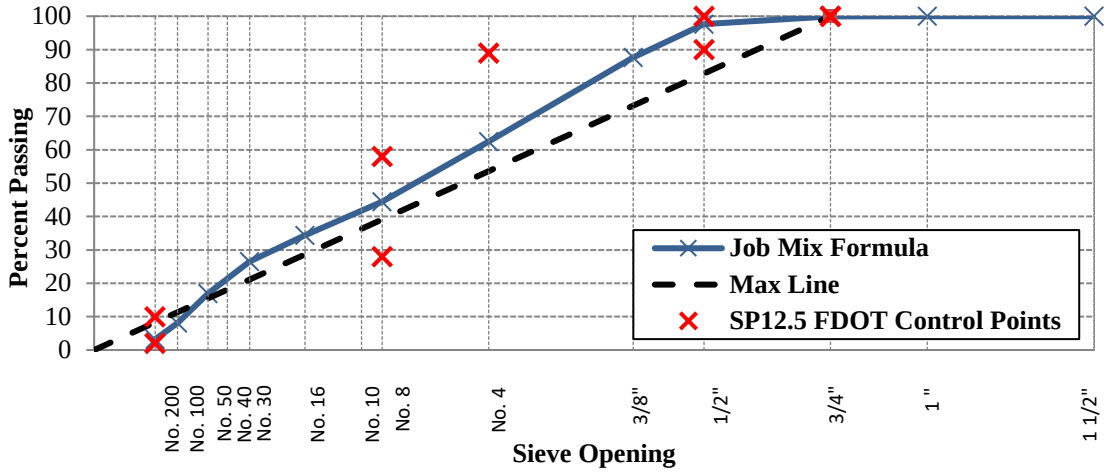


***AGGREGATE GRADATION CURVE***

## *HOT MIX DESIGN DATA*

| $P_b$ (%) | $G_{mb}$ @ $N_{des}$ | $G_{mm}$ | $V_a$ (%) | VMA (%) | VFA (%) | $P_{be}$ (%) | DP = $P_{0.075}/P_{be}$ |
|---|---|---|---|---|---|---|---|
| 3.5 | 2.383 | 2.572 | 7.3 | 15.4 | 52.4 | 3.4 | 0.9 |
| 4.0 | 2.431 | 2.552 | 4.7 | 14.1 | 66.6 | 3.9 | 0.8 |
| 4.5 | 2.466 | 2.532 | 2.6 | 13.4 | 80.5 | 4.4 | 0.7 |
| 5.0 | 2.488 | 2.512 | 1.0 | 13.0 | 92.7 | 4.9 | 0.7 |

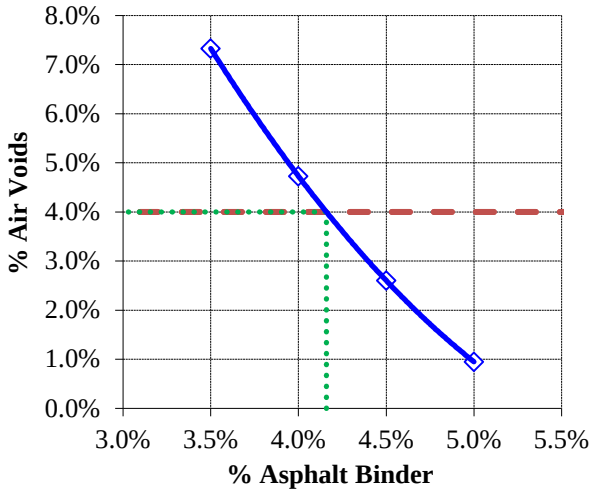


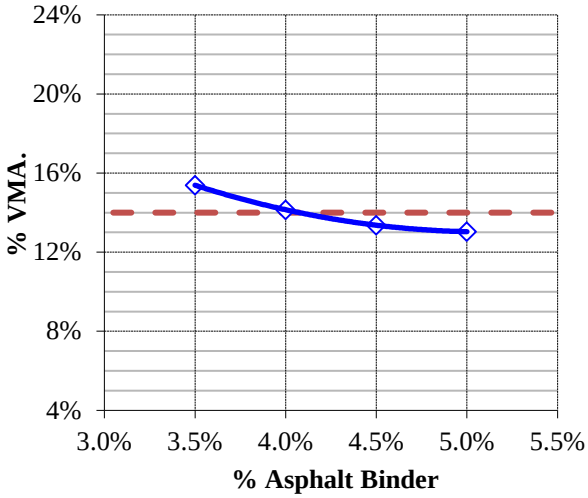


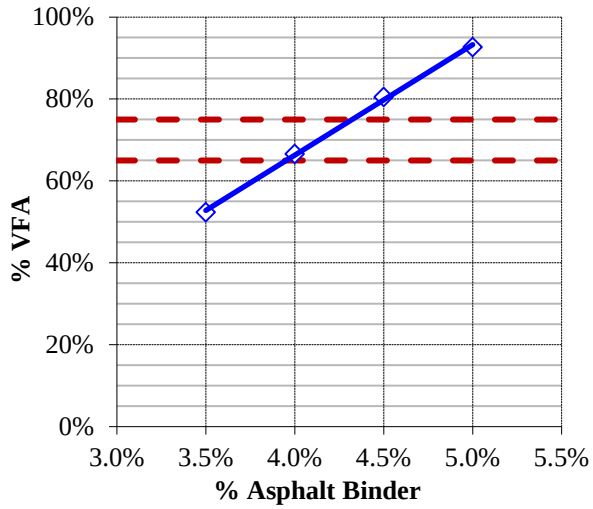


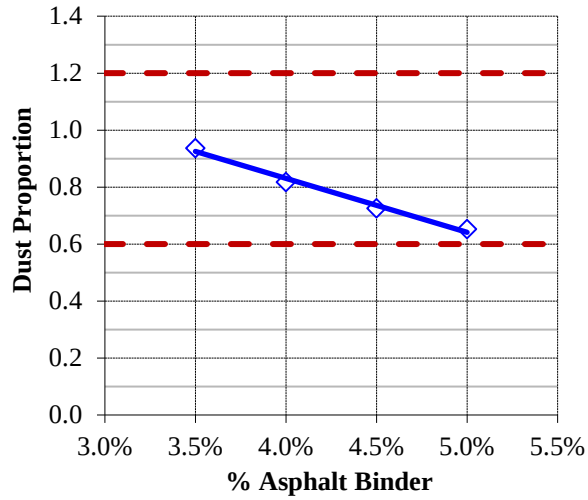


***Optimum Total Binder Content (OBC):*** 4.2 %
***RAP Total Binder Content:*** 6.68%
***RAP Binder Ratio (RBR) at OBC:*** 0.32
***VA at OBC:*** 4.0%
***VMA at OBC:*** 13.9%
***VFA at OBC:*** 71.2%
***DP at OBC:*** 0.8
***Mixing Temperature:*** 325°F (163°C)
***Compaction Temperature:*** 310°F (155°C)
***Additives:*** Antistrip 0.5%

## B.1.16. Mix Design 15: GA125_HP(A)

**Type of Mix:** Fine SP-12.5
**Intended Use of Mix**: Structural
**Design Traffic Level:** D/E
**Gyrations @ $N_{des}$:** 100

| Product Description | Product Code | Producer Name | Product Name | Plant/Pit Number | Bin Percentage (%) |
|---|---|---|---|---|---|
| S1A Stone | C47 | Junction City Mining | #78 Stone | GA553 | 27.96 |
| S1B Stone | C51 | | #89 Stone | GA553 | 12.96 |
| Screenings | F22 | | W-10 Screenings | GA553 | 35.96 |
| Screenings | F23 | | M-10 Screenings | GA553 | 11.96 |
| Sand | 334-LS | Anderson Columbia Company, Inc. | Blossom Loop | -- | 10.96 |
| Generated Dust | -- | -- | GA P200 | -- | 0.20 |

***PERCENTAGE BY WEIGHT TOTAL AGGREGATE PASSING SIEVES***

| Blend | | 27.96% | 12.96% | 35.96% | 11.96% | 10.96% | 0.20% | Job Mix Formula | Control Points |
|---|---|---|---|---|---|---|---|---|---|
| Stockpile ID | | S1A Stone C47 | S1B Stone C53 | Screenings F22 | Screenings F23 | Sand 334-LS | GA P200 | | |
| | 1" (25.00 mm) | 100.0 | 100.0 | 100.0 | 100.0 | 100.0 | 100.0 | 100.0 | |
| SIEVE SIZE | 3/4" (19.00 mm) | 100.0 | 100.0 | 100.0 | 100.0 | 100.0 | 100.0 | 100.0 | 100 |
| | 1/2" (12.50 mm) | 97.0 | 100.0 | 100.0 | 100.0 | 100.0 | 100.0 | 99.2 | 90 – 100 |
| | 3/8" (9.50 mm) | 60.0 | 98.0 | 100.0 | 100.0 | 100.0 | 100.0 | 88.6 | ≤ 90 |
| | No.4 (4.75 mm) | 15.0 | 35.0 | 98.0 | 98.0 | 100.0 | 100.0 | 66.9 | |
| | No.8 (2.36 mm) | 4.0 | 4.0 | 73.0 | 77.0 | 100.0 | 100.0 | 48.3 | 28 – 58 |
| | No.16 (1.18 mm) | 2.0 | 3.0 | 47.0 | 53.0 | 100.0 | 100.0 | 35.3 | |
| | No.30 (0.600 mm) | 1.0 | 2.0 | 32.0 | 38.0 | 88.0 | 100.0 | 26.4 | |
| | No.50 (0.300 mm) | 1.0 | 1.0 | 21.0 | 29.0 | 43.0 | 100.0 | 16.3 | |
| | No.100 (0.150 mm) | 1.0 | 1.0 | 13.0 | 20.0 | 9.0 | 100.0 | 8.7 | |
| | No.200 (0.075 mm) | 1.0 | 1.0 | 5.5 | 15.0 | 4.0 | 100.0 | 4.8 | 2 – 10 |
| | $G_{sb}$ | | | | | | | 2.736 | |

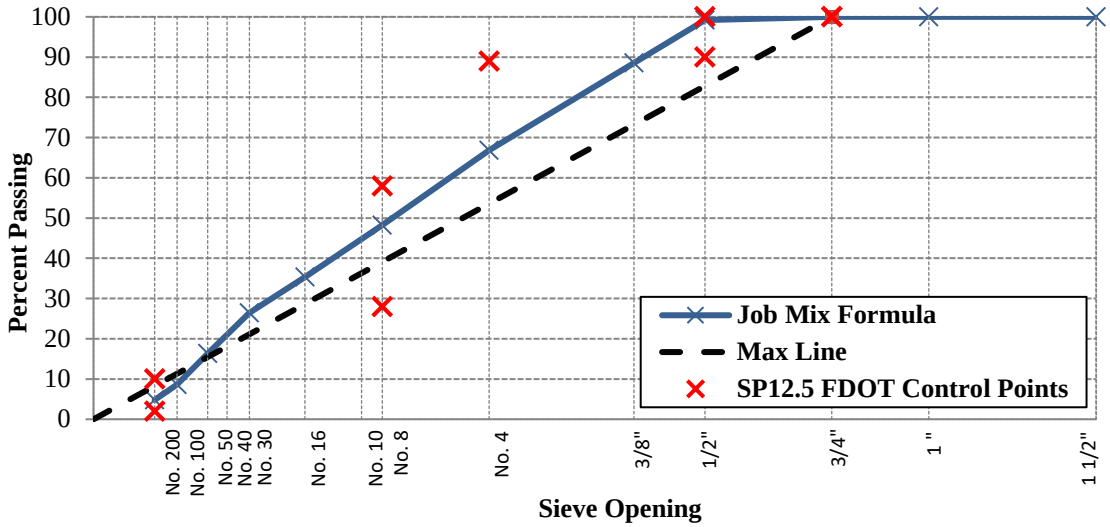


***AGGREGATE GRADATION CURVE***

## *HOT MIX DESIGN DATA*

| $P_b$ (%) | $G_{mb}$ @ $N_{des}$ | $G_{mm}$ | $V_a$ (%) | VMA (%) | VFA (%) | $P_{be}$ (%) | DP = $P_{0.075}/P_{be}$ |
|---|---|---|---|---|---|---|---|
| 4.0 | 2.447 | 2.612 | 6.3 | 14.1 | 55.4 | 3.3 | 1.5 |
| 4.5 | 2.466 | 2.591 | 4.8 | 13.9 | 65.4 | 3.8 | 1.3 |
| 5.0 | 2.482 | 2.570 | 3.4 | 13.8 | 75.2 | 4.3 | 1.1 |
| 5.5 | 2.497 | 2.550 | 2.1 | 13.8 | 84.9 | 4.8 | 1.0 |

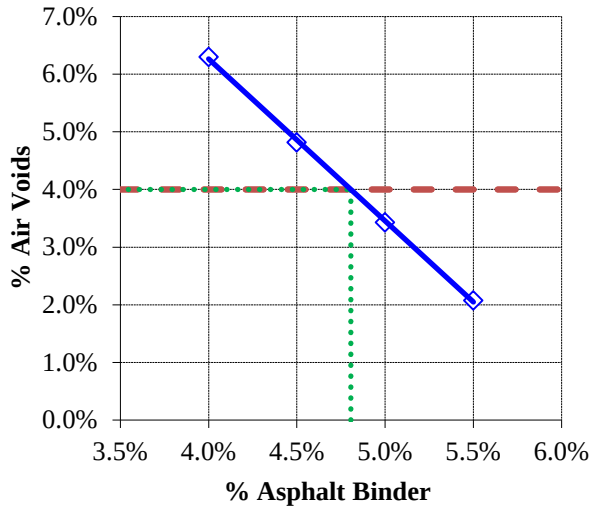


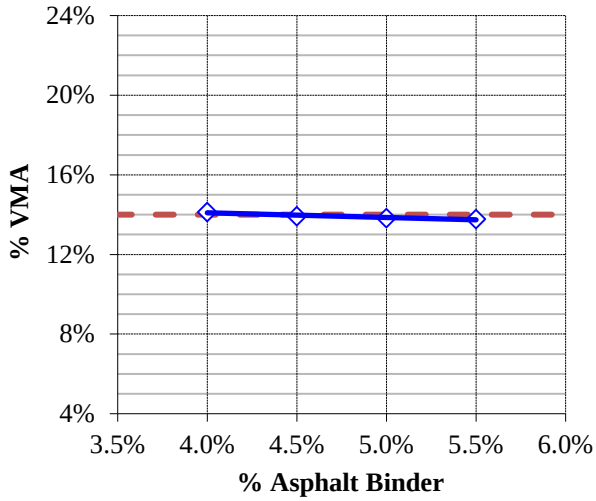


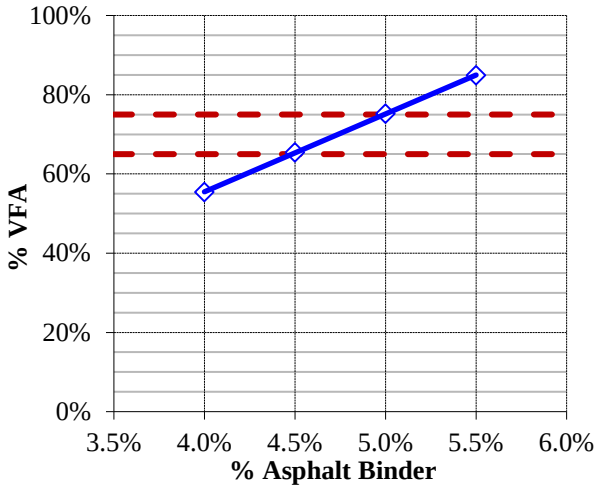


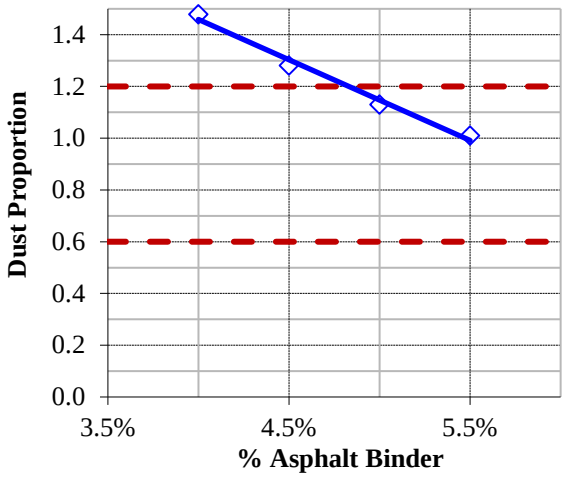


***Optimum Total Binder Content (OBC):*** 4.8 %
***RAP Total Binder Content:*** No Rap was used
***RAP Binder Ratio (RBR) at OBC:*** 0.00
***VA at OBC:*** 4.0%
***VMA at OBC:*** 13.9%
***VFA at OBC:*** 71.4%
***DP at OBC:*** 1.2
***Mixing Temperature:*** 340°F (171°C)
***Compaction Temperature:*** 325°F (163°C)
***Additives:*** Antistrip 0.5%

### B.1.17. Mix Design 16: GA125_HP(B)

**Type of Mix:** Fine SP-12.5
**Intended Use of Mix**: Structural
**Design Traffic Level:** D/E
**Gyrations @ $N_{des}$:** 100

| Product Description | Product Code | Producer Name | Product Name | Plant/Pit Number | Bin Percentage (%) |
|---|---|---|---|---|---|
| S1A Stone | C47 | Junction City Mining | #78 Stone | GA553 | 27.96 |
| S1B Stone | C51 | | #89 Stone | GA553 | 12.96 |
| Screenings | F22 | | W-10 Screenings | GA553 | 35.96 |
| Screenings | F23 | | M-10 Screenings | GA553 | 11.96 |
| Sand | 334-LS | Anderson Columbia Company, Inc. | Blossom Loop | -- | 10.96 |
| Generated Dust | -- | -- | GA P200 | -- | 0.20 |

***PERCENTAGE BY WEIGHT TOTAL AGGREGATE PASSING SIEVES***

| Blend | | 27.96% | 12.96% | 35.96% | 11.96% | 10.96% | 0.20% | Job Mix Formula | Control Points |
|---|---|---|---|---|---|---|---|---|---|
| Stockpile ID | | S1A Stone C47 | S1B Stone C53 | Screenings F22 | Screenings F23 | Sand 334-LS | GA P200 | | |
| | 1" (25.00 mm) | 100.0 | 100.0 | 100.0 | 100.0 | 100.0 | 100.0 | 100.0 | |
| SIEVE SIZE | 3/4" (19.00 mm) | 100.0 | 100.0 | 100.0 | 100.0 | 100.0 | 100.0 | 100.0 | 100 |
| | 1/2" (12.50 mm) | 97.0 | 100.0 | 100.0 | 100.0 | 100.0 | 100.0 | 99.2 | 90 – 100 |
| | 3/8" (9.50 mm) | 60.0 | 98.0 | 100.0 | 100.0 | 100.0 | 100.0 | 88.6 | ≤ 90 |
| | No.4 (4.75 mm) | 15.0 | 35.0 | 98.0 | 98.0 | 100.0 | 100.0 | 66.9 | |
| | No.8 (2.36 mm) | 4.0 | 4.0 | 73.0 | 77.0 | 100.0 | 100.0 | 48.3 | 28 – 58 |
| | No.16 (1.18 mm) | 2.0 | 3.0 | 47.0 | 53.0 | 100.0 | 100.0 | 35.3 | |
| | No.30 (0.600 mm) | 1.0 | 2.0 | 32.0 | 38.0 | 88.0 | 100.0 | 26.4 | |
| | No.50 (0.300 mm) | 1.0 | 1.0 | 21.0 | 29.0 | 43.0 | 100.0 | 16.3 | |
| | No.100 (0.150 mm) | 1.0 | 1.0 | 13.0 | 20.0 | 9.0 | 100.0 | 8.7 | |
| | No.200 (0.075 mm) | 1.0 | 1.0 | 6.0 | 15.0 | 4.0 | 100.0 | 4.8 | 2 – 10 |
| | $G_{sb}$ | | | | | | | 2.736 | |

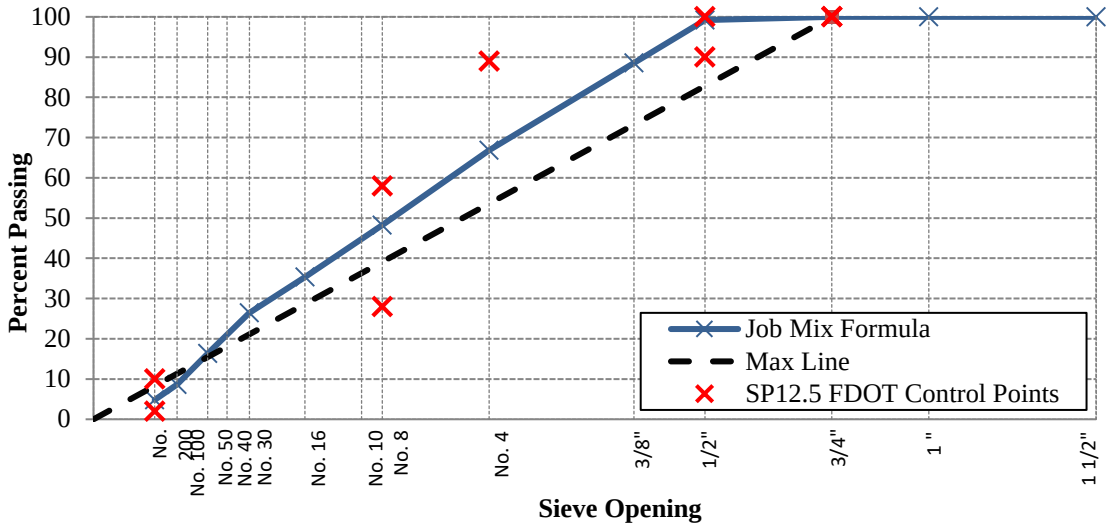


***AGGREGATE GRADATION CURVE***

## *HOT MIX DESIGN DATA*

| $P_b$ (%) | $G_{mb}$ @ $N_{des}$ | $G_{mm}$ | $V_a$ (%) | VMA (%) | VFA (%) | $P_{be}$ (%) | DP = $P_{0.075}/P_{be}$ |
|---|---|---|---|---|---|---|---|
| 4.5 | 2.436 | 2.591 | 6.0 | 15.0 | 60.0 | 3.8 | 1.3 |
| 5.0 | 2.461 | 2.570 | 4.2 | 14.5 | 70.9 | 4.3 | 1.1 |
| 5.5 | 2.481 | 2.550 | 2.7 | 14.3 | 81.2 | 4.8 | 1.0 |
| 6.0 | 2.504 | 2.529 | 1.0 | 14.0 | 92.7 | 5.3 | 0.9 |

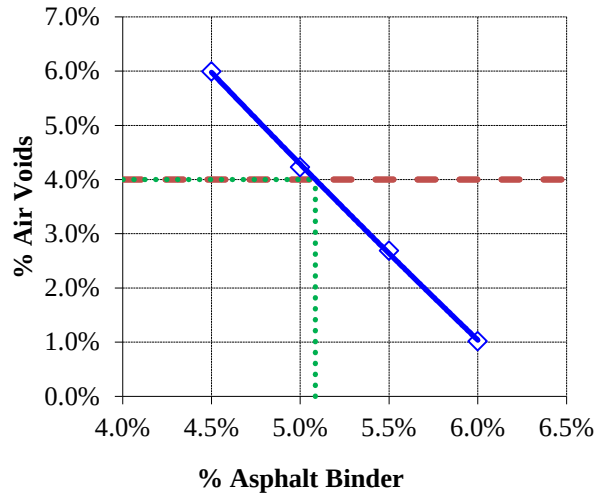


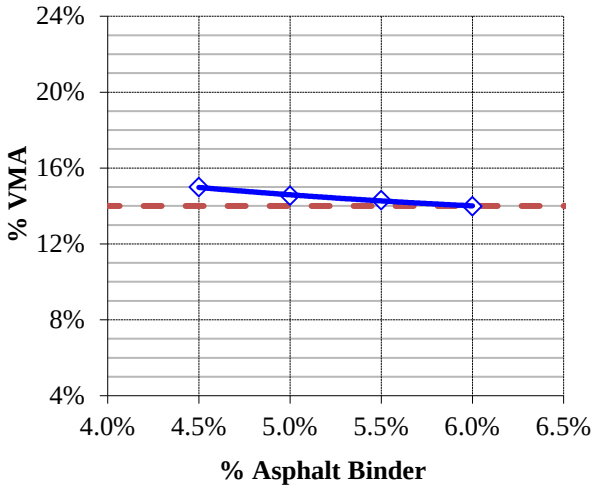


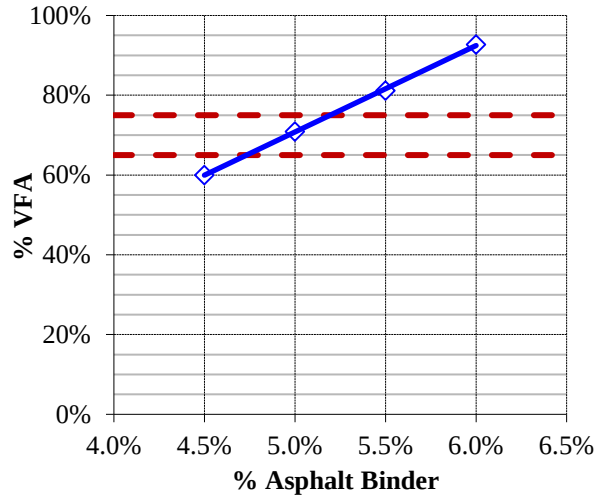


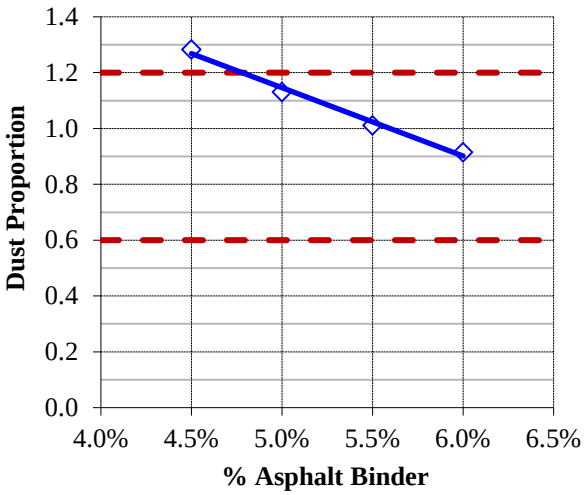


***Optimum Total Binder Content (OBC):*** 5.1 %
***RAP Total Binder Content:*** No Rap was used
***RAP Binder Ratio (RBR) at OBC:*** 0.00
***VA at OBC:*** 4.0%
***VMA at OBC:*** 14.5%
***VFA at OBC:*** 72.5%
***DP at OBC:*** 1.1
***Mixing Temperature:*** 340°F (171°C)
***Compaction Temperature:*** 325°F (163°C)
***Additives:*** Antistrip 0.5%

### B.1.18. Summary of Developed Mix Designs

**Table B.1. Summary of Mix Designs for FL Aggregate 9.5 mm NMAS with PMA and HP Asphalt Binders.**

| Mix Design ID | FL95_PMA(A) | FL95_PMA(B) | FL95_HP(A) | FL95_HP(B) |
|---|---|---|---|---|
| Traffic Level ($N_{design}$) | C (75) | C (75) | C (75) | C (75) |
| OBC by twm, % | 6.2 | 6.2 | 5.9* | 5.9* |
| RAP Binder Ratio, RBR | 0.00 | 0.00 | 0.00 | 0.00 |
| $G_{mm}$ at OBC | 2.368 | 2.362 | 2.356 | 2.370 |
| Va, % | 4.0 | 4.0 | 3.7 | 4.3 |
| VMA, % (min 15%) | 15.0 | 15.3 | 14.9 | 15.2 |
| VFA, % (65 – 75%) | 73.1 | 73.9 | 75.6 | 71.2 |
| $P_{be}$ at OBC, % | 4.99 | 5.13 | 5.05 | 4.79 |
| DP ( 0.6 – 1.2) | 0.8 | 0.8 | 0.8 | 0.8 |

* The recommended OBC is slightly different from the true OBC in order to achieve a consistent mix design for the two binder sources.

**Table B.2. Summary of Mix Designs for FL Aggregate 12.5 mm NMAS with PMA and HP Asphalt Binders.**

| Mix Design ID | FL125_PMA(A) | FL125_PMA(B) | FL125_HP(A) | FL125_HP(B) |
|---|---|---|---|---|
| Traffic Level ($N_{design}$) | D/E (100) | D/E (100) | D/E (100) | D/E (100) |
| OBC by twm[1], % | 5.5* | 5.5* | 5.4 | 5.4 |
| RAP Binder Ratio, RBR | 0.00 | 0.00 | 0.00 | 0.00 |
| $G_{mm}$[2] at OBC | 2.372 | 2.378 | 2.360 | 2.369 |
| Va, % | 3.8 | 4.4 | 4.0 | 4.0 |
| VMA, % (min 15%) | 13.9 | 14.0 | 14.2 | 13.9 |
| VFA, % (65 – 75%) | 72.4 | 69.2 | 71.9 | 71.2 |
| $P_{be}$[3] at OBC, % | 4.49 | 4.38 | 4.60 | 4.44 |
| DP ( 0.6 – 1.2) | 0.8 | 0.8 | 0.8 | 0.8 |

* The recommended OBC is slightly different from the true OBC in order to achieve a consistent mix design for the two binder sources.

**Table B.3. Summary of Mix Designs for GA Aggregate 9.5 mm NMAS with PMA and HP Asphalt Binders.**

| Mix Design ID | GA95_PMA(A) | GA95_PMA(B) | GA95_HP(A) | GA95_HP(B) |
|---|---|---|---|---|
| Traffic Level ($N_{design}$) | C (75) | C (75) | C (75) | C (75) |
| OBC by twm, % | 4.8* | 4.8 | 4.9 | 4.9 |
| RAP Binder Ratio, RBR | 0.23 | 0.23 | 0.00 | 0.00 |
| $G_{mm}$ at OBC | 2.558 | 2.571 | 2.551 | 2.547 |
| Va, % | 3.8 | 4.0 | 4.0 | 4.0 |
| VMA, % (min 15%) | 15.0 | 14.9 | 14.9 | 14.9 |
| VFA, % (65 – 75%) | 75.6 | 72.7 | 73.1 | 73.1 |
| $P_{be}$ at OBC, % | 4.67 | 4.53 | 4.49 | 4.54 |
| DP ( 0.6 – 1.2) | 1.2 | 1.2 | 1.2 | 1.2 |

* The recommended OBC is slightly different from the true OBC in order to achieve a consistent mix design for the two binder sources.

**Table B.4. Summary of Mix Designs for GA Aggregate 12.5 mm NMAS with PMA and HP Asphalt Binders.**

| Mix Design ID | GA125_PMA(A) | GA125_PMA(B) | GA125_HP(A) | GA125_HP(B) |
|---|---|---|---|---|
| **Traffic Level ($N_{design}$)** | D/E (100) | D/E (100) | D/E (100) | D/E (100) |
| **OBC by twm, %** | 4.2* | 4.2 | 4.9* | 4.9* |
| **RAP Binder Ratio, RBR** | 0.32 | 0.32 | 0.00 | 0.00 |
| **$G_{mm}$ at OBC** | 2.555 | 2.545 | 2.574 | 2.574 |
| **Va, %** | 4.4 | 4.0 | 3.8 | 4.6 |
| **VMA, % (min 14%)** | 14.0 | 13.8 | 13.9 | 14.7 |
| **VFA, % (65 – 75%)** | 68.4 | 71.2 | 73.3 | 68.5 |
| **$P_{be}$ at OBC, %** | 3.97 | 4.10 | 4.16 | 4.16 |
| **DP ( 0.6 – 1.2)** | 0.8 | 0.8 | 1.2 | 1.2 |

* The recommended OBC is slightly different from the true OBC in order to achieve a consistent mix design for the two binder sources.

## B.2. RESISTANCE TO MOISTURE DAMAGE

**Table B.5. Moisture Damage Results Summary Table for FL95_PMA(A).**

| Description | Dry Set | | | | Conditioned Set | | | |
|---|---|---|---|---|---|---|---|---|
| Sample ID | D1 | D2 | D3 | D4 | W1 | W2 | W3 | W4 |
| Diameter (in.) | 4.00 | 4.00 | 4.00 | -- | 4.00 | 4.00 | 4.00 | -- |
| Thickness (in.) | 2.49 | 2.49 | 2.49 | -- | 2.49 | 2.49 | 2.49 | -- |
| Air Void (%) | 7.1 | 6.5 | 6.6 | -- | 7.5 | 7.0 | 7.0 | -- |
| Average Air Void (%) | 6.8 | | | | 7.2 | | | |
| Saturation (%) | 0.0 | | | | 72.1 | 70.9 | 71.7 | -- |
| Peak Applied Load (lbs) | 2,714.8 | 2,943.1 | 2,894.3 | -- | 2,800.9 | 3,059.1 | 2,816.6 | -- |
| Tensile Strength TS (psi) | 173.7 | 188.5 | 184.9 | -- | 179.2 | 195.8 | 180.0 | |
| Average TS (psi) | 182.4 | | | | 185.0 | | | |
| Standard Deviation (psi) | 7.7 | | | | 9.3 | | | |
| 95% Confidence Interval (psi) | 8.7 | | | | 9.1 | | | |
| TSR Ratio (%) | 101.4 | | | | | | | |

**Table B.6. Moisture Damage Results Summary Table for FL95_HP(A).**

| Description | Dry Set | | | | Conditioned Set | | | |
|---|---|---|---|---|---|---|---|---|
| Sample ID | D1 | D2 | D3 | D4 | W1 | W2 | W3 | W4 |
| Diameter (in.) | 4.00 | 4.00 | 4.00 | -- | 4.00 | 4.00 | 4.00 | -- |
| Thickness (in.) | 2.49 | 2.48 | 2.48 | -- | 2.49 | 2.48 | 2.48 | -- |
| Air Void (%) | 6.8 | 6.3 | 6.6 | -- | 6.7 | 6.8 | 6.5 | -- |
| Average Air Void (%) | 6.6 | | | | 6.6 | | | |
| Saturation (%) | 0.0 | | | | 72.3 | 78.9 | 79.4 | -- |
| Peak Applied Load (lbs) | 2,670.1 | 2,812.5 | 2,603.1 | -- | 2,487.4 | 2,549.1 | 2,556.7 | -- |
| Tensile Strength TS (psi) | 170.7 | 180.3 | 166.8 | -- | 159.2 | 163.5 | 164.0 | |
| Average TS (psi) | 172.6 | | | | 162.2 | | | |
| Standard Deviation (psi) | 6.9 | | | | 2.6 | | | |
| 95% Confidence Interval (psi) | 7.8 | | | | 2.9 | | | |
| TSR Ratio (%) | 94.0 | | | | | | | |

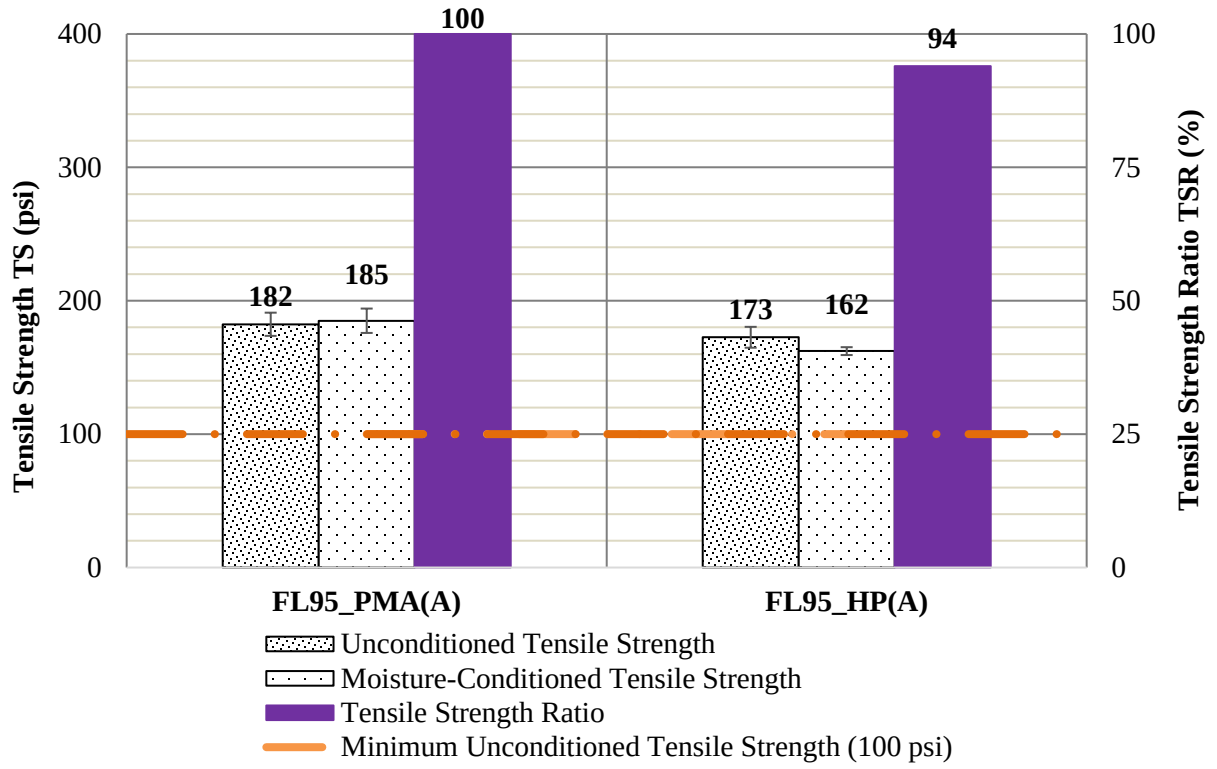


**Figure B.1. Tensile strength statistical representation for FL95_PMA(A) and FL95_HP(A) mixes (Error bars represent the mean values plus or minus 95% confidence interval).**

**Table B.7. Moisture Damage Results Summary Table for FL95_PMA(B).**

| **Description** | **Dry Set** | | | | **Conditioned Set** | | | |
|---|---|---|---|---|---|---|---|---|
| Sample ID | D1 | D2 | D3 | D4 | W1 | W2 | W3 | W4 |
| Diameter (in.) | 4.00 | 4.00 | 4.00 | -- | 4.00 | 4.00 | 4.00 | -- |
| Thickness (in.) | 2.49 | 2.48 | 2.49 | -- | 2.48 | 2.48 | 2.48 | -- |
| Air Void (%) | 7.2 | 6.6 | 7.0 | -- | 7.5 | 7.0 | 7.0 | -- |
| Average Air Void (%) | 6.9 | | | | 7.2 | | | |
| Saturation (%) | 0.0 | | | | 76.7 | 71.9 | 78.7 | -- |
| Peak Applied Load (lbs) | 2,665.7 | 2,607.8 | 2,807.4 | -- | 2,338.1 | 2,296.1 | 2,330.6 | -- |
| Tensile Strength TS (psi) | 170.6 | 167.1 | 179.3 | -- | 150.3 | 147.3 | 149.5 | |
| Average TS (psi) | 172.3 | | | | 149.0 | | | |
| Standard Deviation (psi) | 6.2 | | | | 1.5 | | | |
| 95% Confidence Interval (psi) | 6.1 | | | | 1.7 | | | |
| TSR Ratio (%) | 86.5 | | | | | | | |

**Table B.8. Moisture Damage Results Summary Table for FL95_HP(B).**

| Description | Dry Set | | | | Conditioned Set | | | |
|---|---|---|---|---|---|---|---|---|
| Sample ID | D1 | D2 | D3 | D4 | W1 | W2 | W3 | W4 |
| Diameter (in.) | 4.00 | 4.00 | 4.00 | -- | 4.00 | 4.00 | 4.00 | -- |
| Thickness (in.) | 2.40 | 2.49 | 2.49 | -- | 2.48 | 2.48 | 2.48 | -- |
| Air Void (%) | 6.9 | 6.3 | 6.7 | -- | 7.9 | 7.3 | 7.6 | -- |
| Average Air Void (%) | 6.6 | | | | 7.6 | | | |
| Saturation (%) | 0.0 | | | | 77.5 | 70.8 | 72.6 | -- |
| Peak Applied Load (lbs) | 2,338.3 | 2,516.5 | 2,384.4 | -- | 2,193.8 | 2,323.5 | 2,106.6 | -- |
| Tensile Strength TS (psi) | 150.1 | 161.1 | 152.7 | -- | 141.0 | 149.2 | 135.1 | |
| Average TS (psi) | 154.6 | | | | 141.8 | | | |
| Standard Deviation (psi) | 5.8 | | | | 7.1 | | | |
| 95% Confidence Interval (psi) | 5.7 | | | | 8.0 | | | |
| TSR Ratio (%) | 91.7 | | | | | | | |

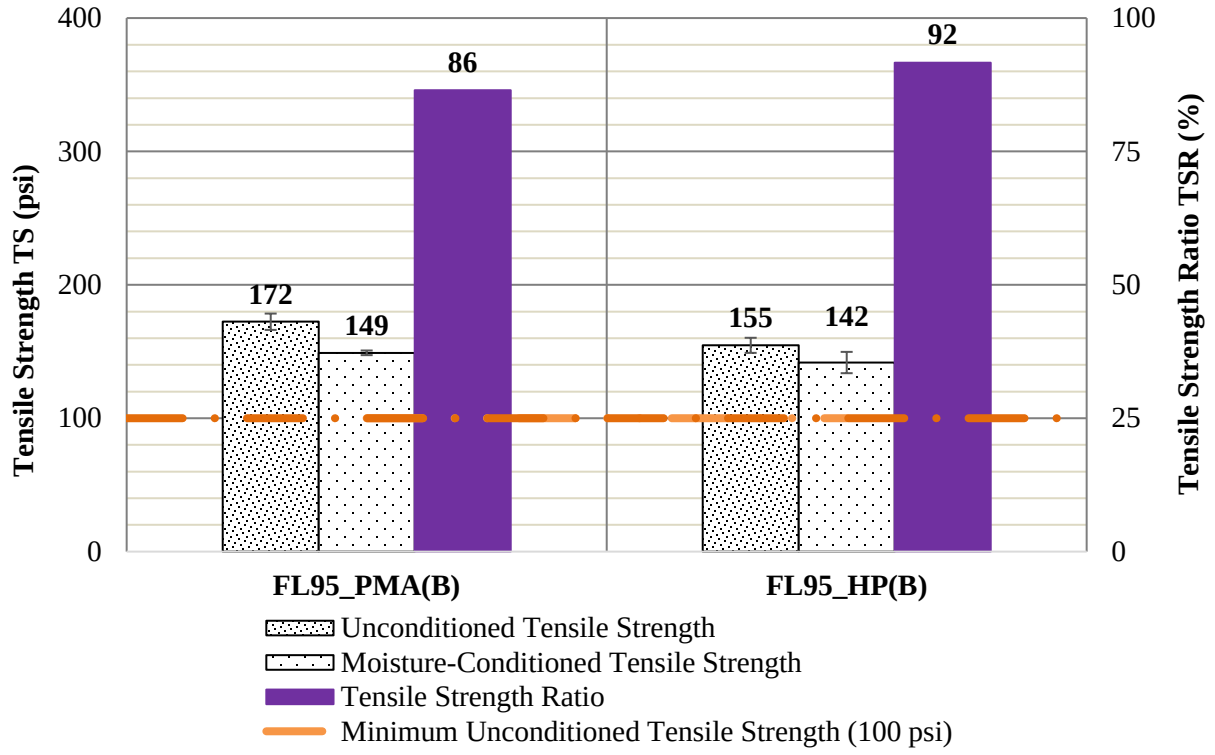


**Figure B.2. Tensile strength statistical representation for FL95_PMA(B) and FL95_HP(B) mixes (Error bars represent the mean values plus or minus 95% confidence interval).**

## Table B.9. Moisture Damage Results Summary Table for FL125_PMA(A).

| Description | Dry Set | | | | Conditioned Set | | | |
|---|---|---|---|---|---|---|---|---|
| Sample ID | D1 | D2 | D3 | D4 | W1 | W2 | W3 | W4 |
| Diameter (in.) | 4.00 | 4.00 | 4.00 | -- | 4.00 | 4.00 | 4.00 | 4.00 |
| Thickness (in.) | 2.49 | 2.49 | 2.49 | -- | 2.50 | 2.49 | 2.50 | 2.49 |
| Air Void (%) | 6.5 | 6.7 | 6.6 | -- | 6.3 | 6.5 | 6.3 | 6.5 |
| Average Air Void (%) | 6.6 | | | | 6.4 | | | |
| Saturation (%) | 0.0 | | | | 72.2 | 77.5 | 79.1 | 79.3 |
| Peak Applied Load (lbs) | 3,418.0 | 3,506.4 | 3,210.1 | -- | 2,914.4 | 2,657.6 | 2,669.2 | 2,931.5 |
| Tensile Strength TS (psi) | 218.4 | 224.3 | 205.4 | -- | 185.8 | 169.8 | 170.2 | 187.6 |
| Average TS (psi) | 216.0 | | | | 178.4 | | | |
| Standard Deviation (psi) | 9.7 | | | | 9.6 | | | |
| 95% Confidence Interval (psi) | 8.5 | | | | 9.5 | | | |
| TSR Ratio (%) | 82.6 | | | | | | | |

## Table B.10. Moisture Damage Results Summary Table for FL125_HP(A).

| Description | Dry Set | | | | Conditioned Set | | | |
|---|---|---|---|---|---|---|---|---|
| Sample ID | D1 | D2 | D3 | D4 | W1 | W2 | W3 | W4 |
| Diameter (in.) | 4.00 | 4.00 | 4.00 | -- | 4.00 | 4.00 | 4.00 | 4.00 |
| Thickness (in.) | 2.48 | 2.49 | 2.49 | -- | 2.49 | 2.48 | 2.48 | 2.48 |
| Air Void (%) | 6.7 | 6.2 | 6.5 | -- | 6.6 | 6.8 | 6.3 | 6.6 |
| Average Air Void (%) | 6.4 | | | | 6.6 | | | |
| Saturation (%) | 0.0 | | | | 78.0 | 76.2 | 79.6 | 70.9 |
| Peak Applied Load (lbs) | 2,479.1 | 2,721.2 | 2,560.9 | -- | 2,022.1 | 2,006.2 | 2,121.1 | 2,173.1 |
| Tensile Strength TS (psi) | 158.8 | 174.1 | 163.8 | -- | 129.5 | 128.5 | 136.0 | 139.7 |
| Average TS (psi) | 165.6 | | | | 133.4 | | | |
| Standard Deviation (psi) | 7.8 | | | | 5.3 | | | |
| 95% Confidence Interval (psi) | 7.6 | | | | 5.2 | | | |
| TSR Ratio (%) | 80.6 | | | | | | | |

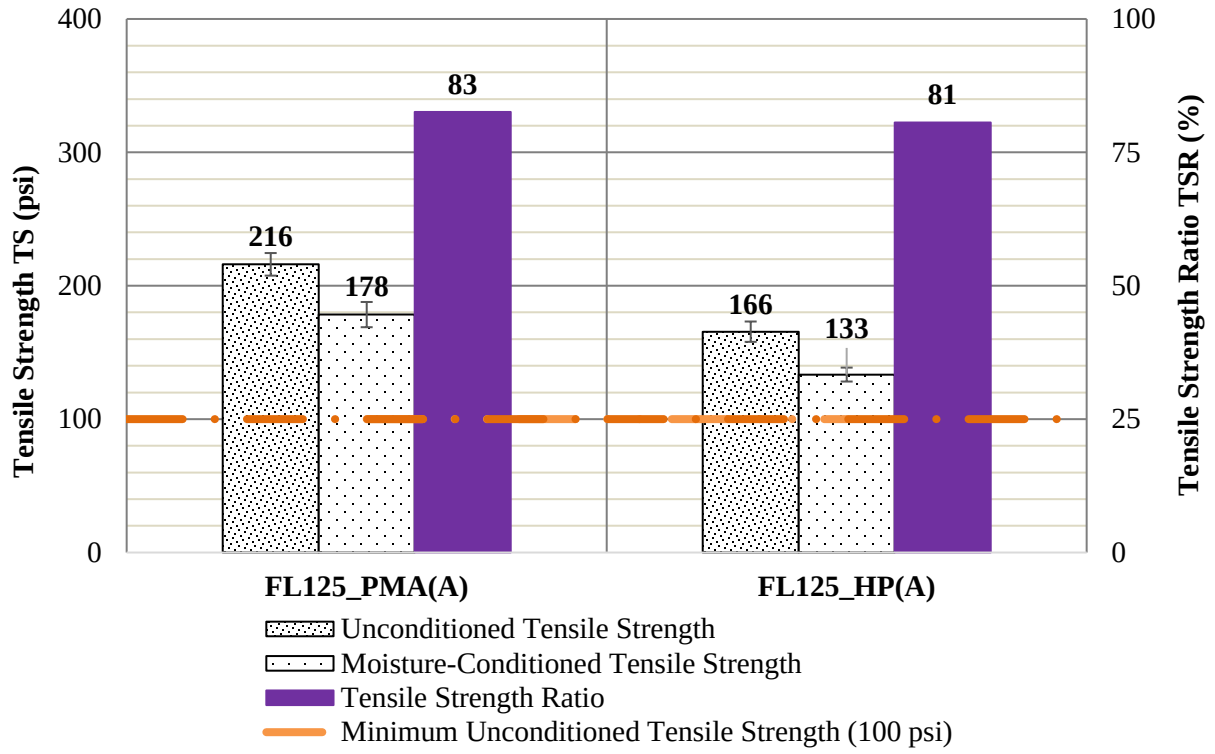


**Figure B.3. Tensile strength statistical representation for FL125_PMA(A) and FL125_HP(A) mixes (Error bars represent the mean values plus or minus 95% confidence interval).**

**Table B.11. Moisture Damage Results Summary Table for FL125_PMA(B).**

| **Description** | **Dry Set** | | | | **Conditioned Set** | | | |
|---|---|---|---|---|---|---|---|---|
| Sample ID | D1 | D2 | D3 | D4 | W1 | W2 | W3 | W4 |
| Diameter (in.) | 4.00 | 4.00 | 4.00 | -- | 4.00 | 4.00 | 4.00 | -- |
| Thickness (in.) | 2.49 | 2.49 | 2.49 | -- | 2.48 | 2.48 | 2.48 | -- |
| Air Void (%) | 6.7 | 6.5 | 7.0 | -- | 6.4 | 6.6 | 6.5 | -- |
| Average Air Void (%) | 6.7 | | | | 6.5 | | | |
| Saturation (%) | 0.0 | | | | 79.5 | 78.1 | 74.3 | -- |
| Peak Applied Load (lbs) | 3,332.6 | 3,204.3 | 3,294.7 | -- | 2,915.9 | 2,710.7 | 3,118.0 | -- |
| Tensile Strength TS (psi) | 212.7 | 204.5 | 210.2 | -- | 186.9 | 173.8 | 199.7 | |
| Average TS (psi) | 209.1 | | | | 186.8 | | | |
| Standard Deviation (psi) | 4.2 | | | | 13.0 | | | |
| 95% Confidence Interval (psi) | 4.1 | | | | 14.7 | | | |
| TSR Ratio (%) | 89.3 | | | | | | | |

**Table B.12. Moisture Damage Results Summary Table for FL125_HP(B).**

| Description | Dry Set | | | | Conditioned Set | | | |
|---|---|---|---|---|---|---|---|---|
| Sample ID | D1 | D2 | D3 | D4 | W1 | W2 | W3 | W4 |
| Diameter (in.) | 4.00 | 4.00 | 4.00 | -- | 4.00 | 4.00 | 4.00 | 4.00 |
| Thickness (in.) | 2.48 | 2.49 | 2.48 | -- | 2.48 | 2.48 | 2.48 | 2.48 |
| Air Void (%) | 6.7 | 6.6 | 6.6 | -- | 6.7 | 6.8 | 6.6 | 6.6 |
| Average Air Void (%) | 6.6 | | | | 6.7 | | | |
| Saturation (%) | 0.0 | | | | 78.0 | 79.4 | 79.1 | 73.8 |
| Peak Applied Load (lbs) | 2,342.4 | 2,669.7 | 2,459.2 | -- | 2,113.0 | 2,098.3 | 2,039.8 | 2,165.6 |
| Tensile Strength TS (psi) | 150.0 | 170.8 | 157.6 | -- | 135.4 | 134.5 | 130.9 | 138.9 |
| Average TS (psi) | 159.5 | | | | 134.9 | | | |
| Standard Deviation (psi) | 10.5 | | | | 3.3 | | | |
| 95% Confidence Interval (psi) | 10.3 | | | | 3.2 | | | |
| TSR Ratio (%) | 84.6 | | | | | | | |

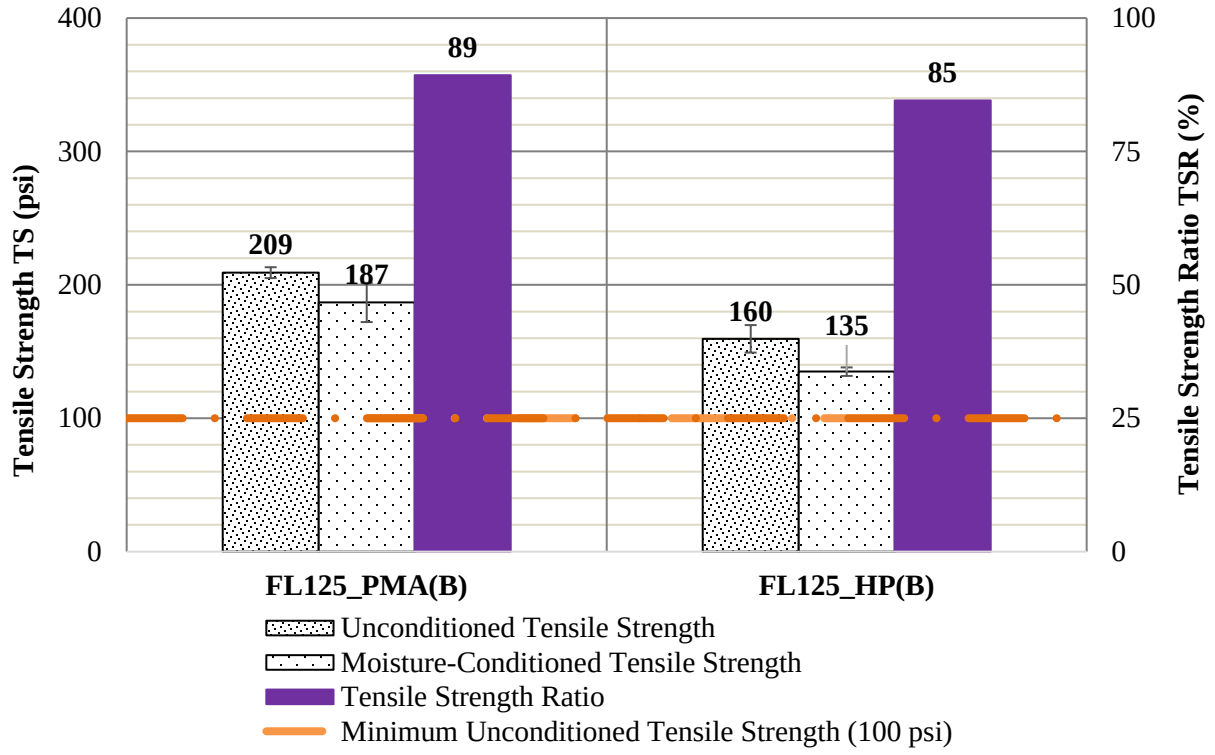


**Figure B.4. Tensile strength statistical representation for FL125_PMA(B) and FL125_HP(B) mixes (Error bars represent the mean values plus or minus 95% confidence interval).**

## Table B.13. Moisture Damage Results Summary Table for GA95_PMA(A).

| Description | Dry Set | | | | Conditioned Set | | | |
|---|---|---|---|---|---|---|---|---|
| Sample ID | D1 | D2 | D3 | D4 | W1 | W2 | W3 | W4 |
| Diameter (in.) | 4.00 | 4.00 | 4.00 | -- | 4.00 | 4.00 | 4.00 | 4.00 |
| Thickness (in.) | 2.50 | 2.49 | 2.49 | -- | 2.49 | 2.49 | 2.49 | 2.50 |
| Air Void (%) | 7.0 | 6.0 | 6.2 | -- | 6.6 | 6.2 | 6.5 | 6.9 |
| Average Air Void (%) | 6.4 | | | | 6.6 | | | |
| Saturation (%) | 0.0 | | | | 70.3 | 76.7 | 70.6 | 77.9 |
| Peak Applied Load (lbs) | 4,229.8 | 4,410.5 | 4,220.3 | -- | 3,611.9 | 3,598.9 | 3,669.3 | 3,643.6 |
| Tensile Strength TS (psi) | 268.9 | 282.2 | 269.7 | -- | 230.8 | 230.0 | 234.8 | 232.4 |
| Average TS (psi) | 273.6 | | | | 232.0 | | | |
| Standard Deviation (psi) | 7.4 | | | | 2.1 | | | |
| 95% Confidence Interval (psi) | 6.5 | | | | 2.1 | | | |
| TSR Ratio (%) | 84.8 | | | | | | | |

## Table B.14. Moisture Damage Results Summary Table for GA95_HP(A).

| Description | Dry Set | | | | Conditioned Set | | | |
|---|---|---|---|---|---|---|---|---|
| Sample ID | D1 | D2 | D3 | D4 | W1 | W2 | W3 | W4 |
| Diameter (in.) | 4.00 | 4.00 | 4.00 | -- | 4.00 | 4.00 | 4.00 | -- |
| Thickness (in.) | 2.49 | 2.49 | 2.49 | -- | 2.48 | 2.49 | 2.48 | -- |
| Air Void (%) | 7.0 | 7.0 | 6.8 | -- | 7.0 | 7.1 | 7.0 | -- |
| Average Air Void (%) | 6.9 | | | | 7.0 | | | |
| Saturation (%) | 0.0 | | | | 73.6 | 79.0 | 76.6 | -- |
| Peak Applied Load (lbs) | 2,975.0 | 3,006.5 | 2,940.5 | -- | 2,821.0 | 2,745.8 | 2,589.0 | -- |
| Tensile Strength TS (psi) | 190.2 | 192.1 | 188.2 | -- | 180.7 | 175.5 | 166.0 | |
| Average TS (psi) | 190.2 | | | | 174.0 | | | |
| Standard Deviation (psi) | 2.0 | | | | 7.5 | | | |
| 95% Confidence Interval (psi) | 1.9 | | | | 8.4 | | | |
| TSR Ratio (%) | 91.5 | | | | | | | |

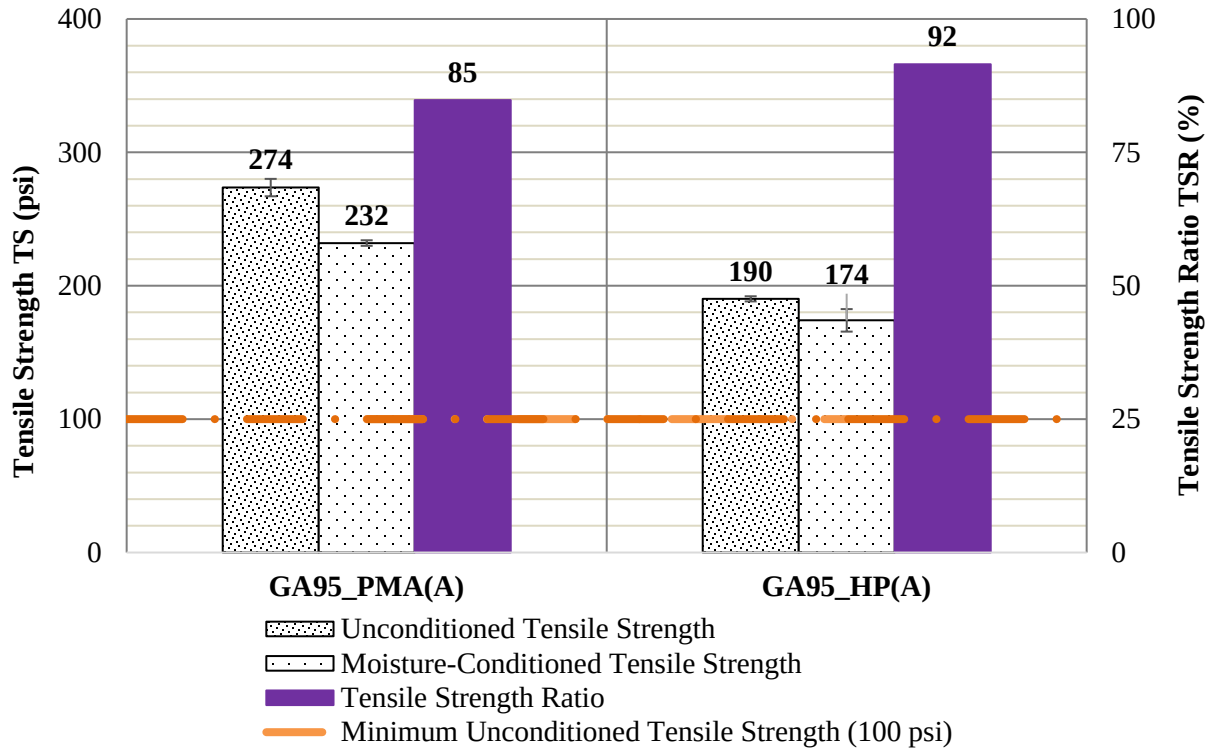


**Figure B.5. Tensile strength statistical representation for GA95_PMA(A) and GA95_HP(A) mixes (Error bars represent the mean values plus or minus 95% confidence interval).**

**Table B.15. Moisture Damage Results Summary Table for GA95_PMA(B).**

| **Description** | **Dry Set** | | | | **Conditioned Set** | | | |
|---|---|---|---|---|---|---|---|---|
| Sample ID | D1 | D2 | D3 | D4 | W1 | W2 | W3 | W4 |
| Diameter (in.) | 4.00 | 4.00 | 4.00 | -- | 4.00 | 4.00 | 4.00 | -- |
| Thickness (in.) | 2.49 | 2.49 | 2.49 | -- | 2.50 | 2.49 | 2.49 | -- |
| Air Void (%) | 6.4 | 6.7 | 6.7 | -- | 6.3 | 6.9 | 6.7 | -- |
| Average Air Void (%) | 6.6 | | | | 6.6 | | | |
| Saturation (%) | 0.0 | | | | 71.1 | 70.4 | 70.6 | -- |
| Peak Applied Load (lbs) | 4,504.9 | 4,548.2 | 4,375.4 | -- | 3,754.1 | 3,527.9 | 3,910.8 | -- |
| Tensile Strength TS (psi) | 287.9 | 290.9 | 279.2 | -- | 239.1 | 225.1 | 249.9 | |
| Average TS (psi) | 286.0 | | | | 238.1 | | | |
| Standard Deviation (psi) | 6.1 | | | | 12.5 | | | |
| 95% Confidence Interval (psi) | 5.3 | | | | 14.1 | | | |
| TSR Ratio (%) | 83.2 | | | | | | | |

**Table B.16. Moisture Damage Results Summary Table for GA95_HP(B).**

| Description | Dry Set | | | | Conditioned Set | | | |
|---|---|---|---|---|---|---|---|---|
| Sample ID | D1 | D2 | D3 | D4 | W1 | W2 | W3 | W4 |
| Diameter (in.) | 4.00 | 4.00 | 4.00 | -- | 4.00 | 4.00 | 4.00 | 4.00 |
| Thickness (in.) | 2.47 | 2.47 | 2.48 | -- | 2.49 | 2.48 | 2.48 | 2.48 |
| Air Void (%) | 6.0 | 6.1 | 6.1 | -- | 7.1 | 7.1 | 7.0 | 7.0 |
| Average Air Void (%) | 6.1 | | | | 7.0 | | | |
| Saturation (%) | 0.0 | | | | 74.8 | 74.9 | 77.0 | 75.4 |
| Peak Applied Load (lbs) | 2,108.6 | 2,216.1 | 2,316.0 | -- | 2,539.3 | 2,306.0 | 2,312.3 | 2,481.5 |
| Tensile Strength TS (psi) | 135.9 | 143.0 | 148.9 | -- | 162.6 | 147.7 | 148.3 | 159.5 |
| Average TS (psi) | 142.6 | | | | 154.5 | | | |
| Standard Deviation (psi) | 6.5 | | | | 7.6 | | | |
| 95% Confidence Interval (psi) | 5.7 | | | | 7.5 | | | |
| TSR Ratio (%) | 108.3 | | | | | | | |

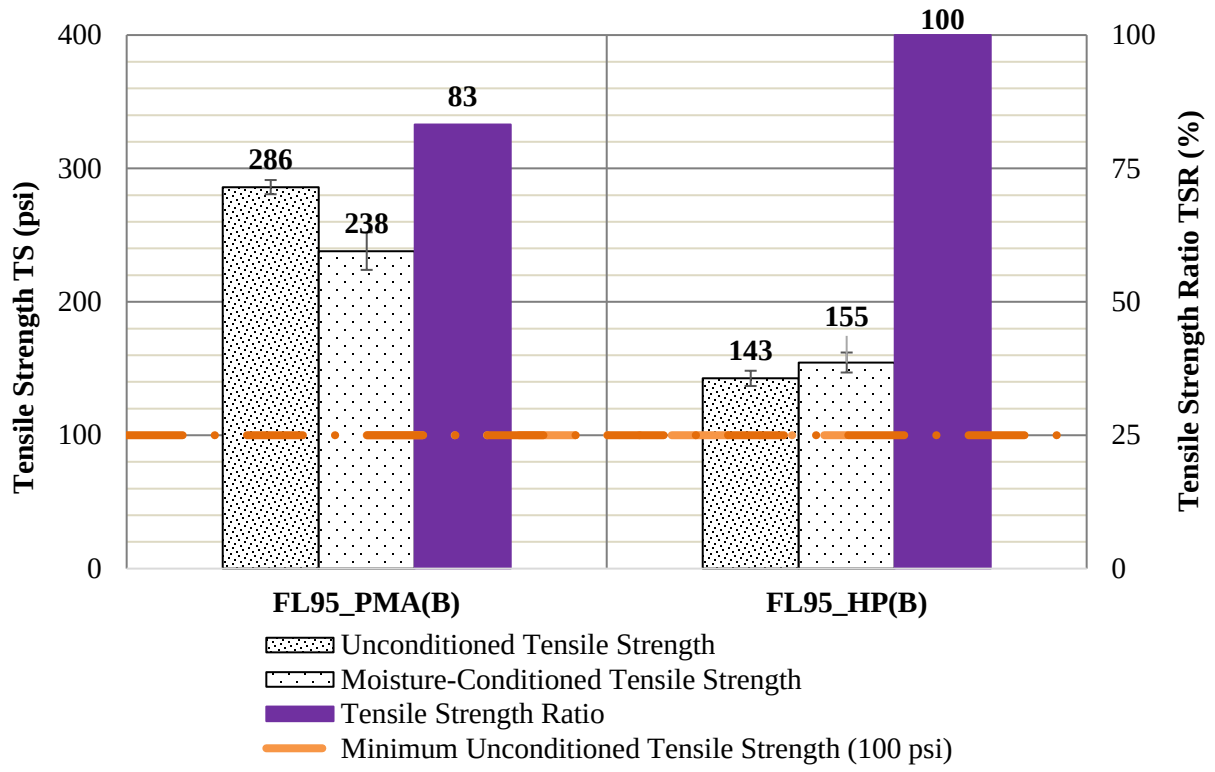


**Figure B.6. Tensile strength statistical representation for GA95_PMA(B) and GA95_HP(B) mixes (Error bars represent the mean values plus or minus 95% confidence interval).**

## Table B.17. Moisture Damage Results Summary Table for GA125_PMA(A).

| Description | Dry Set | | | | Conditioned Set | | | |
|---|---|---|---|---|---|---|---|---|
| Sample ID | D1 | D2 | D3 | D4 | W1 | W2 | W3 | W4 |
| Diameter (in.) | 4.00 | 4.00 | 4.00 | -- | 4.00 | 4.00 | 4.00 | -- |
| Thickness (in.) | 2.49 | 2.49 | 2.49 | -- | 2.50 | 2.50 | 2.49 | -- |
| Air Void (%) | 6.6 | 6.7 | 6.7 | -- | 7.0 | 6.9 | 6.6 | -- |
| Average Air Void (%) | 6.7 | | | | 6.8 | | | |
| Saturation (%) | 0.0 | | | | 76.3 | 73.2 | 78.5 | -- |
| Peak Applied Load (lbs) | 4,532.8 | 4,511.5 | 4,463.4 | -- | 3,879.8 | 3,636.7 | 3,538.6 | -- |
| Tensile Strength TS (psi) | 290.0 | 288.6 | 285.3 | -- | 247.3 | 231.9 | 225.9 | |
| Average TS (psi) | 288.0 | | | | 235.0 | | | |
| Standard Deviation (psi) | 2.4 | | | | 11.1 | | | |
| 95% Confidence Interval (psi) | 2.7 | | | | 12.5 | | | |
| TSR Ratio (%) | 81.6 | | | | | | | |

## Table B.18. Moisture Damage Results Summary Table for GA125_HP(A).

| Description | Dry Set | | | | Conditioned Set | | | |
|---|---|---|---|---|---|---|---|---|
| Sample ID | D1 | D2 | D3 | D4 | W1 | W2 | W3 | W4 |
| Diameter (in.) | 4.00 | 4.00 | 4.00 | 4.00 | 4.00 | 4.00 | 4.00 | 4.00 |
| Thickness (in.) | 2.49 | 2.49 | 2.49 | 2.49 | 2.49 | 2.49 | 2.50 | 2.49 |
| Air Void (%) | 6.4 | 6.6 | 6.6 | 6.3 | 6.7 | 6.4 | 6.8 | 6.3 |
| Average Air Void (%) | 6.5 | | | | 6.5 | | | |
| Saturation (%) | 0.0 | | | | | | | -- |
| Peak Applied Load (lbs) | 3,178.1 | 3,239.1 | 3,184.4 | 3,240.9 | 2,384.3 | 2,641.7 | 2,426.8 | 2,861.8 |
| Tensile Strength TS (psi) | 203.5 | 207.4 | 203.7 | 207.0 | 152.4 | 168.9 | 154.6 | 182.8 |
| Average TS (psi) | 205.4 | | | | 164.7 | | | |
| Standard Deviation (psi) | 2.1 | | | | 14.1 | | | |
| 95% Confidence Interval (psi) | 1.8 | | | | 13.9 | | | |
| TSR Ratio (%) | 80.2 | | | | | | | |

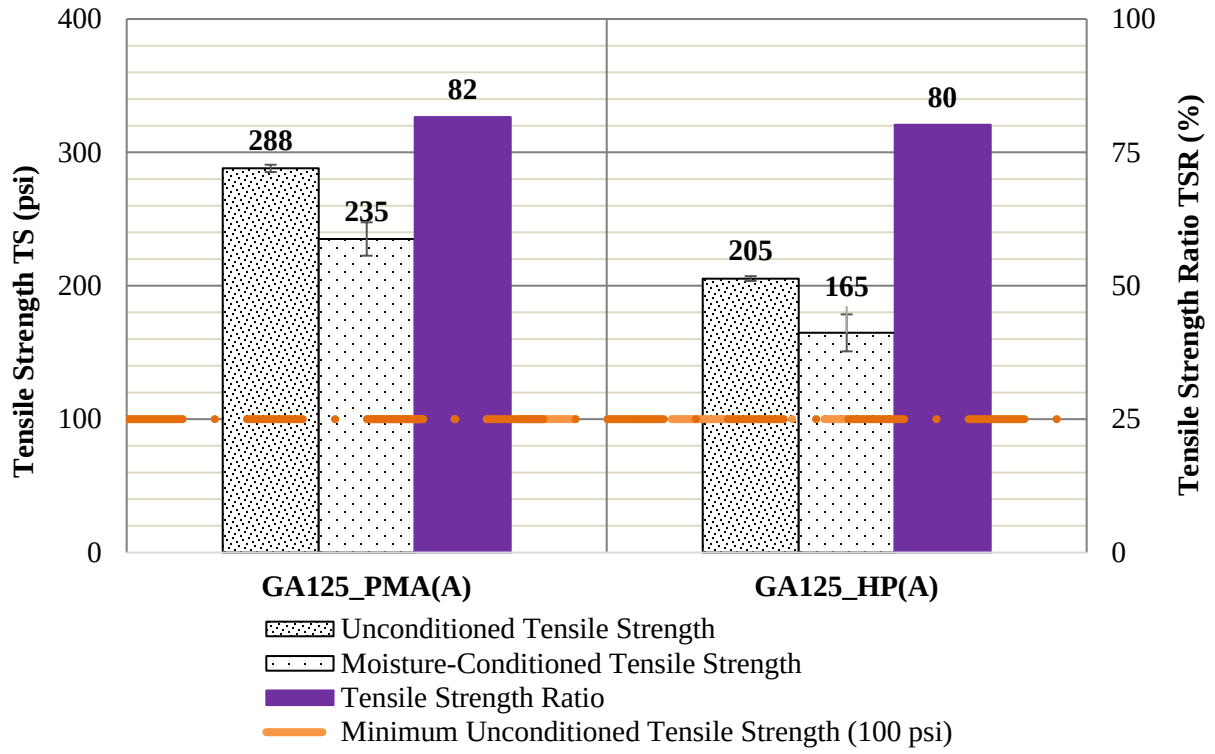


**Figure B.7. Tensile strength statistical representation for GA125_PMA(A) and GA125_HP(A) mixes (Error bars represent the mean values plus or minus 95% confidence interval).**

**Table B.19. Moisture Damage Results Summary Table for GA125_PMA(B).**

| **Description** | **Dry Set** | | | | **Conditioned Set** | | | |
|---|---|---|---|---|---|---|---|---|
| Sample ID | D1 | D2 | D3 | D4 | W1 | W2 | W3 | W4 |
| Diameter (in.) | 4.00 | 4.00 | 4.00 | 4.00 | 4.00 | 4.00 | 4.00 | -- |
| Thickness (in.) | 2.49 | 2.49 | 2.49 | 2.49 | 2.49 | 2.49 | 2.49 | -- |
| Air Void (%) | 6.8 | 6.7 | 6.8 | 6.5 | 6.8 | 6.9 | 6.5 | -- |
| Average Air Void (%) | 6.8 | | | | 6.7 | | | |
| Saturation (%) | 0.0 | | | | 78.5 | 76.6 | 72.1 | -- |
| Peak Applied Load (lbs) | 4,272.2 | 4,338.9 | 4,234.4 | 4,040.7 | 3,505.7 | 3,320.6 | 3,405.9 | -- |
| Tensile Strength TS (psi) | 273.6 | 277.2 | 271.0 | 258.1 | 223.8 | 212.1 | 217.9 | |
| Average TS (psi) | 270.0 | | | | 217.9 | | | |
| Standard Deviation (psi) | 8.3 | | | | 5.9 | | | |
| 95% Confidence Interval (psi) | 8.2 | | | | 6.6 | | | |
| TSR Ratio (%) | 80.7 | | | | | | | |

**Table B.20. Moisture Damage Results Summary Table for GA125_HP(B).**

| Description | Dry Set | | | | Conditioned Set | | | |
|---|---|---|---|---|---|---|---|---|
| Sample ID | D1 | D2 | D3 | D4 | W1 | W2 | W3 | W4 |
| Diameter (in.) | 4.00 | 4.00 | 4.00 | 4.00 | 4.00 | 4.00 | 4.00 | 4.00 |
| Thickness (in.) | 2.49 | 2.49 | 2.49 | 2.49 | 2.51 | 2.48 | 2.49 | -- |
| Air Void (%) | 6.4 | 6.8 | 6.5 | 6.6 | 6.7 | 6.2 | 6.0 | -- |
| Average Air Void (%) | 6.6 | | | | 6.3 | | | |
| Saturation (%) | 0.0 | | | | 72.0 | 70.9 | 77.9 | -- |
| Peak Applied Load (lbs) | 2,882.6 | 2,857.0 | 2,715.8 | 2,742.3 | 2,240.9 | 2,245.2 | 2,399.7 | -- |
| Tensile Strength TS (psi) | 184.5 | 182.8 | 173.6 | 175.2 | 142.9 | 143.8 | 153.5 | |
| Average TS (psi) | 179.0 | | | | 146.7 | | | |
| Standard Deviation (psi) | 5.4 | | | | 5.9 | | | |
| 95% Confidence Interval (psi) | 4.8 | | | | 6.7 | | | |
| TSR Ratio (%) | 81.9 | | | | | | | |

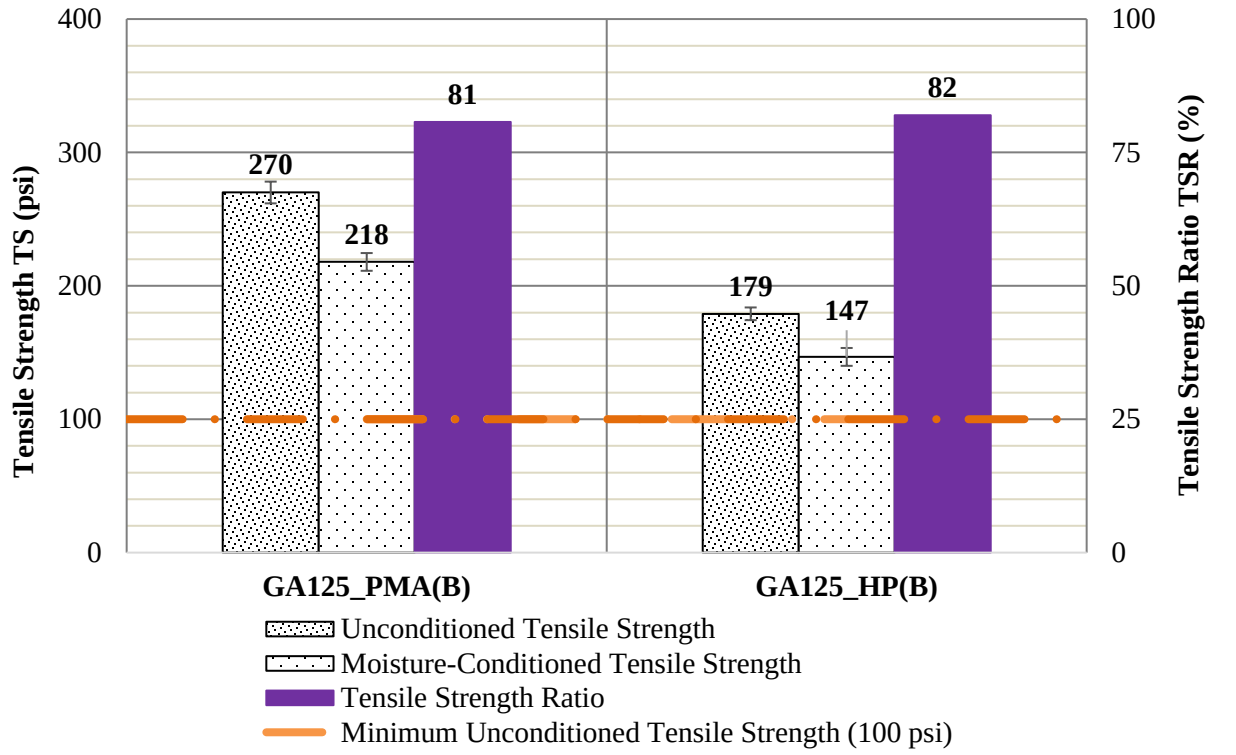


**Figure B.8. Tensile strength statistical representation for GA125_PMA(B) and GA125_HP(B) mixes (Error bars represent the mean values plus or minus 95% confidence interval).**

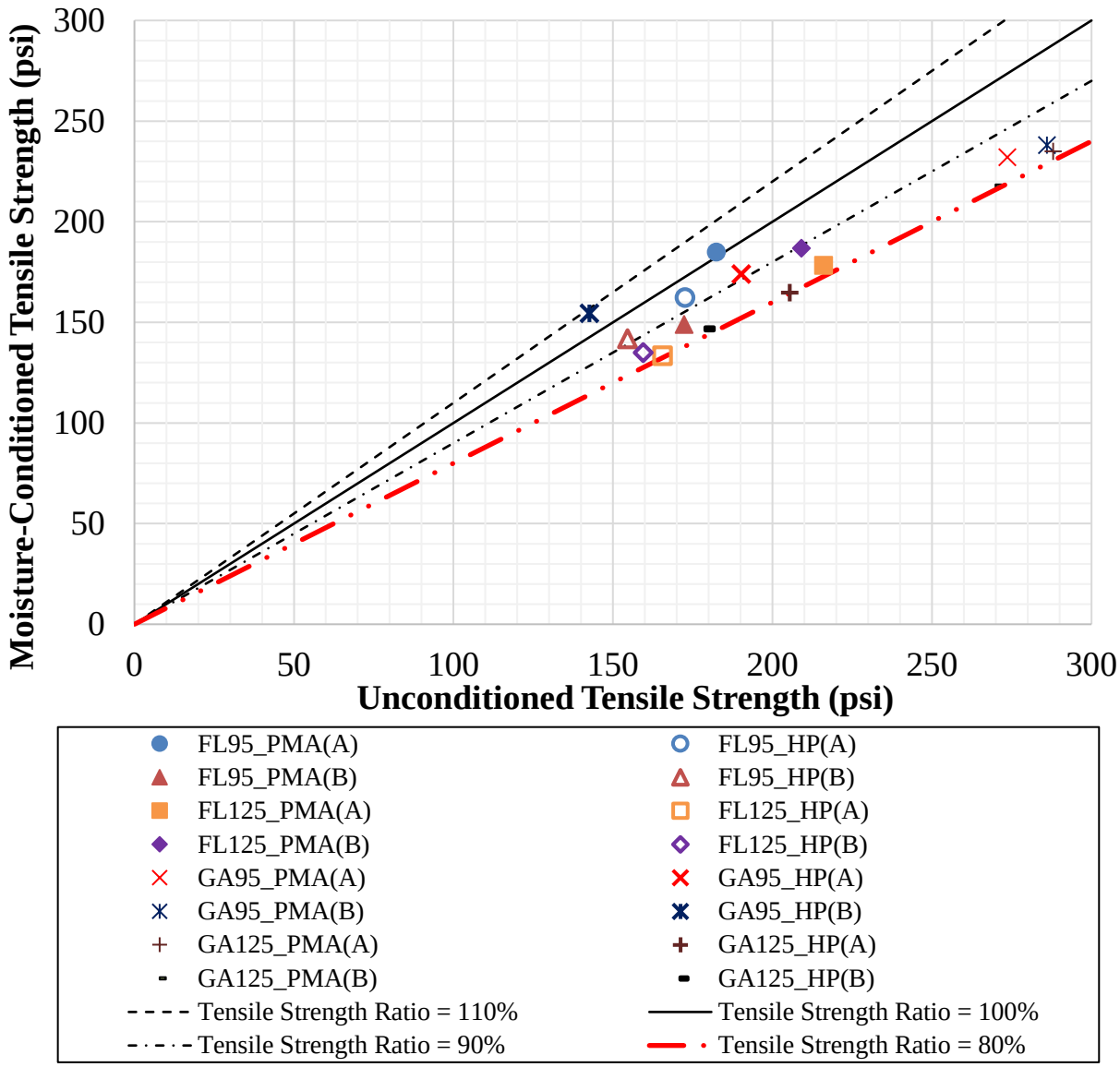


**Figure B.9. Tensile strength representation of the 16 evaluated mixes.**

# APPENDIX C. LABORATORY PERFORMANCE PROPERTIES AND CHARACTERISTIC - DETAILED DATA

## C.1. DYNAMIC MODULUS PROPERTY

### C.1.1. FL95_PMA(A) AC Mix

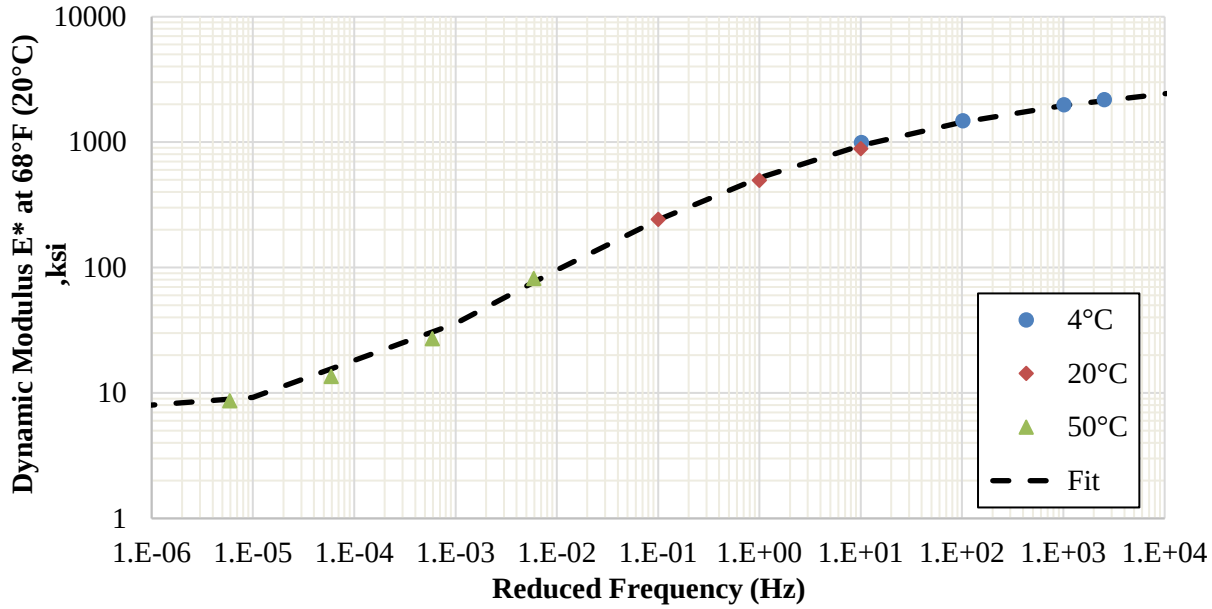


**Figure C.1. Dynamic modulus of FL95_PMA(A) mixture at 68°F (20°C).**

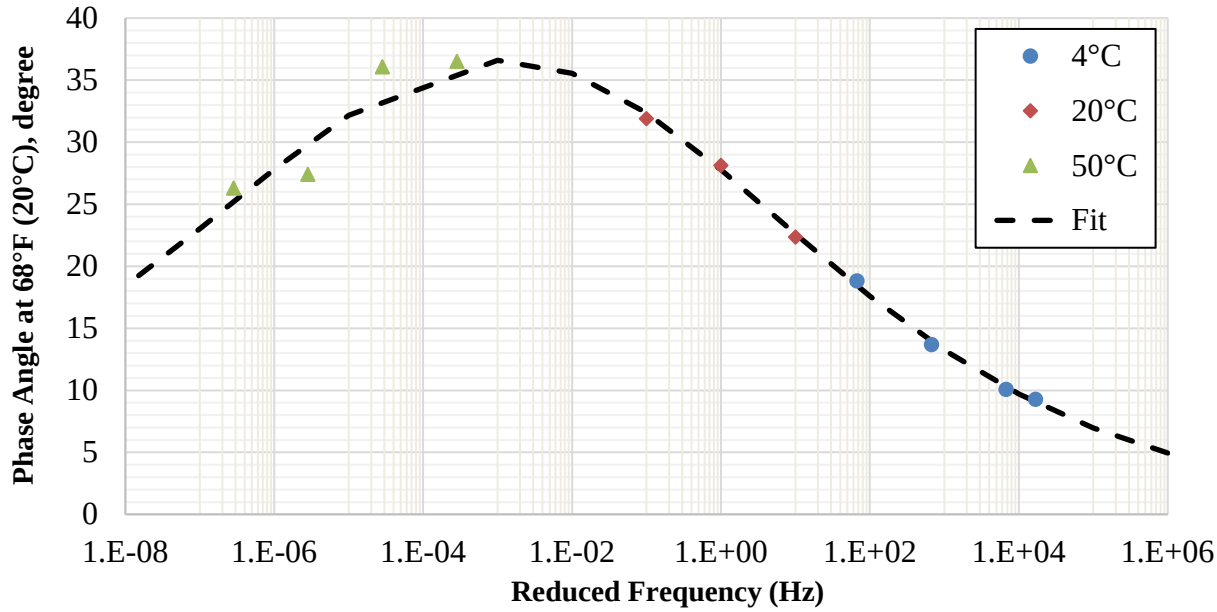


**Figure C.2. Phase angle of FL95_PMA(A) mixture at 68°F (20°C).**

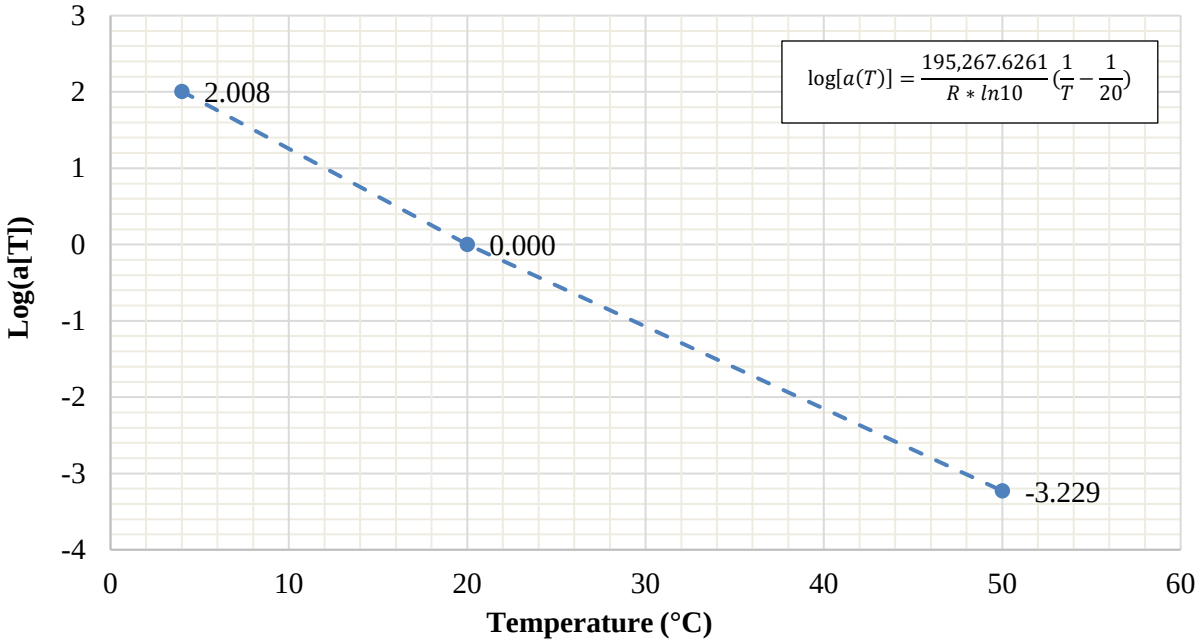


**Figure C.3. Log (a[T]) of FL95_PMA(A) mixture.**

**Table C.1. Dynamic Modulus Input Values for FL95_PMA(A) AC mix.**

| **E*, psi (MPa)** | **Frequency (Hz)** | | | | | |
|---|---|---|---|---|---|---|
| **Temperature, °F (°C)** | 0.1 | 0.5 | 1 | 5 | 10 | 25 |
| 14 (-10) | 1,945,719 (13,415) | 2,281,477 (15,730) | 2,414,749 (16,649) | 2,693,661 (18,572) | 2,800,138 (19,306) | 2,928,378 (20,190) |
| 40 (4) | 913,337 (6,297) | 1,260,750 (8,693) | 1,417,852 (9,776) | 1,784,068 (12,301) | 1,937,760 (13,360) | 2,133,436 (14,710) |
| 70 (21) | 215,122 (1,483) | 380,913 (2,626) | 474,418 (3,271) | 741,742 (5,114) | 876,002 (6,040) | 1,067,179 (7,358) |
| 100 (38) | 36,183 (249) | 71,889 (496) | 96,715 (667) | 186,944 (1,289) | 243,401 (1,678) | 337,210 (2,325) |
| 130 (54) | 10,484 (72) | 15,779 (109) | 19,893 (137) | 37,266 (257) | 49,970 (345) | 74,116 (511) |

**Table C.2. Phase Angle Input Values for FL95_PMA(A) AC mix.**

| **Phase Angle, °** | **Frequency (Hz)** | | | | | |
|---|---|---|---|---|---|---|
| **Temperature, °F (°C)** | 0.1 | 0.5 | 1 | 5 | 10 | 25 |
| 14 (-10) | 8.0 | 6.3 | 5.7 | 4.5 | 4.0 | 3.5 |
| 40 (4) | 18.8 | 15.6 | 14.3 | 11.6 | 10.5 | 9.3 |
| 70 (21) | 33.1 | 30.1 | 28.7 | 25.1 | 23.6 | 21.5 |
| 100 (38) | 35.8 | 36.6 | 36.6 | 35.8 | 35.1 | 33.9 |
| 130 (54) | 27.1 | 30.3 | 31.6 | 34.1 | 35.0 | 35.9 |

### C.1.2. FL95_PMA(B) AC Mix

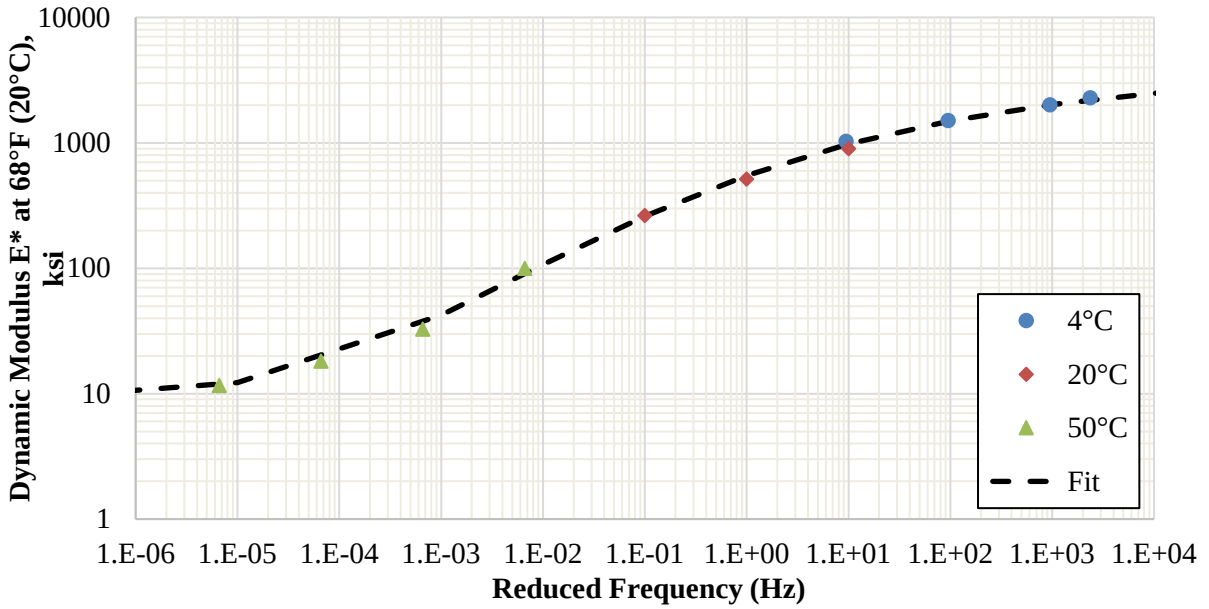


**Figure C.4. Dynamic modulus of FL95_PMA(B) mixture at 68°F (20°C).**

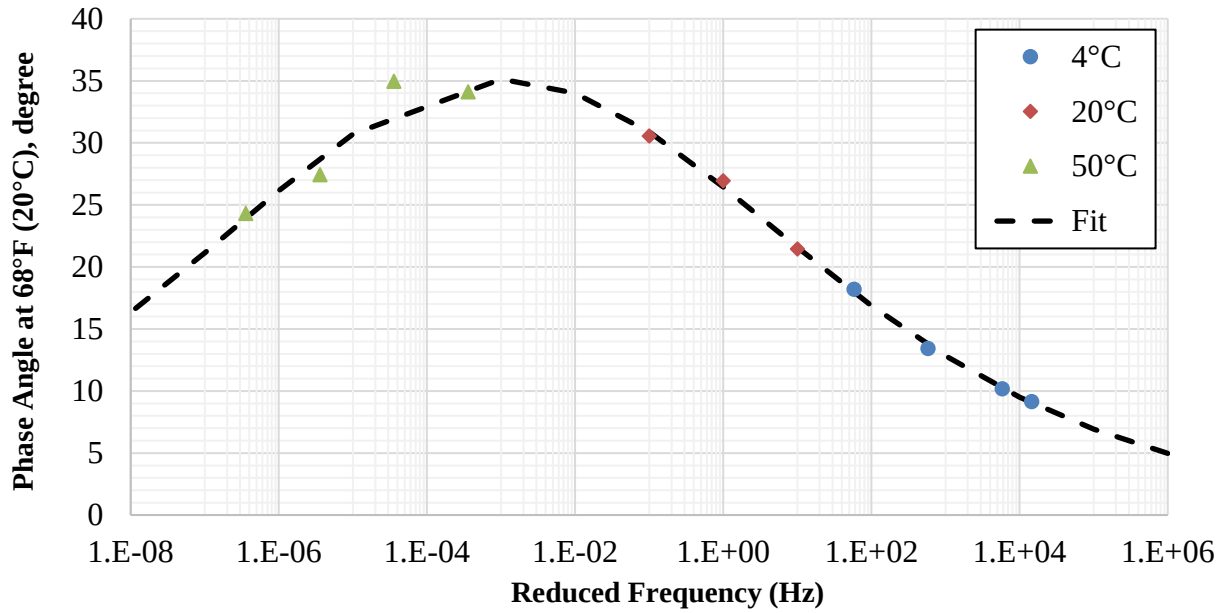


**Figure C.5. Phase angle of FL95_PMA(B) mixture at 68°F (20°C).**

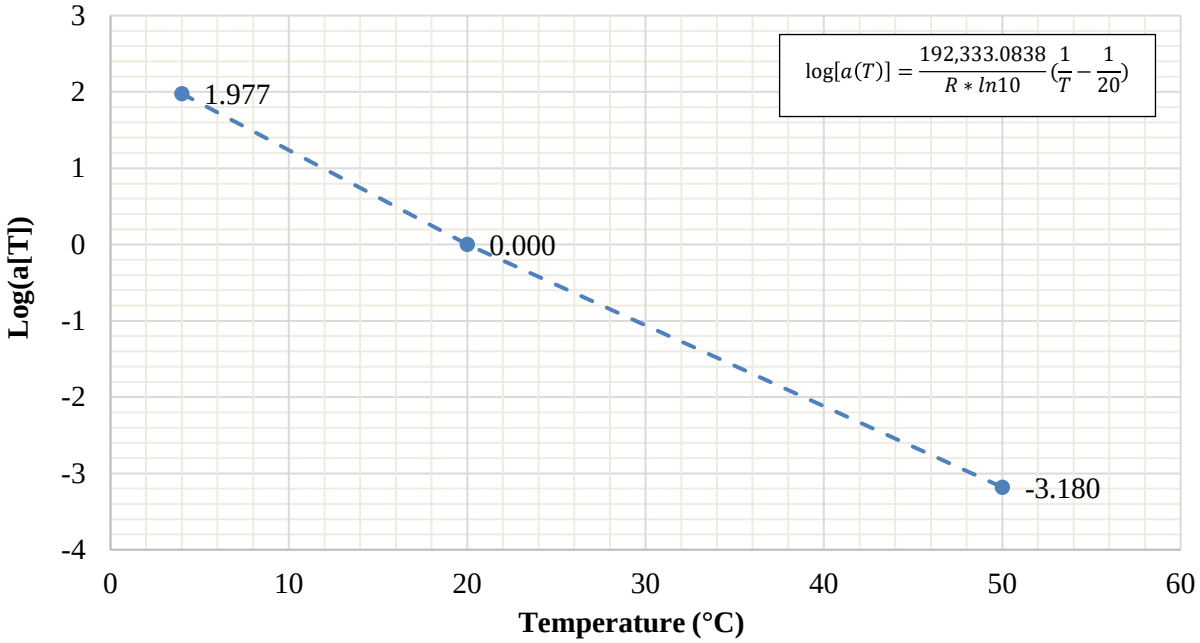


**Figure C.6. Log (a[T]) of FL95_PMA(B) mixture.**

**Table C.3. Dynamic Modulus Input Values for FL95_PMA(B) AC mix.**

| **E*, psi (MPa)** | **Frequency (Hz)** | | | | | |
|---|---|---|---|---|---|---|
| **Temperature, °F (°C)** | 0.1 | 0.5 | 1 | 5 | 10 | 25 |
| 14 (-10) | 1,968,475 (1,3572) | 2,306,516 (15,903) | 2,440,327 (16,825) | 2,719,484 (18,750) | 2,825,674 (19,482) | 2,953,235 (20,362) |
| 40 (4) | 939,556 (6,478) | 1,292,275 (8,910) | 1,451,383 (10,007) | 1,821,152 (12,556) | 1,975,804 (13,623) | 2,172,183 (14,977) |
| 70 (21) | 233,248 (1,608) | 406,176 (2,800) | 503,105 (3,469) | 778,651 (5,369) | 916,333 (6,318) | 1,111,681 (7,665) |
| 100 (38) | 43,861 (302) | 83,748 (577) | 111,028 (766) | 208,643 (1,439) | 268,990 (1,855) | 368,489 (2,541) |
| 130 (54) | 14,084 (97) | 20,652 (142) | 25,630 (177) | 46,118 (318) | 60,789 (419) | 88,261 (609) |

**Table C.4. Phase Angle Input Values for FL95_PMA(B) AC mix.**

| **Phase Angle, °** | **Frequency (Hz)** | | | | | |
|---|---|---|---|---|---|---|
| **Temperature, °F (°C)** | 0.1 | 0.5 | 1 | 5 | 10 | 25 |
| 14 (-10) | 8.2 | 6.6 | 6.0 | 4.7 | 4.3 | 3.7 |
| 40 (4) | 18.3 | 15.3 | 14.0 | 11.5 | 10.5 | 9.3 |
| 70 (21) | 31.6 | 28.7 | 27.3 | 23.9 | 22.5 | 20.5 |
| 100 (38) | 34.5 | 35.1 | 35.1 | 34.1 | 33.4 | 32.1 |
| 130 (54) | 26.0 | 29.3 | 30.6 | 33.1 | 33.9 | 34.6 |

### C.1.3. FL95_HP(A) AC Mix

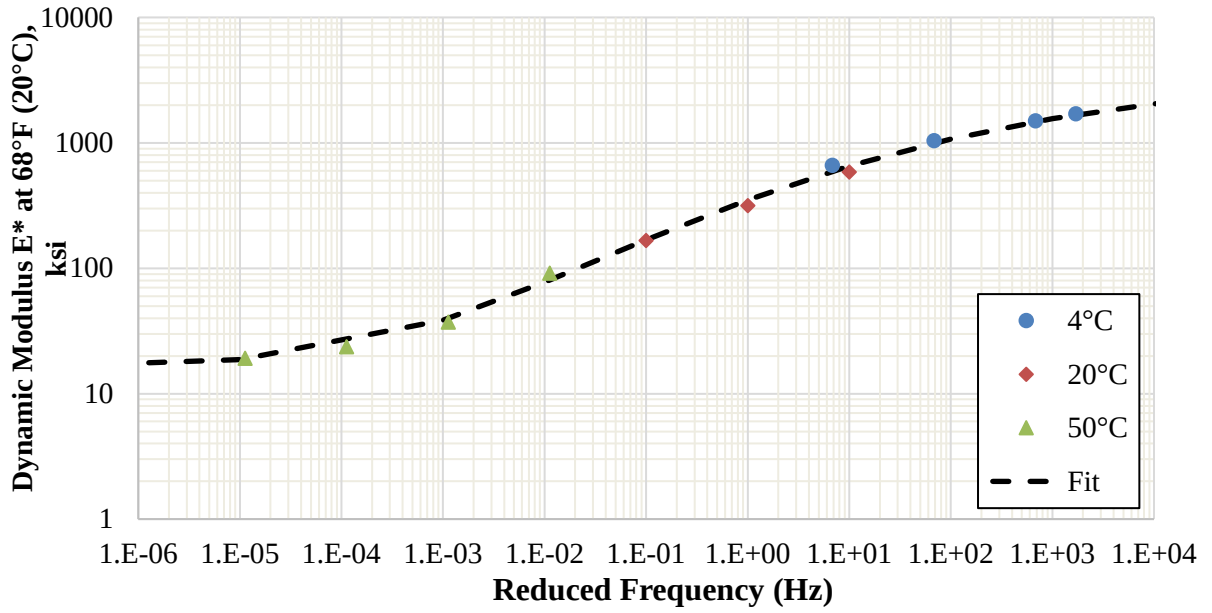


**Figure C.7. Dynamic modulus of FL95_HP(A) mixture at 68°F (20°C).**

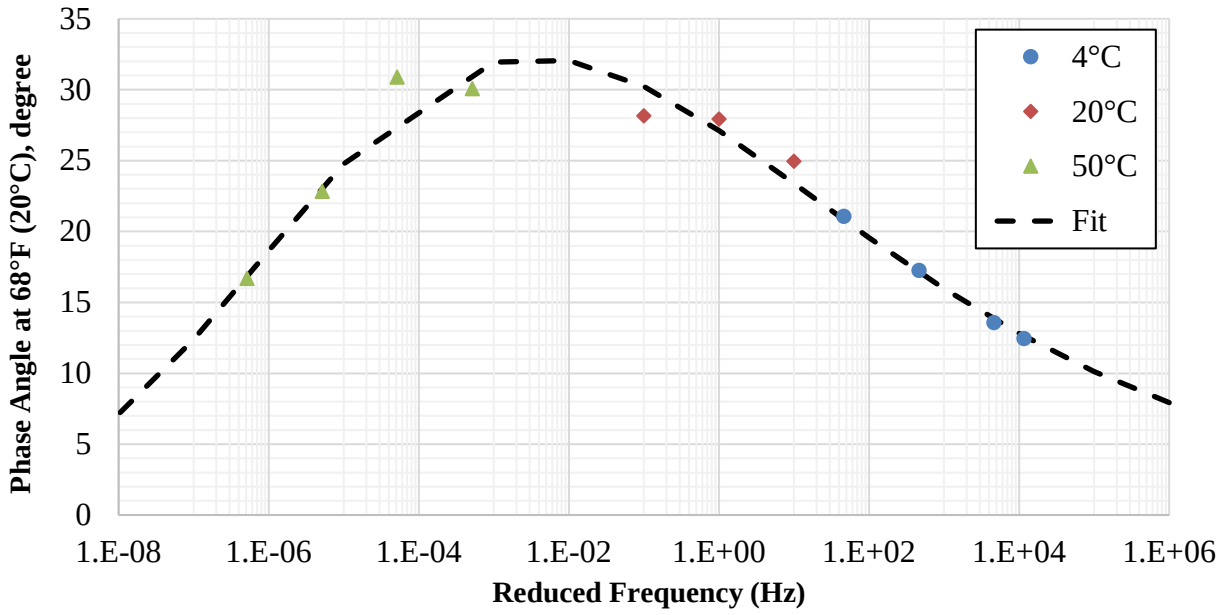


**Figure C.8. Phase angle of FL95_HP(A) mixture at 68°F (20°C).**

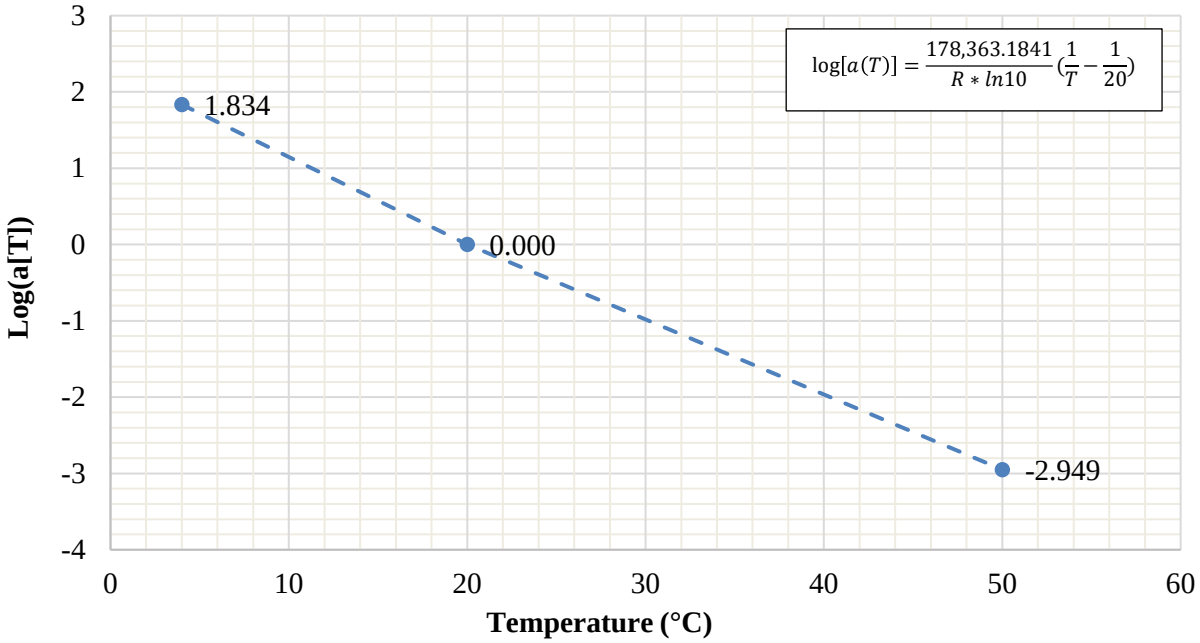


**Figure C.9. Log (a[T]) of FL95_HP(A) mixture.**

**Table C.5. Dynamic Modulus Input Values for FL95_HP(A) AC mix.**

| **E*, psi (MPa)** | **Frequency (Hz)** | | | | | |
|---|---|---|---|---|---|---|
| **Temperature, °F (°C)** | 0.1 | 0.5 | 1 | 5 | 10 | 25 |
| 14 (-10) | 1,369,389 (9,445) | 1,713,661 (11,815) | 1,859,930 (12,824) | 2,185,025 (15,065) | 2,316,221 (15,970) | 2,479,723 (17,097) |
| 40 (4) | 577,508 (3,982) | 843,612 (5,816) | 973,676 (6,713) | 1,300,520 (8,967) | 1,447,680 (9,981) | 1,643,773 (11,333) |
| 70 (21) | 153,206 (1,056) | 260,189 (1,794) | 322,797 (2,226) | 511,678 (3,528) | 612,121 (4,220) | 761,546 (5,251) |
| 100 (38) | 43,213 (298) | 70,748 (488) | 89,002 (614) | 153,519 (1,058) | 193,600 (1,335) | 260,689 (1,797) |
| 130 (54) | 21,229 (146) | 27,313 (188) | 31,684 (218) | 48,553 (335) | 60,016 (414) | 80,795 (557) |

**Table C.6. Phase Angle Input Values for FL95_HP(A) AC mix.**

| **Phase Angle, °** | **Frequency (Hz)** | | | | | |
|---|---|---|---|---|---|---|
| **Temperature, °F (°C)** | 0.1 | 0.5 | 1 | 5 | 10 | 25 |
| 14 (-10) | 12.1 | 10.2 | 9.5 | 8.0 | 7.4 | 6.7 |
| 40 (4) | 21.1 | 18.5 | 17.4 | 15.0 | 14.1 | 12.9 |
| 70 (21) | 30.7 | 28.7 | 27.7 | 25.2 | 24.1 | 22.5 |
| 100 (38) | 30.6 | 32.0 | 32.2 | 32.0 | 31.6 | 30.8 |
| 130 (54) | 19.6 | 23.9 | 25.6 | 28.9 | 30.0 | 31.1 |

### C.1.4. FL95_HP(B) AC Mix

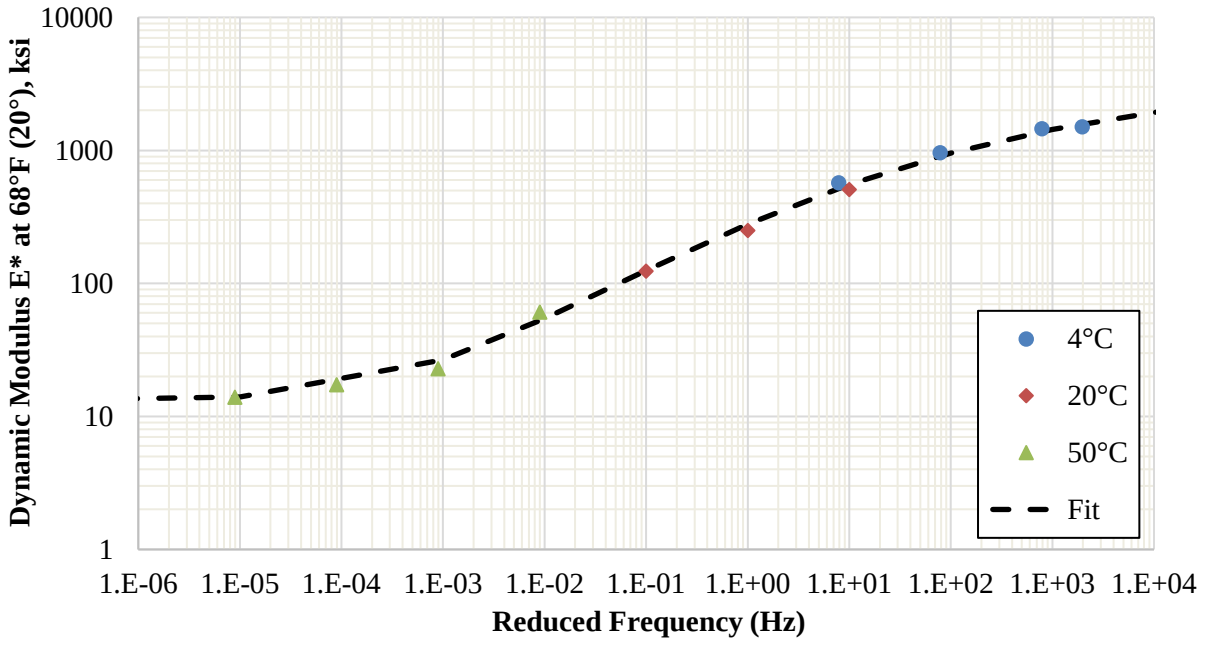


**Figure C.10. Dynamic modulus of FL95_HP(B) mixture at 68°F (20°C).**

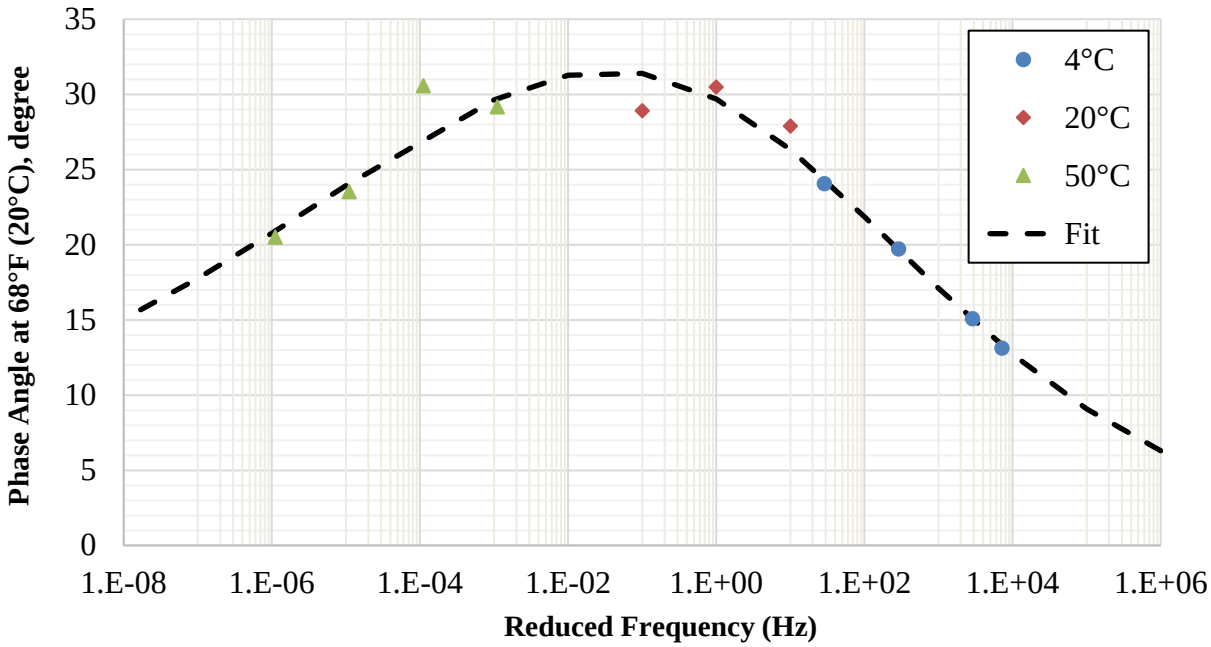


**Figure C.11. Phase angle of FL95_HP(B) mixture at 68°F (20°C).**

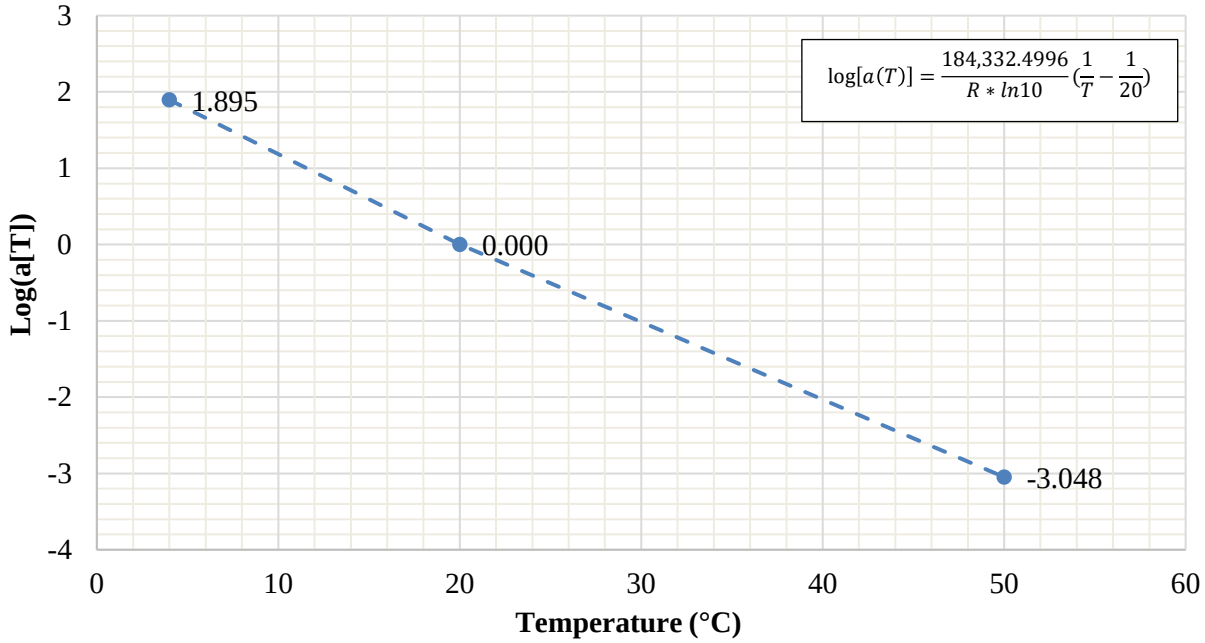


**Figure C.12. Log (a[T]) of FL95_HP(B) mixture.**

**Table C.7. Dynamic Modulus Input Values for FL95_HP(B) AC mix.**

| **E*, psi (MPa)** | **Frequency (Hz)** | | | | | |
|---|---|---|---|---|---|---|
| **Temperature, °F (°C)** | 0.1 | 0.5 | 1 | 5 | 10 | 25 |
| 14 (-10) | 1,306,229 (9,006) | 1,654,600 (11,408) | 1,803,591 (12,435) | 2,135,925 (14,727) | 2,270,390 (15,654) | 2,438,154 (16,810) |
| 40 (4) | 501,085 (3,455) | 755,584 (5,210) | 882,424 (6,084) | 1,206,398 (8,138) | 1,354,233 (9,337) | 1,552,750 (10,706) |
| 70 (21) | 112,803 (778) | 200,603 (1,383) | 253,952 (1,751) | 421,058 (2,903) | 512,821 (3,536) | 652,211 (4,497) |
| 100 (38) | 28,721 (198) | 47,326 (326) | 60,172 (415) | 107,784 (743) | 138,677 (956) | 192,088 (1,324) |
| 130 (54) | 15,055 (104) | 18,309 (126) | 20,831 (144) | 31,148 (215) | 38,472 (265) | 52,186 (360) |

**Table C.8. Phase Angle Input Values for FL95_HP(B) AC mix.**

| **Phase Angle, °** | **Frequency (Hz)** | | | | | |
|---|---|---|---|---|---|---|
| **Temperature, °F (°C)** | 0.1 | 0.5 | 1 | 5 | 10 | 25 |
| 14 (-10) | 13.3 | 10.6 | 9.6 | 7.4 | 6.7 | 5.7 |
| 40 (4) | 24.7 | 21.5 | 20.0 | 16.7 | 15.3 | 13.6 |
| 70 (21) | 31.5 | 30.7 | 30.1 | 28.1 | 27.0 | 25.3 |
| 100 (38) | 28.6 | 30.2 | 30.7 | 31.5 | 31.6 | 31.4 |
| 130 (54) | 22.4 | 24.6 | 25.6 | 27.7 | 28.5 | 29.5 |

### C.1.4. FL125_PMA(A) AC Mix

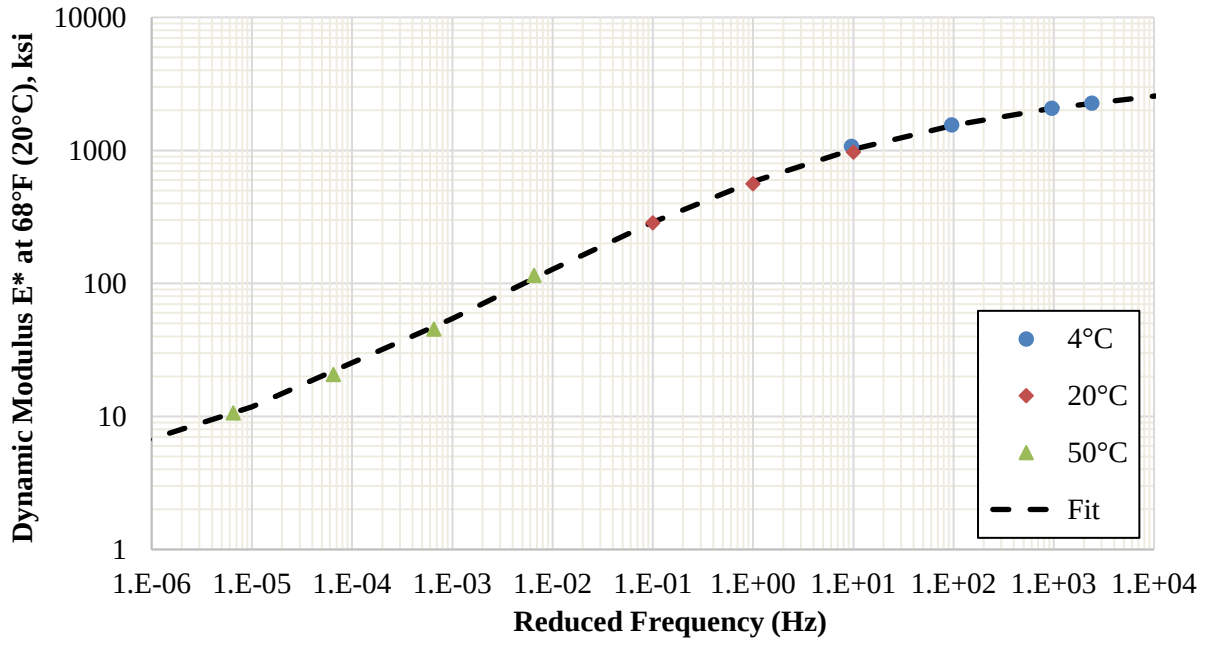


**Figure C.13. Dynamic modulus of FL125_PMA(A) mixture at 68°F (20°C).**

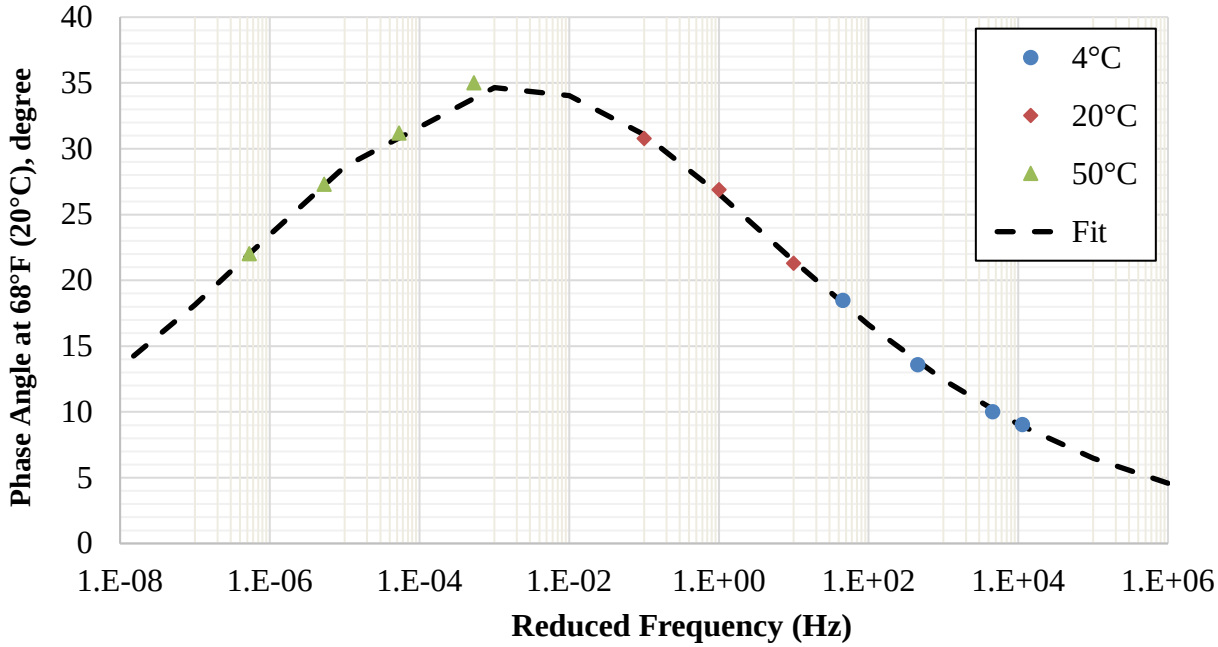


**Figure C.14. Phase angle of FL125_PMA(A) mixture at 68°F (20°C).**

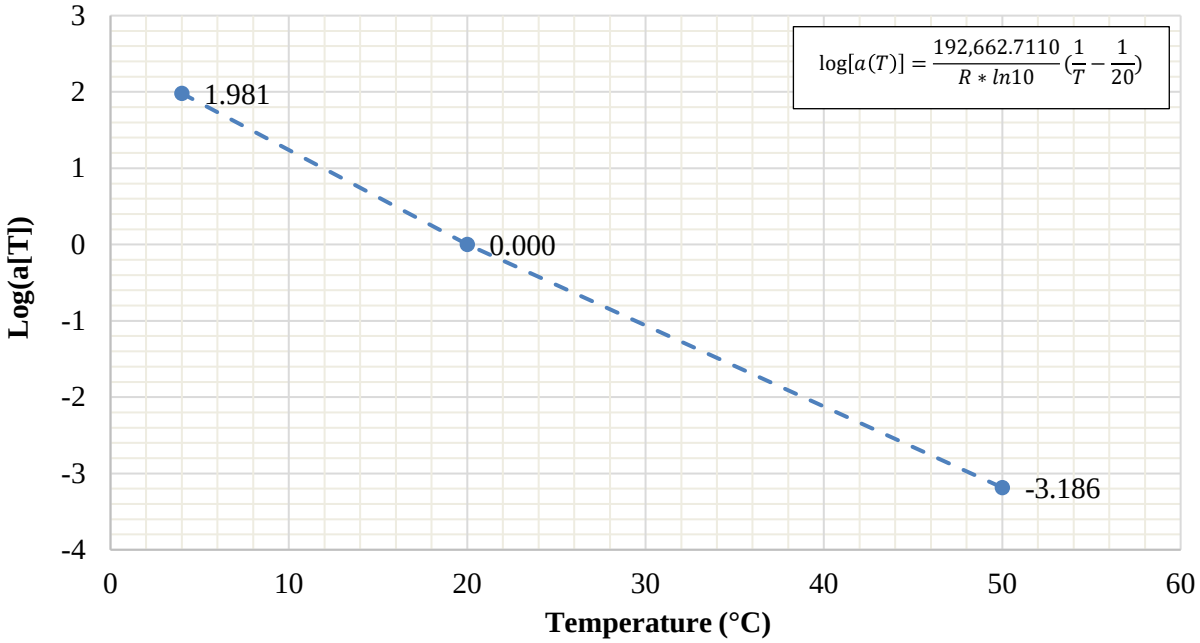


**Figure C.15. Log (a[T]) of FL125_PMA(A) mixture.**

**Table C.9. Dynamic Modulus Input Values for FL125_PMA(A) AC mix.**

| **E*, psi (MPa)** | **Frequency (Hz)** | | | | | |
|---|---|---|---|---|---|---|
| **Temperature, °F (°C)** | 0.1 | 0.5 | 1 | 5 | 10 | 25 |
| 14 (-10) | 2,034,061 (14,024) | 2,379,316 (16,405) | 2,515,240 (17,342) | 2,796,650 (19,282) | 2,902,693 (20,013) | 3,029,132 (20,885) |
| 40 (4) | 979,275 (6,752) | 1,339,161 (9,233) | 1,502,075 (10,356) | 1,881,278 (12,971) | 2,039,802 (14,064) | 2,240,711 (15,449) |
| 70 (21) | 261,138 (1,800) | 437,430 (3,016) | 535,501 (3,692) | 814,254 (5,641) | 953,967 (6,577) | 1,152,829 (7,948) |
| 100 (38) | 56,112 (387) | 102,308 (705) | 132,262 (912) | 235,127 (1,621) | 297,143 (2,049) | 398,332 (2,746) |
| 130 (54) | 15,344 (106) | 25,727 (177) | 32,709 (226) | 58,714 (405) | 76,037 (524) | 107,068 (738) |

**Table C.10. Phase Angle Input Values for FL125_PMA(A) AC mix.**

| **Phase Angle, °** | **Frequency (Hz)** | | | | | |
|---|---|---|---|---|---|---|
| **Temperature, °F (°C)** | 0.1 | 0.5 | 1 | 5 | 10 | 25 |
| 14 (-10) | 8.4 | 6.6 | 6.0 | 4.7 | 4.2 | 3.6 |
| 40 (4) | 18.6 | 15.4 | 14.1 | 11.4 | 10.4 | 9.1 |
| 70 (21) | 31.7 | 28.8 | 27.4 | 23.9 | 22.4 | 20.4 |
| 100 (38) | 33.7 | 34.7 | 34.7 | 33.9 | 33.2 | 31.9 |
| 130 (54) | 24.3 | 27.9 | 29.4 | 32.2 | 33.2 | 34.1 |

### C.1.6. FL125_PMA(B) AC Mix

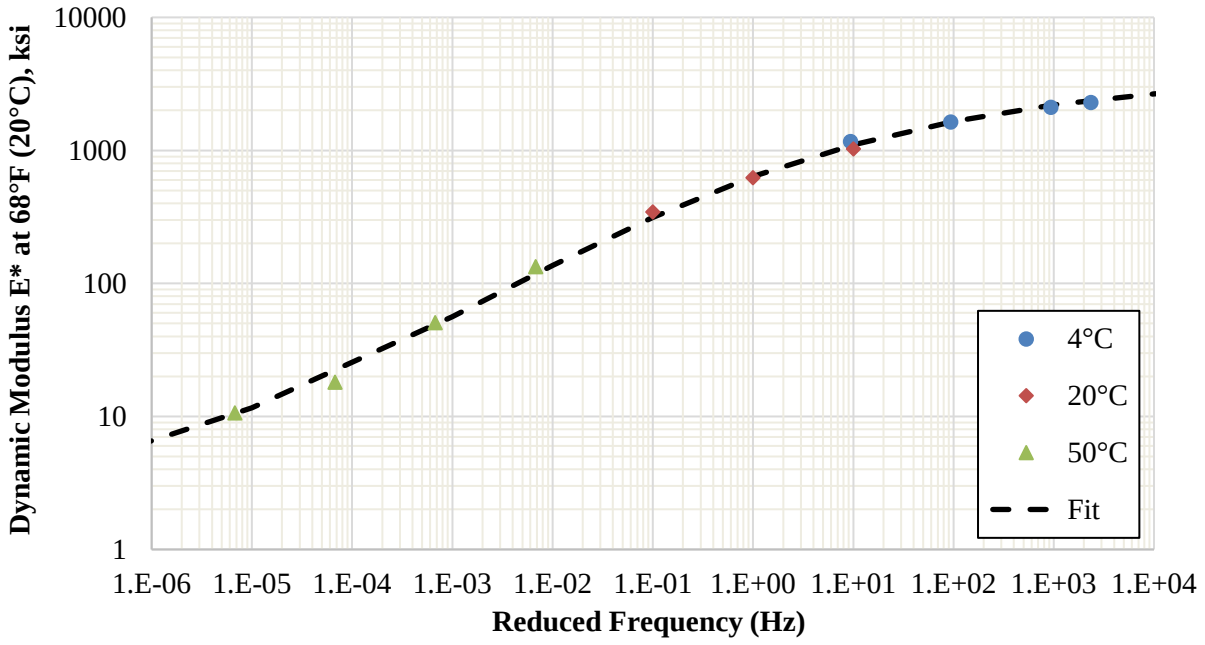


**Figure C.16. Dynamic modulus of FL125_PMA(B) mixture at 68°F (20°C).**

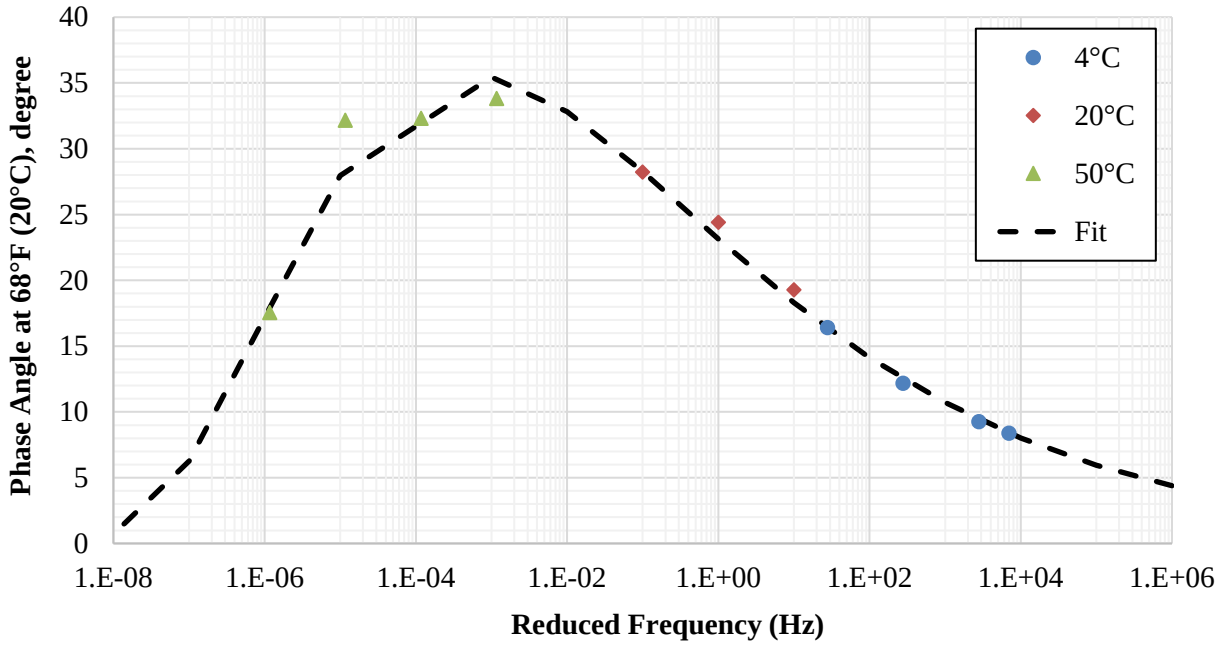


**Figure C.17. Phase angle of FL125_PMA(B) mixture at 68°F (20°C).**

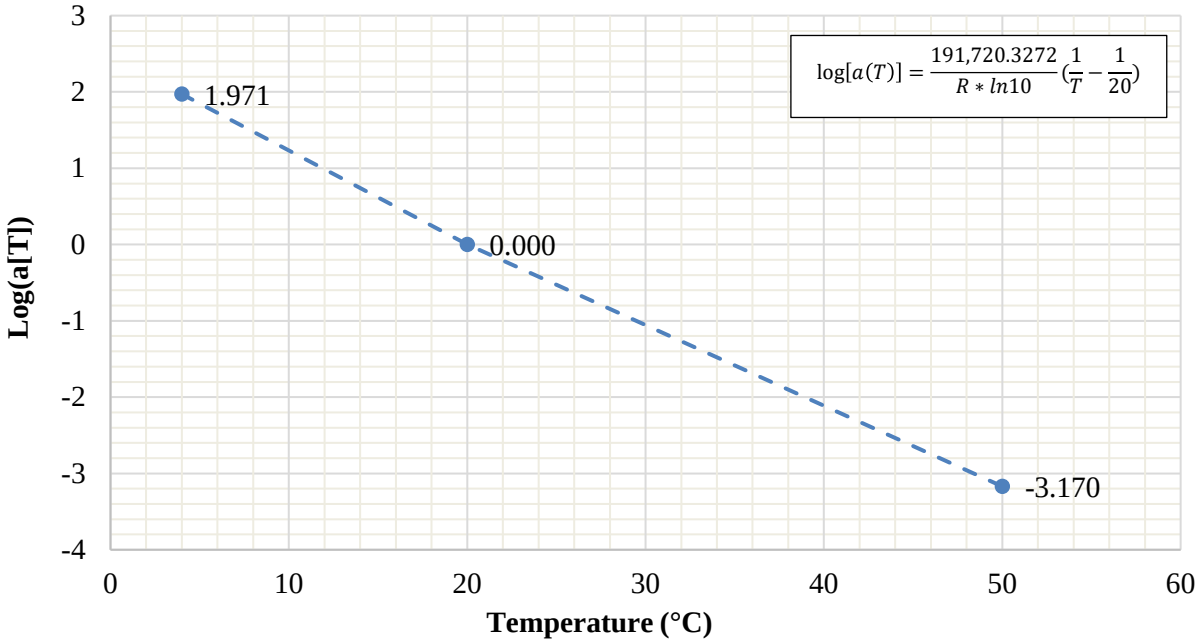


**Figure C.18. Log (a[T]) of FL125_PMA(B) mixture.**

**Table C.11. Dynamic Modulus Input Values for FL125_PMA(B) AC mix.**

| **E*, psi (MPa)** | **Frequency (Hz)** | | | | | |
|---|---|---|---|---|---|---|
| **Temperature, °F (°C)** | 0.1 | 0.5 | 1 | 5 | 10 | 25 |
| 14 (-10) | 2,141,540 (14,765) | 2,485,273 (17,135) | 2,618,831 (18,056) | 2,892,034 (19,940) | 2,993,772 (20,641) | 3,114,157 (21,471) |
| 40 (4) | 1,057,697 (7,293) | 1,436,157 (9,902) | 1,605,099 (11,067) | 1,992,677 (13,739) | 2,152,370 (14,840) | 2,352,778 (16,222) |
| 70 (21) | 283,594 (1,955) | 477,553 (3,293) | 584,798 (4,032) | 886,518 (6,112) | 1,035,945 (7,413) | 1,246,573 (8,595) |
| 100 (38) | 58,832 (406) | 109,489 (755) | 142,600 (983) | 256,744 (1,770) | 325,541 (2,245) | 437,447 (3,016) |
| 130 (54) | 15,396 (106) | 26,344 (182) | 33,819 (233) | 62,104 (428) | 81,172 (560) | 115,560 (797) |

**Table C.12. Phase Angle Input Values for FL125_PMA(B) AC mix.**

| **Phase Angle, °** | **Frequency (Hz)** | | | | | |
|---|---|---|---|---|---|---|
| **Temperature, °F (°C)** | 0.1 | 0.5 | 1 | 5 | 10 | 25 |
| 14 (-10) | 8.4 | 6.9 | 6.3 | 5.1 | 4.6 | 4.1 |
| 40 (4) | 16.7 | 13.9 | 12.8 | 10.5 | 9.6 | 8.6 |
| 70 (21) | 29.1 | 25.5 | 24.0 | 20.5 | 19.0 | 17.2 |
| 100 (38) | 35.5 | 35.0 | 34.3 | 31.7 | 30.3 | 28.4 |
| 130 (54) | 23.4 | 30.0 | 32.1 | 35.0 | 35.5 | 35.4 |

### C.1.7. FL125_HP(A) AC Mix

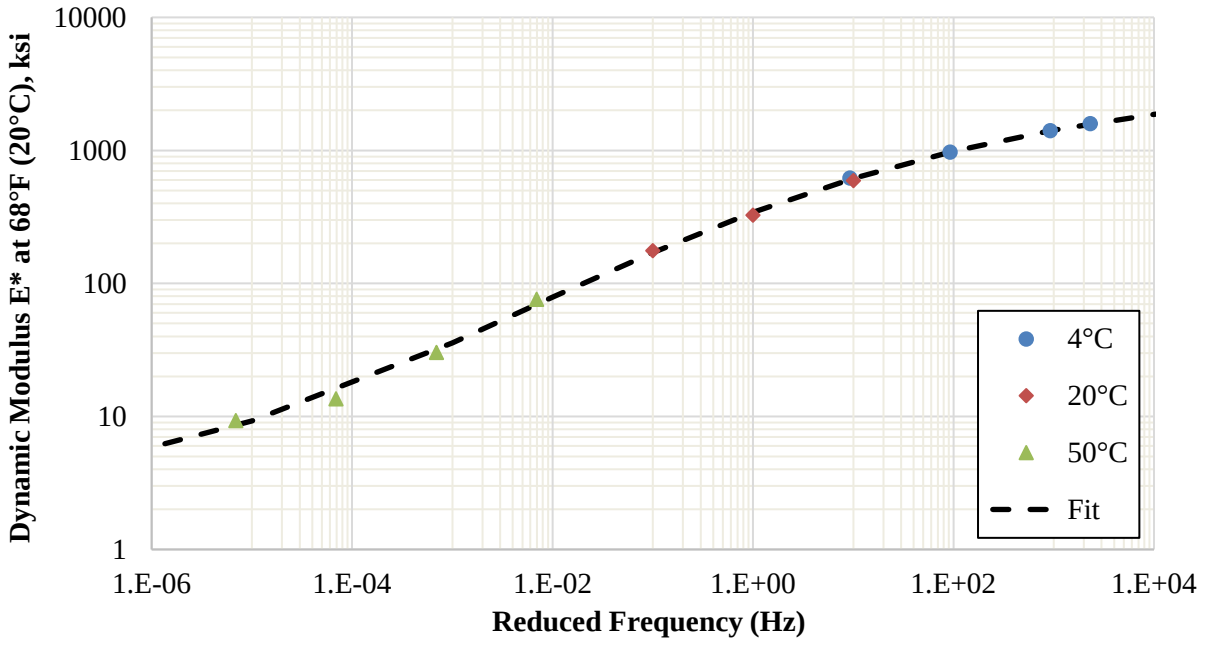


**Figure C.19. Dynamic modulus of FL125_HP(A) mixture at 68°F (20°C).**

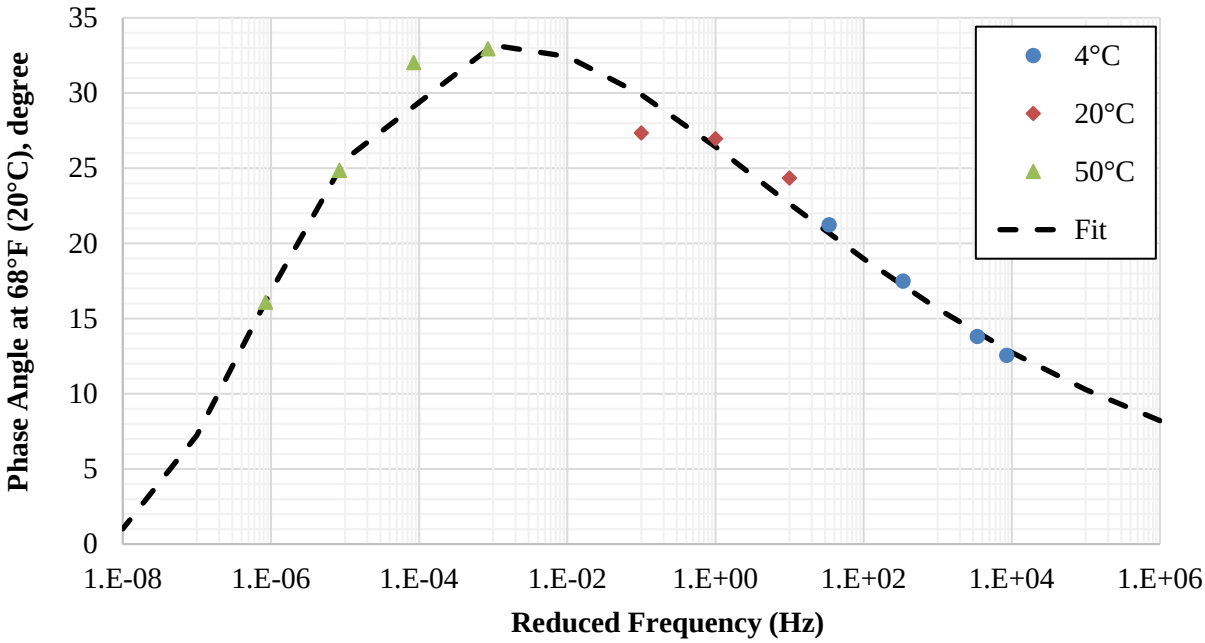


**Figure C.20. Phase angle of FL125_HP(A) mixture at 68°F (20°C).**

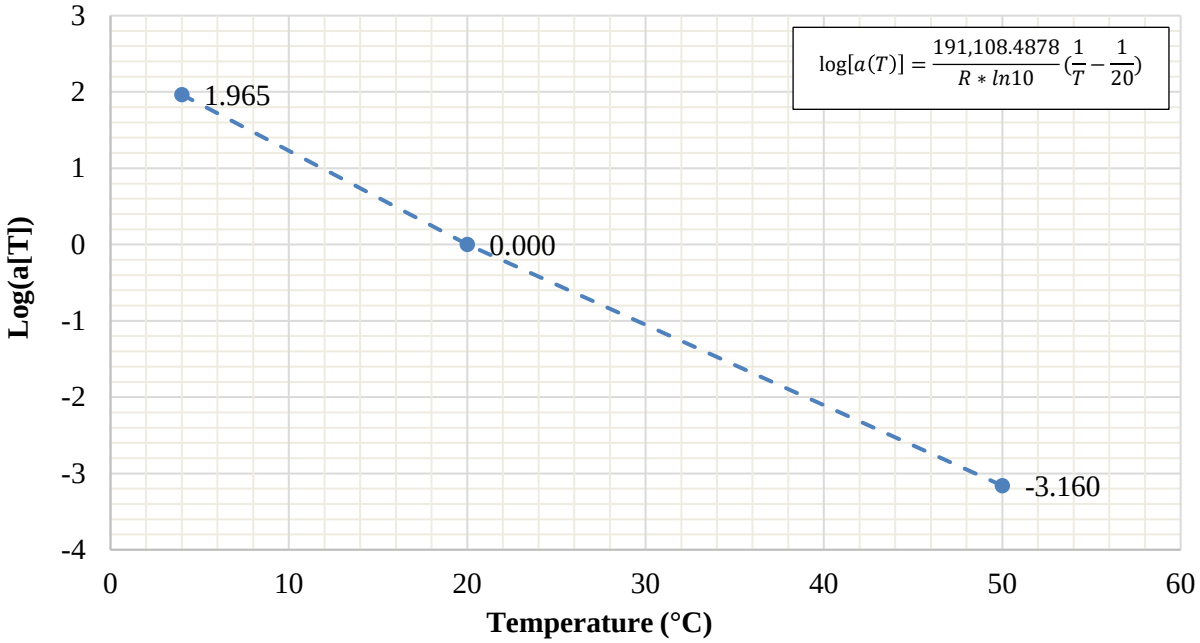


**Figure C.21. Log (a[T]) of FL125_HP(A) mixture.**

**Table C.13. Dynamic Modulus Input Values for FL125_HP(A) AC mix.**

| **E*, psi (MPa)** | **Frequency (Hz)** | | | | | |
|---|---|---|---|---|---|---|
| **Temperature, °F (°C)** | 0.1 | 0.5 | 1 | 5 | 10 | 25 |
| 14 (-10) | 1,366,334 (9,421) | 1,681,304 (11,592) | 1,815,860 (12,520) | 2,117,573 (14,600) | 2,240,777 (15,450) | 2,395,836 (16,519) |
| 40 (4) | 585,609 (4,038) | 830,066 (5,723) | 948,295 (6,538) | 1,244,655 (8,582) | 1,378,478 (9,504) | 1,557,779 (10,741) |
| 70 (21) | 155,026 (1,069) | 256,842 (1,771) | 314,643 (2,169) | 485,048 (3,344) | 574,369 (3,960) | 706,587 (4,872) |
| 100 (38) | 37,199 (256) | 64,710 (446) | 82,224 (567) | 141,734 (977) | 177,584 (1,224) | 236,501 (1,631) |
| 130 (54) | 11,750 (81) | 18,549 (128) | 23,014 (159) | 39,180 (270) | 49,691 (343) | 68,223 (470) |

**Table C.14. Phase Angle Input Values for FL125_HP(A) AC mix.**

| **Phase Angle, °** | **Frequency (Hz)** | | | | | |
|---|---|---|---|---|---|---|
| **Temperature, °F (°C)** | 0.1 | 0.5 | 1 | 5 | 10 | 25 |
| 14 (-10) | 12.7 | 11.0 | 10.3 | 8.8 | 8.2 | 7.5 |
| 40 (4) | 20.9 | 18.4 | 17.4 | 15.2 | 14.3 | 13.1 |
| 70 (21) | 30.4 | 28.1 | 27.0 | 24.4 | 23.3 | 21.8 |
| 100 (38) | 32.5 | 33.2 | 33.1 | 32.1 | 31.4 | 30.2 |
| 130 (54) | 20.5 | 26.2 | 28.2 | 31.4 | 32.3 | 33.0 |

### C.1.8. FL125_HP(B) AC Mix

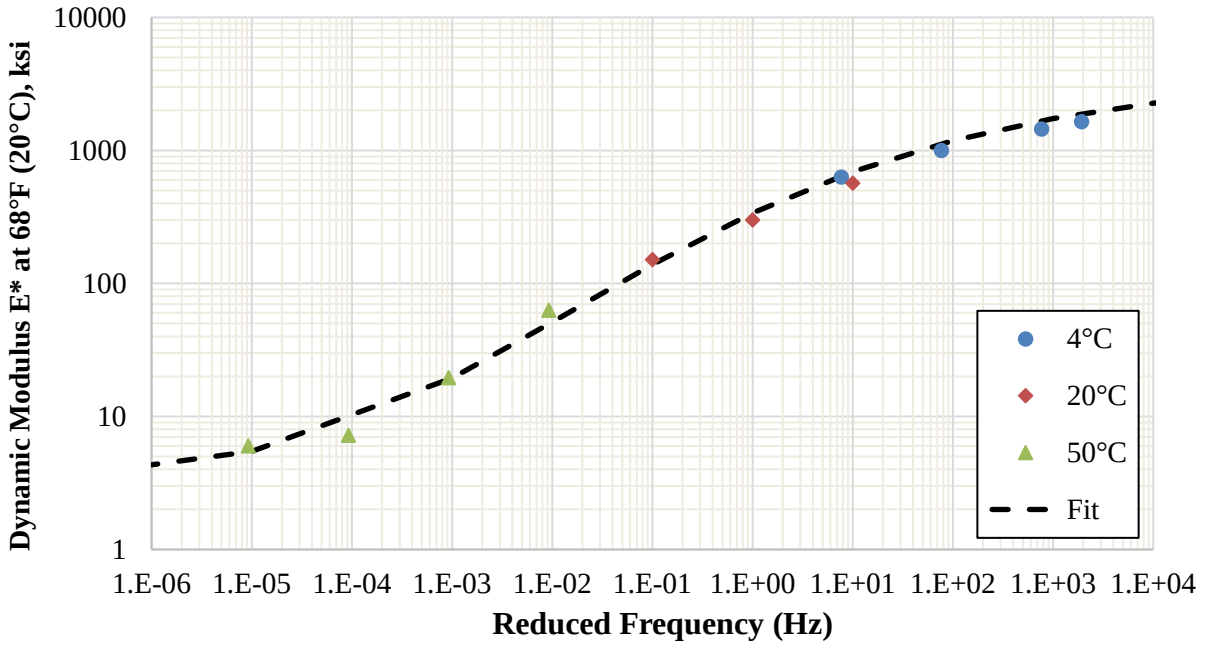


**Figure C.22. Dynamic modulus of FL125_HP(B) mixture at 68°F (20°C).**

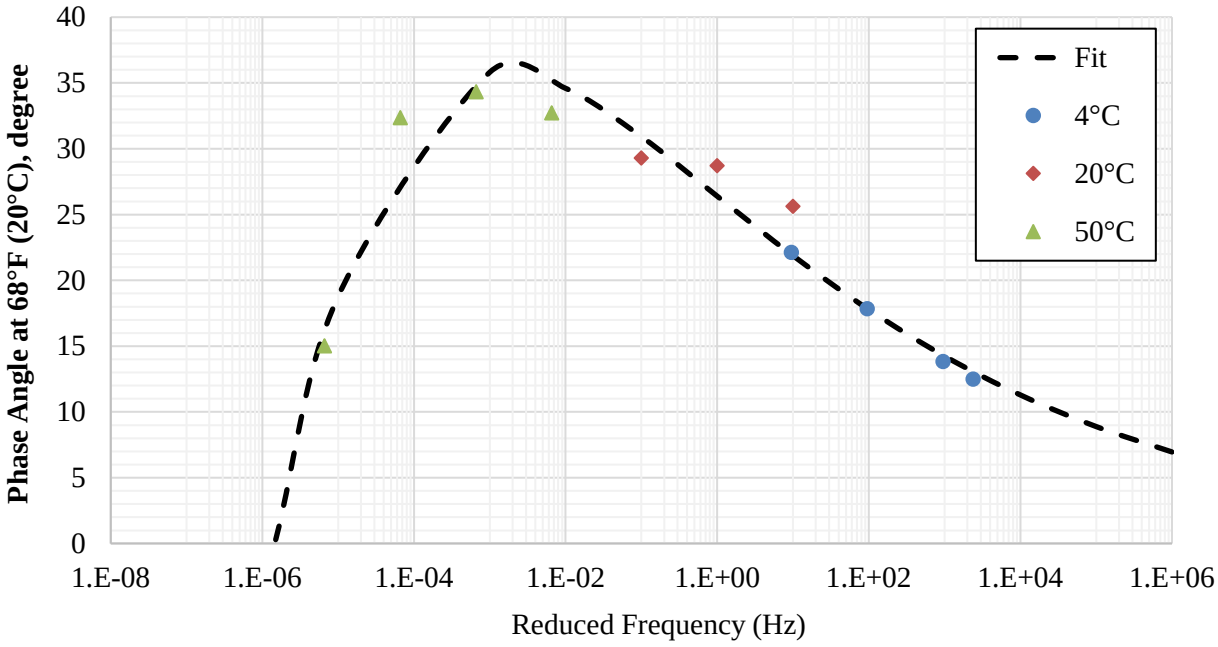


**Figure C.23. Phase angle of FL125_HP(B) mixture at 68°F (20°C).**

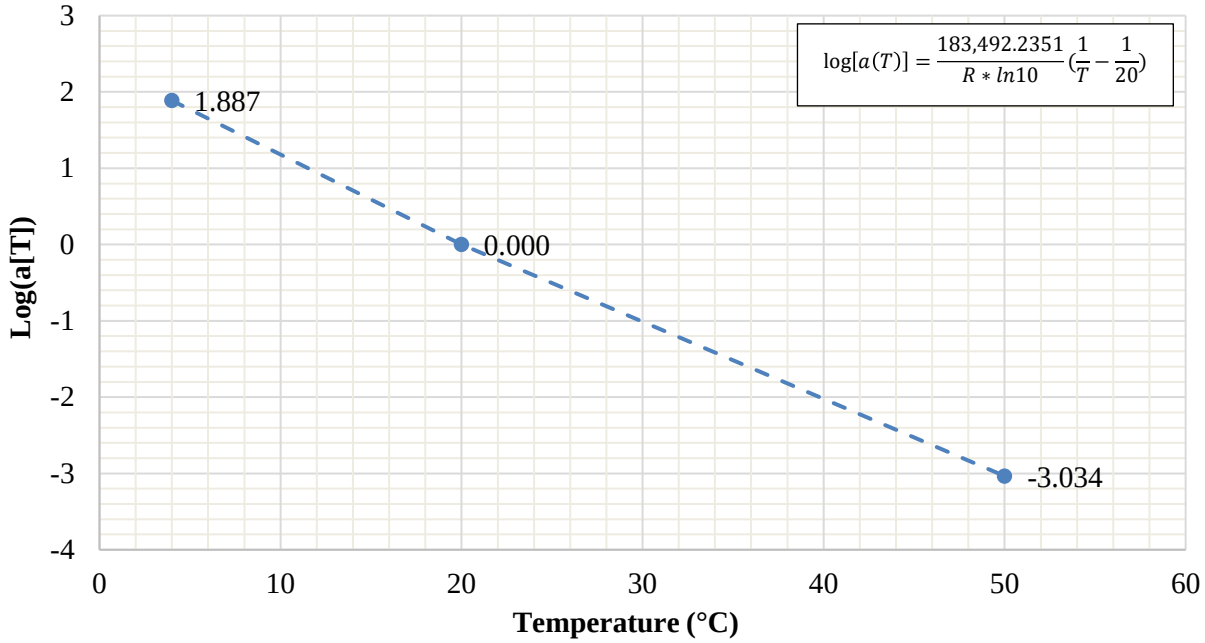


**Figure C.24. Log (a[T]) of FL125_HP(A) mixture.**

**Table C.15. Dynamic Modulus Input Values for FL125_HP(B) AC mix.**

| **E*, psi (MPa)** | **Frequency (Hz)** | | | | | |
|---|---|---|---|---|---|---|
| **Temperature, °F (°C)** | 0.1 | 0.5 | 1 | 5 | 10 | 25 |
| 14 (-10) | 1,584,600 (10,925) | 1,967,828 (13,568) | 2,125,421 (14,654) | 2,463,470 (16,985) | 2,594,957 (17,892) | 2,754,689 (18,993) |
| 40 (4) | 621,763 (4,287) | 940,140 (6,482) | 1,094,550 (7,547) | 1,475,754 (10,175) | 1,643,469 (11,331) | 1,862,650 (12,843) |
| 70 (21) | 123,313 (850) | 236,420 (1,630) | 305,886 (2,109) | 522,761 (3,604) | 640,382 (4,415) | 816,358 (5,629) |
| 100 (38) | 21,871 (151) | 43,149 (297) | 58,497 (403) | 117,876 (813) | 157,523 (1,086) | 226,964 (1,565) |
| 130 (54) | 6,930 (48) | 10,643 (73) | 13,377 (92) | 24,732 (171) | 33,086 (228) | 49,262 (340) |

**Table C.16. Phase Angle Input Values for FL125_HP(B) AC mix.**

| **Phase Angle, °** | **Frequency (Hz)** | | | | | |
|---|---|---|---|---|---|---|
| **Temperature, °F (°C)** | 0.1 | 0.5 | 1 | 5 | 10 | 25 |
| 14 (-10) | 14.5 | 12.4 | 11.5 | 9.8 | 9.1 | 8.3 |
| 40 (4) | 22.2 | 19.3 | 18.1 | 15.5 | 14.5 | 13.2 |
| 70 (21) | 31.5 | 28.4 | 27.0 | 23.8 | 22.4 | 20.7 |
| 100 (38) | 35.8 | 35.2 | 34.5 | 32.0 | 30.7 | 29.0 |
| 130 (54) | 25.3 | 32.6 | 34.3 | 35.9 | 35.8 | 35.1 |

### C.1.9. GA95_PMA(A) AC Mix

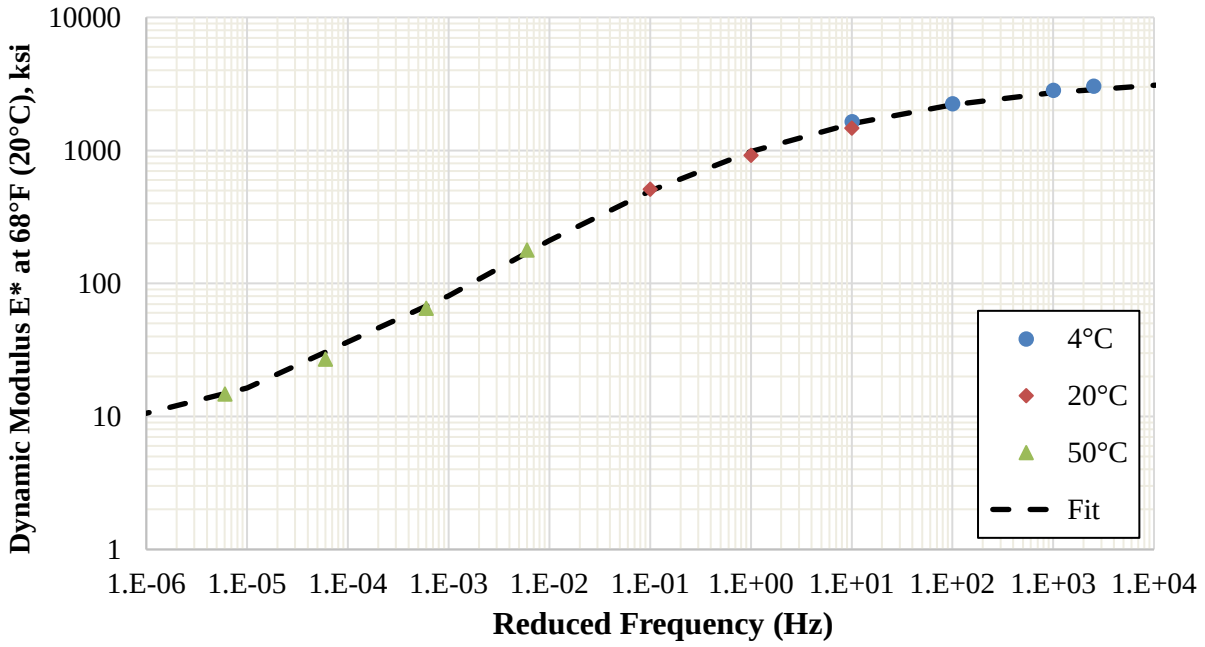


**Figure C.25. Dynamic modulus of GA95_PMA(A) mixture at 68°F (20°C).**

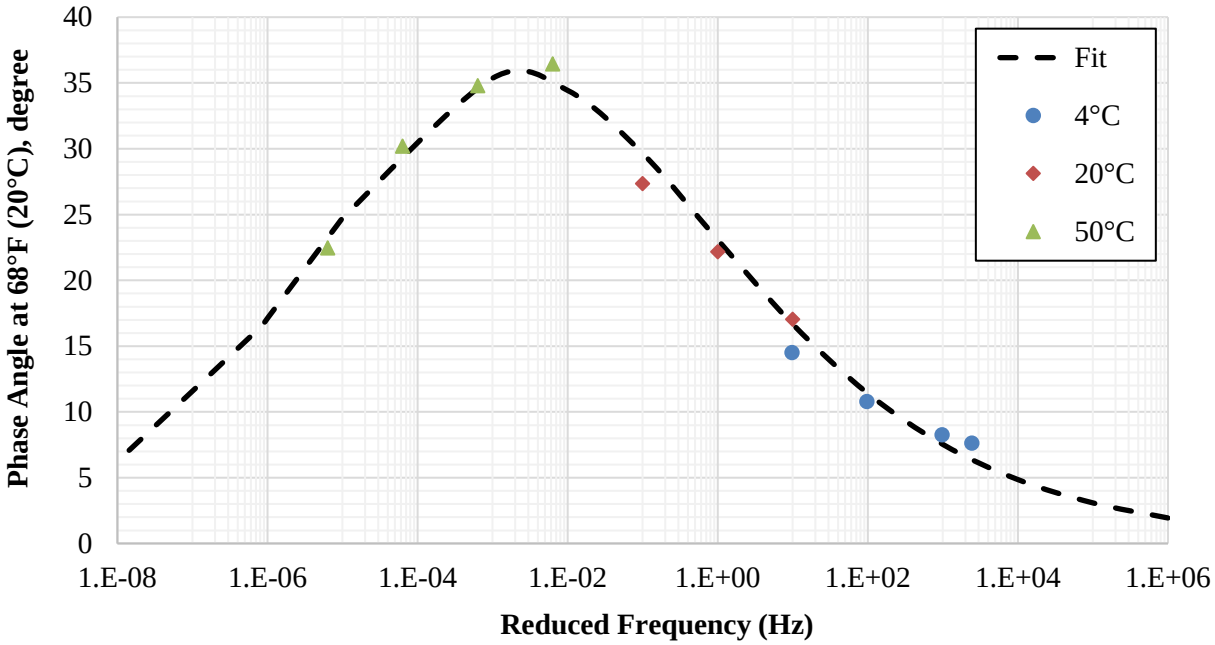


**Figure C.26. Phase angle of GA95_PMA(A) mixture at 68°F (20°C).**

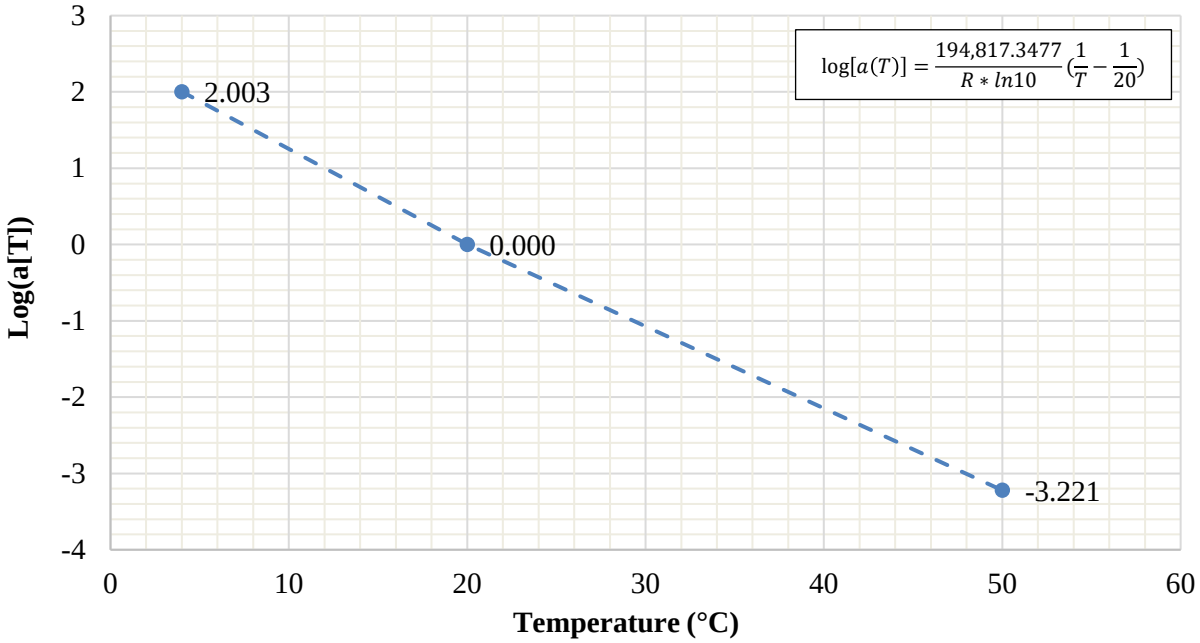


**Figure C.27. Log (a[T]) of GA95_PMA(A) mixture.**

**Table C.17. Dynamic Modulus Input Values for GA95_PMA(A) AC mix.**

| **E*, psi (MPa)** | **Frequency (Hz)** | | | | | |
|---|---|---|---|---|---|---|
| **Temperature, °F (°C)** | 0.1 | 0.5 | 1 | 5 | 10 | 25 |
| 14 (-10) | 2,692,695 (18,565) | 2,977,217 (20,527) | 3,080,088 (21,236) | 3,277,656 (22,599) | 3,346,855 (23,076) | 3,425,645 (23,619) |
| 40 (4) | 1,553,561 (10,711) | 1,989,227 (13,715) | 2,167,618 (14,945) | 2,544,385 (17,543) | 2,687,613 (18,530) | 2,858,202 (19,707) |
| 70 (21) | 448,840 (3,095)) | 748,813 (5,163) | 905,982 (6,247) | 1,317,386 (9,083) | 1,506,022 (13,384) | 1,756,950 (12,114) |
| 100 (38) | 82,120 (566) | 161,032 (1,110) | 213,846 (1,474) | 396,036 (2,731) | 503,868 (3,474) | 674,584 (4,651) |
| 130 (54) | 20,318 (140) | 34,250 (236) | 44,333 (306) | 84,896 (585) | 113,518 (783) | 166,437 (1,148) |

**Table C.18. Phase Angle Input Values for GA95_PMA(A) AC mix.**

| **Phase Angle, °** | **Frequency (Hz)** | | | | | |
|---|---|---|---|---|---|---|
| **Temperature, °F (°C)** | 0.1 | 0.5 | 1 | 5 | 10 | 25 |
| 14 (-10) | 7.8 | 5.7 | 5.0 | 3.7 | 3.2 | 2.7 |
| 40 (4) | 17.1 | 13.2 | 11.7 | 8.8 | 7.8 | 6.5 |
| 70 (21) | 30.4 | 26.0 | 24.0 | 19.3 | 17.4 | 15.1 |
| 100 (38) | 35.4 | 35.1 | 34.3 | 31.2 | 29.5 | 26.9 |
| 130 (54) | 27.6 | 32.1 | 33.6 | 35.5 | 35.6 | 35.0 |

### C.1.10. GA95_PMA(B) AC Mix

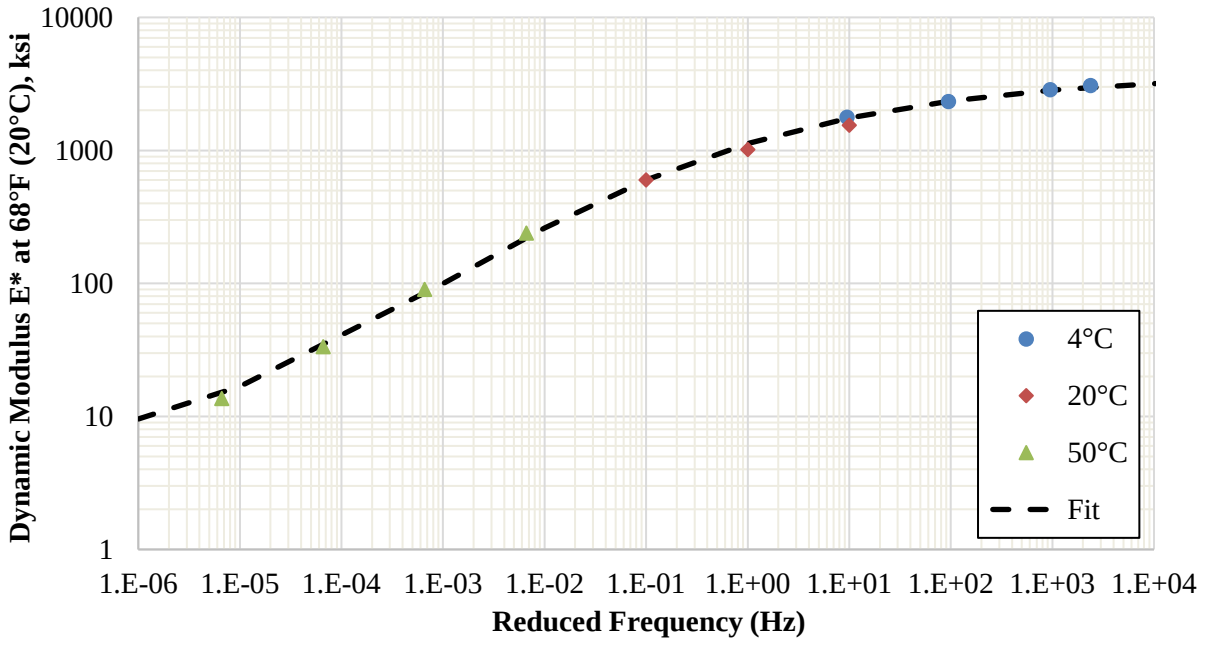


**Figure C.28. Dynamic modulus of GA95_PMA(B) mixture at 68°F (20°C).**

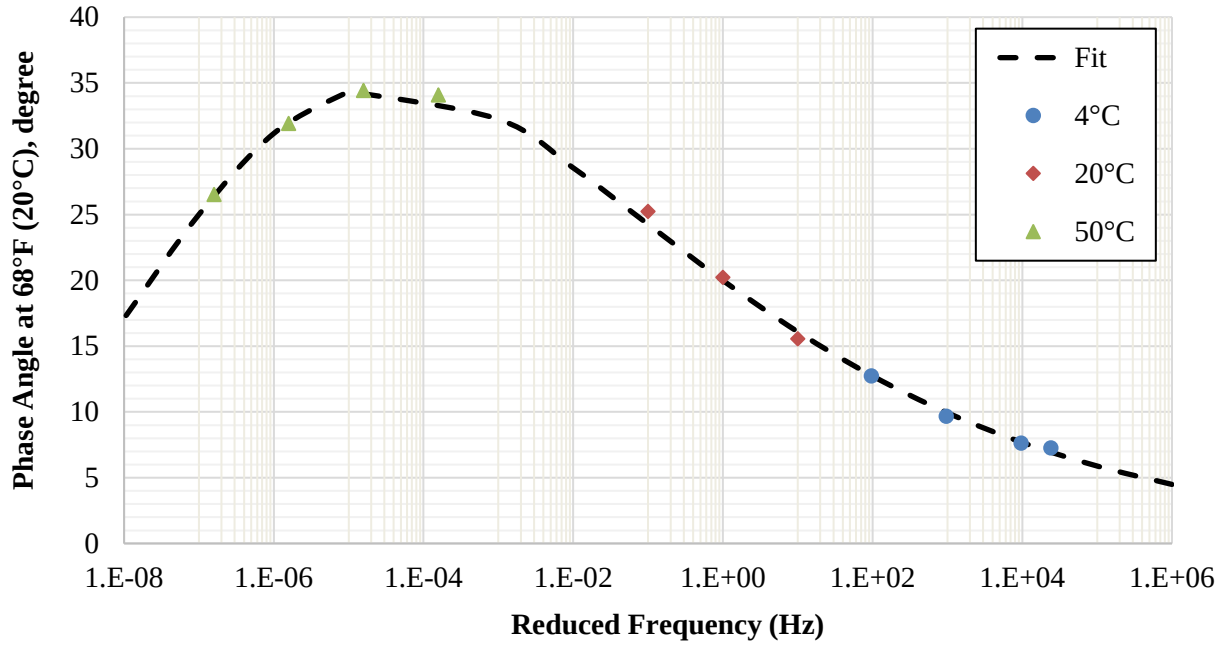


**Figure C.29. Phase angle of GA95_PMA(B) mixture at 68°F (20°C).**

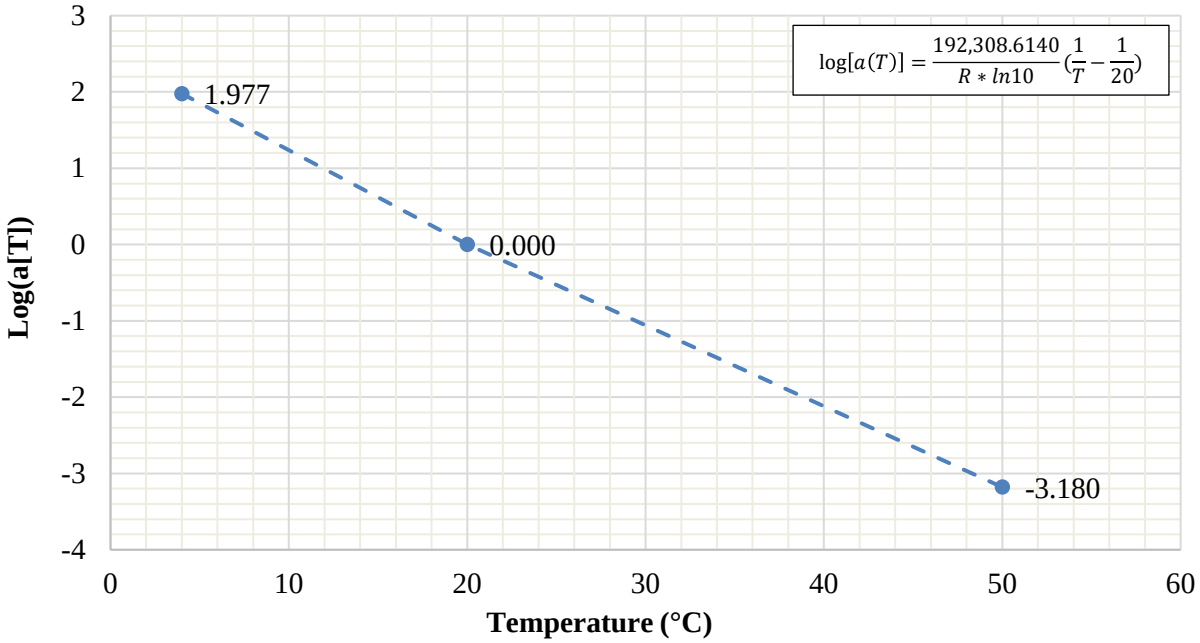


**Figure C.30. Log (a[T]) of GA95_PMA(B) mixture.**

**Table C.19. Dynamic Modulus Input Values for GA95_PMA(B) AC mix.**

| **E*, psi (MPa)** | **Frequency (Hz)** | | | | | |
|---|---|---|---|---|---|---|
| **Temperature, °F (°C)** | 0.1 | 0.5 | 1 | 5 | 10 | 25 |
| 14 (-10) | 2,795,904 (19,277) | 3,059,694 (21,096) | 3,153,911 (21,745) | 3,333,056 (22,981) | 3,395,212 (23,409) | 3,465,580 (23,894) |
| 40 (4) | 1,707,863 (11,775) | 2,138,755 (14,746) | 2,311,237 (15,935) | 2,668,631 (18,400) | 2,802,143 (19,320) | 2,959,511 (20,405) |
| 70 (21) | 544,283 (3,753) | 881,873 (6,080) | 1,052,731 (7,258) | 1,484,918 (10,238) | 1,676,971 (11,562) | 1,927,363 (13,289) |
| 100 (38) | 103,538 (714) | 205,055 (1,414) | 271,360 (1,871) | 492,135 (3,393) | 618,193 (4,262) | 812,316 (5,601) |
| 130 (54) | 22,648 (156) | 41,376 (285) | 54,995 (379) | 109,467 (755) | 147,370 (1,016) | 216,229 (1,491) |

**Table C.20. Phase Angle Input Values for GA95_PMA(B) AC mix.**

| **Phase Angle, °** | **Frequency (Hz)** | | | | | |
|---|---|---|---|---|---|---|
| **Temperature, °F (°C)** | 0.1 | 0.5 | 1 | 5 | 10 | 25 |
| 14 (-10) | 6.1 | 5.0 | 4.6 | 3.8 | 3.5 | 3.1 |
| 40 (4) | 13.0 | 11.0 | 10.2 | 8.5 | 7.9 | 7.1 |
| 70 (21) | 25.1 | 22.1 | 20.8 | 18.0 | 16.8 | 15.4 |
| 100 (38) | 34.4 | 33.0 | 32.1 | 29.6 | 28.4 | 26.7 |
| 130 (54) | 28.8 | 32.3 | 33.4 | 34.7 | 34.8 | 34.5 |

### C.1.11. GA95_HP (A) AC Mix

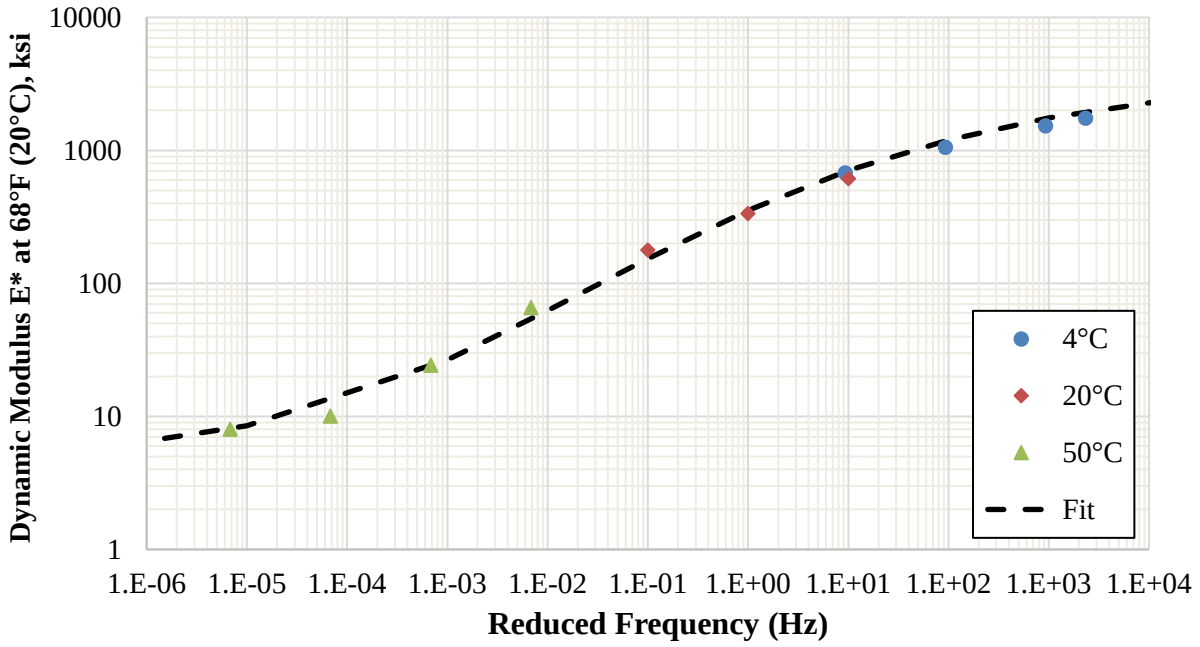


**Figure C.28. Dynamic modulus of GA95_HP(A) mixture at 68°F (20°C).**

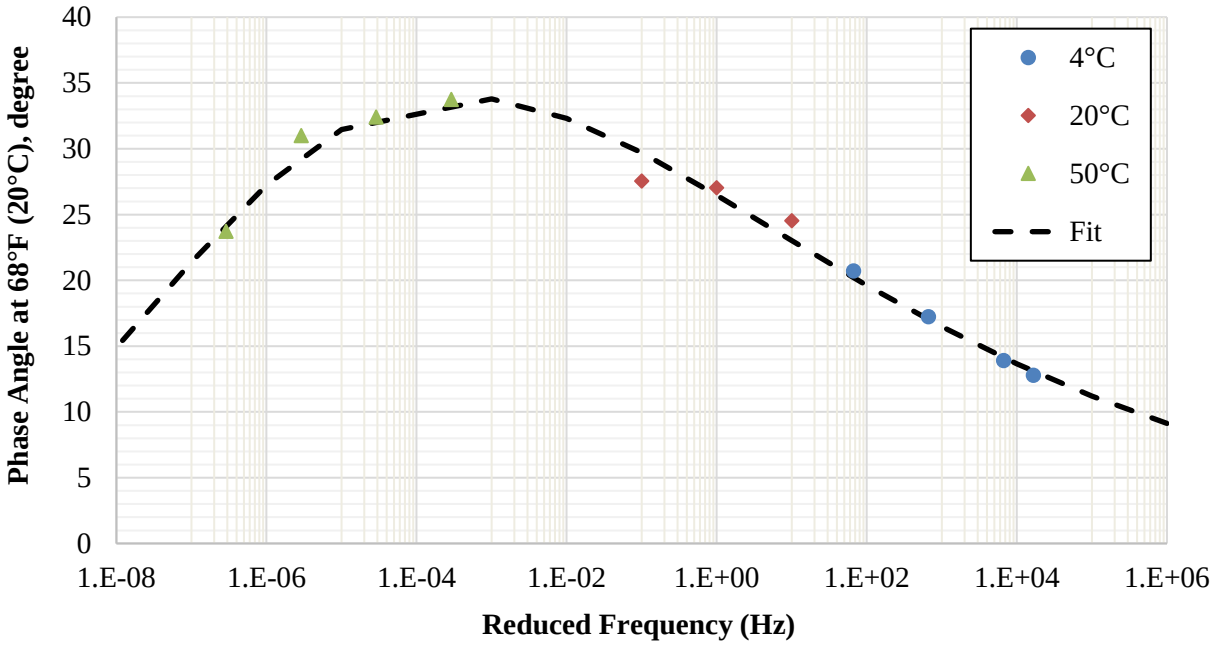


**Figure C.29. Phase angle of GA95_HP(A) mixture at 68°F (20°C).**

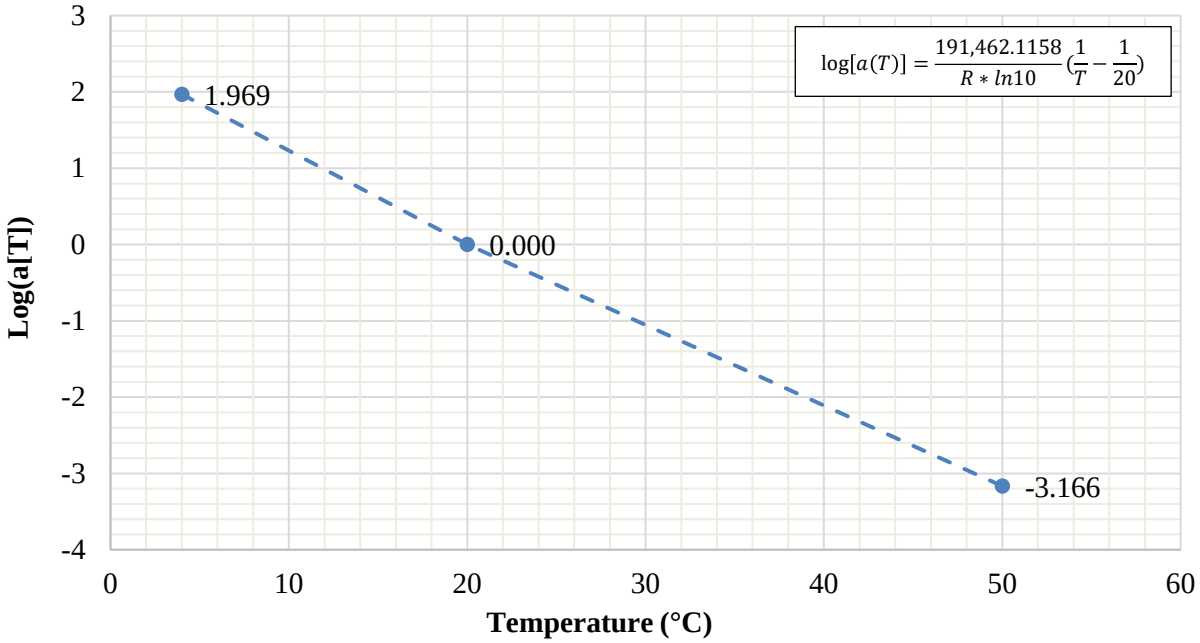


**Figure C.30. Log (a[T]) of GA95_HP(A) mixture.**

**Table C.21. Dynamic Modulus Input Values for GA95_HP(A) AC mix.**

| **E*, psi (MPa)** | **Frequency (Hz)** | | | | | |
|---|---|---|---|---|---|---|
| **Temperature, °F (°C)** | 0.1 | 0.5 | 1 | 5 | 10 | 25 |
| 14 (-10) | 1,690,624 (11,656) | 2,070,626 (14,276) | 2,224,985 (15,341) | 2,552,223 (17,597) | 2,678,006 (16,464) | 2,829,598 (19,509) |
| 40 (4) | 668,930 (4,612)) | 994,007 (6,853) | 1,150,729 (7,934) | 1,535,431 (10,586) | 1,703,696 (11,747) | 1,922,626 (13,256) |
| 70 (21) | 137,104 (945) | 250,923 (1,730) | 320,147 (2,270) | 535,609 (3,693) | 652,534 (4,499) | 827,804 (5,708) |
| 100 (38) | 27,789 (192) | 49,958 (344) | 65,313 (450) | 122,906 (847) | 160,718 (1,108) | 226,602 (1,562) |
| 130 (54) | 10,037 (69) | 14,441 (100) | 17,471 (120) | 29,222 (201) | 37,432 (258) | 52,827 (364) |

**Table C.22. Phase Angle Input Values for GA95_HP(A) AC mix.**

| **Phase Angle, °** | **Frequency (Hz)** | | | | | |
|---|---|---|---|---|---|---|
| **Temperature, °F (°C)** | 0.1 | 0.5 | 1 | 5 | 10 | 25 |
| 14 (-10) | 12.2 | 10.6 | 10.0 | 8.6 | 8.1 | 7.4 |
| 40 (4) | 20.5 | 18.2 | 17.3 | 15.2 | 14.4 | 13.3 |
| 70 (21) | 30.3 | 28.1 | 27.1 | 24.7 | 23.7 | 22.3 |
| 100 (38) | 33.8 | 33.9 | 33.6 | 32.5 | 31.9 | 30.8 |
| 130 (54) | 26.5 | 29.8 | 31.0 | 32.9 | 33.5 | 33.9 |

### C.1.12. GA95_HP (B) AC Mix

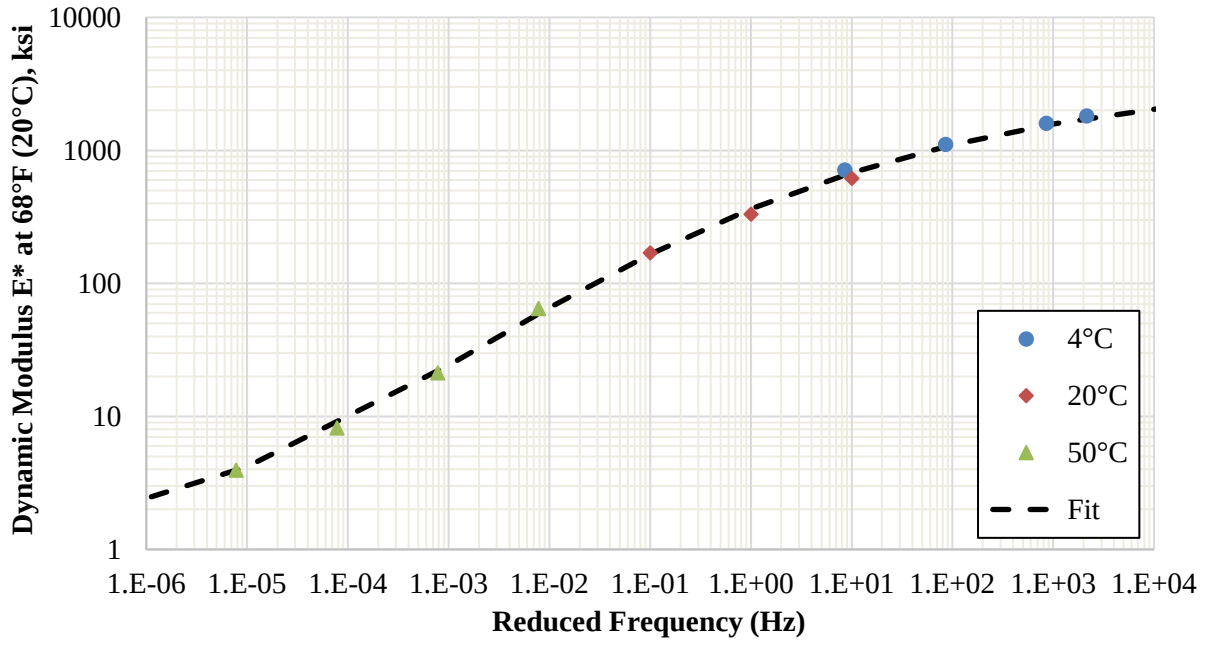


**Figure C.31. Dynamic modulus of GA95_HP(B) mixture at 68°F (20°C).**

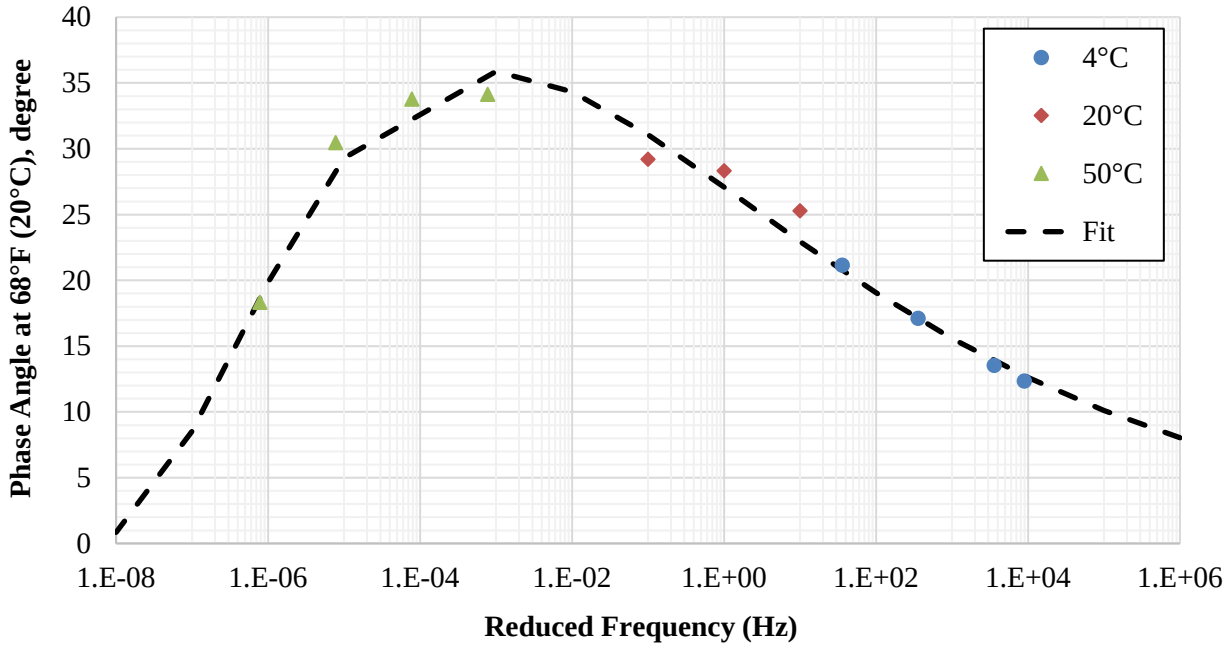


**Figure C.32. Phase angle of GA95_HP(B) mixture at 68°F (20°C).**

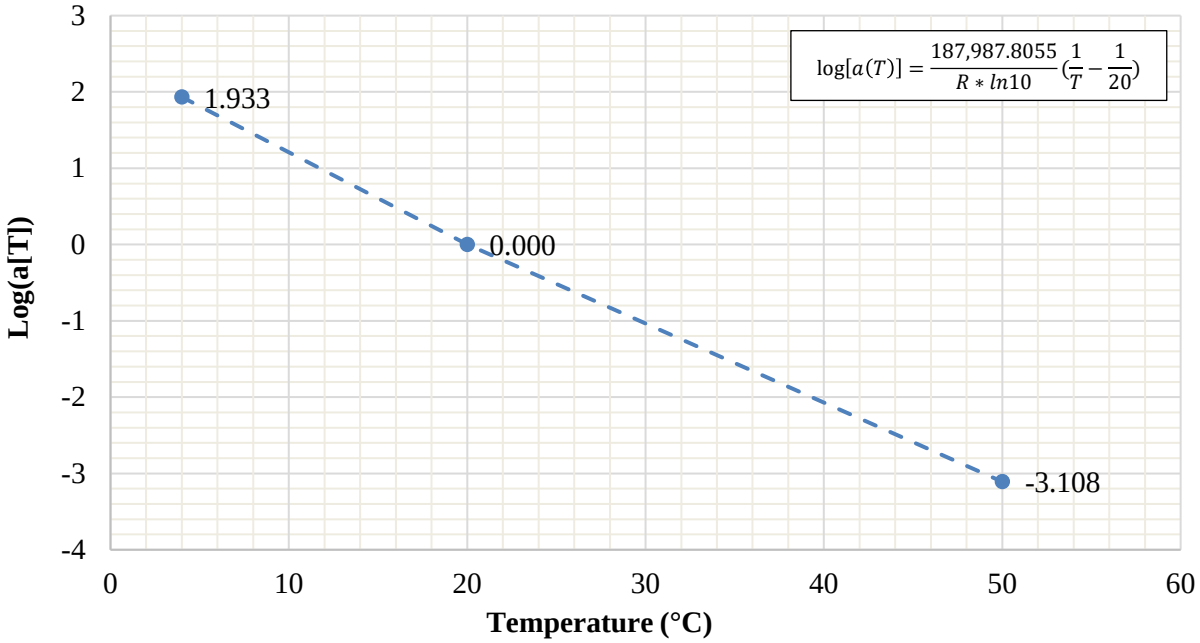


**Figure C.33. Log (a[T]) of GA95_HP(B) mixture.**

**Table C.23. Dynamic Modulus Input Values for GA95_HP(B) AC mix.**

| **E*, psi (MPa)** | **Frequency (Hz)** | | | | | |
|---|---|---|---|---|---|---|
| **Temperature, °F (°C)** | 0.1 | 0.5 | 1 | 5 | 10 | 25 |
| 14 (-10) | 1,488,799 (10,265) | 1,820,909 (12,555) | 1,959,715 (13,512) | 2,264,236 (15,611) | 2,385,901 (16,450) | 2,536,789 (17,491) |
| 40 (4) | 636,248 (4,387) | 914,601 (6,306) | 1,047,226 (7,220) | 1,373,178 (9,468) | 1,517,226 (10,461) | 1,707,143 (11,770) |
| 70 (21) | 148,419 (1,023) | 264,866 (1,826) | 332,137 (2,290) | 531,347 (3,664) | 635,330 (4,380) | 787,998 (5,433) |
| 100 (38) | 26,422 (182) | 53,209 (367) | 71,475 (493) | 137,184 (946) | 178,291 (1,229) | 247,064 (1,703) |
| 130 (54) | 5,962 (41) | 10,920 (75) | 14,520 (100) | 29,007 (200) | 39,253 (271) | 58,327 (402) |

**Table C.24. Phase Angle Input Values for GA95_HP(B) AC mix.**

| **Phase Angle, °** | **Frequency (Hz)** | | | | | |
|---|---|---|---|---|---|---|
| **Temperature, °F (°C)** | 0.1 | 0.5 | 1 | 5 | 10 | 25 |
| 14 (-10) | 12.5 | 10.7 | 10.0 | 8.5 | 8.0 | 7.3 |
| 40 (4) | 21.0 | 18.4 | 17.3 | 15.0 | 14.1 | 12.9 |
| 70 (21) | 31.7 | 29.0 | 27.8 | 24.9 | 23.6 | 22.0 |
| 100 (38) | 35.6 | 35.8 | 35.4 | 33.9 | 32.9 | 31.6 |
| 130 (54) | 23.5 | 29.6 | 31.6 | 34.7 | 35.4 | 35.9 |

### C.1.13. GA125_PMA(A) AC Mix

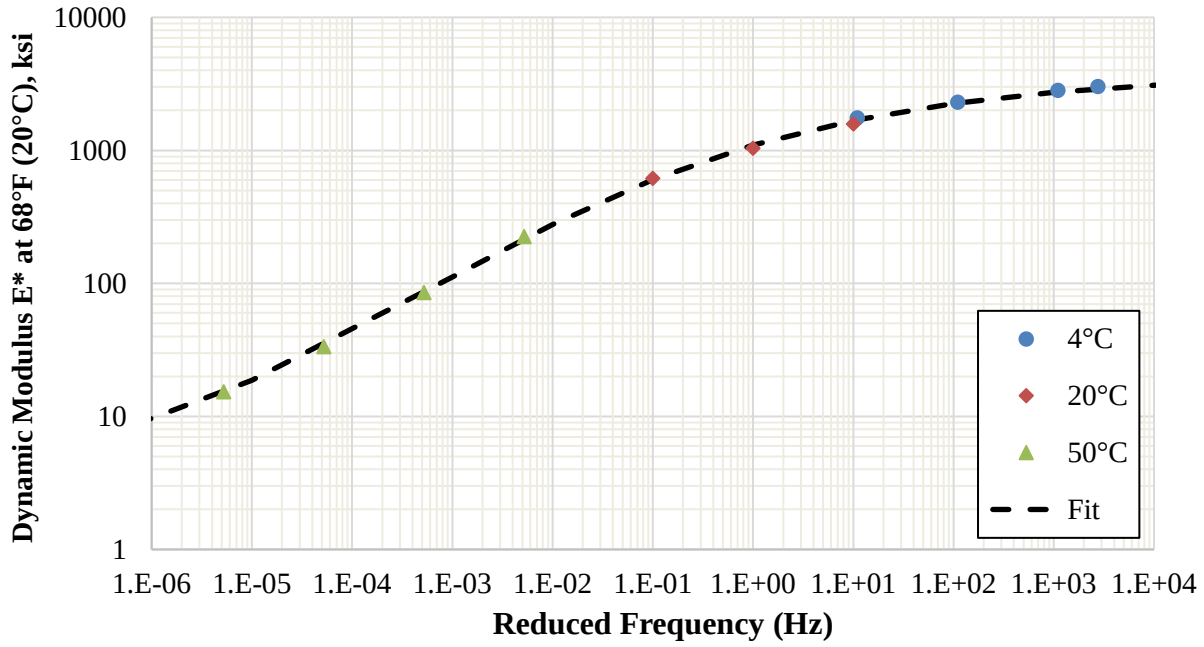


**Figure C.34. Dynamic modulus of GA125_PMA(A) mixture at 68°F (20°C).**

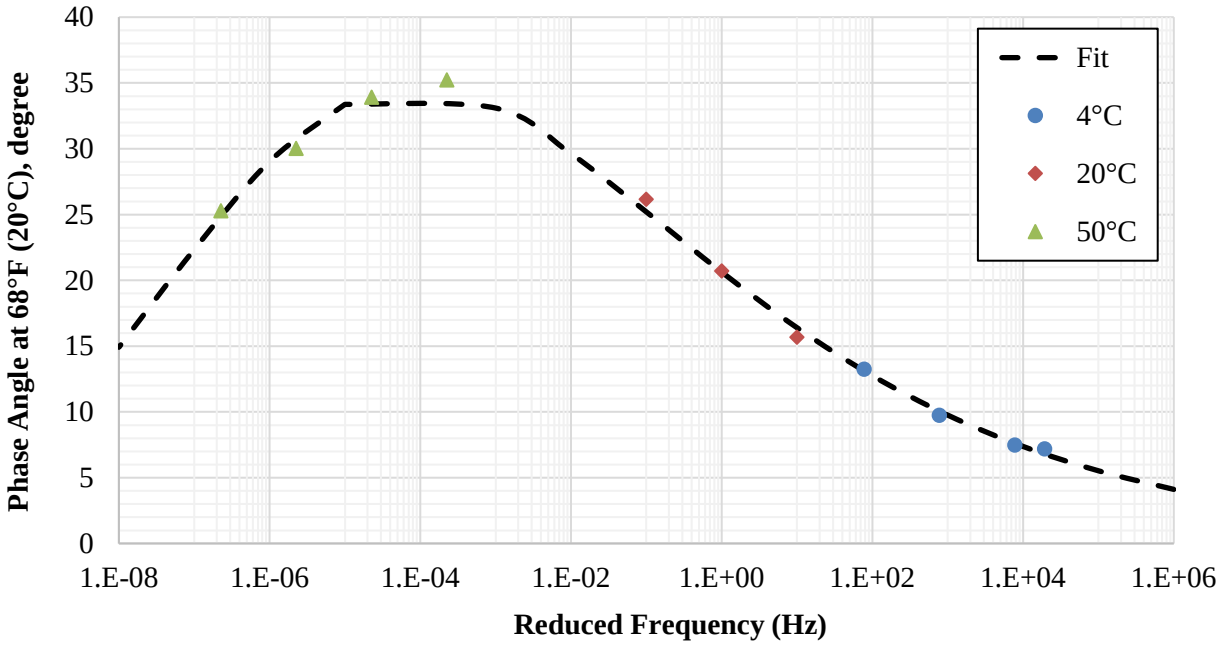


**Figure C.35. Phase angle of GA125_PMA(A) mixture at 68°F (20°C).**

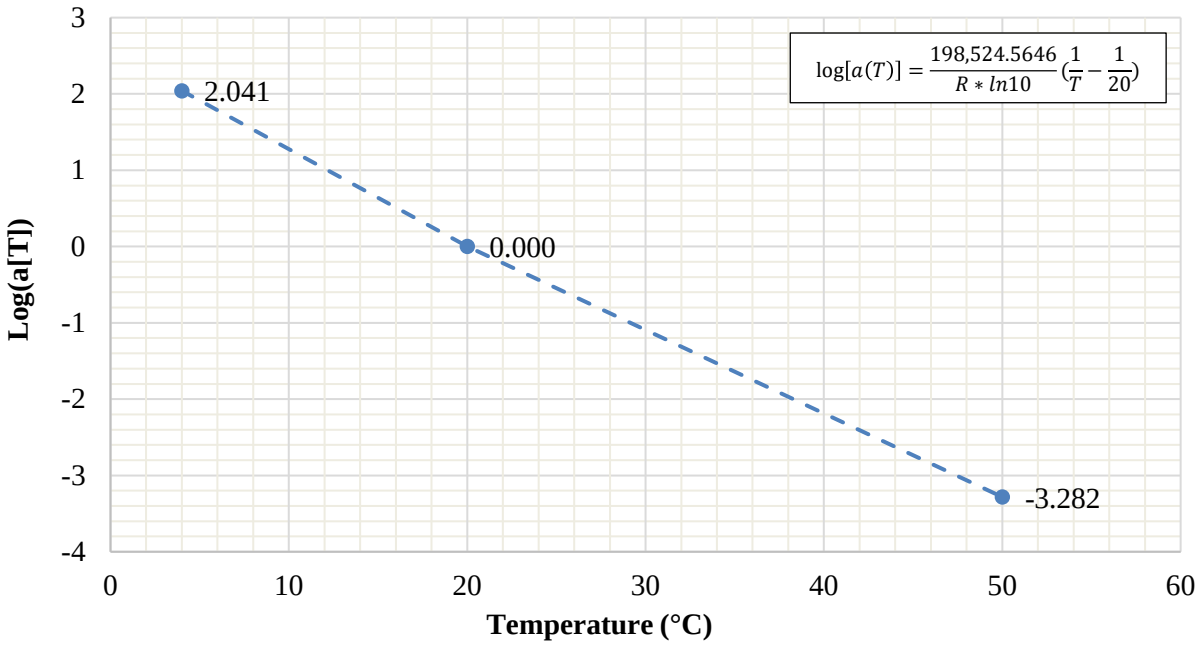


**Figure C.36. Log (a[T]) of GA125_PMA(A) mixture.**

**Table C.25. Dynamic Modulus Input Values for GA125_PMA(A) AC mix.**

| **E*, psi (MPa)** | **Frequency (Hz)** | | | | | |
|---|---|---|---|---|---|---|
| **Temperature, °F (°C)** | 0.1 | 0.5 | 1 | 5 | 10 | 25 |
| 14 (-10) | 2,746,066 (18,933) | 3,008,320 (20,742) | 3,103,855 (21,400) | 3,289,111 (22,678) | 3,354,753 (23,130) | 3,430,140 (23,650) |
| 40 (4) | 1,670,986 (11,521) | 2,078,579 (14,331) | 2,243,960 (15,472) | 2,592,518 (17,875) | 2,725,300 (18,790) | 2,884,070 (19,885) |
| 70 (21) | 548,681 (3,783) | 863,507 (5,954) | 1,021,688 (7,044) | 1,422,703 (9,809) | 1,602,401 (11,048) | 1,838,950 (12,679) |
| 100 (38) | 109,815 (757) | 209,566 (1,445) | 272,763 (1,881) | 478,047 (3,296) | 593,518 (4,092) | 770,501 (5,312) |
| 130 (54) | 23,397 (161) | 42,975 (296) | 56,801 (392) | 110,124 (759) | 146,099 (1,007) | 210,123 (1,449) |

**Table C.26. Phase Angle Input Values for GA125_PMA(A) AC mix.**

| **Phase Angle, °** | **Frequency (Hz)** | | | | | |
|---|---|---|---|---|---|---|
| **Temperature, °F (°C)** | 0.1 | 0.5 | 1 | 5 | 10 | 25 |
| 14 (-10) | 6.0 | 4.9 | 4.5 | 3.6 | 3.3 | 3.0 |
| 40 (4) | 13.4 | 11.2 | 10.3 | 8.5 | 7.8 | 7.0 |
| 70 (21) | 26.1 | 22.9 | 21.5 | 18.4 | 17.2 | 15.6 |
| 100 (38) | 34.6 | 33.5 | 32.7 | 30.3 | 29.0 | 27.3 |
| 130 (54) | 27.5 | 31.3 | 32.5 | 34.3 | 34.6 | 34.6 |

### C.1.14. GA125_PMA(B) AC Mix

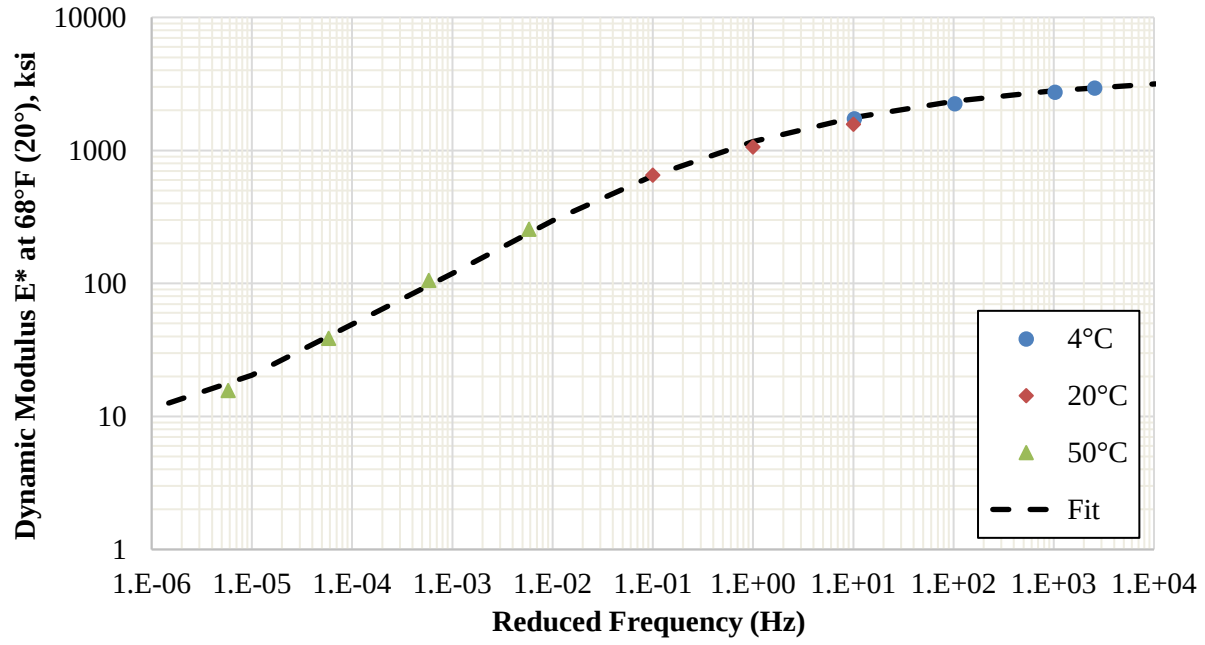


**Figure C.37. Dynamic modulus of GA125_PMA(B) mixture at 68°F (20°C).**

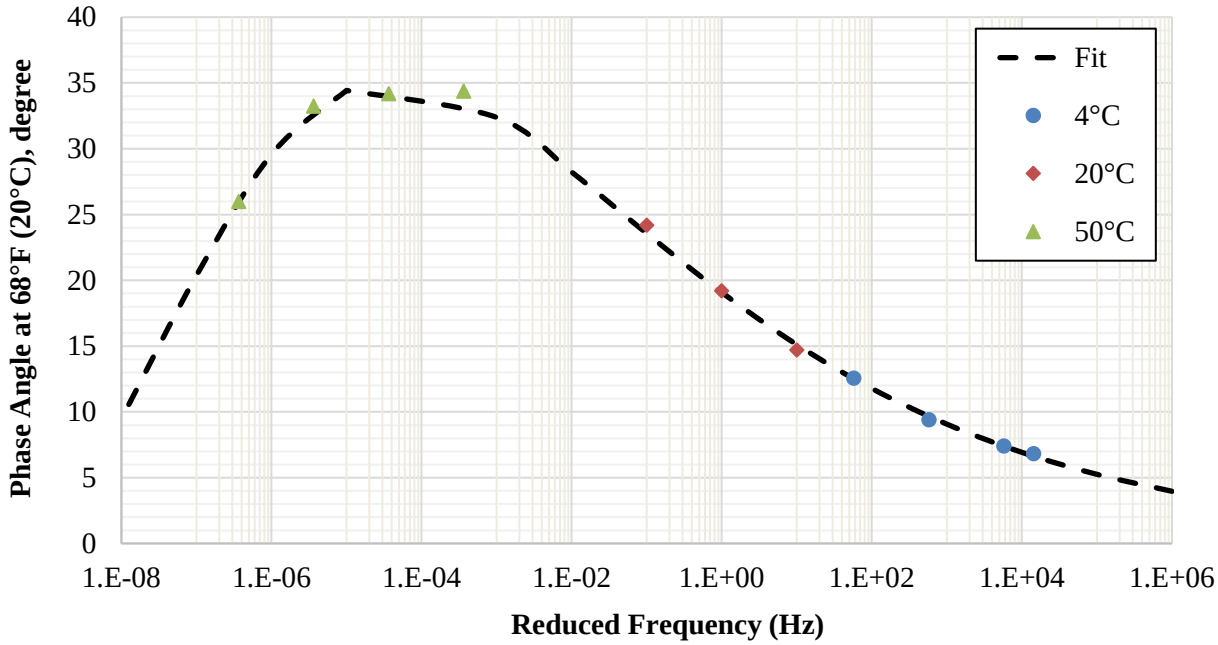


**Figure C.38. Phase angle of GA125_PMA(B) mixture at 68°F (20°C).**

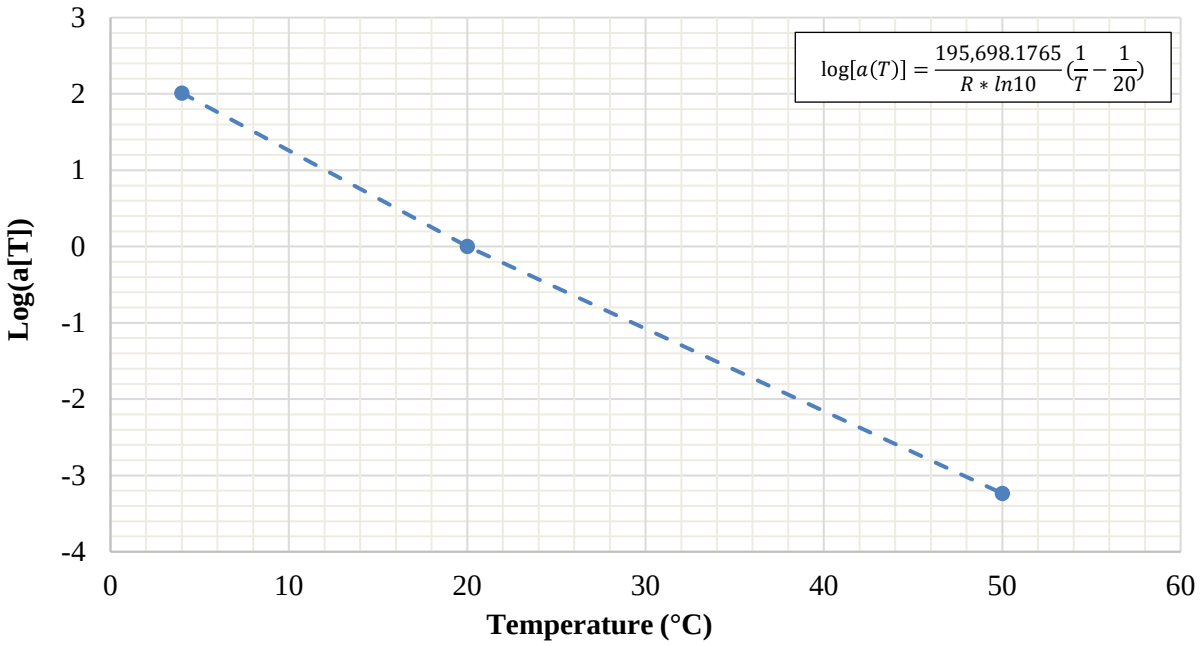


**Figure C.39. Log (a[T]) of GA125_PMA(B) mixture.**

**Table C.27. Dynamic Modulus Input Values for GA125_PMA(B) AC mix.**

| **E*, psi (MPa)** | **Frequency (Hz)** | | | | | |
|---|---|---|---|---|---|---|
| **Temperature, °F (°C)** | 0.1 | 0.5 | 1 | 5 | 10 | 25 |
| 14 (-10) | 2,796,597 (19,982) | 3,052,938 (21,049) | 3,145,648 (21,688) | 3,324,285 (22,920) | 3,387,185 (23,354) | 3,459,138 (23,850) |
| 40 (4) | 1,739,120 (11,991) | 2,149,776 (14,822) | 2,314,599 (15,959) | 2,658,519 (18,330) | 2,788,269 (19,224) | 2,942,460 (20,288) |
| 70 (21) | 588,808 (4,060) | 923,040 (6,364) | 1,089,044 (7,509) | 1,504,225 (10,371) | 1,687,720 (11.636) | 1,926,946 (13,286) |
| 100 (38) | 119,503 (824) | 229,356 (1,581) | 298,935 (2,061) | 523,484 (3,609) | 648,563 (4,472) | 838,469 (5,781) |
| 130 (54) | 26,256 (181) | 47,668 (329) | 62,982 (434) | 122,636 (846) | 163,070 (1,124) | 235,010 (1,620) |

**Table C.28. Phase Angle Input Values for GA125_PMA(B) AC mix.**

| **Phase Angle, °** | **Frequency (Hz)** | | | | | |
|---|---|---|---|---|---|---|
| **Temperature, °F (°C)** | 0.1 | 0.5 | 1 | 5 | 10 | 25 |
| 14 (-10) | 6.1 | 5.0 | 4.6 | 3.8 | 3.5 | 3.1 |
| 40 (4) | 12.8 | 10.7 | 9.9 | 8.2 | 7.6 | 6.8 |
| 70 (21) | 24.4 | 21.2 | 19.9 | 17.0 | 15.8 | 14.3 |
| 100 (38) | 34.5 | 32.5 | 31.4 | 28.4 | 27.0 | 25.1 |
| 130 (54) | 29.4 | 33.4 | 34.4 | 35.2 | 35.0 | 34.3 |

### C.1.15. GA125_HP(A) AC Mix

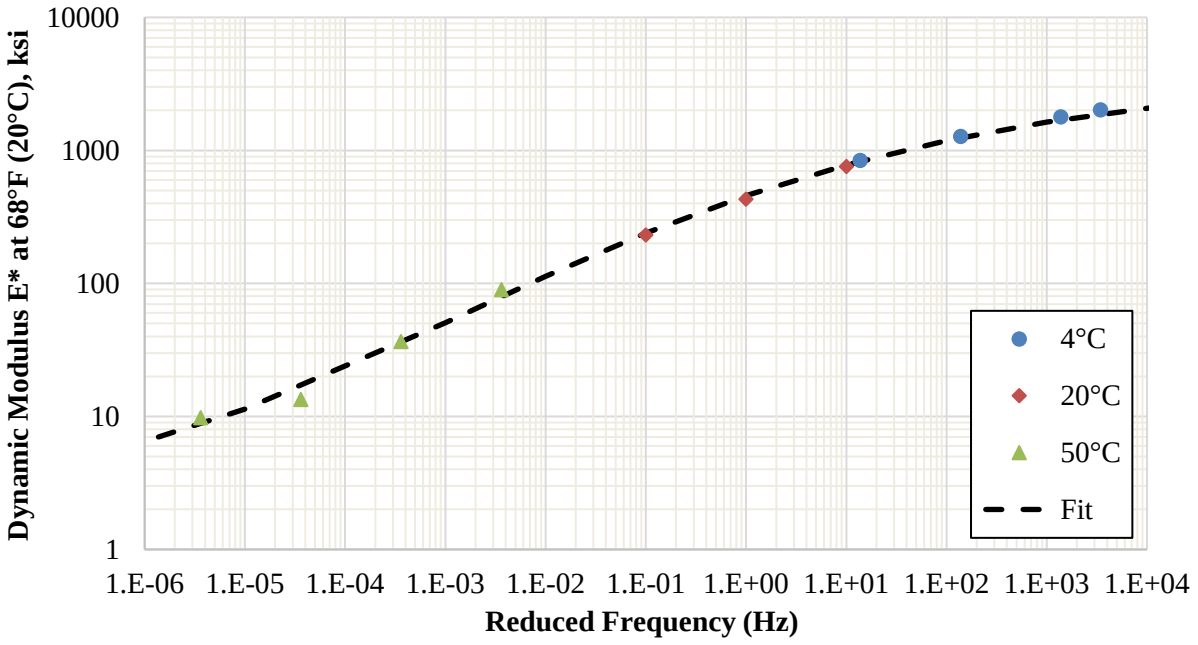


**Figure C.37. Dynamic modulus of GA125_HP(A) mixture at 68°F (20°C).**

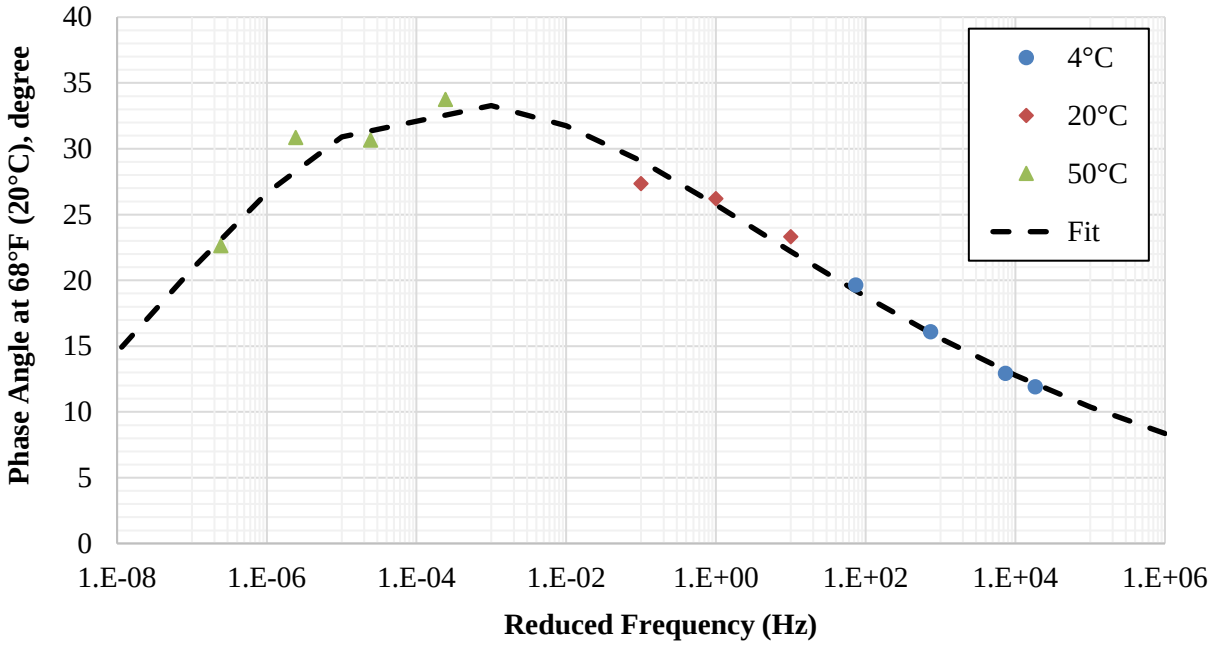


**Figure C.38. Phase angle of GA125_HP(A) mixture at 68°F (20°C).**

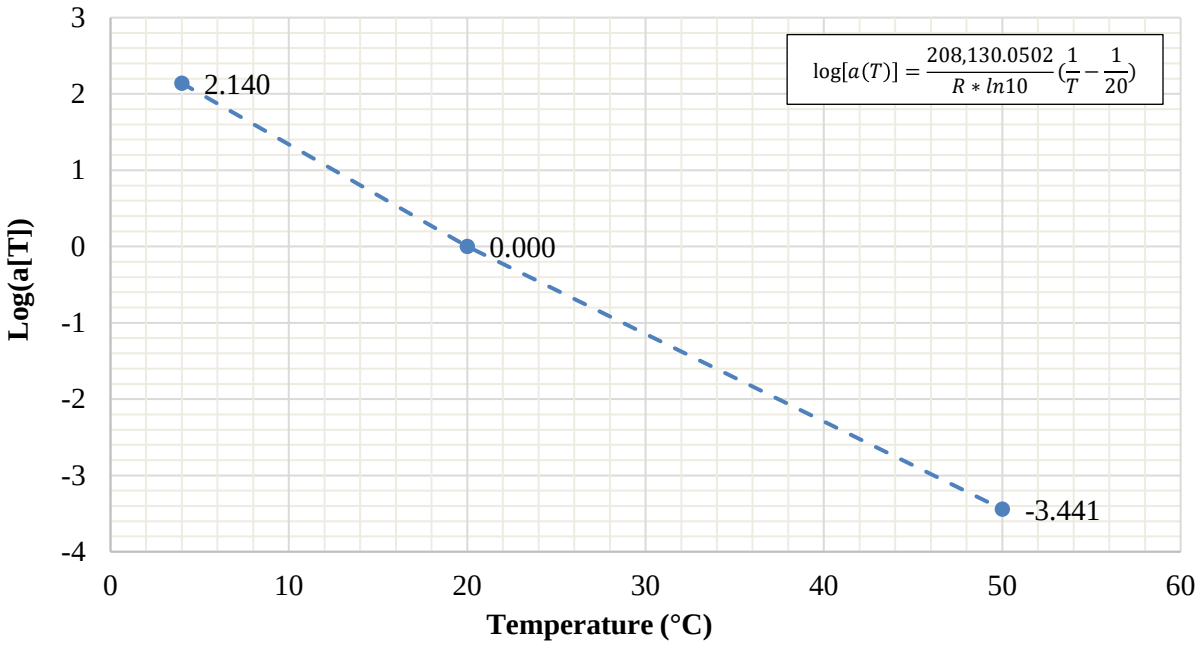


**Figure C.39. Log (a[T]) of GA125_HP(A) mixture.**

**Table C.29. Dynamic Modulus Input Values for GA125_HP(A) AC mix.**

| **E*, psi (MPa)** | **Frequency (Hz)** | | | | | |
|---|---|---|---|---|---|---|
| **Temperature, °F (°C)** | 0.1 | 0.5 | 1 | 5 | 10 | 25 |
| 14 (-10) | 1,729,692 (11,926) | 2,035,060 (14,031) | 2,160,749 (14,898) | 2,433,849 (16,781) | 2,542,276 (17,528) | 2,676,458 (18,454) |
| 40 (4) | 806,581 (5,561) | 1,086,889 (7,494) | 1,216,415 (8,387) | 1,527,779 (10,534) | 1,663,173 (11,467) | 1,840,327 (12,689) |
| 70 (21) | 216,349 (1,492) | 348,034 (2,400) | 420,068 (2,896) | 624,099 (4,303) | 727,134 (5,013) | 875,773 (6.038) |
| 100 (38) | 46,077 (318) | 81,068 (559) | 103,058 (711) | 176,325 (1,216) | 219,553 (1,514) | 289,397 (1,995) |
| 130 (54) | 12,139 (84) | 19,815 (137) | 24,877 (172) | 43,228 (298) | 55,141 (380) | 76,072 (524) |

**Table C.30. Phase Angle Input Values for GA125_HP(A) AC mix.**

| **Phase Angle, °** | **Frequency (Hz)** | | | | | |
|---|---|---|---|---|---|---|
| **Temperature, °F (°C)** | 0.1 | 0.5 | 1 | 5 | 10 | 25 |
| 14 (-10) | 11.1 | 9.6 | 9.0 | 7.7 | 7.2 | 6.6 |
| 40 (4) | 19.5 | 17.2 | 16.2 | 14.2 | 13.4 | 12.3 |
| 70 (21) | 29.6 | 27.4 | 26.4 | 23.9 | 22.9 | 21.5 |
| 100 (38) | 33.3 | 33.4 | 33.1 | 32.1 | 31.4 | 30.4 |
| 130 (54) | 25.4 | 28.9 | 30.1 | 32.2 | 32.8 | 33.3 |

### C.1.16. GA125_HP(B) AC Mix

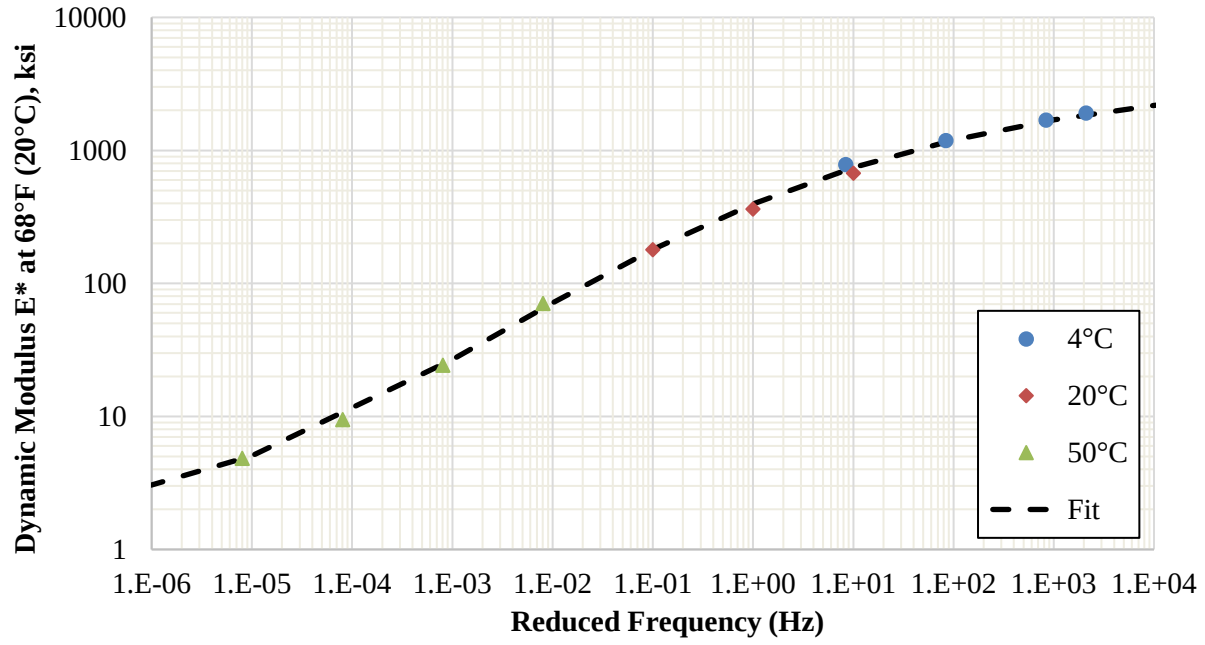


**Figure C.37. Dynamic modulus of GA125_HP(B) mixture at 68°F (20°C).**

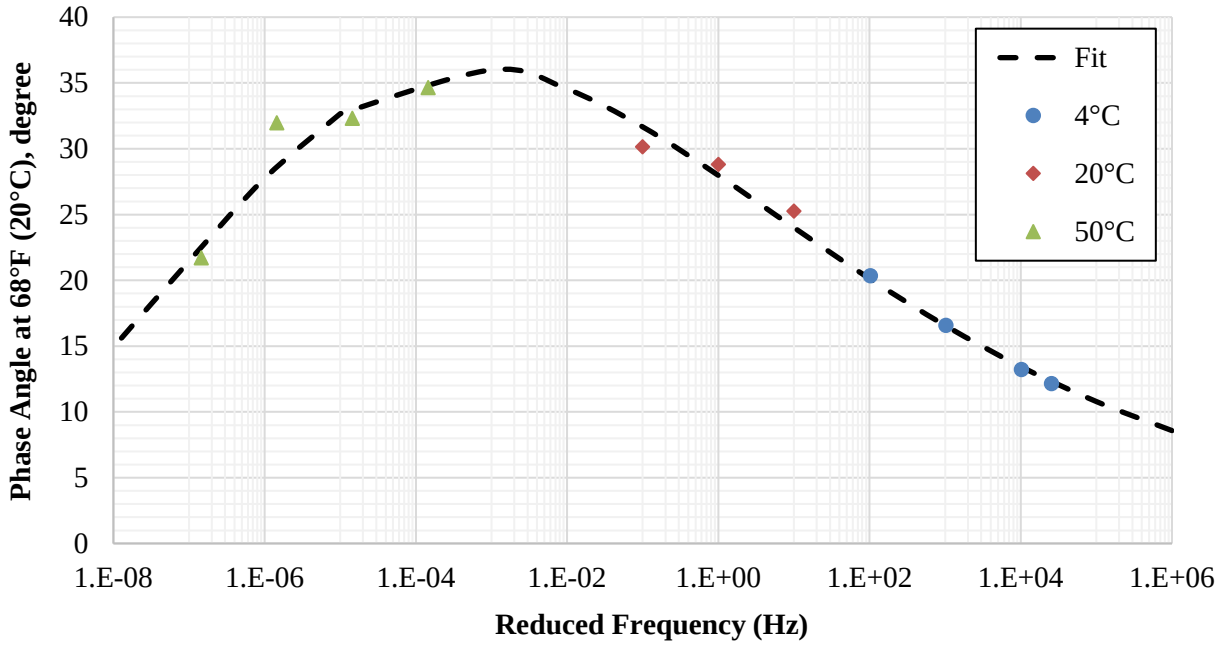


**Figure C.38. Phase angle of GA125_HP(B) mixture at 68°F (20°C).**

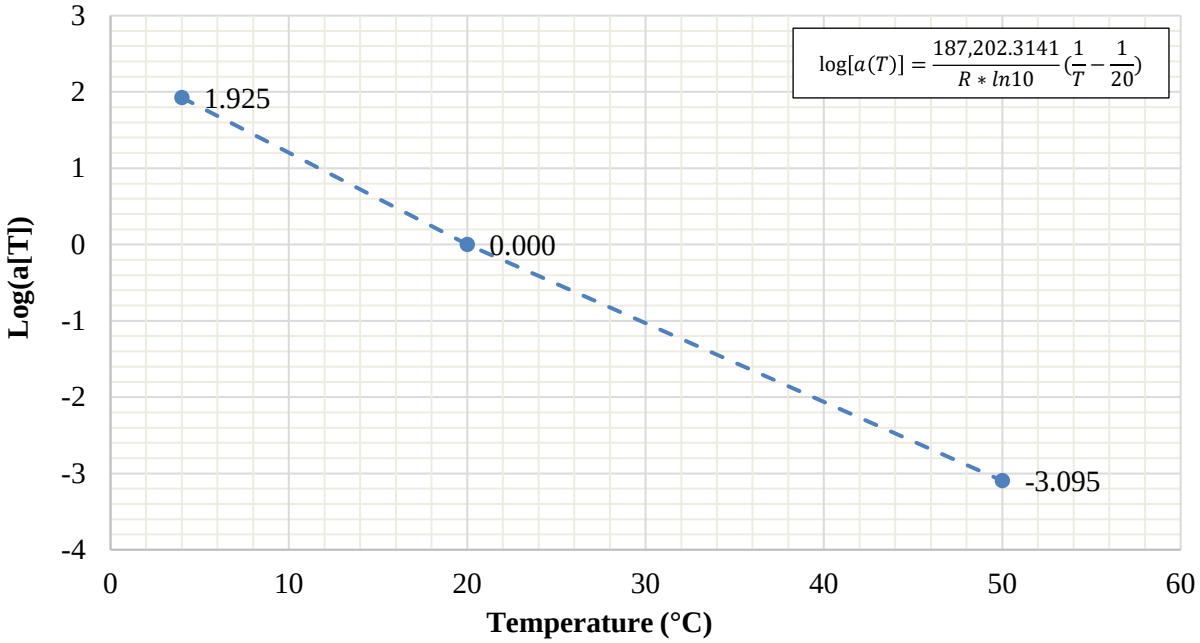


**Figure C.39. Log (a[T]) of GA125_HP(B) mixture.**

**Table C.31. Dynamic Modulus Input Values for GA125_HP(B) AC mix.**

| **E*, psi (MPa)** | **Frequency (Hz)** | | | | | |
|---|---|---|---|---|---|---|
| **Temperature, °F (°C)** | 0.1 | 0.5 | 1 | 5 | 10 | 25 |
| 14 (-10) | 1,597,839 (11,017) | 1,944,810 (13,409) | 2,088,136 (14,397) | 2,398,693 (16,538) | 2,521,155 (17,383) | 2,671,634 (18,420) |
| 40 (4) | 689,423 (4,753) | 990,260 (6,828) | 1,132,727 (7,810) | 1,479,908 (10,204) | 1,631,832 (11,251) | 1,830,577 (12,621) |
| 70 (21) | 161,070 (1,111) | 287,859 (1,985) | 361,254 (2,491) | 578,550 (3,989) | 691,722 (4,769) | 857,357 (5,911) |
| 100 (38) | 29,402 (203) | 58,451 (403) | 78,285 (540) | 149,865 (1,033) | 194,777 (1,343)) | 270,040 (1,862) |
| 130 (54) | 7,111 (49) | 12,614 (87) | 16,574 (114) | 32,419 (224) | 43,602 (301) | 64,425 (444) |

**Table C.32. Phase Angle Input Values for GA125_HP(B) AC mix.**

| **Phase Angle, °** | **Frequency (Hz)** | | | | | |
|---|---|---|---|---|---|---|
| **Temperature, °F (°C)** | 0.1 | 0.5 | 1 | 5 | 10 | 25 |
| 14 (-10) | 10.9 | 9.3 | 8.7 | 7.4 | 6.9 | 6.2 |
| 40 (4) | 20.4 | 17.9 | 16.8 | 14.6 | 13.7 | 12.5 |
| 70 (21) | 32.3 | 29.9 | 28.7 | 26.0 | 24.8 | 23.2 |
| 100 (38) | 35.5 | 36.1 | 36.0 | 35.1 | 34.5 | 33.5 |
| 130 (54) | 24.8 | 29.0 | 30.5 | 33.5 | 34.4 | 35.3 |

### C.1.17. Dynamic Modulus and Phase Angle: Summary of All Mixes

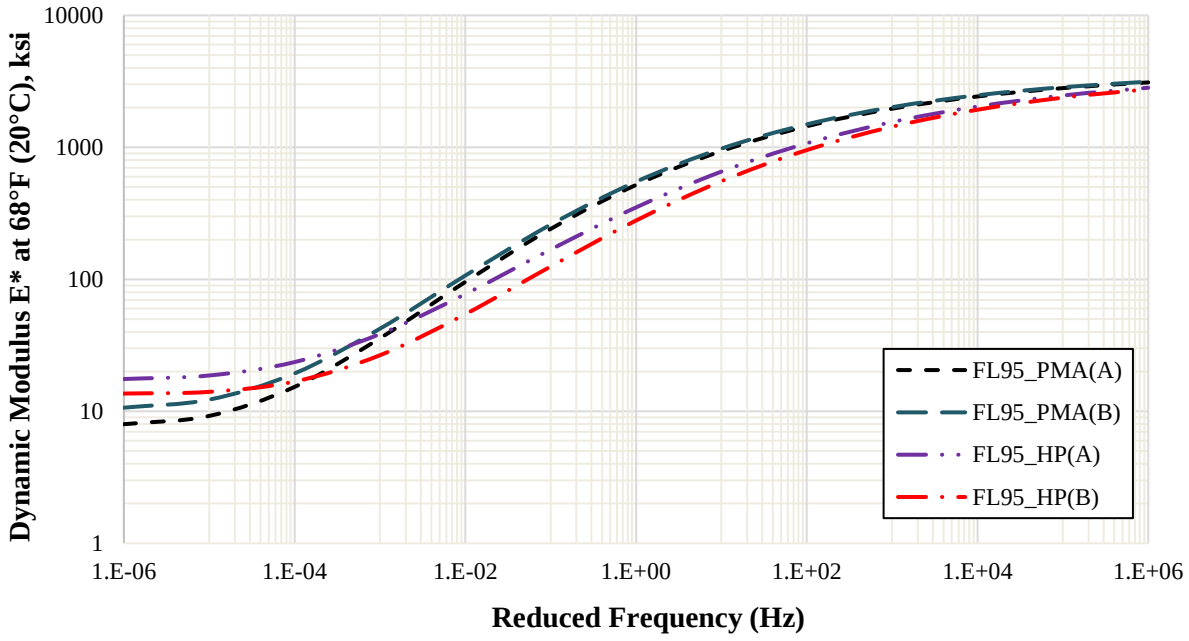


**Figure C.40. Dynamic modulus master curves of FL95_PMA(A), FL95_PMA(B), FL95_HP(A), and FL95_HP(B) mixes at 68°F (20°C).**

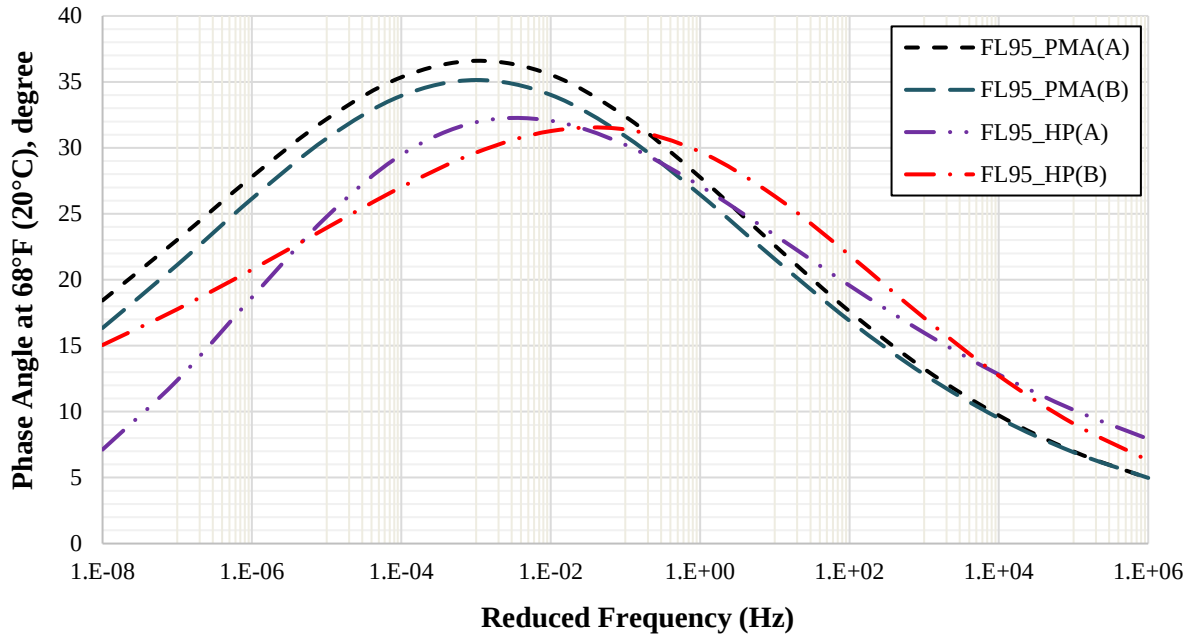


**Figure C.41. Phase angle master curves of FL95_PMA(A), FL95_PMA(B), FL95_HP(A), and FL95_HP(B) mixes at 68°F (20°C).**

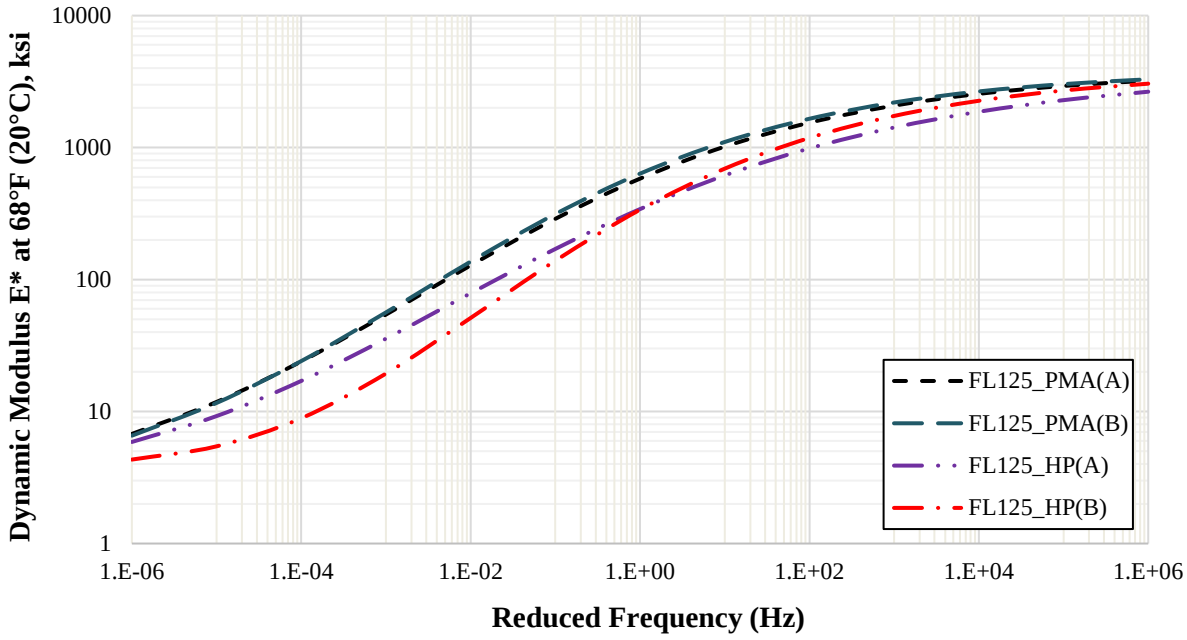


**Figure C.42. Dynamic modulus master curves of FL125_PMA(A), FL125_PMA(B), FL125_HP(A), and FL125_HP(B) mixes at 68°F (20°C).**

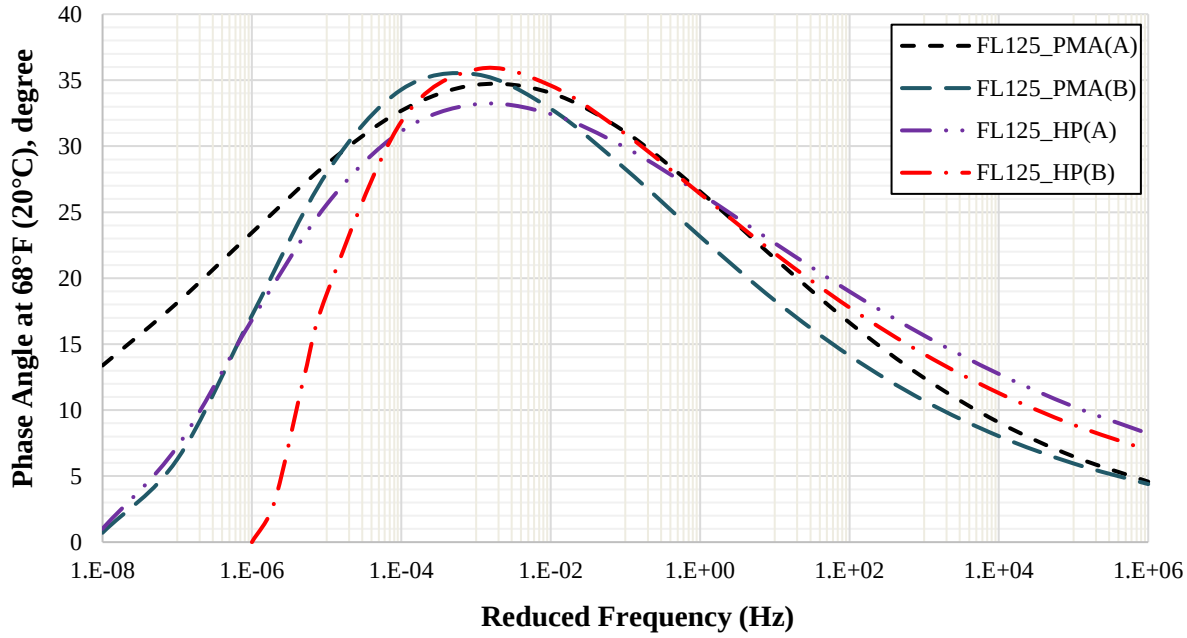


**Figure C.43. Phase angle master curves of FL125_PMA(A), FL125_PMA(B), FL125_HP(A), and FL125_HP(B) mixes at 68°F (20°C).**

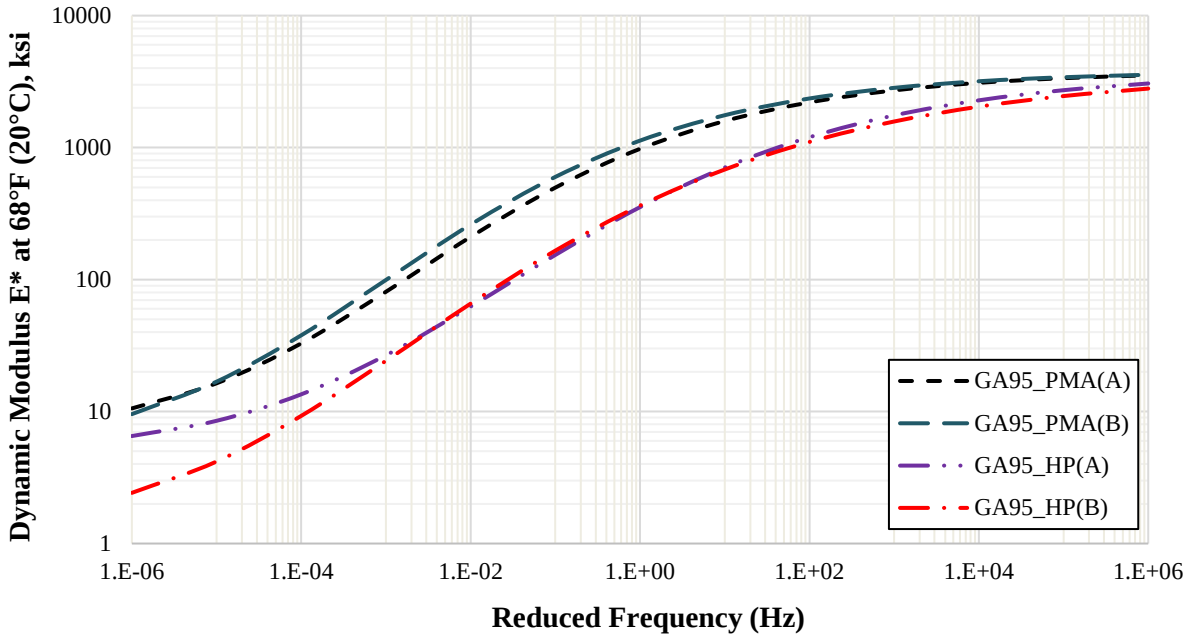


**Figure C.44. Dynamic modulus master curves of GA95_PMA(A), GA95_PMA(B), GA95_HP(A), and GA95_HP(B) mixes at 68°F (20°C).**

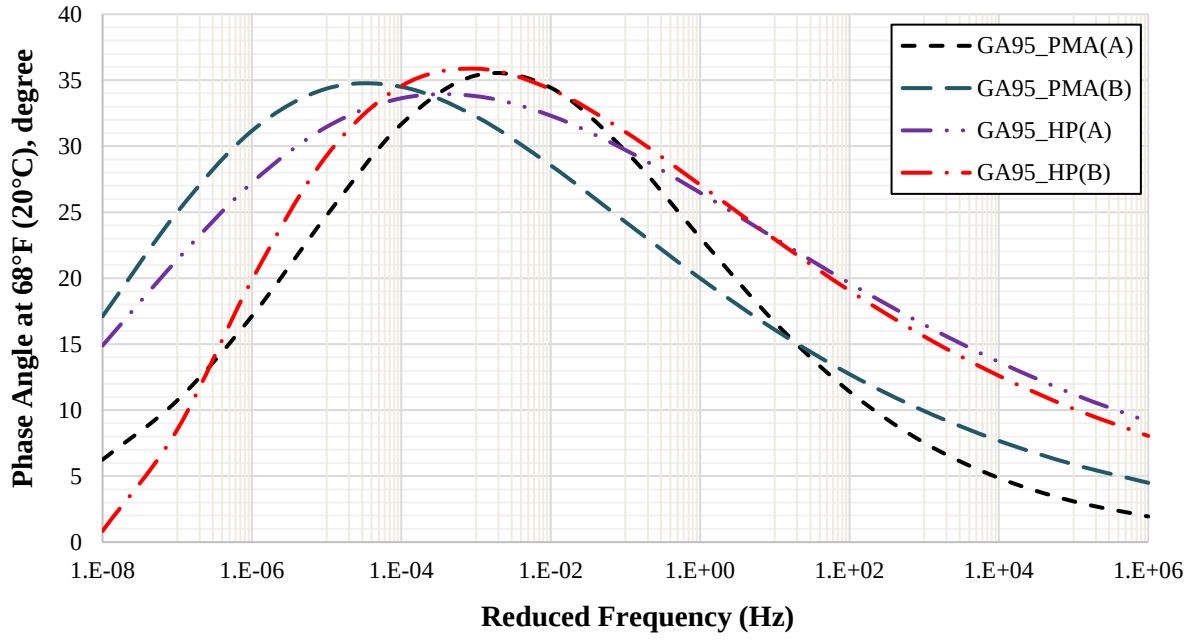


**Figure C.45. Phase angle master curves of GA95_PMA(A), GA95_PMA(B), GA95_HP(A), and GA95_HP(B) mixes at 68°F (20°C).**

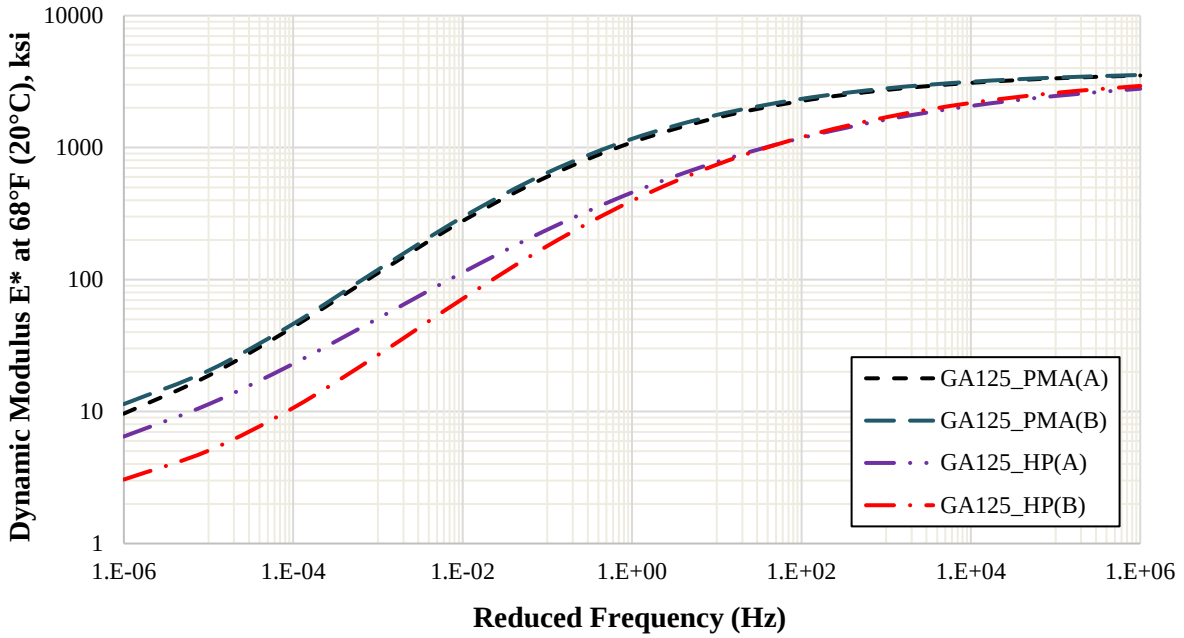


**Figure C.46. Dynamic modulus master curves of GA125_PMA(A), GA125_PMA(B), GA125_HP(A), and GA125_HP(B) mixes at 68°F (20°C).**

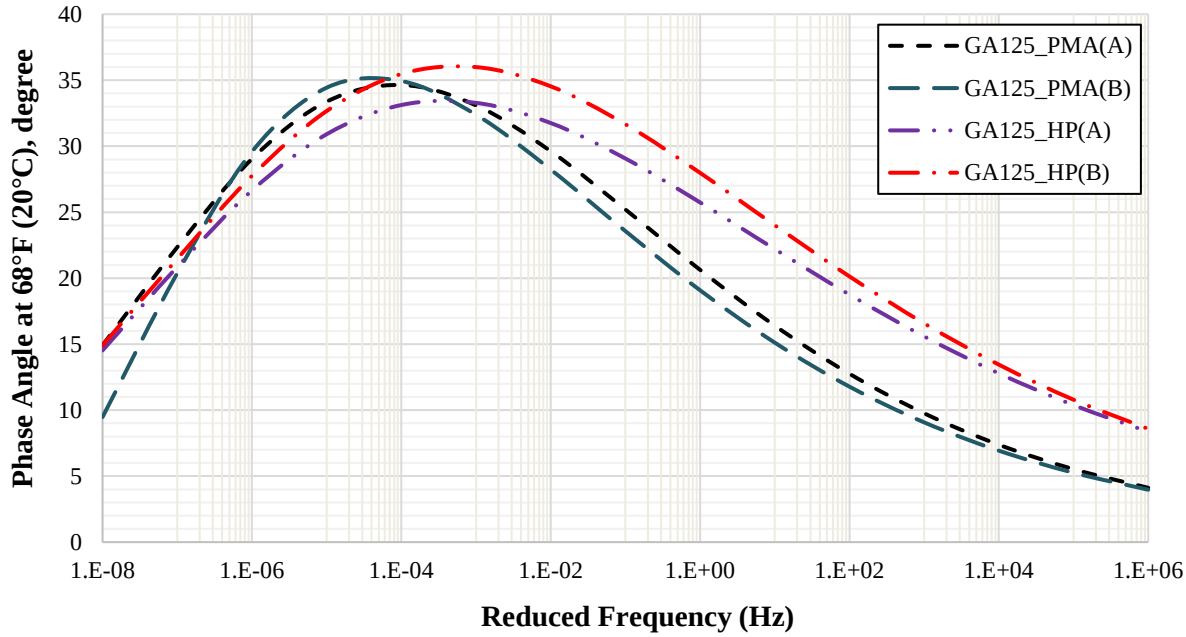


**Figure C.47. Phase angle master curves of GA125_PMA(A), GA125_PMA(B), GA125_HP(A), and GA125_HP(B) mixes at 68°F (20°C).**

## C.2. REPEATED TRIAXIAL LOAD (RLT) TEST - RUTTING

### C.2.1. FL95_PMA(A) AC Mix

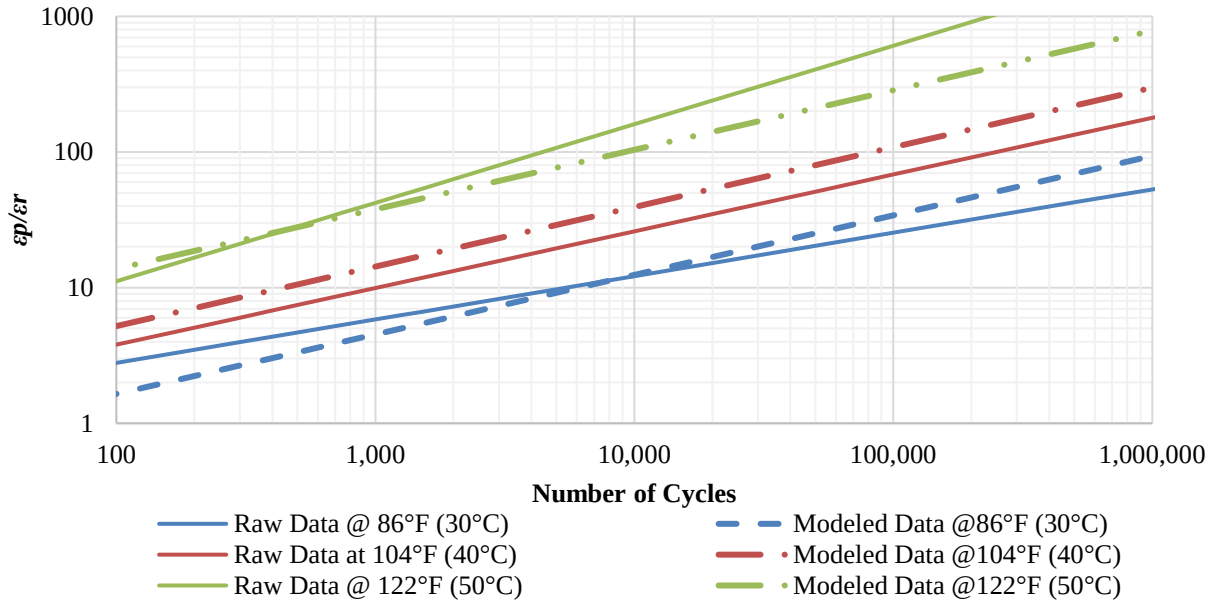


**Figure C.48. Rutting raw and modeled data of FL95_PMA(A) at 86, 104, and 122°F (30, 40, and 50°C).**

### C.2.2. FL95_PMA(B) AC Mix

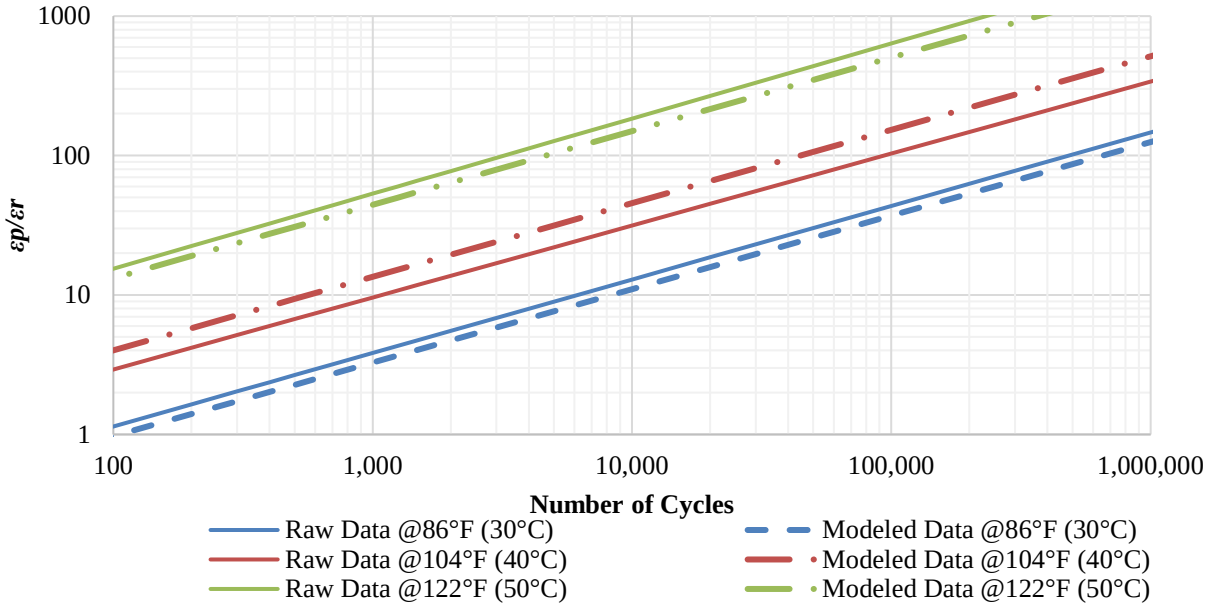


**Figure C.49. Rutting raw and modeled data of FL95_PMA(B) at 86, 104, and 122°F (30, 40, and 50°C).**

### C.2.3. FL95_HP(A) AC Mix

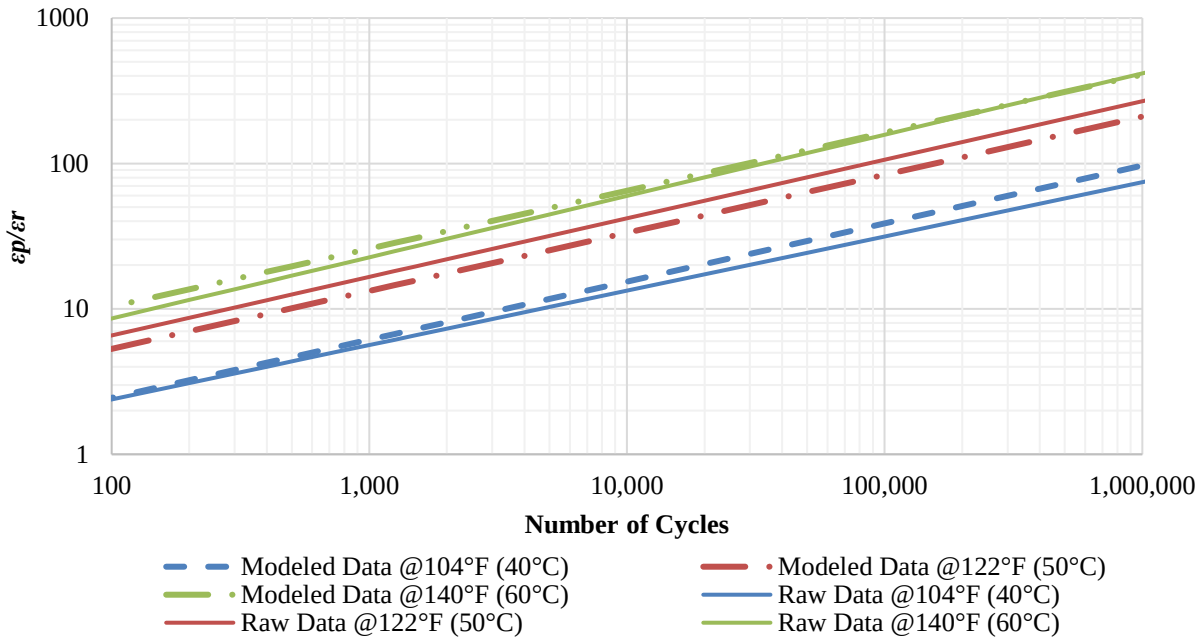


**Figure C.50. Rutting raw and modeled data of FL95_HP(A) at 104, 122, and 140°F (40, 50, and 60°C).**

### C.2.4. FL95_HP(B) AC Mix

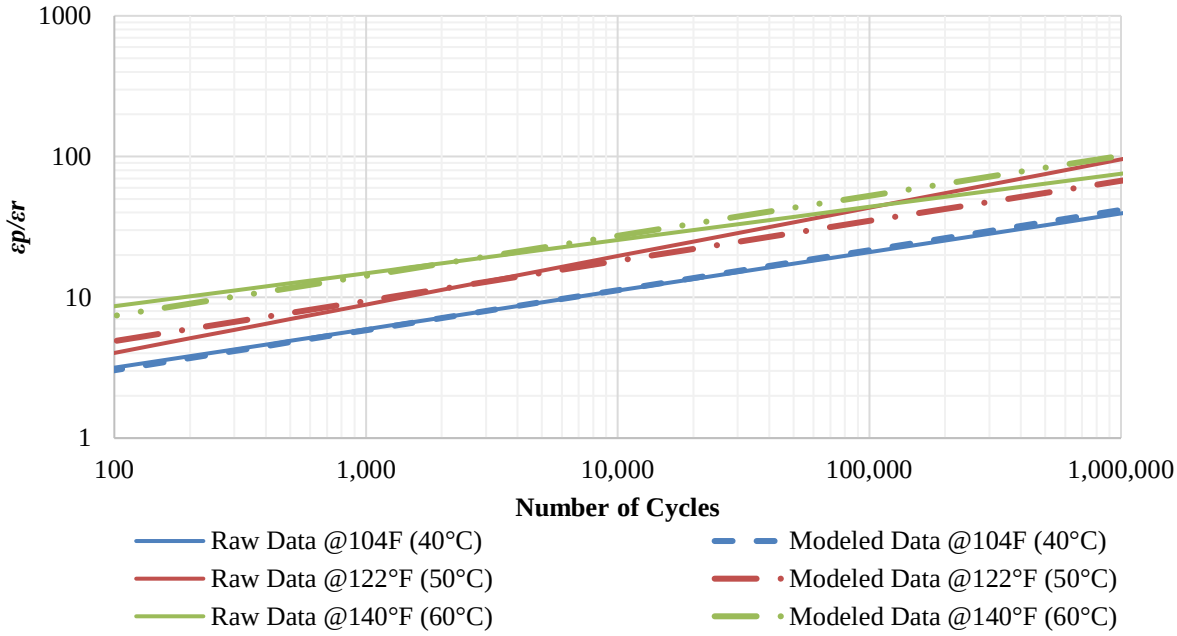


**Figure C.51. Rutting raw and modeled data of FL95_HP(B) at 104, 122, and 140°F (40, 50, and 60°C).**

### C.2.5. FL125_PMA(A) AC Mix

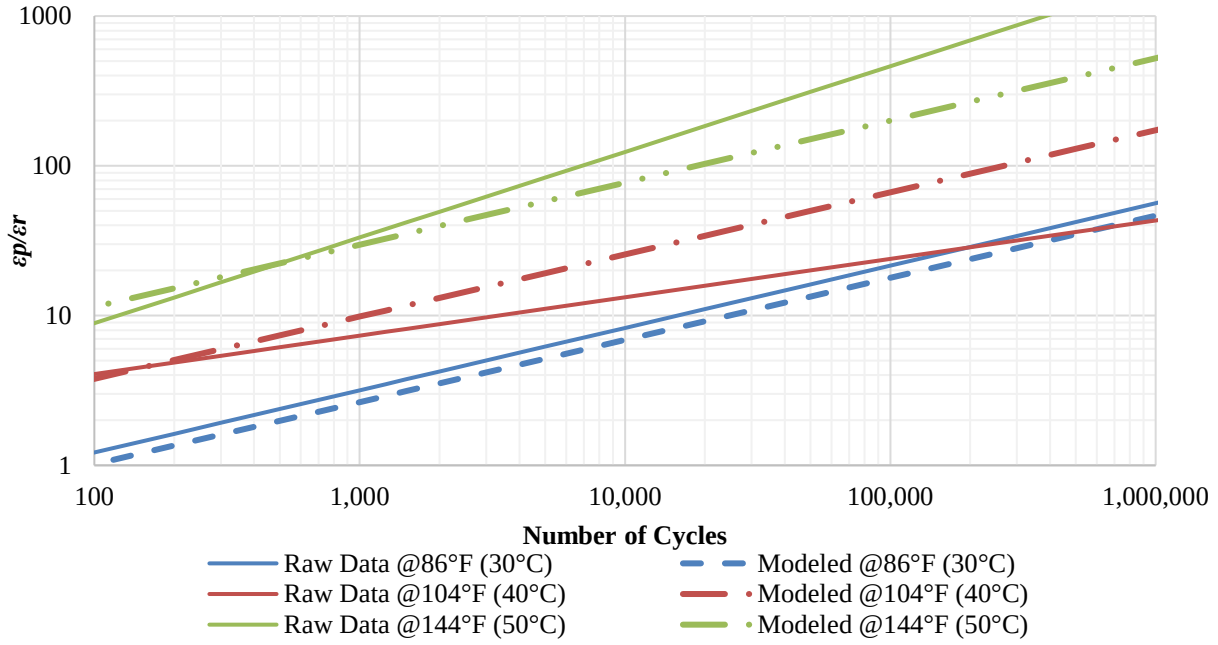


**Figure C.52. Rutting raw and modeled data of FL125_PMA(A) at 86, 104, and 122°F (30, 40, and 50°C).**

### C.2.6. FL125_PMA(B) AC Mix

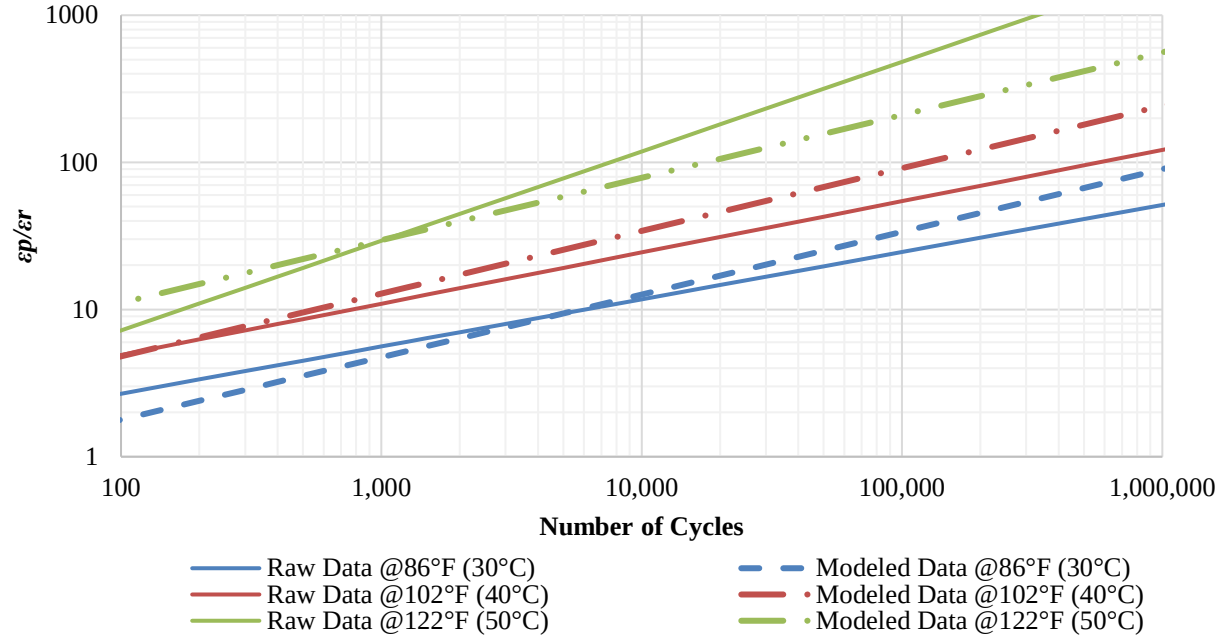


**Figure C.53. Rutting raw and modeled data of FL125_PMA(B) at 86, 104, and 122°F (30, 40, and 50°C).**

### C.2.7. FL125_HP(A) AC Mix

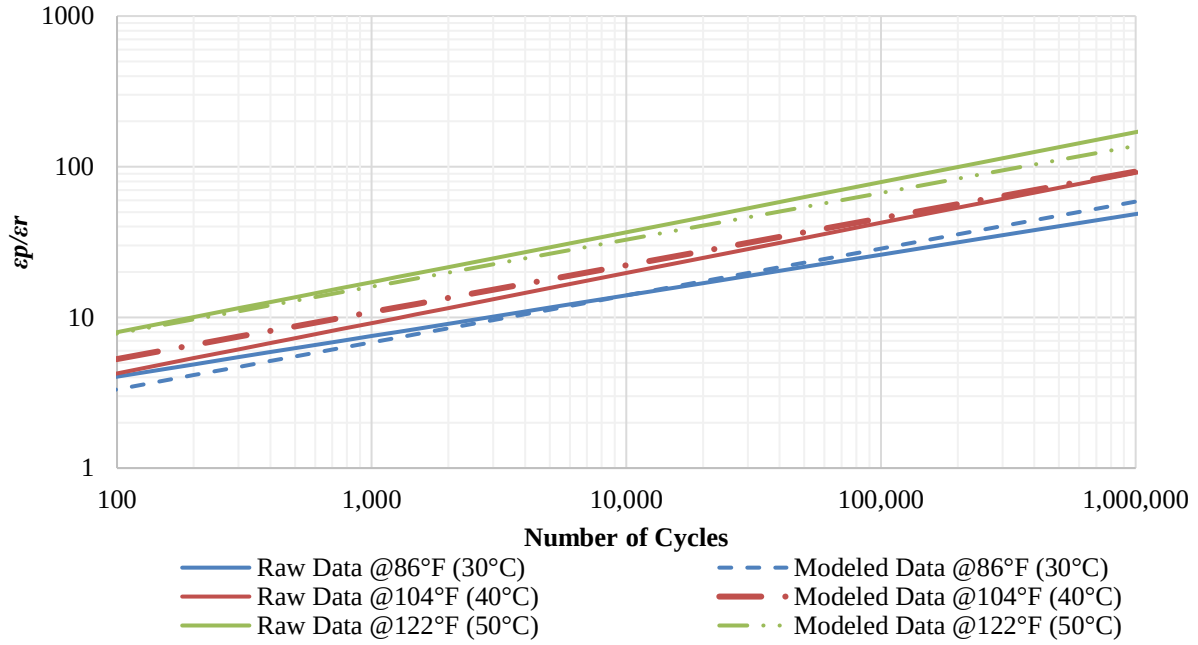


**Figure C.54. Rutting raw and modeled data of FL125_HP(A) at 104, 122, and 140°F (40, 50, and 60°C).**

### C.2.8. FL125_HP(B) AC Mix

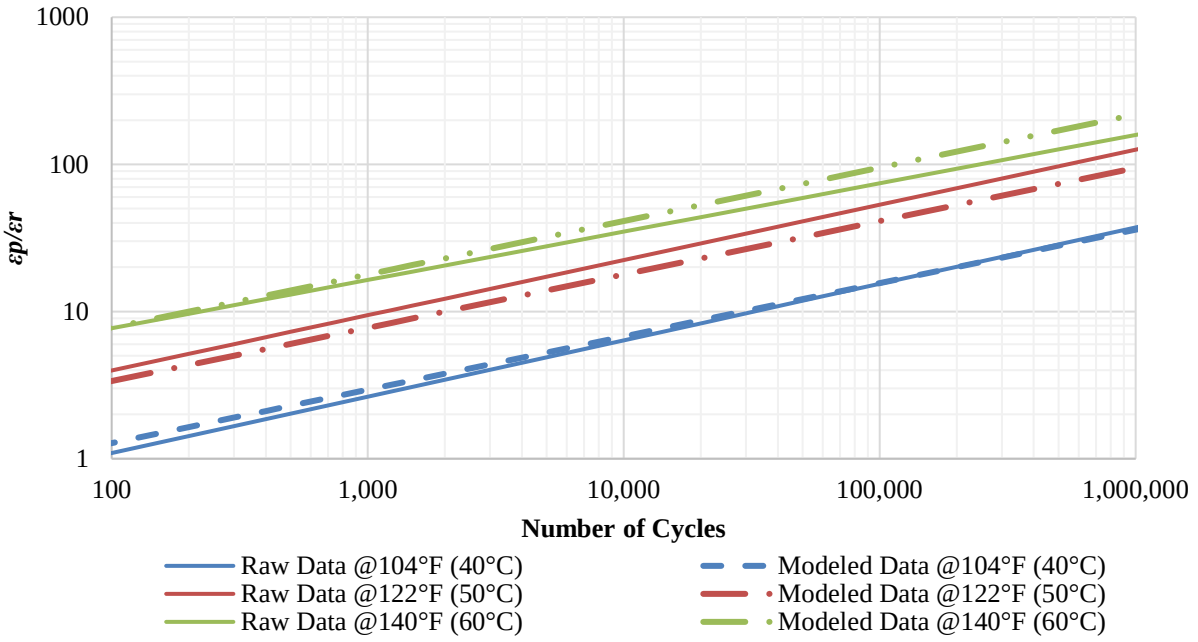


**Figure C.55. Rutting raw and modeled data of FL125_HP(B) at 104, 122, and 140°F (40, 50, and 60°C).**

### C.2.9. GA95_PMA(A) AC Mix

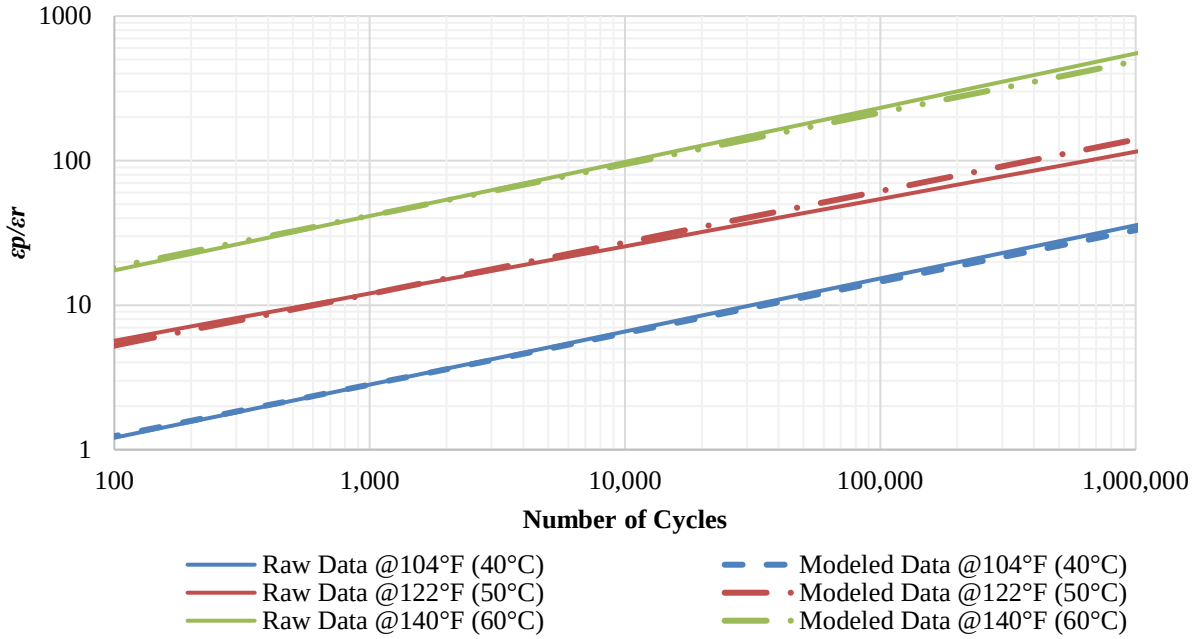


**Figure C.56. Rutting raw and modeled data of GA95_PMA(A) at 104, 122, and 140°F (40, 50, and 60°C).**

### C.2.10. GA95_PMA(B) AC Mix

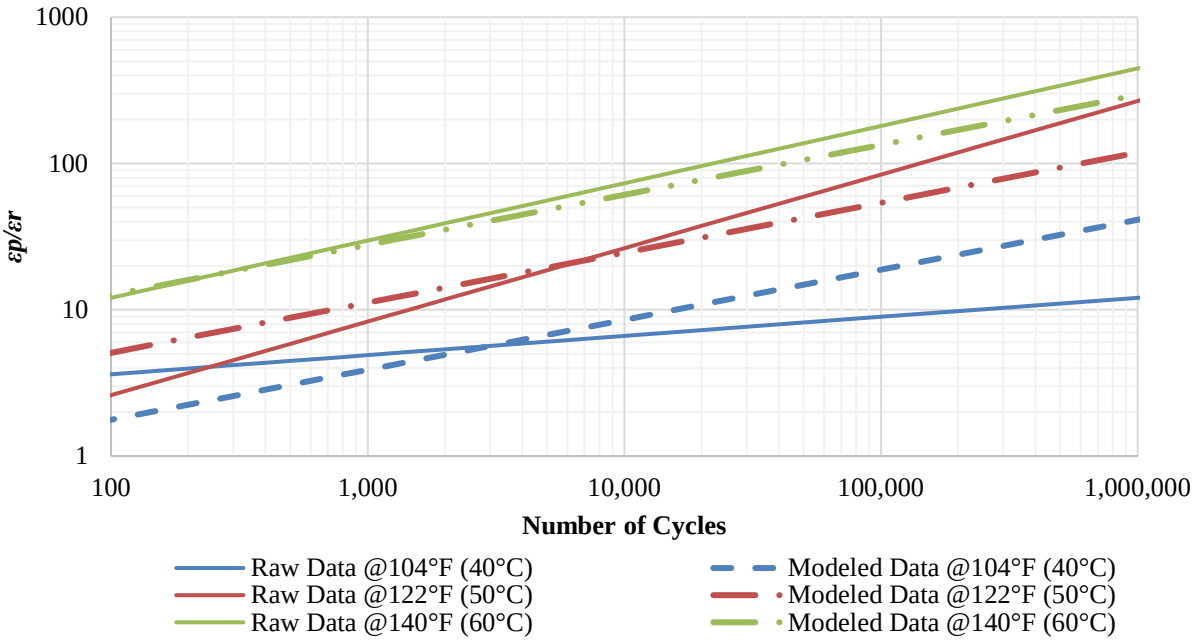


**Figure C.57. Rutting raw and modeled data of GA95_PMA(B) at 104, 122, and 140°F (40, 50, and 60°C).**

### C.2.11. GA95_HP(A) AC Mix

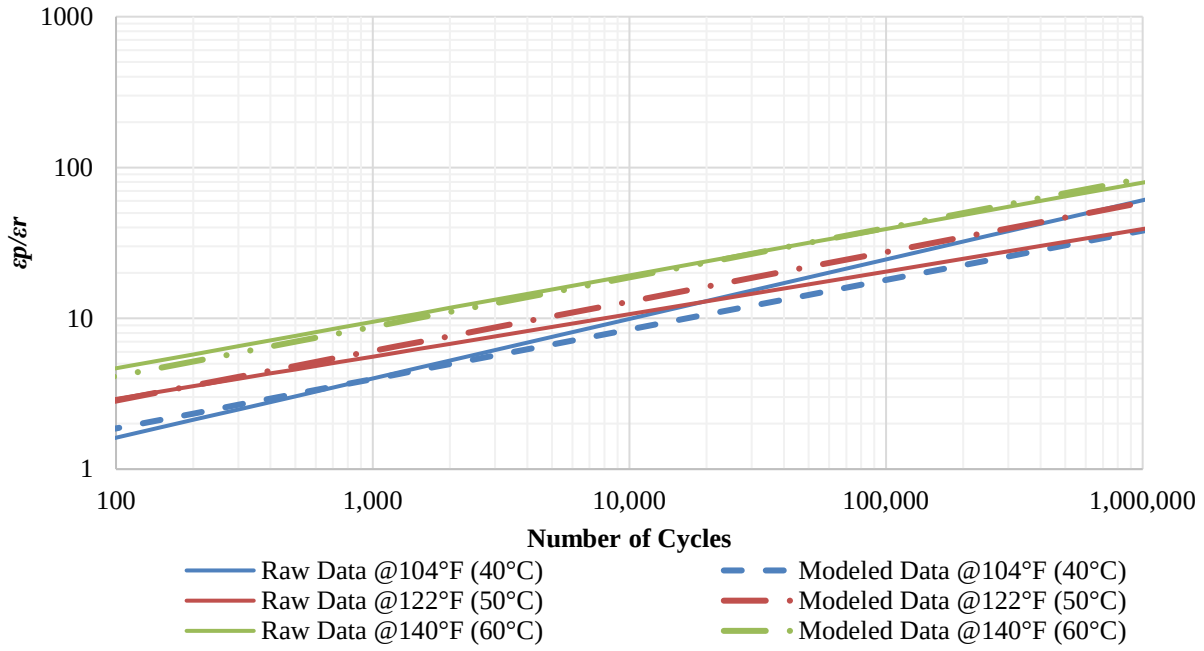


**Figure C.58. Rutting raw and modeled data of GA95_HP(A) at 104, 122, and 140°F (40, 50, and 60°C).**

### C.2.12. GA95_HP(B) AC Mix

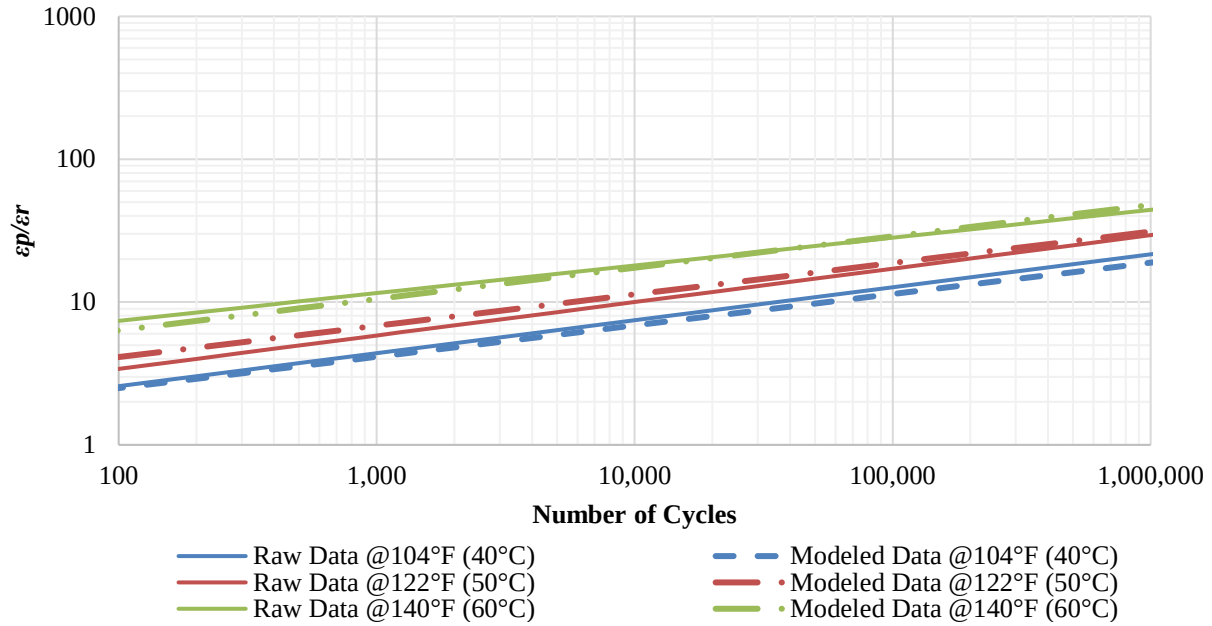


**Figure C.59. Rutting raw and modeled data of GA95_HP(B) at 104, 122, and 140°F (40, 50, and 60°C).**

### C.2.13. GA125_PMA(A) AC Mix

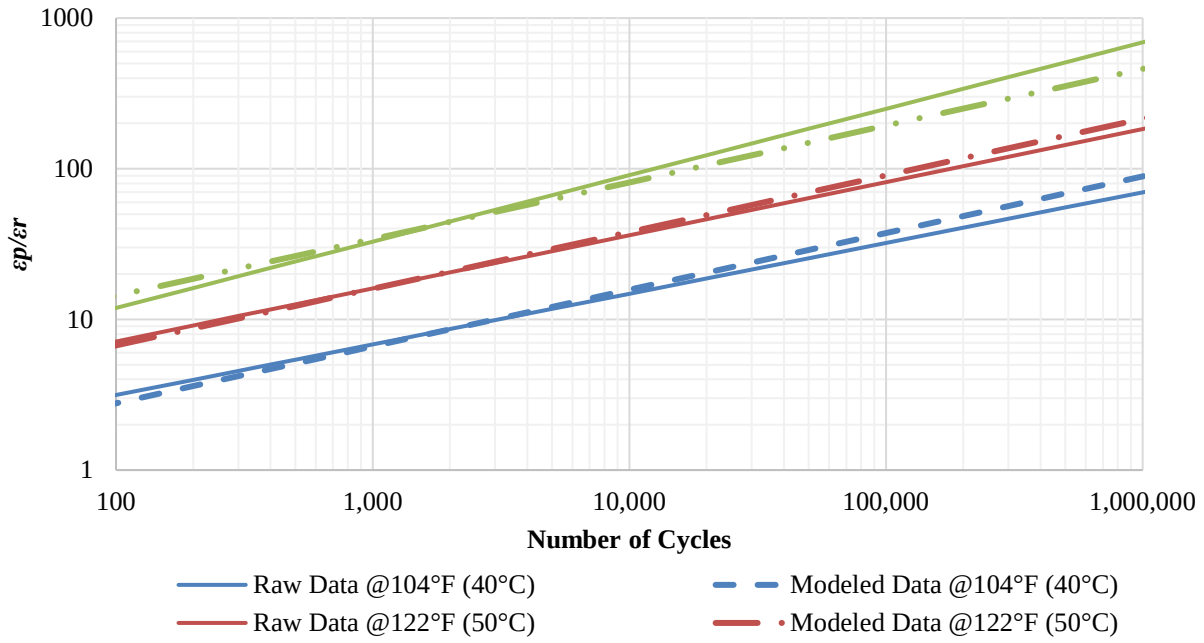


**Figure C.60. Rutting raw and modeled data of GA125_PMA(A) at 104, 122, and 140°F (40, 50, and 60°C).**

### C.2.14. GA125_PMA(B) AC Mix

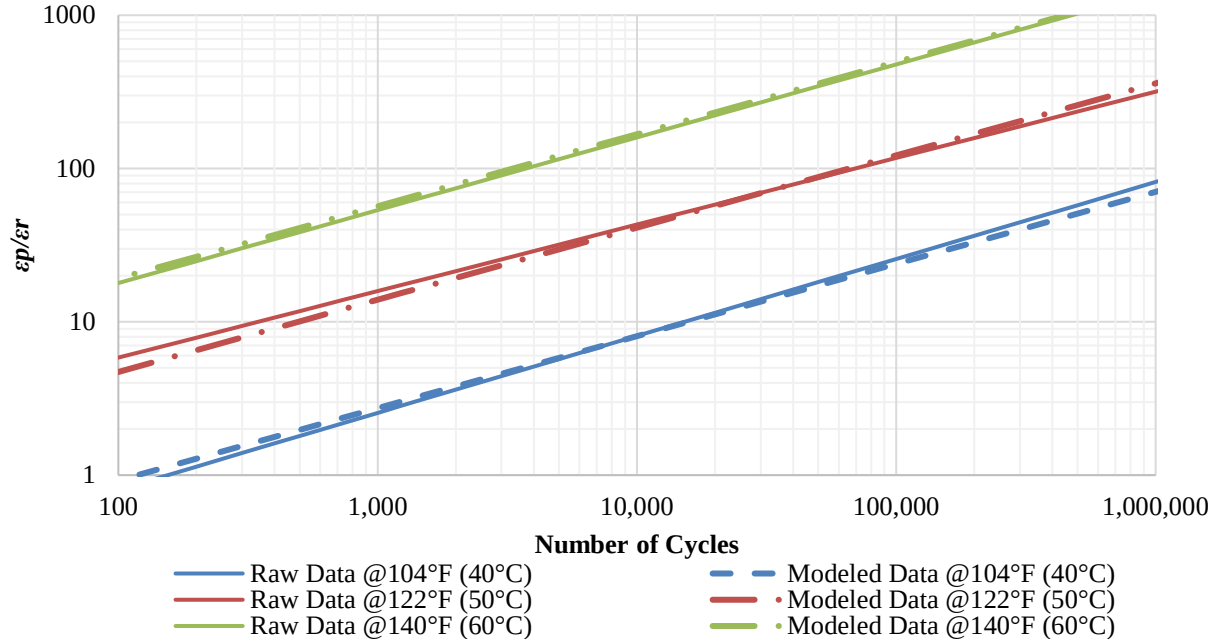


**Figure C.61. Rutting raw and modeled data of GA125_PMA(B) at 104, 122, and 140°F (40, 50, and 60°C).**

### C.2.15. GA125_HP(A) AC Mix

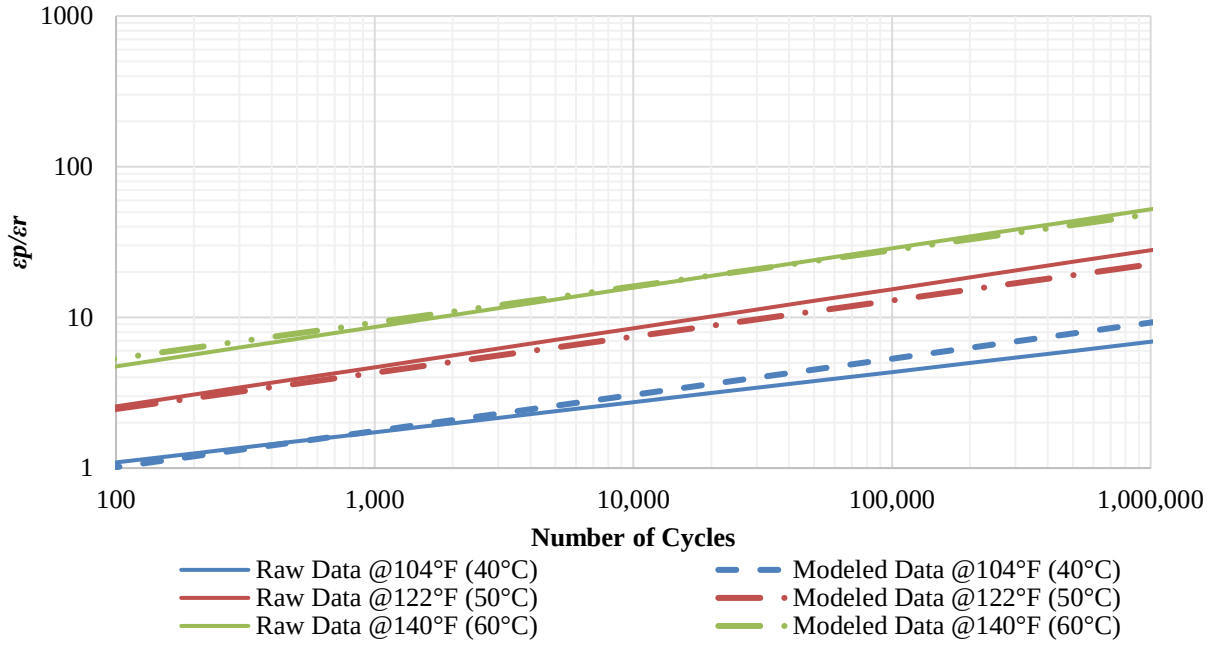


**Figure C.62. Rutting raw and modeled data of GA125_HP(A) at 104, 122, and 140°F (40, 50, and 60°C).**

### C.2.16. GA125_HP(B) AC Mix

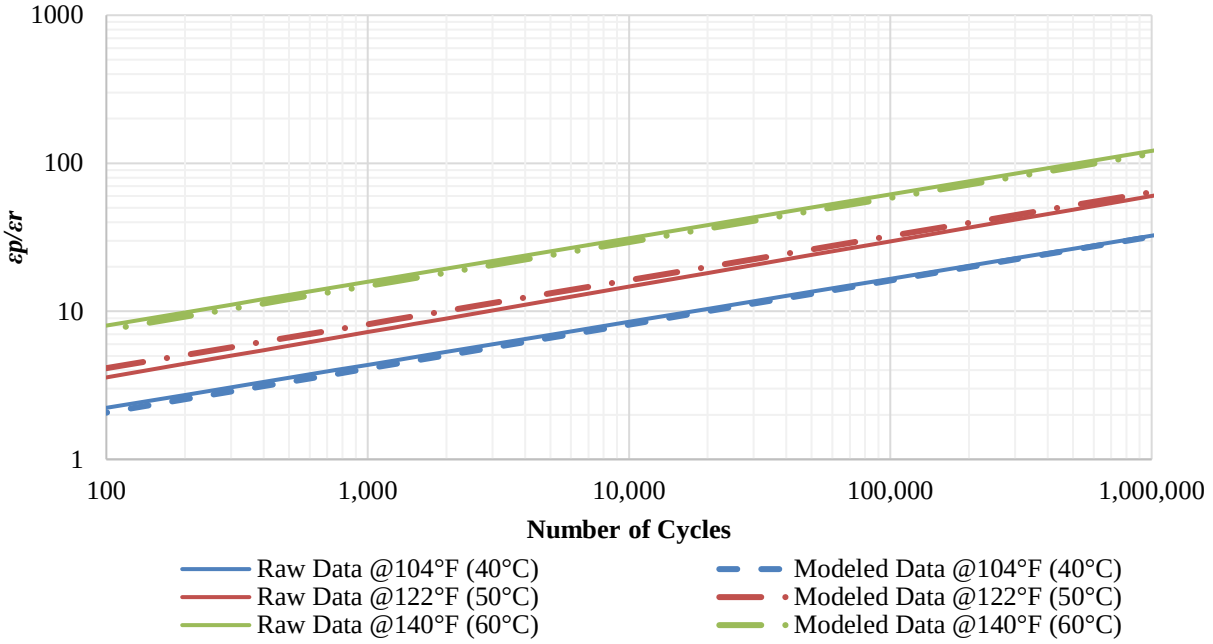


**Figure C.63. Rutting raw and modeled data of GA125_HP(A) at 104, 122, and 140°F (40, 50, and 60°C).**

## C.3. FLEXURAL BEAM FATIGUE TEST – FATIGUE CRACKING

### C.3.1. FL95_PMA(A) AC Mix

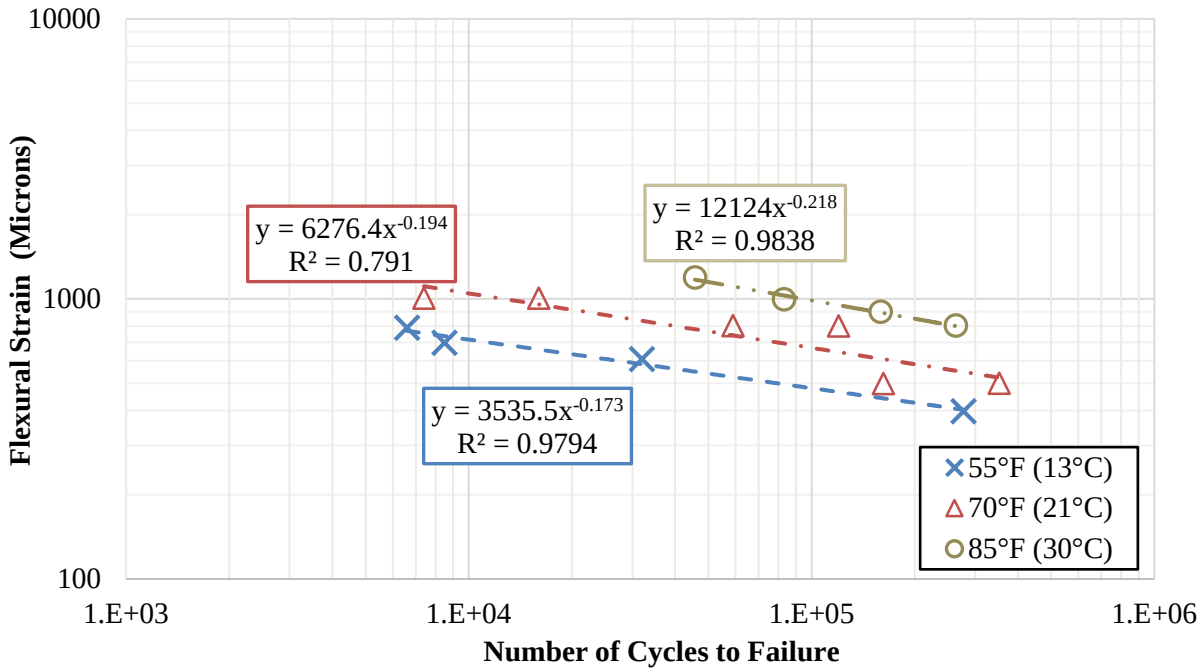


**Figure C.64. Beam fatigue raw data of FL95_PMA(A) at 55, 70, ad 85°F (13, 20, and 30°C).**

## Table C.33. Summary of Beam Fatigue Data for FL95_PMA(A) AC mix.

| Sample ID | Air Voids Level (%) | Testing Temp, °F (°C) | Dynamic Modulus E*, psi (MPa)[a] | Initial Flexural Stiffness $S_0$, psi (MPa) | Initial Dissipated Energy $E_0$, J/m$^3$ | Flexural Strain Level (micro-strain) | Number of Cycles to Failure |
|---|---|---|---|---|---|---|---|
| S1 | 6.7 | 55 (13) | 1,380,800 (9,520) | 1,207,004 (8,322) | 1,385 | 397 | 277,237 |
| S2 | 7.3 | 55 (13) | 1,380,800 (9,520) | 1,166,829 (8,045) | 2,999 | 610 | 32,000 |
| S3 | 7.6 | 55 (13) | 1,380,800 (9,520) | 1,045,287 (7,207) | 3,472 | 697 | 8,500 |
| S4 | 6.4 | 55 (13) | 1,380,800 (9,520) | 982,196 (6,772) | 5,665 | 790 | 6,600 |
| S5 | 7.3 | 70 (21) | 876,600 (6,044) | 699,952 (4,826) | 1,406 | 498 | 162,104 |
| S6 | 6.7 | 70 (21) | 876,600 (6,044) | 678,922 (4,681) | 1,258 | 499 | 352,494 |
| S7 | 6.3 | 70 (21) | 876,600 (6,044) | 548,533 (3,782) | 3,441 | 801 | 120,000 |
| S8 | 7.3 | 70 (21) | 876,600 (6,044) | 586,098 (4,041) | 7,163 | 802 | 59,000 |
| S9 | 7.2 | 70 (21) | 876,600 (6,044) | 585,517 (4,037) | 7,163 | 1,006 | 16,000 |
| S10 | 7.2 | 70 (21) | 876,600 (6,044) | 663,403 (4,574) | 7,307 | 1,007 | 7,400 |
| S11 | 7.3 | 85 (30) | 490,000 (3,378) | 312,556 (2,155) | 3,215 | 804 | 263,000 |
| S12 | 6.3 | 85 (30) | 490,000 (3,378) | 315,312 (2,174) | 3,617 | 901 | 159,000 |
| S13 | 7.5 | 85 (30) | 490,000 (3,378) | 249,610 (1,721) | 3,675 | 998 | 83,000 |
| S14 | 8 | 85 (30) | 490,000 (3,378) | 230,030 (1,586) | 3,215 | 1193 | 45,658 |

[a] Dynamic Modulus E* is determined at the testing temperature and a frequency of 10 Hz

### C.3.2. FL95_PMA(B) AC Mix

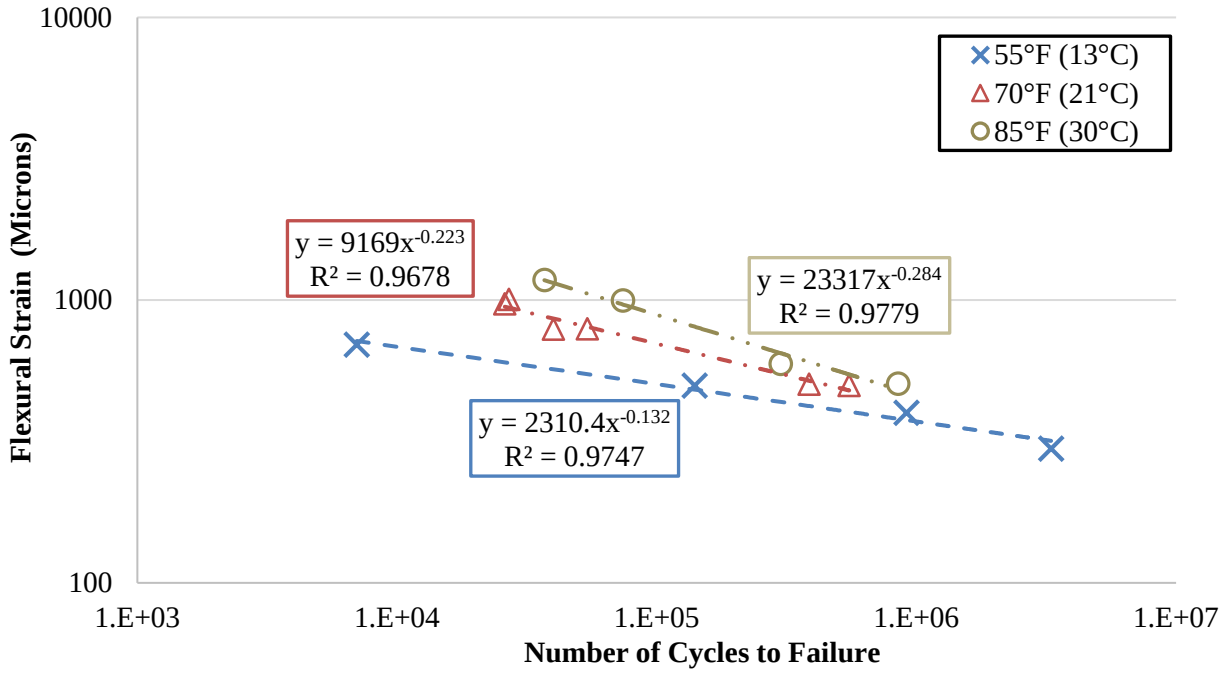


**Figure C.65. Beam fatigue raw data of FL95_PMA(B) at 55, 70, ad 85°F (13, 20, and 30°C).**

## Table C.34. Summary of Beam Fatigue Data for FL95_PMA(B) AC mix.

| Sample ID | Air Voids Level (%) | Testing Temp, °F (°C) | Dynamic Modulus E*, psi (MPa)[a] | Initial Flexural Stiffness $S_0$, psi (MPa) | Initial Dissipated Energy $E_0$, J/m$^3$ | Flexural Strain Level (micro-strain) | Number of Cycles to Failure |
|---|---|---|---|---|---|---|---|
| S1 | 7.7 | 55 (13) | 1,422,400 (9,807) | 1,216,867 (8,390) | 661 | 298 | 3,300,000 |
| S2 | 7.9 | 55 (13) | 1,422,400 (9,807) | 1,048,898 (7,225) | 1,274 | 400 | 917,000 |
| S3 | 7.7 | 55 (13) | 1,422,400 (9,807) | 1,001,921 (6,908) | 1,871 | 499 | 140,000 |
| S4 | 7.8 | 55 (13) | 1,422,400 (9,807) | 981,180 (6,765) | 3,580 | 696 | 7,000 |
| S5 | 7.6 | 70 (21) | 916,900 (6,322) | 636,281 (4,387) | 1,554 | 499 | 551,000 |
| S6 | 7.6 | 70 (21) | 916,900 (6,322) | 771,746 (5,321) | 1,942 | 504 | 386,000 |
| S7 | 7.6 | 70 (21) | 916,900 (6,322) | 476,159 (3,283) | 4,486 | 789 | 40,000 |
| S8 | 8 | 70 (21) | 916,900 (6,322) | 507,052 (3,496) | 9,096 | 792 | 54,000 |
| S9 | 7.6 | 70 (21) | 916,900 (6,322) | 475,144 (3,276) | 5,495 | 971 | 26,000 |
| S10 | 7.8 | 70 (21) | 916,900 (6,322) | 444,541 (3,065) | 4,017 | 1005 | 27,000 |
| S11 | 8 | 85 (30) | 524,300 (3,615) | 285,289 (1,967) | 3,252 | 998 | 74,000 |
| S12 | 8.1 | 85 (30) | 524,300 (3,615) | 271,511 (1,872) | 4,053 | 1,180 | 46,000 |

[a] Dynamic Modulus E* is determined at the testing temperature and a frequency of 10 Hz

### C.3.3. FL95_HP(A) AC Mix

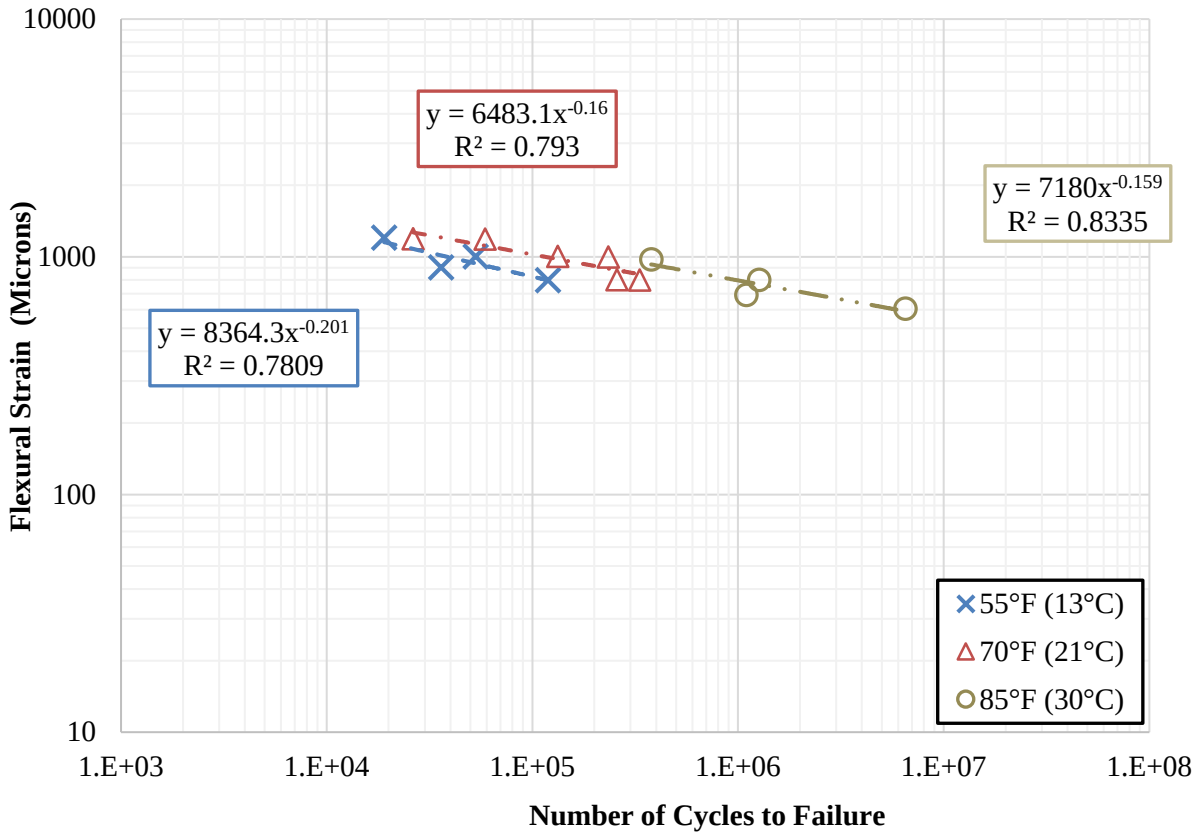


**Figure C.66. Beam fatigue raw data of FL95_HP(A) at 55, 70, ad 85°F (13, 20, and 30°C).**

## Table C.35. Summary of Beam Fatigue Data for FL95_HP(A) AC mix.

| Sample ID | Air Voids Level (%) | Testing Temp, °F (°C) | Dynamic Modulus E*, psi (MPa)[a] | Initial Flexural Stiffness $S_0$, psi (MPa) | Initial Dissipated Energy $E_0$, J/m$^3$ | Flexural Strain Level (micro-strain) | Number of Cycles to Failure |
|---|---|---|---|---|---|---|---|
| S1 | 8 | 55 (13) | 983,500 (6,781) | 493,999 (3,406) | 3,567 | 799 | 119,061 |
| S2 | 7.7 | 55 (13) | 983,500 (6,781) | 586,678 (4,045) | 9,117 | 903 | 36,000 |
| S3 | 7.2 | 55 (13) | 983,500 (6,781) | 619,601 (4,272) | 6,274 | 1,003 | 53,000 |
| S4 | 7.8 | 55 (13) | 983,500 (6,781) | 545,632 (3,762) | 9,117 | 1,206 | 19,000 |
| S5 | 7.1 | 70 (21) | 612,500 (4,223) | 252,366 (1,740) | 3,190 | 801 | 333,000 |
| S6 | 7.1 | 70 (21) | 612,500 (4,223) | 339,388 (2,340) | 3,339 | 801 | 258,000 |
| S7 | 7.1 | 70 (21) | 612,500 (4,223) | 314,152 (2,166) | 3,938 | 999 | 234,000 |
| S8 | 7.1 | 70 (21) | 612,500 (4,223) | 337,503 (2,327) | 4,625 | 1,004 | 133,000 |
| S9 | 7.7 | 70 (21) | 612,500 (4,223) | 276,152 (1,904) | 4,530 | 1,189 | 59,000 |
| S10 | 7.7 | 70 (21) | 612,500 (4,223) | 290,946 (2,006) | 3,938 | 1,192 | 26,313 |
| S11 | 5.9 | 85 (30) | 353,000 (2,434) | 180,282 (1,243) | 1,652 | 607 | 6,497,895 |
| S12 | 8.2 | 85 (30) | 353,000 (2,434) | 161,862 (1,116) | 585 | 692 | 1,095,497 |
| S13 | 8 | 85 (30) | 353,000 (2,434) | 273,541 (1,886) | 1,652 | 801 | 1,264,369 |
| S14 | 6.6 | 85 (30) | 353,000 (2,434) | 157,511 (1,086) | 1,363 | 979 | 377,996 |

[a] Dynamic Modulus E* is determined at the testing temperature and a frequency of 10 Hz

### C.3.4. FL95_HP(B) AC Mix

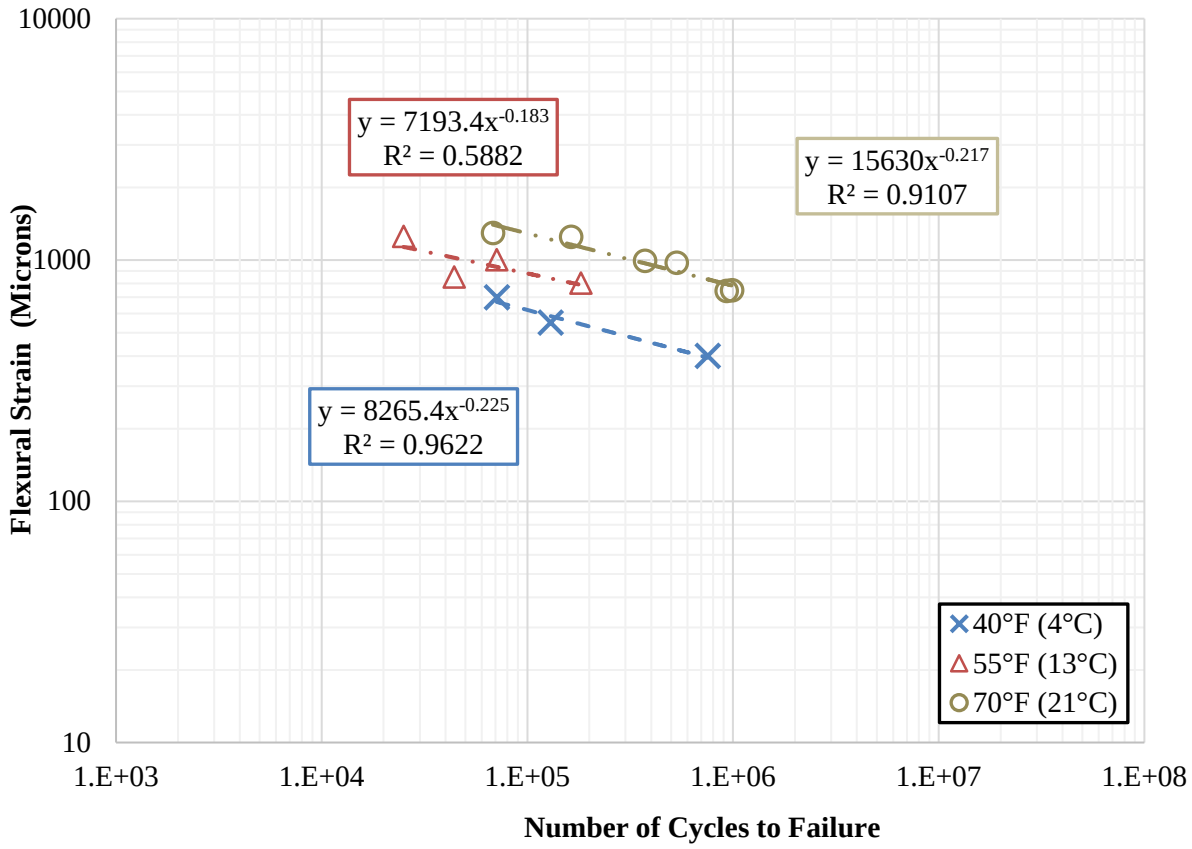


**Figure C.67. Beam fatigue raw data of FL95_HP(B) at 40, 55, ad 70°F (4, 13, and 20°C).**

## Table C.36. Summary of Beam Fatigue Data for FL95_HP(B) AC mix.

| Sample ID | Air Voids Level (%) | Testing Temp, °F (°C) | Dynamic Modulus E*, psi (MPa)[a] | Initial Flexural Stiffness $S_0$, psi (MPa) | Initial Dissipated Energy $E_0$, J/m$^3$ | Flexural Strain Level (micro-strain) | Number of Cycles to Failure |
|---|---|---|---|---|---|---|---|
| S1 | 7.6 | 40 (4) | 1,357,000 (9356) | 1,100,836 (7,590) | 862 | 400 | 759,651 |
| S2 | 7.5 | 40 (4) | 1,357,000 (9356) | 1,259,073 (8,681) | 2,059 | 550 | 130,000 |
| S3 | 7.6 | 40 (4) | 1,357,000 (9356) | 985,967 (6,798) | 4,014 | 701 | 71,000 |
| S4 | 7.4 | 55 (13) | 877,800 (6,052) | 531,853 (3,667) | 4,371 | 802 | 182,000 |
| S5 | 7.1 | 55 (13) | 877,800 (6,052) | 636,281 (4,387) | 9,487 | 849 | 44,000 |
| S6 | 7.6 | 55 (13) | 877,800 (6,052) | 498,930 (3,440) | 5,643 | 1,003 | 71,000 |
| S7 | 7.6 | 55 (13) | 877,800 (6,052) | 440,625 (3,038) | 9,487 | 1,252 | 25,000 |
| S8 | 8 | 70 (21) | 513,200 (3538) | 258,022 (1,779) | 1578 | 746 | 928,000 |
| S9 | 7.2 | 70 (21) | 513,200 (3538) | 249,175 (1,718) | 1813 | 750 | 988,000 |
| S10 | 8 | 70 (21) | 513,200 (3538) | 304,144 (2,097) | 4061 | 976 | 531,000 |
| S11 | 8 | 70 (21) | 513,200 (3538) | 220,893 (1,523) | 2453 | 994 | 373,000 |
| S12 | 7.8 | 70 (21) | 513,200 (3538) | 215,381 (1,485) | 2453 | 1,248 | 163,000 |
| S13 | 7.8 | 70 (21) | 513,200 (3538) | 213,640 (1,473) | 4325 | 1,296 | 68,000 |

[a] Dynamic Modulus E* is determined at the testing temperature and a frequency of 10 Hz

### C.3.5. FL125_PMA(A) AC Mix

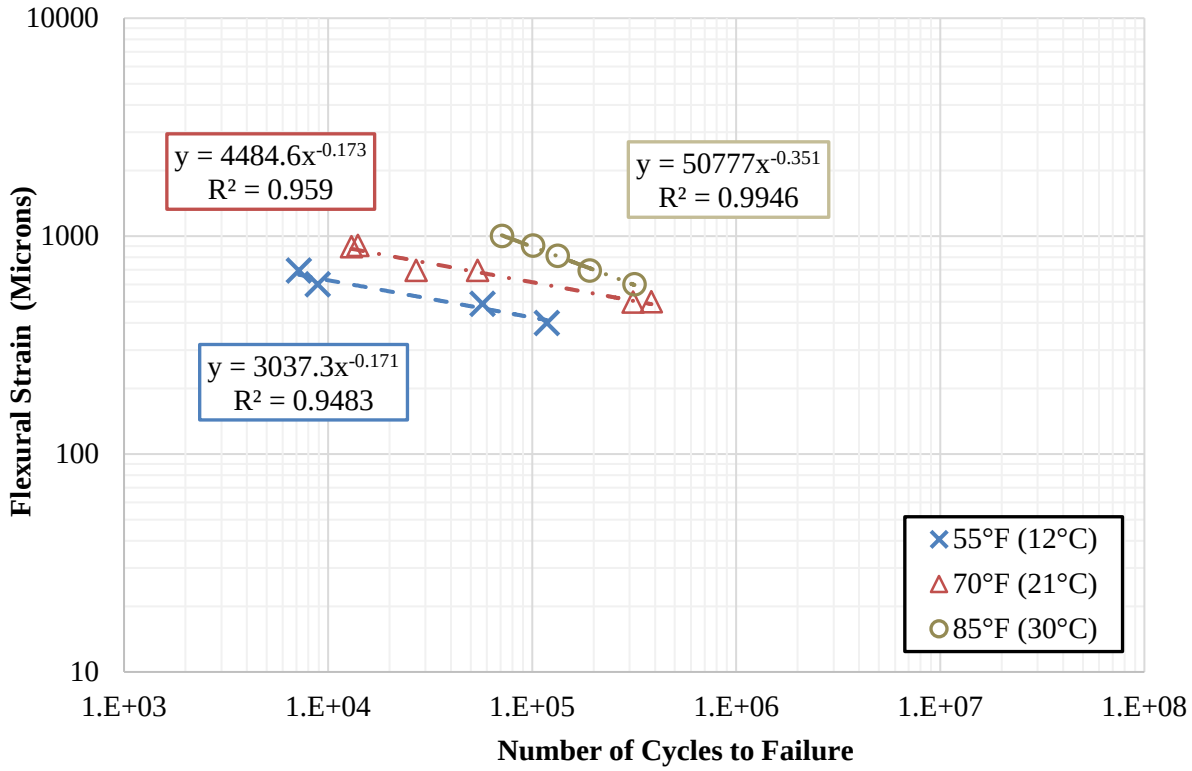


**Figure C.68. Beam fatigue raw data of FL125_PMA(A) at 55, 70, ad 85°F (13, 20, and 30°C).**

## Table C.37. Summary of Beam Fatigue Data for FL125_PMA(A) AC mix.

| Sample ID | Air Voids Level (%) | Testing Temp, °F (°C) | Dynamic Modulus E*, psi (MPa)[a] | Initial Flexural Stiffness $S_0$, psi (MPa) | Initial Dissipated Energy $E_0$, J/m$^3$ | Flexural Strain Level (micro-strain) | Number of Cycles to Failure |
|---|---|---|---|---|---|---|---|
| S1 | 7.2 | 55 (13) | 1,471,400 (10,145) | 1,184,233 (8,165) | 1,294 | 400 | 118,000 |
| S2 | 7.5 | 55 (13) | 1,471,400 (10,145) | 1,264,584 (8,719) | 1,663 | 488 | 57,000 |
| S3 | 8 | 55 (13) | 1,471,400 (10,145) | 986,982 (6,805) | 1,663 | 602 | 8,900 |
| S4 | 7.5 | 55 (13) | 1,471,400 (10,145) | 1,386,271 (9,558) | 5,058 | 695 | 7,200 |
| S5 | 7 | 70 (21) | 954,600 (6,582) | 774,066 (5,337) | 1,602 | 498 | 312,000 |
| S6 | 7.9 | 70 (21) | 954,600 (6,582) | 703,578 (4,851) | 2,793 | 500 | 384,000 |
| S7 | 7.9 | 70 (21) | 954,600 (6,582) | 681,967 (4,702) | 2,793 | 696 | 27,000 |
| S8 | 8 | 70 (21) | 954,600 (6,582) | 615,105 (4,241) | 2,802 | 697 | 54,000 |
| S9 | 8 | 70 (21) | 954,600 (6,582) | 581,021 (4,006) | 4,168 | 893 | 13,000 |
| S10 | 7.7 | 70 (21) | 954,600 (6,582) | 627,578 (4,327) | 6,416 | 906 | 14,000 |
| S11 | 7.6 | 85 (30) | 556,300 (3836) | 267,015 (1,841) | 1864 | 602 | 317,000 |
| S12 | 7.8 | 85 (30) | 556,300 (3836) | 284,854 (1,964) | 3874 | 697 | 191,000 |
| S13 | 7.9 | 85 (30) | 556,300 (3836) | 231,625 (1,597) | 3398 | 812 | 133,000 |
| S14 | 7.3 | 85 (30) | 556,300 (3836) | 277,167 (1,911) | 3874 | 905 | 101,000 |
| S15 | 8.1 | 31700 | 556,300 (3836) | 245,114 (1,690) | 3618 | 1,002 | 71,000 |

[a] Dynamic Modulus E* is determined at the testing temperature and a frequency of 10 Hz

### C.3.6. FL125_PMA(B) AC Mix

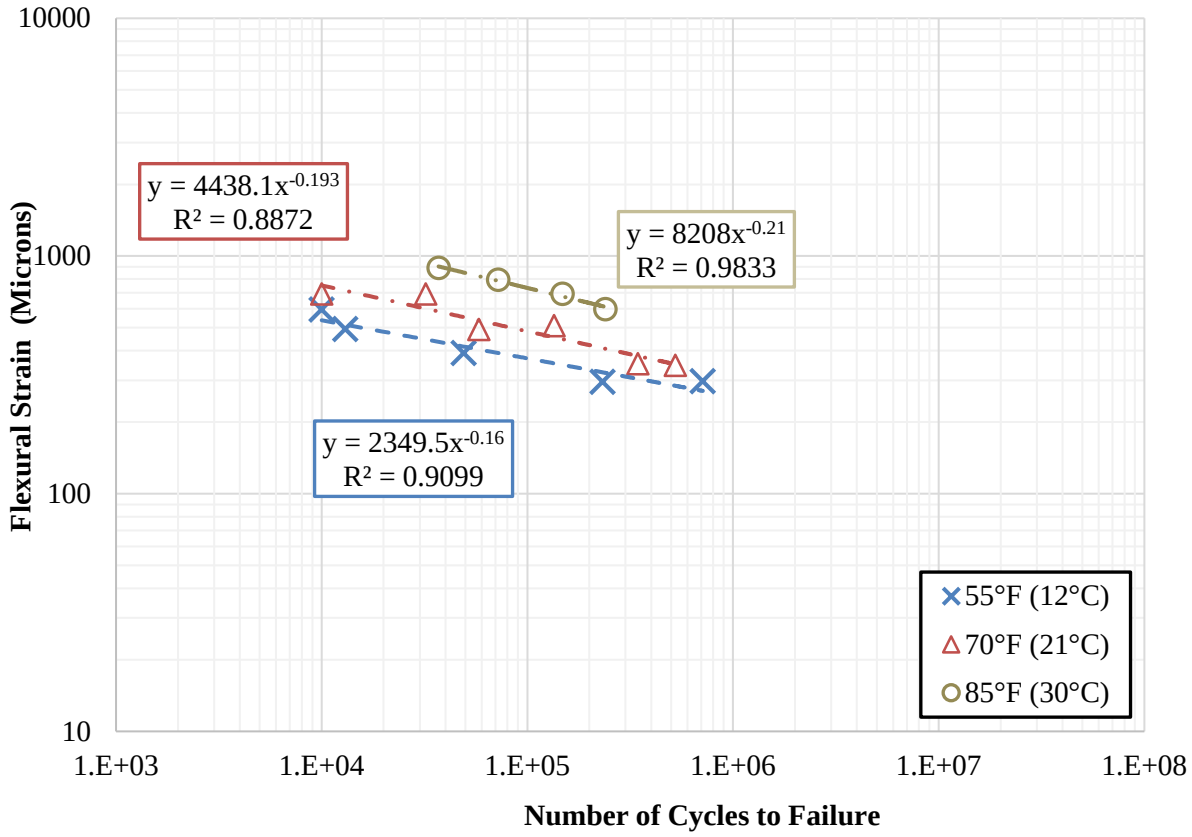


**Figure C.69. Beam fatigue raw data of FL125_PMA(B) at 55, 70, ad 85°F (13, 20, and 30°C).**

## Table C.38. Summary of Beam Fatigue Data for FL125_PMA(B) AC mix.

| Sample ID | Air Voids Level (%) | Testing Temp, °F (°C) | Dynamic Modulus E*, psi (MPa)[a] | Initial Flexural Stiffness $S_0$, psi (MPa) | Initial Dissipated Energy $E_0$, J/m$^3$ | Flexural Strain Level (micro-strain) | Number of Cycles to Failure |
|---|---|---|---|---|---|---|---|
| S1 | 7.4 | 55 (13) | 1,576,300 (10,868) | 1,141,012 (7,867) | 1,212 | 295 | 232,000 |
| S2 | 7.6 | 55 (13) | 1,576,300 (10,868) | 1,215,416 (8,380) | 365 | 298 | 713,000 |
| S3 | 7.5 | 55 (13) | 1,576,300 (10,868) | 1,096,050 (7,557) | 710 | 390 | 49,000 |
| S4 | 8 | 55 (13) | 1,576,300 (10,868) | 891,402 (6,146) | 1,212 | 493 | 13,000 |
| S5 | 7.5 | 55 (13) | 1,576,300 (10,868) | 966,967 (6,666) | 2,712 | 595 | 10,001 |
| S6 | 8 | 70 (21) | 1,036,600 (7,147) | 574,930 (3,964) | 365 | 347 | 524,000 |
| S7 | 7.4 | 70 (21) | 1,036,600 (7,147) | 771,891 (5,322) | 796 | 353 | 345,000 |
| S8 | 7.8 | 70 (21) | 1,036,600 (7,147) | 666,593 (4,596) | 2,377 | 491 | 58,000 |
| S9 | 8 | 70 (21) | 1,036,600 (7,147) | 590,739 (4,073) | 1,213 | 509 | 135,000 |
| S10 | 7.5 | 70 (21) | 1,036,600 (7,147) | 607,853 (4,191) | 2,377 | 692 | 10,001 |
| S11 | 7.6 | 70 (21) | 1,036,600 (7,147) | 627,578 (4,327) | 2,550 | 693 | 32,000 |
| S12 | 7.8 | 85 (30) | 609,300 (4,201) | 368,976 (2,544) | 3,350 | 597 | 239,000 |
| S13 | 8.3 | 85 (30) | 609,300 (4,201) | 330,831 (2,281) | 1,407 | 693 | 148,000 |
| S14 | 7.3 | 85 (30) | 609,300 (4,201) | 350,701 (2,418) | 3,350 | 795 | 72,000 |
| S15 | 8.3 | 85 (30) | 609,300 (4,201) | 321,404 (2,216) | 2,696 | 892 | 37,000 |

[a] Dynamic Modulus E* is determined at the testing temperature and a frequency of 10 Hz

### C.3.7. FL125_HP(A) AC Mix

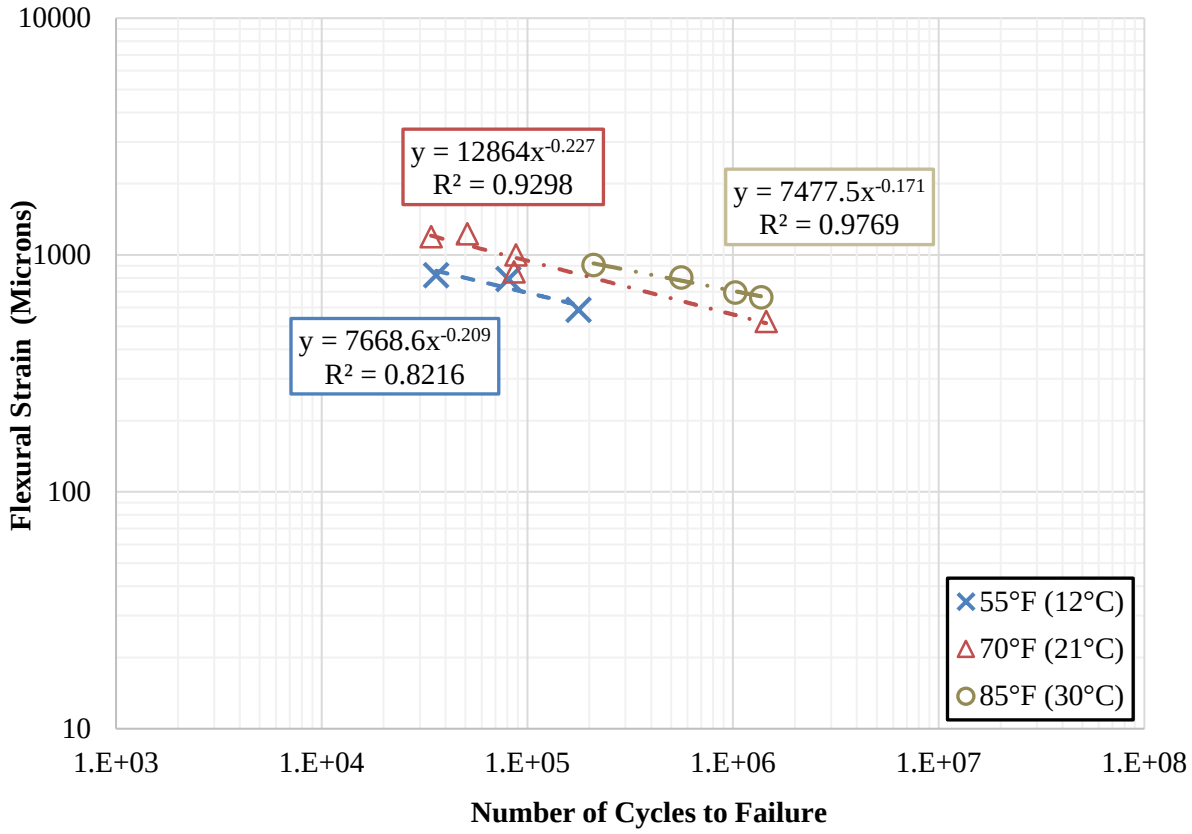


**Figure C.70. Beam fatigue raw data of FL125_HP(A) at 55, 70, ad 85°F (13, 20, and 30°C).**

## Table C.39. Summary of Beam Fatigue Data for FL125_HP(A) AC mix.

| Sample ID | Air Voids Level (%) | Testing Temp, °F (°C) | Dynamic Modulus E*, psi (MPa)[a] | Initial Flexural Stiffness $S_0$, psi (MPa) | Initial Dissipated Energy $E_0$, J/m$^3$ | Flexural Strain Level (micro-strain) | Number of Cycles to Failure |
|---|---|---|---|---|---|---|---|
| S1 | 7.8 | 55 (13) | 929,100 (6,406) | 811,341 (5,594) | 1,516 | 588 | 177,000 |
| S2 | 7.8 | 55 (13) | 929,100 (6,406) | 679,937 (4,688) | 1,516 | 792 | 81,000 |
| S3 | 7.8 | 55 (13) | 929,100 (6,406) | 588,273 (4,056) | 2,423 | 821 | 36,000 |
| S4 | 7.6 | 70 (21) | 574,800 (3,963) | 332,717 (2,294) | 2,476 | 525 | 1,448,169 |
| S5 | 7.4 | 70 (21) | 574,800 (3,963) | 354,182 (2,442) | 3,172 | 848 | 86,000 |
| S6 | 7.6 | 70 (21) | 574,800 (3,963) | 302,404 (2,085) | 3,804 | 1,000 | 88,000 |
| S7 | 7.3 | 70 (21) | 574,800 (3,963) | 313,572 (2,162) | 5,504 | 1,195 | 34,000 |
| S8 | 7.3 | 70 (21) | 574,800 (3,963) | 336,778 (2,322) | 3,172 | 1,230 | 51,000 |
| S9 | 7.8 | 85 (30) | 328,700 (2,266) | 213,496 (1,472) | 628 | 664 | 1,367,721 |
| S10 | 7.7 | 85 (30) | 328,700 (2,266) | 186,229 (1,284) | 744 | 696 | 1,024,926 |
| S11 | 7.7 | 85 (30) | 328,700 (2,266) | 198,992 (1,372) | 1,446 | 806 | 558,104 |
| S12 | 7.7 | 85 (30) | 328,700 (2,266) | 181,297 (1,250) | 628 | 909 | 209,592 |

[a] Dynamic Modulus E* is determined at the testing temperature and a frequency of 10 Hz

### C.3.8. FL125_HP(B) AC Mix

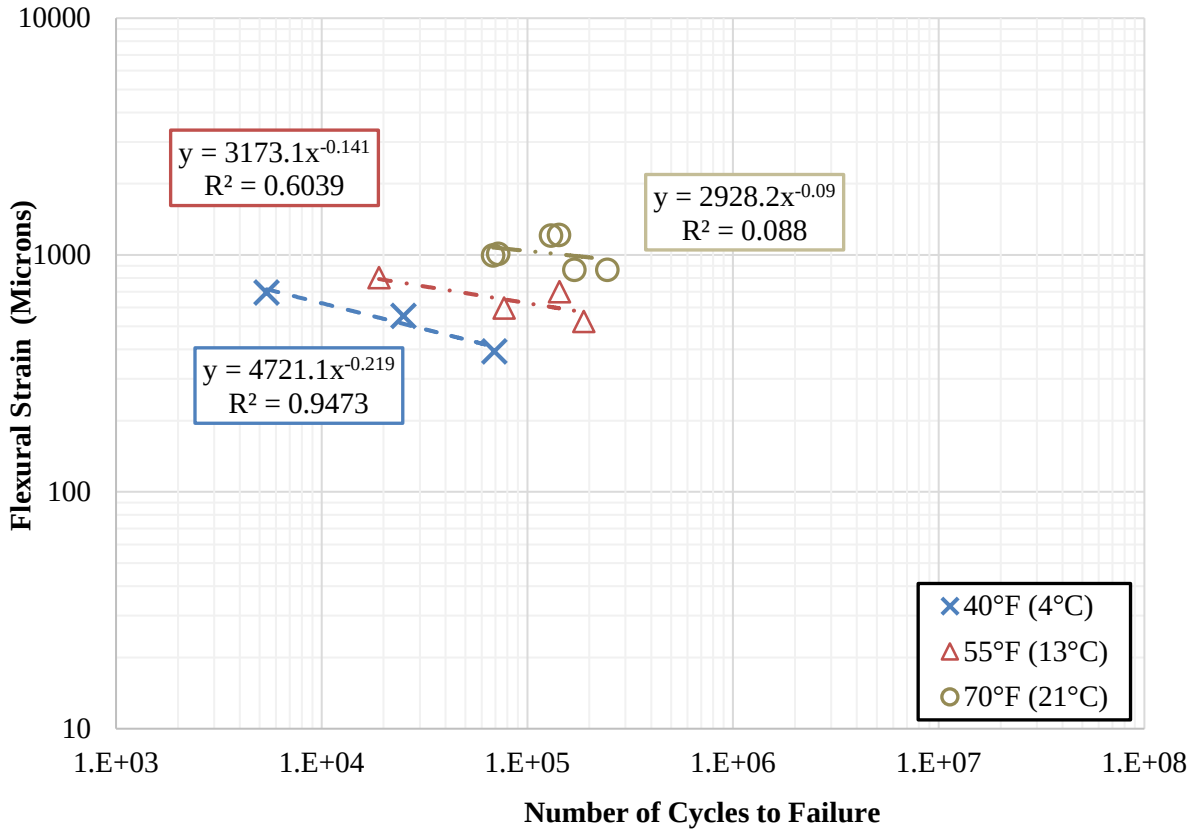


**Figure C.71. Beam fatigue raw data of FL125_HP(B) at 40, 55, ad 70°F (13, 20, and 30°C).**

## Table C.40. Summary of Beam Fatigue Data for FL125_HP(B) AC mix.

| Sample ID | Air Voids Level (%) | Testing Temp, °F (°C) | Dynamic Modulus E*, psi (MPa)[a] | Initial Flexural Stiffness $S_0$, psi (MPa) | Initial Dissipated Energy $E_0$, J/m$^3$ | Flexural Strain Level (micro-strain) | Number of Cycles to Failure |
|---|---|---|---|---|---|---|---|
| S1 | 7.7 | 40 (4) | 1,643,800 (11,334) | 1,336,088 (9,212) | 756 | 362 | 69,000 |
| S2 | 7.7 | 40 (4) | 1,643,800 (11,334) | 1,004,386 (6,925) | 1,957 | 553 | 25,000 |
| S3 | 7.7 | 40 (4) | 1,643,800 (11,334) | 921,280 (6,352) | 3,127 | 695 | 5,400 |
| S4 | 7.4 | 55 (13) | 1,091,400 (7,525) | 634,395 (4,374) | 1,357 | 524 | 188,000 |
| S5 | 6.8 | 55 (13) | 1,091,400 (7,525) | 847,601 (5,844) | 2,363 | 598 | 77,000 |
| S6 | 7.7 | 55 (13) | 1,091,400 (7,525) | 561,441 (3,871) | 2,809 | 699 | 143,000 |
| S7 | 8.2 | 55 (13) | 1,091,400 (7,525) | 607,998 (4,192) | 2,363 | 802 | 19,000 |
| S8 | 7.9 | 70 (21) | 640,900 (4,419) | 294,610 (1,721) | 2,676 | 867 | 169,000 |
| S9 | 7.8 | 70 (21) | 640,900 (4,419) | 296,457 (2,044) | 3,262 | 869 | 244,000 |
| S10 | 7.3 | 70 (21) | 640,900 (4,419) | 336,052 (2,317) | 4,221 | 999 | 68,000 |
| S11 | 8.7 | 70 (21) | 640,900 (4,419) | 221,473 (1,527) | 3,262 | 1,014 | 72,000 |
| S12 | 7.8 | 70 (21) | 640,900 (4,419) | 202,473 (1,396) | 5,160 | 1,210 | 130,000 |
| S13 | 7.8 | 70 (21) | 640,900 (4,419) | 222,778 (1,536) | 6,241 | 1,218 | 142,000 |

[a] Dynamic Modulus E* is determined at the testing temperature and a frequency of 10 Hz

### C.3.9. GA95_PMA(A) AC Mix

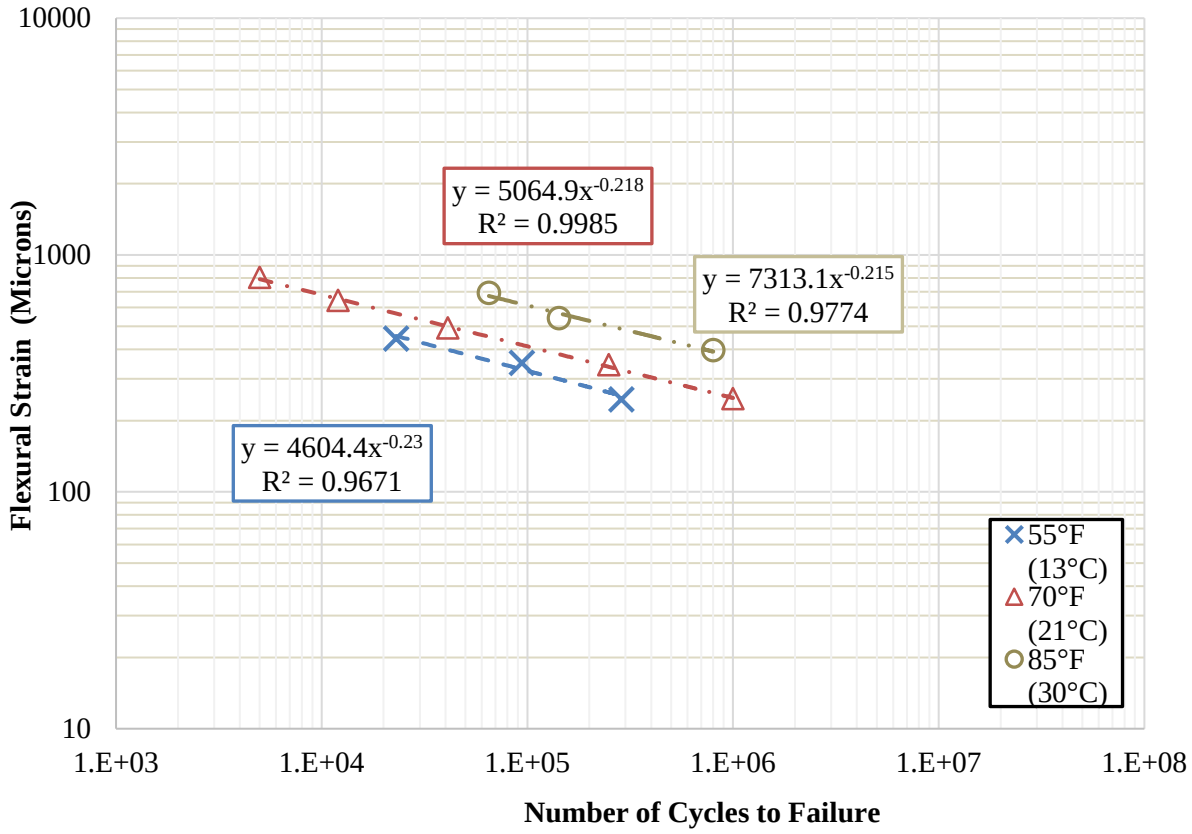


**Figure C.72. Beam fatigue raw data of GA95_PMA(A) at 55, 70, ad 85°F (13, 20, and 30°C).**

## Table C.41. Summary of Beam Fatigue Data for GA95_PMA(A) AC mix.

| Sample ID | Air Voids Level (%) | Testing Temp, °F (°C) | Dynamic Modulus E*, psi (MPa)[a] | Initial Flexural Stiffness $S_0$, psi (MPa) | Initial Dissipated Energy $E_0$, J/m$^3$ | Flexural Strain Level (micro-strain) | Number of Cycles to Failure |
|---|---|---|---|---|---|---|---|
| S1 | 7 | 55 (13) | 2,128,000 (14,672) | 2,265,635 (15,621) | 476 | 246 | 287,000 |
| S2 | 7 | 55 (13) | 2,128,000 (14,672) | 1,801,369 (12,420) | 1,307 | 350 | 94,000 |
| S3 | 7.9 | 55 (13) | 2,128,000 (14,672) | 1,933,353 (13,330) | 1,898 | 443 | 23,000 |
| S4 | 7.9 | 70 (21) | 1,506,800 (10,389) | 1,291,126 (8,902) | 228 | 247 | 1,000,000 |
| S5 | 8.1 | 70 (21) | 1,506,800 (10,389) | 1,274,882 (8,790) | 2,858 | 345 | 249,000 |
| S6 | 7.7 | 70 (21) | 1,506,800 (10,389) | 1,156,821 (7,976) | 1,692 | 492 | 41,000 |
| S7 | 8 | 70 (21) | 1,506,800 (10,389) | 1,059,356 (7,304) | 2,858 | 643 | 12,000 |
| S8 | 6.9 | 70 (21) | 1,506,800 (10,389) | 1,209,615 (8,340) | 7,322 | 805 | 5,000 |
| S9 | 7.5 | 85 (30) | 932,700 (6,431) | 743,754 (5,128) | 948 | 397 | 801,000 |
| S10 | 7.6 | 85 (30) | 932,700 (6,431) | 689,074 (4,751) | 1,661 | 541 | 142,000 |
| S11 | 7.7 | 85 (30) | 932,700 (6,431) | 683,853 (4,717) | 2,887 | 694 | 65,000 |

[a] Dynamic Modulus E* is determined at the testing temperature and a frequency of 10 Hz

### C.3.10. GA95_PMA(B) AC Mix

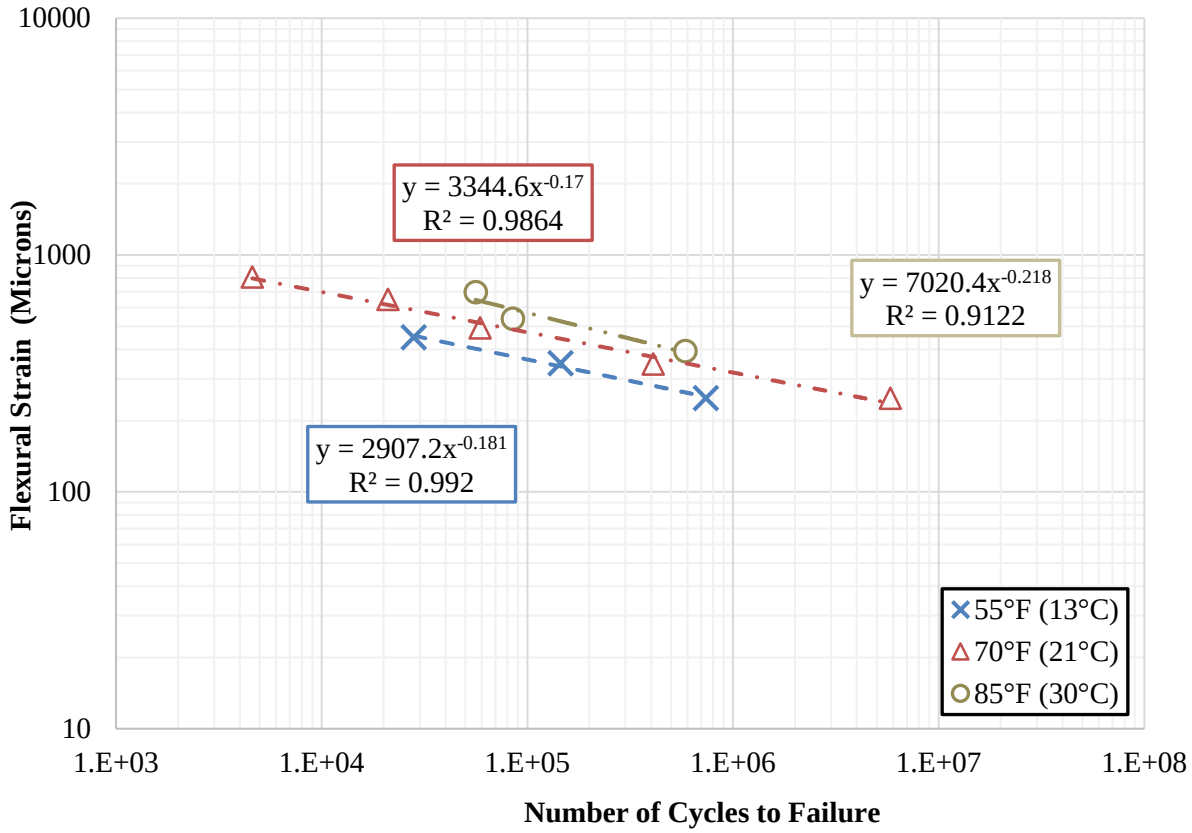


**Figure C.73. Beam fatigue raw data of GA95_PMA(B) at 55, 70, ad 85°F (13, 20, and 30°C).**

## Table C.42. Summary of Beam Fatigue Data for GA95_PMA(B) AC mix.

| Sample ID | Air Voids Level (%) | Testing Temp, °F (°C) | Dynamic Modulus E*, psi (MPa)[a] | Initial Flexural Stiffness $S_0$, psi (MPa) | Initial Dissipated Energy $E_0$, J/m$^3$ | Flexural Strain Level (micro-strain) | Number of Cycles to Failure |
|---|---|---|---|---|---|---|---|
| S1 | 7.9 | 55 (13) | 2,280,800 (15,725) | 1,775,262 (12,240) | 459 | 249 | 737,000 |
| S2 | 7.9 | 55 (13) | 2,280,800 (15,725) | 1,862,720 (12,843) | 1,402 | 349 | 145,000 |
| S3 | 8 | 55 (13) | 2,280,800 (15,725) | 1,832,407 (12,634) | 2,333 | 449 | 28,000 |
| S4 | 8.1 | 70 (21) | 1,677,800 (11,568) | 1,180,462 (8,139) | 392 | 248 | 5,813,780 |
| S5 | 7.9 | 70 (21) | 1,677,800 (11,568) | 1,293,447 (8,918) | 3,290 | 347 | 409,000 |
| S6 | 7.9 | 70 (21) | 1,677,800 (11,568) | 994,379 (8,656) | 1,690 | 493 | 59,000 |
| S7 | 7.7 | 70 (21) | 1,677,800 (11,568) | 1,114,760 (7,686) | 3,290 | 649 | 21,000 |
| S8 | 7.5 | 70 (21) | 1,677,800 (11,568) | 1,074,295 (7,407) | 8,233 | 808 | 4,600 |
| S9 | 7.9 | 85 (30) | 1,088,700 (7,506) | 580,731 (4,004) | 789 | 394 | 585,000 |
| S10 | 7.9 | 85 (30) | 1,088,700 (7,506) | 610,754 (4,211) | 1,753 | 539 | 85,000 |
| S11 | 7.7 | 85 (30) | 1,088,700 (7,506) | 581,456 (4,009) | 2,742 | 697 | 56,000 |

[a] Dynamic Modulus E* is determined at the testing temperature and a frequency of 10 Hz

### C.3.11. GA95_HP(A) AC Mix

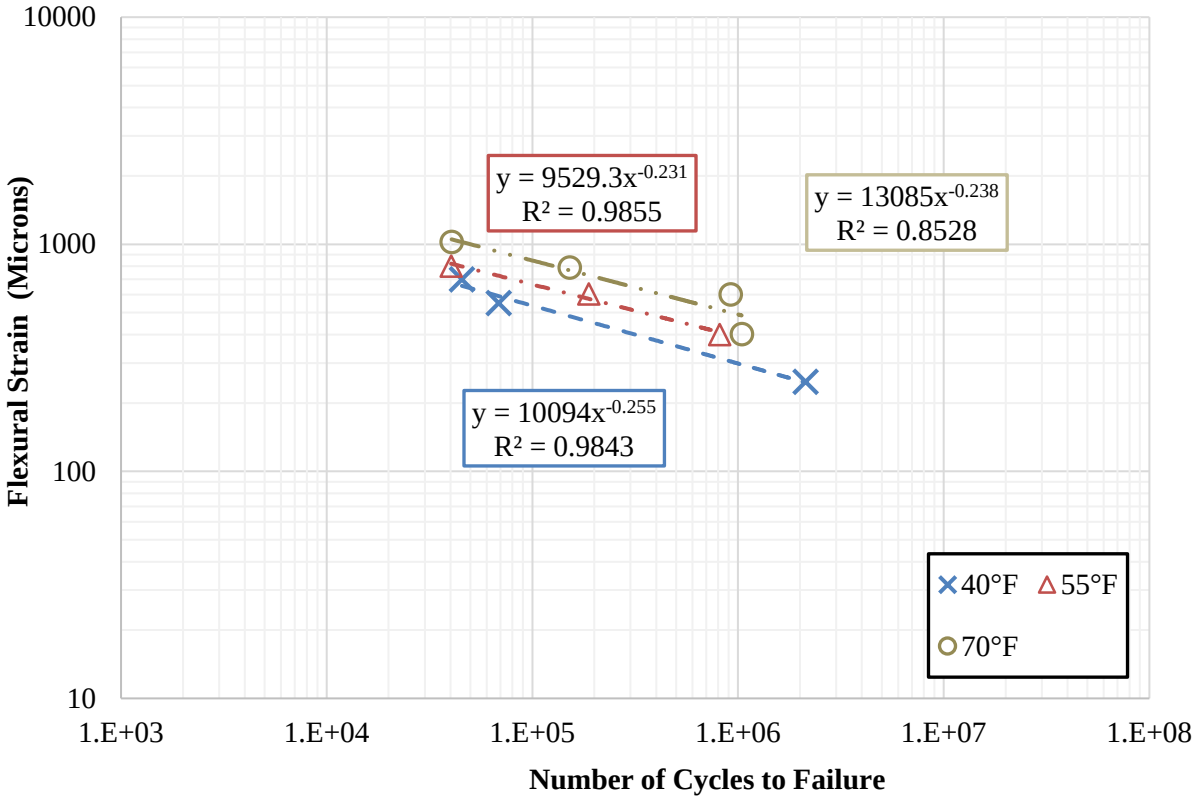


**Figure C.74. Beam fatigue raw data of GA95_HP(A) at 40, 55, ad 70°F (4, 13, and 21°C).**

## Table C.43. Summary of Beam Fatigue Data for GA95_HP(A) AC mix.

| Sample ID | Air Voids Level (%) | Testing Temp, °F (°C) | Dynamic Modulus E*, psi (MPa)[a] | Initial Flexural Stiffness $S_0$, psi (MPa) | Initial Dissipated Energy $E_0$, J/m$^3$ | Flexural Strain Level (micro-strain) | Number of Cycles to Failure |
|---|---|---|---|---|---|---|---|
| S1 | 7.7 | 40 (4) | 1,704,000 (11,748) | 1,095,905 (7,556) | 435 | 248 | 2,127,637 |
| S2 | 8.2 | 40 (4) | 1,704,000 (11,748) | 1,177,271 (8,117) | 2,992 | 550 | 68,656 |
| S3 | 7.8 | 40 (4) | 1,704,000 (11,748) | 1,027,882 (7,087) | 4,454 | 699 | 45,444 |
| S4 | 7.7 | 55 (13) | 1,124,300 (7,752) | 605,967 (4,178) | 1,057 | 400 | 45,444 |
| S5 | 8 | 55 (13) | 1,124,300 (7,752) | 594,220 (4,097) | 2,859 | 604 | 96,000 |
| S6 | 7.7 | 55 (13) | 1,124,300 (7,752) | 608,433 (4,195) | 4,563 | 802 | 51,000 |
| S7 | 7.7 | 70 (21) | 653,100 (4,503) | 299,503 (2,065) | 877 | 403 | 880,000 |
| S8 | 7.9 | 70 (21) | 653,100 (4,503) | 308,205 (2,125) | 1302 | 602 | 522,000 |
| S9 | 7.4 | 70 (21) | 653,100 (4,503) | 328,801 (2,267) | 1302 | 790 | 122,000 |
| S10 | 7.8 | 70 (21) | 653,100 (4,503) | 238,297 (1,643) | 5404 | 1,026 | 146,000 |

[a] Dynamic Modulus E* is determined at the testing temperature and a frequency of 10 Hz

### C.3.12. GA95_HP(B) AC Mix

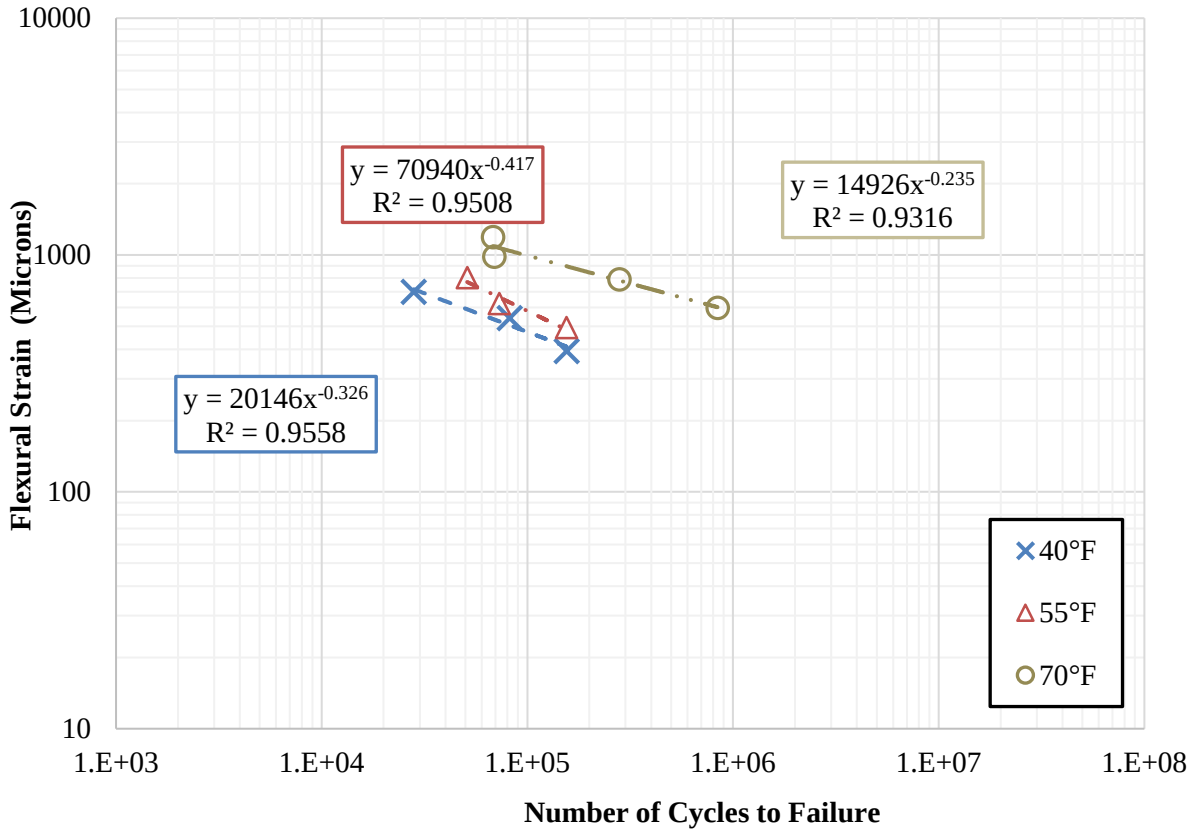


**Figure C.75. Beam fatigue raw data of GA95_HP(B) at 40, 55, ad 70°F (4, 13, and 21°C).**

## Table C.44. Summary of Beam Fatigue Data for GA95_HP(B) AC mix.

| Sample ID | Air Voids Level (%) | Testing Temp, °F (°C) | Dynamic Modulus E*, psi (MPa)[a] | Initial Flexural Stiffness $S_0$, psi (MPa) | Initial Dissipated Energy $E_0$, J/m$^3$ | Flexural Strain Level (micro-strain) | Number of Cycles to Failure |
|---|---|---|---|---|---|---|---|
| S1 | 7.4 | 40 (4) | 1,517,500 (10,463) | 1,177,561 (8,119) | 1,344 | 393 | 155,000 |
| S2 | 7.2 | 40 (4) | 1,517,500 (10,463) | 1,119,256 (7,717) | 2,659 | 541 | 82,000 |
| S3 | 7.7 | 40 (4) | 1,517,500 (10,463) | 998,005 (6,881) | 4,266 | 699 | 28,000 |
| S4 | 7.7 | 55 (13) | 1,033,400 (7,125) | 813,807 (5,611) | 1,792 | 493 | 155,000 |
| S5 | 7.7 | 55 (13) | 1,033,400 (7,125) | 620,181 (4,276) | 1,804 | 623 | 73,000 |
| S6 | 7.7 | 55 (13) | 1,033,400 (7,125) | 519,525 (3,582) | 3,689 | 802 | 51,000 |
| S7 | 7.6 | 70 (21) | 635,800 (4,384) | 299,938 (2,068) | 1,479 | 599 | 840,000 |
| S8 | 7.9 | 70 (21) | 635,800 (4,384) | 311,106 (2,145) | 2,114 | 789 | 280,000 |
| S9 | 7.6 | 70 (21) | 635,800 (4,384) | 325,320 (2,243) | 3,458 | 984 | 69,000 |
| S10 | 7.3 | 70 (21) | 635,800 (4,384) | 261,213 (1,801) | 2,114 | 1,193 | 68,000 |

[a] Dynamic Modulus E* is determined at the testing temperature and a frequency of 10 Hz

### C.3.13. GA125_PMA(A) AC Mix

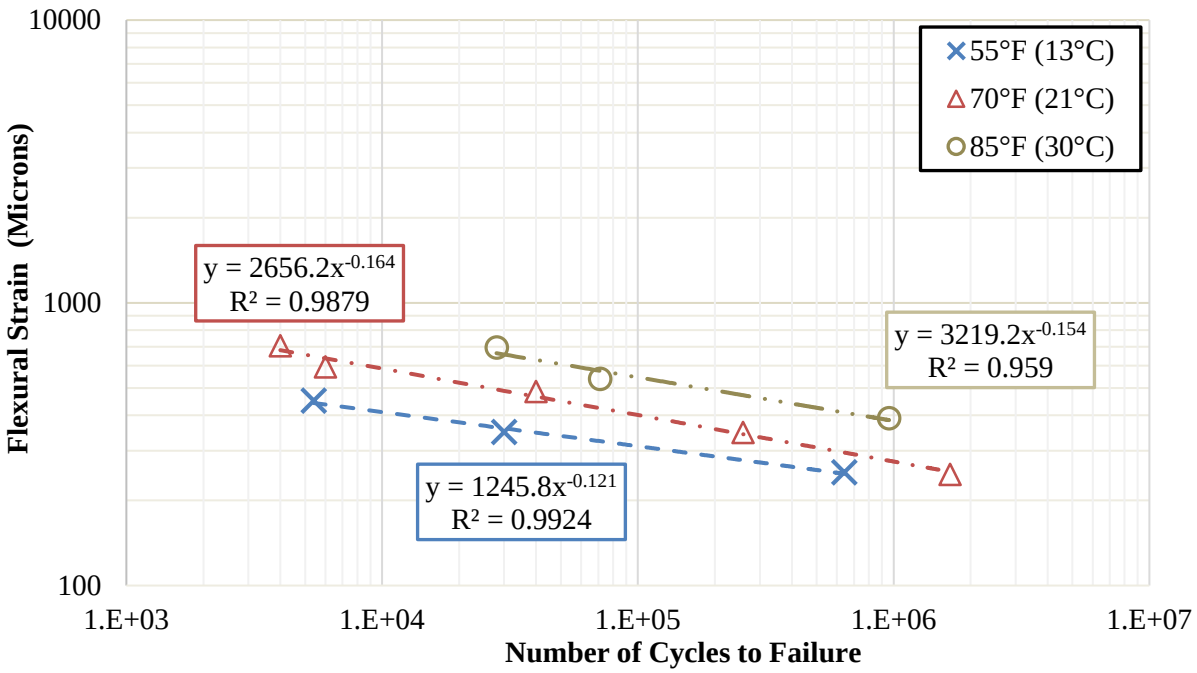


**Figure C.76. Beam fatigue raw data of GA125_PMA(A) at 55, 70, ad 85°F (13, 20, and 30°C).**

## Table C.45. Summary of Beam Fatigue Data for GA125_PMA(A) AC mix.

| Sample ID | Air Voids Level (%) | Testing Temp, °F (°C) | Dynamic Modulus E*, psi (MPa)[a] | Initial Flexural Stiffness $S_0$, psi (MPa) | Initial Dissipated Energy $E_0$, J/m$^3$ | Flexural Strain Level (micro-strain) | Number of Cycles to Failure |
|---|---|---|---|---|---|---|---|
| S1 | 7.9 | 55 (13) | 2,196,200 (15,142) | 1,534,644 (10,581) | 492 | 251 | 642,000 |
| S2 | 7.9 | 55 (13) | 2,196,200 (15,142) | 1,716,522 (11,835) | 1,120 | 349 | 30,000 |
| S3 | 6.8 | 55 (13) | 2,196,200 (15,142) | 1,432,393 (9,876) | 2,282 | 451 | 5,400 |
| S4 | 7.3 | 70 (13) | 1,603,200 (11,054) | 938,249 (6,469) | 247 | 247 | 1,661,054 |
| S5 | 7.3 | 70 (13) | 1,603,200 (11,054) | 892,562 (6,154) | 2,108 | 348 | 258,000 |
| S6 | 6.8 | 70 (13) | 1,603,200 (11,054) | 993,799 (6,852) | 1,417 | 486 | 40,000 |
| S7 | 6.9 | 70 (13) | 1,603,200 (11,054) | 834,112 (5,751) | 2,108 | 593 | 6,000 |
| S8 | 7.6 | 70 (13) | 1,603,200 (11,054) | 897,349 (6,187) | 4,099 | 705 | 4,000 |
| S9 | 7.9 | 85 (30) | 1,038,300 (7,159) | 615,685 (4,245) | 791 | 391 | 959,836 |
| S10 | 7.8 | 85 (30) | 1,038,300 (7,159) | 655,281 (4,518) | 1,851 | 539 | 71,000 |
| S11 | 7.8 | 85 (30) | 1,038,300 (7,159) | 476,014 (3,282) | 2,754 | 696 | 28,000 |

[a] Dynamic Modulus E* is determined at the testing temperature and a frequency of 10 Hz

### C.3.14. GA125_PMA(B) AC Mix

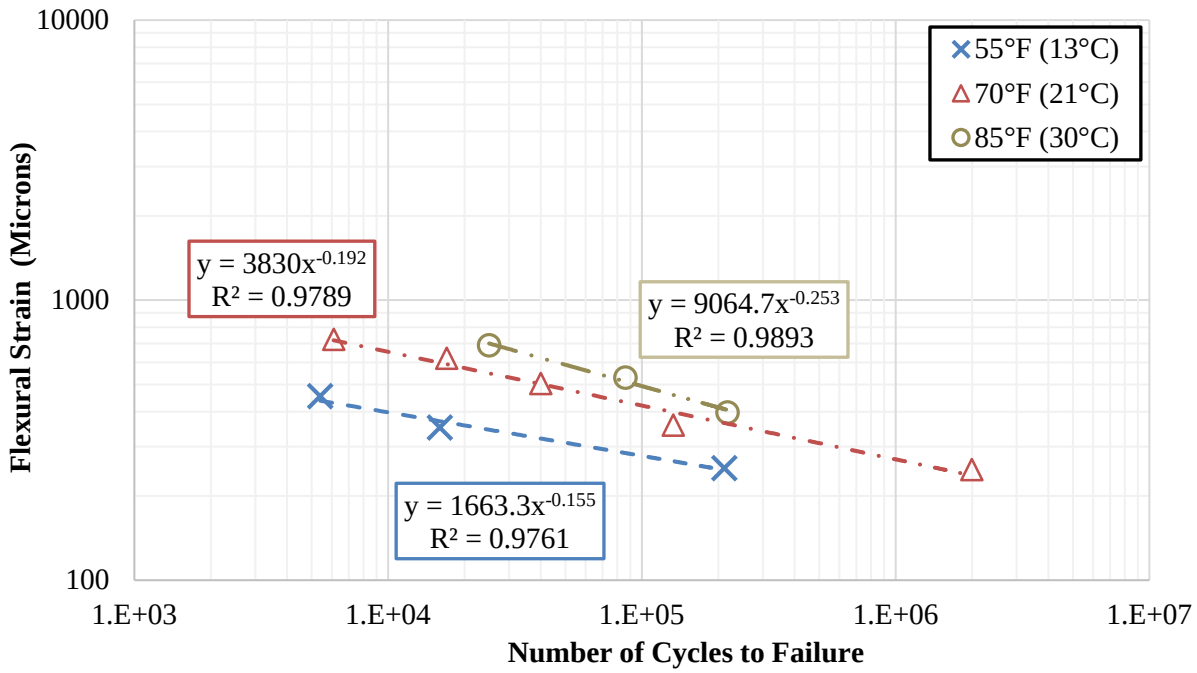


**Figure C.77. Beam fatigue raw data of GA125_PMA(B) at 55, 70, ad 85°F (13, 20, and 30°C).**

## Table C.46. Summary of Beam Fatigue Data for GA125_PMA(B) AC mix.

| Sample ID | Air Voids Level (%) | Testing Temp, °F (°C) | Dynamic Modulus E*, psi (MPa)[a] | Initial Flexural Stiffness $S_0$, psi (MPa) | Initial Dissipated Energy $E_0$, $J/m^3$ | Flexural Strain Level (micro-strain) | Number of Cycles to Failure |
|---|---|---|---|---|---|---|---|
| S1 | 7.8 | 55 (13) | 2,275,500 (15,689) | 1,483,301 (10,227) | 442 | 251 | 211,000 |
| S2 | 7.8 | 55 (13) | 2,275,500 (15,689) | 2,140,612 (14,759) | 1,188 | 351 | 16,000 |
| S3 | 7.8 | 55 (13) | 2,275,500 (15,689) | 1,222,233 (8,427) | 1,811 | 454 | 5,400 |
| S4 | 8.5 | 70 (13) | 1,688,500 (11,642) | 896,043 (6,178) | 326 | 248 | 1,993,970 |
| S5 | 7.9 | 70 (13) | 1,688,500 (11,642) | 901,845 (6,218) | 2,267 | 358 | 133,000 |
| S6 | 7.9 | 70 (13) | 1,688,500 (11,642) | 782,334 (5,394) | 1,026 | 503 | 40,000 |
| S7 | 7.7 | 70 (13) | 1,688,500 (11,642) | 791,906 (5,460) | 2,267 | 620 | 17,000 |
| S8 | 7.5 | 70 (13) | 1,688,500 (11,642) | 893,287 (6,159) | 3,400 | 724 | 6,100 |
| S9 | 8.1 | 85 (30) | 1,114,300 (7,683) | 655,426 (4,519) | 1,140 | 398 | 217,000 |
| S10 | 7.9 | 85 (30) | 1,114,300 (7,683) | 623,372 (4,298) | 1,196 | 530 | 86,000 |
| S11 | 8.3 | 85 (30) | 1,114,300 (7,683) | 527,502 (3,637) | 2,260 | 691 | 25,000 |

[a] Dynamic Modulus E* is determined at the testing temperature and a frequency of 10 Hz

### C.3.15. GA125_HP(A) AC Mix

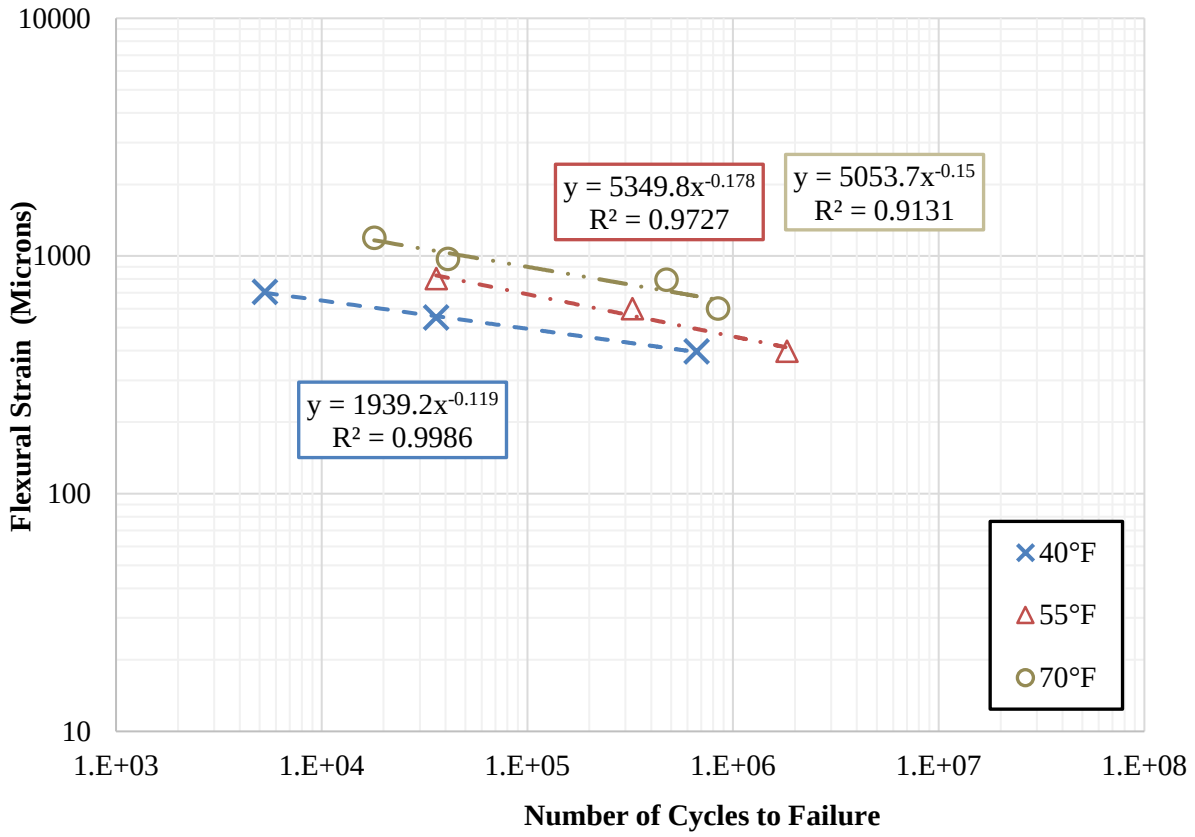


**Figure C.78. Beam fatigue raw data of GA125_HP(A) at 40, 55, ad 70°F (4, 13, and 21°C).**

## Table C.47. Summary of Beam Fatigue Data for GA125_HP(A) AC mix.

| Sample ID | Air Voids Level (%) | Testing Temp, °F (°C) | Dynamic Modulus E*, psi (MPa)[a] | Initial Flexural Stiffness $S_0$, psi (MPa) | Initial Dissipated Energy $E_0$, J/m$^3$ | Flexural Strain Level (micro-strain) | Number of Cycles to Failure |
|---|---|---|---|---|---|---|---|
| S1 | 6.9 | 40 (4) | 1,663,500 (11,469) | 1,268,790 (8,748) | 1,254 | 396 | 666,000 |
| S2 | 6.9 | 40 (4) | 1,663,500 (11,469) | 1,374,958 (9,480) | 3,420 | 551 | 36,000 |
| S3 | 7.1 | 40 (4) | 1,663,500 (11,469) | 1,289,095 (8,888) | 5,659 | 706 | 5,300 |
| S4 | 7.2 | 55 (13) | 1,155,200 (7,965) | 734,906 (5,067) | 1,165 | 397 | 1,826,578 |
| S5 | 7.2 | 55 (13) | 1,155,200 (7,965) | 747,960 (5,157) | 2,977 | 600 | 324,000 |
| S6 | 6.9 | 55 (13) | 1,155,200 (7,965) | 904,310 (6,235) | 6,087 | 804 | 36,000 |
| S7 | 7.7 | 70 (21) | 727,600 (5,017) | 406,541 (2,803) | 4881 | 603 | 845,000 |
| S8 | 6.9 | 70 (21) | 727,600 (5,017) | 512,777 (2,846) | 2699 | 796 | 474,000 |
| S9 | 7.4 | 70 (21) | 727,600 (5,017) | 398,274 (2,746) | 4881 | 975 | 41,000 |
| S10 | 7.6 | 70 (21) | 727,600 (5,017) | 362,159 (2,497) | 5743 | 1195 | 18,000 |

[a] Dynamic Modulus E* is determined at the testing temperature and a frequency of 10 Hz

### C.3.16. GA125_HP(B) AC Mix

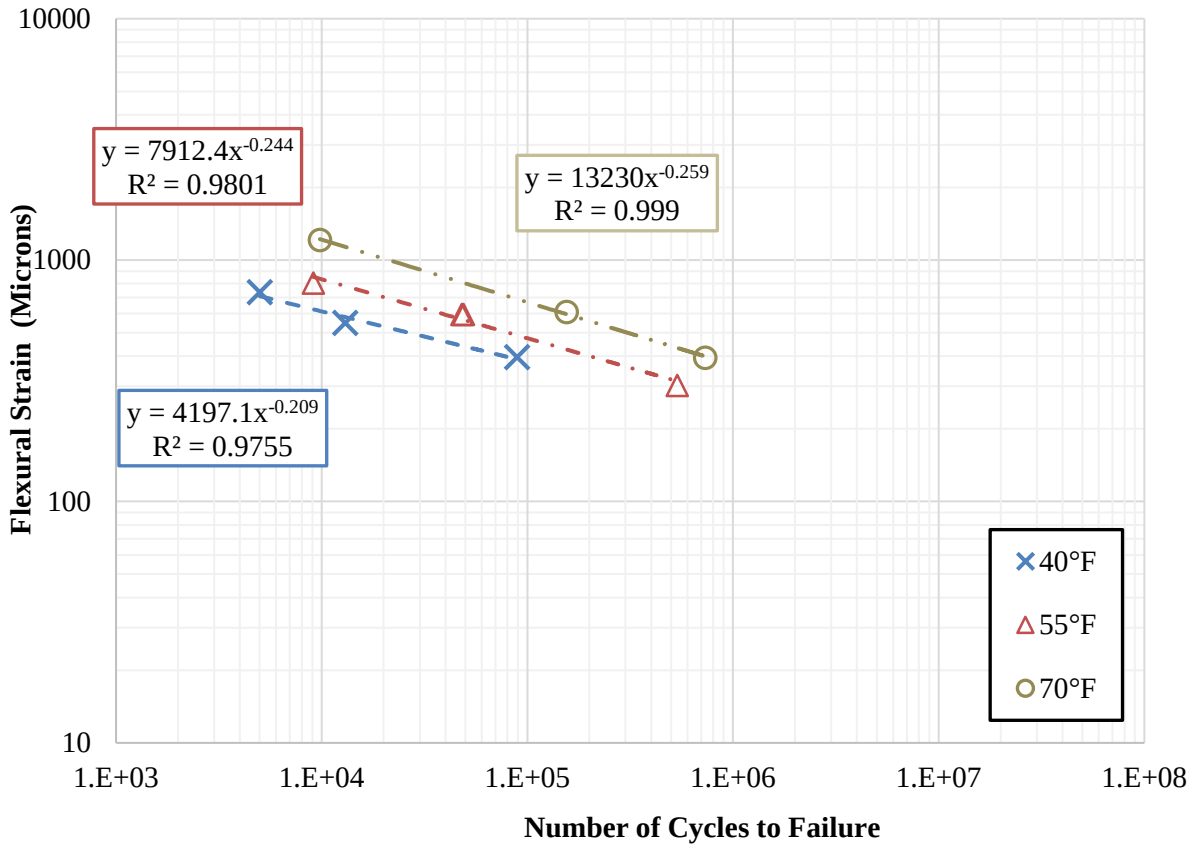


**Figure C.79. Beam fatigue raw data of GA125_HP(B) at 40, 55, ad 70°F (4, 13, and 21°C).**

## Table C.48. Summary of Beam Fatigue Data for GA125_HP(B) AC mix.

| Sample ID | Air Voids Level (%) | Testing Temp, °F (°C) | Dynamic Modulus E*, psi (MPa)[a] | Initial Flexural Stiffness $S_0$, psi (MPa) | Initial Dissipated Energy $E_0$, J/m$^3$ | Flexural Strain Level (micro-strain) | Number of Cycles to Failure |
|---|---|---|---|---|---|---|---|
| S1 | 7.5 | 40 (4) | 1,632,100 (11,253) | 1,732,911 (11,948) | 1,481 | 396 | 89,000 |
| S2 | 7.4 | 40 (4) | 1,632,100 (11,253) | 1,445,156 (9,964) | 3,104 | 549 | 13,000 |
| S3 | 7.5 | 40 (4) | 1,632,100 (11,253) | 1,450,087 (9,998) | 6,169 | 735 | 5,000 |
| S4 | 7.7 | 55 (13) | 1,120,000 (7,722) | 991,768 (6,838) | 1,403 | 302 | 535,051 |
| S5 | 6.5 | 55 (13) | 1,120,000 (7,722) | 853,692 (5,886) | 2,671 | 595 | 48,937 |
| S6 | 7.2 | 55 (13) | 1,120,000 (7,722) | 947,096 (6,530) | 2,808 | 596 | 48,000 |
| S7 | 7.5 | 55 (13) | 1,120,000 (7,722) | 825,700 (5,693) | 5,659 | 804 | 9,100 |
| S8 | 6.5 | 70 (21) | 692,200 (4,773) | 700,387 (4,829) | 646 | 394 | 731,798 |
| S9 | 6 | 70 (21) | 692,200 (4,773) | 393,632 (2,714) | 4,464 | 609 | 154,955 |
| S10 | 6.5 | 70 (21) | 692,200 (4,773) | 403,785 (2,784) | 6,920 | 1,212 | 9,800 |

[a] Dynamic Modulus E* is determined at the testing temperature and a frequency of 10 Hz

## APPENDIX D. BOOTSTRAPPED FUNCTION FOR CONFIDENCE INTERVALS OF MEAN STATISTIC IN R-PACKAGE

### D.1. ENTIRE DATA EVALUATED AS ONE GROUP

```
library(stats)
library(Matrix)
library(car)
x<-matrix(c(0.4, 0.382608695652174, 0.352, 0.88, 1.1, 0.88, 0.517647058823529, 0.676923076923077, 0.8, 0.382608695652174, 0.382608695652174, 0.338461538461538, 0.382608695652174, 0.366666666666667, 0.352, 0.88, 1.1, 0.977777777777778, 0.488888888888889, 0.628571428571429, 0.88, 0.382608695652174, 0.352, 0.338461538461538, 0.416842105263158, 0.396, 0.377142857142857, 0.99, 0.99, 0.792, 0.528, 0.72, 0.792, 0.36, 0.36, 0.344347826086957, 0.459130434782609, 0.502857142857143, 0.48, 1.32, 1.32, 1.32, 0.621176470588235, 0.96, 0.88, 0.502857142857143, 0.502857142857143, 0.459130434782609, 0.396, 0.377142857142857, 0.36, 0.792, 0.99, 0.99, 0.528, 0.66, 0.792, 0.396, 0.36, 0.33, 0.352, 0.406153846153846, 0.528, 0.586666666666667, 0.586666666666667, 0.528, 0.48, 0.586666666666667, 0.48, 0.48, 0.66, 0.528), 72, 1)
x

qqPlot(x)
shapiro.test(x)

boot.mean = function(x,B,binwidth=NULL) {
n = length(x)
boot.samples = matrix( sample(x,size=n*B,replace=TRUE), B, n)
boot.statistics = apply(boot.samples,1,mean)
se = sd(boot.statistics)
require(ggplot2)
if ( is.null(binwidth) )
binwidth = diff(range(boot.statistics))/30
p = ggplot(data.frame(x=boot.statistics),aes(x=x)) +
geom_histogram(aes(y=..density..),binwidth=binwidth) + geom_density(color="red")
plot(p)
interval = mean(x) + c(-1,1)*2*se
print( interval )
return( list(boot.statistics = boot.statistics, interval=interval, se=se, plot = p ) )}

out= with( data.frame(x), boot.mean(x, B=2000))
y<-out$'boot.statistics'

qqPlot(y)
shapiro.test(y)
```

## D.2. DATA BASED ON AGGREGATE SOURCES: FL VS. GA

### D.2.1. FL Data Set

```
library(stats)
library(Matrix)
library(car)
xFL<-matrix(c(0.48, 0.59, 0.75, 0.59, 0.59, 0.59, 0.53, 0.66, 0.48, 0.66, 0.59, 0.53, 0.8, 1.1, 0.68,
0.48, 0.59, 0.48, 0.33, 0.36, 0.4, 0.46, 0.5, 0.5, 0.34, 0.36, 0.36, 0.79, 0.66, 0.53, 0.88, 0.96, 0.62,
0.79, 0.72, 0.53), 36, 1)
xFL

qqPlot(xFL)
shapiro.test(xFL)

boot.mean = function(x,B,binwidth=NULL) {
n = length(x)
boot.samples = matrix( sample(x,size=n*B,replace=TRUE), B, n)
boot.statistics = apply(boot.samples,1,mean)
se = sd(boot.statistics)
require(ggplot2)
if ( is.null(binwidth) )
binwidth = diff(range(boot.statistics))/30
p = ggplot(data.frame(x=boot.statistics),aes(x=x)) +
geom_histogram(aes(y=..density..),binwidth=binwidth) + geom_density(color="red")
plot(p)
interval = mean(x) + c(-1,1)*2*se
print( interval )
return( list(boot.statistics = boot.statistics, interval=interval, se=se, plot = p ) )}

outFL= with( data.frame(xFL), boot.mean(xFL, B=2000))
yFL<-outFL$'boot.statistics'

qqPlot(yFL)
shapiro.test(yFL)
```

### D.2.2. GA Data Set

```
library(stats)
library(Matrix)
library(car)
xGA<-matrix(c(0.44, 0.44, 0.44, 0.37, 0.42, 0.46, 0.53, 0.59, 0.59, 0.53, 0.41, 0.35, 0.49, 0.44,
0.37, 0.53, 0.41, 0.35, 0.99, 0.99, 0.79, 1.32, 1.32, 1.32, 0.79, 0.99, 0.99, 0.36, 0.38, 0.4, 0.48,
0.5, 0.46, 0.38, 0.4, 0.42), 36, 1)
xGA
```

```
qqPlot(xGA)
shapiro.test(xGA)

boot.mean = function(x,B,binwidth=NULL) {
n = length(x)
boot.samples = matrix( sample(x,size=n*B,replace=TRUE), B, n)
boot.statistics = apply(boot.samples,1,mean)
se = sd(boot.statistics)
require(ggplot2)
if ( is.null(binwidth) )
binwidth = diff(range(boot.statistics))/30
p = ggplot(data.frame(x=boot.statistics),aes(x=x)) +
geom_histogram(aes(y=..density..),binwidth=binwidth) + geom_density(color="red")
plot(p)
interval = mean(x) + c(-1,1)*2*se
print( interval )
return( list(boot.statistics = boot.statistics, interval=interval, se=se, plot = p ) )}

outGA= with( data.frame(xGA), boot.mean(xGA, B=2000))
yGA<-outGA$'boot.statistics'

qqPlot(yGA)
shapiro.test(yGA)
```

**D.3. DATA BASED ON NMAS: 9.5 VS. 12.5 MM**

**D.2.1. 9.5 mm Data Set**

```
library(stats)
library(Matrix)
library(car)
x95<-matrix(c(0.48, 0.59, 0.75, 0.59, 0.59, 0.59, 0.53, 0.66, 0.48, 0.66, 0.59, 0.53, 0.8, 1.1, 0.68,
0.48, 0.59, 0.48, 0.44, 0.44, 0.44, 0.37, 0.42, 0.46, 0.53, 0.59, 0.59, 0.53, 0.41, 0.35, 0.49, 0.44,
0.37, 0.53, 0.41, 0.35), 36, 1)
x95

qqPlot(x95)
shapiro.test(x95)

boot.mean = function(x,B,binwidth=NULL) {
n = length(x)
boot.samples = matrix( sample(x,size=n*B,replace=TRUE), B, n)
boot.statistics = apply(boot.samples,1,mean)
se = sd(boot.statistics)
require(ggplot2)
if ( is.null(binwidth) )
```

```
binwidth = diff(range(boot.statistics))/30
p = ggplot(data.frame(x=boot.statistics),aes(x=x)) +
geom_histogram(aes(y=..density..),binwidth=binwidth) + geom_density(color="red")
plot(p)
interval = mean(x) + c(-1,1)*2*se
print( interval )
return( list(boot.statistics = boot.statistics, interval=interval, se=se, plot = p ) )}

out95= with( data.frame(x95), boot.mean(x95, B=2000))
y95<-out95$'boot.statistics'

qqPlot(y95)
shapiro.test(y95)
```

### D.2.2. 12.5 mm Data Set

```
library(stats)
library(Matrix)
library(car)
x125<-matrix(c(0.33, 0.36, 0.4, 0.46, 0.5, 0.5, 0.34, 0.36, 0.36, 0.79, 0.66, 0.53, 0.88, 0.96, 0.62,
0.79, 0.72, 0.53, 0.99, 0.99, 0.79, 1.32, 1.32, 1.32, 0.79, 0.99, 0.99, 0.36, 0.38, 0.4, 0.48, 0.5,
0.46, 0.38, 0.4, 0.42), 36, 1)
x125

qqPlot(x125)
shapiro.test(x125)

boot.mean = function(x,B,binwidth=NULL) {
n = length(x)
boot.samples = matrix( sample(x,size=n*B,replace=TRUE), B, n)
boot.statistics = apply(boot.samples,1,mean)
se = sd(boot.statistics)
require(ggplot2)
if ( is.null(binwidth) )
binwidth = diff(range(boot.statistics))/30
p = ggplot(data.frame(x=boot.statistics),aes(x=x)) +
geom_histogram(aes(y=..density..),binwidth=binwidth) + geom_density(color="red")
plot(p)
interval = mean(x) + c(-1,1)*2*se
print( interval )
return( list(boot.statistics = boot.statistics, interval=interval, se=se, plot = p ) )}

out125= with( data.frame(x125), boot.mean(x125, B=2000))
y125<-out125$'boot.statistics'
qqPlot(y125)
shapiro.test(y125)
```

## APPENDIX E – DAMAGED DYNAMIC MODULUS FOR PMA AC MIXES

**Table E.1. Damaged Dynamic Modulus Input Values for FL95_PMA(A) AC mix.**

| E*, psi (MPa) | Frequency (Hz) | | | | | |
|---|---|---|---|---|---|---|
| Temperature, °F (°C) | 0.1 | 0.5 | 1 | 5 | 10 | 25 |
| 14 (-10) | 1,563,932 (10,783) | 1,833,763 (12,643) | 1,940,866 (13,382) | 2,165,013 (14,927) | 2,250,583 (15,517) | 2,353,643 (16,228) |
| 40 (4) | 734,261 (5,063) | 1,013,459 (6,988) | 1,139,714 (7,858) | 1,434,022 (9,887) | 1,557,536 (10,739) | 1,714,790 (11,823) |
| 70 (21) | 173,143 (1,194) | 306,381 (2,112) | 381,526 (2,631) | 596,360 (4,112) | 704,257 (4,856) | 857,896 (5,915) |
| 100 (38) | 29,340 (202) | 58,035 (400) | 77,986 (538) | 150,498 (1,038) | 195,869 (1,350) | 271,259 (1,870) |
| 130 (54) | 8,687 (60) | 12,942 (89) | 16,249 (112) | 30,210 (208) | 40,420 (279) | 59,824 (412) |

**Table E.2. Damaged Dynamic Modulus Input Values for FL95_PMA(B) AC mix.**

| E*, psi (MPa) | Frequency (Hz) | | | | | |
|---|---|---|---|---|---|---|
| Temperature, °F (°C) | 0.1 | 0.5 | 1 | 5 | 10 | 25 |
| 14 (-10) | 1,582,348 (10,910) | 1,854,013 (12,783) | 1,961,550 (13,524) | 2,185,894 (15,071) | 2,271,233 (15,659) | 2,373,747 (16,366) |
| 40 (4) | 755,461 (5,209) | 1,038,922 (7,163) | 1,166,788 (8,045) | 1,463,952 (10,094) | 1,588,238 (10,951) | 1,746,057 (12,039) |
| 70 (21) | 187,839 (1,295) | 326,812 (2,253) | 404,708 (2,790) | 626,150 (4,317) | 736,798 (5,080) | 893,789 (6,162) |
| 100 (38) | 35,638 (246) | 67,694 (467) | 89,617 (618) | 168,065 (1,159) | 216,563 (1,493) | 296,525 (2,044) |
| 130 (54) | 11,708 (81) | 16,987 (117) | 20,987 (145) | 37,452 (258) | 49,242 (340) | 71,320 (492) |

**Table E.3. Damaged Dynamic Modulus Input Values for FL125_PMA(A) AC mix.**

| E*, psi (MPa) | Frequency (Hz) | | | | | |
|---|---|---|---|---|---|---|
| Temperature, °F (°C) | 0.1 | 0.5 | 1 | 5 | 10 | 25 |
| 14 (-10) | 1,634,910 (11,272) | 1,912,373 (13,185) | 2,021,608 (13,938) | 2,247,762 (15,498) | 2,332,983 (16,085) | 2,434,595 (16,786) |
| 40 (4) | 787,235 (5,428) | 1,076,456 (7,422) | 1,207,381 (8,325) | 1,512,126 (10,426) | 1,639,524 (11,304) | 1,800,984 (12,417) |
| 70 (21) | 210,107 (1,449) | 351,783 (2,425) | 430,597 (2,969) | 654,617 (4,513) | 766,896 (5,289) | 926,711 (6,389) |
| 100 (38) | 45,338 (313) | 82,464 (569) | 106,536 (735) | 189,203 (1,305) | 239,042 (1,648) | 320,362 (2,209) |
| 130 (54) | 12,575 (87) | 20,920 (144) | 26,530 (183) | 47,429 (327) | 61,351 (424) | 86,289 (595) |

**Table E.4. Damaged Dynamic Modulus Input Values for FL125_PMA(B) AC mix.**

| E*, psi (MPa) | Frequency (Hz) | | | | | |
|---|---|---|---|---|---|---|
| Temperature, °F (°C) | 0.1 | 0.5 | 1 | 5 | 10 | 25 |
| 14 (-10) | 1,721,246 (11,868) | 1,997,485 (13,772) | 2,104,819 (14,512) | 2,324,378 (16,026) | 2,406,139 (16,590) | 2,502,886 (17,257) |
| 40 (4) | 850,219 (5,862) | 1,154,367 (7,959) | 1,290,137 (8,895) | 1,601,612 (11,043) | 1,729,949 (11,928) | 1,891,006 (13,038) |
| 70 (21) | 228,114 (1,573) | 383,988 (2,648) | 470,175 (3,242) | 712,651 (4,914) | 832,738 (5,742) | 1,002,008 (6,909) |
| 100 (38) | 47,484 (327) | 88,195 (608) | 114,804 (792) | 206,536 (1424) | 261,824 (1,805) | 351,757 (2,425) |
| 130 (54) | 12,577 (87) | 21,376 (147) | 27,383 (189) | 50,114 (346) | 65,438 (451) | 93,073 (642) |

**Table E.5. Damaged Dynamic Modulus Input Values for GA95_PMA(A) AC mix.**

| E*, psi (MPa) | Frequency (Hz) | | | | | |
|---|---|---|---|---|---|---|
| Temperature, °F (°C) | 0.1 | 0.5 | 1 | 5 | 10 | 25 |
| 14 (-10) | 2,164,493 (14,924) | 2,393,148 (16,500) | 2,475,820 (17,070) | 2,634,595 (18,165) | 2,690,207 (18,548) | 2,753,527 (18,985) |
| 40 (4) | 1,249,033 (8,612) | 1,599,154 (11,026) | 1,742,517 (12,014) | 2,045,304 (14,102) | 2,160,409 (14,895) | 2,297,503 (15,841) |
| 70 (21) | 361,227 (2,491) | 602,299 (4,153) | 728,608 (5,024) | 1,059,231 (7,303) | 1,210,828 (8,348) | 1,412,485 (9,739) |
| 100 (38) | 66,514 (459) | 129,931 (896) | 172,375 (1188) | 318,791 (2,198) | 405,450 (2,795) | 542,646 (3,741) |
| 130 (54) | 16,846 (116) | 28,043 (193) | 36,147 (249) | 68,745 (474) | 91,747 (633) | 134,275 (926) |

**Table E.6. Damaged Dynamic Modulus Input Values for GA95_PMA(B) AC mix.**

| E*, psi (MPa) | Frequency (Hz) | | | | | |
|---|---|---|---|---|---|---|
| Temperature, °F (°C) | 0.1 | 0.5 | 1 | 5 | 10 | 25 |
| 14 (-10) | 2,247,243 (15,494) | 2,459,237 (16,956) | 2,534,953 (17,478) | 2,678,923 (18,471) | 2,728,874 (18,815) | 2,785,426 (19,205) |
| 40 (4) | 1,372,842 (9,465) | 1,719,127 (11,853) | 1,857,742 (12,809) | 2,144,960 (14,785) | 2,252,257 (15,529) | 2,378,725 (16,401) |
| 70 (21) | 437,735 (3,018) | 709,038 (4,889) | 846,348 (5,835) | 1,193,673 (8,230) | 1,348,016 (9,294) | 1,549,243 (10,682) |
| 100 (38) | 83,532 (576) | 165,116 (1,138) | 218,402 (1,506) | 395,826 (2,729) | 497,133 (3,428) | 653,139 (4,503) |
| 130 (54) | 18,525 (128) | 33,576 (231) | 44,521 (307) | 88,297 (609) | 118,757 (819) | 174,095 (1,200) |

**Table E.7. Damaged Dynamic Modulus Input Values for GA125_PMA(A) AC mix.**

| E*, psi (MPa) | Frequency (Hz) | | | | | |
|---|---|---|---|---|---|---|
| **Temperature, °F (°C)** | 0.1 | 0.5 | 1 | 5 | 10 | 25 |
| 14 (-10) | 2,207,116 (15,218) | 2,417,875 (16,671) | 2,494,652 (17,200) | 2,643,532 (18,227) | 2,696,285 (18,590) | 2,756,870 (19,008) |
| 40 (4) | 1,343,131 (9,261) | 1,670,692 (11,519) | 1,803,600 (12,435) | 2,083,717 (14,367) | 2,190,427 (15,102) | 2,318,022 (15,982) |
| 70 (21) | 441,195 (3,042) | 694,204 (4,786) | 821,325 (5,663) | 1,143,599 (7,885) | 1,288,013 (8,881) | 1,478,115 (10,191) |
| 100 (38) | 88,502 (610) | 168,666 (1,163) | 219,454 (1,513) | 384,429 (2,651) | 477,228 (3,290) | 619,459 (4,271) |
| 130 (54) | 19,052 (131) | 34,786 (240) | 45,896 (316) | 88,750 (612) | 117,661 (811) | 169,113 (1,166) |

**Table E.8. Damaged Dynamic Modulus Input Values for GA125_PMA(B) AC mix.**

| E*, psi (MPa) | Frequency (Hz) | | | | | |
|---|---|---|---|---|---|---|
| **Temperature, °F (°C)** | 0.1 | 0.5 | 1 | 5 | 10 | 25 |
| 14 (-10) | 2,247,761 (15,495) | 2,453,769 (16,918) | 2,528,275 (17,432) | 2,671,836 (18,422) | 2,722,386 (18,770) | 2,780,210 (19,169) |
| 40 (4) | 1,397,924 (9,638) | 1,727,946 (11,914) | 1,860,405 (12,827) | 2,136,796 (14,733) | 2,241,068 (15,452) | 2,364,983 (16,306) |
| 70 (21) | 473,479 (3,265) | 742,084 (5,116) | 875,492 (6,036) | 1,209,151 (8,337) | 1,356,616 (9,354) | 1,548,870 (10,679) |
| 100 (38) | 96,324 (664) | 184,607 (1,273) | 240,523 (1,658) | 420,982 (2,903) | 521,501 (3,596) | 674,118 (4,648) |
| 130 (54) | 21,386 (147) | 38,594 (266) | 50,901 (351) | 98,842 (681) | 131,336 (906) | 189,151 (1,304) |